Springer Proceedings in Physics 263

Olena Fesenko
Leonid Yatsenko *Editors*

Nanomaterials and Nanocomposites, Nanostructure Surfaces, and Their Applications

Selected Proceedings of the 8th International Conference Nanotechnology and Nanomaterials (NANO2020), 26–29 August 2020, Lviv, Ukraine

Springer

Springer Proceedings in Physics

Volume 263

Indexed by Scopus

The series Springer Proceedings in Physics, founded in 1984, is devoted to timely reports of state-of-the-art developments in physics and related sciences. Typically based on material presented at conferences, workshops and similar scientific meetings, volumes published in this series will constitute a comprehensive up-to-date source of reference on a field or subfield of relevance in contemporary physics. Proposals must include the following:

- name, place and date of the scientific meeting
- a link to the committees (local organization, international advisors etc.)
- scientific description of the meeting
- list of invited/plenary speakers
- an estimate of the planned proceedings book parameters (number of pages/articles, requested number of bulk copies, submission deadline).

Please contact:

For Americas and Europe: Dr. Zachary Evenson; zachary.evenson@springer.com
For Asia, Australia and New Zealand: Dr. Loyola DSilva; loyola.dsilva@springer.com

More information about this series at http://www.springer.com/series/361

Olena Fesenko · Leonid Yatsenko
Editors

Nanomaterials and Nanocomposites, Nanostructure Surfaces, and Their Applications

Selected Proceedings of the 8th International Conference Nanotechnology and Nanomaterials (NANO2020), 26–29 August 2020, Lviv, Ukraine

Springer

Editors
Olena Fesenko
Institute of Physics
National Academy of Sciences of Ukraine
Kyiv, Ukraine

Leonid Yatsenko
Institute of Physics
National Academy of Sciences of Ukraine
Kyiv, Ukraine

ISSN 0930-8989 ISSN 1867-4941 (electronic)
Springer Proceedings in Physics
ISBN 978-3-030-74740-4 ISBN 978-3-030-74741-1 (eBook)
https://doi.org/10.1007/978-3-030-74741-1

This Springer imprint is published by the registered company Springer Nature Switzerland AG
The registered company address is: Gewerbestrasse 11, 6330 Cham, Switzerland

Preface

This book highlights the most recent advances in nanoscience from leading researchers in Ukraine, Europe, and beyond. It features contributions from participants of the eighth international research and practice conference "Nanotechnology and Nanomaterials" (NANO-2020), held in Lviv, Ukraine, on August 26–29, 2020.

This event was organized jointly by the Institute of Physics of the National Academy of Sciences of Ukraine, Lviv Polytechnic National University (Ukraine), University of Tartu (Estonia), University of Turin (Italy), and Pierre and Marie Curie University (France). Internationally recognized experts from a wide range of universities and research institutes shared their knowledge and key results in the areas of nanocomposites and nanomaterials, nanostructured surfaces, microscopy of nano-objects, nano-optics and nanophotonics, nanoplasmonics, nanochemistry, and nanobiotechnology.

Nowadays, nanotechnology is becoming the most actively developing and promising field of science. Numerous nanotechnology investigations are already producing practical results that can be applied in various areas of human life from science and technology to medicine and pharmacology. The aim of the present book is to highlight the latest investigations from different areas of nanoscience and to stimulate new interest in this field. Volume II of this two-volume work covers such important topics as nanostructured composites, nanocrystals, magnetic and nanoporous structure, and advanced carbon nanomaterials.

This book is divided into two sections—Part I: *Nanomaterials and Nanocomposites* and Part II: *Nanostructure Surfaces*. Sections covering nanobiotechnology, nanodevices and quantum structures, and spectroscopy and nano-optics can be found in Volume I: *Nano-optics and Photonics, Nanochemistry and Nanobiotechnology, and Their Applications*.

We hope that both volumes will be equally useful and interesting for young scientists or PhD students and mature scientists alike.

Kyiv, Ukraine

Olena Fesenko
Leonid Yatsenko

Contents

Contributors

M. Androulidaki Institute of Electronic Structure & Laser (IESL) of Foundation for Research and Technology Hellas (FORTH), Heraklion, Crete, Greece

L. I. Ardanova Minnesota State University, Mankato, MN, USA

A. E. Artyukhov Department of Marketing, Sumy State University, Sumy, Ukraine

N. O. Artyukhova Department of Marketing, Sumy State University, Sumy, Ukraine

A. Yu. Badalian Sumy State University, Sumy, Ukraine

D. V. Baklan Faculty of Chemical Technology, Igor Sikorsky Kyiv Polytechnic Institute, Kyiv, Ukraine

V. F. Bashev Oles Honchar Dnipro National University, Dnipro, Ukraine

O. Yu. Boldyrieva Taras Shevchenko National University of Kyiv, Kyiv, Ukraine

V. A. Borshchak Odesa I.I. Mechnikov National University, Odesa, Ukraine

D. V. Brazhnyk Institute for Sorption and Problems of Endoecology NAS Ukraine, Kyiv, Ukraine

I. V. Brazhnyk Gimasi SA, Mendrisio, Switzerland

I. V. Brytavskyi Odessa I.I. Mechnikov National University, Odessa, Ukraine

Yu. I. Bulyga Odessa I.I. Mechnikov National University, Odessa, Ukraine

A. P. Chebanenko Odessa I.I. Mechnikov National University, Odessa, Ukraine

Xiaohong Chen Physics Department, East China Normal University, Shanghai, China

O. V. Chukova Taras Shevchenko National University of Kyiv, Kyiv, Ukraine

V. V. Datsyuk Taras Shevchenko National University of Kyiv, Kyiv, Ukraine

M. P. Derhachov Physics, Electronics and Computer Systems Department, Oles Honchar Dnipro National University, Dnipro, Ukraine

N. V. Diyuk Taras Shevchenko National University of Kyiv, Kyiv, Ukraine

O. A. Diyuk Institute for Sorption and Problems of Endoecology of National Academy of Sciences of Ukraine, Kyiv, Ukraine

V. E. Diyuk Taras Shevchenko National University of Kyiv, Kyiv, Ukraine

Volodimir Dolgoshey National Technical University of Ukraine "Igor Sikorsky Kyiv Polytechnic Institute", Kyiv, Ukraine

Yuriy Dovhopyatyy Ternopil Ivan Puluj National Technical University, Ternopil, Ukraine

P. Dulian Faculty of Chemical Engineering and Technology, Cracow University of Technology, Cracow, Poland

Yuliya Dzyazko VI Vernadskii Institute of General and Inorganic Chemistry of the National Academy of Science of Ukraine, Kyiv, Ukraine

O. M. Fesenko Institute of Physics of National Academy Sciences of Ukraine, Kyiv, Ukraine

L. M. Filevska Odessa I.I. Mechnikov National University, Odessa, Ukraine

I. I. Gab Frantsevich Institute for Problems of Materials Science of National Academy Sciences of Ukraine, Kyiv, Ukraine

E. I. Get'man Vasyl' Stus Donetsk National University, Vinnytsia, Ukraine

M. A. Glauberman Odesa I.I. Mechnikov National University, Odesa, Ukraine

V. S. Grinevych Odessa I.I. Mechnikov National University, Odessa, Ukraine

L. M. Grishchenko Taras Shevchenko National University of Kyiv, Kyiv, Ukraine

Khalil J. Hamam Applied Physics Department Faculty of Science, Tafila Technical University, Tafila, Jordan

D. O. Holochalov Physics, Electronics and Computer Systems Department, Oles Honchar Dnipro National University, Dnipro, Ukraine

V. V. Honcharov State Establishment "Lugansk State Medical University", Rubizhne, Ukraine

Iryna Ivanenko Department of Inorganic Substances Technology, Water Treatment and General Chemical Engineering of National Technical University of Ukraine, "Igor Sikorsky Kyiv Polytechnic Institute", Kyiv, Ukraine

Hanna V. Karakurkchi National Technical University «Kharkiv Polytechnic Institute», Kharkiv, Ukraine

I. Karbovnyk Ivan Franko National University of Lviv, Lviv, Ukraine

L. S. Kaykan G.V. Kurdyumov Institute for Metal Physics, Kyiv, Ukraine

O. V. Khomenko Sumy State University, Sumy, Ukraine

H. Klym Lviv Polytechnic National University, Lviv, Ukraine

Yuri Kobljanskyj Department of Radiophysics, Kyiv National Taras Shevchenko University, Kyiv, Ukraine

Oleg Kolesnyk Department of Radiophysics, Kyiv National Taras Shevchenko University, Kyiv, Ukraine

Yevhen Kolomiiets VI Vernadskii Institute of General and Inorganic Chemistry of the National Academy of Science of Ukraine, Kyiv, Ukraine

A. M. Korol National University for Food Technologies, Kyiv, Ukraine; Laboratory on Quantum Theory in Linkoping, International Society for Independent Research (ISIR), Linkoping, Sweden

Valery Korskanov Institute of Physics of the National Academy of Sciences of Ukraine, Kyiv, Ukraine

Oleksandr Kramar Ternopil Ivan Puluj National Technical University, Ternopil, Ukraine

J. Krmela Department of Numerical Methods and Computational Modeling, Alexander Dubcek University of Trencin, Puchov, Slovak Republic

V. Krmelova Department of Materials Technologies and Environment, Alexander Dubcek University of Trencin, Puchov, Slovak Republic

Kateryna Kudelko VI Vernadskii Institute of General and Inorganic Chemistry of the National Academy of Science of Ukraine, Kyiv, Ukraine

O. V. Kudryk Vinnytsia National Technical University, Vinnytsia, Ukraine

O. I. Kushnerov Oles Honchar Dnipro National University, Dnipro, Ukraine

V. M. Ledovskykh National Aviation University, Kyiv, Ukraine

Tetiana A. Len Departments of Physics, Taras Shevchenko National University of Kyiv, Kyiv, Ukraine

Ya. I. Lepikh Odesa I.I. Mechnikov National University, Odesa, Ukraine

Serhii Lesik Department of Inorganic Substances Technology, Water Treatment and General Chemical Engineering of National Technical University of Ukraine, “Igor Sikorsky Kyiv Polytechnic Institute”, Kyiv, Ukraine

S. V. Levchenko National Aviation University, Kyiv, Ukraine

O. M. Lysenko Department of Analytical Chemistry, Faculty of Chemistry, Taras Shevchenko National University of Kyiv, Kyiv, Ukraine

A. Maizelis Department of Technical Electrochemistry, National Technical University, "Kharkiv Polytechnic Institute", Kharkiv, Ukraine

Vladimir Malyshev Department of Radiophysics, Kyiv National Taras Shevchenko University, Kyiv, Ukraine

A. Manousaki Institute of Electronic Structure & Laser (IESL) of Foundation for Research and Technology Hellas (FORTH), Heraklion, Crete, Greece

Oleh D. Marinin Departments of Physics, Taras Shevchenko National University of Kyiv, Kyiv, Ukraine

Lyudmila Yu. Matzui Departments of Physics, Taras Shevchenko National University of Kyiv, Kyiv, Ukraine

J. S. Mazurenko Ivano Frankivsk National Medical University, Ivano-Frankivsk, Ukraine

N. V. Medvid National University for Food Technologies, Kyiv, Ukraine

Magdalena Medykowska Faculty of Chemistry, Department of Radiochemistry and Environmental Chemistry, Institute of Chemical Sciences, Maria Curie-Sklodowska University in Lublin, Lublin, Poland

O. V. Mischanchuk Chuiko Institute of Surface Chemistry of the National Academy of Sciences of Ukraine, Kyiv, Ukraine

V. N. Moiseyenko Physics, Electronics and Computer Systems Department, Oles Honchar Dnipro National University, Dnipro, Ukraine

O. V. Myronyuk Faculty of Chemical Technology, Igor Sikorsky Kyiv Polytechnic Institute, Kyiv, Ukraine

S. A. Nedilko Taras Shevchenko National University of Kyiv, Kyiv, Ukraine

S. G. Nedilko Taras Shevchenko National University of Kyiv, Kyiv, Ukraine

Vladimir Ogenko VI Vernadskii Institute of General and Inorganic Chemistry of the National Academy of Science of Ukraine, Kyiv, Ukraine

O. V. Ohiienko Physics, Electronics and Computer Systems Department, Oles Honchar Dnipro National University, Dnipro, Ukraine

Yu. A. Oleksii Vasyl' Stus Donetsk National University, Vinnytsia, Ukraine

Roman Ostapenko Department of Physics, Kyiv National Taras Shevchenko University, Kyiv, Ukraine

Iryna V. Ovsiienko Departments of Physics, Taras Shevchenko National University of Kyiv, Kyiv, Ukraine

A. Papadopoulos Institute of Electronic Structure & Laser (IESL) of Foundation for Research and Technology Hellas (FORTH), Heraklion, Crete, Greece

V. V. Permyakov Institute of Geological Sciences of National Academy of Sciences of Ukraine, Kyiv, Ukraine

Oleksandr Prokopenko Department of Radiophysics, Kyiv National Taras Shevchenko University, Kyiv, Ukraine

S. V. Radio Vasyl' Stus Donetsk National University, Vinnytsia, Ukraine

V. A. Raks Department of Analytical Chemistry, Faculty of Chemistry, Taras Shevchenko National University of Kyiv, Kyiv, Ukraine

Ludmila Rozhdestvenska VI Vernadskii Institute of General and Inorganic Chemistry of the National Academy of Science of Ukraine, Kyiv, Ukraine

S. I. Ryabtsev Oles Honchar Dnipro National University, Dnipro, Ukraine

O. V. Sachuk Institute for Sorption and Problems of Endoecology of National Academy of Sciences of Ukraine, Kyiv, Ukraine

N. N. Sadova Odesa I.I. Mechnikov National University, Odesa, Ukraine

Galyna V. Saenko Departments of Physics, Taras Shevchenko National University of Kyiv, Kyiv, Ukraine

Nikolay D. Sakhnenko National Technical University «Kharkiv Polytechnic Institute», Kharkiv, Ukraine

Bilal Abu Sal Applied Physics Department Faculty of Science, Tafila Technical University, Tafila, Jordan

O. V. Sanzhak Institute for Sorption and Problems of Endoecology NAS Ukraine, Kyiv, Ukraine

K. Savva Institute of Electronic Structure & Laser (IESL) of Foundation for Research and Technology Hellas (FORTH), Heraklion, Crete, Greece

Mykhailo Semenko Department of Physics, Kyiv National Taras Shevchenko University, Kyiv, Ukraine

D. B. Shakhnin University «Ukraine», Kyiv, Ukraine

S. M. Shcherbakov M.G. Kholodny Institute of Botany of the National Academy of Science of Ukraine, Kyiv, Ukraine

N. D. Shcherban L.V. Pisarzhevsky Institute of Physical Chemistry of National Academy of Sciences of Ukraine, Kyiv, Ukraine

O. Shevchenko National University for Food Technologies, Kyiv, Ukraine

V. Y. Shkola Sumy State University, Sumy, Ukraine

L. V. Shmeleva Taras Shevchenko National University of Kyiv, Kyiv, Ukraine

P. V. Sivolapov Faculty of Chemical Technology, Igor Sikorsky Kyiv Polytechnic Institute, Kyiv, Ukraine

Andrii S. Sizhuk Department of Radiophysics, Kyiv National Taras Shevchenko University, Kyiv, Ukraine

Yuriy Skorenkyy Ternopil Ivan Puluj National Technical University, Ternopil, Ukraine

V. A. Smyntyna Odessa I.I. Mechnikov National University, Odessa, Ukraine

A. I. Sokolenko National University for Food Technologies, Kyiv, Ukraine

T. V. Stetsyuk Frantsevich Institute for Problems of Materials Science of National Academy Sciences of Ukraine, Kyiv, Ukraine

E. Stratakis Institute of Electronic Structure & Laser (IESL) of Foundation for Research and Technology Hellas (FORTH), Heraklion, Crete, Greece

Zhuo Sun Physics Department, East China Normal University, Shanghai, China

A. D. Suprun Taras Shevchenko National University of Kyiv, Kyiv, Ukraine

Katarzyna Szewczuk-Karpisz Institute of Agrophysics, Polish Academy of Sciences, Lublin, Poland

G. G. Tsapyuk Taras Shevchenko National University of Kyiv, Kyiv, Ukraine

Tatiana l. Tsaregradskaya Departments of Physics, Taras Shevchenko National University of Kyiv, Kyiv, Ukraine

Tamara Tsebriinko Institute of Physics of the National Academy of Sciences of Ukraine, Kyiv, Ukraine

S. V. Vakal Scientific Research Institute of Mineral Fertilizers and Pigments, Sumy, Ukraine

V. S. Vakal Scientific Research Institute of Mineral Fertilizers and Pigments, Sumy, Ukraine

I. Vasylchyshyn Lviv Polytechnic National University, Lviv, Ukraine

Maryna V. Ved National Technical University «Kharkiv Polytechnic Institute», Kharkiv, Ukraine

T. A. Voitenko Taras Shevchenko National University of Kyiv, Kyiv, Ukraine

Lyudmila l. Vovchenko Departments of Physics, Taras Shevchenko National University of Kyiv, Kyiv, Ukraine

Yu. P. Vyshnevska National Technical University of Ukraine “Igor Sikorsky Kyiv Polytechnic Institute”, Kyiv, Ukraine

Małgorzata Wiśniewska Faculty of Chemistry, Department of Radiochemistry and Environmental Chemistry, Institute of Chemical Sciences, Maria Curie-Sklodowska University in Lublin, Lublin, Poland

G. O. Yanovska Sumy State University, Sumy, Ukraine

Andriy Yaremkevych Institute of Physics of the National Academy of Sciences of Ukraine, Kyiv, Ukraine

T. Y. Yarova Sumy State University, Sumy, Ukraine

A. V. Yatsymyrskyi Taras Shevchenko National University of Kyiv, Kyiv, Ukraine

Iryna Yu. Yermolenko National Technical University «Kharkiv Polytechnic Institute», Kharkiv, Ukraine

S. M. Yezhov Taras Shevchenko National University of Kyiv, Kyiv, Ukraine

O. V. Yushchenko Sumy State University, Sumy, Ukraine

A. N. Zaderko Taras Shevchenko National University of Kyiv, Kyiv, Ukraine

N. P. Zatovskaya Odesa I.I. Mechnikov National University, Odesa, Ukraine

V. A. Zazhigalov Institute for Sorption and Problems of Endoecology of National Academy of Sciences of Ukraine, Kyiv, Ukraine

Zhenjie Zhao Physics Department, East China Normal University, Shanghai, China

Nanomaterials and Nanocomposites

Predicting the Stability of Orthoarsenates $Lu_{1-x}Ln_xAsO_4$, Ln = Sm–Yb, Sc, Y, and $La_{1-x}Ln_xAsO_4$, Ln = Ce, Pr, Nd Solid Solutions

E. I. Get'man, Yu. A. Oleksii, O. V. Kudryk, S. V. Radio, and L. I. Ardanova

1 Prospects for the Practical Use of Solid Solutions of $Ln^{I}_{1-x}Ln^{II}_xAsO_4$, Where Ln^{I}, Ln^{II} = REEs

Orthoarsenates of rare-earth elements (REEs) in composition and crystal structure are analogs of orthophosphates and orthovanadates of REEs, which are studied as materials for lasers, light emitters, catalysts, ionic conductors, and matrices for radioactive waste [1]. REEs orthovanadates of the Ce–Lu series and REEs orthophosphates of the Gd–Lu series with zircon structure [2] activated with REEs are effective phosphors [3]. Recently, luminescent materials have been intensively studied, containing not only the matrix (the "host" of the structure) and activator ions isomorphically included in it, but also containing two or more ions of different REEs in the matrix lattice, the so-called mixed luminophores, for example, composition $Sc_{0.93-x}Ln_xVO_4:Eu^{3+}{}_{0.07}$ [3]. The luminescence intensity of $Sc_{0.93-x}Ln_xVO_4:Eu^{3+}{}_{0.07}$ with partial substitution of Sc for Y, La, Gd, or Lu can be increased by 156%, 120%, 120%, and 133%, respectively. REEs orthophosphates of the La–Dy series with monazite structure [2] are promising materials for matrices that absorb radioactive waste of actinides and lanthanides, and they are superior in radiation resistance to aluminophosphate or borosilicate glasses currently used for these purposes [4–7].

It is known that REEs orthoarsenates of the Sm–Lu series are isostructural to REEs orthovanadates of the Ce–Lu series and REEs orthophosphates of the Gd–Lu series

E. I. Get'man · Yu. A. Oleksii · S. V. Radio (✉)
Vasyl' Stus Donetsk National University, Vinnytsia 21027, Ukraine
e-mail: radio@donnu.edu.ua

O. V. Kudryk
Vinnytsia National Technical University, Vinnytsia 21000, Ukraine

L. I. Ardanova
Minnesota State University, Mankato, MN 56001, USA
e-mail: lyudmyla.stackpool@mnsu.edu

O. Fesenko and L. Yatsenko (eds.), *Nanomaterials and Nanocomposites, Nanostructure Surfaces, and Their Applications*, Springer Proceedings in Physics 263, https://doi.org/10.1007/978-3-030-74741-1_1

with zircon structure [2], which may indicate the presence of luminescent properties in them. Similarly, REEs orthoarsenates of the La–Nd series are isostructural to REEs orthophosphates of the La–Dy series with monazite structure [2], which may indicate the possibility of their use as matrices for waste immobilization. However, much less attention is paid to REEs orthoarsenates, apparently due to the toxicity of arsenic compounds. Even though they are slightly soluble in water and have relatively high thermal decomposition temperatures, a decrease in their mass is observed at temperatures higher than ~1550 K [8, 9], which is significantly higher than the decomposition temperature, for example, of As_2O_5 (~550 K) [9]. This circumstance allows them to be used as matrices for the immobilization of toxic wastes of arsenic and selenium [1, 10]. It is also known that they have ferroelectric [11] and luminescent [12] properties, which have not been practically studied. In the above cases, REEs orthoarsenates can be used in the form of solid solutions, which makes it possible to purposefully control their properties. However, as far as we know, there is practically no information in the literature on the corresponding phase diagrams of systems with the composition $Ln^{I}_{1-x}Ln^{II}_{x}AsO_4$, where Ln^{I}, Ln^{II} = REEs, which are the physicochemical basis for choosing the composition of solid solutions of orthoarsenates and the conditions for their solid-phase synthesis. Usually, there is information on individual compositions, for example, $Pr_{0.502}Nd_{0.478}As_{0.981}O_{4.039}$, $La_{0.427}Pr_{0.487}As_{0.948}O_{4.138}$, $Er_{0.493}Yb_{0.512}As_{0.989}O_{4.006}$ [9], $Nd_{0.65}Sm_{0.35}AsO_4$ [13, 14], $Nd_{0.35}Sm_{0.65}AsO_4$ [14], and $Ce_{0.47}La_{0.20}Nd_{0.18}AsO_4$ [1]. At the same time, to study the dependence of properties on the composition of a solid solution, it is necessary to know both the limits of substitutions and the thermodynamic stability of solid solutions at different temperatures, which makes it possible to avoid their decomposition during synthesis, operation, and storage. However, due to the toxicity of arsenic compounds, experimental studies are difficult, and therefore, it is rational to combine them with calculation methods, as has been done for a long time, for example, when studying isomorphous substitutions of radioactive substances with the aim of their immobilization [4].

Therefore, the work aimed to predict the limits of substitutions and stability regions of solid solutions of the composition $Lu_{1-x}Ln_xAsO_4$, Ln = Sm–Yb, Sc, Y with zircon structure, and $La_{1-x}Ln_xAsO_4$, Ln = Ce, Pr, Nd with monazite structure. The choice of these solid solutions is due to the fact that in the previously studied related orthovanadate and orthophosphate systems with zircon structure, some of the most effective luminescent and laser materials are lutetium compounds [15, 16], and solid solutions $La_{1-x}Ln_xAsO_4$, Ln = Ce, Pr, Nd with monazite structure, have been proposed as matrices for the immobilization of arsenic and selenium [10, 17].

2 Calculation Procedure and Initial Data

The main task in calculating the substitution limits of solid solutions using the Urusov's crystal energy method [18–20] is to determine the mixing energy Q (interaction parameter). In this work, we study the mutual substitution of REEs in systems, both components of which are isostructural. For this case, the mixing energy can be

represented as consisting of two contributions due to the difference in the sizes of the substituted structural units or interatomic distances in the components (Q_R) and the difference in the degrees of ionicity of the chemical bond (Q_ε):

$$Q = Q_R + Q_\varepsilon = Cmnz_m z_x(\Delta R/R_1)^2 + 1390mz_m z_x\alpha(\Delta\varepsilon)^2/(2R_1), \text{ (kJ/mol)},$$

where $C = 112.6$ kJ, a constant calculated from the equation $C = 20(2\Delta\chi + 1)$ [20] based on the difference in electronegativity χ [21] of cations and anion. The value of $\chi(AsO_4^{4-})$, as recommended [22], was accepted equal to $\chi(O^{2-}) = 3.758$.

$m = 2$—the number of formula units in the pseudobinary approximation of components;

$n = 5.3$—effective coordination number according to Batsanov [23], since in the zircon structure, the cation is surrounded by six tetrahedral arsenate anions located at two significantly different distances;

z_m, z_x—charge modulus of structural units (Ln^{3+} and AsO_4^{3-});

R—interatomic distance Cation—central atom of the oxoanion;

R_1—the smaller interatomic distance;

$\alpha = 1.723$, the reduced Madelung constant calculated by Templeton formula [24];

$\Delta\varepsilon$—the difference in the degrees of ionicity of the chemical bond in the components, calculated from the difference in the electronegativity (EN) of REEs cations and anion taken from [16]. According to [19, 20], if the difference between the EN of the substituted components is less than 0.4 or the degree of ionicity of the chemical bond is less than 0.05, the value of Q_ε will be small and can be ignored. As you can see from Tables 1 and 2, in all systems, the value of $\Delta\chi$ is significantly less than 0.4;

Table 1 Initial data and results of calculating the critical temperatures of decomposition for $Lu_{1-x}Ln_xAsO_4$, Ln = Sm–Yb, Sc, and Y solid solutions

Ln	R, Å	$\Delta R/R_1$	Q_R, J/mol	χ_{Ln}	ε_{Ln}	$\varepsilon_{Ln}-\varepsilon_{Sc}$	Q_ε, J/mol	Q, J/mol	T_{cr}, K
Sm	3.688	0.03103	10,343	1.410	0.720	0.004	58	10,444	624
Eu	3.678	0.02824	8567	1.433	0.715	0.001	4	8571	512
Gd	3.662	0.02376	6064	1.386	0.724	0.008	230	6294	376
Tb	3.652	0.02097	4723	1.410	0.720	0.004	58	4781	285
Dy	3.634	0.01594	2729	1.426	0.716	0	0	2729	163
Ho	3.629	0.01454	2271	1.433	0.715	0.001	4	2275	136
Er	3.609	0.00895	860	1.438	0.714	0.002	14	874	52
Tm	3.599	0.00615	406	1.455	0.710	0.006	130	536	32
Yb	3.587	0.00280	84	1.479	0.706	0.010	360	444	26
Lu	3.577	–	–	1.431	0.716	0	0	–	–
Sc	3.477	0.02876	8885	1.415	0.718	0.002	14	8899	530
Y	3.618	0.01146	1411	1.340	0.722	0.006	130	1541	84

Table 2 Initial data and results of calculating the critical decomposition temperatures of $La_{1-x}Ln_xAsO_4$, Ln = Ce–Nd solid solutions

Ln	V, Å^3	$\Delta R/R_1$	Q_R, J/mol	χ_{Ln}	T_{cr}, K
La	331.09	–	–	1.327	–
Ce	327.29	0.0038552	181	1.348	11
Pr	320.24	0.013515	2221	1.374	133
Nd	315.67	0.016024	3122	1.382	186

therefore, the contribution of the difference in the degrees of ionicity to the mixing energy can be ignored.

$\Delta R/R_1$—relative size difference of the substituted structural units (dimensional parameter) calculated by the distance values Ln^{3+}—AsO_4^{3-} for $Lu_{1-x}Ln_xAsO_4$ systems [25] or by cubic roots from the volumes of unit cells for $La_{1-x}Ln_xAsO_4$ systems [1, 11].

The accuracy of calculating the critical temperature according to [19] is less than 13%.

Since the size parameter values in all cases are less than 0.1 (Tables 1 and 2), according to recommendation [18–20], the critical decomposition temperatures of solid solutions were calculated in the approximation of regular solutions using the equation:

$$T_{cr} = Q/2kN,$$

where k is Boltzmann constant, N is the Avogadro number. And the decomposition temperature T_d at a given substitution limit x or the substitution limit x at the decomposition temperature is according to the Becker equation [26]:

$$-(1-2x)/\ln[x/(1-x)] = kN \times T_d/Q$$

The dependence of the decomposition temperatures of solid solutions on the composition (x) in this case will be symmetric.

3 Calculation Results for $Lu_{1-x}Ln_xAsO_4$, Ln = Sm–Yb, Sc, and Y Solid Solutions with Zircon Structure

As can be seen from the data given in Table 1, the calculated values of mixing energies and critical decomposition (stability) temperatures of solid solutions of REE orthoarsenates of the composition $Lu_{1-x}Ln_xAsO_4$ with zircon structure naturally decrease in the Sm–Yb series, which is due to a decrease in the size of substituting structural units. The mixing energy and critical temperature for the

$Lu_{1-x}Y_xAsO_4$ system are between the corresponding values for the $Lu_{1-x}Ho_xAsO_4$ and $Lu_{1-x}Er_xAsO_4$ systems, because the crystalline ionic radius Y^{3+} (1.040 Å, here and further ionic radii are given according to Shannon [27]) has a value that is intermediate between close to each other radii for Ho^{3+} (1.041 Å) and Er^{3+} (1.030 Å) ions. The mixing energy and critical temperature for the $Lu_{1-x}Sc_xAsO_4$ system are in the interval between the corresponding values for the $Lu_{1-x}Sm_xAsO_4$ and $Lu_{1-x}Eu_xAsO_4$ systems due to the fact that the dimensional parameter for the $Lu_{1-x}Sc_xAsO_4$ system (0.02876) lies between the dimensional parameters of the $Lu_{1-x}Sm_xAsO_4$ systems (0.03103) and $Lu_{1-x}Eu_xAsO_4$ (0.02824), although there is a significant difference in the sizes of the radius of the Sc^{3+} ion (0.885 Å) and the radii of the Sm^{3+} (1.098 Å) and Eu^{3+} (1.087 Å) ions. This can be explained by the fact that the ionic radius of the substituted Lu^{3+} ion (1.001 Å) is larger than the ionic radius of the Sc^{3+} ion (0.885 Å), but less than the radii of Sm^{3+} (1.098 Å) and Eu^{3+} (1.087 Å) ions by approximately the same value. As follows from the data given in Table 1, the effect of differences in the degrees of ionicity of the chemical bond in the components on the critical decomposition temperature of solid solutions can indeed be neglected since they are within the range of up to 0.01, which can lead to an error in calculating the mixing energy of 360 J/mol or decomposition temperature of about 20 K. In addition to the critical temperatures, we also calculated the decomposition temperatures of limited series of solid solutions for compositions with x equal to 0.01, 0.05, 0.10, and 0.20, and the dependence of which on the REEs numbers, as well as the dependence for $x = 0.5$, is shown in Fig. 1. It follows from the presented diagram that continuous series of solid solutions are thermodynamically stable in the temperature range above the e curve ($x = 0.5$). At lower temperatures, they can decompose, forming limited series

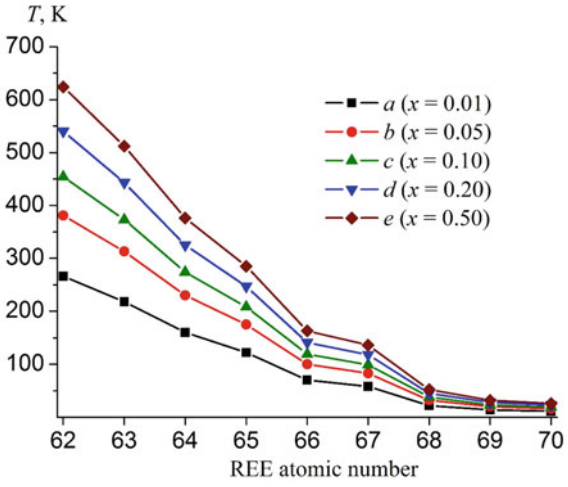

Fig. 1 Dependences of the calculated decomposition temperatures (stability temperatures) of solid solutions of REEs orthoarsenates of the composition $Lu_{1-x}Ln_xAsO_4$ with zircon structure on the REEs atomic number (diagram of the thermodynamic stability of solid solutions)

of solid solutions, if the diffusion rate is sufficient for the formation and growth of a new phase. Similarly, limited solid solutions at temperatures above *a*, *b*, *c*, and *d* curves are thermodynamically stable, and below this curve they can decompose.

Unfortunately, as far as we know, there are no data in the literature on the temperature at which the decomposition of solid solutions $Lu_{1-x}Ln_xAsO_4$ stops during cooling due to kinetic difficulties (spontaneous quenching of the samples). However, it can be assumed that it is close to the temperature at which the components interact in the solid-phase synthesis of REEs orthoarsenates. According to [9], the solid-phase reactions of $LnAsO_4$ formation end at 973 K with a calcination time of 24 h. Therefore, it can be assumed that, in solid solutions of $Lu_{1-x}Ln_xAsO_4$ systems, the transition of samples to a metastable state due to kinetic constraints upon cooling occurs at the same temperature approximately. As follows from the calculation results, in the $Lu_{1-x}Ln_xAsO_4$ systems, the critical temperatures of decomposition of solids (Table 1) are significantly lower than the possible temperature of their spontaneous quenching. Therefore, it can be assumed that continuous series of solid solutions of the composition $Lu_{1-x}Ln_xAsO_4$, Ln = Sm–Yb, Sc, and Y, are thermodynamically stable at temperatures above T_{cr}, metastable at lower temperatures, and do not decompose when cooled to temperatures down to room temperature.

4 Calculation Results for $La_{1-x}Ln_xAsO_4$, Ln = Ce, Pr, and Nd Solid Solutions with Monazite Structure

Prediction of the stability of solid solutions of systems with the composition $La_{1-x}Ln_xAsO_4$, Ln = Ce, Pr, and Nd, was carried out in connection with the fact that in [10, 17] it was proposed to immobilize selenate, selenite, arsenate, and arsenite oxoanions using lanthanum oxide with the addition of one more oxide from among CeO_2, Nd_2O_3, or Pr_6O_{11}. As a result of the interaction of oxoanions with the above oxides, orthoarsenates of lanthanum and second lanthanide (Ce, Pr, Nd, or solid solutions based on them) should be formed, which in the crystalline state can be matrices for immobilizing not only arsenic and selenium compounds but also, possibly, radioactive waste of REEs and actinides. The calculation was carried out without taking into account the effect of differences in the degrees of ionicity of the chemical bond in the components on the mixing energy due to the proximity of the EN of ions La^{3+} (1.327), Ce^{3+} (1.348), Pr^{3+}(1.374), and Nd^{3+} (1.382) [21].

As can be seen from the presented results (Table 2), the values of the mixing energies and the critical decomposition temperatures of solid solutions increase with an increase in the REEs number in the series Ce, Pr, and Nd, which is due to a decrease in the ionic radii and a corresponding increase in the difference in the sizes of La^{3+} and REEs ions. However, such critical temperatures, due to the closeness of the sizes of La^{3+} (1.172 Å) ion with the sizes of Ce^{3+} (1.150 Å), Pr^{3+} (1.130 Å), and Nd^{3+} (1.123 Å) ions [27], are so small (11–186 K) that they are not can lead to the decomposition of solid solutions at lower temperatures due to difficulties of a

kinetic nature and continuous series of solid solutions will be stable over the entire temperature range. Above critical temperatures, continuous series of solid solutions are stable, and below critical temperatures, they are metastable.

As far as we know, there is no information in the literature on the experimentally found mixing energies, substitution limits, and thermodynamic stability of solid solutions in REEs orthoarsenate systems. This does not allow comparing the calculation results with experimental data. At the same time, polymorphic transitions in solid solutions of the $Tb_xY_{1-x}AsO_4$ and $Tb_xTm_{1-x}AsO_4$ systems were studied earlier [28, 29]. It was found that in the $Tb_xY_{1-x}AsO_4$ system, the transition temperature from the tetragonal to the rhombic modification regularly increases from 5.8 to 27.3 K when x changes from 0.32 to 1, and in the $Tb_xTm_{1-x}AsO_4$ system, when x changes from 0 to 1, it increases from 6.1 up to 25.5 K [28, 29], which indicates in the first case about a wide range and in the second about the presence of unlimited miscibility at temperatures of about 30 K. It follows from these experimental results that in the $Tb_xTm_{1-x}AsO_4$ system, the critical decomposition temperature of solid solutions is less than 30 K. In the $Tb_xY_{1-x}AsO_4$ system, it should be even lower, since the sizes of the crystal ionic radii (for the coordination number 8) of Tb (1.18 Å) and Y (1.159 Å) differ to a lesser extent than Tb (1.18 Å) and Tm (1.134 Å) [27].

Therefore, we also performed calculations for the $Tb_xY_{1-x}AsO_4$ and $Tb_xTm_{1-x}AsO_4$ systems. The results obtained on the critical decomposition temperatures in these systems (56 and 139 K, respectively [30]) considering the accuracy of the calculation method (13%) agree with the literature data [28, 29].

5 Conclusions

The crystal-chemical approach in the approximation of regular solutions was used to calculate the mixing energies and critical decomposition (stability) temperatures of solid solutions in the $Lu_{1-x}Ln_xAsO_4$, Ln = Sm–Yb, Sc, and Y, systems with zircon structure and $La_{1-x}Ln_xAsO_4$, Ln = Ce, Pr, and Nd, systems with monazite structure. For systems $Lu_{1-x}Ln_xAsO_4$, Ln = Sm–Yb with REEs atomic number increasing calculated mixing energy and critical temperature of decomposition of solid solutions evidently decrease, which is caused by the decrease in REEs ionic radii. In the $La_{1-x}Ln_xAsO_4$, Ln = Ce–Nd systems, they increase for the same reason. The differences in the degrees of ionicity of the chemical bond in the components of the systems are small and practically do not affect the calculation results. The mixing energy and critical temperature for the $Lu_{1-x}Y_xAsO_4$ system are in the interval between the corresponding values for the $Lu_{1-x}Ho_xAsO_4$ and $Lu_{1-x}Er_xAsO_4$ systems and for the $Lu_{1-x}Sc_xAsO_4$ system—in the interval between the corresponding values for the $Lu_{1-x}Sm_xAsO_4$ and $Lu_{1-x}Eu_xAsO_4$ systems. The obtained diagram of thermodynamic stability allows one to evaluate the stability of $Lu_{1-x}Ln_xAsO_4$ solid solutions in a wide range of compositions and temperatures.

Also, the critical decomposition temperatures (56 and 139 K) in related systems $Tb_{1-x}Ln_xAsO_4$, Ln = Y, and Tm, were calculated, which within the accuracy of the calculation method (13%) agree with the previously obtained experimental results for these systems.

Acknowledgements This study was carried out within the Fundamental Research Programme funded by the Ministry of Education and Science of Ukraine (grants ID 0119U100025 and 0120U102059).

References

1. Clavier N, Podor R, Dacheux N (2011) Crystal chemistry of the monazite structure. J Eur Ceram Soc 31:941–976
2. Boatner LA (2002) Synthesis, structure, and properties of monazite, pretulite, and xenotime. Rev Mineral Geochem 48:87–121
3. Ye X, Wu D, Yang M, Li Q, Huang X, Yang Y, Nie H (2014) luminescence properties of fine-grained $ScVO_4:Eu^{3+}$ and $Sc_{0.93-x}Ln_xVO_4:Eu^{3+}{}_{0.07}$ (Ln = Y, La, Gd, Lu) phosphors. ECS J Solid State Sci Technol 3:R95–R99
4. Grechanovsky AE, Eremin NN, Urusov VS (2013) Radiation resistance of $LaPO_4$ (monazite structure) and $YbPO_4$ (zircon structure) from data of computer simulation. Phys Solid State 55:1929–1935
5. Schlenz H, Heuser J, Neumann A, Schmitz S, Bosbach D (2013) Monazite as a suitable actinide waste form. Z Kristallogr-Cryst Mater 228:113–123
6. Meldrum A, Boatner LA, Wang LM, Ewing RC (1997) Ion-beam-induced amorphization of $LaPO_4$, and $ScPO_4$. Nucl Instrum Method B 127–128:160–165
7. Meldrum A, Boatner LA, Ewing RC (2000) A comparison of radiation effects in crystalline ABO_4-type phosphates and silicates. Mineral Mag 64:185–194
8. Bondar IA, Vinogradova NV, Demyanets LN, Yezhova ZhA, Ilyukhin VV, Kara-Ushanov VYu, Komissarova LN (1983) Soyedineniya redkozemel'nykh elementov. Silikaty, germanaty, fosfaty, arsenaty, vanadaty [Compounds of rare earth elements. silicates, germanates, phosphates, arsenates, vanadates]. Nauka, Moscow, 288 p. (in Russian)
9. Schmidt M, Muller U, Gil RC, Milke E, Binnewies M (2005) Chemical vapour transport and crystal structure of rare-earth arsenates (V). Z Anorg Allg Chem 631:1154–1162
10. Harck JF, Wilkis S, Winters I (2004) Composition and process for removing arsenic and selenium from aqueous solution: U.S. patent US 6800204 B2. Int. Cl. C02F 1/28. Date of patent: 5 Oct 2004; prior publication: 21 Aug 2003
11. Ismailzade IH, Alekberov AI, Ismailov RM, Asadova RK, TsD G, YeM N (1980) Ferroelectricity in the crystals $RAsO_4$ (R = Pr, Nd, Eu, Gd, Tb, Dy, Er, Yb). Ferroelectrics 23:35–38
12. Samarium-doped scandium arsenate luminescent film, electroluminescent device containing samarium-doped scandium arsenate luminescent film and their preparation methods: China patent CN 104673306 A. Int. Cl. C09K 11/78 (2006.01), H01L 33/50 (2010.01). Priority date: 27 Nov 2013; publication: 03 June 2015. (in Chinese)
13. Kolitsch U, Holtstam D (2004) Crystal chemistry of $REEXO_4$ compounds (X = P, As, V). II. Review of $REEXO_4$ compounds and their stability fields. Eur J Mineral 16:117–126
14. Feigelson RS (1967) Crystal growth of rare-earth orthoarsenates. J Am Ceram Soc 50:433–434
15. Zagumennyi AI, Popov PA, Zerouk F, Zavartsev YuD, Kutovoi SA, Shcherbakov IA (2008) Heat conduction of laser vanadate crystals. Quantum Electron 38:227–232
16. Yu HH, Zhang HJ, Wang ZP, Wang JY, Yu YG, Cheng XF, Shao ZS, Jiang MH (2007) Characterization of mixed Nd: $Lu_xGd_{1-x}VO_4$ laser crystals. J Appl Phys 101:113109

17. Burba J, Hassler C, Pascoe J, Wright B, Whitehead C, Lupo J, O'Kelley CB, Cable R (2010) Target material removal using rare earth metals: U.S. patent US 2010/0155330 A1. Int. Cl. C02F 1/42, C09K 3/00 (2006.01). Publication: 24 June 2010
18. Urusov VS (1975) Energetic theory of miscibility gaps in mineral solid solutions. Fortschr Mineral 52:141–150
19. Urusov VS (1977) Teoriia izomorfnoi smesimosti (Theory of isomorphous miscibility). Nauka, Moscow, 251 p (in Russian)
20. Urusov VS, Tauson VL, Akimov VV (1997) Geokhimiya tverdogo tela [Geochemistry of solid state]. GEOS, Moscow, 500 p. (in Russian)
21. Li K, Xue D (2006) Estimation of electronegativity values of elements in different valence states. J Phys Chem A 110(39):11332–11337
22. Batsanov SS (1968) The concept of electronegativity. Conclusions and prospects. Russ Chem Rev 37(5):332–351
23. Batsanov SS (1977) Ob effektivnom koordinatsionnom chisle atomov v kristallakh [About the effective coordination number of atoms in crystals]. Zhurn Neorgan Khimii 22:1155–1159 (in Russian)
24. Templeton DH (1953) Madelung constants and coordination. J Chem Phys 21:2097–2098
25. Get'man EI (1985) Izomorfnye zameshcheniia v volframatnyh i molybdatnyh sistemah [Isomorphous substitutions in tungstate and molybdate systems]. Nauka, Novosibirsk, 214 p. (in Russian)
26. Becker R (1937) Über den Aufbau binarer Legierungen. Z Metallkunde 29:245–249
27. Shannon RD (1976) Revised effective ionic radii and systematic studies of interatomic distances in halides and chalcogenides. Acta Cryst A32:751–767
28. Schwab M (1978) Phase transition in the mixed crystals $Tb_pY_{1-p}AsO_4$. Phys Status Solidi B 86:195–203
29. Kasten A, Kahle HG, Klöfer P, Schäfer-Siebert D (1987) Specific heat experiments at the cooperative Jahn-Teller transition in the mixed crystal systems $(Tb_xTm_{1-x})AsO_4$ and $(Tb_xTm_{1-x})VO_4$. Phys Status Solidi B 144:423–436
30. Get'man EI, Oleksii YuA, Radio SV (2020) Predicting the stability of orthoarsenates $Sc_{1-x}Ln_xAsO_4$ and $Tb_xLn_{1-x}AsO_4$ solid solutions. Nanosistemi, Nanomateriali, Nanotehnologii (in press)

Novel Silica-Based Material with Nano-functional Groups for Analytical Application

V. A. Raks, O. V. Myronyuk, D. V. Baklan, O. M. Lysenko, and P. V. Sivolapov

Acronyms

TGA Thermogravimetric analysis (change of remaining mass fraction with temperature),
DTG Derivative thermogravimetric (−dm/dt),
DTA Change in temperature (temp./mg),
SPE Solid-phase extraction.

1 Introduction

Free radicals damage the cell membrane in the human body, causing much pathology such as atherosclerosis, diabetes, rheumatism, inflammation, diseases of the musculoskeletal system and eyes, premature aging and cancer [1, 2]. To prevent such harmful influence of the radicals, it is recommended to use healthy food, beverage or to take medicines/supplements with health-promoting phytochemicals such as *myo*-inositol and inositol derivatives [3, 4]. Most of these compounds are present in some fruits and herbs and honey. Herbs with their structural and stereochemical complexity provide an alternate source of medicinal phytochemicals for drugs development. The study of herbs as phytochemicals source for drug development is likely richly rewarding. Analysis of publications on use of drugs based on *myo*-inositol (Myo-In)

V. A. Raks (✉) · O. M. Lysenko
Department of Analytical Chemistry, Faculty of Chemistry, Taras Shevchenko National University of Kyiv, Volodymyrska 64, Kyiv 01033, Ukraine

O. V. Myronyuk · D. V. Baklan · P. V. Sivolapov
Faculty of Chemical Technology, Igor Sikorsky Kyiv Polytechnic Institute, Peremohy Ave, 37, Kyiv 03056, Ukraine

O. Fesenko and L. Yatsenko (eds.), *Nanomaterials and Nanocomposites, Nanostructure Surfaces, and Their Applications*, Springer Proceedings in Physics 263, https://doi.org/10.1007/978-3-030-74741-1_2

shows that it has significant effects on the functioning of cells, tissue and the whole body [5]. The primary function of Myo-In and its derivatives is their involvement in intracellular signal transmission and in the functioning of such important as receptors of insulin [6], catecholamine [7] and metabotropic neurotransmitter [8] receptors. Most inositol-dependent proteins with known functions are involved in the support of vital functions of the cardiovascular system [9], immune system [10] and in the structure of connective tissue [11]. The role of Myo-In in maintaining the functioning of the central nervous system [12, 13], *myo*-inositol hexaphosphate in functioning of kidneys [14] and pinitol in a protective effect against chemically induced liver damage [15] is no less important. Taking into account the interaction of inositol derivatives with specific proteins active in the reproductive system and embryonic development [16], the application of Myo-In in obstetric practice shows prospects. Furthermore, Myo-In- and InDrs-containing herbs are also enriched with health-promoting phytochemicals with antioxidant properties [17, 18]. Polyphenolic compounds (PCs), such as myricetin, luteolin-7-O-glucoside, p-coumaric acid, ferulic acid and resveratrol, behave as antioxidants, and they are found with Myo-In and its derivatives in the same herbs, for example, Alfalfa (*Medicago sativa L.*) [17, 19–21]. Glycyrrhiza glabra [22] and fagopyrum esculentum [23] are also rich for Myo-In and PCs.

Isolation of myo-I and InDrs from plant matrices, their separation from other components in extracts as well as their analysis, is of great interest in several fields, such as pharmaceutical and food industries, biochemistry, medical cell biology and biotechnology research. These examples underline the need for research and development of isolation strategies for phytochemicals.

Isolation and separation of phytochemicals are complicated by the chemical nature of the matrix, properties of individual or combined components and the method of sample analysis. Solvent extraction [24, 25], solid-phase extraction (SPE) [26–28] or supercritical fluid extraction (SFE) [29–31] are traditionally widely used to isolate phytochemicals from plants prior their chromatographic analysis. However, these approaches only allow isolation using costly and multi-step, time-consuming procedures. Because of the different biological activity of phytochemicals stereoisomers, there is a strong demand for their selective isolation from herbs.

The most important and challenging step faced by researchers in the study of complex natural compounds is the need for thorough pre-cleaning of plant extracts before analysis. During extraction and purification, significant loss of these compounds occurs, and their deactivation can be observed. K. Pyrzynska et al. [32] have described application of four different solid-phase extraction approaches for pre-concentration of phenolic compounds. As it can be seen, the C18 SPE cartridge is not optimal. For most of the selected phenolic compounds, extraction to solid phase is less than 50%. By contrast, ion-exchange phases (XAD-2) are more effective with extraction efficiencies of 60–100%. The authors explain this effect through π-π interactions between the aromatic structure of the polymeric XAD-2 phase and the phenols. However, XAD-2 has a major disadvantage—it has a polymeric support—which results in very slow adsorption kinetics that are unacceptable for unstable, easily oxidized compounds such as polyphenolic one is.

State-of-the-art analytical techniques generally used for these tasks are HPLC–MS [26, 33] and GC–MS [34], but, because of low selectivity for the complex plant matrices, HPLC–MS and GC–MS analyses require substantial sample preparation. Until now no acceptable universal approach for sample preparation has been proposed.

The aim of work was to develop novel silica-based solid-phase extraction (SPE) cartridges to extract, separate and purify myo-inositol from herbs. Developed materials have been surface modified with a range of hydrophobicities/hidrophilicities to give selective recovery of individual classes of natural compounds. Surface modification with different functional groups might tune selectivity of component recovery. The work comprised the application of known methodologies for chemical synthesis of novel SPE-phases. Surfactants with amphiphilic nature would provide the best functionality for targeted extraction of phytochemicals. Hence, initial extraction agents included surfactants Triton X-100, Brij® C10 and Brij® S10. The SPEs cartridges are organosilica composites made from a bifunctional immobilized layer comprising a major fraction of hydrophilic diol groups and minor fraction of the amphiphilic long-chain nonionic surfactant.

2 Materials and Methods

2.1 Materials

(3-(2,3-Epoxypropoxy)-propyl)-trimethoxysilane, Triton X-100, Brij C10 and Brij S10 (all reagent grade), toluene anhydrous (99.8%) and isopropanol, silica (high-purity grade, 150 Å) were purchased from Sigma-Aldrich and used without purification.

2.2 Silanization Procedures

Macroporous silica (silica gel, pore size 150 Å, 200–425 mesh, high-purity grade, Sigma-Aldrich) was calcined in a vacuum oven at 120 °C for 24 h. It was carried out in a four-necked reactor equipped with a mechanical stirrer and a condenser. The reactor was heated by immersing it in a thermostated oil bath. Subsequently, 13.59 mmol (4 mL) of (3-(2,3-epoxypropoxy)-propyl)-trimethoxysilane was added to 30 g silica in 100 mL toluene. The resulting suspension was stirred at reflux for 10 h under nitrogen (to prevent possible hydrolysis of epoxy groups). The solid phase was separated by filtration and washed with toluene (48 h in a Soxhlet apparatus). The Epoxy-SiO_2 prepared in such a manner was dried at 100 °C in vacuum. 3.22 mmol of modifiers (Triton X-100, Brij C10, Brij S10) was added to 10 g Epoxy-SiO_2 in 40 mL toluene, and the mixture was heated at 110 °C for 10 h. The solid phase was

filtered and washed with isopropanol in a Soxhlet apparatus for 48 h and drying in an oven at 110 °C.

The concentration of grafted groups was determined by differential thermal analysis and C, H elemental analysis. Functionalized supports were denoted using the abbreviation of the corresponding grafted functional groups. Epoxypropoxypropyl is denoted as Epoxy-SiO_2. Surfactant-containing silicas with grafted groups of Triton X-100, Brij C10, Brij S10 are denoted as TX-SiO_2, Brij C10-SiO_2 and Brij S10-SiO_2, respectively.

2.3 Methods

2.3.1 Fourier Transform Infrared Spectroscopy

Fourier transform infrared spectroscopy (FT-IR) spectra were recorded using a **FT-IR** microscope—hyperion 1000/2000 from Bruker optics spectrophotometer in order to determine functional groups on the silica surface after its modification. Each spectrum scan was recorded at a resolution of 8 cm^{-1}. FT-IR spectra in the wavenumber range from 400 to 4000 cm^{-1} were recorded without KBr in powder.

2.3.2 Differential Thermal Analysis

Thermal behavior of silica samples was investigated in the temperature range of 20–800 °C using a SDT 2960 derivatograph (simultaneous DSC-TGA, firmy TA Instruments). Analysis was conducted employing a linear heating rate of 10 °C/min in an air flow.

The concentration of functional groups on the surface of epoxypropoxypropyl silica (Epoxy-SiO_2) was calculated from thermogravimetric data using Eq. (1):

$$C_L(\text{mol} \cdot \text{g}^{-1}) = \frac{\Delta m}{M_r \cdot g} \tag{1}$$

where Δm is mass loss (g) of modified silica in the temperature range 200–800 °C, corresponding to thermal decomposition of organic fragments; M_r is the formula molecular weight of the 2,3-epoxypropoxypropyl group (115 g·mol^{-1}); g is a mass of modified silica (g). Concentrations of polyoxyethylated isooctylphenolic groups, polyethylene glycol octadecyl ether and polyethylene glycol hexadecyl ether groups covalently linked to the surface of TX-SiO_2, Brij C10-SiO_2 and Brij S10-SiO_2 accordingly were calculated using the same equation, where Δm is the difference between mass loss of TX-SiO_2/Brij C10-SiO_2/Brij S10-SiO_2 and Epoxy-SiO_2, and Mr is average formula molecular weight of Triton X-100 (for n = 10), Brij C10 and Brij S10.

2.4 LC Instruments and Chromatographic Conditions

LC analysis was performed on Agilent Technologies S 1260 Infinity Series system equipped with LC-1260 quaternary gradient pump, 380 evaporative light scattering detector. Separation was achieved on an Obelisc N column (15 × 4.6 mm, 5 μm, SIELC Technologies) maintained at 25 °C with a mobile phase flow rate of 0.6 mL min^{-1}. The mobile phase contained acetonitrile (ACN) and water. Isocratic elution was employed at 77% ACN and 23% 10 Mm ammonium formate in water (pH = 3.0). Injection volume was 20 μL. The detection of analytes was carried out by evaporative light scattering detection which detects all non-volatile solutes after light dispersion on analyte particles and hence is useful in quantitative determination of non-chromophoric compounds. The drift tube and evaporator temperatures were set at 30 and 90 °C, respectively, and nebulizing gas (N_2) flow rate was 2.0 SLM. Samples for calibration curve were prepared in a mixture of H_2O and ACN solvents as a ratio of 40–60%.

2.5 Adsorption Studies of SPE-Phases

The adsorption capacity of SPE-phases was studied in static conditions. 250 mg of SPE-phases was mixed with 25 mL of 50 mg·L^{-1} solution of Myo-In at pH range from 2 to 8 and shaken during fixed time interval (60 min). The solution was analyzed for Myo-In contents by HPLC.

Ground leaves of *M. Sativa L.* (20 g, May 2019) were stirred with distilled water (100 mL) twice for 3 h in a conical flask (250 mL). The total filtrates were combined and evaporated to 10 mL. The remaining extract (1 mL) was pre-cleaned and deionized on columns linked in series. The first was C18 (cartridge J. T. Baker) followed by H_2O-Phobic SA-DVB. Then, extract was concentrated on Triton-SiO_2, and extract was eluted with ACN (100%) and diluted with water (40%), and such prepared sample was analyzed. Activation of SPE cartridges was conducted with methanol (4 mL), then with water (2 mL). The extract was filtered through a 0.45 μm millipore membrane, and an aliquot of 20 μL was used for LC analysis.

2.6 Calibration Curves, Limits of Detection and Quantification

Stock solution was prepared by taking 5 mg of Myo-In in 5 mL of analysis solvent. The stock solution was diluted to six appropriate concentrations, and 20 μL of each solution was injected six times for the construction of calibration curves. The LOD and LOQ under the present chromatographic conditions were determined at signal-to-noise ratio (S/N) of 3 and 10, respectively.

3 Results and Discussion

3.1 Immobilization of Surfactants

The anhydrous synthetic path to Epoxy-SiO_2 involves grafting (3-(2,3-epoxypropoxy)-propyl)-trimethoxysilane in a media of non-polar solvent–toluene (Fig. 1). Immobilization of surfactants with alkyl and aromatic groups onto the silica surface was achieved by a two-step synthetic path using epoxy-silica. M. K. Abderrezak et al. have described the reaction of Epoxy-SiO_2 with amines and alcohols, resulting in the immobilization of the latter on the surface [35]. Our assumption was that polyoxyethylated surfactans with different variety of alkyl and aromatic incorporated fragments could also react with Epoxy-SiO_2, forming silica-based SPEs according to Figs. 2, 3 and 4.

Surfactants immobilization was monitored using 13C NMR. C-1 and C-2 appear upfield from the others as they are surrounded by the silicium atom and the carbon atom (C-3), while their electronegativities are lower than for the oxygen atom (Fig. 5). An electronegative atom such as oxygen moves a peak further downfield. Therefore, the chemical shifts of C-4 and C-3 are higher than those of C-5 and C-6. Thus, C-4 and C-3 appear downfield from C-5 and C-6 because of the nature of oxirane ring. The chemical shift of C-1 is at 7.7 ppm. The unshared pairs on the oxirane oxygen make it a Bronsted base, which can be protonated. This makes ring opening even easier.

After immobilization of Triton X-100 to the surface of Epoxy-SiO_2, four small peaks are recorded. Molecule of Triton X-100 has four different types of aromatic carbons, so four different peaks between 100 and 160 ppm can be observed (Fig. 6). It is difficult to distinguish $–CH_2–$ groups in such long chains using solid phase NMR. They are all in the area of a wide peak with a maximum at 71.41 ppm. The signals at 29.6 ppm fall in the aliphatic region and belong to the $–CH_3$ carbon. Quaternary carbons usually give sharper signals than other carbons and usually give weaker signals. Therefore, the signal at 38.1 and 35 ppm is assigned to C-13 and C-17. New small peak appeared near 65 ppm that can be related to the carbon atom of $–CH_2–$ (b)

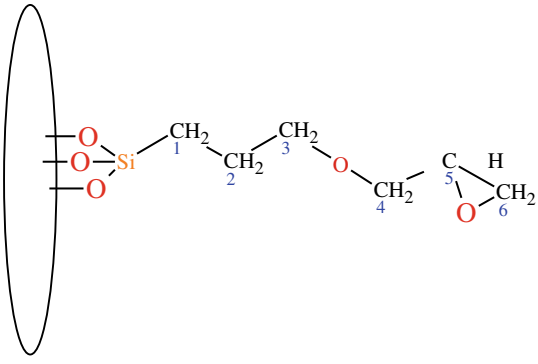

Fig. 1 Silica surface of epoxy-SiO_2

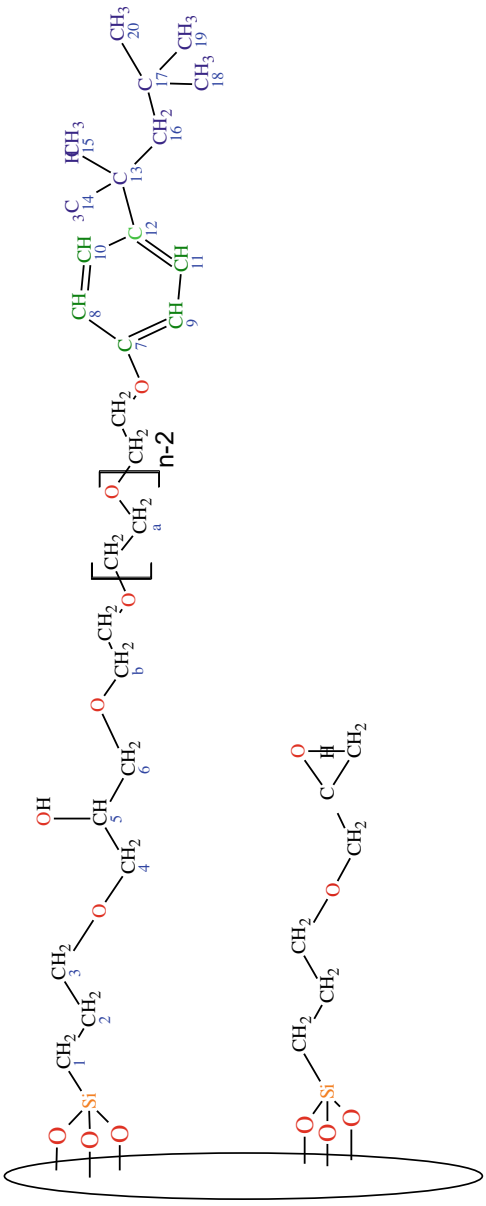

Fig. 2 Silica surface of TX-SiO_2

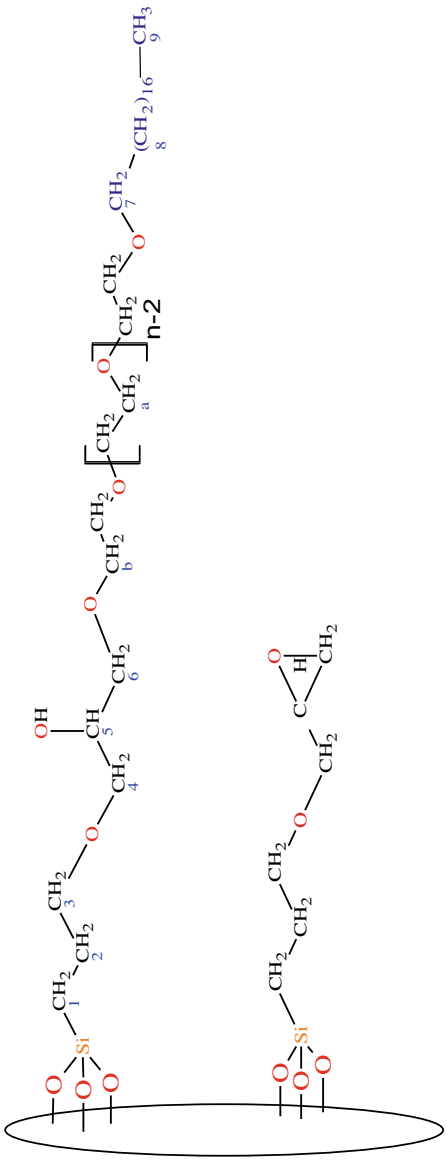

Fig. 3 Silica surface of Brij$S10$-SiO_2

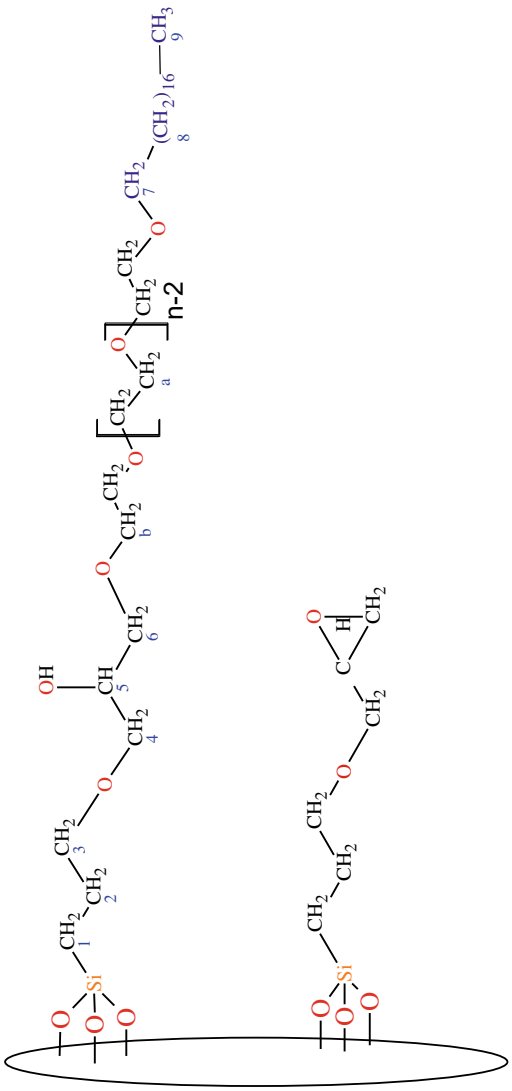

Fig. 4 Silica surface of BrijS10-SiO_2

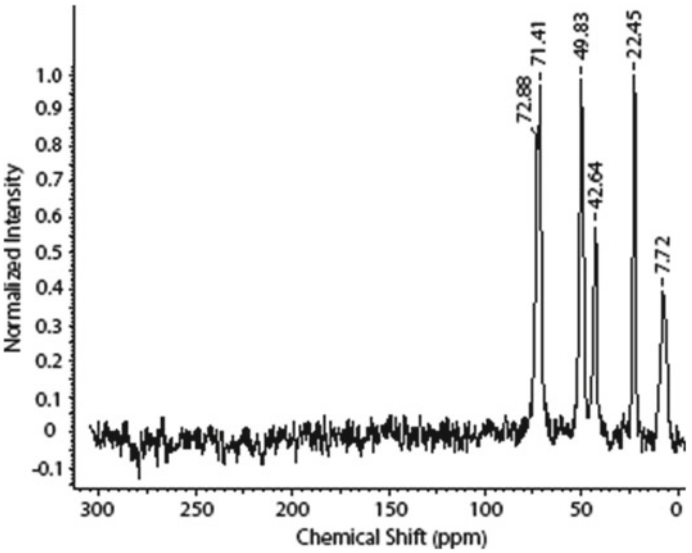

Fig. 5 13C NMR of Epoxy-SiO_2: δ72.8 (C-3), 71.4 (C-4), 49.8 (C-5), 42.6 (C-6), 22.4 (C-2), 7.7 (C-1)

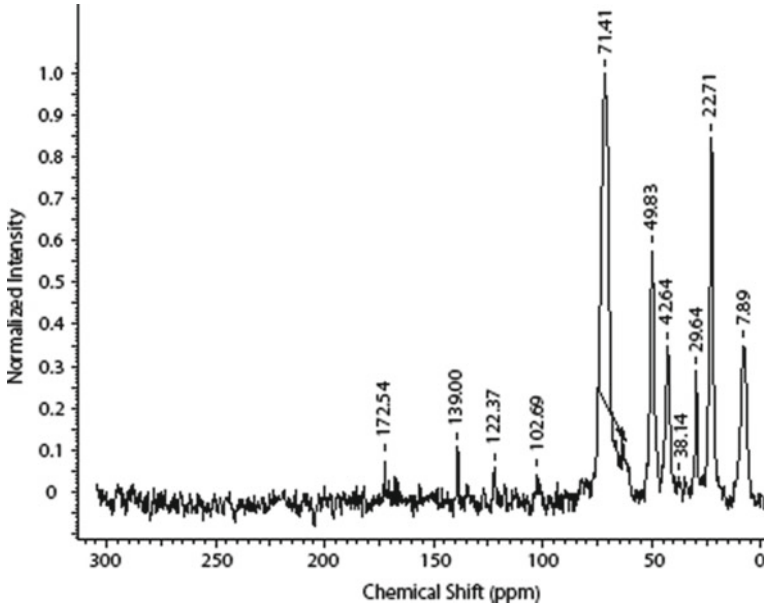

Fig. 6 13C NMR of TX-SiO_2: δ172.5 (C-7), 138.9 (C-12), 122.3 (C-10,11), 102.6 (C-8,9), 71.4 (C-4, C-16, C-a,), 49.8 (C-5), 42.6 (C-6), 38.1 (C-13), 35 (C-17), 29.629 (C-14,15, 18, 19, 20), 22.71 (C-2), 7.8 (C-1)

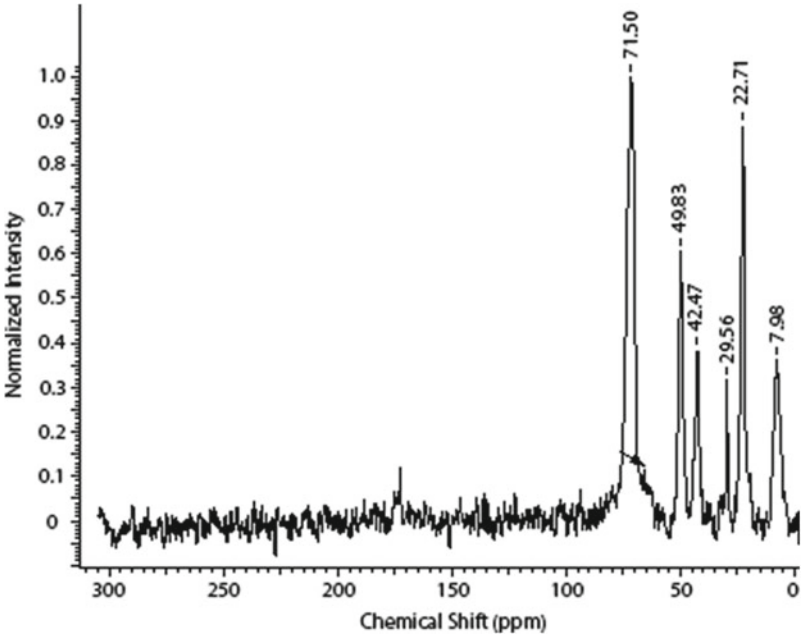

Fig. 7 13C NMR of Brij S10-SiO_2: δ71.5 (C-4, C-3, C-7, C-8, c-a), 49.8 (C-5), 42.4 (C-6), 29.5 (C-9), 22.5 (C-2), 7.9 (C-1)

group as a result of formation new bond C–O–C. This signal appeared also in spectra of Brij C10-SiO_2 and Brij S10-SiO_2.

^{13}C NMR spectra of Brij S10-SiO_2 exhibits an additional peak at 29.5 ppm corresponding to the –CH3 groups (Fig. 7). Alkyl –CH_2– groups are all in the area of a wide peak with a maximum at 71.5 ppm.

^{13}C NMR spectra of Brij C10-SiO_2 and Brij S10-SiO_2 are almost identical with slight changes in shift of the carbon atom C-9 at 30.4 ppm (Fig. 8).

3.2 Fourier Transform Infrared (FTIR) Spectroscopy

Surfactants immobilization was monitored using Fourier transform infrared (FTIR) spectroscopy. FTIR spectroscopic data provide evidence for the immobilization of (3-(2,3-epoxypropoxy)-propyl)-trimethoxysilane (Fig. 1). Alkane C-H stretching absorption just below 3000 cm^{-1} demonstrates the presence of saturated carbons. Absorption bands occur in the FTIR spectrum of Epoxy-SiO_2 that are characteristic of the stretching and deformation vibrations of alkyl fragments [36]: ν(C–H) assym at 2947 (CH_3), ν(C–H) sym at 2876 (CH_3), ν(C–H) sym (CH_2) at 2850 cm^{-1} and δ(C–H) at 1460 cm^{-1}. Symmetrical CH_3 banding band at 1380 cm^{-1} is visible in spectrum of TX-SiO_2. These groups belong to grafted molecules of surfactants, and

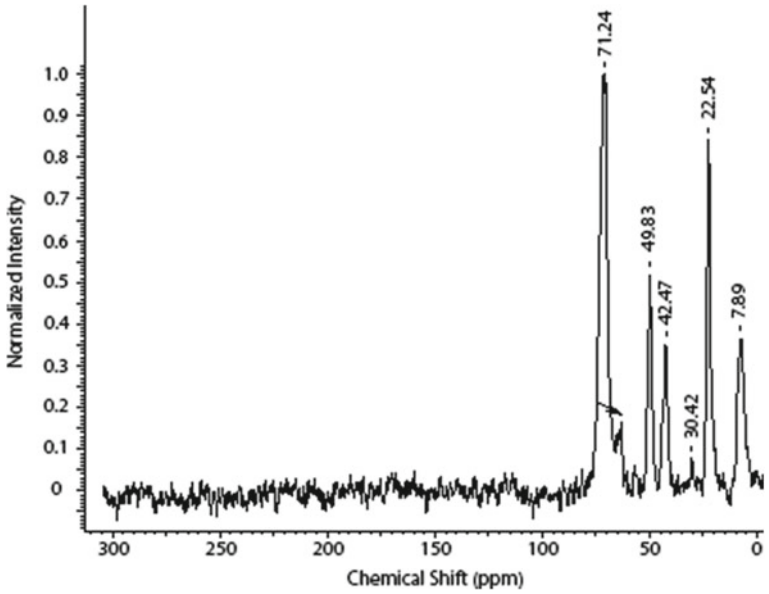

Fig. 8 13C NMR of Brij C10-SiO_2: δ71.2 (C-4, C-3, C-7, C-8, c-a), 49.8 (C-5), 42.4 (C-6), 30.4 (C-9), 22.6 (C-2), 7.8 (C-1)

this peak is not visible in spectrum of Epoxy-SiO_2. Absorption band at 1513 cm^{-1} occurs in the FTIR spectrum of TX-SiO_2 comparing to Epoxy-SiO_2. The intensity of vibrations of alkyl fragments (ν(C–H)) increases in the FTIR spectrum of TX-SiO_2. Bands with a maximum at 1513 cm^{-1} are characteristic of stretching vibrations of aromatic rings ν(–C = C–), which confirms that the TX-SiO_2 synthesis proceeded according to Fig. 2.

3.3 Differential Thermal Analysis (DTA)

Under oxygen flow, curves of TGA-DTG-DTA show thermal decomposition of unmodified silica. There are two clearly visible phases in a temperature range from 25 to 800 °C. Weight loss in the first phase begins at 25 °C. First phase shows a 4.07% decline of the TGA thermal curve from 25 to 120 °C, while there is a maximum on the DTG curve at 46 °C, and endothermic effect is visible on the DTA curve. In this phase, physically adsorbed water is eliminated. Dehydration process occurs through cleavage of hydrogen bonds between molecules of water and silanol groups of the silica surface and thus elimination of molecules of water. Second phase, in a temperature range from 120 to 700 °C, is characterized by lowest rate of change on the weight loss curve that has a 2.22% decline. It corresponds to 1.306 mmol OH-silanols per 1 g of SiO_2 (0.022/17 = 1.306 mmol). Heating of silica gel above 200 °C decreases

its mass as a result of dehydroxylation of vicinal silanols forming strained siloxane bonds. Therefore, desorption of chemically adsorbed water is kinetically slow. The DTA thermal curve shows an exothermal effect of dehydroxilation process with a maximum at 252 °C. Total loss of water in the entire temperature range is 6.29%. Effect of modification of the silica surface gives three phases of transformation its surface: from 25 to 120 °C, from 206 to 290 °C and from 290 to 700 °C.

TGA-DTG-DTA curves of synthesized Epoxy-SiO_2, TX-SiO_2, Brij C10-SiO_2 and Brij S10-SiO_2 have another behavior. First phase exhibits a 1.02, 1.30, 1.13, 1.33% decline on the TGA thermal curve from 25 to 120 °C for synthesized Epoxy-SiO_2, TX-SiO_2, Brij C10-SiO_2 and Brij S10-SiO_2, respectively. Therefore, weight loss of physically adsorbed water for synthesized SPE-phases is about three times less than for a sample of unmodified silica. It might be attributed to the amphiphilic nature of modified silicas, which show higher hydrophobicity because of incorporated alkyl and aryl-fragment compared to the nature of unmodified silica (4.07%). There are no peaks on DTG thermal curves, and there are typical endothermic peaks on DTA thermal curves for all synthesized SPE-phases in the first phase when compared to unmodified silica. Second phase is observed for all SPE-phases and characterized with a 6.34% weight loss for the Epoxy-SiO_2 and 6.83% weight loss for Brij S10-SiO_2, which occurs between 214.76 and 292.14 °C on the TGA curve, which is also reflected by DTA and DTG peaks with a specific exothermal effect of decoupling of organic groups from the silica surface. There are sharp and clear visible bands with maxima at 247.15 °C, 265.58 °C, 233.96 °C, 240.34 °C on thermal curves of Epoxy-SiO_2, TX-SiO_2, Brij C10-SiO_2 and Brij S10-SiO_2, respectively. Those peaks are not visible on thermal curves of unmodified silica. Obviously that weight loss is related to decomposition of the organic layer of modified silicas. The weight loss temperature range for the second thermal phase of all the SPE-phases is precisely indicated in the figures. It is interesting that flash points of modifiers: (3-(2,3-epoxypropoxy)-propyl)-trimethoxysilane (110 °C), Triton X-100 [37] (251 °C), Brij S10 (100 °C), Brij C10 (150 °C) are near the area of inflection points of DTA thermal curves. In our case, process of decoupling of bonds through which modifiers are grafted to the silica surface is shifted to higher temperatures. For instance, the weight loss for Epoxy-SiO_2 starts at 212 °C, while the flash point is 110 °C. However, the thermal stability of such phases is not very high: up to around 200 °C, a temperature suitable for SPE conditions. Third phase of the DTA curves for SPE-phases starts at 290–315 °C. Estimating a temperature interval from 200 to 700 °C for Epoxy-SiO_2: 883.0 μmol g^{-1} of functional groups is calculated from Eq. 1. Heating the SPE-phases above 300 °C decreases their masses as a result of further decomposition of modifiers and as well as due to condensation of vicinal hydroxyl groups, leaving strained siloxane groups as in the case of silica gel.

This third phase is characterized by a 3.57, 5.22, 3.93 and 4.79% decline of the TGA thermal curve from 290 to 700 °C for Epoxy-SiO_2, TX-SiO_2, Brij S10-SiO_2 and Brij C10-SiO_2, respectively. The decline is more clearly visible for TGA curves of SPE-phases when compared to that of SiO_2. DTA curves do not display a wide band of exothermal effects when comparing to unmodified silica.

Table 1 Concentration of targeted functional groups on the surface of SPEs

SPEs	$C_{epoxy\ groups}$, μmol g^{-1}	C_L, μmol g^{-1}
Epoxy-SiO_2	883.0	883.0
TX-SiO_2	854.2	28.8
Brij S10-SiO_2	874.0	9
Brij C10-SiO_2	857.8	25.2

First thermal phase of SPE-phases is characterized by a low rate of change on the weight loss curve, and it is kinetically the slowest. Second thermal phase of SPE-phases is characterized by a fast rate of change and thus fast chemical transformation of grafted molecules within it. Third phase is kinetically moderate.

Values of the concentration of targeted groups grafted to the silica surface estimated from the value of thermogravimetric data in the temperature range of 200–700 °C are given below (Table 1).

3.4 Elemental Analysis

According to elemental analysis, the content of carbon atoms comprising the SPE-phases varies from 5.741 to 6.858% of carbon for Epoxy-SiO_2 and TX-SiO_2, respectively (Table 2). Epoxy-SiO_2 was synthesized at the first step of modification, and other SPE-phases were synthesized at the second step of modification. Content of carbon atoms (C^2, %) in covalently linked polyoxyethylated isooctylphenolic groups, polyethylene glycol octadecyl ether and polyethylene glycol hexadecyl ether groups to the silica surface (column 3 in Table 2) is the difference between total content of carbon atoms (C^1, %) for TX-SiO_2/Brij S10-SiO_2/Brij C10-SiO_2 phases and content of carbon atoms for Epoxy-SiO_2. Content of targeted groups (C_L, %) was calculated using Eq. 2:

$$\frac{C, \%}{C, \%} = \frac{A \cdot n(C)}{M} \tag{2}$$

Table 2 Concentration of targeted functional groups on the surface of SPEs estimated from the value of elemental analysis

SPEs	C^1, %	C^2, %	C_L, %	m_L, mg on a gram of SPE	M, mg m mol^{-1}	C_L, μmol g^{-1}
Epoxy-SiO_2	5.741	5.741	9.16	91.6	115	797
TX-SiO_2	6.858	1.117	1.711	17.11	625	27.4
Brij S10-SiO_2	6.705	0.964	1.503	15.03	711	21.1
Brij C10-SiO_2	6.701	0.960	1.517	15.17	683	22.2

C^1—Total content of carbon atoms, %
C^2—Content of carbon atoms in targeted groups: Epoxy/Triton X-100/Brij S10/Brij C10, %

where C, % is content of carbon atoms in SPE-phases, A—atomic mass of carbon atom, $n(C)$—number of carbon atoms in targeted groups, M is the molecular weight of targeted groups: 2,3-epoxypropoxypropyl group (115 mg $mmol^{-1}$); polyoxyethylated isooctylphenolic groups (625 mg $mmol^{-1}$), polyethylene glycol octadecyl ether (711 mg $mmol^{-1}$) and polyethylene glycol hexadecyl ether groups (683 mg $mmol^{-1}$). Concentrations of targeted groups on the SPE-phases vary from 21.1 to 27.4 $\mu mol\ g^{-1}$ for grafted molecules of Triton X-100, Brij S10 and Brij C10. At the same time, concentration of 2,3-epoxypropoxypropyl group is much higher (797 $\mu mol\ g^{-1}$). Values of the concentration of targeted groups calculated from elemental analysis (Table 2) are well-correlated to those of thermogravimetric data. For example, according to TGA and elemental analysis, data transformation of silanol groups to 2,3-epoxypropoxypropyl groups reaches up 67.61% and 61.02%, respectively. Slightly higher value for TGA is related to condensation of residual vicinal hydroxyl groups in the same temperature interval.

3.5 Determination of Myo-Inositol in Medicago Sativa L.

The developed method for determination of Myo-In using ELSD was validated for linearity, precision, accuracy, limits of detection (LODs) and quantification (LOQs) according to Reference [38]. A calibration curve showed good linear regression ($R^2 = 0.993$). The LODs (S/N = 3) and LOQs (S/N = 10) for Myo-In were 1.27 and 5.59 μg per column, respectively. In the studied conditions, the calibration graph (i.e., correlation between log (S) and log (m)) appeared perfectly linear in 15–200 mg L^{-1} Myo-In concentration range; the line equation is

$$y = 1.43x + 3.12$$

The precision results showed the low values of intra- and inter-day % RSD of retention times and peak areas (<1%). Therefore, the developed method is precise, accurate for determination of Myo-In in herb extracts.

In this work, SPE-phases, containing polyoxyethylated groups covalently linked to the surface, are proposed as sorbents, capable of the extraction of Myo-In from water solutions. The proposed SPE-phases are amphiphilic as they contain both hydrophilic (oxyethyl and diol) and hydrophobic (isooctylphenol or alkyl) groups on the surface. The amphiphilicity of the proposed SPE's surface may increase the selectivity of its interaction with Myo-In and reduce nonspecific sorption of hydrophobic organic compounds from matrix. Surprisingly, the Myo-In adsorbs on SPE-phases in noticeable amount under the selected conditions (pH 2); total adsorption capacity did not exceed 2.65 mg g^{-1}. Adsorption of Myo-In on SPE-phases was studied at the range of pH values from 2 to 8.0. Optimal recovery of Myo-In was achieved at pH 2, and thus, all the procedure was conducted at this pH value. Such a specificity of

Table 3 Recovery of Myo-In using SPE-phases

SPE-phases	Myo-In added, μg mL^{-1}	Mean recovery, %	RSD, %
TX-SiO_2	50	53	2.4
Brij C10-SiO_2	50	51	3.6
Brij S10-SiO_2	50	50	2.0

SPE-phases to Myo-In can be explained by binding accelerated through interactions between the functional groups of modifiers, such as hydroxyl groups and polar groups of Myo-In, the additional forces being dipole–dipole interactions (O-fragments of Triton X-100 and Brijs ligands) and slight disperse interactions (between alkyl fragments of molecules of Myo-In and alkyl fragments of Triton X-100 and Brijs ligands) which also play some part in the binding.

Values of recoveries (see Table 3) of SPE-phases to Myo-In enable their application for pre-concentration of Myo-In and structured-liked compounds from water samples.

Subsequently, extract of ground leaves of *M. Sativa L.* was analyzed using developed methods with Triton-SiO_2 (Fig. 9), and 2.6 g of Myo-In per 1 kg was found in herb leaves.

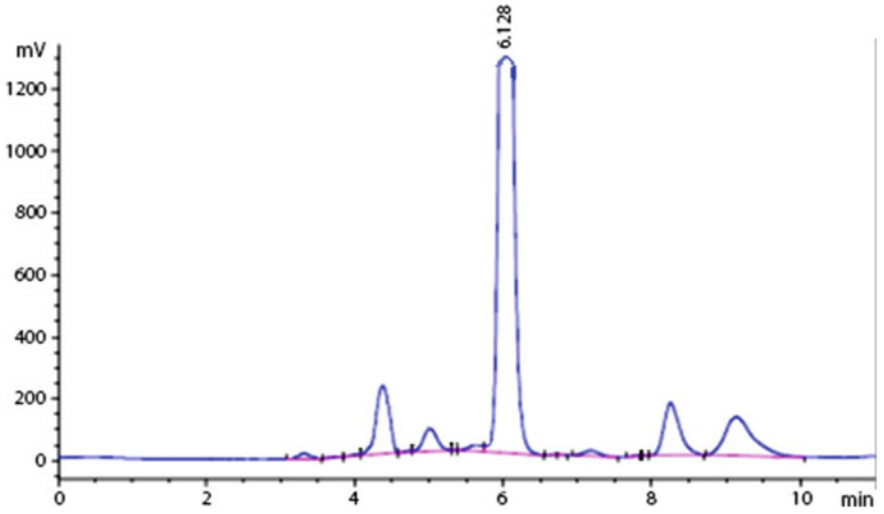

Fig. 9 LC chromatogram of extract from leaves of *M. Sativa L*

4 Conclusion

A surface-assemblage starting with silica gel was used to prepare grafted (3-(2,3-epoxypropoxy)-propyl), polyoxyethylated isooctylphenolic, polyethylene glycol octadecyl ether and polyethylene glycol hexadecyl ether groups. According to differential thermal analysis data, the grafted layer of silica-based SPE cartridges is stable in O_2 flow up to 200 °C. Its decomposition begins on exposure to O_2 at 210–300 °C. Silica-based SPE cartridges with satisfactory densities (20–30 μmol g^{-1}) are thermally stable and can contribute to the materials, desirable for analytical application.

Resulted SPE cartridges can adsorb Myo-In from water solution. 0.25 g of the adsorbent can remove Myo-In (up to 53%) from 25 mL of water under static conditions. Adsorbed Myo-In can be easily eluted with acetonitrile for further analysis or quantitative determination on the phase of adsorbent by HPLC. The sensitivity of developed SPE procedure is sufficient for analysis of myo-inositol in water extract at the level of 1.27 μg of Myo-In per column.

References

1. Ambigaipalan P, de Camargo AC, Shahidi F (2017) Identification of phenolic antioxidants and bioactives of pomegranate seeds following juice extraction using HPLC-DAD-ESI-MSn. Food Chem 221:1883–1894. https://doi.org/10.1016/j.foodchem.2016.10.058
2. Ahmad SR, Gokulakrishnan P, Giriprasad R, Yatoo MA (2015) Fruit-based natural antioxidants in meat and meat products: a review. Crit Rev Food Sci Nutr 55(11):1503–1513. https://doi.org/10.1080/10408398.2012.701674
3. Parazzini F (2014) Resveratrol, inositol, vitamin D and K in the prevention of cardiovascular and osteoporotic risk: a novel approach in peri- and postmenopause. Minerva Ginecol 66(5):513–518. http://www.ncbi.nlm.nih.gov/pubmed/25245999.
4. Celentano C, Matarrelli B, Mattei PA, Pavone G, Vitacolonna E, Liberati M (2016) Myo-Inositol supplementation to prevent gestational diabetes mellitus. Curr Diab Rep 16(3):30. https://doi.org/10.1007/s11892-016-0726-6
5. Gill BD, Indyk HE, Woollard DC (2016) Current methods for the analysis of selected novel nutrients in infant formulas and adult nutritionals. J AOAC Int 99(1):30–41. https://doi.org/10.5740/jaoacint.15-0247
6. Bizzarri M, Fuso A, Dinicola S, Cucina A, Bevilacqua A (2016) Pharmacodynamics and pharmacokinetics of inositol(s) in health and disease. Expert Opin Drug Metab Toxicol 12(10):1181–1196. https://doi.org/10.1080/17425255.2016.1206887
7. Sasakawa N, Ohara-Imaizumi M, Fukuda M, Kabayama H, Mikoshiba K, Kumakura K (2011) Dissociation of inositol polyphosphates from the C2B domain of synaptotagmin facilitates spontaneous release of catecholamines in adrenal chromaffin cells. A suggestive evidence of a fusion clamp by synaptotagmin. Neuropharmacology 60(7–8):1364–1370. https://doi.org/10.1016/j.neuropharm.2011.03.005
8. Vadnal R, Parthasarathy L, Parthasarathy R (1997) Role of inositol in the treatment of psychiatric disorders. CNS Drugs 7(1):6–16. https://doi.org/10.2165/00023210-199707010-00002
9. Salehpour S, Nazari L, Hoseini S, Saharkhiz N, Ghazi F, Sohrabi MR (2016) A potential therapeutic role of myoinositol in the metabolic and cardiovascular profile of PCOS Iranian

women aged between 30 and 40 years. Int J Endocrinol. 2016:1–5. https://doi.org/10.1155/2016/7493147
10. Wu J, Tang C, Yao S et al (2015) Anti-inflammatory inositol derivatives from the whole plant of *Inula cappa*. J Nat Prod 78(10):2332–2338. https://doi.org/10.1021/acs.jnatprod.5b00135
11. Bole GG, Castor CW (1964) Characterization of lipid constituents of human "fibroblasts" cultivated in vitro. Exp Biol Med 115(1):174–179. https://doi.org/10.3181/00379727-115-28862
12. Qureshi NA, Al-Bedah (May 2013) Mood disorders and complementary and alternative medicine: a literature review. Neuropsychiatr Dis Treat 639. https://doi.org/10.2147/NDT.S43419.
13. Thomas MP, Mills SJ, Potter BVL (2016) The "other" inositols and their phosphates: synthesis, biology, and medicine (with recent advances in myo-inositol chemistry). Angew Chemie Int Ed 55(5):1614–1650. https://doi.org/10.1002/anie.201502227
14. Sanchis P, Buades JM, Berga F et al (2016) Protective effect of myo-inositol hexaphosphate (phytate) on abdominal aortic calcification in patients with chronic kidney disease. J Ren Nutr 26(4):226–236. https://doi.org/10.1053/j.jrn.2016.01.010
15. Magielse J, Arcoraci T, Breynaert A et al (2013) Antihepatotoxic activity of a quantified desmodium adscendens decoction and d-pinitol against chemically-induced liver damage in rats. J Ethnopharmacol 146(1):250–256. https://doi.org/10.1016/j.jep.2012.12.039
16. Tsui MM, York JD (2010) Roles of inositol phosphates and inositol pyrophosphates in development, cell signaling and nuclear processes. Adv Enzyme Regul 50(1):324–337. https://doi.org/10.1016/j.advenzreg.2009.12.002
17. Oh M-M, Rajashekar CB (2009) Antioxidant content of edible sprouts: effects of environmental shocks. J Sci Food Agric 89(13):2221–2227. https://doi.org/10.1002/jsfa.3711
18. Silva LR, Pereira MJ, Azevedo J et al (2013) Glycine max (L.) Merr *Vigna radiata L.* and *Medicago sativa L.* sprouts: a natural source of bioactive compounds. Food Res Int 50(1):167–175. https://doi.org/10.1016/j.foodres.2012.10.025
19. Hipskind JD, Paiva NL (2000) Constitutive accumulation of a resveratrol-glucoside in transgenic alfalfa increases resistance to phoma medicaginis. Mol Plant-Microbe Interact 13(5):551–562. https://doi.org/10.1094/MPMI.2000.13.5.551
20. Horbowicz M, Obendorf RL, McKersie BD, Viands DR (1995) Soluble saccharides and cyclitols in alfalfa (*Medicago sativa L.*) somatic embryos, leaflets, and mature seeds. Plant Sci. https://doi.org/10.1016/0168-9452(95)04155-N
21. Raks V, Al-Suod H, Buszewski B (2018) Isolation, separation, and preconcentration of biologically active compounds from plant matrices by extraction techniques. Chromatographia 81:189–202. https://doi.org/10.1007/s10337-017-3405-0)
22. Biondi DM, Rocco C, Ruberto G (2005) Dihydrostilbene derivatives from Glycyrrhiza g labra leaves. J Nat Prod 68(7):1099–1102. https://doi.org/10.1021/np050034q
23. Gui W, Lemley BA, Keresztes I, Condo AM, Steadman KJ, Obendorf RL (2013) Purification and molecular structure of digalactosyl myo-inositol (DGMI), trigalactosyl myo-inositol (TGMI), and fagopyritol B3 from common buckwheat seeds by NMR. Carbohydr Res 380:130–136. https://doi.org/10.1016/j.carres.2013.08.004
24. Rodríguez-Sánchez S, Ruiz-Matute AI, Alañón ME et al (2010) Analysis of cyclitols in different Quercus species by gas chromatography-mass spectrometry. J Sci Food Agric 90(10):1735–1738. https://doi.org/10.1002/jsfa.4009
25. Duquesnoy E, Castola V, Casanova J (2008) Identification and quantitative determination of carbohydrates in ethanolic extracts of two conifers using 13C NMR spectroscopy. Carbohydr Res 343(5):893–902. https://doi.org/10.1016/j.carres.2008.01.001
26. Rougemont B, Fonbonne C, Lemoine J, Bourgeaux V, Salvador A (2016) Liquid chromatography coupled to tandem mass spectrometry for the analysis of inositol hexaphosphate after solid-phase extraction. J Liq Chromatogr Relat Technol 39(8):408–414. https://doi.org/10.1080/10826076.2016.1169427
27. Zhang J, Chu C-J, Li X-L et al (2014) Isolation and identification of antioxidant compounds in Vaccinium bracteatum Thunb. by UHPLC-Q-TOF LC/MS and their kidney damage protection. J Funct Foods 11:62–70. https://doi.org/10.1016/j.jff.2014.09.005

28. Buszewski B, Szultka M (2012) Past, present, and future of solid phase extraction: a review. Crit Rev Anal Chem 42(3):198–213. https://doi.org/10.1080/07373937.2011.645413
29. Talmaciu AI, Volf I, Popa VI (2015) A Comparative Analysis of the "Green" Techniques Applied for Polyphenols Extraction from Bioresources. Chem Biodivers 12(11):1635–1651. https://doi.org/10.1002/cbdv.201400415
30. Cháfer A, Berna A (2014) Study of kinetics of the d-pinitol extraction from carob pods using supercritical CO_2. J Supercrit Fluids 94:212–215. https://doi.org/10.1016/j.supflu.2014.07.015
31. Liu J, Lin S, Wang Z et al (2011) Supercritical fluid extraction of flavonoids from Maydis stigma and its nitrite-scavenging ability. Food Bioprod Process 89(4):333–339. https://doi.org/10.1016/j.fbp.2010.08.004
32. Pyrzynska K, Biesaga M (2009) Analysis of phenolic acids and flavonoids in honey. TrAC Trends Anal Chem 28(7):893–902. https://doi.org/10.1016/j.trac.2009.03.015
33. Mirnaghi FS, Mousavi F, Rocha SM, Pawliszyn J (2013) Automated determination of phenolic compounds in wine, berry, and grape samples using 96-blade solid phase microextraction system coupled with liquid chromatography–tandem mass spectrometry. J Chromatogr A 1276:12–19. https://doi.org/10.1016/j.chroma.2012.12.043
34. Katona Z, Sass P, Molnár-Perl I (1999) Simultaneous determination of sugars, sugar alcohols, acids and amino acids in apricots by gas chromatography–mass spectrometry. J Chromatogr A 847(1–2):91–102. https://doi.org/10.1016/S0021-9673(99)00333-7
35. Shibata M, Enjoji M, Sakazume K, Ifuku S (2016) Bio-based epoxy/chitin nanofiber composites cured with amine-type hardeners containing chitosan. Carbohydr Polym 144:89–97. https://doi.org/10.1016/j.carbpol.2016.02.033
36. Renuga S, Karthikesan M, Muthu S (2014) FTIR and Raman spectra, electronic spectra and normal coordinate analysis of N, N-dimethyl-3-phenyl-3-pyridin-2-yl-propan-1-amine by DFT method. Spectrochim Acta Part A Mol Biomol Spectrosc 127:439–453. https://doi.org/10.1016/j.saa.2014.02.068
37. Kellogg TF (1982) A water-miscible, nonhazardous liquid scintillation cocktail. Anal Biochem. 120(2):414–419. http://www.ncbi.nlm.nih.gov/pubmed/7091667
38. Eurachem guide: the fitness for purpose of analytical methods—a laboratory guide to method validation and related topics (2014) 2nd edn, ISBN 978-91-87461-59-0

FINEMET Micro-ribbons: The Experimental Identification of the Object

Yuri Kobljanskyj, Andrii S. Sizhuk, Mykhailo Semenko, Roman Ostapenko, Zhenjie Zhao, Zhuo Sun, Xiaohong Chen, Oleg Kolesnyk, Vladimir Malyshev, and Oleksandr Prokopenko

1 Introduction

The study of the specific susceptibility dependent on temperature, the X-ray structural analysis, the ferromagnetic resonance spectrums in the field of super high frequency, and the mechanical vibrations in the soft magnetic materials can provide us with the deeper understanding of the distribution of magnetization, collective spin excitations, etc.

In this work, we pretended to conduct a comprehensive analysis in defining the physical properties of FINEMET (FeCuNbSiB) micro-ribbons, allowing the determination of the application in magnetic and electrical mini-devices. The analysis of the chemical elements, the micro-ribbons are made of, is discussed in order to confirm the stated by the vendor formula for the composition. The experimental data for the specific susceptibility dependent on temperature, the X-ray fluorescent spectroscopy, the X-ray structural analysis, the ferromagnetic resonance spectrums in the field of super high frequency, the amplitude–frequency characteristics in the rectangular resonator in one-mode regime, the complex impedance as the function of frequency of the applied voltage, and the mechanical vibrations in the soft magnetic materials are presented.

Nanocrystalline alloys produced by the partial crystallization of FeCuNbSiB amorphous alloys are one of the best known soft magnetic alloys [1–4]. These alloys possess excellent permeability while maintaining a relatively high saturation magnetization, low coercivity, high electrical resistivity, high Curie temperatures, and low energy losses. All of the mentioned properties make the material suitable candidates

Y. Kobljanskyj · A. S. Sizhuk (✉) · O. Kolesnyk · V. Malyshev · O. Prokopenko
Department of Radiophysics, Kyiv National Taras Shevchenko University, Acad. Glushkova Avenue 4-g, Kyiv 03022, Ukraine
e-mail: cannabiss@univ.kiev.ua

M. Semenko · R. Ostapenko
Department of Physics, Kyiv National Taras Shevchenko University, Acad. Glushkova Avenue 4, Kyiv 03022, Ukraine

Z. Zhao · Z. Sun · X. Chen
Physics Department, East China Normal University, Shanghai 200062, China

O. Fesenko and L. Yatsenko (eds.), *Nanomaterials and Nanocomposites, Nanostructure Surfaces, and Their Applications*, Springer Proceedings in Physics 263, https://doi.org/10.1007/978-3-030-74741-1_3

for most industrial and technological applications [4–6]. Being one of the pioneers of soft nanocrystalline alloys, a lot of research has been done on the FeCuNbSiB alloy most of which is geared toward tailoring the properties to suit a specific application (see, for example, [7–11]). Some of the methods, used to tailor these properties, are annealing, that is microstructural modification process [12, 13], and addition of other alloying elements, such as Co, Ni, Mo, Zr, Ta, and Cr.

Ever since the FINEMET alloy material, represented by $Fe_{73.5}Cu_1Nb_3Si_{13.5}B_9$, was prepared by amorphous crystallization by Yoshizawa et al. (see [3]), its excellent comprehensive soft magnetic properties and giant magneto-impedance effect [6–14] have received great attentions from the scientific community. The special structure and excellent magnetic properties of FINEMET alloy are closely related to the five components of the alloy. The influences of Cu and Nb components on the structure and performance of the alloy are the subjects of research interest, since they are not only important in theory but also practical for material performance improvement and new technique development . It has been done a lot of research on the microstructure of the nanocrystal by X-ray diffraction, transmission electron microscope, Mössbauer spectrum, positron annihilation, etc.

The amorphous alloy Fe-Si-B can get grain organization of 0.1-μm after crystallization, while Fe-Si-B-Cu and Fe-Si-B-Nb cannot get homogeneous crystallization phase with big volumetric factor. A large amount of works indicates that the alloy of $Fe_{73.5}Cu_1Nb_3Si_{13.5}B_9$ can get homogeneous nanocrystalline structure with α–Fe(Si) phase, relevant with the coactions of Cu and Nb and that the best magnetic property can be achieved by annealing the $Fe_{73.5}Cu_1Nb_3Si_{13.5}B_9$ amorphous ribbon at $(540 \pm 10)\,^{\circ}C$ for 1 h. Corresponding to these notable magnetic properties, microstructure is represented by the nanocrystalline grain of α-Fe(Si) with DO3 type and typical grain size of 10–15 nm embedded in the amorphous matrix.

Based on the experiment, in which α-Fe(Si) nanocrystal can be generated by adding Cu into the amorphous ribbon of Fe-Si-B-Nb during annealing, Yoshizawa et al. [3] claimed the following principled idea on the crystallization mechanism of amorphous alloy Fe-Si-B-Cu-Nb. The Fe-rich, Cu-rich, and Nb-rich areas are created in alloy organization during annealing, and the alloy crystallization starts at Fe-rich area for its lower crystallization temperature. The growth of α-Fe(Si) grain is inhibited by the higher crystallization temperature in Cu-rich area and Nb-rich area around α-Fe(Si) grain.

Now, amorphous and nanocrystalline materials work effectively in the frequency range up to several megahertz (transformers, chokes, and sensors). However, related magnetic materials, such as permalloy ($Ni_{80}Fe_{20}$), are also used in the microwave range, in particular in the manufacture of structured nano-objects [15, 16]. Further investigations of amorphous and nanostructured materials, including structural, magnetic, mechanical properties, as well as resonance properties by radio-spectroscopic methods, are required to advance into the high-frequency range [17]. The comprehensive studies of the dependence of the specific susceptibility on the temperature, the Cu K X-ray diffraction patterns, the ferromagnetic resonance spectrums, and the resonant mechanical vibrations for the amorphous and nanocrystalline micro-

Table 1 Report of elemental analysis. X-ray fluorescent spectroscopy. Commercial spectrometer produced by Elvatech. It is not sensible for the element B. Annealed sample

At. N.	El.	Ser.	Intensity	Concentr. (%)
14	Si	K	75,093	7.9213 ± 0.0586
15	P	K	1133	0.0795 ± 0.0279
24	Cr	K	1326	0.0411 ± 0.0165
25	Mn	K	3271	0.1380 ± 0.0129
26	Fe	K	2,713,483	85.9121 ± 0.0580
28	Ni	K	550	0.0401 ± 0.0113
29	Cu	K	31,096	1.6004 ± 0.0195
41	Nb	K	242,092	2.8777 ± 0.0125
42	Mo	K	112,365	1.3898 ± 0.0092

ribbons, claimed by a provider to correspond to $Fe_{73.5}Cu_1Nb_3Si_{13.5}B_9$, are presented in this paper.

In the next section, we start with the investigation of the possibility of determining the elementary composition by widely used techniques.

The investigation is provided for the stated by a vendor composition $Fe_{73.5}Cu_1Nb_3Si_{13.5}B_9$. Some amorphous micro-ribbons underwent annealing at about 540 °C. The samples have the surface roughness within 100 nm, while their thickness and width are about 20 μm and 0.5 mm, accordingly.

2 Experimental Observations

2.1 Elemental Analysis. X-Ray Fluorescent Spectroscopy

The X-ray fluorescent spectroscopy was provided us by two different laboratories with the different X-ray spectroscopes. Both methods used in the analysis are non-sensitive to the light elements, such as B. Therefore, to confirm the stated by the vendor elemental composition for the provided us samples, we need to find the way how correctly to take into account the assumption about the present element B in the micro-samples.

Tables 1, 2, 3, and 4 represent the analysis of the composition of chemical elements obtained from the X-ray fluorescent spectroscopy.

As it was expected, the found concentrations of elements are not coinciding with the given at the beginning formula. Nevertheless, if to assume the presence of the chemical element B in the stated by the vendor concentration of 9%, then the appropriately introduced corrections in the concentrations can give the confirmation of the initial formula. In order to take into account the assumption about the present element

Table 2 Report of elemental analysis. X-ray fluorescent spectroscopy. Commercial spectrometer produced by Elvatech. It is not sensible for the element B. As-cast sample

At. N.	El.	Ser.	Intensity	Concentr. (%)
14	Si	K	36,694	7.7848 ± 0.0844
15	P	K	758	0.1068 ± 0.0452
22	Ti	K	454	0.0601 ± 0.0771
24	Cr	K	890	0.0428 ± 0.0205
25	Mn	K	2260	0.1479 ± 0.0160
26	Fe	K	1,751,113	85.9662 ± 0.0795
28	Ni	K	207	0.0234 ± 0.0139
29	Cu	K	20,189	1.6106 ± 0.0245
41	Nb	K	155,007	2.8553 ± 0.0158
42	Mo	K	73,158	1.4023 ± 0.0118
45	Rh	K	4140	< 0.0001

Table 3 Report of elemental analysis. X-ray fluorescent spectroscopy. Laboratory non-commercial spectrometer, Ukrainian National Institute of Physics. It is not sensible for the element B. Annealed sample

At. number	Element	Series	Concentr. (%) (RDFS)	$\tilde{x}$ (At. %)
14	Si	K	8.203	15.3321
25	Mn	K	0.095	0.0892
26	Fe	K	86.341	81.1761
29	Cu	K	1.543	1.2706
41	Nb	K	2.578	1.4544
42	Mo	K	1.240	0.6773

Table 4 Report of elemental analysis. X-ray fluorescent spectroscopy. Laboratory non-commercial spectrometer, Ukrainian National Institute of Physics. It is not sensible for the element B. As-cast sample

At. Number	Element	Series	Concentr. (%) (RDFS)	$\tilde{x}$ (At. %)
14	Si	K	8.227	15.2575
25	Mn	K	0.095	0.8855
26	Fe	K	86.250	80.4447
29	Cu	K	1.521	1.2449
33	As	K	0.0339	0.0208
41	Nb	K	2.603	1.4585
42	Mo	K	1.271	0.6876

B in the micro-samples, we discuss the definition of the used here percentages as follows.

Assume that the intensities I_i of the X-ray fluorescence, detected for each element i, are proportional to the amount of matter of the elements (mole of atoms), denoted here ν_i, in the sample (more strictly, concentrations). That is $I_i \propto k_i \nu_i$, where k_i is the characteristic coefficient, depending on the absorption/re-emission of the i-th chemical element in the sample. Then, the definition of the normalized amount of matter for a component, denoted as x_i, can be written down in the following manner:

$$x_i = \frac{I_i/k_i}{\sum_j I_j/k_j + I_B/k_B} = \frac{\nu_i}{\sum_j \nu_j + \nu_B}. \tag{1}$$

Here, the sum over the index $j = \{\text{Si, Mn, Fe, Cu, Nb, Mo, } \ldots\}$ does not take into account the chemical element B. The corresponding term for the element B is taken into account by adding I_B/k_B to the sum over j.

Next, suppose the presence of the atoms B does not significantly influence the fluorescent properties of the sample in the X-ray range of frequencies. Therefore, the above expression can be rewritten

$$x_i = \frac{\nu_i}{\sum_j \nu_j} \frac{1}{1 + \nu_B/\sum_j \nu_j} \approx \tilde{x}_i \frac{1}{1 + x_B}, \tag{2}$$

where $\tilde{x}_i$ corresponds to the normalization of the concentrations x_i without taking into account the element B. Note, it is assumed that $x_B \ll x_{Fe}$.

Applying the last expression to the experimentally found atomic percents without element B ($\tilde{x}_i$) in the Tables 1, 2, 3 and 4, one can find the following. For example, from Table 4 that $x_{\text{Fe}} \approx \tilde{x}_{\text{Fe}} * (1/1.09) = 80.45/109.00 \approx 0.7381 = 73.81\%$, while $x_{\text{Si}} \approx \tilde{x}_{\text{Si}} * (1/1.09) = 15.26/109.00 = 0.14 = 14.00\%$. Taking into account the other tables, the proposed estimation does not require the restriction $\tilde{x}_B \ll \tilde{x}_j$ if the traces of such atoms like Mo are neglected. Thus, the stated by vendor formula can be confirmed within our elemental analysis with the described uncertainty about 0.5%.

Therefore, there is a necessity to test the presence of a lighter component, the stated by the vendor element Boron, in the formula of the material. In the next subsection, the results of the analysis by the method of laser mass spectroscopy are provided. In comparison with the previous method of X-ray spectroscopy, the method of laser mass spectroscopy is destructive (based on the vaporization and ionization of the surface layers of a sample).

2.2 Elemental Analysis. The Data from the Laser Mass Spectroscopy

To qualitatively prove the formula of the chemical elements for the micro-ribbons, the laser mass spectroscopy was used. The results of the scans are shown in graphs 1 and 2 for the as-cast and annealed samples, correspondingly.

The results shown in graphs 1 and 21 represent the induced voltage drop (amplified) on the detector, depending on the atomic mass and the number of bombarding atoms per unit of time. The lower and higher resolutions of the scans are presented in the top and bottom of the figure, accordingly.

Some picks correspond to the double- and triple-ionized anions. The atoms in the samples can be multiply ionized during the laser pulse. The laser pulse is used in the mass spectrometer to evaporate the elements into the analyzer of the spectrometer.

For example, as it is shown in Figs. 1 and 2, the line at $A = 28$ g/mol can represent the overlapping of different multi-ionized elements, such as Si^+ and Fe^{2+} (compare with [18]). It is known that iron relatively easy frees up two external electrons. It is obvious that the samples consists of iron, silicon, niobium, and copper. The peak at $A = 46$ g/mol and $A = 93$ g/mol can be corresponding to titanium or double-ionized niobium and niobium, correspondingly. The titanium was not found in X-ray spectroscopy and is the suspect for being added as a debris of used glue before scanning if the double ionization interpretation fails. Despite of the low peak, not corresponding to the stated amount of atoms per mole, the presence of boron is confirmed. The rest of the lines that are not seen by X-ray spectroscopy can be due to the leak of the chamber of the mass spectrometer. Note, the detected amount of niobium is much more significant in comparison with the element of molybdenum contrary to the observed (more exactly interpreted) by X-ray method.

2.3 The Cu K_α X-Ray Diffraction Patterns

The Cu K_α X-ray diffraction patterns of the as-cast and annealed ribbons of $Fe_{73.5}Cu_1Nb_3Si_{13.5}B_9$ are shown in Graphs 3 and 4 (coincides with [19]) (Figs. 3 and 4).

It can be seen the relatively pronounced peaks at the diffraction angles $2\theta = 42.74°$ and $2\theta = 45.00°$. The peak at $2\theta = 42.74°$ in the Graph 3 is not interpreted by us and requires reexamination.

The estimated crystal interplanar spacing for each observed diffraction angle, $2\theta = 42.74°$ and $2\theta = 45.00°$, corresponds to the distance, that is about 0.7–0.9 Å smaller in comparison with the length of the side of the unit cell for the iron crystal (in the case of body centered cubic structure). Note, the found in [20] values of the distances between the two nearest atoms Fe and Si in α-$FeSi_2$ phase are around 2.30 Å and for Fe-Fe(Si) in the phase of Fe_3Si are about 2.45 Å with the lattice parameters 2.70 Å and 5.60 Å, accordingly.

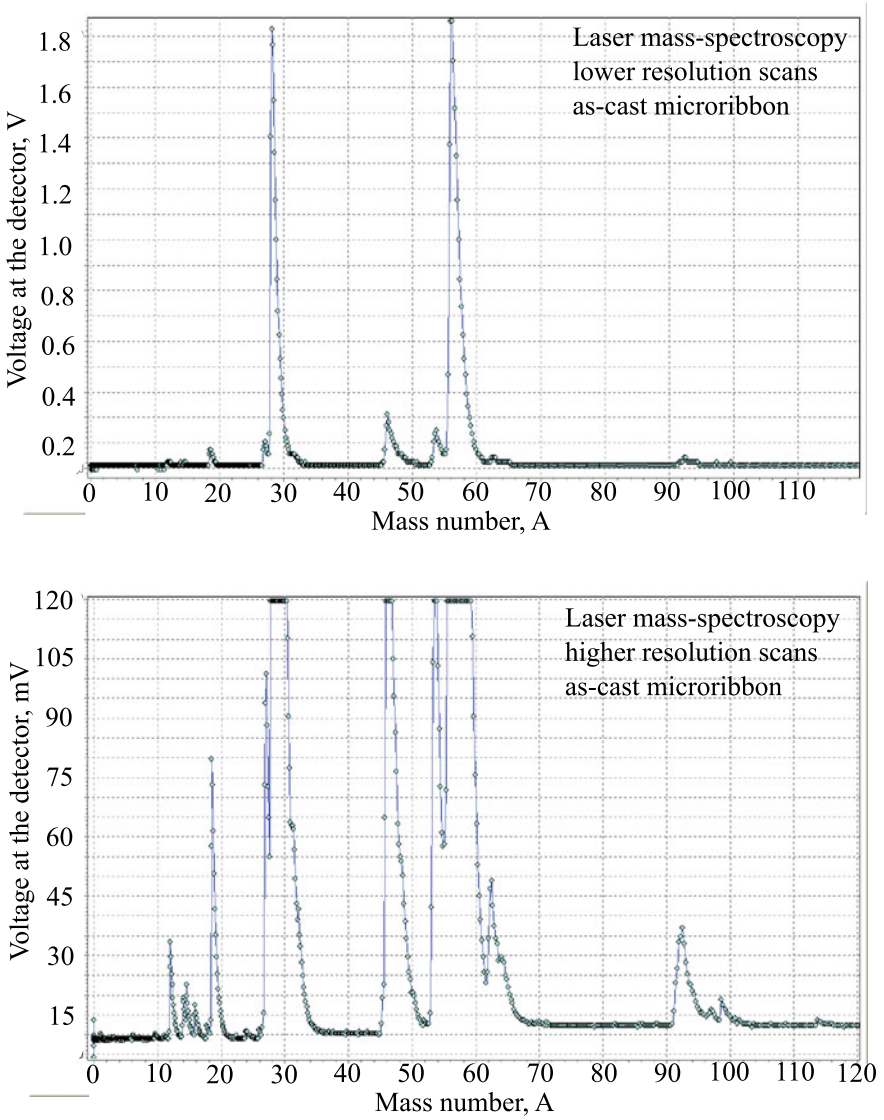

Fig. 1 Laser mass spectroscopy for the as-cast sample. The lower and higher resolutions of the scans are presented in the top and bottom of the figure, accordingly. $[A] = \text{g/mol}$

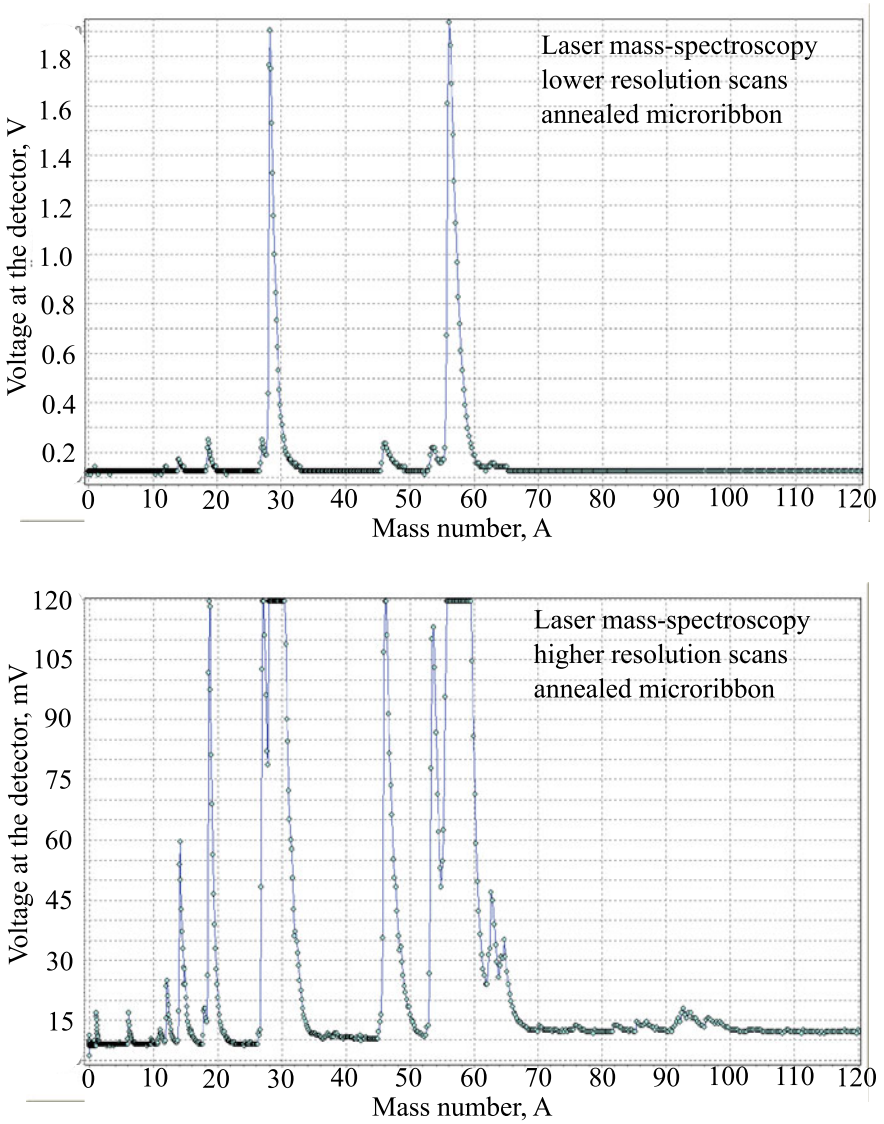

Fig. 2 Laser mass spectroscopy for the annealed sample. The lower and higher resolutions of the scans are presented in the top and bottom of the figure, accordingly. $[A] = \text{g/mol}$

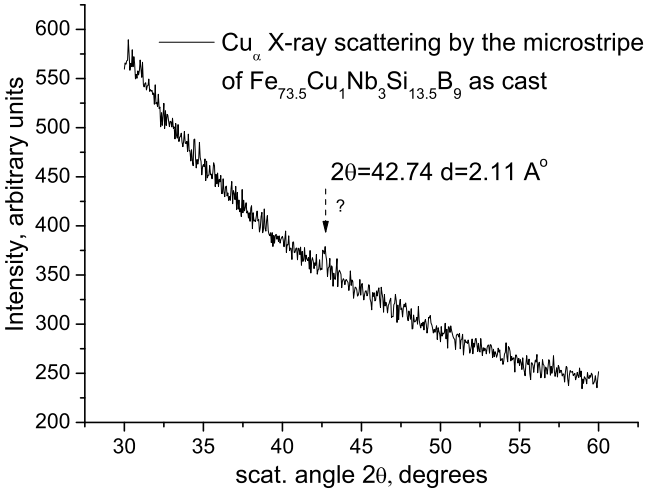

Fig. 3 Cu K_α X-ray diffraction pattern of $Fe_{73.5}Cu_1Nb_3Si_{13.5}B_9$ as-cast ribbon. It can be seen the peak at the diffraction angle $2\theta = 42.74°$. Cited from [19]

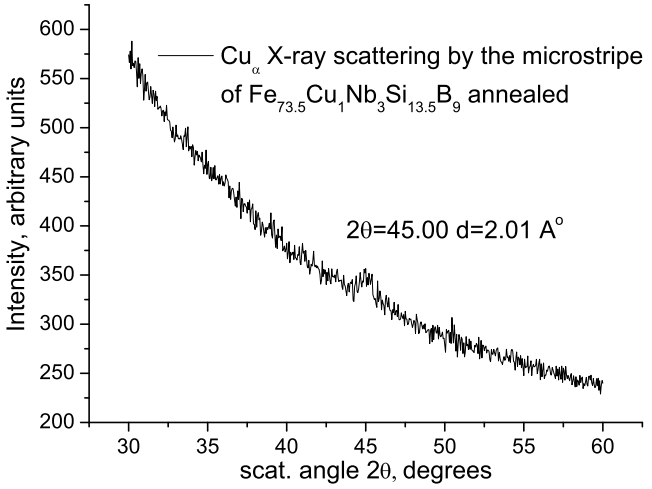

Fig. 4 Cu K_α X-ray diffraction pattern of $Fe_{73.5}Cu_1Nb_3Si_{13.5}B_9$ annealed ribbon. It can be seen the peak at the diffraction angle $2\theta = 45.00°$. Cited from [19]

Except for the low sensitivity of the used x-ray detector, the observed difference in the X-ray diffraction patterns in Graphs 3 and 4 can be due to the quite small size of iron nanoparticles used in production of the as-cast samples, the appearance of multiplets during the irradiation by the Cu K_α X-rays, and the formation of different quite large crystalline phases, etc.

2.4 The Magnetic Susceptibility as the Function of Temperature

The specific susceptibility of the soft magnetic ribbons was measured by a Faraday balance in the magnetic field of magnitude 6911.5 Oe. The obtained data of the specific susceptibility of $Fe_{73.5}Cu_1Nb_3Si_{13.5}B_9$ as-cast and annealed ribbons are shown in Figs. 5 and 6, correspondingly.

The phase transition of the micro-ribbon from amorphous to crystalline state can be seen in 5. The temperature of the phase transition is about 600 K.

In the majority of works, the observed abrupt change of magnetic susceptibility at 600 K and at 850 K, shown in Fig. 5, is attributed to the induction of the chemical bonds of Fe with Si and B, such as FeSi, Fe_2Si, Fe_3Si, Fe_2B and Fe_3B, and the grows of the interfaced surfaces between the different crystalline and amorphous phases.

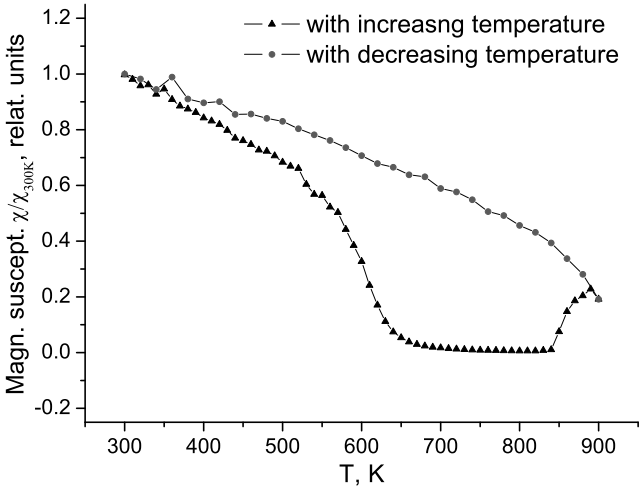

Fig. 5 Relative (related to the value at 300 K) magnetic susceptibility of $Fe_{73.5}Cu_1Nb_3Si_{13.5}B_9$ as-cast ribbon, measured by a Faraday balance. The mass of the sample is equal to 0.300 ± 0.001 mg. Cited from [19]

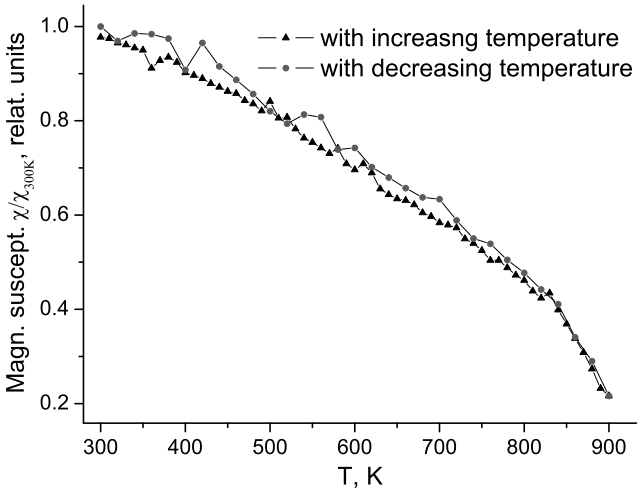

Fig. 6 Relative (related to the value at 300 K) magnetic susceptibility of $Fe_{73.5}Cu_1Nb_3Si_{13.5}B_9$ annealed ribbon, measured by a Faraday balance. The mass of the sample is equal to 0.255 ± 0.001 mg. Cited from [19]

2.5 The Ferromagnetic Resonance

The FMR spectrums, differential signal power dP/dH, of the amorphous (as-cast) and annealed ribbons $Fe_{73.5}Cu_1Nb_3Si_{13.5}B_9$ at 9.4 GHz and room temperature are shown in Fig. 7.

The top left and right and the bottom left graphs in Fig. 7 demonstrate the dependence of the spectra of the as-cast sample on the angle between the applied in-planar (the plain of the ribbon is parallel to the direction of the field) strong magnetic field and the main axis of the ribbon, denoted as θ (do not be confused with the scattering angle for the X-ray pattern). Both curves, for the as-cast (solid thin) and the annealed (bold dashed) ribbons, are represented in the bottom right graph in 7.

The relatively symmetric line shape of ferromagnetic resonance was observed for the annealed (nanocrystalline) ribbon (see the right bottom graph in Fig. 7). In comparison with the amorphous ribbon (see Fig. 7), the signal swing is approximately two times higher. Note the shifts of the peaks, the changes in the width of the line for the different angles θ, and the appearance of the additional red-shifted lower peak at $\theta = 90°$ in the left and right upper and the left bottom graphs in 7. Some authors refer the latter to certain non-planar features of FMR, such as induced by the bulk collective spin effects.

If to make an attempt to interpret the data, then it could be tested the quite elaborated two-dimensional model of soft magnetic (but strictly saying, not yet ferromagnetic), appealing to the absolute and relative sizes of the samples. Still, it does not guarantee a success in explaining the appearance of the additional peaks on the left wing of the resonant curve at the angle $\theta = 90°$ or even in having the ferromagnetic

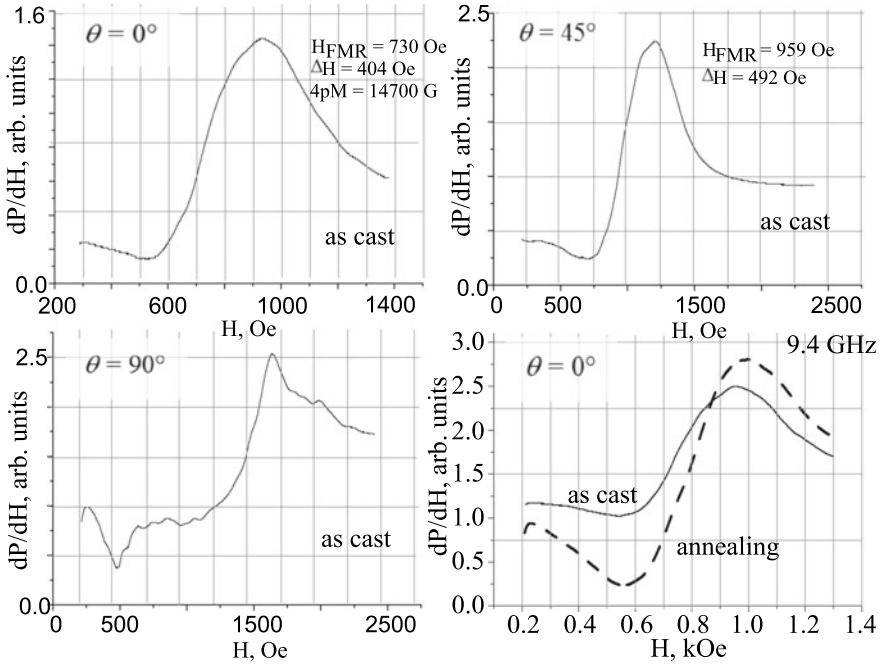

Fig. 7 Spectrum of ferromagnetic resonance, differential signal power dP/dH. The top left and right and the bottom left graphs are for the amorphous (as-cast) ribbons $Fe_{73.5}Cu_1Nb_3Si_{13.5}B_9$ at 9.4 GHz and room temperature. θ is the angle between the main axis of the ribbon and the applied magnetic field. Both curves, for the as-cast (solid thin) and the annealed (bold dashed) ribbons, are represented in the bottom right graph (compared with the data in [19])

ordering of spin-spin and spin-lattice (amorphous subsystem) subsystems (see the notes about the possible transition to a ferromagnetic ordering: comparison between the Ising and Heisenberg models in [21]). In our opinion, the three-dimensional model of spin system, including the interaction with the "multi-dimentional field" of the environment (many-atomic subsystem), has to be founded in building the macroscopic theory.

As it is demonstrated in next subsection, the role of a microscopic state, in determining the response to the field of super high frequency, is indirectly justified by the results of experiments with the sample in the resonator.

2.6 The Behavior in the Surface Electromagnetic Wave Resonator

The research was carried out by the method of reflectometry using a Network Analyzer P2-61 in the reflection measurement scheme in the X-band range, as shown in

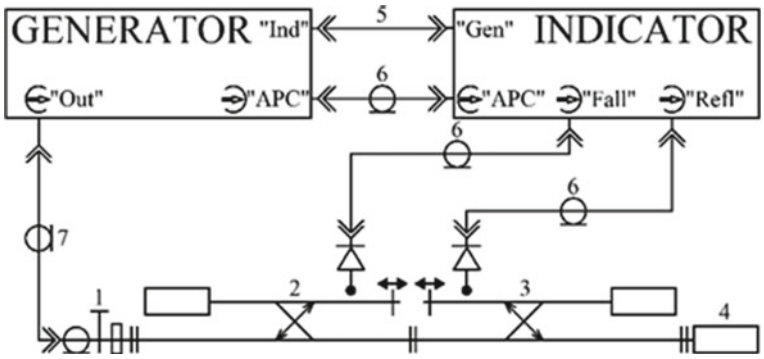

Fig. 8 Experimental setup of network analyzer R2-61. Transition coaxial waveguide (1), directional detector "falling" (2), direction detector "reflected" (3), measurable object (4), cable (5), connecting coaxial cable HF (6), microwave coaxial cable connecting (7)

Fig. 8. As you know, the surface electromagnetic wave resonators (SWR) are excited by the main wave of a rectangular waveguide H_{10}. Oscillations exist along the resonant size l and along the size w [22]. But the modes along w are undesirable, so the resonator is located in an out-of-band waveguide. This allowed to eliminate in the spectra of the amplitude–frequency characteristics effect associated with oscillations of longitudinal modes [23].

In order to obtain a high Q-factor of SWR, it is located at the center of the waveguide as far away as possible from the walls, parallel to the wider wall of the outer waveguide and at the optimum distance z, as shown in Fig. 9. The optimal condition for determining the distance z was to obtain a critical connection of a resonator of a surface electromagnetic wave with an electromagnetic wave in a regular waveguide. For this purpose, dielectric inserts are used on the basis of dielectrics with low dielectric constant and low losses in the microwave range. Dielectric inserts made of styrofoam were used for the research.

The ferromagnetic surface electromagnetic wave resonator (FSEWR) is represented by the conducting surface of ferromagnetic material. It was used a FINEMET micro-ribbon with the size of $l \times w \times d$ as the conducting surface. In order to ensure the one-mode regime, the FSEWR has only the lowest transversal mode in the standard rectangular waveguide.

The microwave properties of FSEWR with the FINEMET are experimentally investigated for the cases of the as-cast sample (see Fig. 10) with the approximate size of 12.00 mm $\times$ 0.60 mm $\times$ 0.02 mm ($l \times w \times d$) and the annealed sample (see Fig. 11) of 12.10 mm $\times$ 0.60 mm $\times$ 0.02 mm ($l \times w \times d$).

The measurement of the Q-factors of the resonators yields $Q_0 = 61$ for the as-cast micro-ribbon at the frequency $f_0 = 10.537$ GHz and $Q_0 = 75$ for the annealed micro-ribbon at the frequency $f_0 = 10.411$ GHz.

In the resonators with the FINEMET micro-ribbons, it can also be observed the so-called ferromagnetic surface electromagnetic wave resonance. For example, the

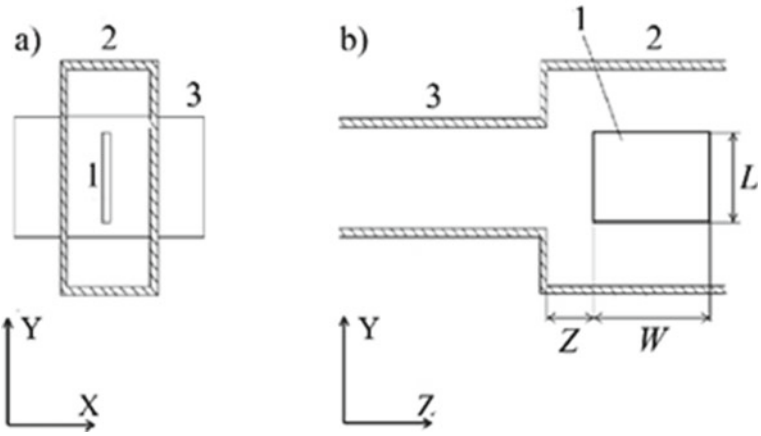

Fig. 9 Waveguide section in the plane xy (**a**); the waveguide section in the plane yz (**b**). SWR with dimensions L and W in an extinct rectangular waveguide. 1—SWR, 2—outermost waveguide, 3—regular waveguide, L is the length of the resonator, and W is the width of the resonator

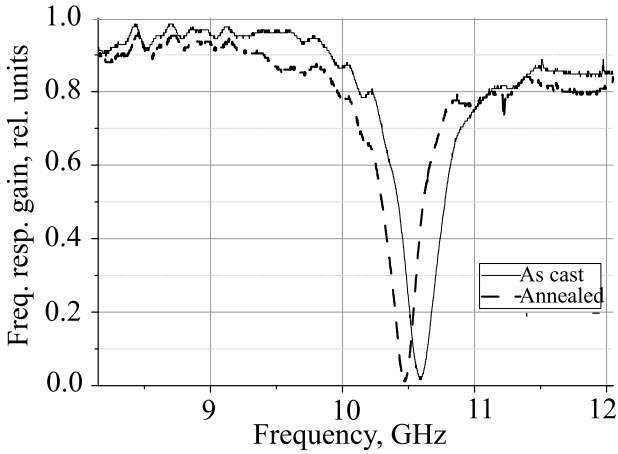

Fig. 10 Frequency response curve with standing wave ratio at voltage (SWRV) = 1.20 for the as-cast (solid thin) and annealed (bold dash) FINEMET samples without applying a constant external magnetic field

change of the frequency response curve of such a resonator with the as-cast microstripe under the applied constant magnetic field is represented in the experimental data Fig. 12.

The present additional constant magnetic field in the resonator changes the order of rearrangement of the spin-spin interaction. This causes the shifts of the observed resonant peak. It is interesting to note that the additional magnetic field induces the splitting of the resonant curve for the non-ferromagnetic materials, but the nature of

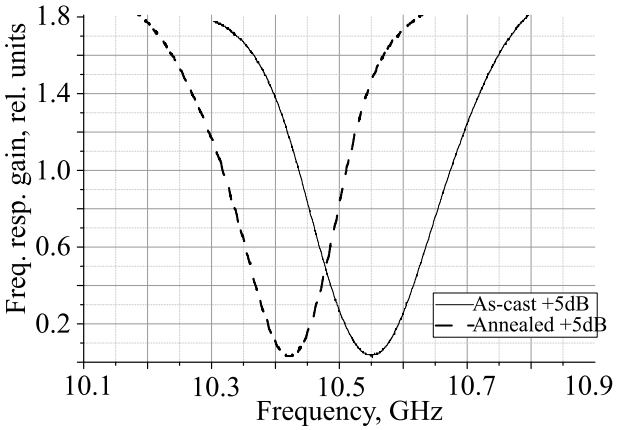

Fig. 11 Frequency response curve with standing wave ratio at voltage (SWRV) = 1.20 with the amplification equal to +5 dB for the as-cast (solid thin) and annealed (bold dash) FINEMET samples without applying a constant external magnetic field

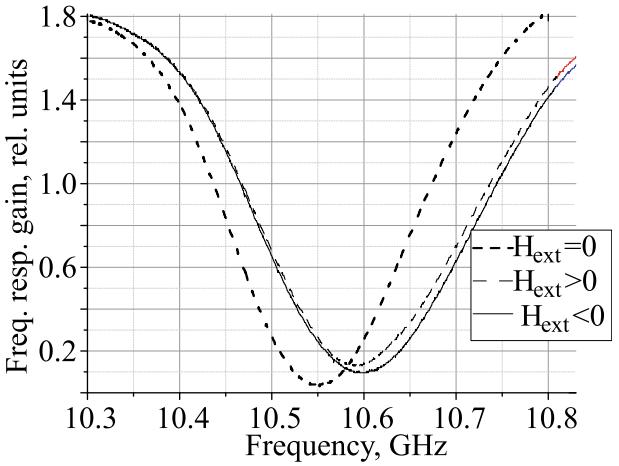

Fig. 12 Frequency response curve with SWRV = 1.20 for the as-cast FINEMET sample of the size 12.1 mm × 0.6 mm × 0.03 mm with the amplification equal to +5 dB at the applied external magnetic field (zero (bold dash), greater (dash), and less (solid thin line for the opposite direction of the constant magnetic field) than the zero value)

the effect is different (see, for example, [24]). Herewith, the process, determining the Q-factor of the resonator with the sample, is the power (resistance) dissipation.

In the next subsection, the complex impedance is measured for the microscopic stripes in MHz frequency range.

2.7 *The Complex Impedance of the FINEMET Micro-samples as the Function of Frequency*

The complex impedance of the FINEMET micro-samples as the function of frequency for the applied voltage was measured by the commercial impedancemeter Z-2000 of the company Elins. The most typical behavior of the samples is represented by the experimental data in the Graphs 13 and 14 (Figs. 13 and 14).

Therefore, the absolute values of the active (real) and reactance (imaginary) components of the complex resistance for the FINEMET as-cast and annealed samples are growing with frequency of the applied voltage. It appears that the active (supposedly complying with the Ohm's law) component has much higher values than the resistance of the same piece of iron. If the increase of the reactance could be explained by the Drude model (by introducing the relaxation time for the free electrons in the metal lattice), then the growing with the frequency active component of the resistance does not support the concept of high-mobility two-dimensional electron gas (see, for example, [25, 26]).

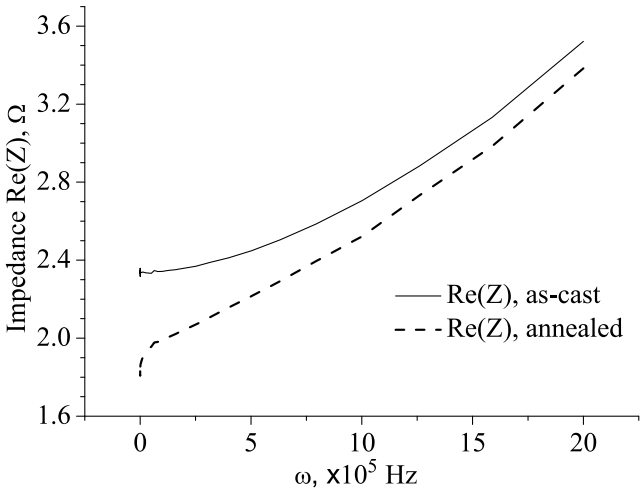

Fig. 13 Real part of the impedance (complex resistance) of the FINEMET micro-ribbon as the function of frequency of the applied voltage. The solid thin curve corresponds to the as-cast sample, while the bold dash line is related to the annealed microstrip

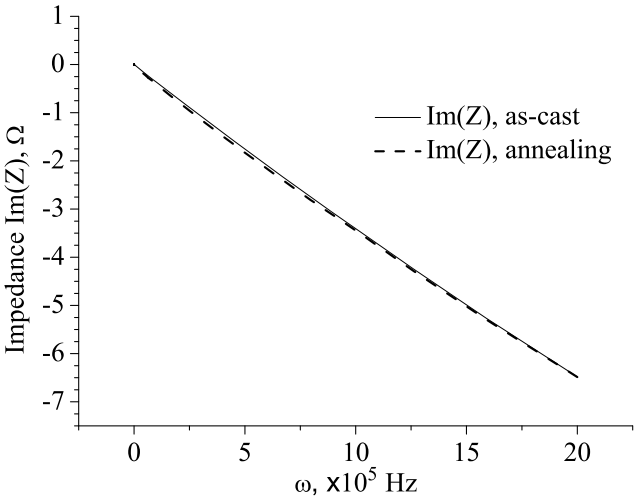

Fig. 14 Imaginary part of the impedance (complex resistance) of the FINEMET micro-ribbon as the function of frequency of the applied voltage. The solid thin curve corresponds to the as-cast sample, while the bold dash line is related to the annealed microstrip

Such feature of the microscopic samples can be related to the sort of inductance in the sense of possible applications.

2.8 Excited Transversal Mechanical Vibration of the Micro-ribbon with an Unfixed End

The vibrations at low frequencies were observed for the samples with one fixed end and the loose end placed at the outer edge of the electromagnet coil (see Fig. 15).

The frequency of the electromagnet was ranged from 0 to 100 Hz. The shorter as-cast ribbon (17.0 ± 0.5 mm in length) has lower frequency of self-excitation vibrations than the annealed sample (20.0 ± 0.5 mm in length), i.e., 28 ± 2 Hz

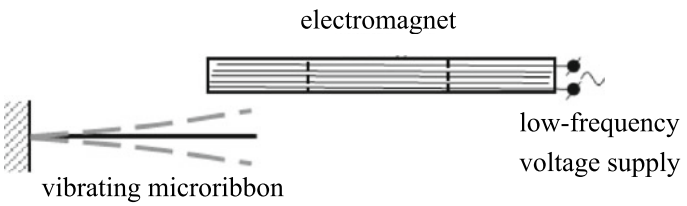

Fig. 15 Schematic illustration of the excited transversal mechanical vibration of the micro-ribbon with an unfixed. The illustrated scheme was used for the experimental setup

and 34 ± 2 Hz, correspondingly. When a relatively weak permanent magnet was approached to the ribbon in the perpendicular to the vibration direction, the vibrations ceased for both samples. The larger ribbons of copper or iron did not stop vibration in the additionally applied perpendicular magnetic field. If we assume the average density of the ribbons is about 7.3 ± 1 g/cm^3, then the observed self-excitation frequencies were estimated to correspond to the Young's modulus equal to 62.9 ± 5.0 GPa and 177.7 ± 15.0 GPa (compare with the value 211 GPa of Young's modulus for iron), for the as-cast and annealed ribbons, accordingly (more accurately, that is the mixture effect including shear stress during bending motion).

3 Discussion of the Experimental Data

Thus, the X-ray spectroscopic determination of the elementary composition for the micro-sample has to be supplemented by spectroscopic methods sensitive for lighter elements. One of the nondestructive methods is spectroscopy in optical region. But, in our case, the identification procedure may require special technique to separate the lighter atoms from the sample to avoid the widening and shift of the resonant lines by other surrounding atoms.

We can assume that the laser spectroscopy is one of the perspective supplementary modernization for the existing scanning devices, such as laser mass spectroscopy. For example, the characteristic lines of boron can be obtained even by recombination of the ionized and evaporated atoms against a special detector with the low mutual chemical activity for the element.

Because, for the samples of annealed iron, the intrinsic local magnetic field can in principle be three orders of magnitude greater than the inducing external field, and the discussion of the phonon–electron interaction becomes mandatory. This is because the sizes of the crystalline nanophases (see for example, [27]) vary depending on the applied external field. Therefore, the space anisotropy of the micro-samples defines its macroscopic properties (see [28, 29]). For example, according to the results of the work [16], at the concentrations of Si higher than a certain value (12.5% of the total amount of atoms in the sample as in [30]), the formation of the nanocrystalline phases of Fe3Si during annealing can be assumed. Then, the magnetic properties of the samples can also be defined by the excitation of the surface spin waves on the interfaces between the different phases of the FINEMET alloy. Besides the mentioned nano-crystals Fe3Si, according to the work [31], there can also be formed such types of structures as Fe3B (or/and Fe2B, etc.) in the sample. The relatively broad diffraction line at 45° testifies in favor of the latter.

It appears that the annealed sample reveals typical for high-quality ferromagnetic films behavior in the super high-frequency domain. At the same time, the role of microscopic system state in defining the response to a super high-frequency field is indirectly confirmed by the experimentation with the micro-samples in the specific resonator setup.

Note here, that the widely used macroscopic theory of ferromagnetic resonance applies thermodynamic expressions for the system of bose particles in the Gibbs Grand canonical ensemble (see for more details, for instance, [32]). Here, it arises the necessity of the argumentation for such an point of view because spontaneous magnetization, attributed to the ferromagnetic materials of a macroscopic size, and the corresponding long range correlation order in crystals cannot be described without three-dimensional spin dynamics of electrons. That is, the statistical properties of the fermi-system in thermodynamic equilibrium (without an external high frequency magnetic field) with the nano-lattice determine the resonant absorption in static magnetic fields.

Besides, it turns out that the increase of ohmic (active) component of the complex resistance cannot be explained in terms of the Drude model. Assume the dependence of the active resistance on the frequency is caused by skin effect. This probably explains the linear dependence on the frequency of the applied voltage in the micro-sample of 20 μm in thickness. Then, in accordance with the Drude model, such dependence has to cause a quadratic growth with frequency for the reactance (imaginary). Hence, it differs from the classical behavior and requires testing for higher frequencies to exclude experimental errors in formulating a hypothesis.

Also, the observed induced mechanical low frequency resonant vibrations of the micro-ribbons are of interest for more careful identification of the soft magnetic micro-systems. Taking into account the relatively high resistance of the samples, electrically open circuit, and the assumed low coercivity, a synchronous magnetization with the electromagnet is supposed to be the nature of the excited resonant bending (vibration). The latter may not be so trivial in description in terms of the scalar magnetic dipole-field coupling (or in terms of the corresponding vector-space gradient).

4 Conclusions

Thus, the following was experimentally identified: the importance to combine different method of elemental analysis for micro-objects containing light chemical elements; the difficulties to apply commonly used models for the description of the micro-ribbons, in particular the Drude model and therefore the two-dimensional spin system of electrons; the observed properties of the soft magnetic have the potential of various applications in electronic miniaturization, including GHz technology; the necessity of the further development of comprehensive analytical methods for the correct prediction of new properties for FINEMET.

Recall the main features, revealed in the micro-ribbons of Fe–Cu–Nb–Si–B by the provided in this work analysis.

X-ray diffraction patterns showed the appearance of the ordered (probably, various crystalline substructures) phases after annealing.

The transition from amorphous phase to crystalline phases (probably, the induction of the chemical bonds between Fe and Si, B is involved in the process) was also

observed at 600 K during the increase of the temperature of the as-cast sample. The observed abrupt change of magnetic susceptibility can also be testifying the transition to the long range order in spin-spin coupling or/and more correlated states between the different phases.

The peak of ferromagnetic resonance was observed for both crystalline and the amorphous phases within the same magnitude of in-plane external magnetic field. The annealed sample shows behavior typical for high-quality ferromagnetic films (such as permalloy) in the field of GHz region.

The perturbation of the magnetic field in the ribbon's plane (perpendicular to the direction of the mechanical self-resonant vibration) can cause the change in the intrinsic state of the system (ribbon) that defines the elasticity (more accurately, the reaction of the sample on the external low frequency magnetic fields) of the ribbon. Actually, the latter can be explained also by the induction of the additional longitudinal current that, in turn, interacts with the perturbed in-plane magnetic field and compensates the elastic force exerted by the low frequency field of the electromagnet. Therefore, in this case, it is interesting to discover, does the additional static magnetic field change the intrinsic long range order of spin-spin coupling, or the effect is due to the induced longitudinal current? The fact is that the cessation of the mechanical vibration in the direction perpendicular to the plane of the sample and parallel to the axis of the electromagnet is not observed for much larger (in proportional scale) samples of iron or copper.

The theoretical description of the soft magnetic multi-component micro-ribbons probably requires the formulation of the correct model Hamiltonian and the corresponding structure of a pure quantum state that can be useful for the micro-samples made of nanoparticles. The transition to a macroscopic description (or the statistical system of quite large sizes) is the subject of additional investigation that did not yet reach necessary analytical (and applicable) stage of development in the theory.

Acknowledgements This work was supported in part by the grant No. 19BF052-01 from the Ministry of Education and Science of Ukraine. Special thanks to company Elvatech, National Institute of Physics, Physics Department at Lesya Ukrainka EENU for the provided additional experimental facility and support.

References

1. Askeland DK, Fulay PP, Wright WJ (2010) The science and engineering of materials. Cengage Learning Inc, Boston
2. Callister WD Jr (2007) Materials science and engineering—an introduction. Wiley, Hoboken
3. Yoshizawa Y, Oguma S, Yamauchi K (1988) New Fe-based soft magnetic alloys composed of ultrafine grain structure. J Appl Phys 64:6044–6046. https://doi.org/10.1063/1.342149
4. Herzer G (1989) Grain structure and magnetism of nanocrystalline ferromagnets. IEEE Trans Magn 25:3327–3329. https://doi.org/10.1109/20.42292
5. Yoshizawa Y, Yamauchi K (1990) Fe-based soft magnetic alloys composed of ultrafine grain structure. Mat Trans IJM 31:307–314. https://doi.org/10.2320/matertrans1989.31.307

6. Martienssen W, Warlimont H (2005) Springer handbook of condensed matter and materials data. Springer, Berlin, Heidelberg. https://doi.org/10.1007/3-540-30437-1
7. Wei L (2015) Advances on FeCuNbSiB nanocrystalline soft magnetic powder cores. Mat Sci Forum 815:233–237
8. Lashgari HR, Chu D, Xie S, Sun H, Ferry M, Lia S (2014) Composition dependence of the microstructure and soft magnetic properties of Fe-based amorphous/nanocrystalline alloys: a review study. J Non-Crystal Solids 391:61–82
9. Xiao H, Dong Y, He A, Sun H, Anding Wang H, Li LL, Liu X, Li R (2019) Magnetic softness and magnetization dynamics of FeSiBNbCu(P, Mo) nanocrystalline alloys with good high-frequency characterization. J Magn Magn Mat 478:192–197
10. Guotai W, Ting L, Xu J, Yuanzheng Y (2020) Composition dependence of amorphous forming, crystallization behavior, magnetic and electronic properties of silicon-rich FeSiBCuNb alloys. J Magn Magn Mater 505
11. Mikhalitsyna EA, Kataev VA, Larrañaga A, Lepalovskij VN, Kurlyandskaya GV (2020) Nanocrystallization in FINEMET-type Fe73.5Nb3Cu1Si13.5B9 and Fe72.5Nb1.5Mo2Cu1.1Si14.2B8.7 thin films. Materials 13, 348:1–16
12. Le Breton JM, Zorkovsk A, Kasiarova M (2004) Crystallization of Fe73.5Cu1RE3Si13.5B9 ribbons with RE = Pr, Nd, Gd. J Phys Condensed Matter 16:5555–5568. https://doi.org/10.1088/0953-8984/16/30/016
13. Yoshizawa Y, Yamauchi K (1991) Magnetic properties of Fe-Cu-M-Si-B (M=Cr, V, Mo, Nb, Ta, W) alloys. Mater Sci Eng A 133:176–179
14. Tejedor M et al (1998) Magnetoimpedance effect in zero magnetostriction nanocrystalline Fe73.5Cu1Nb3Si16.5B6 ribbons. J Magn Magn Mater 185:61–65
15. Chumak AV, Vasyuchka VI, Serga AA, Hillebrands B (2015) Magnon spintronics. Nat Phys 11:453–461. https://doi.org/10.1038/nphys3347
16. Kobljanskyj Y et al (2015) Nonlinear dynamic properties of two-dimensional arrays of magnetic nanodots. In: Lukaszew R (ed) Handbook of nanomagnetism: applications and tools, pp 97–116
17. Schmool DS, Rocha R, Sousa JB, Santos JAM, Kakazei GN, Garitaonandia JS, Martín Rodríguez D, Lezama L, Barandiarán JM (2004) Ferromagnetic resonance in nanometric magnetic systems. J Optoelectron Adv Mater 6(2):541–550
18. Hono K, Hiraga K, Wang Q, Inoue A, Sakurai T (1992) The microstructure evolution of a $Fe_{73.5}\ Si_{l3.5}\ B_9\ Nb_3\ Cu_1$, nanocrystalline soft magnetic material. Acta Metall Mat 40(9):2137–2147
19. Kobljanskyj Y, Sizhuk A, Semen'ko M, Ostapenko R, Zhuo S, Zhenjie Z, Xiaohong C, Kolesnyk O, Malyshev V (2020) About some resonance, structural, and magnetic properties of amorphous and nanocrystalline FeCuNbSiB ribbons. In: 2020 IEEE Ukrainian microwave week, 2020 IEEE 10th international kharkiv symposium on physics and engineering of microwaves, millimeter and submillimeter waves (MSMW), Kharkiv, Ukraine, September 21–25, Proceedings book, vol 3, Radiospectroscopy, pp 829–832
20. Sandalov I et al (2015) Effect of electron correlations on the Fe3Si and α-FeSi2 band structure and optical properties. Phys Rev B 92
21. Svidzinsky AV (1998) Mathematical methods of theoretical physics, Olena Teliga Publication, Kyiv, pp 417–442
22. Melkov GA et al (1998) Surface wave HTS resonators. In: MSMW symposium proceedings, pp 625–630
23. Melkov GA et al (2002) Microwave properties of the surface wave resonator in the below-cutoff waveguide. Modern Probl Radio Eng Telecommun Comput Sci IEEE Proc 75–77
24. Malyshev VY, Zavislyak IV, Melkov GA, Popov MO, Prokopenko OV (2020) Microwave magnon-plasmon-polaritons in the ferromagnetic metal-screened insulator structure. Ukr J Phys 65(10):939–948
25. Dressel M, Scheffler M (2006) Verifying the Drude response. Annalen der Physik 15(7–8):535–544. https://doi.org/10.1002/andp.200510198
26. Burke PJ, Spielman IB, Eisenstein JP, Pfeiffer LN, West KW (2000) High frequency conductivity of the high-mobility two-dimensional electron gas. Appl Phys Lett 76(6):745–747. https://doi.org/10.1063/1.125881

27. I. V. Lyasotsky, N. B. Dyakonova, D. L. Dyakonov, E. N. Vlasova and M. Yu. Jazvitsky, Metastable phases and nanostructuring of fe-nb-si-b base rapidly quenched alloys, Rev. Adv. Mater. Sci. 18, 695 - 702, pp. 18., 2008
28. Xie J, Liao Y-F, Dong-Ni W, Xiao W-J, Xie Quan (2020) The of order dependent electronic structures and magnetic properties of Fe3Si alloys. Physica Status Solidi (b). https://doi.org/10.1002/pssb.201900667
29. Anton T et al (2019) Spin-dependent electrical hole extraction from low doped p-Si via the interface states in a Fe3Si/p-Si structure. Semicond Sci Technol 34(3):1–16
30. Tetsuo M et al (2017) Mechanical properties of Fe-rich Si alloy from Hamiltonian NPJ. Comput Mat 10:1–6. https://doi.org/10.1038/s41524-017-0012-4
31. Sun X et al (2000) Nanocrystallization behavior and magnetic properties of amorphous Fe78Si9B13 ribbons. Physica B 291:173–179
32. Ahiezer AI, Barjakhtar VG, Peletminsky SV (1967) Spin waves. Moscow, Nauka, pp 172–175

Heavy Metals Removal Using Nanostructured Carbon-Based Composites in the Presence of Various Organic Compounds

Magdalena Medykowska, Małgorzata Wiśniewska, and Katarzyna Szewczuk-Karpisz

1 Structure of Composites

Composites are widespread materials due to their special properties, for example high strength and stiffness or low density and corrosion resistance or even lighter weight. They are defined as a combined materials created of two or more constituent in order to receive specific characteristic and better properties than constituents have used separately. In their construction the reinforcement or selected filler and the matrix binder can be distinguished. Moreover, both ingredients keep their physical, chemical, and mechanical properties. Composites are obtained in a synthetic way and may include various materials, e.g., metal, metal oxide, carbon, ceramics, glass, polymers.

In general, the reinforcement is in the form of particles or fiber and brings hardness, stiffness, and strength. The matrix phase is responsible for keeping the fibers in required orientation and protecting them from external factors. Most commonly used matrix is a metal, polymer, or ceramics. Furthermore the constituents do not dissolve in themselves or merge completely in any other way, so they can be physically identified in composite structure. Composites can be divided into fibrous (consisted of fibers in a matrix), laminar (consisted of layers of materials), or particulate (consisted of particles in a matrix) ones [1–3].

M. Medykowska · M. Wiśniewska (✉)
Faculty of Chemistry, Department of Radiochemistry and Environmental Chemistry, Institute of Chemical Sciences, Maria Curie-Sklodowska University in Lublin, Maria Curie-Sklodowska Sq. 3, 20-031 Lublin, Poland
e-mail: wisniewska@hektor.umcs.lublin.pl

M. Medykowska
e-mail: m.medykowska@poczta.umcs.lublin.pl

K. Szewczuk-Karpisz
Institute of Agrophysics, Polish Academy of Sciences, Doświadczalna 4, 20-290 Lublin, Poland

O. Fesenko and L. Yatsenko (eds.), *Nanomaterials and Nanocomposites, Nanostructure Surfaces, and Their Applications*, Springer Proceedings in Physics 263, https://doi.org/10.1007/978-3-030-74741-1_4

Composites are widely used in various fields of human activity. Besides their application in environmental protection for removal of hazardous substances from gas and liquid phases, they can be used as construction materials in many technical fields (including architecture), in aeronautics and astronautics (elements of airplanes, rockets, artificial satellites), in the wheel and rail transport as well as in stomatology and medicine (implants and tissue regeneration systems).

2 Heavy Metal Removal Using Natural and Modified Sorbents

Removal processes of heavy metals with high toxicity [4, 5] engages many kinds of sorbents like natural or synthetic zeolites. This minerals possess an important properties such as ion-exchange capability. One of the naturally occurring zeolites is clinoptilolite, which reveals great selectivity for heavy metal ions like Pb(II), Cd(II), Cu(II), and Zn(II) [6, 7]. The ability of selective adsorption of certain heavy metals depends on solutions pH in the case of both natural and synthetic zeolites. Na-A zeolite and 4A zeolite remove Cr(III) ions at neutral pH value. The last of them was made by dehydroxylation of low-grade kaolin.

Cr(VI) was removed at acidic pH, Cu(II) and Zn(II) at neutral and alkaline pH, whereas Mn(IV) was adsorbed at highly alkaline pH values [8–10]. For this purpose, the synthetic zeolites and coal flay ash were used. In turn, MMZ, which is synthetic zeolite that was magnetically modified by iron oxide, was used in the process of Pb(II) ions removal [11]. Another effective adsorbents are clay–polymer composites synthesized by modification of natural clay mineral with a polymeric material [12–14]. To separate heavy metal, ions from aqueous solutions have been used various phosphates: calcined phosphate at 900 °C, phosphate activated with nitric acid, and zirconium phosphate [15–17].

Next group of heavy metal removing sorbents are chemically modified industrial by-products like waste iron, hydrous titanium oxide, or fly ash. For example, iron slags were used to effective adsorption of Cu(II) and Pb(II) ions [18]; different fly ashes remove Cd(II), Ni(II) [19] and Cu(II), Pb(II) ions [20] from wastewaters. Sawdust modified with 1,5-disodium hydrogen phosphate removed favorably Cr(VI) ions [21]. Likewise iron-based sorbents—FerroSorp Plus [22] and synthetic nano-crystalline akaganeite [23] were successfully used for simultaneous removal of heavy metal ions (As, Cd, Cr, Cu, Ni, and Zn). Hydrous titanium oxide was also investigated in order to adsorption of Cr(VI) and Cu(II) ions [24–26].

3 Carbon-Based Composites in Heavy Metal Removal

Adsorbents containing carbon such as carbon nanotubes, activated carbon, biochar, graphene, and its derivatives are widely used in process of heavy metals removal. This kind of adsorption depends on the type of surface functional groups of carbon materials and its interactions with heavy metal ions which has great impact on adsorption mechanism. This mechanism include ion exchange, electrostatic interaction, surface complexation, precipitation, and physical adsorption (Fig. 1) [27]. Surface modification of carbon materials are essential to selective adsorption of heavy metal ions. There are carbon adsorbents modified by chemical methods such as nitrogenation, oxidation, and sulfuration.

Oxidation modificators such as nitric acid, ozone, and electrochemical oxidation techniques upgrade Cd(II) sorption capacity of carbon nanotubes (CNTs), activated carbon cloth (ACC), activated carbon (AC), and carbon nanofibers. On the other hand, cationic surfactant oxidation of AC improves adsorption rate of Cr(VI) ions [28–30]. Coconut shell carbon coated by chitosan modified with phosphoric acid effectively removes Zn(II) ions [1]. Carbon nanotube sheets stands out with good potential application in environmental purification. It was found that oxidized CNT sheets removes favorably metal ions in the following order: Pb(II), Cd(II), Co(II), Zn(II), and Cu(II) [31].

Nitrogenation is a popular technique to add nitrogen-included functional groups on the surface of carbon adsorbents. Manufacture of amino functional groups on the surface of CNTs or amino-functionalization of them was recently investigated [32, 33]. Nitrogenation of AC under ammonia atmosphere with preoxidation with HNO_3 has a good effect on Cu(II) adsorption rate, whereas modification of AC using nitric acid, thionyl chloride, and ethylenediamine reaction improves adsorption of Hg(II) ions [34, 35]. Likewise, recently was examined amino-modified biochar for

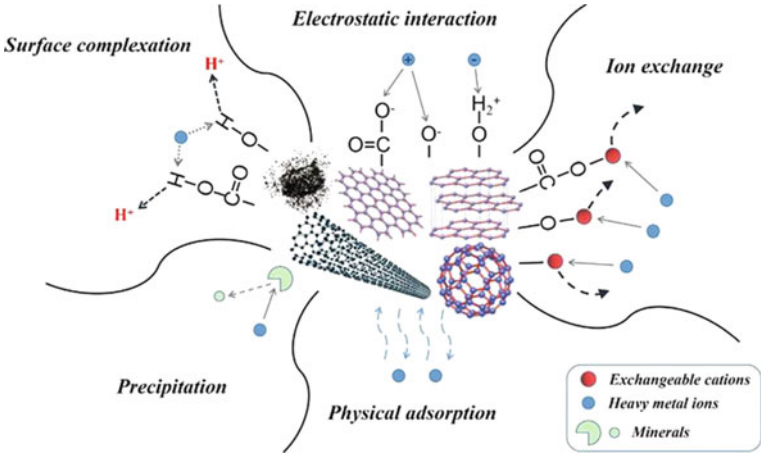

Fig. 1 Mechanisms of heavy metals ions separation [27]

Cu(II) removal and magnetic carbon nanoparticles doped with nitrogen for Cr(III) ions adsorption [36, 37].

Sulfuration allows to add sulfur containing functional groups on the surface of carbon adsorbents. For example, the surface modification of AC derived from nut shells with SO_2 at ambient temperature and AC modified by SO_2 in 900 °C improves process of Cd(II) ions removal [38, 39], as well as AC modification with SO_2 and/or H_2S at varying temperatures increases level of Pb(II) ions separation [40]. Sulfonated graphene is an excellent adsorbent for removal of Cd(II) ions [41] and the sulfhydryl functionalized GO effectively absorbs U(VI) ions from aqueous solutions [27, 42].

Carbon aerogel can be used as an adsorbent in process of heavy metal removal, such as Cd(II), Hg(II), Pb(II), Cu(II), Ni(II), Mn(II), and Zn(II) ions, from aqueous solutions. This process strictly depends on conditions like solution pH, contact time, temperature, and adsorbent dose [43]. Highly efficient technique for lead, arsenic, and mercury removal is usage of functionalized carbon nanotubes sheets with deep eutectic solvents. Two types of carbon nanotubes—containing one graphene sheet (SWCNTS) and containing more than one sheet (MWCNTS)—were examined (Fig. 2) [44].

Carbon composites are characterized by great thermal and chemical stability in inert environment as well as high strength and stiffness potential [45]. One of the composite suitable for heavy metal removal is common granular activated carbon that was covered with polymers subjected to acyl chlorination in order to add soft bases and thiols. This material was investigated toward Cd(II) ions removal from stormwater [46]. Activated carbon (AC) and silica/activated carbon composite (drawn up in rate 2:3) capacities of heavy metal ions removal were compared. Research showed that the silica/AC composite was the most effective sorbent for nickel ions removal from water [47].

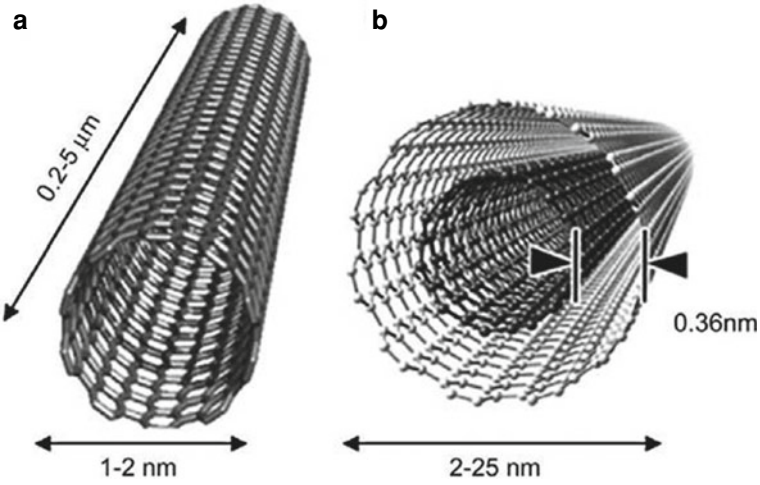

Fig. 2 Two types of CNTs [44]

There was developed carbon paper at magnesium silicate composite films for efficient adsorption of Zn(II) and Cu(II) ions which can be used in adsorption–filtration systems [48]. Low cost of adsorbents removing heavy metals is also important. Due to this issue, a novel composite was created from porous puffed rice carbon with attached metal iron and sulfur for Hg(II) ions removal (Fig. 3) [49].

Next innovative composite is magnetic Fe/Zn-layered double oxide-covered carbon nanotubes, which was successfully used in U(VI) and ^{241}Am(III) removal [50]. Carbon nitride with polydopamine (PDSA) was instilled with polyethyleneimine (PEI) brush to create a composite for U(VI) elimination from aqueous environment. It was also successfully used in ^{241}Am(III), Cu(II), and Pb(II) adsorption [51]. To dispose of As(V) from raw groundwater, zero-valent iron supported by activated carbon (NZVI/AC) was synthesized (Fig. 4) [52]. Nanoscale zero-valent iron particles was also used with carbon nanotubes in filter removing toxic Sb(III), by its transformation in Sb(III) [53] and with porous activated carbon balls for Cr(VI) ions removal from aqueous solutions [54]. Additionally, zero-valent

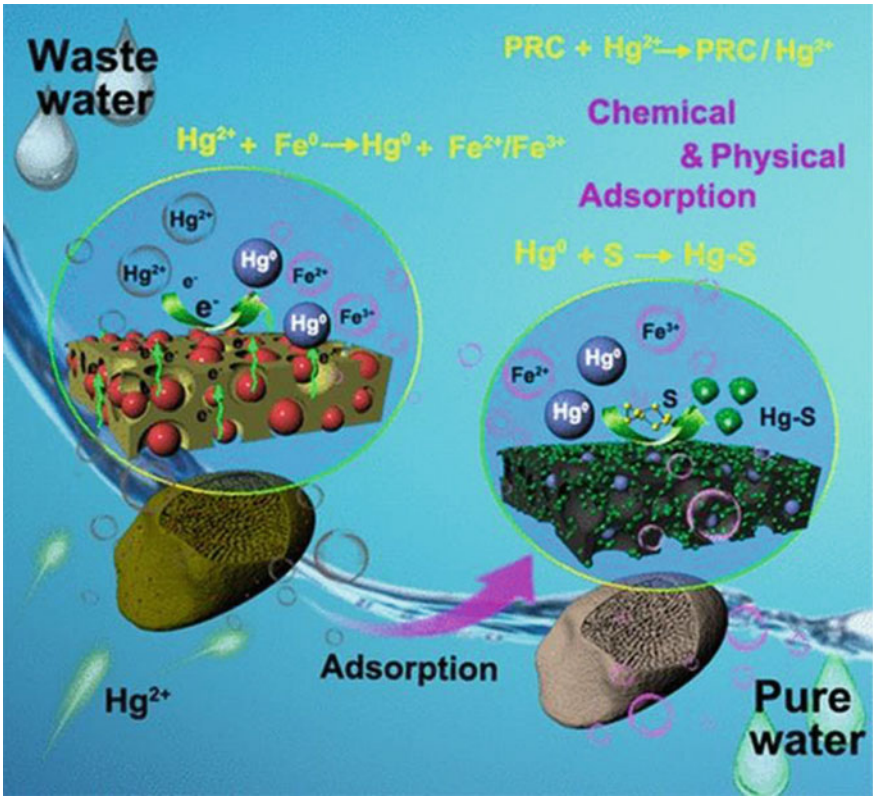

Fig. 3 Schema of Hg(II) ions adsorption on carbon-based composite [49]

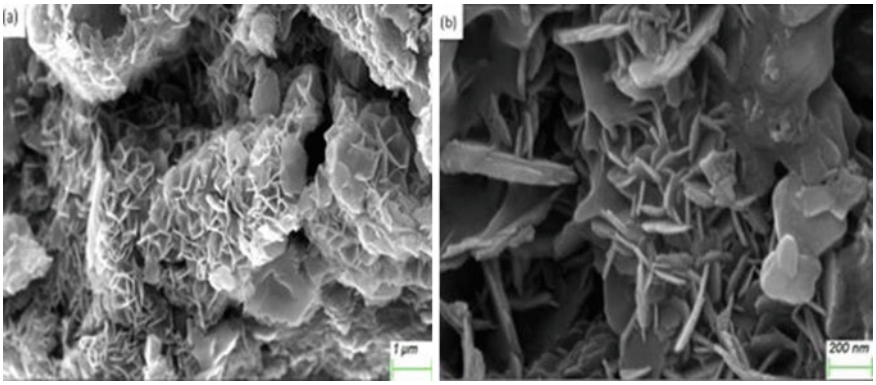

Fig. 4 SEM of NZVI/AC composite: **a** in low extension and **b** in high extension [52]

iron particles was used in Cr(VI) ions removal after their coverage with starch and immobilization on activated carbon surface [55].

Activated carbon derived from peanut shell synthesized with iron oxide (Fe_3O_4/PSAC) gave nano-composite adsorbent, which was very useful in Cr(VI) ions removal [56]. Separation of trace amounts of Pb(II) ions was realized with the use of recently synthesized mesoporous carbon which was doped by boron. Adsorption efficiency of both single carbon and composite was growing as pH value was increasing [57]. Iron cross-linked sodium alginate (SA-Fe) was used to maintain an Fe/C composite (SA-Fe-C) with large content of reducible Fe for Cr(VI) removal [58]. For a similar application, a zero-valent iron@carbon@polianniline was designed [59]. Another adsorbent for water treatment is polyaminoxime-modified magnetic-activated carbon (PAMC). It was used successfully for chromium and thallium separation [60]. The composite of carbon sphere-layered double hydroxide was synthesized and applied for U(VI) removal from wastewater [61].

4 Carbon-Based Composites in Heavy Metal Removal from Solutions Containing Additional Substances

There are rare scientific reports concerning the removal process of heavy metal ions in the systems of mixed adsorbates. One of them is focusing on the usage of titanium dioxide-covered carbon sphere composites in simultaneous graphene oxide (GO) and Cr(VI) ions separation from wastewater [62]. Another promising composite is zero-valent iron based on biochar carrier (nZVI-BC). It was used in Cd(III) and As(III) co-adsorption investigation in process of these ions removal from aqueous systems [63]. There was designed for heavy metal ions and toxic organic compounds elimination adsorbent containing alginate bead and active carbon (AC-AB). It was effectively used to reduce amount of organic compounds like p-Toluic acid. Moreover, it copes

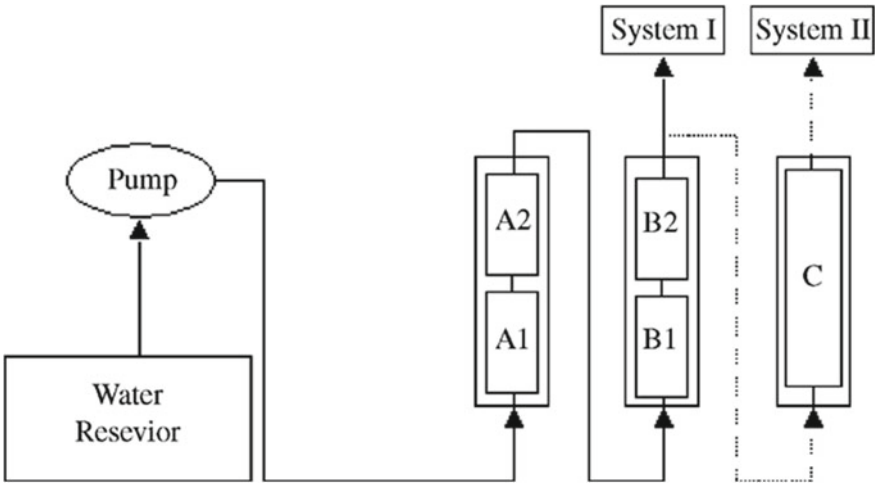

Fig. 5 Water treatment with filter consisting of alginate gel-coated AC-AB: system I—only filter cartridge used and system II—with additional AC-BC filter [64]

with simultaneous deletion of heavy metal ions like Pb(II), Mn(II), Cd(II), Cu(II), Zn(II), Fe(II), Al(III), and Hg(II) and passing of useful and essentials minerals (K^+, Mg^{2+}, Na^+, Ca^{2+}). It also can be easily regenerated by eluents like HNO_3 without losing its adsorption capacity, therefore can be used in cleaning water environment (Fig. 5) [64].

Enhancement of the multi-walled carbon nanotubes by addition of alumina onto their surface (Al_2O_3/MWCNT) leads to the obtaining of valuable adsorbent for simultaneous Cd(II) and trichloroethylene (TCE) removal from groundwater [65]. For separation of co-occurring Cr(VI) ions and aniline, there was designed a composite synthesized with active carbon and chitosan [66].

Fly ash that contains unburned carbon, silica, alumina, and iron oxide was used for separation of copper, nickel, and cadmium ions in the presence of methylene blue (MB) dye [67]. Composites synthesized of graphite phase carbon nitride and zero-valent iron with reduced graphene oxide showed better stability and protection against oxidation. It was used to simultaneous dispose of rhodamine B (RhB) and Cr(VI), and thus, it can be adapt in the future photocatalyst for environmental remediation [68]. Next successful way used in simultaneous elimination of dyes and heavy metals from industrial wastewater is application of novel developed composite made of derived from banana peels porous carbon (BPCA) and porous carbon oxide (BPCAO). It was applied for Co(II) and methylene blue elimination at the same time [69]. Activated carbon derived from walnut wood was used to dispose of Pb(II) and methylene blue dye. It is fast, cheap, and efficient way to purify aquatic environment from hazardous substances [70]. To dispose of Acid Blue 23 (AB25) dye and heavy metal ions, such as Zn(II), Ni(II), and Cd(II) at the same time, the activated carbon with structure modified by calcium solution stamped from egg shells was applied [71].

There was developed magnetic ion-imprinted chitosan with Fe(III) modified with carbon disulfide for contemporary removal of an antibiotic such as tetracycline and a heavy metal ions, namely Cd(II) from aqueous environment [72]. Magnetic and multi-walled carbon nanotubes (MMWCNT) were designed for simultaneous removal of herbicide—atrazine and heavy metal ion—Cu(II) from wastewater [73]. Multi-walled carbon nanotubes were modified with trimethoxysilylpropanethiol (MPTs), hydrazine, ammonium ferric sulfate, and ammonium ferrous sulfate to add Fe_3O_4, amino, and thiol groups on the sidewalls of nanotubes. Next, it was proved that these composites can be used as an adsorbents for zinc, lead, and phenol molecules at the same time [74].

Graphene oxide synthesized with 2,20-dipyridylamine gives a composite that is able to simultaneously remove four heavy metal ions, such as Pb(II), Cd(II), Ni(II), and Cu(II) from aqueous solution [75]. On the other hand, magnetic graphene oxide (MGO) was synthesized and used as an adsorbent for elimination of Cd(II) and ionic dyes, such as methylene blue and orange G (OG) from real water samples [76]. Elimination of atrazine and Cu(II) ions at the same time was achieved by using functionalized (by polyacrylic acid) magnetic-ordered mesoporous carbon (P-MMC). The obtained results were compared with those of ordered mesoporous carbon (OMC) and also with magnetic-ordered mesoporous carbon (MMC). The first material has great potential in hazardous pollutants removal [77].

The carbon–silica composite (C-SiO_2) properties, i.e., aggregation tendency and adsorptive capacity relative to proteins (ovalbumin (OVA) and lysozyme (LSZ)) in the heavy metal ions—copper(II) presence—were determined [78]. It was observed that the C-SiO_2 composite was a good sorbent relative to proteins, especially at protein isoelectric point (pI). Addition of Cu(II) ions causes significant reduction of the protein adsorption on the composite surface. The strongest aggregation of the C-SiO_2 particles was noted in the simultaneous presence of ovalbumin and Cu(II) ions. The same composite was applied in the system of mixed adsorbates—ionic polyacrylamides (PAM) and Cu(II) ions [79]. The obtained results indicated that both Cu(II) ions and ionic polyacrylamide were adsorbed on the composite surface at pH 6. Cu(II) ions presence in the solution results in the increase of the anionic PAM adsorbed amount and in the decrease of the cationic PAM adsorption.

Novel, highly effective adsorbent of Cu(II) ions, hybrid carbon-mineral nanocomposites with metallic cores (Mn/Fe in the case of B-6, Mn—B-8) were examined [80]. The effect of the presence of poly(acrylic acid) (PAA)—a macromolecular compound commonly used in industry and agriculture—was determined. Under examined conditions (at pH 5 and 6), Cu(II) adsorbed amount was significantly higher on the B-8 surface. Moreover, anionic polymer limited the Cu(II) adsorbed amount on the nanocomposite surface.

5 Conclusions

Carbon-based composites show great application potential toward removal of hazardous pollutants from aqueous environment. Innovative modifications of these materials allow to increase the range of possible applications. However, there is only few studies concerning mixed adsorbate systems containing carbon-based composites. Most of them are focused onto heavy metal ions and dyes removal. Few papers showed results concerning elimination of hazardous organic compounds in the presence of heavy metals. For this reason, there is still a need to elaboration of new carbon-based composites toward their wide use for the treatment of the aquatic environment contaminated with various substances and examination of removal mechanisms in more complex adsorbate systems (which are similar composition to the real wastewater).

References

1. Lubin G (1982) Handbook of composites
2. Campbell FC (2010) Structural composite materials
3. Peters ST (1998) Handbook of composites, 2nd edn
4. Rout G, Das P (2003) Effect of metal toxicity on plant growth and metabolism. Agronomie 23:3–11
5. Jaishankar M, Tseten T, Anbalagan N, Mathew BB, Beeregowda KN (2014) Toxicity, mechanism and health effects of some heavy metals. Interdiscip Toxicol 7:60–72
6. Babel S, Kurniawan TA (2003) Low-cost adsorbents for heavy metals uptake from contaminated water: a review. J Hazard Mater 97:219–243
7. Bose P, Bose MA, Kumar S (2002) Critical evaluation of treatment strategies involving adsorption and chelation for wastewater containing copper, zinc, and cyanide. Adv Environ Res 7:179–195
8. ElI B, Vazquez PG, Iucolano F, Caputo D (2007) Chromium removal from water using LTA zeolites: effect of pH. J Colloid Interface Sci 313:574–578
9. Ríos CA, Williams CD, Roberts CL (2008) Removal of heavy metals from acid mine drainage (AMD) using coal fly ash, natural clinker and synthetic zeolites. J Hazard Mater 156:23–35
10. Barakat MA (2008) Adsorption of heavy metals from aqueous solutions on synthetic zeolite. Res J Environ Sci 2:13–22
11. Nah IW, Hwang KY, Jeon C, Choi HB (2006) Removal of Pb ion from water by magnetically modified zeolite. Min Eng 19:1452–1455
12. Vengris T, Binkiene R, Sveikauskaite A (2001) Nickel, copper, and zinc removal from wastewater by a modified clay sorbent. Appl Clay Sci 18:183–190
13. Solener M, Tunali S, Ozcanc AS, Ozean A, Gedikbey T (2008) Adsorption characteristics of lead(II) ions onto the clay/poly(methoxyethyl)acrylamide (PMEA) composite from aqueous solutions. Desalination 223:308–322
14. Abu-Eishah SI (2008) Removal of Zn, Cd, and Pb ions from water by Sarooj clay. Appl Clay Sci 42:201–205
15. Aklil A, Mouflihb M, Sebti S (2004) Removal of heavy metal ions from water by using calcined phosphate as a new adsorbent. J Hazard Mater 112:183–190
16. Moufliha M, Aklila A, Sebti S (2005) Removal of lead from aqueous solutions by activated phosphate. J Hazard Mater 119:183–188

17. Pan BC, Zhang QR, Zhang WM, Pana BJ, Dua W, Lvb L, Zhanga QJ, Xua ZW, Zhang QX (2007) Highly effective removal of heavy metals by polymer-based zirconium phosphate: a case study of lead ion. J Colloid Interface Sci 310:99–105
18. Feng D, Van Deventer JSJ, Aldrich C (2004) Removal of pollutants from acid mine wastewater using metallurgical by-product slags. Sep Purif Technol 40:61–67
19. Gupta VK, Jain CK, Ali I, Sharma M, Saini SK (2003) Removal of cadmium and nickel from wastewater using bagasse fly ash—a sugar industry waste. Water Res 37:4038–4044
20. Alinnor J (2007) Adsorption of heavy metal ions from aqueous solution by fly ash. Fuel 86:853–857
21. Uysal M, Ar I (2007) Removal of Cr(VI) from industrial wastewaters by adsorption. Part I: determination of optimum conditions. J Hazard Mater 149:482–491
22. Genc-Fuhrman H, Wu P, Zhou Y, Ledin A (2008) Removal of As, Cd, Cr, Cu, Ni and Zn from polluted water using an iron based sorbent. Desalination 226:357–370
23. Deliyanni EA, Peleka EN, Matis KA (2007) Removal of zinc ion from water by sorption onto iron-based nanoadsorbent. J Hazard Mater 141:176–184
24. Ghosh UC, Dasgupta M, Debnath S, Bhat SC (2003) Studies on management of chromium(VI)-contaminated industrial waste effluent using hydrous titanium oxide (HTO). Water, Air, Soil Pollut 143:245–256
25. Barakat MA (2005) Adsorption behavior of copper and cyanide ions at TiO_2–solution interface. J Colloid Interface Sci 291:345–352
26. Barakat MA (2011) New trends in removing heavy metals from industrial wastewater. Arab J Chem 4:361–377
27. Yang X, Wan Y, Zheng Y, He F, Yu Z, Huang J, Gao B (2019) Surface functional groups of carbon-based adsorbents and their roles in the removal of heavy metals from aqueous solutions: a critical review. Chem Eng J 366:608–621
28. Al-Khaldi FA, Abusharkh B, Khaled M, Atieh MA, Nasser M, Saleh TA, Agarwal S, Tyagi I, Gupta K (2015) Adsorptive removal of cadmium (II) ions from liquid phase using acid modified carbon-based adsorbents. J Mol Liq 204:55–263
29. Rangel-Mendez J, Streat M (2002) Adsorption of cadmium by activated carbon cloth: influence of surface oxidation and solution pH. Water Res 36:1244–1252
30. Choi H-D, Jung W-S, Cho J-M, Ryu B-G, Yang J-S, Baek K (2009) Adsorption of Cr(VI) onto cationic surfactant-modified activated carbon. J Hazard Mater 166:642–646
31. Tofighy MA, Mohammadi T (2011) Adsorption of divalent heavy metal ions from water using carbon nanotube sheets. J Hazard Mater 185:140–147
32. Alireza Y, Ali R (2018) Synthesis of amino-functionalized carbon nanotubes and their applications. Curr Org Chem 22:1505–1522
33. Das R, Hamid SBA, Ali ME, Ismail AF, Annuar MSM, Ramakrishna S (2014) Multifunctional carbon nanotubes in water treatment: the present, past and future. Desalination 354:160–179
34. Kasnejad MH, Esfandiari A, Kaghazchi T, Asasian N (2012) Effect of pre-oxidation for introduction of nitrogen containing functional groups into the structure of activated carbons and its influence on Cu (II) adsorption. J Taiwan Inst Chem Eng 43:736–740
35. Zhu J, Deng B, Yang J, Gang D (2009) Modifying activated carbon with hybrid ligands for enhancing aqueous mercury removal. Carbon 47:2014–2025
36. Yang G-X, Jiang H (2014) Amino modification of biochar for enhanced adsorption of copper ions from synthetic wastewater. Water Res 48:396–405
37. Shin K-Y, Hong J-Y, Jang J (2011) Heavy metal ion adsorption behavior in nitrogen-doped magnetic carbon nanoparticles: isotherms and kinetic study. J Hazard Mater 190:36–44
38. Tajar AF, Kaghazchi T, Soleimani M (2009) Adsorption of cadmium from aqueous solutions on sulfurized activated carbon prepared from nut shells. J Hazard Mater 165:1159–1164
39. Macıas-Garcıa A, Gomez-Serrano V, Alexandre-Franco M, Valenzuela- Calahorro C (2003) Adsorption of cadmium by sulphur dioxide treated activated carbon. J Hazard Mater 103:141–152
40. Macias-Garcıa A, Valenzuela-Calahorro C, Espinosa-Mansilla A, Bernalte- Garcia A, Gómez-Serrano V (2004) Adsorption of Pb^{2+} in aqueous solution by SO_2-treated activated carbon. Carbon 42:1755–1764

41. Shen Y, Chen B (2015) Sulfonated graphene nanosheets as a superb adsorbent for various environmental pollutants in water. Environ Sci Technol 49:7364–7372
42. Zhao DL, Gao X, Chen SH, Xie FZ, Feng SJ, Alsaedi A, Hayat T, Chen CL (2018) Interaction between U(VI) with sulfhydryl groups functionalized graphene oxides investigated by batch and spectroscopic techniques. J Colloid Interface Sci 524:129–138
43. Meena AK, Mishra GK, Rai PK, Rajagopal C, Nagar PN (2005) Removal of heavy metal ions from aqueous solutions using carbon aerogel as an adsorbent. J Hazard Mater 122:161–170
44. Fiyadh SS, AlSaadi MA, Binti Jaafar WZ, AlOmar MK, Fayaed SS, Binti Mohd NS, El-Shafie A (2019) Review on heavy metal adsorption processes by carbon nanotubes. J Cleaner Prod 230:783–793
45. Buckley JD, Edie DD (1993) Carbon–Carbon materials and composites. Park Ridge, N.J. : Noyes Publications
46. Ko D, Mines PD, Jakobsen MH, Yavuz CT, Hansen HCB, Andersen HR (2018) Disulfide polymer grafted porous carbon composites for heavy metal removal from stormwater runoff. Chem Eng J 348:685–692
47. Karnib M, Kabbani A, Holail H, Olama Z (2014) Heavy metals removal using activated carbon, silica and silica activated carbon composite. Energy Procedia 50:113–120
48. Huang R, He L, Zhang T, Li D, Tang P, Feng Y (2018) Novel carbon paper@magnesium silicate composite porous films: design, fabrication, and adsorption behavior for heavy metal ions in aqueous solution. ACS Appl Mater Interf 10:22776–22785
49. Fang R, Lu Ch, Zhong Y, Xiao Z, Liang Ch, Huang H, Gan Y, Zhang J, Pan G, Xia X, Xia Y, Zhang W (2020) Puffed rice carbon with coupled sulfur and metal iron for high-efficiency mercury removal in aqueous solution. Environ Sci Technol 54:2539–2547
50. Chen H, Zhang Z, Wang X, Chen J, Xu C, Liu Y, Yu Z, Wang X (2018) Fabrication of magnetic Fe/Zn layered double oxide@carbon nanotube composites and their application for U(VI) and ^{241}Am(III) removal. ACS Appl Nano Mater 1:2386–2396
51. Wang P, Yin L, Wang J, Xu C, Liang Y, Yao W, Wang X (2017) Superior immobilization of U(VI) and ^{243}Am(III) on polyethyleneimine modified lamellar carbon nitride composite from water environment. Chem Eng J 326:863–874
52. Zhu H, Shi M, Zhang X, Liu B, Yao D (2020) Adsorption kinetics of arsenic (V) on nanoscale zero-valent iron supported by activated carbon. Nanomaterials 10:1791
53. Liu F, Liu Y, Ding N, Yang S, Shen C, Li F, Sand W (2020) An affordable carbon nanotube filter functionalized with nanoscale zerovalent iron for one-step Sb(III) decontamination. Environ Eng Sci 37:490–496
54. Song Y, Wang L, Lv B, Chang G, Jiao W, Liu Y (2020) Removal of trace Cr(VI) from aqueous solution by porous activated carbon balls supported by nanoscale zero-valent iron composites. Environ Sci Pollut Res 27:7015–7024
55. Ji B, Shu Y, Li Y, Wang J, Shi Y, Chen W (2019) Chromium (VI) removal from water using starch coated nanoscale zerovalent iron particles supported on activated carbon. Chem Eng Commun 206:708–715
56. Bharath G, Rambabu K, Banat F, Hai A, Arangadi AF, Ponpandian N (2019) Enhanced electrochemical performances of peanut shell derived activated carbon and its Fe_3O_4 nanocomposites for capacitive deionization of Cr(VI) ions. Sci Total Environ 691:713–726
57. Liu Y, Xiong Y, Xu P, Pang Y, Du C (2020) Enhancement of Pb (II) adsorption by boron doped ordered mesoporous carbon: isotherm and kinetics modeling. Sci Total Environ 708:134918
58. Wu J, Zheng H, Zhang F, Zeng RJ, Xing BS (2019) Iron-carbon composite from carbonization of iron-crosslinked sodium alginate for Cr(VI) removal. Chem Eng J 362:21–29
59. Gong K, Hu Q, Xiao Y, Cheng X, Liu H, Wang N, Qiu B, Guo Z (2018) Triple layered core–shell ZVI@carbon@polyaniline composite enhanced electron utilization in Cr(VI) reduction. J Mater Chem A 6:11119–11128
60. Adio SO, Asif M, Mohammed A-RI, Baig N, Al-Arfaj AA, Saleh TA (2019) Poly (amidoxime) modified magnetic activated carbon for chromium and thallium adsorption: statistical analysis and regeneration. Process Saf Environ Protect 121:254–262

61. Wang X, Yu S, Wu Y, Pang H, Yu S, Chen Z, Wang S (2018) The synergistic elimination of uranium (VI) species from aqueous solution using bi-functional nanocomposite of carbon sphere and layered double hydroxide. Chem Eng J 342:321–330
62. Wang J, Liang Y, Jin Q, Hou J, Liu B, Li X, Wang X (2017) Simultaneous removal of graphene oxide and chromium(VI) on the rare earth doped titanium dioxide coated carbon sphere composites. ACS Sustain Chem Eng 5:5550–5561
63. Yang D, Wang L, Li Z, Tang X, He M, Yang S, Xu J (2019) Simultaneous adsorption of Cd(II) and As(III) by a novel biochar-supported nanoscale zero-valent iron in aqueous systems. Sci Total Environ 708:134823
64. Park HG, Kim TW, Chae MY, Yoo I-K (2007) Activated carbon-containing alginate adsorbent for the simultaneous removal of heavy metals and toxic organics. Process Biochem 42:1371–1377
65. Liang J, Liu J, Yuan X, Dong H, Zeng G, Wu H, Wang H, Liu J, Hua S, Zhang S, Tu Z, He Z, He Y (2015) Facile synthesis of alumina-decorated multi-walled carbon nanotubes for simultaneous adsorption of cadmium ion and trichloroethylene. Chem Eng J 273:101–110
66. Huang R, Yang B, Liu Q, Liu Y (2013) Simultaneous adsorption of aniline and Cr(VI) ion by activated carbon/chitosan composite. J Appl Polym Sci 131:39903
67. Visa M, Bogatu C, Duta A (2010) Simultaneous adsorption of dyes and heavy metals from multicomponent solutions using fly ash. Appl Surf Sci 256:5486–5491
68. Wang X, Lu M, Ma J, Ning P (2019) Preparation of air-stable magnetic g-C_3N_4@Fe0-graphene composite by new reduction method for simultaneous and synergistic conversion of organic dyes and heavy metal ions in aqueous solution. Sep Purif Technol 212:586–596
69. Yu D, Wang L, Wu M (2018) Simultaneous removal of dye and heavy metal by banana peels derived hierarchically porous carbons. J Taiwan Inst Chem Eng 93:543–553
70. Ghaedi M, Mazaheri H, Khodadoust S, Hajati S, Purkait MK (2015) Application of central composite design for simultaneous removal of methylene blue and Pb^{2+} ions by walnut wood activated carbon. Spectrochim Acta Part A: Molec Biomolec Spectrosc 135:479–490
71. Tovar-Gómez R, Rivera-Ramírez DA, Hernández-Montoya V, Bonilla-Petriciolet A, Durán-Valle CJ, Montes-Morán MA (2012) Synergic adsorption in the simultaneous removal of acid blue 25 and heavy metals from water using a $Ca(PO_3)^{2-}$ modified carbon. J Hazard Mater 199–200:290–300
72. Chen A, Shang C, Shao J, Lin Y, Luo S, Zhang J, Huang H, Lei M, Zeng Q (2017) Carbon disulfide-modified magnetic ion-imprinted chitosan-Fe(III): a novel adsorbent for simultaneous removal of tetracycline and cadmium. Carbohydr Polym 155:19–27
73. Tang W-W, Zeng G-M, Gong J-L, Liu Y, Wang X-Y, Liu Y-Y, Liu Z-F, Chen L, Zhang X-R, Tu D-Z (2012) Simultaneous adsorption of atrazine and Cu:(II) from wastewater by magnetic multi-walled carbon nanotube. Chem Eng J 211–212:470–478
74. Jiang L, Li S, Yu H, Zou Z, Hou X, Shen F, Yao X (2016) Amino and thiol modified magnetic multi-walled carbon nanotubes for the simultaneous removal of lead, zinc, and phenol from aqueous solutions. Appl Surf Sci 369:398–413
75. Zare-Dorabei R, Ferdowsi SM, Barzin A, Tadjarodi A (2016) Highly efficient simultaneous ultrasonic-assisted adsorption of Pb(II), Cd(II), Ni(II) and Cu(II) ions from aqueous solutions by graphene oxide modified with 2,2'-dipyridylamine: Central composite design optimization. Ultrason Sonochem 32:265–276
76. Deng J-H, Zhang X-R, Zeng G-M, Gong J-L, Niu Q-Y, Liang J (2013) Simultaneous removal of Cd(II) and ionic dyes from aqueous solution using magnetic graphene oxide nanocomposite as an adsorbent. Chem Eng J 226:189–200
77. Zhou Y, Zhang F, Tang L, Zhang J, Zeng G, Luo L, Liu X (2017) Simultaneous removal of atrazine and copper using polyacrylic acid-functionalized magnetic ordered mesoporous carbon from water: adsorption mechanism. Sci Rep 7:43831
78. Szewczuk-Karpisz K, Wiśniewska M, Medykowska M, Bogatyrov V, Sokołowska Z (2020) Adsorption layer structure on the surface of carbon-silica composite in the presence of proteins of different internal stability and Cu(II) ions—the effect on solid aggregation. J Mol Liq 309:113072

79. Szewczuk-Karpisz K, Bogatyrov VM, Galaburda M, Sokołowska Z (2020) Study on adsorption and aggregation in the mixed system of polyacrylamide, Cu(II) ions and innovative carbon-silica composite. Polymers 12:961
80. Szewczuk-Karpisz K, Wiśniewska M, Medykowska M, Galaburda MV, Bogatyrov VM, Oranska OI, Błachnio M, Oleszczuk P (2021) Simultaneous adsorption of Cu(II) ions and poly(acrylic acid) on the hybrid carbon-mineral nanocomposites with metallic cores. J Hazard Mater 412: 125138

On the Crystallization Ability of $80GeSe_2$-$20Ga_2Se_3$ Glasses

H. Klym, I. Karbovnyk, and I. Vasylchyshyn

1 Introduction

The current state of the art of the modern photonics indicates on significant importance of glassy functional materials with improved exploitation properties [1–5]. Main developments concerning preparation of such materials are known to include different methods of their technological and post-technological structural modification using external factors, such as thermal annealing, high-energy irradiation, and laser-beam treatment. [6, 7]. However, the technical possibilities of these modification methods are significantly restricted by physical–chemical peculiarities of vitreous state with character effects of natural physical aging (both physical and chemical), functional non-reproducibility and thermodynamic instability in view of high affinity to spontaneous crystallization and chemical reactivity [8–11].

That is why, at the present, glass-science specialists and device manufacturers are more and more dealing with traditional chemical–compositional modification based on doping possibilities with additional components introduced in a glass matrix to attain new, sometimes unusual properties. Thus, for example, the principal functionality of chalcogenide glasses (ChG) revealed in their excellent IR transparency (in a wide spectral region, including both commercially important atmospheric telecommunication windows at 3–5 and 8–12 μm up to space telecommunication domain at 20–25 μm), can be effectively combined with high transparency

H. Klym (✉) · I. Vasylchyshyn
Lviv Polytechnic National University, S. Bandery Str., 12, Lviv 79013, Ukraine
e-mail: halyna.i.klym@lpnu.ua

I. Vasylchyshyn
e-mail: Ivanna.i.vasylchyshyn@lpnu.ua

I. Karbovnyk
Ivan Franko National University of Lviv, Lviv, Ukraine

O. Fesenko and L. Yatsenko (eds.), *Nanomaterials and Nanocomposites, Nanostructure Surfaces, and Their Applications*, Springer Proceedings in Physics 263, https://doi.org/10.1007/978-3-030-74741-1_5

of halide compounds in a visible range by developing mixed chalcogenide–halogenide (chalcohalide) glassy alloys [12–14]. But this idea seems to be impossible for successful performance at all because chemical doping substances possess, as a rule, too poor solubility in ChG systems. To ensure optimal exploitation properties in such mixed glassy solids, their "pure" atomic sub-system should be effectively "working" along with atomic-deficit sub-system. This is proper, in part, to ChG of quasi-binary stoichiometric $GeSe_2$-Ga_2Se_3 cut-section.

Unique multifunctional possibilities of novel photonic devices based on this large $GeSe_2$-Ga_2Se_3 ChG family has appeared owing to luminescence phenomena, e.g., intense radiative photoemission of some rear-earth doping additives introduced in ChG [15–17], ion-conductive phenomena: abnormal conductivity of Li^+ ions in solid electrolytes [18–20], diffusive-related phenomena: reversible self-healing effects observed in photo-induced refraction owing to ion-conducting AgI additives [21, 22].

In all the above cases, just optimized inner-pore structure of basic $GeSe_2$-Ga_2Se_3 ChG is a determinant of their final glassy-like state—its stretched functionality connected with possibility to accommodate alien atoms and their groups. It is of high importance that under controlled halide additives these ChG can be easily transformed in chalcogenide ceramics transparent in IR region, as it is well demonstrated in [23].

Despite successes achieved, generally due to empirical determination of compositional boundaries for doping and component variation in stoichiometric $GeSe_2$-Ga_2Se_3 ChG, which allow a full absence of monolithic crystallization effects for germanium bi-chalcogenides in a wide temperature range, the functionality mechanism of these systems left unknown up to now, significantly limited the further progress in the modern IR photonics.

In our previous works [24–26], we investigated the inner free-volume structure in $80GeSe_2$-$20Ga_2Se_3$ chalcogenide glass with controlled crystallization, after thermal annealing above glass transition temperature over different time frames. We also analyzed interface void volumes formed by nanocrystals using the $\times 3$– $\times 2$-decomposition procedure described in [27], optical properties in IR region [28, 29], structural transformation caused by crystallization in the Ge-Ga-S(CsCl) glass–ceramics [30–32], effects of radiation in nanocomposites [33, 34], functional ceramics [35], etc. The goal of this work is described and generalize in one-work peculiarities of crystallization ability of the $80GeSe_2$-$20Ga_2Se_3$ ChG caused by thermal treatment for 10, 25, 50, 80, and 100 h using X-ray diffraction (XRD) probes.

2 Sample Preparation and Experimental Setup

The $80GeSe_2$-$20Ga_2Se_3$ ChG were prepared from melting mixture of highly pure raw materials (Ge, Ga, and Se: 99.999%) in sealed silica ampoule kept under 10^{-6} Pa vacuum detail described in [24, 25, 36]. The ampoule of 9 mm inner diameter was placed in a rocking furnace. The raw materials were heated from 20 to 850 °C using 2 °C/min heating rate and maintained at this temperature for 12 h at least. Then, the

silica tube was quenched in water at room temperature, annealed 30 °C below the glass transition temperature (T_g = 370 °C) for 3 h to minimize inner strains, and finally slowly cooled down to room temperature. Glass rods were cut into slices of 1 mm thickness and polished for further optical measurements [36].

The crystallization of the $80GeSe_2$-$20Ga_2Se_3$ was performed with a single step of heat treatment at T_g + 10 °C. This temperature has been chosen as an optimal temperature of ceramization as it permits to control the generation by simultaneous nucleation and growth of nanoparticles within the glassy matrix according to the heat treatment time [24]. Thus, glass samples were placed in a ventilated furnace where the accuracy of temperature is ±2 °C for various time varying from 10 to 100 h.

XRD measurements with $CuK_{\alpha 1}$ radiation were performed to determine crystalline phases in the studied samples. Solid-rock plates of powdered $80GeSe_2$-$20Ga_2Se_3$ ChG deposited on amorphous substrate were prepared to arrange experiments in optimal transmittance geometry [24, 25]. The measured X-ray beam intensities and reflection angles 2θ were obtained using automatic STOE STADI P diffractometer ("STOE & Cie GmbH, Germany) with a linear position-precision detector. Experimental linear absorption coefficients were determined as logarithmic ratio of primary beam intensities after passing through background and studied samples. All measurements were conducted in 2θ-step regime, the profiles of peaks being refined using WinPLOTR and PowderCell software [37].

3 Results and Discussion

3.1 XRD Study at Crystallization of $GeSe_2$–Ga_2Se_3 Glasses

For precise calculations the change in preFSDP and FSDP (which is manifested in the change in intensity, shift of the maximum FSDP, and in the change offull width at half maximum (FWHM) for normalized samples, the procedure of description of the profile of peaks was carried out by means of the WinPLOTR software package with the subsequent mathematical processing of FSDP parameters for semi-morphic halos [38, 39]. In addition, for $80GeSe_2$-$20Ga_2Se_3$ glasses and samples crystallized at 10, 25 and 50 h, the calculation of microstructural parameters (sizes of coherent scattering domains, which in the approximation can be considered as the grain size of the phase and internal stresses) in the isotropic approximation by the methods of integral width of diffraction peaks was performed [40]. Selection of the instrumental component of device is carried out by the primary beam.

In results of calculations, the following microstructural parameters were obtained (see Tables 1, 2, 3, and 4; Figs. 1, 2, 3, and 4): position of the halo maximum (2θ) for λ = 1.540598 Å, $CuK_{\alpha 1}$ radiation; standard deviation (sigma 2θ); peak area (I); the full width of the half-height diffraction peak (FWHM); maximum peak intensity (I_{max}); average maximum domain size (AS_{av}) average maximum internal voltage

Table 1 Microstructural parameters of the $80GeS_2$-$20Ga_2S_3$ glasses before annealing obtained by XRD method

Peak no.	2θ, °	$\delta 2\theta$, °	I	δI	FWHM, °2θ	δFWHM	I_{max}	AS_{av}, Å
1	5.993546	0.104791	86.69	8.66	2.161456	0.267143	670.9	32.84
2	13.850087	0.008325	2963.86	13.30	3.702218	0.021589	1262.49	19.28
3	28.926701	0.005937	7714.85	19.11	5.318455	0.017024	1703.02	13.76
4	50.15329	0.012372	5187.05	17.10	7.745533	0.032889	962.56	10.10
Peak no.	R(Ernest), Å		$S_{av,max}$, %		Q, $Å^{-1}$		ΔQ, $Å^{-1}$	
1	18.12304891		2243.21		0.426435857		0.15384683	
2	7.858189031		1656.77		0.983473147		0.263484054	
3	3.793502631		1120.84		2.037251229		0.378440374	
4	2.235488741		899.81		3.457104371		0.550919907	
Peak no.	R, Å		L, Å		D, Å		V, $Å^3$	
1	14.73418615		40.84052508		11.04503742		705.7089266	
2	6.388771588		23.84654861		4.78914957		57.53064434	
3	3.08414849		16.60284083		2.311938721		6.472215842	
4	1.817470526		11.40489791		1.362411861		1.32449183	

Table 2 Microstructural parameters of the $80GeS_2$-$20Ga_2S_3$ glasses after annealing at 380 °C for 10 h obtained by XRD method

Peak no.	2θ, °	$\delta 2\theta$, °	I	δI	FWHM, °2θ	δFWHM	I_{max}	AS_{av}, Å
1	5.671628	0.082769	146.65	9.35	2.672626	0.209961	661.57	26.91
2	13.860976	0.008219	2808.85	12.80	3.608578	0.021116	1239.79	20.05
3	28.839653	0.005744	7687.95	18.93	5.256596	0.016317	1718.12	14.10
4	50.112957	0.013039	5180.52	17.11	8.160301	0.034196	935	9.71
Peak no.	R(Ernest), Å		$S_{av,max}$, %		Q, $Å^{-1}$		ΔQ, $Å^{-1}$	
1	19.15078869		2893.06		0.403550894		0.190224617	
2	7.852045843		1592.13		0.984242585		0.256821998	
3	3.804708858		1096.52		2.031250796		0.374041837	
4	2.237171629		936.26		3.454503801		0.580372677	
Peak no.	R, Å		L, Å		D, Å		V, $Å^3$	
1	15.56974695		33.03034794		11.67139032		832.7062339	
2	6.383777126		24.46513678		4.785405623		57.39582498	
3	3.093259243		16.79808161		2.318768322		6.529743347	
4	1.818838728		10.82612182		1.363437492		1.327485337	

Table 3 Microstructural parameters of the $80GeS_2$-$20Ga_2S_3$ glasses after annealing at 380 °C for 25 h obtained by XRD method

Peak no.	2θ, °	$\delta 2\theta$, °	I	δI	FWHM, °2θ	δFWHM	I_{max}	AS_{av}, Å
1	6.037445	0.087041	130.42	9.92	2.529246	0.244078	609.12	27.83
2	14.13869	0.009257	2316.14	19.94	3.533708	0.029669	1065.19	20.04
Peak no.	R(Ernest), Å		$S_{av,max}$, %		Q, $Å^{-1}$		ΔQ, $Å^{-1}$	
1	17.99139464		2627.96		0.429556355		0.180021225	
2	7.698575459		1561.67		1.003863369		0.251495217	
Peak no.	R, Å		L, Å		D, Å		V, $Å^3$	
1	14.62715015		34.90246935		10.96480112		690.4405862	
2	6.259004456		24.98331925		4.691873561		54.0957238	

Table 4 Microstructural parameters of the $80GeS_2$-$20Ga_2S_3$ glasses after annealing at 380 °C for 25 h obtained by XRD method

Peak no.	2θ, °	$\delta 2\theta$, °	I	δI	FWHM, °2θ	δFWHM	I_{max}	AS_{av}, Å
1	6.19921	0.063222	258.16	11.75	3.01856	0.182818	642.04	21.85
2	14.286976	0.009529	2322.37	19.67	3.402784	0.032427	1056.78	19.51
Peak no.	R(Ernest), Å		$S_{av,max}$, %		Q, $Å^{-1}$		ΔQ, $Å^{-1}$	
1	17.52235933		3259.49		0.441054641		0.214841161	
2	7.619079178		1587.74		1.014337523		0.242180103	
Peak no.	R Å		L Å		D Å		V $Å^3$	
1	14.24582063		29.24572403		10.67894897		637.8367961	
2	6.194373333		25.94426723		4.643424792		52.43717465	

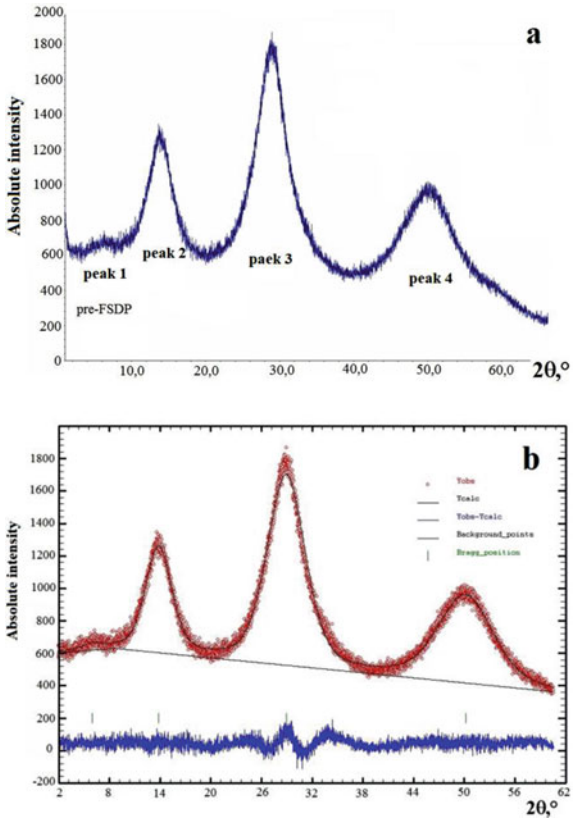

Fig. 1 Probable change of preFSDP and FSDP for $80GeSe_2$-$20Ga_2Se_3$ glasses before treatment (**a**) and after the procedure of describing the peak profile using WinPLOTR (**b**)

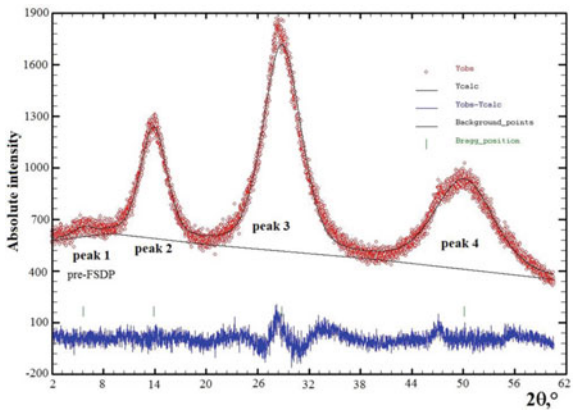

Fig. 2 Probable change of preFSDP and FSDP for $80GeSe_2$-$20Ga_2Se_3$ glasses annealed at 380 °C for 10 h after the procedure of describing the peak profile using WinPLOTR

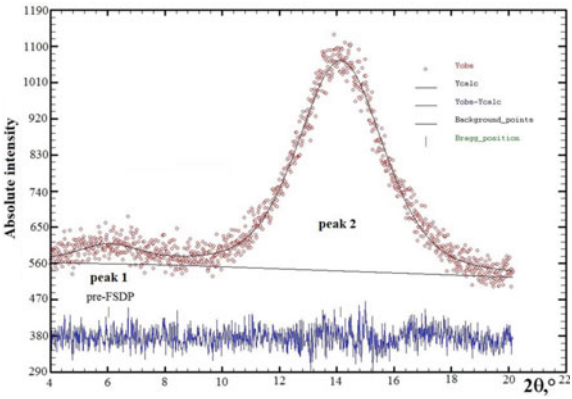

Fig. 3 Probable change of preFSDP and FSDP for $80GeSe_2$-$20Ga_2Se_3$ glasses annealed at 380 °C for 25 h after the procedure of describing the peak profile

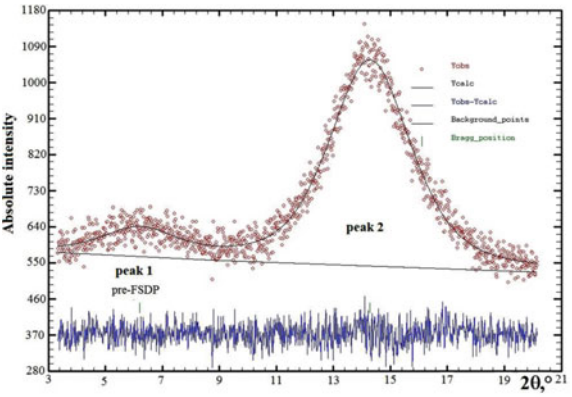

Fig. 4 Probable change of preFSDP and FSDP for $80GeSe_2$-$20Ga_2Se_3$ glasses annealed at 380 °C for 50 h after the procedure of describing the peak profile using WinPLOTR

($S_{av.max}$); the radii of the coordination spheres (R (Ernest); position of the halo (Q); FWHM of halo (ΔQ).

It should be noted that in ChG thermally annealed for 25 and 50 h crystallization processes begin to occur, which are reflected in changes of peak 3 (see Fig. 2) transforming from amorphous to crystalline [24, 25].

The generalized results of XRD results for $80GeSe_2$-$20Ga_2Se_3$ glasses before and after thermal annealing at 380 °C for 10, 25, and 50 h, in comparison with the theoretical reflexes of the known crystallization $GeGa_4Se_8$, $GeSe_2$, and Ga_2Se_3 phases are shown in Figs. 5 and 6.

Polythermal and isothermal cut-sections of crystalline phases possible in Ge-Ga-Se system were studied in [41]. In part, the ternary $GeGa_4Se_8$ phase ($Ga_{0.5}Ge_{0.13}Se$) having polymorph transformation near ~898 K (625 °C) was identified, the high-temperature modification being crystallized in ZnS structural type (cubic syngony, F-43 m space group, lattice parameter a ~5.45 Å, most essential XRD reflexes of $CuK_{\alpha 1}$ radiation being grouped near $2\theta = 28°$, 47°, 56°, 68.5°, 76° 87.5°), while low temperature one being of unknown structure but of close subcell parameter a ~

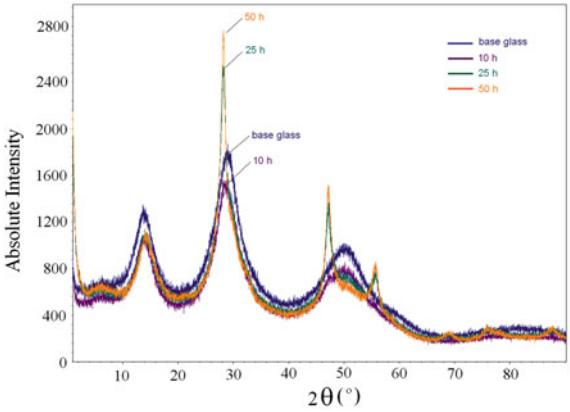

Fig. 5 Comparison of experimental XRD profiles for $80GeSe_2$-$20Ga_2Se_3$ glass before annealing (base glass, 0 h) and annealed at 380 °C for 10, 25, and 50 h

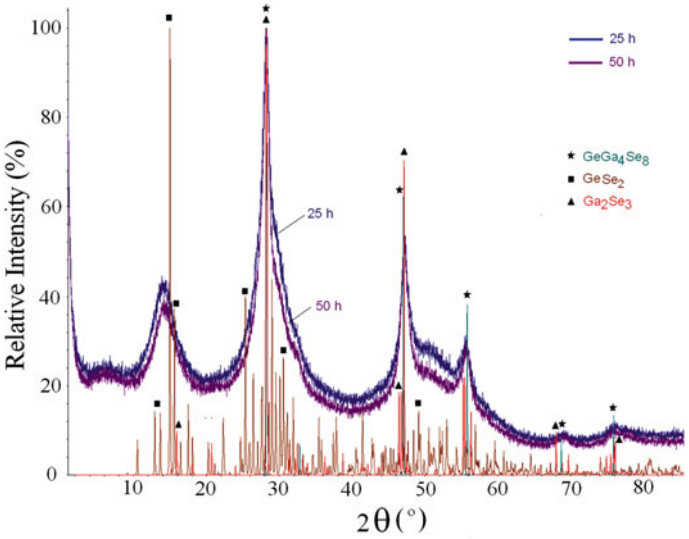

Fig. 6 Comparison of XRD patterns of $80GeSe_2$-$20Ga_2Se_3$ glass annealed at 380 °C for 25 and 50 h with theoretical patterns of crystallized $GeGa_4Se_8$, $GeSe_2$, and Ga_2Se_3 phases

5.461 Å type (main XRD reflexes of $CuK_{\alpha 1}$ radiation are observed near $2\theta = 28°$, 47°, 56°). Two other ternary phases $GeGa_2Se_3$ and $GeGaSe_3$ were also detected after 25 or 50 h of annealing. General structural similarity between these phases as well as binary Ga_2Se_3 (main XRD reflexes of $CuK_{\alpha 1}$ radiation are observed near $2\theta = 28°$, 47°, 55.5°) and $GeSe_2$ phases (main XRD reflexes of $CuK_{\alpha 1}$ radiation are observed near $2\theta = 15°$, 25°, 29°) of different modifications is their tetrahedral arrangement based on (Ge, Ga)[Se_4] tetrahedra.

It was established previously [42] that reproducible glass ceramics based on $80GeSe_2$-$20Ga_2Se_3$ alloy can be obtained using appropriate heat treatment at the temperature of 380 °C. At short heating durations up to 25–50 h, the small nanosized particles of $GeGa_4Se_8$ of about 10 nm appear. These crystallized inclusions aggregates in larger ones of about 100 nm in size uniformly distributed within the glass structure, the nanocrystallites of $GeSe_2$ phase being detected in addition to growing content of $GeGa_4Se_8$ ones [42]. Our XRD results confirm, in principal features, these conclusions.

With respect to our results, the extended gallous in XRD patterns of non-annealed $80GeSe_2$-$20Ga_2Se_3$ glasses near $2\theta = 12°$, 30° and 50° (Fig. 6) can be ascribed to typical signatures of amorphous structure. Obviously, these peaks are predetermined by cumulative inputs of some pre-cursors caused by different phases possible in this cut-section.

Annealing at 380 °C for 10 h does not change significantly the structure of ChG, since no sharp crystalline patters appear in their XRD patterns apart from noticeable decrease in gallous. Therefore, we can assume that even under this short-time heat treatment there are some transformations in the intrinsic structure of ChG, which do not contribute essentially to crystallization ordering. Nevertheless, slight decrease in the gallous intensities indicates that some changes are still occurred in this ChG. We can speculate that underlying transformations can be probably associated with inner phase separation in $80GeSe_2$-$20Ga_2Se_3$ cut-section on individual boundary components (stoichiometric binary $GeSe_2$ and Ga_2Se_3), which serve as prerequisites for further disproportionality reaction to form ternary $GeGa_4Se_8$ phase:

$$GeSe_2 + 2Ga_2Se_3 \rightarrow GeGa_4Se_8. \quad (1)$$

It means that stoichiometry of base $80GeSe_2$-$20Ga_2Se_3$ cut-section provides an excellent condition for crystallization of $GeGa_4Se_8$ phase through segregation of previously extracted $GeSe_2$ and Ga_2Se_3 phases accompanied by formation of $GeSe_2$-rich remainder. Since stoichiometric germanium selenide $GeSe_2$ is out of glass-forming region [30], under quite large amount of latter it will be extracted in a separate crystallized phase.

With increasing annealing time from 10 to 25 h and further to 50 h, the well-pronounced crystalline peaks at $2\theta \sim 28°$ are observed (see Figs. 5 and 6). The positions of this peak are in good agreement with $GeGa_4Se_8$ and Ga_2Se_3 phase indexation. Both phases have sharp reflexes near $2\theta \sim 28°$, which cannot be well separated [41]. In fact, all principal XRD peaks of $GeGa_4Se_8$ and Ga_2Se_3 phases coincide, so we considered them in crystallized $80GeSe_2$-$20Ga_2Se_3$ glass as signatures of both these phases (Ga_2Se_3 and $GeGa_4Se_8$). The broadness of this peak ($2\theta \sim 28°$) confirms the presence of dispersed nanoparticles in a glassy matrix as nanocrystalline inclusions of near 9–10 nm in sizes (determined in respect to Debay–Scherrer equation [43]).

The maximums associated with $GeSe_2$ phase appear on the XRD patterns of thermally annealed $80GeSe_2$-$20Ga_2Se_3$ glass too, but (in contrast to [42]) it cannot be well distinguished as separate crystalline peaks even for long annealing durations (50 h). It means that $GeSe_2$ crystals appear only in a small amount, probably as

surface inclusions [24, 25]. It can be imagined that $GeSe_2$ crystals grow among glass remainder after Ga_2Se_3 and $GeGa_4Se_8$ crystals extraction as a result of ceramization process governed by reaction (1).

The XRD peaks of ChG annealed during 25 and 50 h reveal quick enhancement at small scattering angles $2\theta < 1.5°$ that can be probably attributed to some kinds of fractal structures [41].

It is shown that semi-amorphous halos present on XRD patterns for non-annealed ChG and annealed for 10 h do not disappear. This is clearly seen in a detailed consideration of the region of the two maximum peaks at comparison (Fig. 7). In general, the picture is fully consistent with the results presented in [25]. For samples annealed for 25 and 50 h in the region of small diffraction angles 2θ, there is an increase in intensity, which indicates that fractal formations in the glass during annealing do not disappear but become larger (Fig. 8).

However, at detailed analysis of the maximum halo, it can be seen that even with a small heat treatment time (10 h), changes begin to occur in the glass structure (Fig. 9)

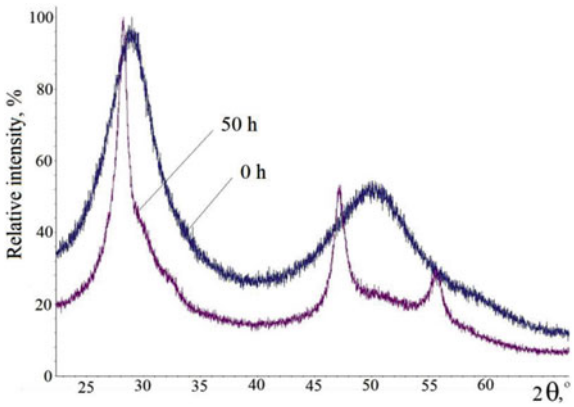

Fig. 7 Comparison of diffraction patterns for non-annealed (0 h) ChG and annealed for 50 h

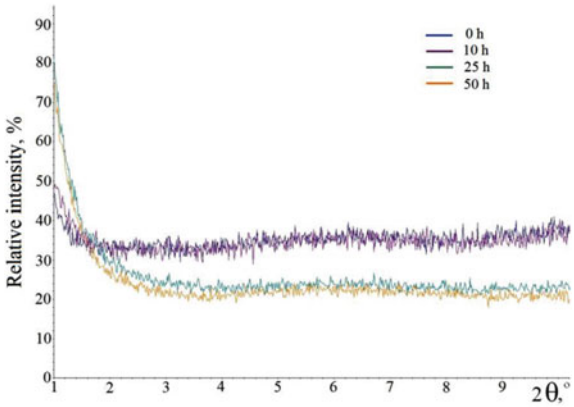

Fig. 8 Comparison of the small-angle section of XRD patterns for non-annealed (0 h) ChG and annealed for 10, 25 and 50 h

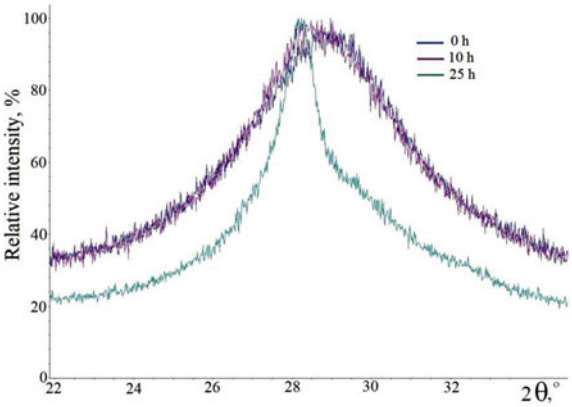

Fig. 9 Comparison maximum reflection on the XRD patterns for non-annealed (0 h) ChG and annealed for 10 and 50 h

accompanied by crystallization of the $GeGa_4Se_8$ phase in the glass structure from the chaotic arrangement of Ga tetrahedra [Se_4], Ge [Se_4]. These are characterized only by the short order, and there is a transition to the formation of the long order, characteristic of the crystal $GeGa_4Se_8$ structure).

Further increase for annealing duration to 80 and 100 h does not affect the diffraction maxima reflecting mainly the formation of triple $GeGa_4Se_8$ and double Ga_2Se_3 phases, similar to $80GeSe_2$-$20Ga_2Se_3$ glass annealed for 50 h (Fig. 10). Thus, process of crystallization and formation of a long-range order during this time of annealing does not occur. The first maximum of the semi-amorphous halo at ~14.6° 2θ (Fig. 11)

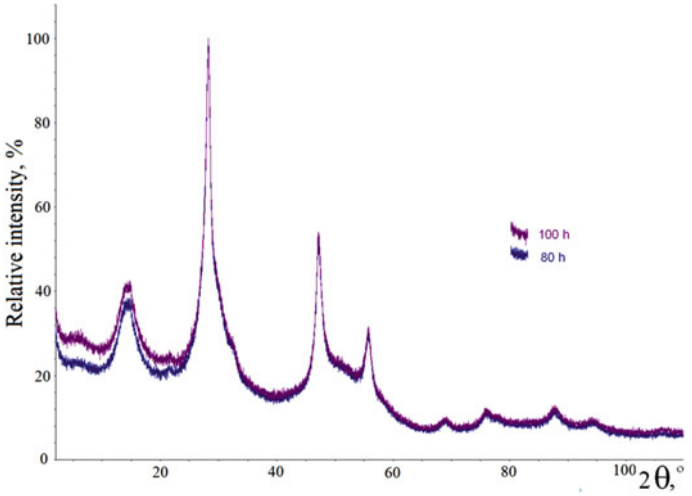

Fig. 10 XRD patterns of non-annealed (0 h) $80GeSe_2$-$20Ga_2Se_3$ glass and annealed at 380 °C for 80 and 100 h

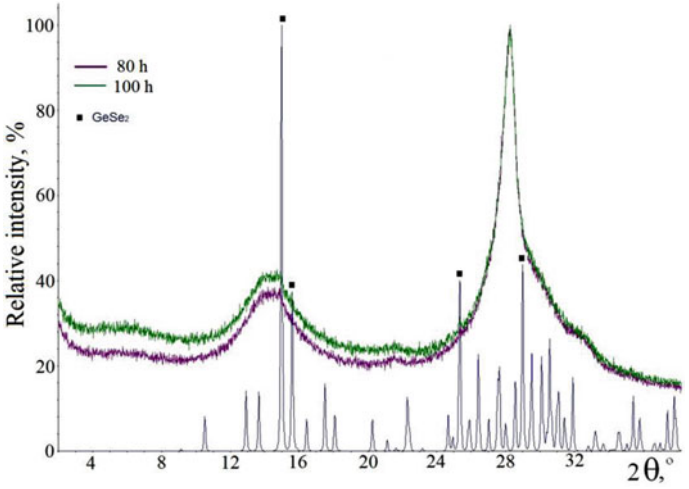

Fig. 11 Comparison of the small-angle section of experimental XRD patterns for $80GeSe_2$-$20Ga_2Se_3$ glass annealed for 80 and 100 h with theoretical reflexes of the $GeSe_2$ phase (monoclinic syngony)

corresponds to the maximum intensity reflection (002) of $GeSe_2$ phase (monoclinic syngony and spatial group $P2_1/c$).

For ChG annealed at 80 and 100 h additional analysis of crystallization, Ga_4GeSe_8 and Ga_2Se_3 phases were performed. Taking into account the state diagram of the Ga-Se system, the temperature of existence of cubic Ga_2Se_3 (high-temperature $Ga_{0.67}Se$) begins above $T = 730$ °C. Below this temperature is a low-temperature monoclinic modification of Ga_2Se_3. Distinguish between monoclinic and cubic modification of the Ga_2Se_3 phase is possible only on samples with a high degree of crystallinity.

Assuming that pure high-temperature Ga_2Se_3 crystallizes in the studied samples, it is most likely a modification of α-Ga_2Se_3 (for which $a \sim 5.44$ Å). However, taking into account that the peaks are extended, simultaneously with α-modification of Ga_2Se_3, the γ-modification of Ga_2Se_3 is also possible (Fig. 12).

However, it should also pay attention to the raising of the background on the XRD patterns (indicated by ellipses in Fig. 13).

These uplifts correspond to the peaks from the experimental XRD patterns for high-temperature and low-temperature modifications of Ga_4GeSe_8 phase (Fig. 14). Otherwise, it can assume that the ChG samples have a crystallized high-temperature α-Ga_2Se_3 phase (stabilization with minor impurities of Ge reduces its temperature from 730 to 385 °C, which corresponds to the annealing of glass) and the amorphous phase of glass, which is responsible for halo.

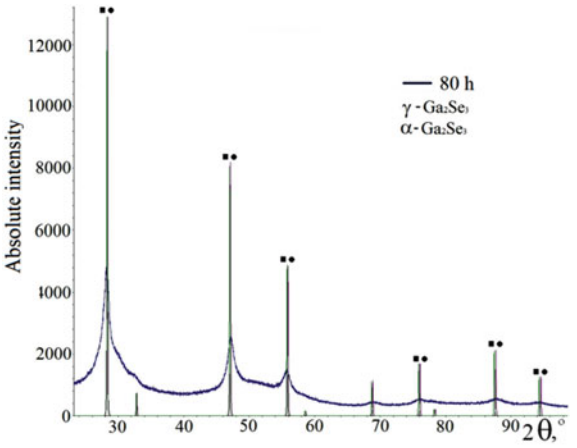

Fig. 12 Comparison of experimental XRD pattern for $80GeSe_2$-$20Ga_2Se_3$ glass annealed for 80 h with theoretical reflexes of α-Ga_2Se_3 та γ- Ga_2Se_3 phases

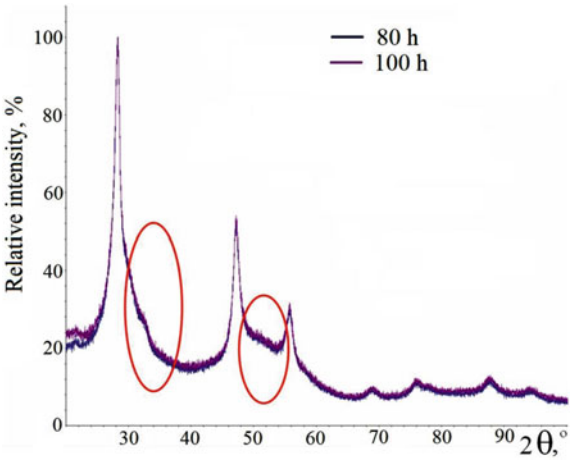

Fig. 13 Raising background on experimental XRD patterns of $80GeSe_2$-$20Ga_2Se_3$ glass annealed for 80 h and 100 h

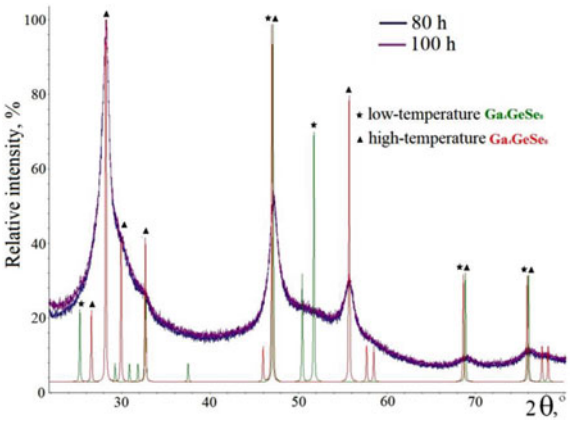

Fig. 14 Width of the peak at $2\theta \sim 28.22°$ indicates the presence in the crystal matrix of dispersed nanoparticles in the form of nanocrystalline inclusions with a size of 9–10 nm (determined by the Debye-Scherer equation)

4 Conclusions

Crystallization ability of the $80GeSe_2$-$20Ga_2Se_3$ glasses during annealing at 380 °C for 10 h, 25 h, 50 h 80 h and 100 h was analyzed by XRD technique. It is established that crystallization is accompanied by formation of $GeGa_4Se_8$ of low- and high-temperature modification, as well as α-Ga_2Se_3 and γ-Ga_2Se_3 phases. The size of nanocrystallites determined with respect to Debay–Scherrer equation is near 9–10 nm. The most significant crystallization processes occur at 380 °C for 25 and 50 h. Further annealing at 80 and 100 h does not show crystallization changes in the inner structure of the $80GeSe_2$-$20Ga_2Se_3$ glasses.

Acknowledgements H. Klym thanks to the Ministry of Education and Science of Ukraine for support, Dr. L. Calvez for sample preparation, Prof. O. Shpotyuk for discussion, and Dr. P. Demchenko for assistance in XRD experiments.

References

1. Kokenyesi S (2006) Amorphous chalcogenide nano-multilayers: research and development. J Optoelectron Adv Mater 8(6):2093–2096
2. Singh PK, Dwivedi DK (2017) Chalcogenide glass: fabrication techniques, properties and applications. Ferroelectrics 520(1):256–273. https://doi.org/10.1080/00150193.2017.1412187
3. Shen W, Zeng P, Yang Z, Xia D, Du J, Zhang B, Li Z (2020) Chalcogenide glass photonic integration for improved 2 μm optical interconnection. Photonics Res 8(9):1484–1490. https://www.osapublishing.org/prj/fulltext.cfm?uri=prj-8-9-1484&id=437499
4. Ahluwalia G (2018) Applications of chalcogenides: S, Se, and Te. 2018-Sustain Ind Process Summit 6:297–304. https://www.flogen.org/sips2018/paper-6-164.html
5. Macak JM, Kohoutek T, Wang L, Beranek R (2013) Fast and robust infiltration of functional material inside titania nanotube layers: case study of a chalcogenide glass sensitizer. Nanoscale 5(20):9541–9545. https://pubs.rsc.org/en/content/articlehtml/2013/nr/c3nr03014h
6. Wang J, Yu X, Lon, N, Su, X, Yin G, Jiao Q, Lin C (2019) Spontaneous crystallization of $PbCl_2$ nanocrystals in GeS_2-Sb_2S_3 based chalcogenide glasses. J Non-Cryst Solids. 521:119543. https://www.sciencedirect.com/science/article/abs/pii/S0022309319304144
7. Abe K, Takebe H, Morinaga K (1997) Preparation and properties of Ge-Ga-S glasses for laser hosts. J Non-Cryst Solids 212(2–3):143–150. https://doi.org/10.1016/S0022-3093(96)00655-2
8. Ledemi Y, Messaddeq SH, Skhripachev I, Ribeiro SJL, Messaddeq Y (2009) Influence of Ga incorporation on photoinduced phenomena in Ge–S based glasses. J Non-Cryst Solids 355(37–42):1884–1889. https://doi.org/10.1016/j.jnoncrysol.2009.04.046
9. Lin C, Rüssel C, Dai S (2018) Chalcogenide glass-ceramics: functional design and crystallization mechanism. Prog Mater Sci 93:1–44. https://www.sciencedirect.com/science/article/abs/pii/S0079642517301317
10. Elliott SR (2015) Chalcogenide phase-change materials: past and future. Int J Appl Glass Sci 6(1):15–18. https://doi.org/10.1111/ijag.12107
11. Lotnyk A, Hilmi I, Behrens M, Rauschenbach B (2021) Temperature dependent evolution of local structure in chalcogenide-based superlattices. Appl Surf Sci 536:147959. https://www.sciencedirect.com/science/article/abs/pii/S0169433220327161
12. Calvez L, Lucas P, Rozé M, Ma HL, Lucas J, Zhang XH (2007) Influence of gallium and alkali halide addition on the optical and thermo–mechanical properties of $GeSe_2$-Ga_2Se_3 glass. Appl Phys A 89(1):183–188. https://doi.org/10.1007/s00339-007-4081-y

13. Masselin P, Le Coq D, Calvez L, Petracovschi E, Lépine E, Bychkov E, Zhang X (2012) CsCl effect on the optical properties of the $80GeS_2$–$20Ga_2S_3$ base glass. Appl Phys A 106(3):697–702. https://doi.org/10.1007/s00339-011-6668-6
14. Ledemi Y, Calvez L, Rozé M, Zhang XH, Bureau B, Poulain M, Messaddeq Y (2007) Totally visible transparent chloro-sulphide glasses based on Ga_2S_3-GeS_2-CsCl. J Optoelectron Adv Mater 9(12):3751. http://hdl.handle.net/11449/38619
15. Seddon AB, Tang Z, Furniss D, Sujecki S, Benson TM (2010) Progress in rare-earth-doped mid-infrared fiber lasers. Opt Express 18(25):26704–26719. https://www.osapublishing.org/oe/fulltext.cfm?uri=oe-18-25-26704&id=208653
16. Ren J, Wagner T, Bartos M, Frumar M, Oswald J, Kincl M, Chen G (2011) Intense near-infrared and midinfrared luminescence from the Dy^{3+}-doped $GeSe_2$–Ga_2Se_3–MI (M= K, Cs, Ag) chalcohalide glasses at 1.32, 1.73, and 2.67 μ m. J Appl Phys 109(3):033105. https://doi.org/10.1063/1.3531555
17. Lin C, Dai S, Liu C, Song BA, Xu Y, Chen F, Heo J (2012) Mechanism of the enhancement of mid-infrared emission from GeS_2-Ga_2S_3 chalcogenide glass-ceramics doped with Tm^{3+}. Appl Phys Lett 100(23):231910. https://doi.org/10.1063/1.4727900
18. Yao W, Martin SW (2008) Ionic conductivity of glasses in the MI+M_2S+($0.1Ga_2S_3$+ $0.9GeS_2$) system (M= Li, Na, K and Cs). Solid State Ionics 178(33–34):1777–1784. https://www.sciencedirect.com/science/article/abs/pii/S0167273807003098
19. Bhattacharya S, Acharya A, Das AS, Bhattacharya K, Ghosh CK (2019) Lithium ion conductivity in Li_2O–P_2O_5–ZnO glass-ceramics. J Alloy Compd 786:707–716. https://www.sciencedirect.com/science/article/abs/pii/S0925838819302373
20. Kuo PH, Du J (2019) Lithium ion diffusion mechanism and associated defect behaviors in crystalline $Li_{1+x}Al_xGe_{2-x}(PO_4)_3$ solid-state electrolytes. J Phys Chem C 123(45):27385–27398. https://doi.org/10.1021/acs.jpcc.9b08390
21. Ren J, Wagner T, Orava J, Frumar M, Frumarova B (2008) Reversible photoinduced change of refractive index in ion-conducting chalcohalide glass. Appl Phys Lett 92(1):011114. https://doi.org/10.1063/1.2830941
22. Ren J, Wagner T, Orava J, Kohoutek T, Frumarova B, Frumar M, Jain H (2008) In-situ measurement of reversible photodarkening in ion-conducting chalcohalide glass. Opt Express 16(3):1466–1474. https://www.osapublishing.org/oe/abstract.cfm?uri=OE-16-3-1466
23. Zhang XH, Calvez L, Seznec V, Ma HL, Danto S, Houizot P, Lucas J (2006) Infrared transmitting glasses and glass-ceramics. J Non-Cryst Solids 352(23–25):2411–2415. https://www.sciencedirect.com/science/article/abs/pii/S0022309306004704
24. Shpotyuk O, Calvez L, Petracovschi E, Klym H, Ingram A, Demchenko P (2014) Thermally-induced crystallization behaviour of $80GeSe_2$-$20Ga_2Se_3$ glass as probed by combined X-ray diffraction and PAL spectroscopy. J Alloy Compd 582:323–327. https://doi.org/10.1016/j.jallcom.2013.07.127
25. Klym H, Ingram A, Shpotyuk O, Calvez L, Petracovschi E, Kulyk B, Serkiz R, Szatanik R (2015) Cold'crystallization in nanostructurized $80GeSe_2$-$20Ga_2Se_3$ glass. Nanoscale Res Lett 10(1):1–8. https://doi.org/10.1186/s11671-015-0775-9
26. Klym H, Shpotyuk O, Karbovnyk I, Calvez L, Popov AI (2019) Structural investigation of crystallized Ge-Ga-Se chalcogenide glasses. IOP Conf Ser Mater Sci Eng 503(1):012020. https://doi.org/10.1088/1757-899X/503/1/012020
27. Klym H, Ingram A, Shpotyuk O (2016) Free-volume nanostructural transformation in crystallized GeS_2–Ga_2S_3–CsCl glasses. Materialwiss Werkstofftech 47(2–3):198–202. https://doi.org/10.1002/mawe.201600476
28. Klym H, Ingram A, Shpotyuk O, Karbovnyk I (2016) Influence of CsCl addition on the nanostructured voids and optical properties of $80GeS_2$-$20Ga_2S_3$ glasses. Opt Mater 59:39–42. https://doi.org/10.1016/j.optmat.2016.03.004
29. Klym H, Karbovnyk I, Cestelli Guidi M, Hotra O, Popov AI (2016) Optical and vibrational spectra of CsCl-enriched GeS_2-Ga_2S_3 glasses. Nanoscale Res Lett 11(1):1–6. https://doi.org/10.1186/s11671-016-1350-8

30. Klym H, Ingram A, Shpotyuk O, Hotra O, Popov AI (2016) Positron trapping defects in free-volume investigation of Ge-Ga-S-CsCl glasses. Radiat Meas 90:117–121. https://doi.org/10.1016/j.radmeas.2016.01.023
31. Klym H, Ingram A, Shpotyuk O, Szatanik R (2015) Free-volume study in GeS_2-Ga_2S_3-CsCl chalcohalide glasses using positron annihilation technique. Phys Procedia 76:145–148. https://doi.org/10.1016/j.phpro.2015.10.026
32. Klym H, Kozdras A, Ingram A, Calvez L (2020) Structural transformation caused by crystallization in the Ge-Ga-S (CsCl) glasses. Mol Cryst Liq Cryst 700(1):34–47. https://doi.org/10.1080/15421406.2020.1732550
33. Karbovnyk I, Olenych I, Aksimentyeva O, Klym H, Dzendzelyuk O, Olenych Y, Hrushetska O (2016) Effect of radiation on the electrical properties of PEDOT-based nanocomposites. Nanoscale Res Lett 11(1):84. https://doi.org/10.1186/s11671-016-1293-0
34. Karbovnyk I, Collins J, Bolesta I, Stelmashchuk A, Kolkevych A, Velupillai S, Klym H, Fedyshyn O, Tymoshyk S, Kolych I (2015) Random nanostructured metallic films for environmental monitoring and optical sensing: experimental and computational studies. Nanoscale Res Lett 10(1):1–5. https://doi.org/10.1186/s11671-015-0855-x
35. Shpotyuk O, Brunner M, Hadzaman I, Balitska V, Klym H (2016) Analytical description of degradation-relaxation transformations in nanoinhomogeneous spinel ceramics. Nanoscale Res Lett 11(1):499. https://doi.org/10.1186/s11671-016-1722-0
36. Calvez L, Lin C, Rozé M, Ledemi Y, Guillevic E, Bureau B, Allix M, Zhang X (2010) Similar behaviors of sulfide and selenide-based chalcogenide glasses to form glass ceramics. Proc SPIE 7598:759802–759808. https://doi.org/10.1117/12.840968
37. Rodriguez-Carvajal J, Roisnel T (2000) WinPLOTR: a windows tool for powder diffraction pattern analysis. Mater Sci Forum 378–381
38. Elliott SR (1991) Origin of the first sharp diffraction peak in the structure factor of covalent glasses. Phys Rev Lett 67(6):711–714. https://doi.org/10.1103/PhysRevLett.67.711
39. Elliott SR (1995) Extended-range order, interstitial voids and the first sharp diffraction peak of network glasses. J Non-cryst Solids 182(1–2):40–48. https://www.sciencedirect.com/science/article/abs/pii/0022309394005397
40. De Keijser TH, Langford JI, Mittemeijer EJ, Vogels ABP (1982) Use of the voigt function in a single-line method for the analysis of X-ray diffraction line broadening. J Appl Crystallogr 15(3):308–314. https://scripts.iucr.org/cgi-bin/paper?a21783
41. Lozac'h AL, Guittard M (1977) Systeme ternaire La_2Se_3-Ga_2Se_3-$GeSe_2$ diagramme de phase. Mater Res Bull 12:887–893
42. Roze M, Calvez L, Ledemi Y, Allix M, Matzen G, Zhang XH (2008) Optical and mechanical properties of glasses and glass–ceramics based on the Ge–Ga–Se system. J Am Ceram Soc 91(11):3566–3570. https://doi.org/10.1111/j.1551-2916.2008.02684.x
43. Keshari AK, Pandey AC (2008) Size and distribution: a comparison of XRD, SAXS and SANS study of II–VI semiconductor nanocrystals. J Nanosci Nanotechnol 8(3):1221–1227. https://www.ingentaconnect.com/content/asp/jnn/2008/00000008/00000003/art00024

Kinetics of $ZnMoO_4 \cdot 0.8H_2O$ and α-$ZnMoO_4$ Formation at Ultrasonic Treatment of ZnO and MoO_3 Mixture

O. A. Diyuk, V. A. Zazhigalov, N. D. Shcherban, V. V. Permyakov, N. V. Diyuk, S. M. Shcherbakov, O. V. Sachuk, and P. Dulian

1 Introduction

Currently, zinc molybdate $ZnMoO_4$ is an interesting material thanks to the wide range of its application: luminescent materials [1–8], bolometers, scintillation humidity sensors, gas sensors [2, 9–13], photocatalysts and catalysts of partial hydrocarbons oxidation [4, 14, 15], the anode materials in Li-ion batteries [16–19], and as additives for improvement the mechanical, thermal and sensing properties of composites [13], anticorrosion properties [13, 20] and as smoke suppressant [21, 22].

The modern traditional methods of zinc molybdate synthesis are based on the reactions between components and in most cases metal salts as raw materials are used,

O. A. Diyuk (✉) · V. A. Zazhigalov · O. V. Sachuk
Institute for Sorption and Problems of Endoecology of National Academy of Sciences of Ukraine, 13, General Naumov Str., Kyiv 03164, Ukraine
e-mail: diyukhelen@ukr.net

N. D. Shcherban
L.V. Pisarzhevsky Institute of Physical Chemistry of National Academy of Sciences of Ukraine, 31 pr. Nauky, Kyiv 03028, Ukraine

V. V. Permyakov
Institute of Geological Sciences of National Academy of Sciences of Ukraine, 55-b, O. Gonchar str., Kyiv 01054, Ukraine

N. V. Diyuk
Taras Shevchenko National University of Kyiv, 60, Volodymyrska str., Kyiv 01033, Ukraine

S. M. Shcherbakov
M.G. Kholodny Institute of Botany of the National Academy of Science of Ukraine, 2, Tereshchenkivska str., Kyiv 01004, Ukraine

P. Dulian
Faculty of Chemical Engineering and Technology, Cracow University of Technology, 24, Warszawska str., 31-155 Cracow, Poland

O. Fesenko and L. Yatsenko (eds.), *Nanomaterials and Nanocomposites, Nanostructure Surfaces, and Their Applications*, Springer Proceedings in Physics 263, https://doi.org/10.1007/978-3-030-74741-1_6

in solutions (impregnation, deposition-precipitation, sol–gel, ion exchange, etc.), in gas-phase processes (grafting, combustion, etc.) or solid-state high-temperature synthesis. In these syntheses, organic and inorganic solvents (citric acid, ethylene glycol, etc.) and additional reagents (reducing agents, stabilizers, surfactants) are used often. For example, the synthesis of $ZnMoO_4$ usually uses co-precipitation method proceeds with the use of soluble salts as the initial materials $Zn(NO_3)_2 \cdot 6H_2O$ and $Na_2MoO_4 \cdot 2H_2O$ or $(NH_4)_6Mo_7O_{24}$ [23–25]. Besides for the preparation of this compound constructed from nanostructure particles, additional different organic substances for example citric acid and ethylene glycol [23, 26] or other surfactants $C_{12}H_{25}SO_4Na$ or $(C_{16}H_{33})N(CH_3)_3Br$ [9] are used. This synthesis method requires a lot of water to remove water-soluble by-products; however, they still can be present in the final product [13]. The preparation of $ZnMoO_4$ by solid-phase reaction can be realized with ZnO and MoO_3 or their salts as raw materials [5, 6, 27, 28]. However, this method leads to the formation of a product with impurity of the initial oxides [6] and accompanied by high-power consumption.

So, all these methods of zinc molybdate synthesis are accompanied by the pollutions to environment because they are characterized by the presence of significant amount of liquid and gaseous emissions and not environmentally friendly processes. Such factors determine the need of the creation of new solutions in the technology of the zinc molybdate nanomaterials preparation.

The different conventional syntheses for decreasing of the reaction time, preparation of zinc molybdate nanoparticles, the wastes and power consumption were proposed also. The influence of hydrothermal, solvothermal and microwave methods on the formation of $ZnMoO_4$ phase from soluble salts has been studied [1, 23, 26]. As the promising and innovative methods, the mechanochemical treatment and ultrasonic irradiation treatment (UST) with the use of metal oxides as raw materials were studied also [15, 29–31]. It was shown that the mechanochemical treatment of the oxides mixture (1:1) after 4 h leads to the formation of a mixture of β-$ZnMoO_4$, ZnO, $MoO_3 \cdot 0.5H_2O$ phases, and only an increase of the treatment time up to 8 h permits to obtain a pure β-$ZnMoO_4$ phase in the form of nano-rods [29]. Very interesting results were obtained after ultrasonic treatment ZnO and MoO_3 mixture during 1 h. It was shown that this process leads to the formation of $ZnMoO_4$ with low content β-MoO_3 impurity [15, 31].

In this investigation, the influence of ultrasonic treatment duration of ZnO and MoO_3 as raw materials mixture ($ZnO/MoO_3 = 1:1$) on the formation of zinc molybdates phases was studied in detail.

2 Experimental

The Samples Preparation

The mixture of ZnO and MoO_3 powders at 1:1 molar ratio was loaded in glass reactor with an addition of distilled water. The mixture of the powder of ZnO (3.61 g) and

MoO_3 (6.39 g) was loaded into a glass reactor, and 80 ml of distilled water was added. The weight ratio of the oxides mixture to distillate water was 1:8. Ultrasonic treatment (UST) of the oxides mixture was carried out at room temperature for 5, 10, 20, 40 and 60 min using UZDN-A ultrasonic dispersant operating in acoustic cavitations mode at a frequency of 22 kHz. The samples synthesized by ultrasonic method can be combined into two groups. The first group of the samples was dried at 100 °C in air, and dry precipitates were obtain and labeled as Zn-Mo-O_5_100; Zn-Mo-O_10_100; Zn-Mo-O_20_100; Zn-Mo-O_40_100 and Zn-Mo-O_60_100.

The second group of the samples was dried at 300 °C in air for 3 h and was labeled: Zn-Mo-O_5_300; Zn-Mo-O_10_300; Zn-Mo-O_20_300; Zn-Mo-O_40_300 and Zn-Mo-O_60_300, where the first number determines the UST time and second one—the treatment temperature.

For comparison, the preparation of $ZnMoO_4$ by co-precipitation method using $Na_2MoO_4 \cdot 2H_2O$ and $Zn(NO_3)_3 \cdot 6H_2O$ or $Zn(OAc)_2$ as raw materials [21] was realized.

First synthesis:

Sodium molybdate ($Na_2MoO_4 \cdot 2H_2O$) 3.226 g and zinc nitrate 3.959 g ($Zn(NO_3)_3 \cdot 6H_2O$) separately were dissolved in 100 ml deionized water and heated up to 80 °C. Then the hot $Na_2MoO_4 \cdot 2H_2O$ solution was added drop by drop to the hot $Zn(NO_3)_3 \cdot 6H_2O$ solution at stirring. The obtained solution was kept at room temperature without any stirring or shaking.

Second synthesis:

Sodium molybdate ($Na_2MoO_4 \cdot 2H_2O$) 3.226 g and zinc acetate ($Zn(CH_3COO)_2$, $Zn(OAc)_2$) 2.926 g were used as raw materials for this synthesis. The reaction conditions were similar to the first synthesis.

The samples synthesized by co-precipitation method were washed 5 times by 500 ml deionized water and dried at 100 °C.

According to the X-ray diffraction data, $NaZn_2(MoO_4)_2OH \cdot H_2O$ is a main product obtained by both these syntheses instead of $ZnMoO_4$. In spite of numerous publications [1, 17, 21, 24] which show the formation of $ZnMoO_4$ from sodium molybdate in several publications [32, 33], the formation of $NaZn_2(MoO_4)_2OH \cdot H_2O$ as main or impurity phase was determined.

The solid-state (SS) reaction was also used to synthesize $ZnMoO_4$. ZnO and MoO_3 powders (1:1 molar ratio) were loaded into an agate mortar and grinded. The obtained mixture was transferred into alumina crucible and calcined at 900 °C for 4 h. The prepared sample was named Zn-Mo-O_SS.

Characterization of the Samples

The phase composition of the prepared samples was determined using Bruker D8 Advance diffractometer equipped with Cu K_α ($\lambda = 0.15406$ nm) X-ray source. The average crystalline sizes ($L_{(hkl)}$, nm) were calculated according to the broadening of the reflex by the Scherrer formula.

To analyze the sample's composition and their morphology, scanning electron microscope (SEM JSM6490 LV, JEOL, Japan) with an integrated system for electron microprobe analysis INCA energy based on energy-dispersive and wavelength-dispersive spectrometers (EDS + WDS, OXFORD, UK) with HKL channel system was used.

Transmission electron microscopy (TEM) for the obtained materials was carried out on transmission electron microscope JEM-1200 EX (JEOL, Japan).

The nitrogen adsorption isotherms at −196 °C were obtained on a Quantachrome NOVA-220e Gas Sorption Analyzer. Specific surface area S_{BET} was estimated using the BET equation [34].

The H_2-TPR (temperature programmed reduction) analysis was carried out on H_2-Ar atmosphere (H_2:Ar = 1:1) in the temperature range of 30–800 °C at heating rate 5 °C/min, and volume rate of the mixture was equal to 80 ml/min. The sample weight was 50 mg, scales sensitivity was -3.4×10^{-5} g, and rate registration of data was −10 point/min. The scheme of the used device was published early in [35].

3 Results and Discussion

XRD

XRD patterns of the initial mixture of ZnO (JCPDS 00-080-0075) and MoO_3 (JCPDS 00-005-0508) are shown in Fig. 1a. Despite the fact that the ZnO to MoO_3 molar ratio was 1:1, the reflexes for MoO_3 were more intensive than for ZnO.

X-ray diffractogram of Zn-Mo-O_5_100 (Fig. 1b) shows an appearance of new weak reflections corresponded to $ZnMoO_4 \cdot 0.8H_2O$ phase (JCPDS 00-025-1025). An increase of treatment time up to 10 min (sample Zn-Mo-O_10_100) leads to a significant increase of $ZnMoO_4 \cdot 0.8H_2O$ reflections intensity and disappearance of MoO_3 reflections. X-ray diffraction patterns of the Zn-Mo-O_20_100 sample (Fig. 1d) show the total disappearance of the reflections corresponding to MoO_3, and only reflections of $ZnMoO_4 \cdot 0.8H_2O$ are presented in diffractogram. This fact indicates the formation of $ZnMoO4 \cdot 0.8H_2O$ phase after this time treatment. An increase of treatment time up to 40 and 60 min (the samples Zn-Mo-O_40_100 and Zn-Mo-O_60_100) does not lead to the appearance of new reflections, and only $ZnMoO_4 \cdot 0.8H_2O$ phase was observed. The change of the structural parameters of the formed $ZnMoO_4 \cdot 0.8H_2O$ phase in dependence on the time treatment is demonstrated in Table 1. The large crystallites are formed at the beginning of the synthesis. The increase of treatment time from 5 up to 40 min leads to a decrease of particles size from 42 to 24 nm and is accompanied by the gradual change of the ratio of (010)/(100) reflections intensity of $ZnMoO_4 \cdot 0.8H_2O$. Further increase of time treatment from 40 up to 60 min does not affect particles size, which remains practically the same (Table 1), but the strong increase of (010) reflection intensity at $2\Theta = 13.2°$ was observed (Table 1). These facts can indicate that after $ZnMoO_4 \cdot 0.8H_2O$ phase formation on the first step of

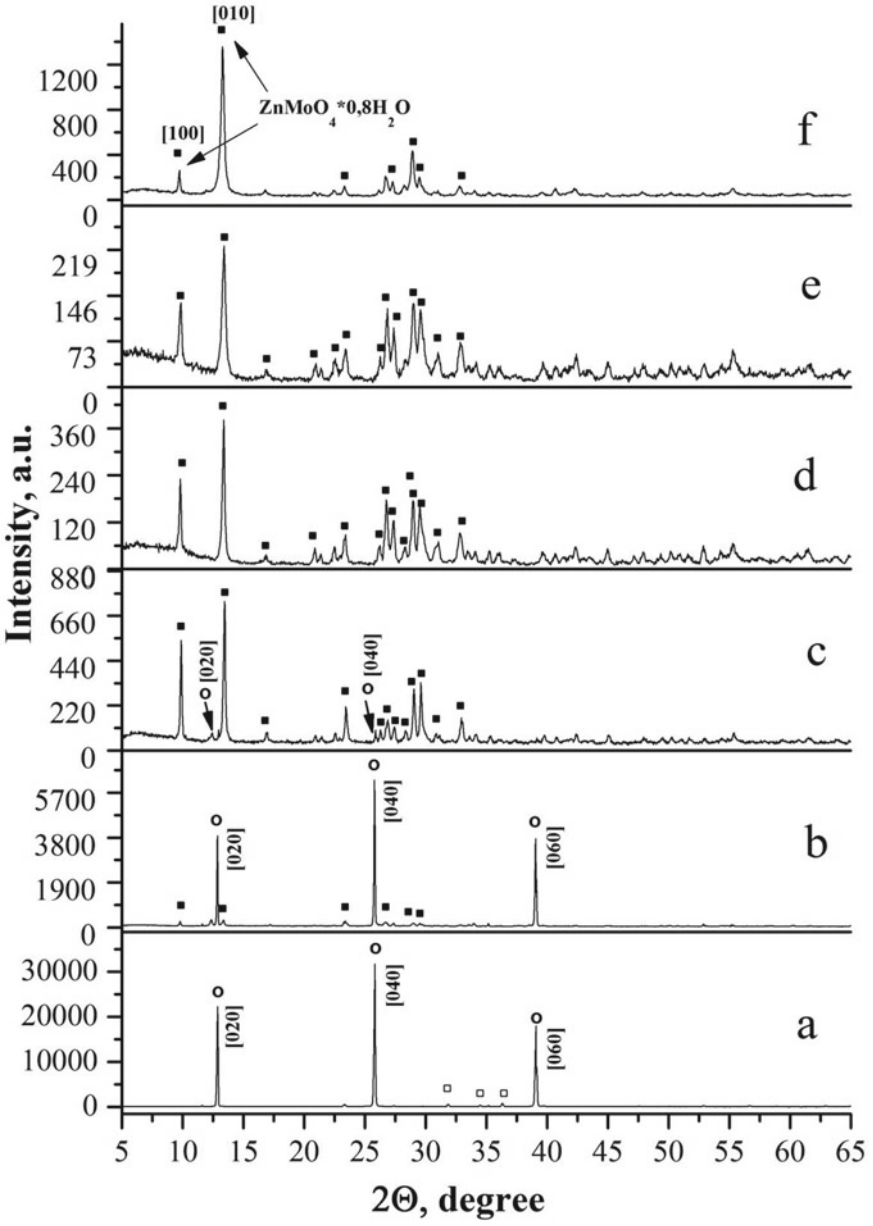

Fig. 1 X-ray diffractograms of the samples: **a** the initial mixture of ZnO and MoO_3, **b** Zn-Mo-O_5_100; **c** Zn-Mo-O_10_100; **d** Zn-Mo-O_20_100; **e** Zn-Mo-O_40_100, **f** Zn-Mo-O_60_100. **O**–MoO_3, □—ZnO, ■—α-$ZnMoO_4$

Table 1 Structural characteristics of the $ZnMoO_4 \cdot 0.8H_2O$ (XRD data)

Sample	I_{010}/I_{100}	Average crystalline size L_{010}, nm
$ZnMoO_4 \cdot 0.8H_2O_{(JCPDS\ 00\text{-}025\text{-}1025)}$	1	–
Zn-Mo-O_5_100	1.21	42
Zn-Mo-O_10_100	1.60	37
Zn-Mo-O_20_100	2.12	32
Zn-Mo-O_40_100	2.17	24
Zn-Mo-O_60_100	8.77	25

UST, the further treatment leads to anisotropic destruction or oriented growth of this phase crystallites.

The XRD data of the samples synthesized by UST followed by the temperature treatment at 300 °C in air for 3 h are presented in Fig. 2. These results show that the temperature treatment of the samples leads to the transformation of $ZnMoO_4 \cdot 0.8H_2O$ to α-$ZnMoO_4$ (JCPDS No 00-035-0765). In the same time, an increase of temperature treatment of the samples does not accompanied by reaction between initial reagents what can be confirmed by the presence of MoO_3 reflexes after 10 min of UST (Figs. 1 and 2). The preferable orientation of the α-$ZnMoO_4$ nanocrystals [the samples have two most intense reflections (Fig. 2c–f)] determined by its presence in synthesized $ZnMoO_4 \cdot 0.8H_2O$ phase rests and the difference with α-$ZnMoO_4$ which was synthesized by the SS method (Fig. 2a) can be observed. The α-$ZnMoO_4$ phase synthesized by the SS method (Fig. 2a) has a larger number of reflections with high intensity, while the samples prepared by the UST method demonstrate only two high intensity reflections which correspond to (−220) and (120) planes (Fig. 2d–f). It is necessary to note that α-$ZnMoO_4$ synthesized by the SS method has larger average crystal size (102 nm) than α-$ZnMoO_4$ synthesized by the UST method where the formation of the nanocrystals with dimension about 35 nm was observed (Table 2).

SEM and EDS Data

In accordance with the data of XRD analysis, the formation of practically pure phase $ZnMoO_4 \cdot 0.8H_2O$ was observed after 20 min of UST. The results presented in Fig. 3 demonstrate the change of samples morphology after UST for 20, 40 and 60 min. Materials consisting of nano-filamentary structures are formed (sample Zn-Mo-O_20_100, Figs. 3a and 4). The cross section of the filaments is near 100 nm, and their length is more than 200 μm. The interwoven nano-filamentary structures form a secondary structure in the form of a fabric. A sufficient number of publications in which SEM images demonstrate the morphology of $ZnMoO_4 \cdot 0.8H_2O$ and α-$ZnMoO_4$ in the form of plate-like or rhombus-like [3, 4, 23, 26], needle-like or rod-like [3, 4, 10, 16, 23, 26, 29, 30] and a flower-like structure [2, 7] are known. However, we have not found literary data about the formation of the particles with the morphology similar to long nano-filamentary structures tending to weaving. Therefore, these results are in accordance with XRD data which demonstrate the formation

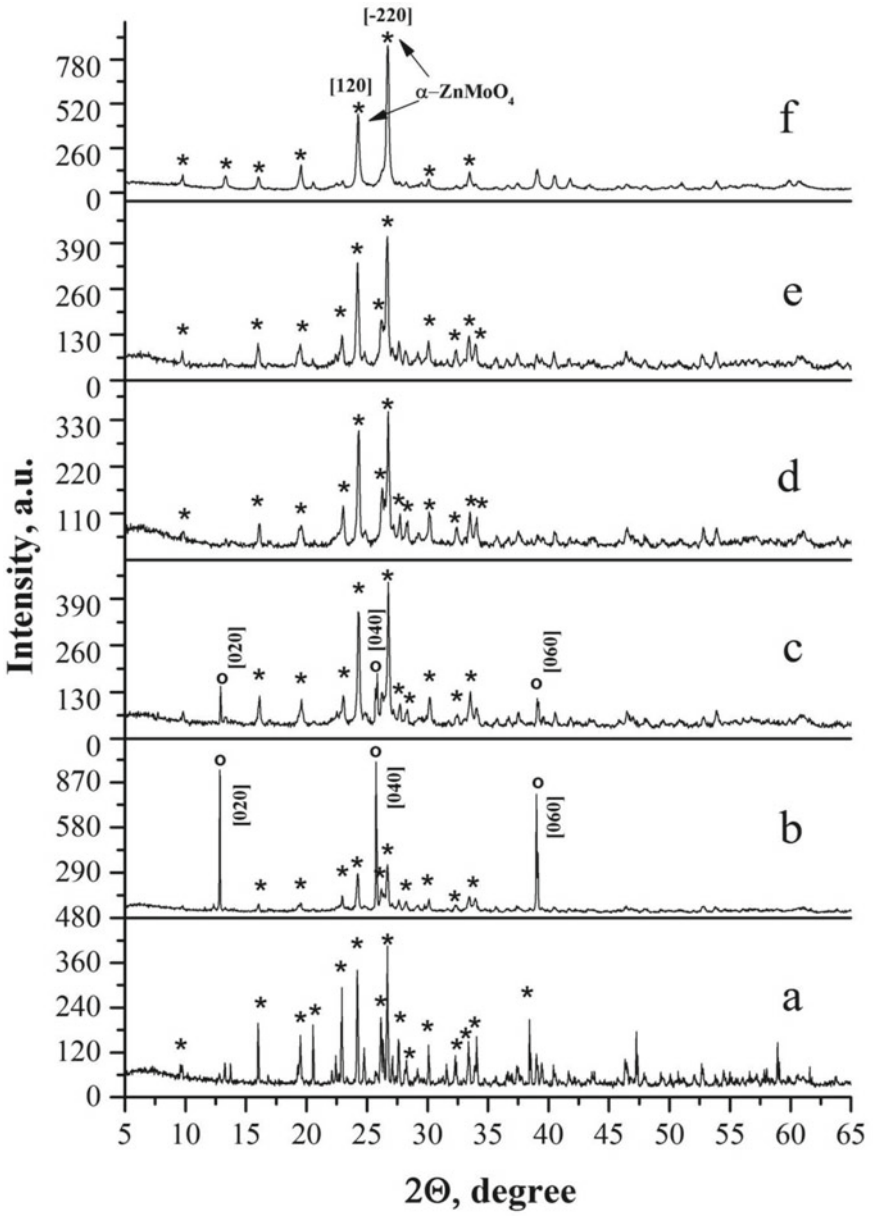

Fig. 2 X-ray diffractograms of the samples: **a** Zn_Mo_O_SS, **b** Zn-Mo-O_5_300, **c** Zn-Mo-O_10_300, **d** Zn-Mo-O_20_300, **e** Zn-Mo-O_40_300, **f** Zn-Mo-O_60_300. *α-$ZnMoO_4$, **o**–MoO_3

Table 2 Structural characteristics of the α-$ZnMoO_4$ (XRD data)

Sample	I_{-220}/I_{120}	L_{-220}, nm
JCPDS 00-035-0765	1.1	–
Zn-Mo-O_SS	1.2	102
Zn-Mo-O_5_300	1.2	46
Zn-Mo-O_10_300	1.2	41
Zn-Mo-O_20_300	1.2	38
Zn-Mo-O_40_300	1.2	35
Zn-Mo-O_60_200	1.8	35

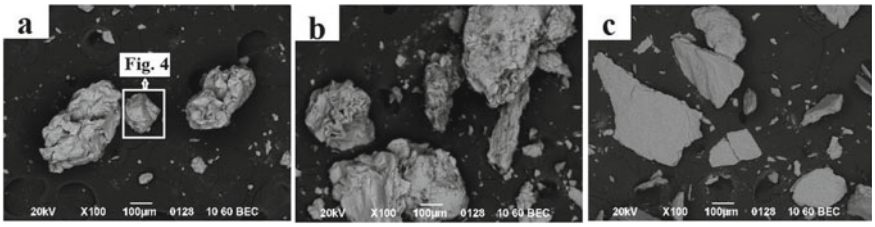

Fig. 3 SEM images of the $ZnMoO_4 \cdot 0.8H_2O$ prepared by US treatment **a** Zn-Mo-O_20_100, **b** Zn-Mo-O_40_100 та **c** Zn-Mo-O_60_100

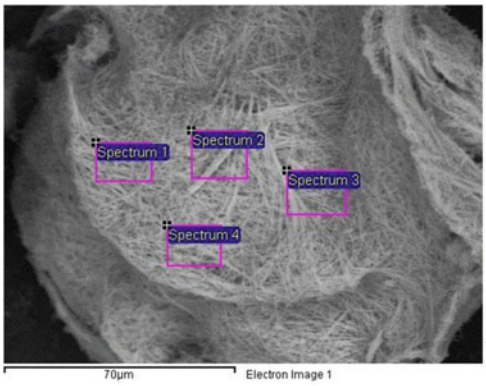

Spectrum	Zn	Mo	O
Spectrum 1	11.37	19.32	69.32
Spectrum 2	11.41	19.30	69.30
Spectrum 3	10.67	19.67	69.67
Spectrum 4	12.70	18.65	68.65
Mean	11.54	19.23	69.23
Std. deviation	0.85	0.42	0.42

Fig. 4 SEM images of the Zn-Mo-O_20_100 (Fig. 3a) at high resolution with EDX (Atomic %)

of $ZnMoO_4 \cdot 0.8H_2O$ preferably oriented in two planes. At the same time, the data of EDX analysis (Fig. 4) show the excess of molybdenum on these filaments which can testify that the process of $ZnMoO_4 \cdot 0.8H_2O$ phase formation is not finished after this time treatment.

The increase of time treatment up to 40 and 60 min leads to partial compressing of long filamentary structures (Fig. 3b, c). The existence of compacting rod-like nanostructures which preferably oriented about one plane was observed at high resolution

(Fig. 5a). These results are in a good agreement with the XRD data (Fig. 1 and Table 1). It is necessary to note that for this sample the uniform elements distribution (EDX analysis) was observed. So, it is possible to conclude that the process of $ZnMoO_4 \cdot 0.8H_2O$ phase formation was finished after 60 min treatment.

The thermal treatment (300 °C) of synthesized $ZnMoO_4 \cdot 0.8H_2O$ phase does not lead to the change of the sample morphology (Fig. 5a, b). The same rod-like structures of α-$ZnMoO_4$ are formed (Fig. 5b), however with an increase of their cross section what correspond to preferably orientation to two planes (Fig. 2 and Table 2). The uniform distribution of elements was determined also.

In contrast to this, a-$ZnMoO_4$ obtained by solid-state reaction demonstrates non-uniform distribution of the elements (Fig. 6). This fact could be explained by partial sublimation of molybdenum oxide before its melting and beginning $ZnMoO_4$ synthesis. It is necessary to note that it [6] was reported that the sample synthesized by SS method has the small amount of impurity phases Mo_4O_{11}, ZnO detected by XRD analysis.

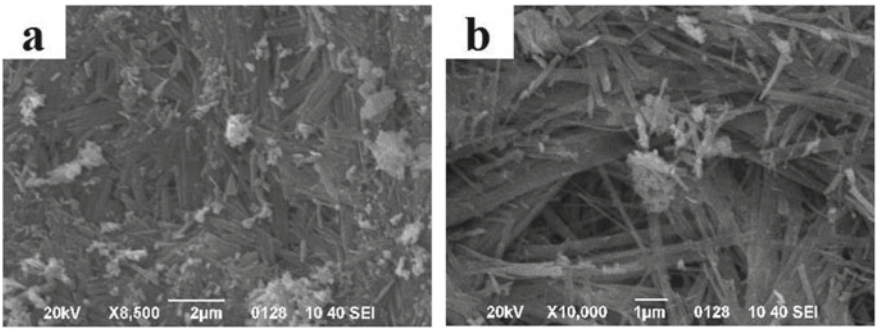

Fig. 5 SEM images of samples at high resolution: **a** Zn-Mo-O_60_100 and **d** Zn-Mo-O_60_300

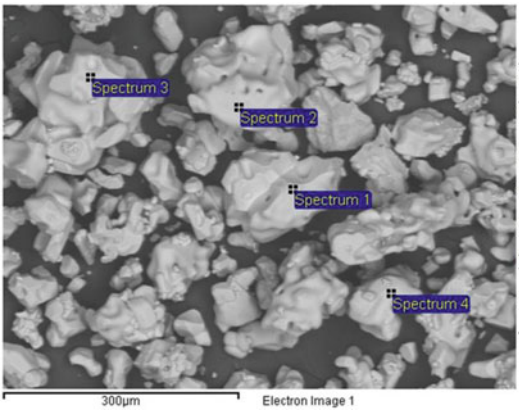

Spectrum	Zn	Mo	O
Spectrum 1	11.27	19.37	69.37
Spectrum 2	24.99	12.50	62.50
Spectrum 3	12.33	18.83	68.83
Spectrum 4	42.02	3.99	53.99
Mean	22.65	13.67	63.67
Std. deviation	14.34	7.17	7.17

Fig. 6 SEM images of the $ZnMoO_4$ prepared by solid-state reaction with EDX (Atomic %)

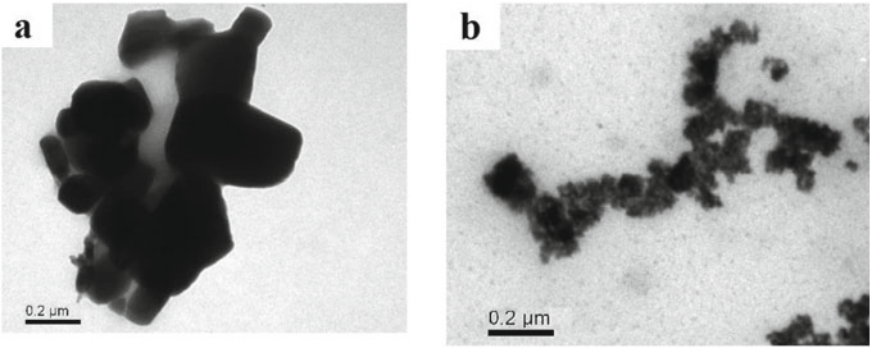

Fig. 7 TEM images of initial oxides **a** MoO_3 and **b** ZnO

TEM

The TEM images of the initial oxides ZnO and MoO_3 are presented in Fig. 7a, b, respectively. It is possible to observe the presence of large compressed particles of MoO_3 and small loose structure particles of ZnO. This fact can explain the presence of high intensity peaks of molybdenum oxide and lower intensity of the peaks of zinc oxide in XRD pattern of the initial mixture (Fig. 1a). After 20 min of UST (Zn-Mo-O_20_100), complete disappearance of the particles characteristic for the initial oxides and formation of new rod-like structure particles were observed (Fig. 8a). Generally, TEM data are in a good agreement with XRD and SEM results demonstrating the transformation of initial oxides to new compound $ZnMoO_4 \cdot 0.8H_2O$ phase as the result of their ultrasound treatments.

The TEM data for the α-$ZnMoO_4$ phase formed after temperature treatment (Zn-Mo-O_60_300, Fig. 8b) and not containing crystallization water demonstrate that rod-like particles (Fig. 5b) consist the long needle-like nanocrystals of this phase.

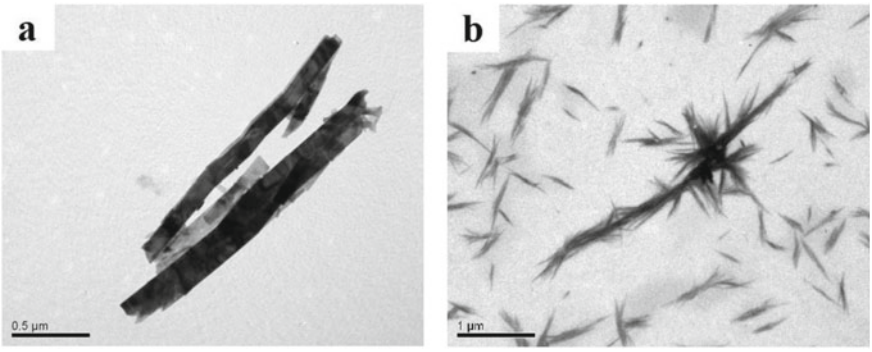

Fig. 8 TEM images of **a** Zn-Mo-O_20_100 and **b** Zn-Mo-O_60_300

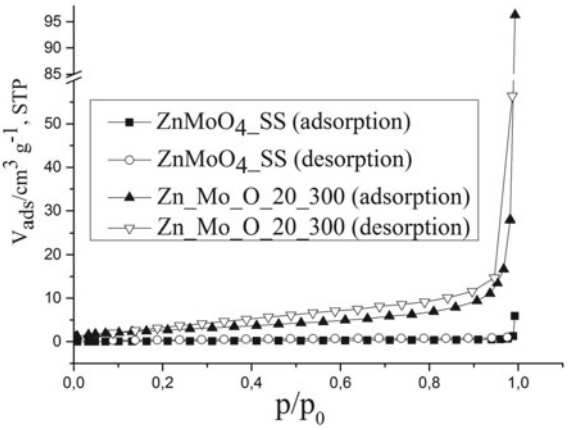

Fig. 9 Nitrogen ad(de)sorption isotherms (77 K) for the $ZnMoO_4$_SS and Zn-Mo-O_20_300

Specific Surface Area

The data of nitrogen ad(de)sorption (Fig. 9) show that α-$ZnMoO_4$ obtained by solid-state reaction is characterized by a low specific surface area (S_{BET} near to 0,7 $m^2\ g^{-1}$). In the same time, the samples prepared by ultrasound method have higher specific surface area (10–13 $m^2\ g^{-1}$) than Zn-Mo-O_SS sample. For example, Fig. 9 presented ad(de)sorption isotherms obtained for Zn-Mo-O_20_300 (S_{BET} = 11 $m^2 g^{-1}$) possessing hysteresis loop in a wide area of relative nitrogen pressure which indicate the presence of mesopores with different sizes.

H_2-TPR

The data of H_2-TPR and corresponding thermogravimetric profiles of Zn-Mo-O_20_100 sample containing $ZnMoO_4 \cdot 0.8H_2O$ phase (see above) are shown in Fig. 10. These curves can be conditionally divided into four regions, each of which contains one derivative peak. The observed weight loss is equal to 1.8; 4.0; 9.3 and 47.1% for each section, correspondingly. The first two effects with maximum of weight loss at T_1 = 105 °C and T_2 = 225 °C can be connected with two steps desorption of crystallization water (5.8% which is close to the theoretical value equal to 6.0 wt%) and formation of the $ZnMoO_4$ phase which is in a well agreement with the presented results. In the same time, the obtained results show that the $ZnMoO_4 \cdot 0.8H_2O$ phase contains two different forms of crystallization water. First form of crystallization water is removed between 20 and 140 °C and can be renewable at the sample cooling (confirmed experimentally). The second form of crystallization water is removed irreversibly in the range of 140–280 °C, and this process leads to the formation of α-$ZnMoO_4$ what corresponds to XRD data. The increase of the temperature treatment of the Zn-Mo-O_20_100 sample is accompanied by the next weight loss (9.3%) and an appearance of the third maximum at 432 °C. This effect can be connected with decomposition of α-$ZnMoO_4$ and formation of new phases as shown in reaction (1) in accordance with [36]. The part of the formed MoO_3 can be reduced to MoO_2 in accordance with the reaction (2) [37, 38] (weight loss is equal to 8.3%)

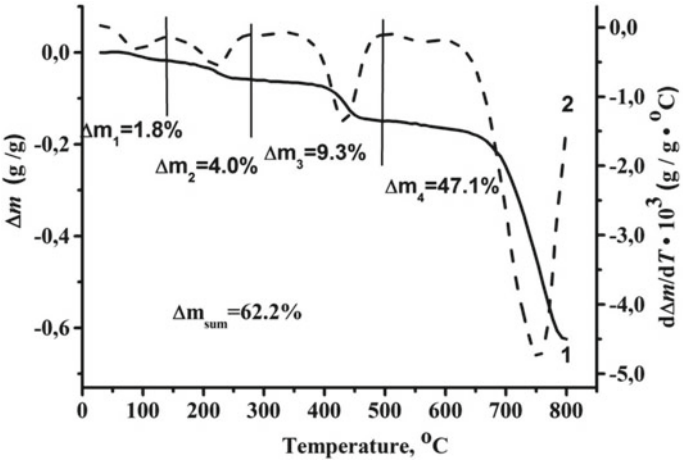

Fig. 10 Thermogravimetric profile and relative derivative curve for Zn-Mo-O_20_100 H_2-TPR analysis

and partially evaporated. The last effect of weight loss (47.1%) with a maximum at 750 °C can be associated with further decomposition of $Zn_3Mo_2O_9$ and evaporation of reduction products, since after H_2-TPR Zn-Mo-O_20_100 (800 °C) the final product presented the black powder demonstrated in XRD only MoO_2 reflexes.

$$3ZnMoO_4 \rightarrow Zn_3Mo_2O_9 + MoO_3 \quad (1)$$

$$MoO_3 \rightarrow MoO_2 \quad (2)$$

4 Conclusion

It was established that the nano-phase of $ZnMoO_4 \cdot 0.8H_2O$ can be synthesized by simple ultrasound method from the mixture of the initial oxides as basic components. The low-temperature treatment (300 °C) of this prepared product permits to obtain the nanodispersed phase of α-$ZnMoO_4$. The synthesized $ZnMoO_4 \cdot 0.8H_2O$ and $ZnMoO_4$ have unique morphology long filamentous with secondary fabric-like structure and demonstrate the higher specific surface area that the samples prepared by traditional methods. As a result, a simple energy-saving and environmentally friendly synthesis method was proposed.

Acknowledgements This work was financially supported by NASU Program "New functional substances and materials of chemical production" (project 1-20) and Program for Young Scientists Group "Synthesis of selective catalysts of pure hydrogen obtaining from ethanol at low temperatures" (Project 22/02-2020).

References

1. Cavalcante LS, Sczancoski JC, Siu Li M, Longo E, Varela JA (2012) β-$ZnMoO_4$ microcrystals synthesized by the surfactant-assisted hydrothermal method: Growth process and photoluminescence properties. Colloids Surf A Physicochem Eng Aspects 396:346–351
2. Chernyak DM, Danevich FA, Degoda VY, Dmitruk IM, Ferri F,Galashov EN, Giuliani A, Ivanov IM, Kobychev VV, Mancuso M, Marnieros S, Mokina VM, Nones C, Olivieri E, Pessina G, Rusconi C, Shlegel VN, Stanovyi OP, Tenconi M, Tretyak VI, Tupitsyna IA (2013) Optical, luminescence and thermal properties of radiopure $ZnMoO_4$ crystals used in scintillating bolometers for double beta decay search. Nucl Instrum Methods Phy Res A 729:856–863
3. Zhaia B, Mab Q, Yanga L, Huanga YM (2017) Growth of $ZnMoO_4$ nanowires via vapor deposition in air. Mater Lett 188:119–1224
4. Wang D, Huang M, Zhuang Y, Jia H, Sun J, Guan M (2017) Phase- and morphology-controlled synthesis of zinc molybdate for excellent photocatalytic property. Eur J Inorg Chem 42:4939–4946
5. Hizhnyia Y, Zatovskya I, Nedilkob S, Boikoc R, Lid J, Hana W, Klyuia NI (2019) Origin of luminescence in $ZnMoO_4$ crystals: Insights from spectroscopic studies and electronic structure calculations. J Lumin 211:127–137
6. Jin Y, Pang T (2019) Highly efficient green upconversion luminescence of $ZnMoO_4$:Yb3+/Er3+/Li+ for accurate temperature sensing. Spectrochimica Acta Part A Mol Biomol Spectrosc 211:306–312
7. Tiwari SK, Singh A, Yadav P, Bibek KS, Rolly V, Rout SK, Ela S (2020) Structural and dielectric properties of Cu-doped α-$ZnMoO_4$ ceramic system for enhanced green light emission and potential microwave applications. J Mater Sci: Mater Electron 27(4):594–599
8. Degodaa VY, Koguta YP, Moroza IM, Danevichb FA, Nasonovc SG, Makarovc EP, Shlegel VN (2017) Temperature dependence of luminescence intensity in $ZnMoO_4$ crystals. Mater Res Bull 89:139–149
9. Beeman JW, Bellini F, Capelli S, Cardani L, Casali N, Dafinei I, Di Domizio S, Ferroni F, Galashov EN, Gironi L, Orio F, Pattavina L, Pessina G, Piperno G, Pirro S, Shlegel VN, Vasilyev YV, Tomei C, Vignati M (2012) $ZnMoO_4$: a promising bolometer for neutrinoless double beta decay searches. Astropart Phy 35:813–820
10. Gironi L, Arnaboldi C, Beeman JW, Cremonesi O, Danevich FA, Degoda VY, Ivleva LI, Nagornaya LL, Pavan M, Pessina G, Pirro S, Tretyak VI, Tupitsyna IA (2010) Performance of $ZnMoO_4$ crystal as cryogenic scintillating bolometer to search for double beta decay of molybdenum. J Instrum 5:1–12
11. Edwin Suresh Raj AM, Mallika C, Swaminathan K, Sreedharan OM, Nagaraja KS (2002) Zinc(II) oxide-zinc(II) molybdate composite humidity sensor. Sens Actuators B 81:229–236
12. Shahri Z, Bazarganipour M, Salavati-Niasari M (2013) Controllable synthesis of novel zinc molybdate rod-like nanostructures via simple surfactant-free precipitation route. Superlattices Microstruct 63:258–266
13. Bhanvase BA, Darda NS, Veerkar NC, Shende AS, Satpute SR, Sonawane SH (2015) Ultrasound assisted synthesis of PANI/$ZnMoO_4$ nanocomposite for simultaneous improvement in anticorrosion, physico-chemical properties and its application in gas sensing. Ultrason Sonochem 24:87–97

14. Oudghiri-Hassani H, Rakass S, Abboudi M, Mohmoud A, Al Wadaani F (2018) Preparation and characterization of α-zinc molybdate catalyst: efficient sorbent for methylene blue and reduction of 3-nitrophenol. Molecules 23:1462
15. Zazhigalov VO, Sachuk OV, Diyuk OA, Kopachevska NS, Starchevskyy VL, Kurmach MM (1919) The effect of ultrasonic treatment on the physical–chemical properties of the ZnO/MoO_3 System. In: Fesenko O, Yatsenko L (eds) Nanocomposites, nanostructures, and their applications, Springer proceedings in physics book series, vol 221, pp 153–166
16. Fei J, Sun Q, Cui Y, Li J, Huang J (2017) Sodium carboxyl methyl cellulose and polyacrylic acid binder with enhanced electrochemical properties for $ZnMoO_4 \cdot 0.8H_2O$ anode in lithium ion batteries. J Electroanal Chem 804:158–164
17. Masood KB, Parte G, Jain N, Dwivedi PK, Kumar P, Shelke MV, Patel RP, Singh J (2020) Electrochemical performance of pre-lithiated $ZnMoO_4$ and r-GO@$ZnMoO_4$ composite anode for lithium-ion battery application. J Taiwan Inst Chem Eng 112:60–66
18. Xue R, Hong W, Pan Z, Jin W, Zhao H, Song Y, Zhou J, Liu Y (2016) Enhanced electrochemical performance of $ZnMoO_4$/reduced grapheme oxide composites as anode materials for lithium-ion batteries. Electrochim Acta 222:838–844
19. Wang L, Liang W, He S, Liu M, Zhao Y, Zhang W, Chen Y, Lai X, Bi J, Gao D (2020) Realization of superior electrochemical performances for $ZnMoO_4$ anode material through the construction strategy of 3D flower-like single crystalline. J Alloy Compd 816:152673
20. Karekara SE, Bagalec UD, Sonawanec SH, Bhanvase BA, Pinjari DV (2018) A smart coating established with encapsulation of zinc molybdate centred nanocontainer for active corrosion protection of mild steel: release kinetics of corrosion inhibitor. Compos interfaces 785–808
21. Jr Rodolfo A, Innocentini-Mei LH (2020) Synthesis of copper(II)-zinc-molybdenum compounds as smoke suppressants for PVC compositions. Fire Mater:1–10
22. Zhang X, Zhang W, Zeng G, Du J, Zhang W, Yang R (2019) The effect of different smoke suppressants with APP for enhancing the flame retardancy and smoke suppression on vinyl ester resin. Polym Eng Sci 60(2):314–322
23. Zhang G, Yu S, Yang Y, Jiang W, Zhang S, Huang B (2010) Synthesis, morphology and phase transition of the zinc molybdates $ZnMoO_4 \cdot 0.8H_2O$/a-$ZnMoO_4$/$ZnMoO_4$ by hydrothermal method. J Cryst Growth 312:1866–1874
24. Ait ahsaine H, Zbair M, Ezahri M, Benlhachemi A, Arab M, Bakiz B, Guinneton F, Gavarri J –R (2015) Rietveld refinements, impedance spectroscopy and phase transition of the polycrystalline $ZnMoO_4$ ceramics. J Ceram Int Part B 41(10):15193–15201
25. Hizhnyi Y, Zatovsky I, Nedilko S, Boiko R, Li J, Han W, Klyui NI (201) Origin of luminescence in $ZnMoO_4$ crystals: insights from spectroscopic studies and electronic structure calculations. J Lumin 211:127–137
26. Keereeta Y, Thongtem T, Thongtem S (2014) Effect of medium solvent ratios on morphologies and optical properties of α-$ZnMoO_4$, β-$ZnMoO_4$ and $ZnMoO_4 0.8H_2O$ crystals synthesized by microwave-hydrothermal/solvothermal method. Superlattices Microstruct 69:253–264
27. da Silva Filho JG, Saraiva GD, de Castro AJR, Neto VOS, SaraivaSouza A, Silva CB, Lima JA, Teixeira AMR, Freire PTC, Paraguassu W, de Sousa FF (2020) Vibrational spectroscopy study and ab initio calculation on $ZnMoO_4$ system. J Mol Struct 1206:127776
28. Peng C, Gao L, Yang S, Sun J (2008) A general precipitation strategy for large-scale synthesis of molybdate nanostructuresw. Chem Commun 5601–5603
29. Zazhigalov VA, Sachuk EV, Kopachevskaya NS, Bacherikova IV, Wieczorek-Ciurowa K, Shcherbakov SN (2016) Mechanochemical synthesis of nanodispersed compounds in the ZnO-MoO_3 system. Theor Exp Chem 52:97–103
30. Sachuk1 O, Kopachevska1 N, Kuznetsova L, Zazhigalov V, Starchevskyy V (2017) Influence of ultrasonic treatment on the properties of Zno-MoO_3 oxide system. Chem Chem Technol 11(2):152–157
31. Zazhigalov VA, Sachuk OV, Kopachevska NS, Starchevskyy VL, Sawlowicz Z (2017) Effect of ultrasonic treatment on formation of nanodimensional structures in ZnO–MoO_3 system. Theor Exp Chem 53:53–59

32. Grzywa M, Łasochaa W, Surga W (2007) Synthesis, characterization and crystal structure of zinc dimolybdatepentahydrate $ZnMo_2O_7 \cdot 5H_2O$. J Solid State Chem 180:1590–1594
33. Clearfield A, Sims MJ, Gopal R (1976) Studies in heavy-metal molybdates. I. Crystal structure of a basic zinc molybdate, $NaZn_2OH(H_2O)(MoO_4)_2$. Inorg Chem 15(2):335–338
34. Gregg SJ, Sing KS (1982) Adsorption, surface area and porosity. Academic Press, New York, p 310
35. Zazhigalov VA, Diyuk OA, Sachuk OV, Diyuk NV, Starchevsky VL, Sawlowicz Z, Bacherikova IV, SM Shcherbakov (1919) The effect of mechanochemical and ultrasonic treatments on the properties of composition CeO_2–$MoO_3 = 1{:}1$. In: Fesenko O, Yatsenko L (eds) Nanocomposites, nanostructures, and their applications, Springer proceedings in physics book, vol 221, pp 109–223
36. Galashov EN, Galkin PS, Plusnin PE, Shlegel VN (2014) Specific features of the phase formation, synthesis, and growth of $ZnMoO_4$ Crystals. Crystallogr Rep 59(2):288–290
37. Lalik E (2011) Kinetic analysis of reduction of MoO_3 to MoO_2. Catalysis Today 169:85–92
38. Ressler T, Wienold J, Jentoft RE (2001) Formation of bronzes during temperature-programmed reduction of MoO with hydrogen—an in situ XRD and XAFS study. Solid State Ionics 141–142:243–251

Ti-Implanted Nanoscale Layers for the Chloramphenicol Photocatalytic Decomposition

O. V. Sanzhak, D. V. Brazhnyk, V. V. Honcharov, and V. A. Zazhigalov

1 Introduction

Pollution of the environment is an acute problem today. At the same time, important factors are not only emissions from transport and energetics, but also waste pollution from various industries, including pharmaceuticals [1–6].

Photocatalysis is one of the effective solutions to this problem. In particular, photocatalysts were used in the study of chloramphenicol utilization problems [7–11]. Moreover, although catalysts with an active ingredient based on silver have proven themselves well [12], the search for active compositions with cheaper components is in progress. Titanium oxides can be considered promising in this regard [3, 8, 9, 13, 14].

Due to a number of disadvantages of existing titanium (low activity in the visible light, use in the form of a solution, etc. [15, 16]) one of the main issues is the structure and composition of existing titanium photocatalysts.

Given the above, we can assume that the most optimal designs of photocatalysts for operation under irradiation conditions will be supported systems [8, 17, 18]. In addition, an important factor is the dimensionality of the structure. It is shown that nanoscale structures achieve a significant effect in catalysis [7, 9, 11, 19, 20].

Therefore, to obtain effective photocatalysts, it is necessary to determine the preparation technology and composition of the supported system.

O. V. Sanzhak · D. V. Brazhnyk · V. A. Zazhigalov
Institute for Sorption and Problems of Endoecology NAS Ukraine, Kyiv, Ukraine
e-mail: zazhigal@ispe.kiev.ua

V. V. Honcharov (✉)
State Establishment "Lugansk State Medical University", Rubizhne, Ukraine
e-mail: milostiprosim@i.ua

O. Fesenko and L. Yatsenko (eds.), *Nanomaterials and Nanocomposites, Nanostructure Surfaces, and Their Applications*, Springer Proceedings in Physics 263, https://doi.org/10.1007/978-3-030-74741-1_7

Supports from metallic foil have advantages compared with glass, ceramics, etc. They are strong, stable in many environments, conduct heat well, and durable. In addition, their plasticity allows to creating of catalysts of almost any shape.

As a method of synthesis supported catalysts, ion-plasma technologies have a number of advantages [19, 21–23]. In particular, ionic implantation technology is attractive for the treatment of catalytic carriers [24–26]. It permits to obtain a thin surface layer active component due to its bombardment by target ions with significant energies. Due to the emission of surface atoms and mixing with implanted ions, new compounds are formed and the surface layer of the sample is strengthened. In contrast to the traditional applied layers, the obtained modified surface has significant strength and heat resistance. Therefore, the structural properties of implants obtained by implanting titanium ions in steel and aluminum were studied. Some samples were oxidized at different temperatures and investigated in the reaction of chloramphenicol photodegradation.

2 The Experimental Part

The detail of synthesis technology of nanoscaled modified layers is described in [19, 27]. Stainless steel foil (100 μm) and aluminum foil (50 μm) were treated by titanium ions according to this method. The samples are marked: Ti/SS and Ti/Al accordingly. After implantation, some of the samples were calcinated on air at different temperatures (200, 300, 400, 500, 600 °C). Calcination time of the sample at each temperature was equal to two hours.

Methods SEM (scanning electron microscopy) and EDXS (energy-dispersive X-ray spectroscopy) were used to determine the qualitative and quantitative composition of the samples. The research was performed using scanning electron microscope Tescan Vega3 LMU and an energy-dispersive X-ray microanalyzer (Oxford Instruments Aztec ONE with X-MaxN20 detector) at the Center for Collective Use "Laboratory of Materials Science of Intermetallic Compounds" at Lviv National University named after Ivan Franko.

Scanning of the surface of the samples (sections) was carried out using an electron beam (generated by a gun W-thermocathode) with a diameter of several nanometers and accelerated voltage of ~25 kV. The maximum resolution reaches 30.0 Å at high vacuum and voltage of 30 kV (increase ~1,000,000 times). The operating distance from the gun to the sample in the SEM method varies from the required increase, for sections of metal alloys is 15–20 mm. The microscope is designed to study samples in high and variable vacuum. At high vacuum (9.9–10^{-3} Pa), it is possible to investigate conductive samples (typical alloys of intermetallics), partially conductive samples (semiconductor alloys, films, crystals) or non-conductive samples (polymers, objects of biological origin, etc.) with a sprayed layer of conductive coatings (such as carbon or gold). Variable vacuum is more often used in the study of nano-objects with a developed surface. The microscope is equipped with two detectors SE and BSE. In the SE-detector mode ("secondary electrons"), the surface condition (topographic

contrast) of the sample can be estimated, and in the BSE-detector mode ("reflected secondary electrons") phases can be identified based on the contrast by the average atomic number (the phase with more electrons will be colored lighter than the phase based on elements with a smaller sequence number). The range of quantitative determination of elements is from Be to Cf. The optimal working distance from the gun to the sample in EDRS methods is 15–17 mm for conductive samples.

Arrays of experimental intensities and angles from the studied samples were obtained on an automatic diffractometer STOE STADI P (manufactured by STOE & Cie GmbH, Germany). It is equipped with a linear position-precision PSD detector according to the scheme of modified Guine geometry and the method of passing bending (CuKα1 radiation; concave Ge monochromator (111) of Johann type; range of angles 2θ was $4.000 \leq 2\theta \leq 99.985°$ with a step of 0.015° 2θ; step of the detector was equal to 0.480° (2θ).

The detail of the samples study by SAXS and XPS methods was reported in [19, 27, 28]. The procedure of determination of elements distribution in surface layer by XPS method was described in [27].

The photocatalytic properties of the samples in degradation of chloramphenicol (50 threshold limit values (TLV)) was determined under visible and UV irradiation. The study was carried out in a cylindrical reactor (9 cm diameter) with a wall-placed 10 cm height sample (implantation on both sides of the foil) and immersed thermostatically controlled radiation source. The source of radiation (high-pressure mercury or sodium lamps were used) was placed in reactor center, which permits to implement the investigation in both UV and visible range. The reaction products were analyzed on a SelmiChrom-2 gas chromatograph equipped with a FID on a stainless steel column (length 1 m, diameter 3 mm) filled with Porapak Q.

3 Results and Discussion

The data obtained by XRD method (Figs. 1 and 2) demonstrate the presence of (111) (200) and (220) planes austenite reflexes (initial stainless steel) in diffractograms of all synthesized samples with implanted titanium. This fact coincides with the results obtained in the work [27].

A similar situation is observed for samples on aluminum foil (Figs. 3, and 4).

The lack of reflexes other than the original ones can be explained by the fact that ionic implantation does not create distinct crystalline structures in the surface layer.

From the SEM data (cross section) [19, 27], it is known that the stainless steel surface after titanium implantation has the new layer (thickness of this layer is near to 80 nm).

The results of XPS study demonstrate the presence of titanium (target ions), oxygen (from air), and nitrogen (from plasma of the ion source) in this nanolayer [27] and the formation of amorphous titanium oxynitride and nitride of titanium in this layer on stainless steel surface as result of titanium implantation. It was shown [27] that treatment of this sample at 600 °C led to formation of titanium oxide in

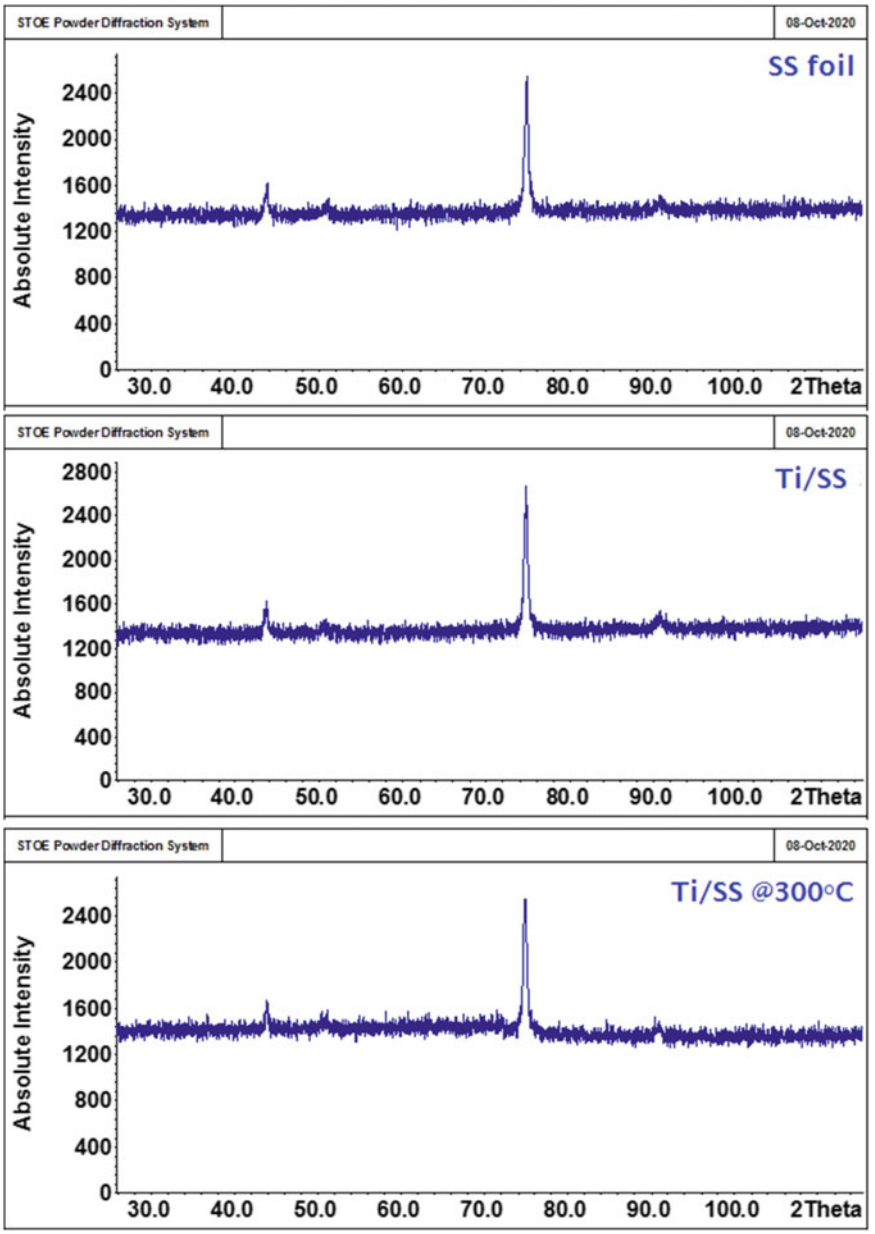

Fig. 1 Data of XRD analysis for initial SS foil, Ti/SS, and Ti/SS oxidized at 300 °C

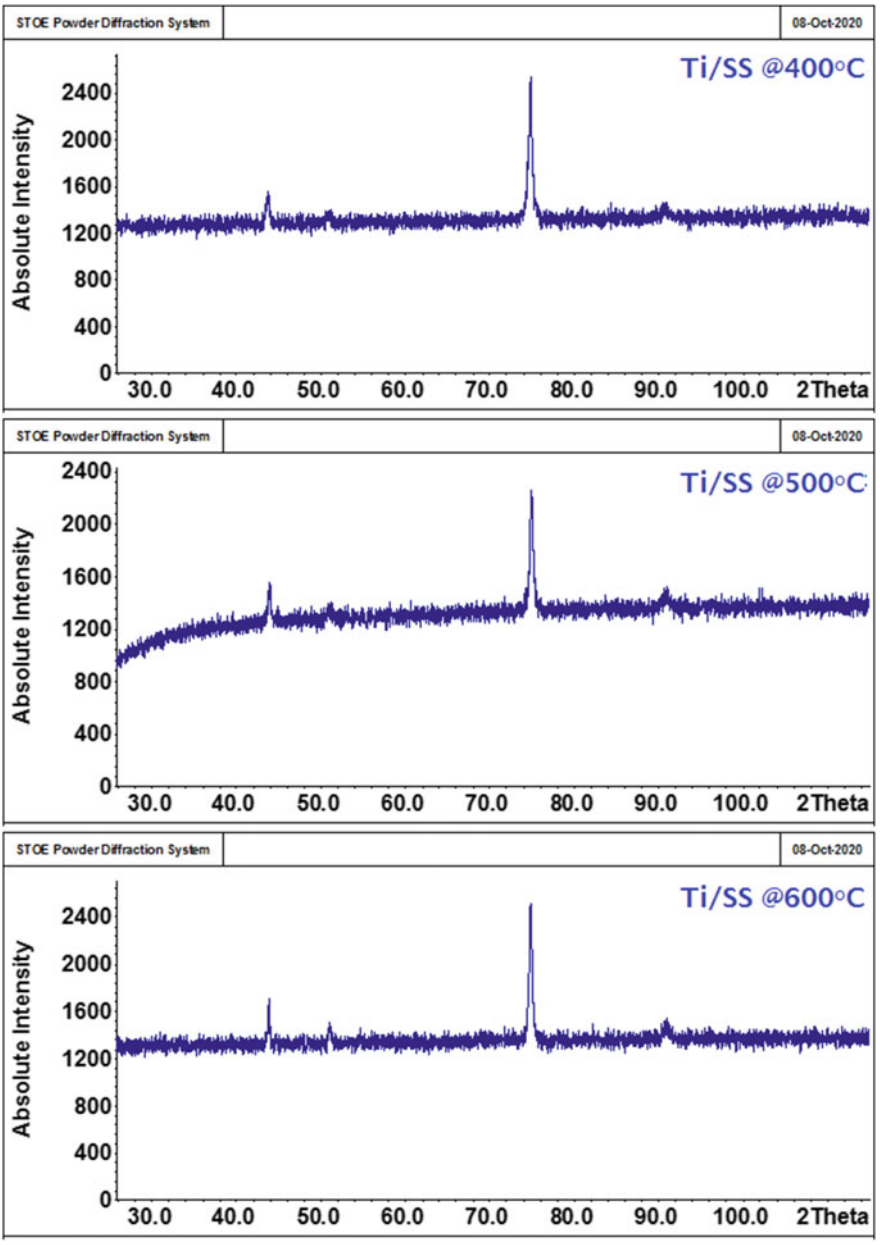

Fig. 2 data of XRD analysis for Ti/SS oxidized at 400, 500, and 600 °C

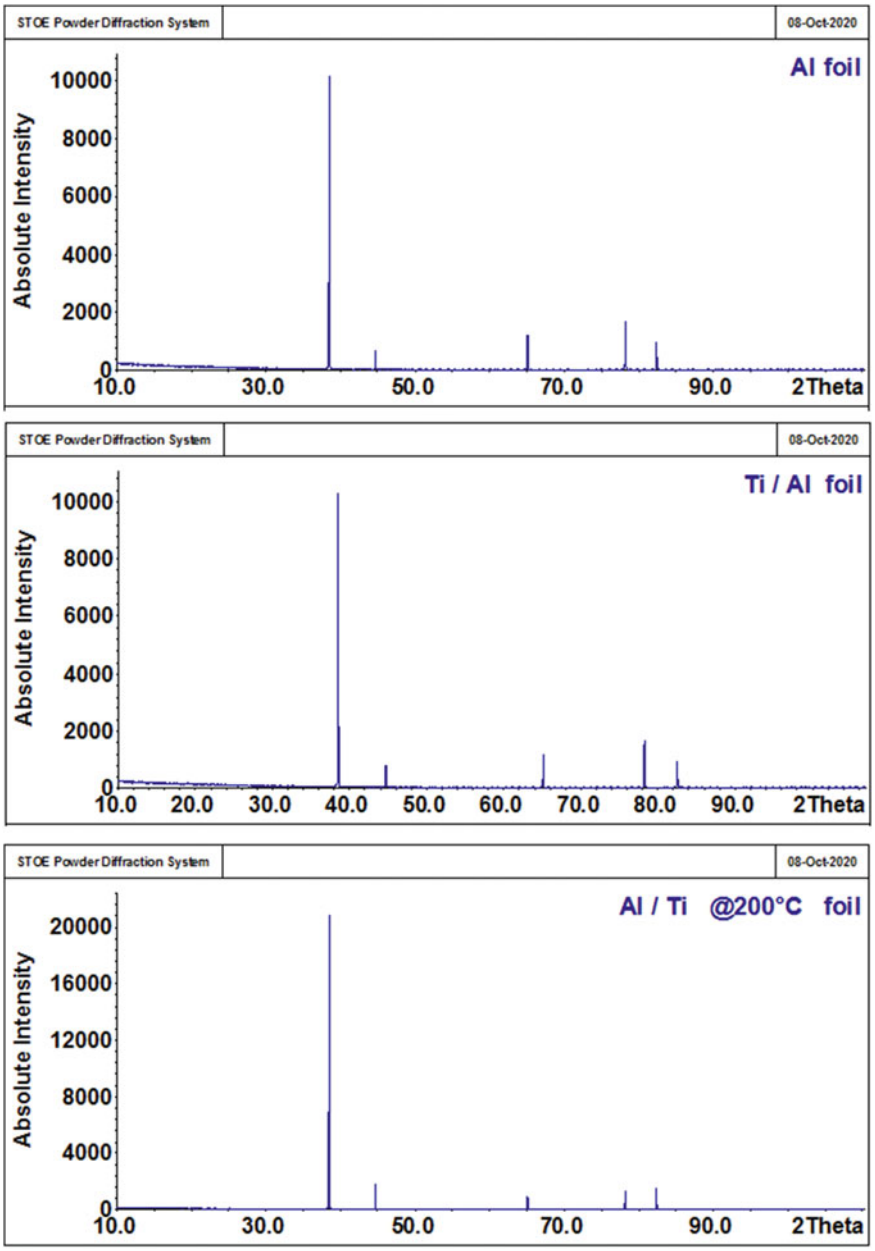

Fig. 3 Data of XRD analysis for initial Al foil, Ti/Al, and Ti/Al oxidized at 200 °C

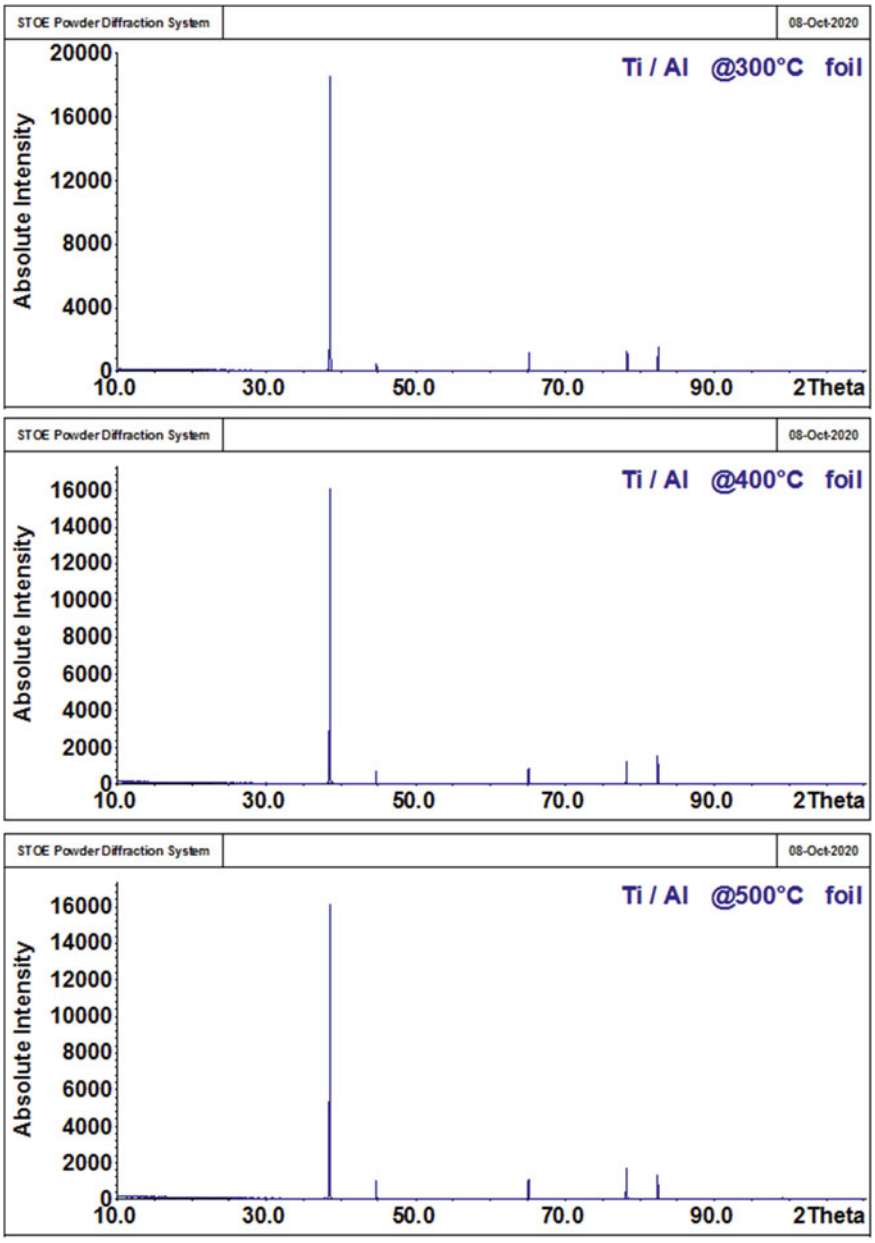

Fig. 4 Data of XRD analysis for Ti/Al oxidized at 300, 400, and 500 °C

this surface layer. The influence of other temperatures of the sample treatment on its properties was not studied. Therefore, an elemental analysis and morphology of the surface layer was performed using SEM and EDXS.

The results (Fig. 5) of the study of morphology (SEM) show that the treatment of the steel sample with titanium ions leads to the severity of the relief. Smaller formations are smoothed, and larger ones are enlarged. After annealing of the samples, the microgeometry changes again—there is a smoothing and averaging of defects. With increasing of the treatment temperature, this effect increases.

On initial sample of aluminum foil (Fig. 6), the defects are visible in the form of stripes, which is the result of production technology. After implantation of titanium, as well as for steel foil, there is an expression of a relief, which is smoothed at oxidation, leaving only technological strips.

The similarities in the behavior of implants on different media confirm the results of EDXS.

EDXS analysis of aluminum-based implants (Fig. 7) shown in the original sample only the components that must be according to the production technology. After implantation, the amount of oxygen in the samples increases and nitrogen appears which enters with the ion stream from the ion source plasma.

It is determined that after oxidation with a temperature of 500 °C (Fig. 7c) only the ratio of nitrogen–oxygen changes in favor of the latter.

Similarly, the composition of the sample synthesized by processing steel foil is changed (Fig. 8).

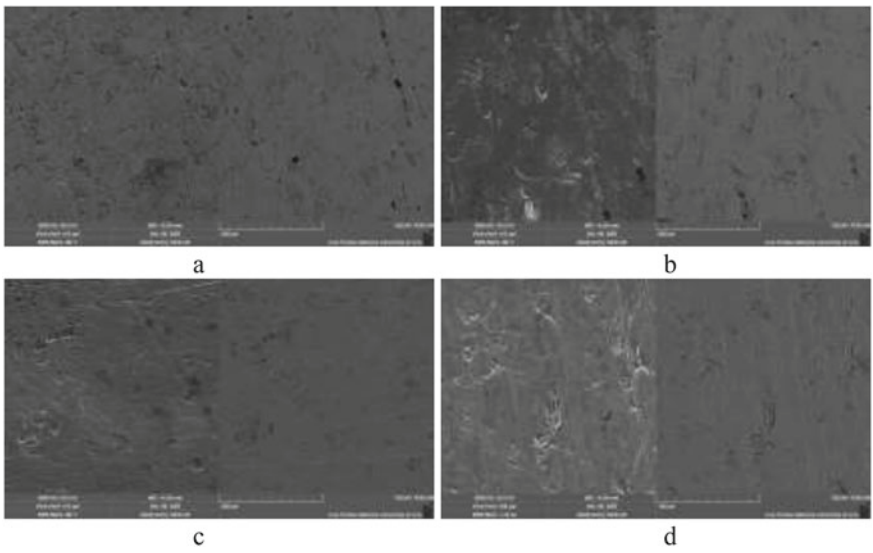

Fig. 5 Data of SEM investigation of initial steel SS (**a**), sample Ti/SS (**b**) and after its temperature treatment under 300 °C (**c**) and 400 °C (**d**)

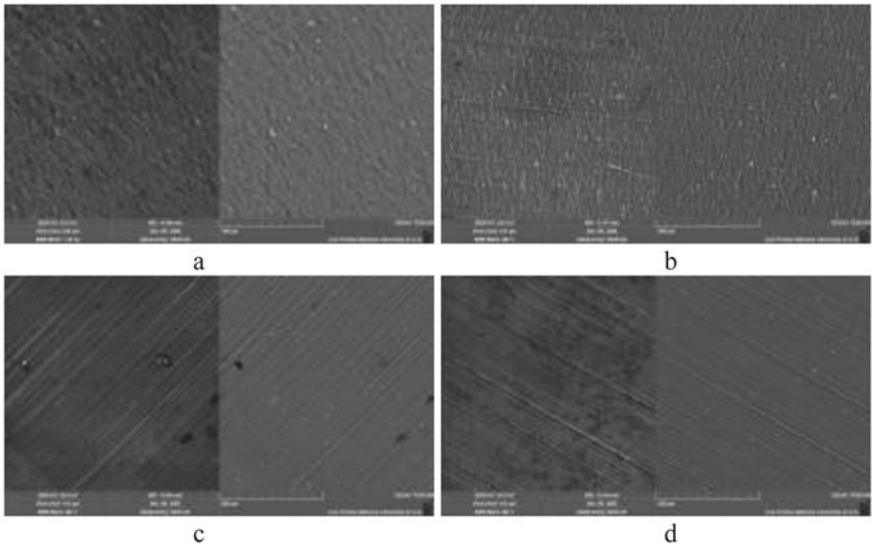

Fig. 6 Data of SEM investigation of initial foil Al (**a**), sample Ti/Al (**b**), and after its temperature treatment under 200 °C (**c**) and 300 °C (**d**)

The original sample (Fig. 8a) corresponds to the standard composition of the components.

During processing, it receives oxygen (Fig. 8b), which the amount increases after oxidation (Fig. 8c).

The obtained results of the samples investigation and the literature data [19, 27] show the perspective of the study of the synthesized implants in the reaction of chloramphenicol (CAP) decomposition (Fig. 9).

The obtained results of photocatalytic activity of implants with titanium ions demonstrate that the chloramphenicol degradation at UV irradiation (all samples were inactive in visible light irradiation) proceed with an offset toward the visible range. Moreover, the magnitude of this shift depends on the exposure time of the sample (Fig. 9). So, it is possible to suppose that photocatalytic activity of the catalysts prepared by ionic implantation of titanium on stainless steel depend on surface composition and morphology, which allows the selection of the appropriate catalyst.

4 Conclusions

The samples were synthesized on aluminum and steel carriers by ion implantation. It is shown that there are no newly formed crystalline structures in the surface layer of the support samples and this state is observed for oxidized carriers as well. The formation of surface nanolayer of implanted titanium was established.

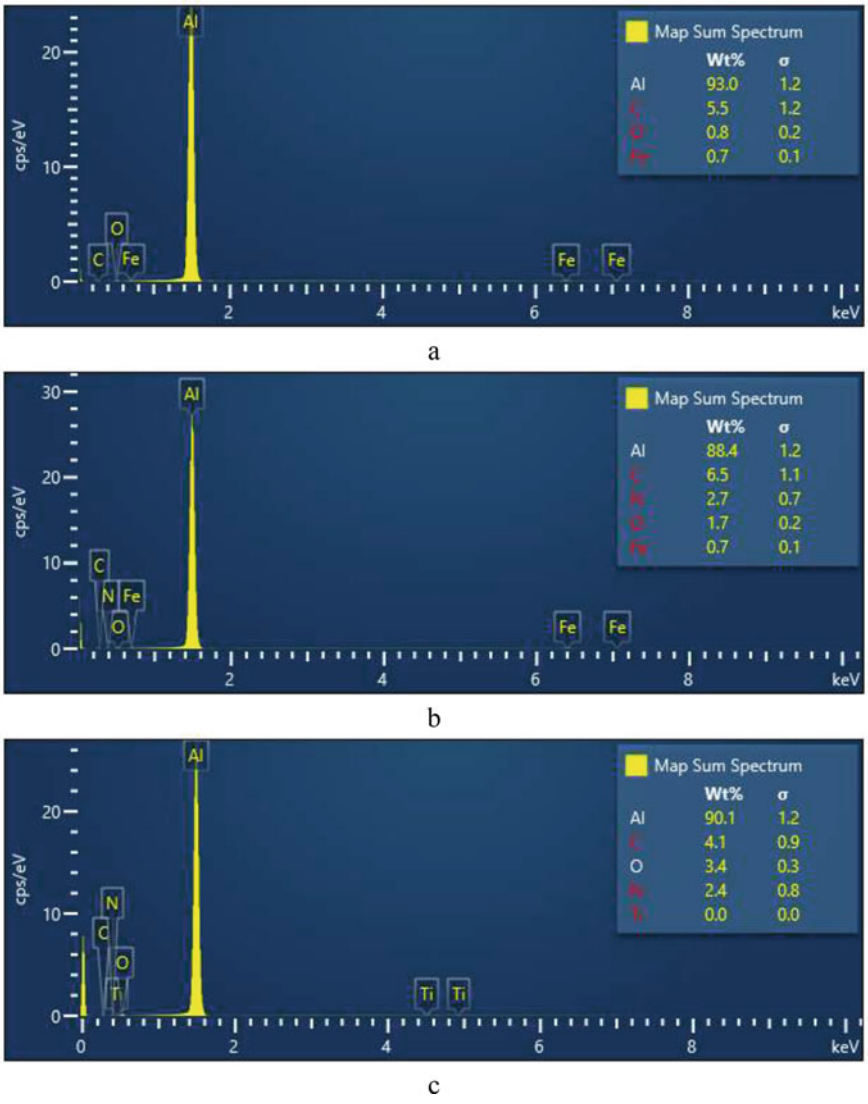

Fig. 7 Data of EDXS analysis of initial foil Al (**a**), sample Ti/Al (**b**), and after its temperature treatment under 500 °C (**c**)

It was found that the samples synthesized on stainless steel by ionic implantation change their morphology during oxidation in the same way as the samples on aluminum foil. It is shown that the nature of changes in surface composition for samples on different supports is similar. It was found that the implants show some photocatalytic activity in the decomposition reaction of chloramphenicol.

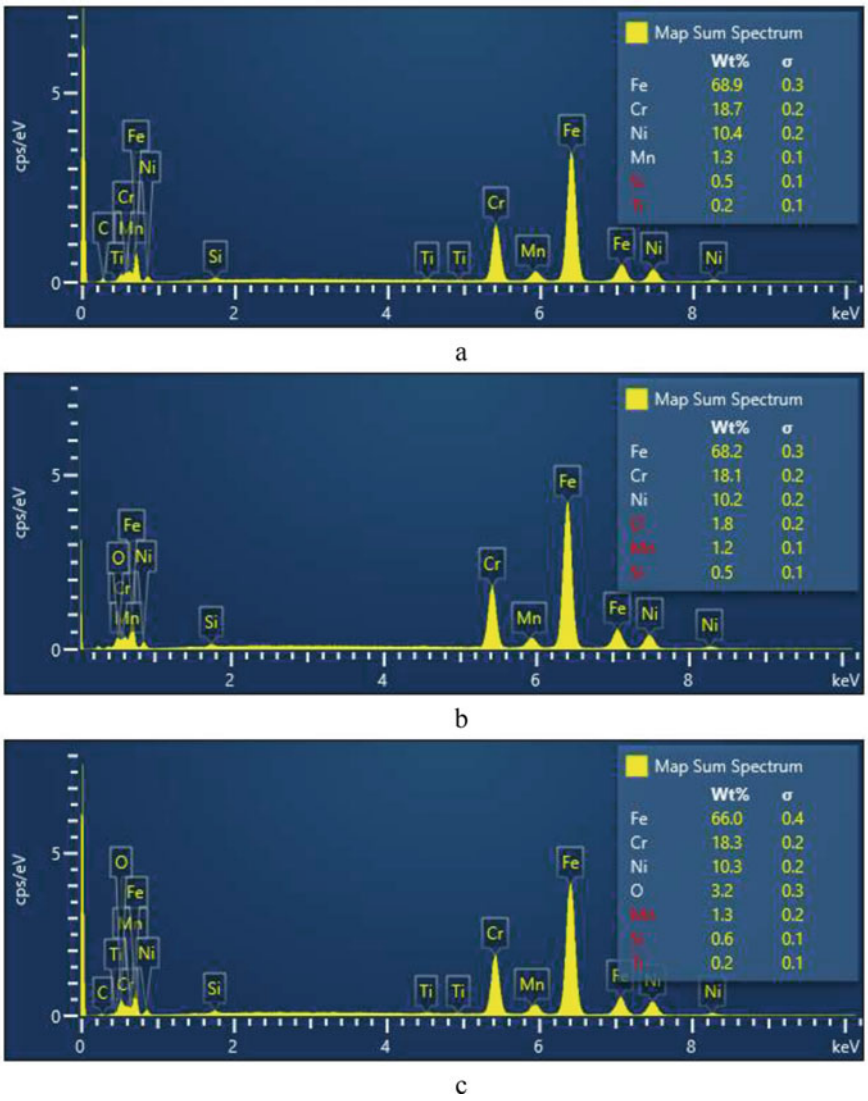

Fig. 8 Data of EDXS analysis of initial foil SS (**a**), initial sample Ti/SS (**b**), and after its temperature treatment under 500 °C (**c**)

Thus, ionic implantation has significant potential as a technology for the synthesis of photocatalysts, which is relevant for environmental catalysis, energetics, pharmaceutical industry and more.

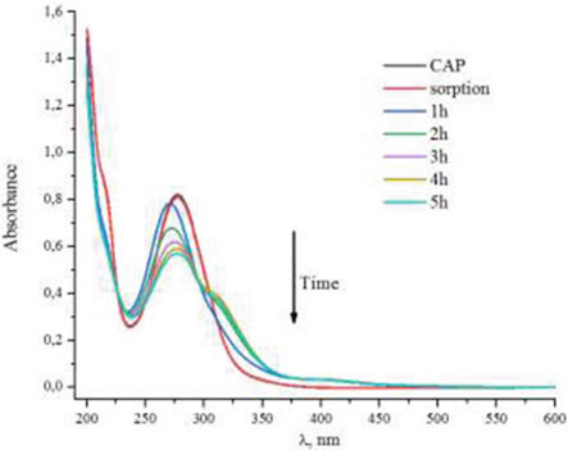

Fig. 9 Photocatalytic degradation of the chloramphenicol on the Ti/SS sample treated at 200 °C

Acknowledgements The investigations were realized with partial financial support of NAS of Ukraine Fundamental Programme "Fine Chemicals," Project 20-(14-16).

References

1. Homem V, Santos L (2011) Degradation and removal methods of antibiotics from aqueous matrices—a review. J Environ Manage 92:2304–2347
2. Michael I, Rizzo L, McArdell CS et al (2013) Urban wastewater treatment plants as hotspots for the release of antibiotics in the environment: a review. Water Res 47:957–995
3. Chatzitakis A, Berberidoua C, Paspaltsisb I et al (2008) Photocatalytic degradation and drug activity reduction of chloramphenicol. Water Res 42:386–394
4. Akimenko YuV, Kazeev KSh, Kolesnikov SI et al (2013) Ecological consequences of pollution of soils antibiotics. Izvestiya Samarskogo nauchnogo tsentra Rossiyskoy akademii nauk 15(3):1196–1199
5. Sarmah AK, Meyer MT, Boxall ABA (2006) A global perspective on the use, sales, exposure pathways, occurrence, fate and effects of veterinary antibiotics (VAs) in the environment. Chemosphere 65:725–759
6. Dolina LF, Savina OP (2018) Water cleaning from residues of medicinal preparations. Nauka ta prohres transportu. Visnyk Dnipropetrovs'koho natsional'noho universytetu zaliznychnoho transportu 3(75):36–51
7. Kulkarnia RM, Malladi RS (1989) Hanagadakara MS (20018) Ba-ZnO nanoparticles for photocatalytic degradation of chloramphenicol. AIP Conf Proc 020026:1–9
8. Baezab B, Lizamaa C, Caneob C et al (2007) Factorial design for the photodegradation of chloramphenicol with immobilized TiO_2. J Adv Oxid Techno 10(2):411–414
9. Palma TL, Vieira B, Nuneset J et al (2020) Photodegradation of chloramphenicol and paracetamol using PbS/TiO_2 nanocomposites produced by green synthesis. J Iran Chem Soc 17:2013–2031
10. Csay T, Racz G, Takacs E et al (2012) Radiation induced degradation of pharmaceutical residues in water: Chloramphenicol. Radiat Phys Chem 81:1489–1494
11. Qin Xu, Song Z, Ji S et al (2019) The photocatalytic degradation of chloramphenicol with electrospun Bi2O2CO3-poly(ethylene oxide) nanofibers: the synthesis of crosslinked polymer, degradation kinetics, mechanism and cytotoxicity. RSC Adv 9:29917–29926

12. Ma Y, Dongyao Wu, Liu C et al (2018) Preparation of Fe-Ag3VO4/GO composite photocatalyst for enhanced photodegradation of chloramphenicol. ICACEES 2018:199–203
13. Malato S, Fernandez-Ibanez P, Maldonado et al (2009) Decontamination and disinfection of water by solar photocatalysis: recent overview and trends. Cataly Today 147:1–59
14. Thompson TL, Yates JT (2006) Surface science studies of the pho-toactivation of TiO_2 new photochemical processes. Chem Rev 106:4428–4453
15. Hiroshi I, Yuka W, Kazuhito H (2003) Carbon-doped anatase TiO_2 powders as a visible-light sensitive photocatalyst. Chem Lett 32(8):772–773
16. Lin X, Rong F, Fu D, Yuan C (2012) Enhanced photocatalytic activity of fluorine doped TiO_2 by loaded with Ag for degradation of organic pollutants. Powder Tech 219:173–178
17. Ang YS, Tinia IMG., Suraya AR (2010) Immobilisation of titanium dioxide onto supporting materials in heterogeneous photocatalysis—a review. Appl Catal A General 389:1–8
18. Rachel A, Subrahmanyan M, Boule P (2002) Comparison of photocatalytic efficiencies of TiO2 in suspended and immobilised form for photocatalytic degradation of nitrobenzenesulfonic acids. Appl Catal B Environm 37:301–308
19. Honcharov V, Zazhigalov V, Sawlowicz Z, Socha R, Gurgol J (2017) Structural, catalytic, and thermal properties of stainless steel with nanoscale metal surface layer. In: Fesenko O, Yatsenko L (eds) Nanophysics, nanomaterials, interface studies, and applications. NANO 2016. Springer Proceedings in Physics, vol 195. Springer, Cham, pp 355–364
20. Chena J, Li Y, Li Z et al (2004) Production of COx-free hydrogen and nanocarbon by direct decomposition of undiluted methane on Ni–Cu–alumina catalysts. Appl Catal A 269:179–186
21. Magali BK, Sven GJ (1996) A review of the use of plasma techniques in catalyst preparation and catalytic reactions. Appl Catal A 147:1–21
22. Liu CJ, Vissokov G, Jang BWL (2002) Catalyst preparation using plasma technologies. Catal Today 72:173–184
23. Durme JV, Dewulf J, Leys C et al (2008) Combining non-thermal plasma with heterogeneous catalysis in waste gas treatment: a review. Appl Catal B 78:324–333
24. June KT, Jeong-Gil K, Ho-Young L et al (2014) Modification of optical and mechanical surface properties of sputter-deposited aluminum thin films through ion implantation. Int J Precis Eng Manuf 15(5):889–894
25. Kalin BA (2001) Radiatsionno-puchkovyye tekhnologii obrabotki konstruktsionnykh materialov. Fiz Khim Obrab Mater 4:5–16
26. Wang H, Zhang S, Yu D et al (2011) Surface modification of (Tb, Dy)Fe_2 alloy by nitrogen ion implantation. J Rare Earths 29(9):878–882
27. Zazhigalov VA, Honcharov VV, Bacherikova IV, Socha R, Gurgul J (2018) Formation of nanodimension layer of catalytically active metals on stainless stail surface by ionic implantation. Theor Experim Chem 34(2):128–137
28. Zazhigalov VA, Honcharov VV (2014) Formirovaniye nanorazmernogo pokrytiya na stali 12H18N10T pri ionnoy implantatsii. Metallofizika i Noveishie Tekhnologii 6(36):757–766

Impedance Spectroscopy of $NaBi(MoO_4)_2:Gd^{3+}$ Nanocrystals in the Pores of an Opal Matrix

Bilal Abu Sal, Khalil J. Hamam, V. N. Moiseyenko, O. V. Ohiienko, M. P. Derhachov, and D. O. Holochalov

1 Introduction and Background

The creation and study of the physical properties of new nanomaterials based on synthetic opals and active dielectric crystals are of fundamental interest from the point of view of the physics of low-dimensional systems. Such materials are 3D periodic structures of nanocrystals of active dielectrics formed in the pores of the opal matrix [1–3]. The unique physical properties of dielectric nanocrystals are due to size effects, which are caused by the increasing role of the surface with a decrease in size to less than 100 nm. In this case, the structure and properties of the surface of nanocrystals are radically different from the properties in the bulk of the crystal due to surface structural relaxation [4]. In [5], within the framework of the model of surface tension in nanoparticles, it was found that the activation energy of ionic conductivity decreases with decreasing nanoparticle size, while the conductivity increases. The revealed theoretical regularities are confirmed by the results of measurements of the temperature and size dependences of the conductivity of oxygen ions in nanograined ceramics ZrO_2:16% Y [6].

The aim of this work was to study the regularities of the temperature–frequency dependence of the electrical conductivity of $NaBi(MoO_4)_2:Gd^{3+}$ nanocrystals in the pores of the opal matrix by impedance spectroscopy.

Single crystals of $NaBi(MoO_4)_2$ doped with rare-earth metal ions are promising materials for solid lasers and require comprehensive study. The crystals are disordered in the distribution of Na^+ and Bi^{3+} ions in two non-equivalent type positions, while

B. A. Sal · K. J. Hamam
Applied Physics Department Faculty of Science, Tafila Technical University, Al-Eis 66141, P.O. Box 40, Tafila, Jordan

V. N. Moiseyenko · O. V. Ohiienko (✉) · M. P. Derhachov · D. O. Holochalov
Physics, Electronics and Computer Systems Department, Oles Honchar Dnipro National University, Prospect Gagarina, 72, Dnipro 49010, Ukraine

O. Fesenko and L. Yatsenko (eds.), *Nanomaterials and Nanocomposites, Nanostructure Surfaces, and Their Applications*, Springer Proceedings in Physics 263, https://doi.org/10.1007/978-3-030-74741-1_8

gadolinium ions Gd^{3+} occupy the position of bismuth [7]. Earlier, the study of the total conductivity in alternating fields in bulk single crystals of $NaBi(MoO_4)_2$ was carried out in [8], in which it was concluded the hopping mechanism of conductivity in these materials.

2 Sample Preparation and Experimental Techniques

2.1 Synthetic Opals and Nanocomposite Based on Them

Original synthetic opals were grown by natural sedimentation of monodisperse SiO_2 spheres synthesized by using the modified Stober technique [1, 9]. $NaBi(MoO_4)_2$:Gd^{3+} single crystal was grown by the Czochralski technique. The filling of the pores of opal samples was carried out by their impregnation with a melt of a single crystal ($T_m = 1133$ K) under the action of capillary forces [1]. The fact of the melt entering the opal pores was recorded by the shift of the maximum of the Bragg reflection band to the long-wavelength region.

2.2 X-ray Diffraction Patterns

XRD measurements on polycrystals powder of $NaBi(MoO_4)_2$:Gd^{3+} and composite were carried out on a DRON-3 diffractometer using Cu K_α radiation ($\lambda = 1.5418°$A).

2.3 Raman Spectra

Raman spectra were recorded in reflection geometry using a LabRamHR800 confocal Raman microscope (HORIBA Scientific, Jobin Yvon). Raman spectra were measured at various points of the (111) surface of the samples at room temperature after removing the remnants of the melt from the surface by grinding it.

2.4 Impedance Measurements

The powder of the composite was compressed into circular pellets (10 mm diameter and 1 mm thickness) under 10 tons (1 MPa) using a hydraulic press at room temperature. Both faces of the pellets were silvered to reduce possible surface current and achieved a good conductivity. Finally, pellets were sandwiched between two parallel electrodes to carry out measurements. The real and imaginary components of the

complex impedance as well as the phase shift were measured in the frequency range from 1 Hz to 1 MHz and temperature range from 290 to 390 K using Solartron-1260 Impedance/Gain Phase Analyzer with 1294 Dielectric Interface, UK. The applied voltage signal has an amplitude of 0.2 V with an accuracy of 0.1%. The real and imaginary components of the complex impedance as well as the phase shift were measured in the frequency range from 1 Hz to 1 MHz and temperature range from 363 to 473 K using LCR meter from Hioki. The applied voltage signal had an amplitude of 0.5 V. The temperature dependence measurements were measured inside an oven, under ambient atmospheric conditions.

3 Characterization of the Opal-$NaBi(MoO_4)_2$:Gd^{3+} Nanocomposite

3.1 X-ray Diffractograms

X-ray diffractograms (XRD) of opal-$NaBi(MoO_4)_2$:Gd^{3+} nanocomposite and polycrystalline powder of $NaBi(MoO_4)_2$:Gd^{3+} were measured (as shown in Fig. 1).

The comparison of X-ray bands of opal-$NaBi(MoO_4)_2$:Gd^{3+} nanocomposite and polycrystalline powder of $NaBi(MoO_4)_2$:Gd^{3+} is given in Table 1.

As can be seen from the table, the angular positions of the diffraction maxima for the opal-$NaBi(MoO_4)_2$:Gd^{3+} nanocomposite coincide with the data for the bulk

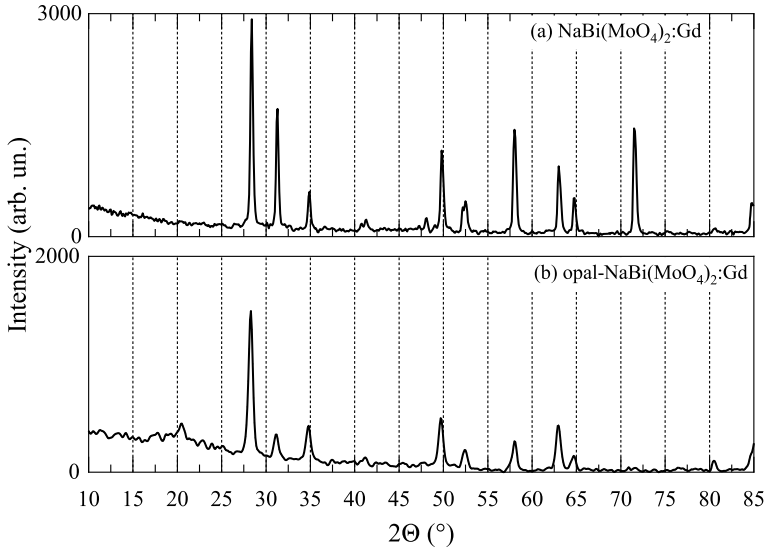

Fig. 1 X-ray diffraction patterns

Table 1 X-ray diffraction bands

$NaBi(MoO_4)_2:Gd^{3+}$ crystal		opal-$NaBi(MoO_4)_2:Gd^{3+}$	
2Θ (°)	Intensity (arb. units)	2Θ (°)	Intensity (arb. units)
28.4	2925.3	28.3	1414.8
31.3	1719.1	31.2	349.1
34.9	602.1	34.8	430.2
40.8	172.7		
41.3	227.1	41.2	133.8
49.8	1156.4	49.7	500.4
48.1	246.8		
52.3	371.6		
52.5	459.8	52.5	204.5
58.0	1439.6	58.1	280.8
63.0	945.5	62.9	434.5
64.8	517.5	64.8	146.7
71.5	1457.5		
		80.5	106.5

monocrystal within the measurement accuracy (±0.1 (°)). However, the intensities and half-widths of the reflexes differ. It is known that a decrease in the size of crystallites causes broadening of diffraction lines and that the integral width of the diffraction line profile is inversely proportional to the size of crystallites in the sample. Thus, broader diffraction peaks in the nanocomposite may indicate the presence of a nanocrystalline phase in the sample opal-$NaBi(MoO_4)_2:Gd^{3+}$.

3.2 Raman Spectra

Raman spectra of $NaBi(MoO_4)_2:Gd^{3+}$ nanocrystals in the pores of the opal matrix were measured in various points on the (111) surface of the composite sample (Fig. 2). The spectra had resonant and outwardly similar to the spectra of single crystals. The broadening of the lines in the low-frequency region, as indicated earlier, is associated with the disordering of Na^+ and Bi^{3+} ions in the crystal sublattice [10].

After subtracting the wing of the scattered light of the exciting radiation, the measured spectra were decomposed into spectral components. The results of the decomposition of the spectra into spectral components are shown in Fig. 3. The table shows the results of comparing a number of frequencies of the observed bands (Table 2).

Comparison of the spectral components frequencies in the Raman spectra of the opal-$NaBi(MoO_4)_2:Gd^{3+}$ nanocomposite and $NaBi(MoO_4)_2:Gd^{3+}$ single crystals

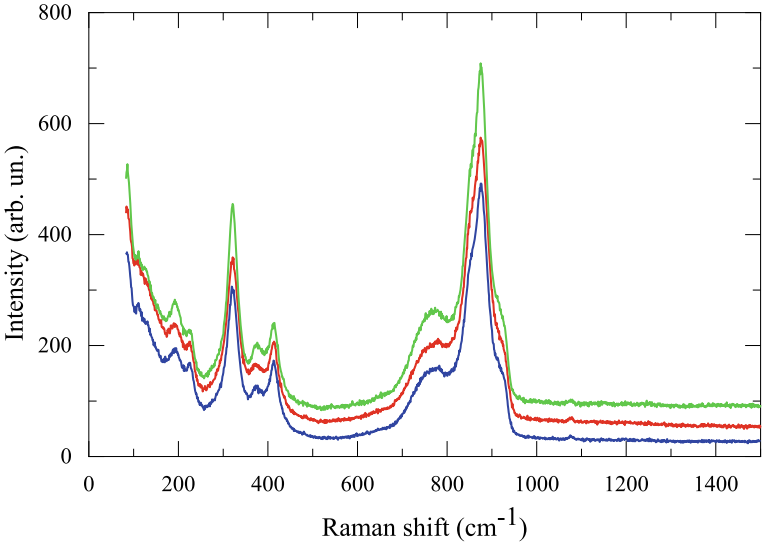

Fig. 2 Raman spectra of $NaBi(MoO_4)_2$:Gd^{3+} nanocrystals in the pores of the opal matrix, measured from different points of the (111) surface of the nanocomposite sample

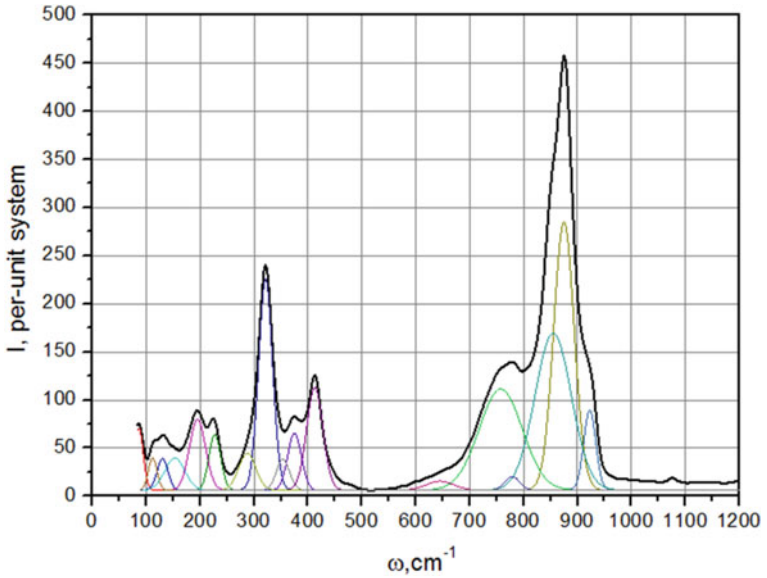

Fig. 3 Result of decomposition of the Raman spectra of $NaBi(MoO_4)_2$:Gd^{3+} nanocrystals in the pores of the opal matrix into spectral components

Table 2 Frequencies (cm^{-1}) of the bands in the opal—$NaBi(MoO_4)_2$ nanocomposite Raman spectrum

Nanocrystals in the opal matrix pores	Monocrystal [10]
	45 X(ZZ)Y
86	84 X(ZZ)Y
112	110 X(ZZ)Y
130	136 X(ZZ)Y
153	143 Z(XX)Y
	174 X(ZZ)Y
195	195 Z(YX)Y
227	236 Z(XZ)Y
	278 X(ZZ)Y
287	283 Z(YZ)Y
	313 X(ZZ)Y
	322 X(ZZ)Y
354	366 X(ZZ)Y
375	370 Z(YX)Y
381	397 X(ZZ)Y
412	410 Z(XX)Y
	476 X(ZZ)Y
	568 X(ZZ)Y
645	681 Z(XZ)Y
758	749 Z(XZ)Y
779	778 Z(YX)Y
	803 X(ZZ)Y
855	860 X(ZZ)Y
875	876 X(ZZ)Y
	911 X(ZZ)Y
925	925 Z(YX)Y
	957 X(ZZ)Y

[10] revealed differences: frequencies in the spectrum of a single crystal 143, 236, 366, 397, 681 cm^{-1} correspond to frequencies in the spectrum of nanocrystals in the opal matrix pores 153, 227, 354, 381 and 645 cm^{-1}. These changes can indirectly indicate a change in the lattice parameters and bond lengths on the surface and in the bulk of nanocrystals in the pores of the opal matrix.

4 Impedance Spectroscopy of Opal-$NaBi(MoO_4)_2$:Gd^{3+} Nanocomposite

Impedance hodographs (Nyquist plots) for nanocomposite are shown in Figs. 4 and 7. The temperature dependence measurements of impedance from 290 to 390 K are shown in Fig. 4a, b.

Samples were heated and then cooled in one cycle, and the measured impedance was recorded as shown in Fig. 4a, b. Impedance hodographs (Nyquist plots) for nanocomposite were undeformed semicircles. The semicircle centers were below the abscissa, which indicates a deviation from the ideal Debye behavior and is a characteristic of ionic conductors. Figure 4a shows that the bulk resistance of the material is increasing as the temperature increases, which is most probably due to the releasing of moisture from the material, while the impedance spectra (Nyquist plots) as shown in Fig. 4b indicate the semiconducting behavior of the material (the decreases of the bulk resistance of the material). The bulk conductivity was given by $\sigma_b = t/RA$, where A is the area of the electrodes, t is the thickness of the sample, and

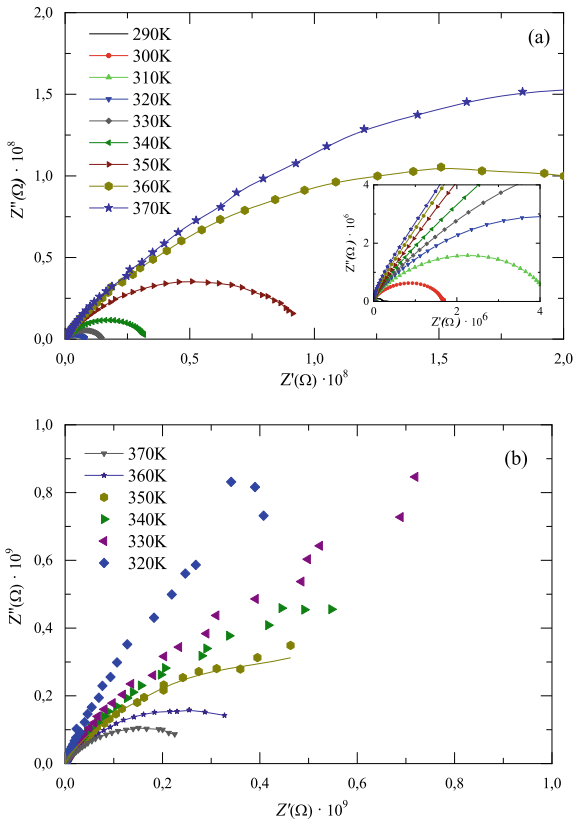

Fig. 4 Sample measured under increased temperature (**a**); sample measured when the temperature decreased (**b**)

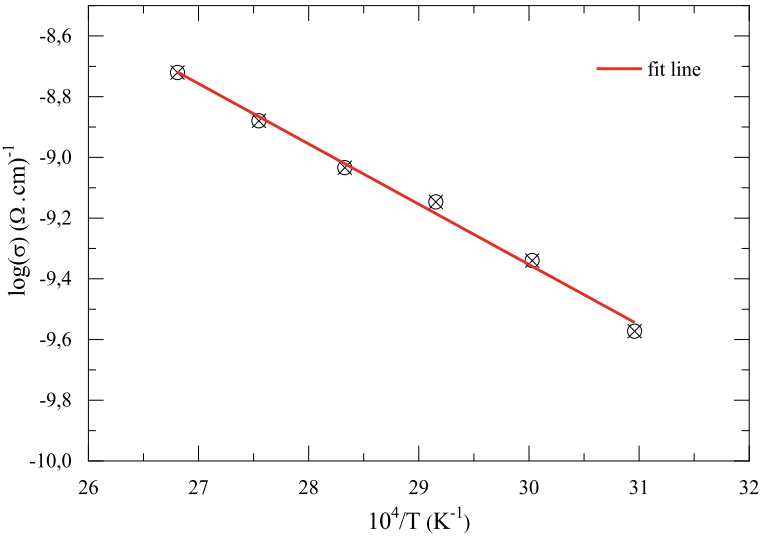

Fig. 5 Bulk conductivity as a function of temperature

R is the bulk resistance (determine from the diameter of the semicircle). Figure 5 shows that bulk conductivity (σ_b) has a temperature-independent activation energy and can be described by an Arrhenius equation as follows:

$$\sigma_b = \sigma_0 \exp\left(\frac{-E_b}{K_R T}\right)$$

where σ_o is the pre-exponent factor, E_b is the activation energy, T is the absolute temperature, and k_B is Boltzmann constant (8.61×10^{-5} eV K^{-1}). The calculated value of the bulk activation energy is $E_b = 0.17$ eV.

The type of conduction mechanism in the material can be determined by studying the frequency-dependent conductivity (σ_{ac}). σ_{ac} is usually expressed within the framework of the universal power law by Jonscher's power law (JPL) $\sigma_{ac} = A\,\omega^n$ [11], where A is a temperature-dependent parameter and n is the exponent factor. Figure 6 shows the temperature dependence of the exponent factor (n), where n is decreasing as the temperature increases. Such behavior of n was observed in many materials such as lithium phosphate glasses [12], silver phosphate glasses [13] and ceramic composites such as barium strontium titanate [14] and organic semiconducting materials as well [15]. The exponent factor behavior (decreases as temperature increases) and its recorded values ($n < 1$) make the correlated barrier hopping (CBH) model as proposed by Elliot [16] to be the most suitable model to describe the conduction mechanism inside of our present material. In CBH model, the charge carriers are assumed to hop between site pairs over the potential barrier separating them.

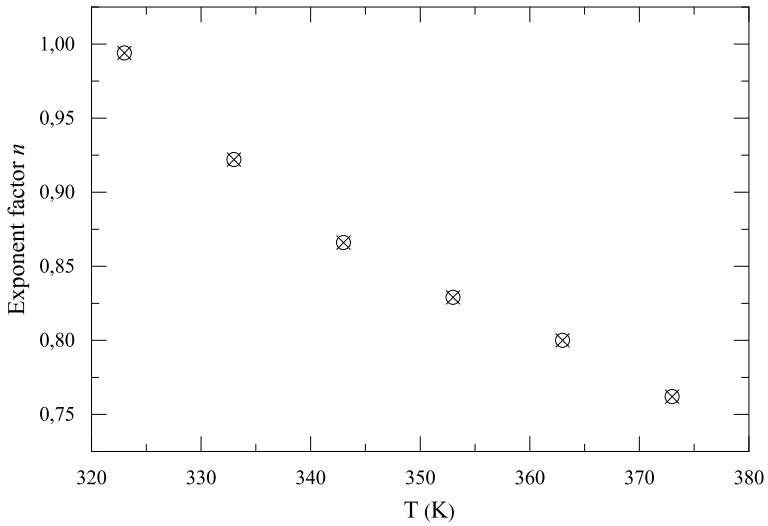

Fig. 6 Exponent factor of AC conductivity

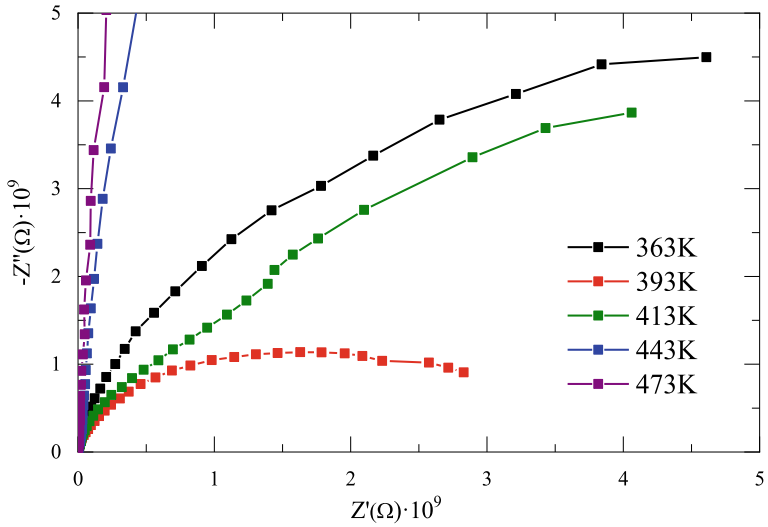

Fig. 7 Nyquist plot of real and imaginary parts of our material

The temperature dependence measurements of impedance from 363 to 473 K are shown in Fig. 7:

Figure 7 shows the Nyquist plot of the nanocomposite material under temperature range from 363 to 473 K. As observed from Fig. 7, it shows that the bulk resistance of the material does not have a specific trend which could be probably due to the

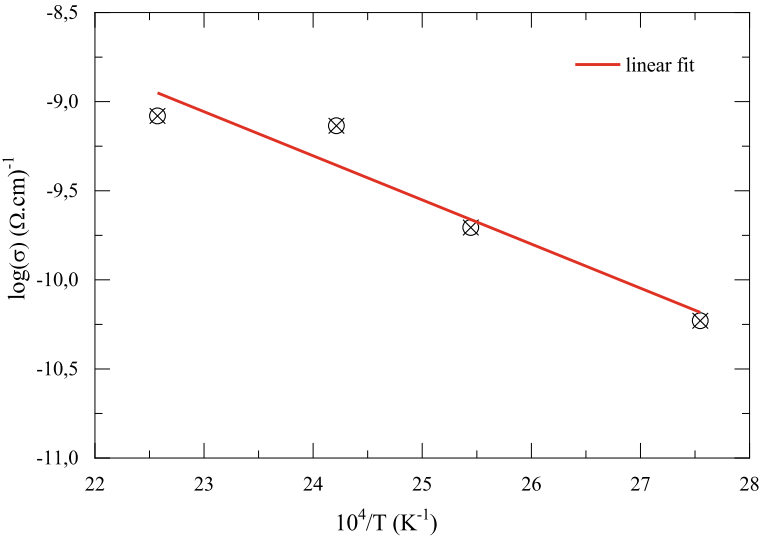

Fig. 8 Bulk conductivity as a function of temperature

desorption of oxygen and moisture from the material. At high temperature, the material tends to lose the semicircle behavior and a parallel line to the vertical line and shows the insulator behavior rather than a semiconducting property. In Fig. 8 shows the temperature dependence of bulk conductivity (σb) in the temperature range from 363K to 473K, which can also be described by the Arrhenius equation. The calculated value of the bulk activation energy is $E_b = 0.213$ eV (Fig. 8).

The obtained values of the activation energy of motion are the characteristics of superionic conductors. The type of conduction mechanism in the material can be determined by studying the frequency-dependent conductivity (σ_{ac}). σ_{ac} is usually expressed within the framework of the universal power law by Jonscher's power law (JPL) $\sigma_{ac} = A\ \omega^n$ [11], where A is a temperature-dependent parameter and n is the exponent factor. Figure 9 shows the temperature dependence of the exponent factor (n) at frequency higher than 10^4 Hz, where n is decreases as the temperature increases.

The theoretical dependence of the ionic conductivity was calculated using the formula from Glinchuk et al. [5], assuming that the main contribution to the conductivity is made by Na^+ ions as follows:

$$\frac{I_0}{A} \approx \exp\left(\frac{E_0}{kT}\right) \sinh\left(\frac{2\alpha V}{R_0 kT}\right)$$

The following values were used as the initial parameters: $E_0 = 1.2$ eV [8], the volume of the sodium ion $V = 3.94 \times 10^{-3}$ nm^3. A comparison of theory with experiment and the selected values of the surface tension coefficient α and the average radius of the nanocrystal R_0 are shown in Fig. 10.

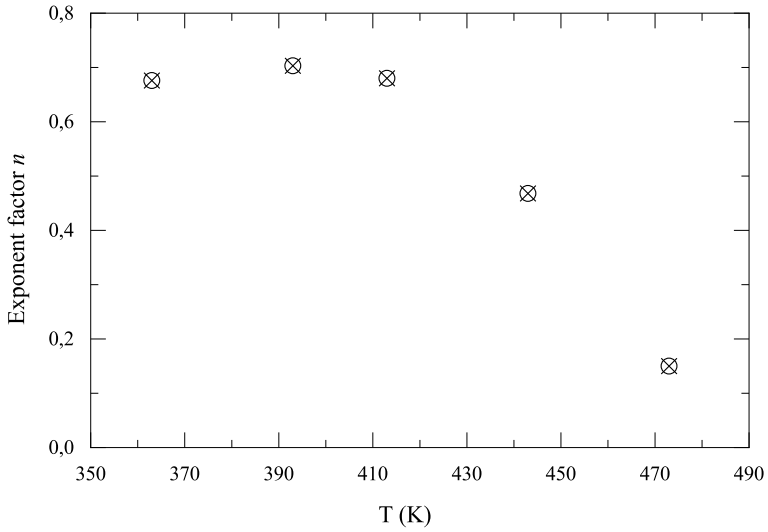

Fig. 9 exponent factor of ac conductivity

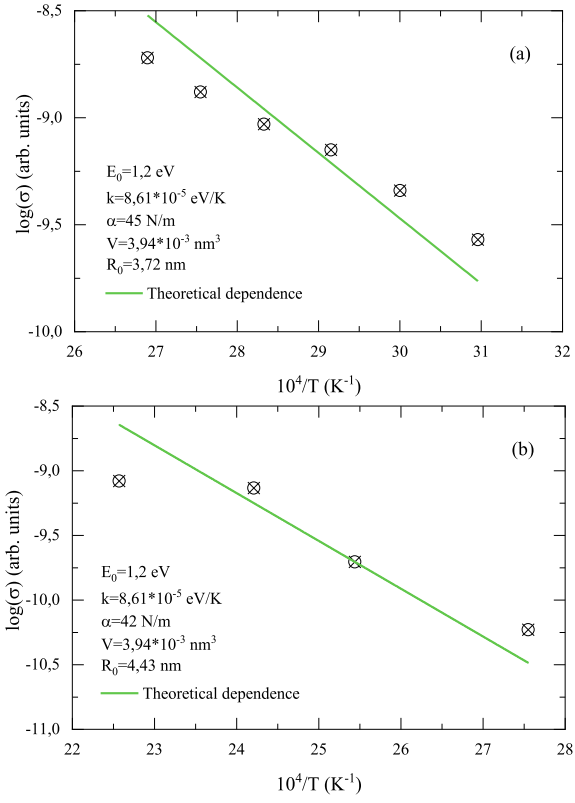

Fig. 10 Comparison of theory with experiment for the temperature dependence of the ionic conductivity of the opal-$NaBi(MoO_4)_2$:Gd^{3+} nanocomposite: $R_0 =$ 3.72 nm (a) and $R_0 =$ 4.43 nm (b)

As can be seen from Fig. 10a, b, the experimental points are in good agreement with the theoretical dependences in different temperature ranges. The thus obtained values of the nanocrystal sizes $R_0 \approx 4$ nm confirm the hypothesis that nanocrystallization occurs on the surface of globules, which has its own substructure of the same scale, the details of which are the centers of nanocrystallization.

Figure 11a, b shows the frequency dependences of the real and imaginary components of the impedance for different temperatures in the range 323–423 K. This is due to the fact that the contribution to the polarization with increasing frequency is made by the lighter O^{2-} ions, due to the non-stoichiometry of the crystals with respect to Mo, and other light ions of uncontrollable impurities concentrated on the nanocrystals surface.

Figure 12 shows the frequency dependence of the sample capacity for different temperatures in the range 323–423 K.

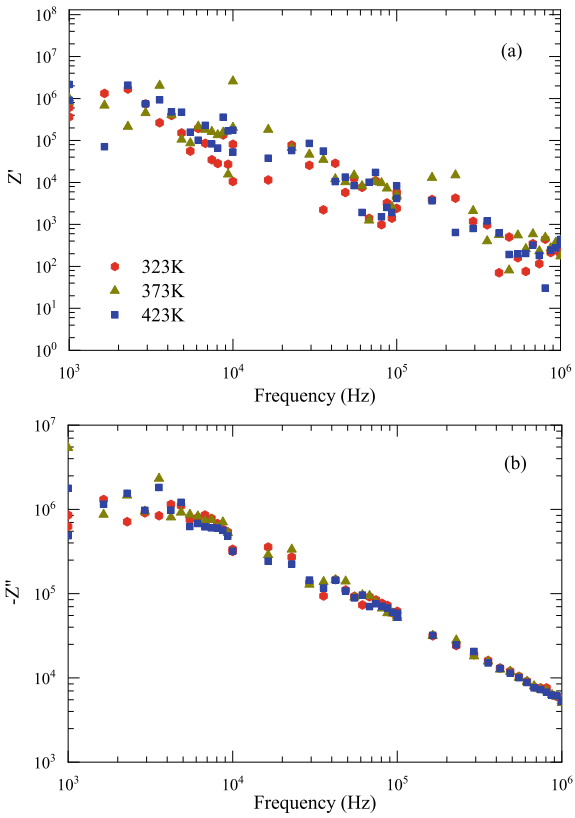

Fig. 11 Dependences of the real (**a**) and imaginary (**b**) components of the impedance for different temperatures in the range 323–423 K

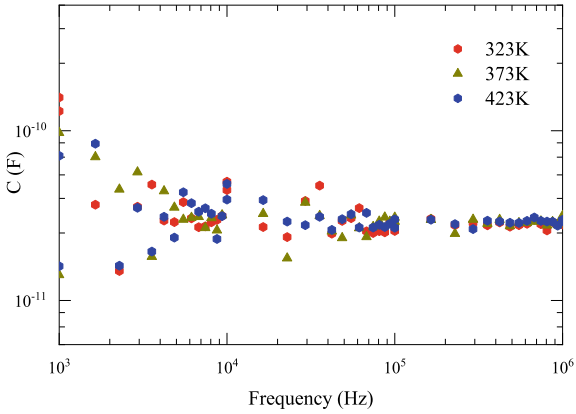

Fig. 12 Dependence of sample capacity for different temperatures in the range of 323–423 K

The average dielectric constant is 100 at 1 MHz, which is considered as high dielectric constant. The high values of the low-frequency dielectric constant of the $NaBi(MoO_4)_2$ crystals indicate a significant contribution to its value of the polarizability of Na^+ and O^{2-} ions, which is associated with their hopping over defects in the Na–Bi sublattice. The contribution of the electronic polarizability in these crystals is small and amounts to $\varepsilon_\infty \approx 5$ for $\lambda = 706$ nm [8]. Figure 12 shows that capacitance is independent from frequency. These results revealed an insulating behavior.

5 Conclusions

Measurements performed confirm the hopping mechanism of conductivity in the nanocomposite. The results obtained suggest that the conductivity in the nanocomposite is mainly ionic and is due to the migration, which includes alternating jumps of Na^+ cations (main contribution to conductivity) and oxygen ions (O^{2-}). In this case, one cannot exclude an additional electronic contribution to the conductivity due to the electron hopping in the impurity band [17]. The value of the activation energy of conduction ($\approx$0.2 eV) obtained from the dependence $\sigma\ (T)$ differs markedly from the corresponding value in the bulk of a single crystal (1.2 eV) [8]. The result obtained indicates the dependence of the activation energy on the particle size and correlates well with the results of calculating this dependence for particles $\leq$40 nm at different values of the surface tension coefficient α [5]. It should also be noted that, in the case of nanocrystals in opal pores, the conductivity is predominant of a surface nature. In this case, the structure and properties of the surface of nanocrystals differ from the properties in the bulk of the crystal by a large number of defects and the effect of surface tension on the value of energy barriers to ion diffusion and, accordingly, the activation energy of conduction [5].

Acknowledgements Special thanks to Deutsche Forschung gemeinschaft for the grant which offered one of us to use the Raman in Technische Universität Chemnitz, Institute of Chemistry.

References

1. Moiseienko V, Derhachov M, Abu Sal B, Holze R, Brynza M (2017) Nanocomposites on the base of synthetic opals and nanocrystalline phases of Bi-containing active dielectrics. Springer Proc Phys 50(195):661–674
2. Derhachov M, Moiseienko V, Kutseva N, Abu Sal B, Holze R, Pliaka S, Yevchyk A (2018) Structure, optical and electric properties of opal-bismuth silicate nanocomposites. Acta Phys Pol A 133(4):847–850
3. Derhachov M, Moiseienko V, Kutseva N, Abu Sal B, Holze R (2019) Fabrication and characterization of crystalline Bi_2TeO_5–$Bi_4Si_3O_{12}$–SiO_2 nanocomposite. Eur Phys J Plus 134
4. Boyko YI, Korshak VF (2015) Poverkhnostnaya strukturnaya relaksatsiya i plastichnost' nanokristallov. VANT 5(99):77–80
5. Glinchuk MD, Bykov PI, Khilcher B (2006) Osobennosti ionnoy provodimosti kisloroda v oksidnoy nanokeramike. Fizika tverdogo tela 48(11):2079–2084
6. Kosacki I, Anderson H (2000) Ionics 6:294
7. Ryadun AA, Nadolinnyy VA, Tsydypova BN, Pavlyuk AA (2015) EPR i fotolyuminestsentsiya kristallov $NaBi(MoO_4)_2$, aktivirovannykh ionami gadoliniya. Fizika tverdogo tela 57(6):1168–1171
8. Koleschnichenko KA, Korkin SG, Kudzin AY, Stolpakova TM, Gontarenko YV (1991) Pryzhkovaya provodimost' v kristallakh. Fizika tverdogo tela 33(3):751–754
9. Stöber W, Fink A, Bohn E (1968) Controlled growth of monodisperse silica spheres in the micron size range. J Colloid Interface Sci 26(2):62–69
10. Moiseyenko VN, Bogatirjov YI, Jeryemenko AM et al (2000) Raman spectra of acoustooptic $NaBi(MoO4)_2$. J Raman Spectroscopy 31:539–541
11. Jonscher AK (1999) Dielectric relaxation in solids. J Phys D Appl Phys 32.https://doi.org/10.1088/0022-3727/32/14/201
12. Hamam KJ, Salman F (2019) Dielectric constant and electrical study of solid-state electrolyte lithium phosphate glasses. Appl Phys A 125.https://doi.org/10.1007/s00339-019-2868-2
13. Cutroni M, Mandanici A, Mustarelli P, Tomasi C, Federico M (2002) Ionic conduction and dynamical regimes in silver phosphate glasses. J Non Cryst Solids 307–310. https://doi.org/10.1016/S0022-3093(02)01561-2
14. Saif AA, Poopalan P (2011) Correlation between the chemical composition and the conduction mechanism of barium strontium titanate thin films. J Alloys Compd 509:7210–7215. https://doi.org/10.1016/j.jallcom.2011.04.068
15. Hamam KJ, Mezei G, Khattari Z (2019) Temperature and frequency effect on the electrical properties of bulk nickel phthalocyanine octacarboxylic acid (Ni-Pc(COOH)8). Appl Phys A 125:7. https://doi.org/10.1007/s00339-018-2147-7
16. Elliott SR (1987) A.c. conduction in amorphous chalcogenide and pnictide semiconductors. Adv Phys 36:135–217. https://doi.org/10.1080/00018738700101971
17. Milnes AG (1973) Deep impurities in semiconductors. John Wiley & Sons, New York, London, Sydney, Toronto

The Practical and Industrial Significance of Magnetic Materials Based on $NiFe_2O_4$. A Review

Iryna Ivanenko and Serhii Lesik

1 Introduction to Nickel Ferrites

Well-known spinels of nickel ferrites were first synthesized a long time ago. The first reliable mentioning of nickel ferrites dates back to [1]. Until the 1990s, only a few scientific papers on this material had been published. However, the great development of science has significantly increased the potential application of nickel ferrites spinels, and therefore, more and more scientists are involved in this area of investigation every year. A graphical representation of the publication numbers is presented in Fig. 1.

Nickel ferrites have a large number of favorable properties that distinguish this material from others. These properties include: high electrical resistance, low hysteresis losses, high permeability at high frequencies, chemical stability, mechanical stability and hardness, low dielectric losses, and the most important characteristics is their reasonable cost.

Due to its high characteristics, this material has been used in many applications in various fields, such as catalysis, electronic media, water treatment, energy, telecommunications, protective nanocoatings [3], medicine, biotechnology, magnetic fluids [4], and sensors [2, 5, 6].

I. Ivanenko (✉) · S. Lesik
Department of Inorganic Substances Technology, Water Treatment and General Chemical Engineering of National Technical University of Ukraine, "Igor Sikorsky Kyiv Polytechnic Institute", 4 building, 37 Peremohy ave., 03056 Kyiv, Ukraine

O. Fesenko and L. Yatsenko (eds.), *Nanomaterials and Nanocomposites, Nanostructure Surfaces, and Their Applications*, Springer Proceedings in Physics 263, https://doi.org/10.1007/978-3-030-74741-1_9

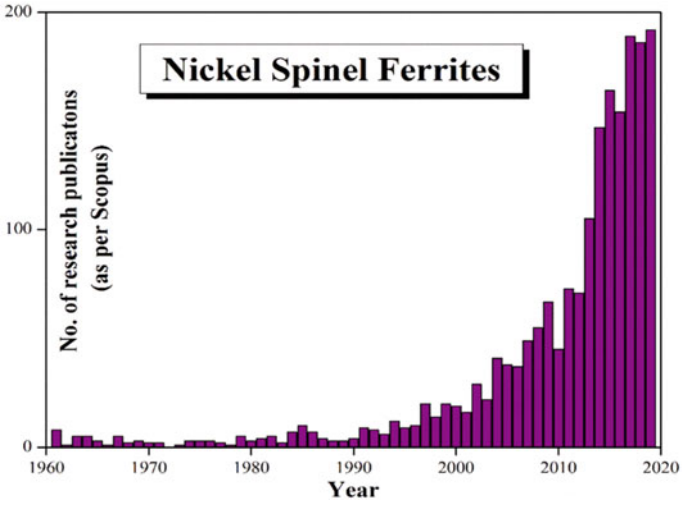

Fig. 1 Number of publications on nickel ferrites in the years 1960–2019 [2]

2 Brief Description of Nickel Ferrites and Methods of Their Obtaining

Nickel ferrites were called the spinels because of their original structure coming from the natural mineral $MgAl_2O_4$, named spinels, and, in general, they have a formula AB_2O_4. It also should be underlined that nickel ferrites are unordinary spinels. They are inverse spinels. A typical structure of normal spinel can be seen in Fig. 2a, thanks to our colleagues for the source [5] and (Fig. 2b) for the source [7].

In the spinel ferrites, the oxygen anions are arranged in a cubic close-packed lattice and the cations of Me and Fe occupy two different crystallographic sites, namely, the tetrahedral (A) and the octahedral (B) sites. The cubic unit cell consists of 56 atoms,

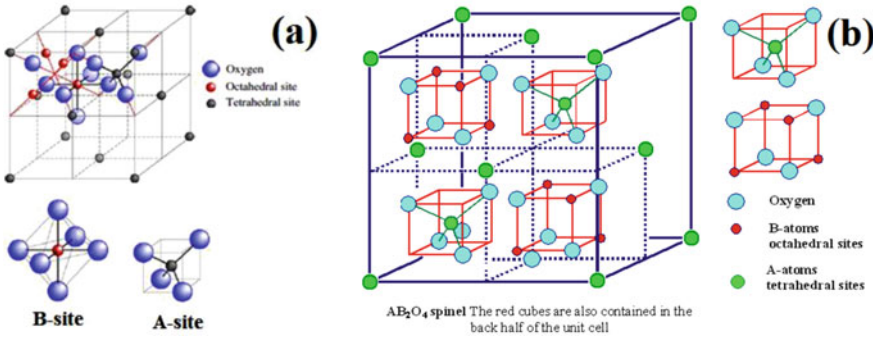

Fig. 2 Typical structure of the spinel (AB_2O_4) [5, 7]

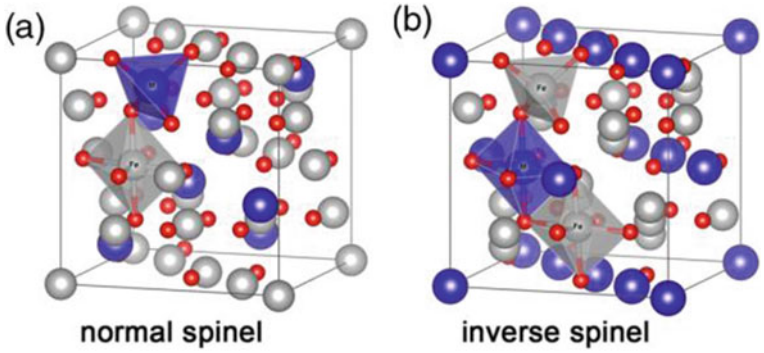

Fig. 3 Unit cell structure of **a** a normal spinel ferrite, and **b** an inverse spinel ferrite [10]

32 oxygen anions, and 24 cations, 8 of which occupy tetrahedral sites and the other 16 ones are located at the octahedral sites [7–9].

In a normal spinel, Me ions are located in the tetrahedron, while Fe^{3+} ions are in the octahedron. In inverse spinels, the opposite situation is observed, when Fe^{3+} ions are located in the tetrahedron, and Me and Fe^{3+} ions are evenly distributed in the octahedron. The visualized structure is presented in Fig. 3.

High electrical and magnetic properties of $NiFe_2O_4$ depend on the nature, charges, and distribution of metal ions. However, $NiFe_2O_4$ exhibits ferromagnetism, which causes the magnetic moment of the antiparallel spins between the Fe^{3+} ions on A-sites and the Ni^{2+} on B-sites [10].

There are many different methods of the nickel ferrites spinels synthesis. In chronological order, the first of the methods is: the hydrothermal [11], the arc image furnace [12], the mechanical activation [13], the ball milling [14], the self-propagating high-temperature synthesis [15], the high-energy mechanical milling [16], the sol–gel using polyacrylic acid [17], the co-precipitation [18], the spin spray ferrite plating [19], the micro-emulsion [20], the precursor approach with ultra-sound radiation [21], the sol–gel based on vacuum sublimation (2007) [22], the melt-injection-decomposition (2018) [23], and others.

Let us consider the main of them: the sol–gel method [3, 24–30], the combustion under the action of microwave radiation [31], the hydrothermal [32], the co-precipitation [17, 33, 34], the electrodeposition [35].

2.1 Sol–gel Method

Traditionally, the essence of the method constitutes the preparation of nitrates solution (Ni^{2+} and Fe^{3+}) in a ratio of 1:2. The nitrate salts of the corresponding metals, being natural minerals, are widely used, due to their easy accessibility, and a high degree of dissolution in water. Polyvinyl alcohol [24], glycolic acid [25], citric acid

[26], and others usually are usually used for the formation of the gel. A typical diagram is shown in Fig. 4 [23].

The final solution is dehydrated by stirring for 2 h, and the resulting gel is calcined at different temperatures. During the calcination, nickel ferrites are formed through the ash stage. As a result of this synthesis, some dependence of the main characteristics was discovered. They are presented in Fig. 5 and Table 1.

As far as the above-mentioned dependencies are concerned, with the increasing of calcination temperature, both the size of the obtained nanoparticles and the degree of their magnetic saturation rise.

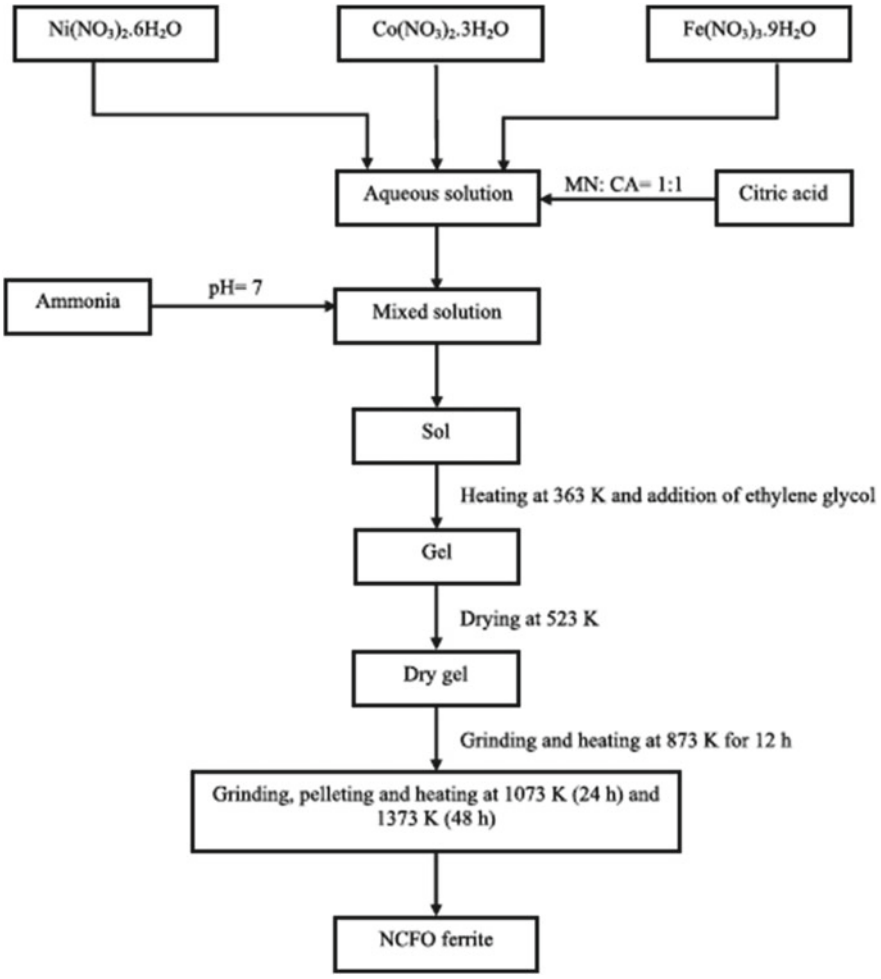

Fig. 4 Block diagram of Pechini sol–gel technique adopted by Hcini et al. for the synthesis of Ni-Co and Mg-Co ferrites [23]

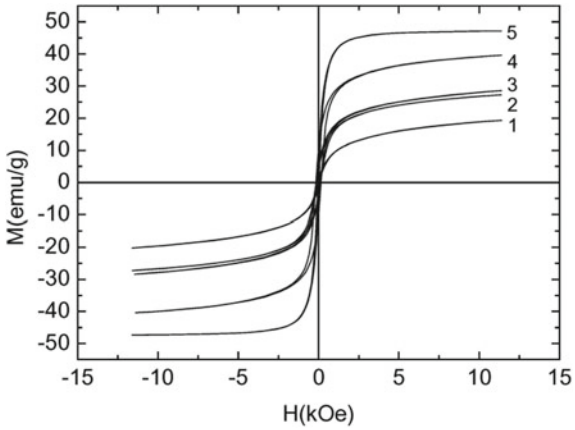

Fig. 5 Magnetic hysteresis loops at 300 K for $NiFe_2O_4$ samples with different sizes [24]

Table 1 Particle size of $NiFe_2O_4$ samples annealed at different temperatures [24]

T, K	673	773	823	1073	1373
D, nm	12	21	24	46	114

It should be emphasized, that the sol–gel method has a number of advantages over other methods, namely the purity of the product, chemical homogeneity, the ability to obtain nanoparticles with predetermined sizes, etc.

2.2 Combustion Under the Influence of Microwave Radiation

As it was mentioned in the previous method, the solution of nitrates Ni^{2+} and Fe^{3+} in a ratio of 1:2 is prepared. In addition, trisodium citrate (in the concentration of 0.2 M) is added to the mixture, as a fuel for combustion. The following mixture is evaporated at the temperature of 80 °C. The evaporated mixture is adjusted to pH 13 with the help of sodium hydroxide and placed under microwave radiation (2.45 GHz, 700 W) for 30 min. The resulting mixture is burned and ground [31].

The EDX spectrum is shown in Fig. 6. According to the obtained spectrum, the calculated ratio of Ni:Fe is 16.48%:31.13%, which is close to the stoichiometry [31].

This method is the fastest one among the others, but the biggest flaw of it is the lack of variety.

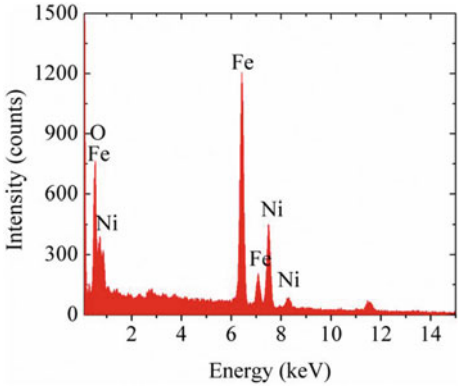

Fig. 6 EXD spectrum [31]

2.3 *Hydrothermal Method*

The hydrothermal method of producing nickel ferrites has long been an advanced method. The essence of the method is to prepare a solution of nitrates Ni^{2+} and Fe^{3+} in a ratio of 1:2, to obtain 0.1 M and 0.2 M solutions, respectively, in 40 mL of deionized water. 10 mL of 8 M NaOH are added to this solution. The resulting mixture is autoclaved for 10 h at the temperature of 180 °C. The resulting powder is washed with plenty of water and dried in vacuum at 50 °C for 4 h [32].

The obtained results are shown as the XRD pattern in Fig. 7. As we can see from the spectrum, the obtained powder has a high purity. The conducted magnetic researches also confirm the reception of nickel ferrites spinel.

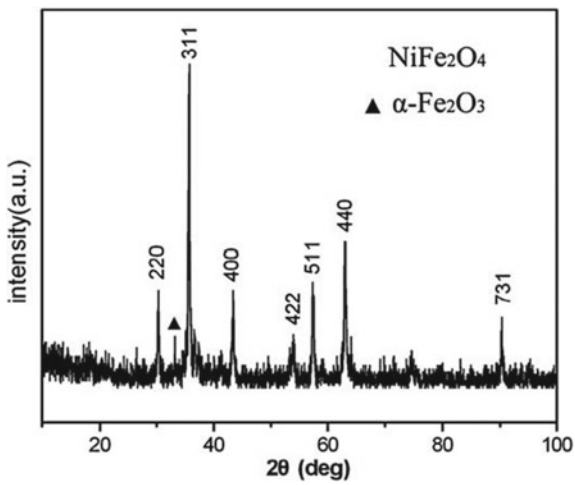

Fig. 7 XRD pattern of the as-synthesized nickel ferrite powder [32]

The method is definitely one of the best in terms of obtaining pure and homogeneous nickel ferrites, but the main flaws of it are the duration and the cost of the method.

2.4 Co-precipitation

According to the study [33], the starting materials were $FeCl_2 \cdot 4H_2O$ and $NiCl_2 \cdot 6H_2O$. The prepared crystal hydrates are dissolved in deionized water, evaporated at the temperature of 313 K for 3 h with constant stirring. The products are washed with a large amount of deionized water and then calcined for 6 h in a muffle furnace at the temperatures of 823, 1023, 1223 K.

As a result of the analysis of the obtained powders, it was found that with the increasing of the annealing temperature the content of the nickel ferrite phase decreases sharply, as is shown in Table 2.

The co-precipitation method was one of the first methods of the nickel ferrites synthesis, but it was not widely used due to the inability of controlling the formation of spinel particles.

3 Practical and Industrial Significance and Application of the Newest Materials Based on Nickel Ferrites

After considering the basic facts about nickel ferrites, it is necessary to pass on the most important part of review, which is their practical application and prospects of development.

Table 2 Phase composition of $NiFe_2O_4$ samples [33]

Temperature, K	Phase	%
823 K	$NiFe_2O_4$	99.13
	Fe_2O_3	0.87
1023 K	$NiFe_2O_4$	93.04
	Fe_2O_3	6.96
1223 K	$NiFe_2O_4$	46.94
	Fe_2O_3	54.00
	NiO_2	2.06

3.1 Energy

The latest direction of nanocomposite power carriers has drawn the scientist's attention to the spinel of nickel ferrites. The tested composite (GNP) was obtained from nickel ferrite, graphene, and polypyrrole. Its formation method is shown in Fig. 8.

According to Koop's theory, the formation of a multilayer capacitor was admitted to be in excellent suitability with the Maxwell–Wagner model. Hence, the dielectric permittivity has been increased. The formation of one and two semicircles in Nyquist plot revealed the existence of grain boundaries and grains effects. The effect of grain boundaries and grains themselves could be distinguished by the Nyquist plot. The non-Debye-type relaxation phenomenon has been observed from the complex electric modulus analysis. The GNP sample efficiently offers its potential use in energy storage devices.

Another promising area for the development of "green energy" [36] is microbial fuel cells with their minimal greenhouse gas emissions. The method is based on the release of energy as a result of the metabolism of living organisms using electrocatalysis. The main problem in this area is the creation of catalytic anodes, quite stable and active, with high biocompatibility. Fe_3O_4 with the necessary active centers does not

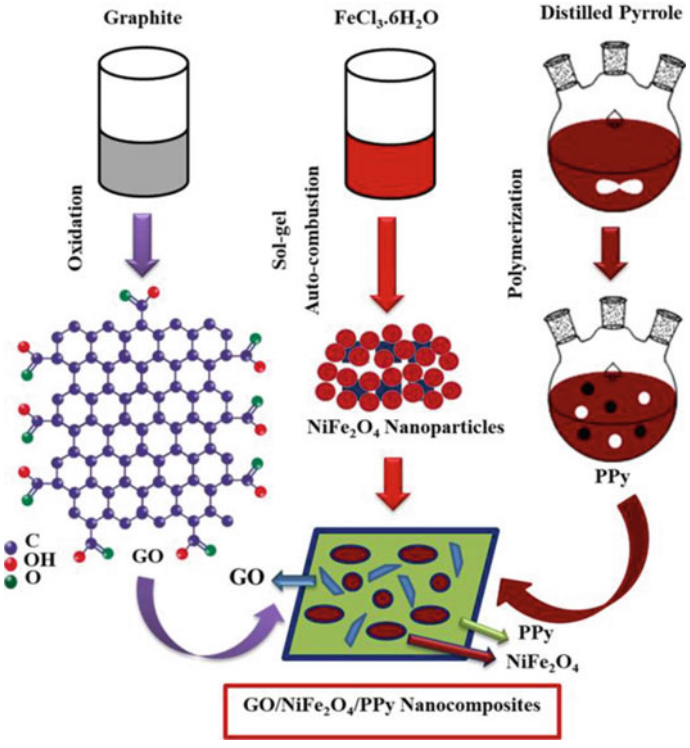

Fig. 8 Schematic illustration of the synthesis [35]

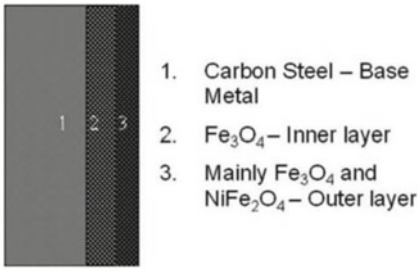

Fig. 9 Modified material [3]

show sufficient electrical conductivity and stability. Nickel ferrites having variable valence cations in their structure (Ni(III)/Ni(II) and Fe(III)/Fe(II)) show excellent electrocatalytic activity and conductivity, relative to individual oxides of the respective metals. These variable valence cations increase the electrocatalytic activity of the anode [37]. This study demonstrated the influence of nickel ferrites on the efficiency of the process. The resulting $NiFe_2O_4$-MXene combined anode showed higher power density and very low resistance (198 Ω) relative to its predecessors. These results provide us with a new understanding of the preparation of efficient electrodes for usage in renewable energy sources.

3.2 Nanocoating

Nanocoating is a relatively new area of research, but it has an incredibly high value due to its low cost of existing material's modification, (coating thickness can range from a few mm to nm), in order to obtain improved properties.

The basis for these studies was the system of primary heat transport of heavy water reactors under pressure. Carbon steel was used for that. The modified material is shown in Fig. 9 [3].

Nickel ferrite was obtained by co-precipitation method. It was coated with PLD technique onto carbon steel. After conducting a number of studies, it was found that the coating of a stable material with a layer of $NiFe_2O_4$ significantly increases the corrosion resistance, which increases with the thickening of the layer, as it can be seen in Fig. 10 [3]. We can make sure, that the high chemical and mechanical resistance of nickel ferrite materials.

3.3 Sensory

The study of sensory properties was performed using the example of polypyrrole and polypyrrole–chitosan in the method of surface plasma resonance in aqueous solutions. This method allows to determine the content of the following elements: Ni,

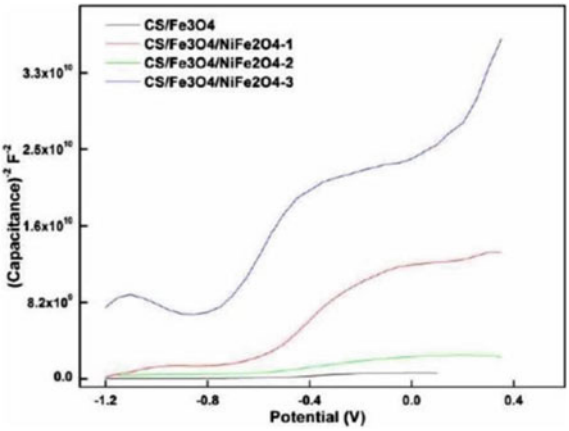

Fig. 10 MS plot of CS, Fe_3O_4, and $NiFe_2O_4$ coating CS [3]

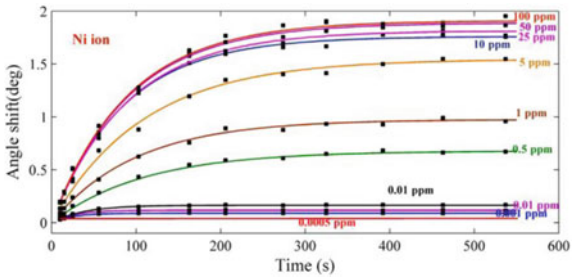

Fig. 11 Variation of resonance angle shift in time to detect the Ni ions [38]

Fe, Co, Al, Mn, Hg, and Pb. While modifying the sensor surface, which was made of polypyrrole–chitosan with nickel ferrite, the increase in the shift of the resonant angle was observed [38]. Moreover, with the increase of the coating thickness, the sensitivity of the sensor increased. Let us consider the example of the nickel definition, as shown in Fig. 11.

3.4 Microbiology

In 2016, Kariim Ishaq together with his colleagues highlighted the results of the studies of nickel ferrites modified with α-alumina effect. The antibacterial activity of the developed nanopowder of nickel ferrite was tested on the selected microbes: Escherichia coli, Pseudomonas aeruginosa, and Staphylococcus aureus. In order to determine the most effective dosing load for the best antibacterial activity, the dose ratio of nickel ferrite to solvent (DMSO) was changed. The results of the antibacterial activity were presented as a zone of inhibition, as shown in Fig. 12, while the diameter of inhibition is shown in Table 3 [39].

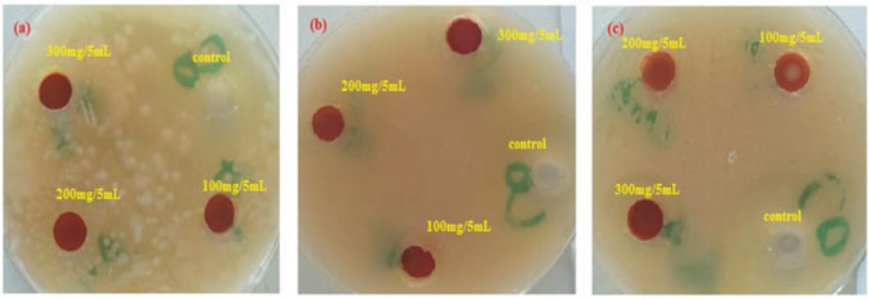

Fig. 12 Antibacterial activity of nickel ferrites on **a** Escherichia coli **b** Pseudomonas aeruginosa, and **c** Staphylococcus aureus [39]

Table 3 Zone of inhibition (mm) of the nickel ferrite loading on waterborne microbes

Bacterial	Zone of inhibition (mm)		
	100 mg/5 mL DMSO	200 mg/5 mL DMSO	300 mg/5 mL DMSO
E. coli	–	–	–
Pseudomonas aeruginosa	–	13.00	17.00
Staphylococcus aureus	0.07	1.20	1.20

The mechanism of cell fragmentation has also been observed in the works of Amro et al. [40] and Hyosuk et al. [41], who reported about the effect of CNT-Ag and GO-Ag nanocomposites against Gram-negative and Gram-positive Bacteria. This excellent antibacterial property possesses the developed nickel ferrites nanoparticles on Staphylococcus aureus and Pseudomonas aeruginosa, which makes it a good source of disinfectant, with effective properties that enhance microbe inhibition even in polluted water.

3.5 Catalysis

Nickel ferrites have found their application in catalysis as well. For example, the effect of nickel ferrites nanoparticles on the oxidation of glucose, b-nicotiamide adenine dinucleotide, and methanol was investigated. R. Galindo and others [42] found that the combined electrode of graphite paste (30% of nickel ferrite nanoparticles, 30% of graphite, 40% of mineral oil) catalyzes these processes. It has been proved that the oxidation of NADH by these nanoparticles requires the modification of the electrode by adding carbon nanotubes and ionic liquid in order to improve the productivity. The increase of the current and potential displacement to further negative values was explained by the better dispersion of nanoparticles in the electrode of the graphite paste.

In 2019, Muhammad Bilal Tahir conducted a study on hydrogen release under the action of visible light in microbiological electrolytic cells (IEC) [43], consisting of a bio-photoelectrochemical cell and a microbiological fuel cell [44]. Nickel ferrite which was modified with tungsten oxide WO_3 was used in this study. The results of this study are shown in Figs. 13 and 14.

The prepared thin films contain different amounts of nickel ferrites: NFW-0.5 (0.5 wt.%), NFW-1.0 (1.0 wt.%), NFW-1.5 (1.5 wt.%), and NFW-2.0 (2.0 wt.%). The prepared doped photocatalyst was used in IEC chambers as an electrode to study the conversion of biomass into hydrogen gas energy. As we can see from Fig. 14, the 1.5% content shows us a twofold increase in hydrogen evolution. The acceleration of the photoelectrons consumption can become a vital way to increase the potential of a semiconductor, based on $NiFe_2O_4/WO_3$, which is used in the IEC with a photocatalytic system [43].

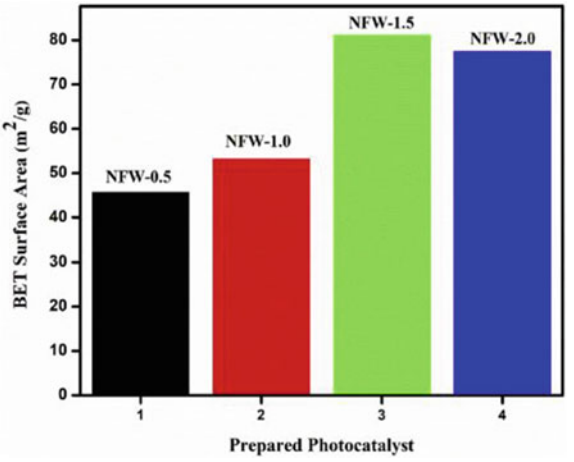

Fig. 13 BET surface of prepared samples [43]

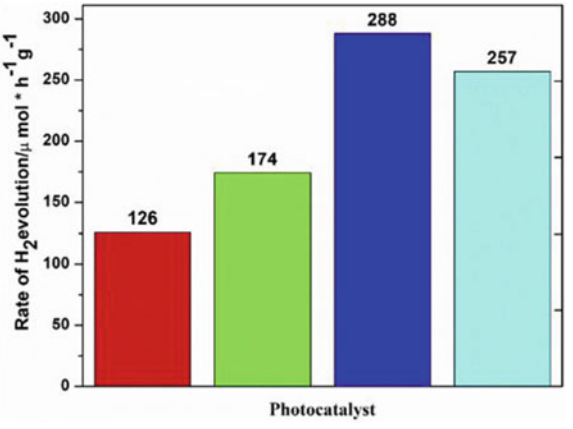

Fig. 14 H_2 evolution of prepared thin films [43]

3.6 Medicine

Maqusood A. and others studied spinel nickel ferrites in the molecular biology of cancer, particularly on cancer cells HepG2 (immortal liver cancer cell line) and MCF-7 (human mammary duct adenocarcinoma cell line). Scientists have been able to prove that nickel ferrites cause cytotoxicity and oxidative stress in human liver cells (HepG2), and breast (MCF-7) depended on the given dosage [45]. Real-time quantitative PCR analysis showed that the levels of genes involved in the apoptosis also decreased under the influence of nickel ferrite. There are only several unique studies, which are extremely important in nowadays world; thus, the further research to establish the potential mechanisms of differential toxicity of nickel ferrites in different in vitro models is necessary.

3.7 Water and Water Treatment

One of the latest growing problems is the increase in the content of pharmaceuticals and related compounds in water [46], namely antibiotics, antidepressants, estrogens, analgesics, and others which become common in reservoirs and wastewater. Nickel ferrites have not found widespread scientific interest in this gas, but already have some positive results in different studies; for example—the removal of dipyrones [47] and phosphate adsorption [48].

A separate branch of water treatment consists of the removal of highly toxic elements from the water. Scientists from Saudi Arabia have achieved the best-known degree of adsorption of Hg^{2+} from aqueous solutions, using the composites, based on carbon, doped with nickel ferrites [49]. These results are presented in Table 4.

The obtained adsorbent is restored with partial storage of its properties, as it can be seen in Fig. 15.

Scientists from the UAE have conducted a number of studies with electrodes, based on nickel ferrite composites. The results discovered that $Co_{0.5}Ni_{0.5}Fe_2O_4$ electrodes showed excellent regeneration ability and the highest electrosorption capacity of 21.84 mg/g, with a slight decrease in salt removal efficiency (<5%), even after 6 cycles of desalination and regeneration [52]. Thus, cobalt and nickel ferrite materials, especially ferrite $Co_{0.5}Ni_{0.5}Fe_2O_4$, can be considered as promising electrode materials for the usage in water desalination.

Table 4 Comparative adsorption capacities of various adsorbents for Hg^{2+} adsorption [49]

Adsorbent	Adsorption capacity (mg/g)	References
$Fe_3O_4/SiO_2/NH/CS_2$	206.0	[50]
Fe_3O_4-GS	23.10	[51]
$NiFe_2O_4$-NC	476.20	[49]

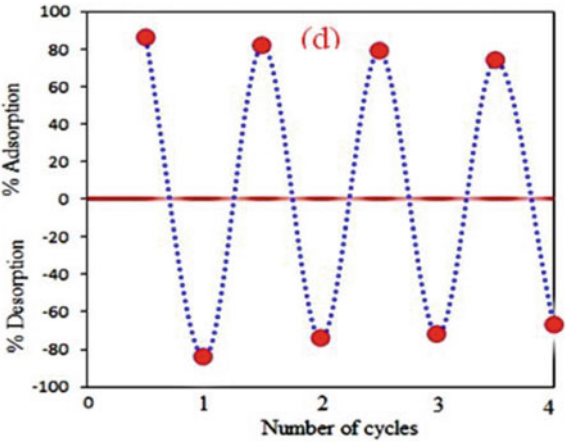

Fig. 15 Regeneration studies of Hg^{2+} metal ion, using $NiFe_2O_4$-NC [49]

4 Modern Trends in Nickel Ferrites Applications

The modern trend uses the composites instead of pure nickel ferrites. The researchers tested new combinations of these ferrites with different materials. One of the most popular alloying elements is Co.

Alloying cobalt into nickel ferrite improves the chances of spinel phase formation. With the increase of Co (x), the increase in the ferrite phase of spinel, (%) in nickel ferrites (72, 94, 90, and 87% at $x = 0.0$, 0.25, 0.5, and 0.75, respectively) was discovered. This indicates the fact, that Co doping stabilizes Fe ions during crystallites formation and Ni ions during crystallites modification [53].

Cobalt doping also increases the crystallinity of spinel ferrite [54]. This conclusion was made on the basis of the X-ray diffraction results, in which the width of the diffraction peak decreased with the increase of Co content in the ferrite, as it is shown in Fig. 16a [54] and Fig. 16b [28].

The addition of cobalt leads to: the increase in the limiting power of nickel ferrites, better optimization of electrical resistance, dielectric constant, and dielectric loss of values, and hence, to good isolation properties [55]. The modification with cobalt leads to the growth in dielectric constant and permeability, with the increase of the cobalt content. The effect of cobalt ion on permeability is due to the distortion of octahedral areas [56, 57].

The lattice constant increases gradually, with the increase of doped cobalt, which can be attributed to the higher ionic radius of the Co^{2+} ion (0.74 Å), compared to the ion of Ni^{2+} (0.695 Å), as can be seen in Fig. 17 [58].

The second most popular element for alloying is zinc. Let us consider the main trends in the results of the research in this type of composites.

The lattice constant increases with the increase of Zn content, which is an admitted fact, considering the difference of ionic radii of Zn^{2+} (0.83 Å) and Ni^{2+} (0.78 Å) [59]. Zn doping reduces the frequency of ferromagnetic resonance [60]. The coercive force

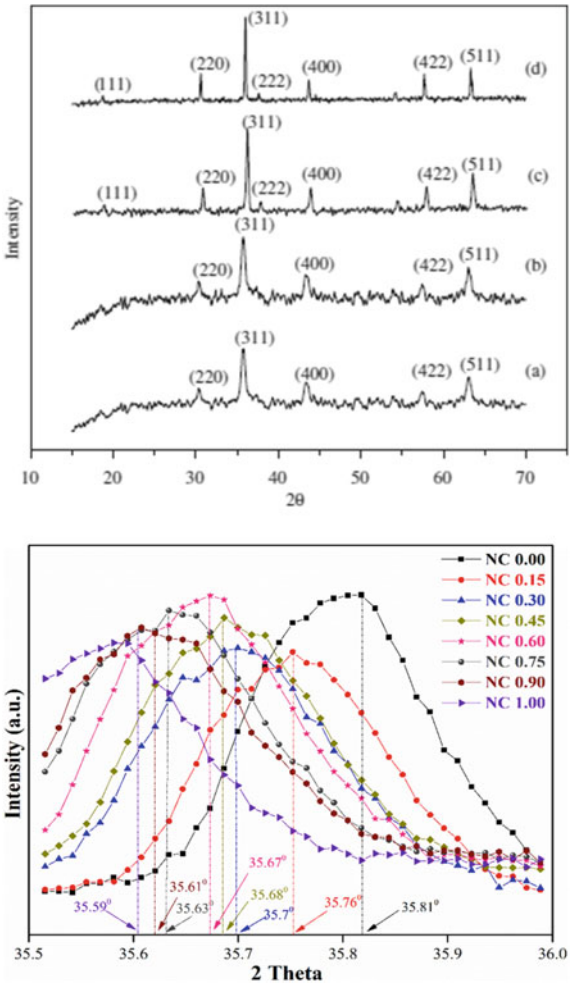

Fig. 16 Increase in crystallinity, indicated by a reduction in the peak broadening (**a**) [54] and **b** for Ni-Co ferrite [28]

increases with the addition of Zn (Fig. 18). The power increase is due to the increase in grain size [60]. The decrease in the magnetic saturation was discovered, which is due to the replacement of ferromagnetic Ni with diamagnetic Zn [59].

The chromite doping of ferrites leads to the decrease in the magnetic saturation and magnetic moment, as well as, to the increase in the coercive power (Table 5).

5 Conclusions

The proposed review represents the important place of nickel ferrite spinels in modern science and technology. Due to their extraordinary characteristics, these nanoparticles have become the basis for many studies in various scientific and practical areas,

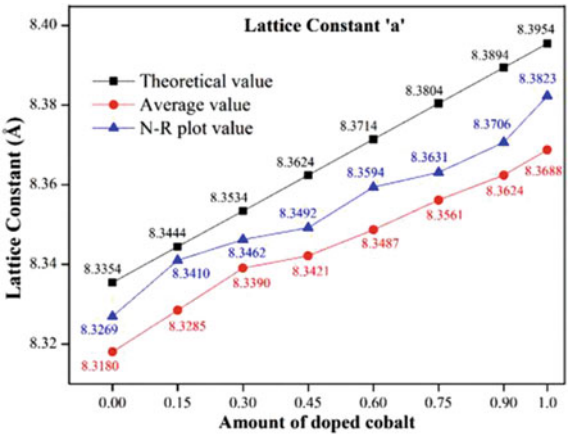

Fig. 17 Increase in lattice constant with cobalt amount in Ni-Co ferrite [58]

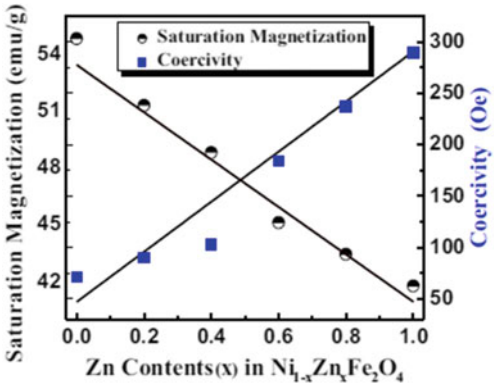

Fig. 18 Magnetic saturation and coercivity in depending on zinc content in Ni ferrite [59]

Table 5 Magnetic properties reported for Cr-doped nickel ferrites [61]

Degree of substitution	M_s (emu/g)	H_c (Oe)	Anisotropy Constant (erg/cm^3)	n_B	Cation distribution	
					A site	B site
0.0	53.38	16	872	2.28	$(Ni_{0.04}Fe_{0.96})$	$[Ni_{0.96}Fe_{1.04}]$
0.2	38.25	33	1288	1.62	$(Fe_{1.00})$	$[Ni_{1.0}Fe_{0.8}Cr_{0.2}]$
0.4	28.78	54	1586	1.28	$(Fe_{1.00})$	$[Ni_{1.0}Fe_{0.6}Cr_{0.4}]$
0.6	19.25	92	1807	0.82	$(Fe_{1.00})$	$[Ni_{1.0}Fe_{0.4}Cr_{0.6}]$
0.8	15.45	184	2901	0.64	$(Ni_{0.04}Fe_{0.96})$	$[Ni_{0.96}Fe_{0.24}Cr_{0.8}]$
1.0	10.18	320	3324	0.4	$(Ni_{0.07}Fe_{0.93})$	$[Ni_{0.93}Fe_{0.07}Cr_{1.0}]$

with different alloying elements. By varying the composition of the original spinel, you can get the improved properties. Pure nickel ferrites and their composites have already demonstrated high achievements in such fields as water treatment, medicine, microbiology, sensorics, catalysis, energy (including "green"), and many others. Therefore, it is extremely important to continue the research on this unique structure and look for the ways to use these results in practice, making the particular area cheaper, faster, and with less waste.

References

1. Hastings JM et al (1953) Neutron diffraction studies of zinc ferrite and nickel ferrite. Rev Mod Phy 25:114
2. Sukhleen BN et al (2020) Nickel spinel ferrites: a review. J Magn Magn Mat 159:167163
3. Sumathi S et al (2017) Evaluation of corrosion resistance of nano nickel ferrite and magnetite double layer coatings on carbon steel. Thin Sol Films 645:77
4. Evrim U et al (2019) Nickel ferrite nanoparticles for simultaneous use in magnetic resonance imaging and magnetic fluid hyperthermia. J Coll Interf Sci 550:199
5. Özgür U et al (2009) Microwave ferrites, part 1: fundamental properties. J Mater Sci Mater Electron 20:789
6. Sugimoto M et al (1999) The past, present, and future of ferrites. J Am Cer Soc 82:269
7. https://www.tf.uni-kiel.de/matwis/amat/def_en/kap_2/basics/b2_1_6.html
8. Goldman A, Marcel D (1993) Modern ferrite technology. 2nd edn. New York, p 438, ISBN 978–0387281513
9. Li D et al (2014) Structural and magnetic properties of nickel ferrite nanoparticles synthesized via a template-assisted sol-gel method. Ceram Int 40:16529
10. Dereje HT et al (2019) Photoelectrochemical and theoretical investigations of spinel type ferrites ($M_xFe_{3-x}O_4$) for water splitting: a mini-review. J Photo En 7:012009
11. Saito S et al (1966) Studies on the formation of nickel ferrite by hydrothermal method. Pow Pow Metall 13:60
12. Poplawsky R (1967) Nickel iron ferrite crystals using arc image furnace techniques. J Cry Growth 1:139
13. Pavlyukhin YT et al (1984) On the consequences of mechanical activation of zinc and nickel ferrites. J Solid State Chem 53:155
14. Jovalekić C et al (1995) Mechanochemical synthesis of $NiFe_2O_4$ ferrite. Mat Lett 24:365
15. Cross WB et al (1999) Self-propagating high-temperature synthesis of ferrites MFe2O4 (M=Mg, Ba Co, Ni, Cu, Zn); reactions in an external magnetic field. J Mat Chem 9:2545
16. Shi Y et al (2000) Strong uni-directional anisotropy in disordered $NiFe_2O_4$. Solid State Commun 115:237
17. Chen DH et al (2001) Synthesis of nickel ferrite nanoparticles by sol-gel method. Mater Res Bull 36:1369
18. Lee JH et al (2001) Microwave-hydrothermal versus conventional hydrothermal preparation of Ni-and Zn-ferrite powders. J All Comp 325:276
19. Hai TH et al (2003) Spinel ferrite thin-film synthesis by spin-spray ferrite plating. Conden Matt 327:194
20. Misra RDK et al (2003) Synthesis of nanocrystalline nickel and zinc ferrites by microemulsion technique. Mat Sci Techn 19:826
21. Lu WZ et al (2006) Experimental study on flow structure at open channel confluences. Shenzhen Daxue Xuebao (Ligong Ban). J Shenzhen Univ Sci Engg 23:329
22. Han DQ et al (2018) Facile synthesis and characterization of spinel ferrite $NiFe_2O_4$ nanowire arrays with a high-aspect-ratio. Ceram Int 44:22997

23. Hcini S et al (2017) The evaluation of temperature in synthesizing process of natural iron sand based Fe_3O_4 nanoparticles for Ni ion adsorption. Ceram Int 43:2529
24. Liu JH et al (2005) Magnetic properties and Mossbauer studies of nanosized $NiFe_2O_4$ particles. J Mat Sci 40:2573
25. Bharvi V et al (2020) Synthesis of magnetic nickel ferrites nanocomposites: an advanced remediation of electroplating wastewater. J Taiwan Inst Chem Eng 112:106
26. Sivakumar P et al (2011) Synthesis and characterization of nickel ferrite magnetic nanoparticles. Mat Res Bull 46:2208
27. Chatterjee A et al (1993) Synthesis of nanocrystalline nickel-zinc ferrite by the sol-gel method. J Magn Magn Mat 127:214
28. George M et al (2006) Finite size effects on the structural and magnetic properties of sol-gel synthesized $NiFe_2O_4$ powders. J Magn Magn Mater 302:190
29. Manish S et al (2009) Synthesis and optical characterization of nanocrystalline $NiFe_2O_4$ structures. J All Comp 481:515
30. Ivanenko I et al (2019) The perspective synthesis methods and research of nickel ferrites. Nanocomposites Nanostruct Appl 221:527
31. Venkatesh M et al (2016) Microwave assisted combustion synthesis and characterization of nickel ferrite nanoplatelets. Mod Elect Mat 2:74
32. Huo J et al (2009) Characterization and magnetic properties of nanocrystalline nickel ferrite synthesized by hydrothermal method. Mater Lett 63:1183
33. Hosni N et al (2018) Synthesis of (2D) MNPs nanosheets of nickel ferrite using a low-cost co-precipitation process. Mater Sci Eng 232–235:48
34. Doh SG et al (2004) Characteristics and synthesis of Cu-Ni ferrite nanopowders by coprecipitation method with ultrasound irradiation. J Magn Magn Mater 272:2238
35. Hafiza VH et al (2020) Polymer based nickel ferrite as dielectric composite for energy storage applications. Synth Met 268:116507
36. Lesik S et al (2018) Magnetically separable catalysts for the hydrolysis of borohydrides. In: Proceeding of the 2018 IEEE 8th international conferences nanomaterials 4:80
37. Khurram T et al (2020) Nickel ferrite/MXene-coated carbon felt anodes for enhanced microbial fuel cell performance. Chem 128784
38. Amir RS et al (2017) Polypyrrole-chitosan/nickel-ferrite nanoparticle composite layer for detecting heavy metal ions using surface plasmon resonance technique. Opt Las Tech 93:216
39. Kariim I et al (2016) Characterization and antibacterial activity of nickel ferrite doped α-alumina nanoparticle. Eng Sci Tech Int J 20:563
40. Amro NA et al (2000) High-resolution atomic force microscopy studies of the Escherichia coli outer membrane: structural basis for permeability. Langmuir 16:2789
41. Hyosuk Y et al (2013) Antibacterial activity of CNT-Ag and GO-Ag nanocomposites against gram-negative and gram-positive bacteria. Bull Korean Chem Soc 34:3261
42. Galindo R et al (2013) Catalytic properties of nickel ferrites for oxidation of glucose, β-nicotiamide adenine dinucleotide (NADH) and methanol. J All Comp 586:S511
43. Tahir MB (2019) Microbial photoelectrochemical cell for improved hydrogen evolution using nickel ferrite incorporated WO_3 under visible light irradiation. Int J Hydrogen Energy 44:17316
44. Oh S et al (2005) Hydrogen and electricity production from a food processing wastewater using fermentation and microbial fuel cell technologies. Water Res 39:4673
45. Ahamed M et al (2015) Comparative cytotoxic response of nickel ferrite nanoparticles in human liver HepG2 and breast MFC-7 cancer cells. Chemosphere 135:278
46. Kyrii S et al (2020) Local wastewater treatment by effective coagulants based on wastes. J Ec Eng 21:34
47. Valeria S et al (2016) Magnetic nickel ferrite nanoparticles for removal of dipyrone from aqueous solutions. J Env Chem Eng 4:3882
48. Daou TJ et al (2007) Phosphate adsorption properties of magnetite-based nanoparticles. Chem Mater 19:4494
49. Naushad M et al (2017) Nickel ferrite bearing nitrogen-doped mesoporous carbon as efficient adsorbent for the removal of highly toxic metal ion from aqueous medium. Chem Eng J 330:1351

50. Freundlich HMF (1906) Over the adsorption in solution. J Phys Chem 57:385
51. Ghasemi M et al (2014) A novel agricultural waste based adsorbent for the removal of Pb(II) from aqueous solution: kinetics, equilibrium and thermodynamic studies. J Ind Eng Chem 20:454
52. Hai A et al (2020) Cobalt and nickel ferrites based capacitive deionization electrode materials for water desalination applications. Electrochimica Acta 363:137083. https://doi.org/10.1016/j.electacta.2020.137083
53. Rodrigues APG et al (2015) Nanoferrites of nickel doped with cobalt: Influence of Co^{2+} on thestructural and magnetic properties. J Magn Magn Mater 374:748
54. Pardavi-Horvath M (2000) Microwave applications of soft ferrites. J Magn Magn Mater 215–216:171
55. Pubby K et al (2018) Cobalt substituted nickel ferrites via Pechini's sol-gel citrate route: X-band electromagnetic characterization. J Magn Magn Mater 466:430
56. Kulikowski J (1984) Soft magnetic ferrites—development or stagnation? J Magn Magn Mater 41:56
57. Pereira SL et al (1999) Microwave absorption properties of radar absorbing nanosized cobalt ferrites for high frequency applications. Mater Res 3:231
58. Javed TA et al (2011) Structural, electrical and dielectric properties of Co–Mn spinel nanoferrites prepared by co-precipitation technique. J Superconduct Novel Magnet 24:2137
59. Atiq S et al (2017) Synthesis and investigation of structural, morphological, magnetic, dielectric and impedance spectroscopic characteristics of Ni-Zn ferrite nanoparticles. Ceram Int 43:2486
60. Stergiou C (2017) Microwave absorption properties of cobalt-zirconium doped strontium hexaferrites in Ku-frequency band. J Magn Magn Mater 426:629
61. Panatage SM et al (2012) Cation distribution study of nanocrystalline $NiFe_{2-x}Cr_xO_4$ ferrite by XRD, magnetization and Mössbauer spectroscopy. Phys Status Solidi A 209:347

Membranes Modified with Advanced Carbon Nanomaterials (Review)

Yuliya Dzyazko, Ludmila Rozhdestvenska, Kateryna Kudelko, Vladimir Ogenko, and Yevhen Kolomiiets

1 Introduction

Nowadays, the membrane technologies are main widespread separation processes in the world. The global forecast up to 2024 has been reported regarding membrane materials (polymers and ceramics), technologies (reverse osmosis, RO, nanofiltration, NF, ultrafiltration, UF, microfiltration, MF), application (water and wastewater treatment and industrial processing), region (North America, Asia-Pasific, Europe, Middle East and Africa, South America) [1]. The global membranes market is expected to grow up to USD 8.3 billion by 2024. According to the forecast, the position of membrane processes on the life cycle curve is determined. With the given curve, H. Strathmann described the level of profits from sales of membrane technologies on the market as a function of development (Fig. 1) [2].

The main efforts of investigators, who deals with membrane materials, are directed to: (i) development of membranes combining high performance and high separation ability under operating conditions that are so mild, as much as possible, (ii) improvement of mechanical durability, chemical and thermal stability of membrane materials and (iii) membrane resistance against fouling with organic substances and biofouling. Earlier these problems were solved in a direction of the development of organic–inorganic polymers [3–5] or modifying of commercial polymer membranes with inorganic particles: zirconium hydrophosphate [6–11], oxides of zirconium [6, 7, 12, 13], titanium [13–16], zinc [13], silica [16–18], Fe_3O_4 [19–21]. Other way is modifying of polymer and ceramics with advanced carbon nanomaterials: one-dimensional multi-walled nanotubes (MWCNTs), two-dimensional graphenes (oxidized, GO, or reduced graphenes, rGO) and three-dimensional fullerenes (Fig. 2).

Y. Dzyazko · L. Rozhdestvenska · K. Kudelko · V. Ogenko · Y. Kolomiiets (✉)
VI Vernadskii Institute of General and Inorganic Chemistry of the National Academy of Science of Ukraine, Kyiv, Ukraine

O. Fesenko and L. Yatsenko (eds.), *Nanomaterials and Nanocomposites, Nanostructure Surfaces, and Their Applications*, Springer Proceedings in Physics 263, https://doi.org/10.1007/978-3-030-74741-1_10

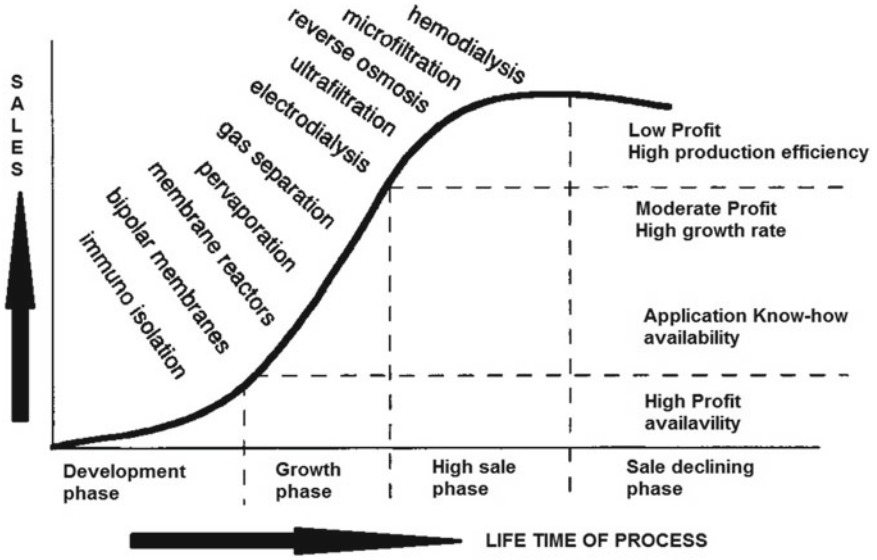

Fig. 1 Life cycle curve of membrane processes (adapted from [2]). Sales are shown as a function of the state of development of the membrane market

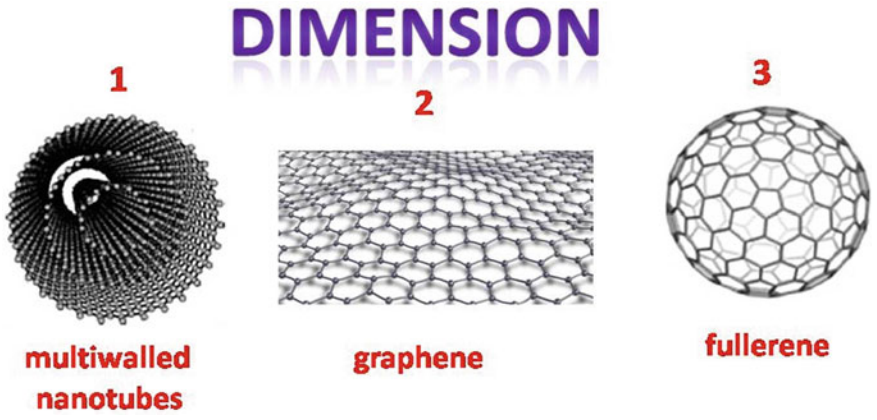

Fig. 2 Carbon nanomaterials for membrane modifying

The modifier can be inserted inside a membrane: this is important both for porous and for non-porous materials. In the case of porous membrane, a modifier fills its pores affecting selectivity. Regarding non-porous polymers, their permeability depends on the packing density, the polymer chain mobility, and the free volume. The hardsphere properties of fullerenes provide high free volume of the polymer and compaction of its chains improving permeability [22]. The internal diameters MWCNTs are

comparable to those of many small molecules, which raises the prospect of size-based exclusion and the separation of chemical compounds [23]. Moreover, the transport of gas and water molecules through the central channels of individual nanotubes would be extraordinarily fast due to their smooth, defect-free walls. At last, graphene is characterized by high specific surface area, mechanical strength and hydrophilicity due to carboxyl, phenolic and epoxy groups (for GO) [24]. Thus, GO looks attractive as a hydrophilizing agent for the enhancement of antifouling stability of the membranes.

A modifier can be inserted to the reaction mixture, when polymer is formed. Other way is its insertion to preliminarily formed membrane. In this case, additional binder is used. Only outer surface of a membrane can be modified. Graphene can be used as filtration membrane without polymer or ceramic support.

In this review, the effect of carbon nanomaterials on separation properties of membranes is considered.

2 Membranes Modified with Carbon Nanotubes

Carbon nanotubes (CNTs) have been of interest to researchers as modifiers and fillers since their discovery in 1993, due to their mechanical, surface, electrical and chemical properties. Carbon nanotubes are being actively studied to purify numerous impurities from aqueous solutions [25]. It is known that in these materials carbon exists in allotropic modifications. CNTs are cylindrical graphite sheets rolled into a tubular structure, and it is customary to distinguish between single-walled and multi-walled nanotubes (SWCNT and MWCNT, respectively). It should be noted that CNT nanoparticles differ significantly in their properties (Table 1).

Due to the properties of CNT, namely elasticity, low density, homogeneity and the possibility of aromatic interaction due to π-π-bonds, they are of interest for research as surface fillers for separation membranes. To date, mainly multi-walled CNT are used in order to modify the surface of the membranes.

CNTs have been used quite successfully in biological research and are also used as drug delivery materials because they are known for their antibacterial properties [25]. Numerical studies of the mechanism of interaction of carbon nanotubes with the bacterial environment have shown that such factors as the diameter of the tubes and its length are quite significant. In addition, the presence of functional groups on the surface of the nanotube can greatly affect the degree of disinfection of bacterial cells.

Table 1 Water flux through the membranes and their selectivity (adapted from [25])

Structure and properties	SWCNTs	MWCNTs
Layers	1	Several
Thermal conductivivty, W mK^{-1}	6000	2000
Electrical conductivity, S sm^{-1}	10^2–10^6	10^3–10^5
Thermal stability in air, °C	>600	>600

It is believed that the shorter the nanotube is, the more toxic effect on microorganisms it has [25]. In particular, the characteristics of the ends of the carbon tube (closed or open) when interacting with the membrane of living cells are important. However, it should be noted that the impact of environment in which the CNTs are located is significant. Namely, in a liquid medium, shorter nanotubes are easily aggregated, and it is unlikely to capture a large number of bacterial membranes, while longer nanotubes in a liquid medium are aggregated less and therefore show greater biological toxicity to microorganisms. It is believed that the phenomenon of agglomeration of nanotubes [26] is associated with the van der Waals interaction.

The effect of nanotubes with a small diameter (about 1.5 nm) on bacterial cells can be compared with the action of a needle, which with a sharp end can damage the bacterial membrane. The nature of the effect of nanotubes with a larger diameter (about 20–30 nm) is more likely related to the interaction of the walls of the tubes on bacterial cells. In addition, the degree of toxicity of carbon nanotubes to microorganisms depends on the shape of bacterial cells; in particular, spherical, rod-shaped bacteria are known. That is, in summary, many factors and parameters determine the toxic effects of carbon nanotubes on microorganisms. It should be noted that the mechanism of toxic action of CNT on microorganisms has not been studied enough.

Mechanical and conductive characteristics of CNT are well-known. Thus, when carbon materials are added to metals or polymers, more functional materials are obtained, lighter and stronger [27]. Together with fullerenes, single-walled and multi-walled CNTs are characterized by photoactivity. These materials were tested for the release of reactive oxygen species (ROS) during UV irradiation.

Multi-walled carbon nanotubes (MWCNT) is a material used in modifying membranes with composites to solve the problem of fouling. Thus, Weiming Yu et al. [28] studied the effect of a composite of magnetic particles with multi-walled nanotubes in a polysulfone membrane. The triple increase in flux through the composite membrane was found, and the effect of membrane functionalization is explained by the fact that MWCNT acts as free channels. The authors report that the modified membrane has pronounced antifouling properties. Fouling is considered according to the theory of XDLVO (extended Derjaguin–Landau–Verwey–Overbeek) [29]. In [28], the indicators of electron-donor components (γ-) of modified membranes were calculated and are 9.79 and 33.29. The authors point out that such modified membranes have a higher ability to donate an electron and therefore show an increased ability against clogging of the membrane in the filtration process. Convective flows through membranes for solutions of bovine serum albumin (BSA), sodium alginate, yeast solution, humic acids were studied. Flux recovery rate (FRR) was 67.89, 85.53, 60.28 and 90.12%.

Khoerunnisa et al. [30] modified the membranes by introducing chitosan/PEG/MWCNT/iodine, the components were introduced at the stage of phase inversion. Spectroscopic data showed that the added polymers together with nanotubes enhanced the interaction of iodine (0.10–0.31 wt.%) with the membrane matrix. The mechanism is described in terms of the interaction of components through hydrogen bonds, which in turn improves the membrane properties (smoothness and roughness) and performance. Changed: contact angle from 70.3 to

59.3°, porosity (average pore radius from 13.3 to 23.2 nm) and mechanical strength (Young's modulus from 6138.6 to 7824.9 MPa), permeability (flow from 212.8 to 220.4 $dm^3\ m^{-2}\ h^{-1}$).

The study [31] demonstrated the use of O-MWCNT for ultrafiltration sulfone membranes with a thin polyamide layer. The presence of hydrophilic O-MWCNT in the PES/SPSf support membrane is explained by the interaction of the monomer due to hydrogen bonding. As a result, a thin polyamide layer is formed on the surface of the support, which improves the permeability and elimination of organic matter in the support layer through the pore channels.

Multi-walled carbon nanotubes with an outer diameter of 30–50 nm and a length of 5–20 μm were used to modify hollow-fibre membranes [32] to remove organic matter from wastewater. Pre-ozonation and the use of modified membranes have been found to improve permeate quality with increasing flux. The rate of contamination of the modified membrane decreased, and the cleaning of the surface by washing was more effective. In addition, pre-ozonation has led to the stability of carbon nanotubes on the membrane surface during chemical cleaning.

Polysulfone membranes modified with PEG-CNT were studied for use in a membrane bioreactor [33]. The optimal percentage of membrane filler was 0.25 wt%. According to the filtration results, the modified membrane showed a fourfold increase in the permeability of water and protein solution by $16.8 + 0.5$ and $110.8 + 0.8$ $Lm^{-2}\ h^{-1}\ bar^{-1}$. It was found that the addition of carbon nanotubes to the polymer reduced the interaction of the protein with the membrane surface, which improved the resistance to contamination by $72.9 \pm 1\%$.

Amino-functionalized multi-walled carbon nanotubes were used to modify polyethersulfone (PES) membranes [34]. The modification led to an increase in the porosity, pore size, surface roughness of the membranes containing modified carbon nanotubes with an amino group up to 1 wt.%. Subsequent addition of the component reduces the porosity and roughness of the formed membrane. Membranes with the addition of 0.5–1 wt.% showed better filtering properties than the original membrane. The initial flow through the pristine membrane (10 $dm^3\ m^{-2}\ h^{-1}$) increased to 32 $dm^3\ m^{-2}\ h^{-1}$ for the modified one. The addition of amino-modified nanotubes increased the separation properties for BSA and the antifouling properties for the PES membrane. Depending on the amount of introduced nanotubes in the polymer from 0.05 to 2%, the rejection of BSA increases from 81 to 88%.

Polysulfone membranes functionalized with a carboxyl group and multi-walled carbon nanotubes (dispersion in chitosan) were studied [35]. The biopolymer chitosan is known for its sorption properties to heavy metal ions. The resulting composite was part of a selective layer of polysulfone membrane. The aim was to increase the separation of heavy metal ions. It was found that the membranes effectively recovered Cu(II), Ni(II), Pb(II), Cd(II) and Co(II) from aqueous solutions at pH 3 and 10. At pH 6–8 the studied membranes showed increased performance for recovery of Cu(II) and Pb(II). At pH 3, the recovery of metal ions increases from 71 to 92.2%. At pH 10, the recovery of metal ions is 93.4–99.9%.

In [36], the authors functionalized CNT, performed oxidation, acylation, azidation and subsequently introduced modifiers to the polysulfone membrane. It is shown that

with increasing of the amount of carbon tubes in the membrane, the smoothness of the surface increases. According to thermal analysis, it was found that the introduction of CNT in the amount of 0.1–0.5% in the polymer increases its thermal stability. The CNT modifier with an azide group (1%) changes the contact angle from 77.7 to 26.3°. Membrane removal of metal ions with a modified polysulfone membrane with oxidized CNT at 0.49 MPa increased the selective properties: for Cr(IV) from 10.2 to 86.2%, for Cu(II) from 10.1 to 79.3%, for Pb(II) from 10.5 to 41.3%, for Cd(II) from 9.9 to 71.6%, for As(III) 10.9 to 83.6%. Introduced into the polymer, the carbon modifier reduces the pore size range of 20–30 nm.

In the study [37], the polyamide membrane was improved by the introduction of multi-walled CNT by grafting. As a result, the contact wetting angle increased from 45 to 75°, with increasing content of modifier in the polymer from 0 to 10 mg g^{-1}. The stress–strain diagrams for the samples were studied, and it was found that the strength of the modified membrane increases in 3 times at a component content of 15 mg g^{-1} (from the original 10 mPa increased to 35 mPa). Removal of humic acids from solutions by composite membranes is increased from 54 to 90%, when administered from 0 to 10 mg g^{-1}.

A two-layer membrane modified with CNT for forward osmosis was described in [38]. The membrane was obtained by interfacial polymerization of polydopamine/CNT components with trimesol chloride in polysulfone (PSf) polymer matrix. The modified two-layer membranes showed higher values of water flow through the membrane without reducing the amount of solutes. TFN0.05 sample was characterized as very highly resistant to fouling due to the content of CNT (0.05%) in both layers of the membrane.

Multi-walled CNTs were introduced into the substrate of the surface of polyvinyl fluoride (PVDF) using vacuum filtration of the suspension of 0.15 g/l [39]. As a result of the modification, the contact wetting angle decreased from 91.2 to 64.6°. The processes of separation were studied in time. For $CaHCO_3$ solution, the modified membrane works more efficiently (flow reduction from 98 to 95%), and for the same period, unmodified recorded flow parameters change from 96 to 90%; for BSA solution: modified membrane is 97–67% and unmodified is 95–57%.

3 Membranes Containing Fullerenes

Fullerene is the allotropic form of carbon, molecule of which is a closed sphere consisting of carbon atoms (see Fig. 2). The shape of this molecule is empty spherical carcass. The formula of fullerenes is C_n, where $n = 20, 24, 28, 32, 36, 50, 60, 70, 74, 76, 84, 164, 192, 216$ and so on [40]. The most stable is C_{60} form, which consists of 12 pentagonal and 20 hexagonal faces [41]. This form has been first obtained by thermal evaporation of graphite in an electric arc. The nanomaterials based on C_{60} are prospective for solar cells and semi-conductors, and they are applied to producing cosmetics and drugs.

Use of fullerenes in combination with UV irradiation is considered as a refined disinfection process for virus inactivation [42]. Fullerenes are also applied for the modifying of membrane surface to prevent biofouling, particularly to depress biofilm formation. Fullerenes are characterized by considerable electron affinity and reactivity, and they produce reactive oxygen species: singlet oxygen and superoxides. Thus, the membranes containing fullerenes are able to inactivate microorganisms and oxidize organic substances. When fullerenes are included to polymer matrix, they save their unique properties [43]. However, the functional properties of polymer are changed.

Limited solubility of fullerenes impedes their application for membrane modifying [44]. The problem can be solved by means of chemical functionalization of their surface, for instance, by the attachment of polar groups to the C_{60} molecules. Different derivatives of fullerenes containing hydrophilic or hydrophobic groups were considered in [45]. Following materials were in a focus of attention: water-soluble carbon nanoclusters containing hydroxyl and carboxyl groups and hydrophobic fullerenes, such as metal- and methanofullerenes. For instance, fullerenols contain different amounts of hydroxyl groups: these compounds are a complex anion-radical of fullerene, chemical formula of which is $C_{60}(OH)_x(O)_y$ $(x + y = 24 - 26)$ (Fig. 3). This is an average formula, which corresponds to the mixture of fullerenes containing different amount of hydroxyl groups. Their content determines water solubility of fullerenols. This distinguishes them from fullerenes, which are completely insoluble in water.

Both fullerenes and low-hydroxylated fullerenols are applied to modifying of membranes for (i) low-temperature fuel cells, (ii) pervaporation and (iii) filtration. The first direction provides membrane obtaining for direct methanol fuels cells (DMFC), where methanol used directly as a fuel instead of its preliminarily decomposition, which as accompanied by hydrogen generation. Catalytic oxidation of methanol occurs on an anode:

$$CH_3OH + H_2O \rightarrow CO_2 + 6H^+ + 6e^- \quad (1)$$

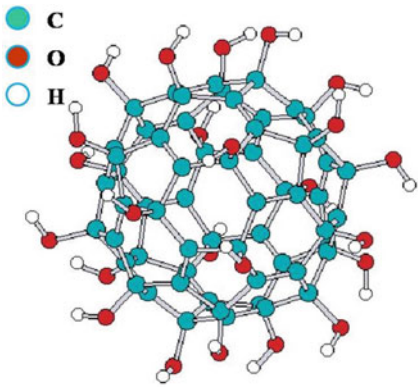

Fig. 3 Fullerenol (adapted from [46])

Protons pass through a proton-conducting membrane towards a cathode, where they interact with oxygen:

$$1.5O_2 + 6H^+ + 6e^- \rightarrow 3H_2O \quad (2)$$

Electrons pass through the external circuit from an anode to cathode. The resulting equation is as follows:

$$CH_3OH + 1.5O_2 \rightarrow CO_2 + 2H_2O \quad (3)$$

Proton-conducting membrane is a key element of DMFC (Fig. 4a). Nafion perfluorinated polymer membranes are used traditionally. This polymer is formed by branched hydrophobic fluorocarbon backbones containing hydrophilic sulfo groups. These groups are deployed to each other forming water-containing clusters and channels, where the proton transport is realized (Fig. 4b). The mechanism of conductivity through clusters and channels is described in numerous reviews, for instance, in [47].

Proton conductivity strongly depends on water content in clusters and channels. The temperature interval of operation is limited by 90 °C. Under higher temperature, the membrane is dehydrated, and as a result, proton conductivity rapidly decreases. In order to expand this temperature diapason to provide water retention and to prevent methanol crossover, new proton-conducting materials are developed. The first approach is modifying of commercial polymers. Other approach provides adding fullerenes to the polymer casting solution before the membrane formation.

According to the first approach, composite proton-conducting membranes were obtained by addition of fullerene to sulfonated polystyrene [49]. Insertion of fullerene to the membranes sufficiently improved its stability against oxidation and depressed the methanol crossover. No effect of the carbon addition on mechanical durability of the membranes has been found. DMFC with composite membrane containing 1.4-mass % of fullerene showed the highest power density of 47 mW sm^{-2} at the current density of 200 mA cm^{-2} (the power density value is lower in 1.7 times comparing with that for DMFC with Nafion membrane). Based on TEM images, it was assumed that high dispersion of fullerene in the polymer provides its performance in the fuel cell. Other assumption is screening of the membrane micropores with fullerene

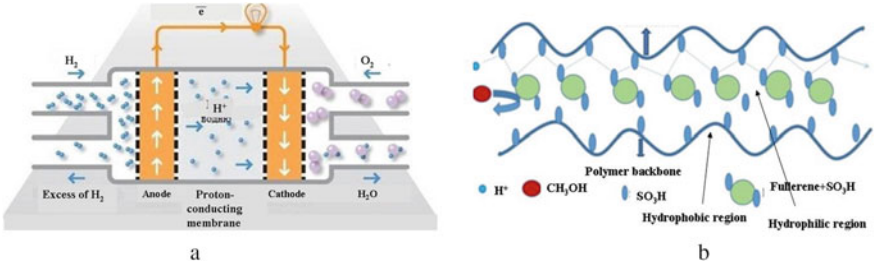

Fig. 4 Typical schemes of DMFC (**a**) and Nafion membrane (**b**, adapted from [48])

nanoparticles. As shown, fullerene nanoparticles-depress methanol crossover: it is lower by 50% comparing with the pristine membrane.

In accordance to the second approach, functionalized fullerene was inserted to Nafion membrane [48]. DMFC containing this membrane was tested under different methanol concentration. C_{60} fullerene was functionalized with 4-benzene diazonium sulfonic acid. Composite membrane was obtained using casting technique. Fullerene has found to be located in clusters of the polymer.

The modifier makes the surface more embossed. Other effect of the carbon additions is increase of proton conductivity of the membrane. DMFC with this membrane demonstrates higher enhanced power output (146 mW cm^{-2}) in comparison with the pristine membrane. Lower methanol crossover as well as less sufficient polarization was found for the DMFC with a membrane containing 1 wt % of functionalized fullerene. The optimal conditions of the DMFC operation are realized, when the methanol concentration is 2 M.

Such fullerene derivatives, as tri-cyanohydrofullerene, $HC_{60}(CN)_3$, and poly{4-[2-[2-(2-methoxyethoxy)ethoxy]ethoxy]benzyl}fullerene, $C_{60}(TEO)_n$, have been synthesized and inserted to the casting Nafion solution [50]. $C_{60}(TEO)_n$ has also been found to be very effective in improving the dispersion of $HC_{60}(CN)_3$ in the Nafion matrix. The fullerene composite membranes have demonstrated enhanced proton conductivity under low relative humidity conditions compared to the pristine polymer.

Modifying of Nafion 117 membrane with fullerene and fullerenol $C_{60}(OH)_{12}$ caused an increase of proton conductivity and water retention by the polymer comparing with the pristine membrane [51]. The improvement of these functional properties is observed at 20–80 °C, especially at low relative humidity (<50%).

The composite membrane based on sulfonated polyvinyl alcohol containing phosphorilated fullerene has been synthesized [52]. The proton conductivity, water uptake and ion-exchange capacity of the composite were estimated as 11.7×10^{-2} S cm^{-1}, 120% and 1.67 mg-eq g^{-1}, respectively. Open-circuit voltage was found to reach 801 mV, and power density was 499.1 mW m^{-2}. The membrane was studied in microbial fuel cell for removal of Cu^{2+} ions simultaneously with the power generation. The maximum removal degree was 73.2%. Besides fuel cell, the field of membrane application is water and wastewater treatment.

Other important field of the application of fullerenes modifiers is the membranes for gas separation and pervaporation. Polystyrene is one of the first materials, which was modified with this carbon nanomaterial [53]. Permeability of the pristine polymer and composite containing 1 wt % of fullerene was investigated towards O_2, N_2, CO_2, C_2H_6 and C_2H_4. Comparing with the unmodified membrane, the permeability increment for the composite is (%): 47 (N_2), 75 (C_2H_6), 41 (C_2H_4). However, selectivity for such gas pairs as O_2/N_2, C_2H_6/C_2H_4 is comparable for these two membranes. The improvement of permeability is explained by an increase of the free volume of polymer due to fullerene insertion.

Increasing amount of the carbon modifier causes enlargement of the size of polymer defects, and their number grows [54]. Moreover, large agglomerates of fullerenes are formed, and the agglomerates are weakly fixed in polymer matrix.

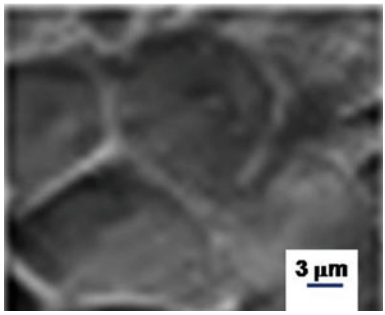

Fig. 5 Poly(phenylene-iso-phthalamide) membrane containing 5% of fiullerenol. Adapted from [54]

For this reason, the membranes containing high amount of fullerene or its derivatives show poor transport properties during pervaporation. The surface of membranes containing fullerenol looks like honeycomb (Fig. 5).

Only small clusters of fullerene are formed, when its amount in polymer (polystyrene) is 1 wt % [55]. Dielectric studies showed increasing relaxation time of α-transition in polysulfone under heating in air-free media to the temperature higher than the polymer glass transition. This effect is due to strong interaction of the polystyrene chains via fullerene molecules.

The measurements of wetting angle indicate the enhancement of the hydrophilicity of poly(phenylene-iso-phthalamide) membranes containing hydrophobic fullerene (Table 2) [56]. The wetting angle that was measured for water and methanol decreases with increasing the fullerene amount. The membranes were used for the separation of methanol/cyclohexane mixture. It was found that all membranes were essentially permeable with respect to methanol. As compared with pure PA, the selectivity and permeability increase for membranes containing 2 and 5 wt.-% C_{60}, whereas these transport parameters are all out of this proportion for membrane containing 10% of fullerene.

This anomalous deviations are connected with heterogeneity of the membrane containing 10 wt.-% C_{60}, where the part of fullerene is not bonded to the polymer chains.

Composite membranes for pervaporation were obtained by means of modifying of polyphenylene oxide and polyphenylene isophtalamide with C_{60} fullerene [57]. Their

Table 2 Properties of poly(phenylene-iso-phthalamide) membrane containing C_{60} (adapted from [56])

C_{60} content, mass %	Contact angle, degree			Diffusion coefficient of CH_3OH, $m^2\ s^{-1}$
	Water	Cyclohexane	Methanol	
–	79.7	25.5	18.8	2.2×10^{-14}
2	78.9	26.3	17.7	3.3×10^{-14}
5	77.5	27.7	16.9	7.2×10^{-14}
10	76.8	29.1	16.5	1.1×10^{-13}

transport properties were tested using the mixtures of ethanol/acetic acid/water/ethyl acetate and methanol/cyclohexane. As shown, the modifier provides the enhancement of the transport properties of membranes.

Fullerene-containing asymmetric composite membranes, particularly based on polyphenylene oxide, can be also applied to baromembrane separation [58]. The membranes were tested by means of filtration of proteins-calibrants with different molecular masses.

One of the promising areas of application of composite membranes is the estrogen extraction from water (as a rule, hydrophobic polymer membranes are used for this purpose [59]). These compounds, which disrupt the endocrine system, are usually present in surface water: their concentration is in the range of 1–30 ppt [60]. Regarding hydrophobic membranes, the estrogen rejection is caused mainly by adsorption on polymer [59]. The rejection can be enhanced when micro- or ultra-filtration are combined with adsorption on activated carbon [61]. Since fullerenes are more effective adsorbents towards both hydrophilic and hydrophobic organic compounds comparing with activated carbon or soot [62], they can be applied to the mentioned combining technique as adsorbents of estrogens or to modifying polymers for baromembrane separation of these compounds [63, 64].

Poly(2, 6-dimethyl-1, 4-phenylene oxide) asymmetric membranes modified with C_{60} fullerene (2 or 10 mass %) were used for this purpose (fullerene was added to the polymer casting solution before the membrane formation) [64]. The membrane cross section is shown in Fig. 6. In the case of pristine membrane, the structure of macroporous support is sponge-like. Cross-linking of the polymer chains with fullerene causes formation of rather straight perforating pores—this facilitates the liquid flux during baromembrane separation. Increasing in C_{60} content up to 2 and 10% leads to a growth of permeate flux in 2 and 8 times, respectively.

The highest selectivity towards estrogen (98.8%) has been found for the membrane containing 2% of fullerene. Further increasing in the C_{60} content causes deterioration of selectivity (96.8), which becomes worse comparing with the pristine membrane (97.2). It should be noted that in the last case the rejection depends on permeate volume: it is 95–99% when the permeate volume is varied from 100 to 600 cm^3. The

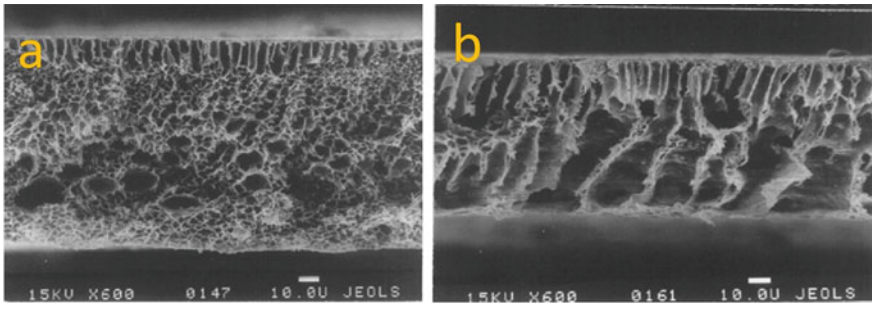

Fig. 6 Cross sections of the poly(2, 6-dimethyl-1, 4-phenylene oxide) membranes: pristine polymer (**a**), containing 10 mass % of C_{60} fullerene (**b**). Adapted from [64]

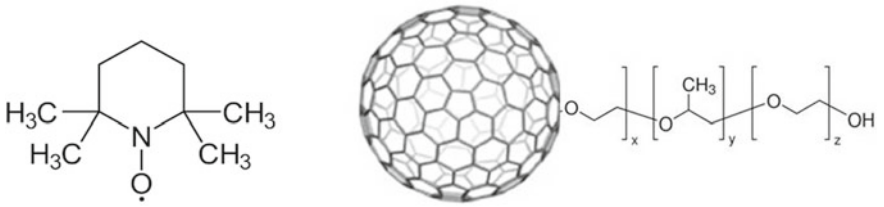

Fig. 7 TEMPO nitroxyl radical (**a**) and fullerene modified with Pluronic F-127 (**b**)

rejection is mainly due to estrogen adsorption on membranes similarly to behaviour of other organic compounds relatively the polymer containing no fullerene [59]. The membrane containing 2% C_{60} shows the highest adsorption rate of estrogen [63].

Considered adsorption capacity towards TEMPO nitroxyl radical (Fig. 7a) has been found for fullerene-containing track membrane. The structure of this chemically stable radical involves a six-member ring similarly to fullerene [65]. In general, adsorption properties of fullerenes are summarized in [66].

A series of ultrafiltration membranes based on polyvinylidene fluoride/polyvinyl butyral containing 0.025–0.1 mass % of fullerene was obtained [67]. Preliminarily, the fullerene was modified with Pluronic F-127 (Fig. 7b). The optimal ratio of mass percentage of fullerene and Pluronic F-127 has been found to reach 0.1:1. The membrane containing the modifier of this composition provides selective rejection for bromelain (33 kDa), ovalbumin (OVA, 45 kDa) and bovine serum albumin (BSA, 68 kDa) up to 98.6%.

4 Membranes Modified with Graphene

Graphene is a two-dimensional allotrope modification of carbon consisting of a single layer of atoms arranged in a honeycomb-like lattice. This advanced carbon material was isolated and characterized in 2004 [68]. A thickness of one graphene sheet is one atom (0.54 nm). For membrane modifying, chemical methods are used to obtain oxidized graphene (GO) from graphite [69]. This technique allows us to obtain graphene-like materials, which involve several layers. Other approach is opening carbon nanotubes [70]: carbon addition of this type was used only for modifying inorganic sorbents [71]. Oxidized graphene can be further transformed to reduced graphene (rGO). When the membrane is formed, rGO is sometimes added to GO in order to affect its functional properties [72]. As opposed to rGO, GO contains hydrophilic fragments: carboxyl, phenolic and epoxy groups. Reduced graphene is free from oxygen-containing groups. Carboxyl groups and a part of phenolic groups are located along the perimeter of GO flakes, epoxy groups and other part of phenolic groups are placed on their basal plane.

Some remarkable properties are attributed to GO: high mechanical strength, ability to form stable colloid solutions and structural transformability. It adsorbs inorganic particles from a solution covering them. This provides the formation of GO-containing composites, which can be deposited from sol of insoluble nanoparticles of insoluble hydroxocomplexes of multivalent metals [71, 73–76]. Other attractive property of graphene is high specific surface area: the theoretical value is 2600 $m^2 g^{-1}$ [77]. As a rule, much lower magnitudes are obtained by the method of nitrogen adsorption–desorption. The method of standard contact porosimetry (MSCP) gives the value, which is close to theoretical one [78]. This is caused by the disjoining pressure of octane (ideally wetting liquid). Octane wets graphene completely penetrating between its sheets. Since octane completely wets the internal surface of any solid, pores determined using these liquids are considered as total porosity [78–83]. Hydrophilic pores are estimated from the measurements with water. Hydrophobic porosity is a difference between the values obtained using octane and water.

Figure 8a illustrates integral pore size distributions obtained for GO and rGO [82]. In the case of rGO, higher 'octane' porosity has been found comparing with 'water' porosity. It means both hydrophilic and hydrophobic pores in reduced graphene. As opposed to this carbon material, GO shows higher water porosity than that determined in octane. Thus, hydrophobic pores cannot be recognized. This phenomenon shows superhydrophilicity of GO pores. Similar results were obtained in [74, 83]. The GO behaviour is similar to that of ion-exchange resins [84] or gas diffusion layer of the electrodes in proton-exchange membrane fuel cells [85]. HZD-GO composites demonstrate similar properties: micropores are superhydrophilic (the intersection of integral curves with ordinate axis) (Fig. 8b) [74]. Further, the difference is constant (no superhydrophilicity) up to $\log r = 0.5$ (nm), i.e. at pore radius of 3 nm. This property, which is recognized according to the increase of a difference between

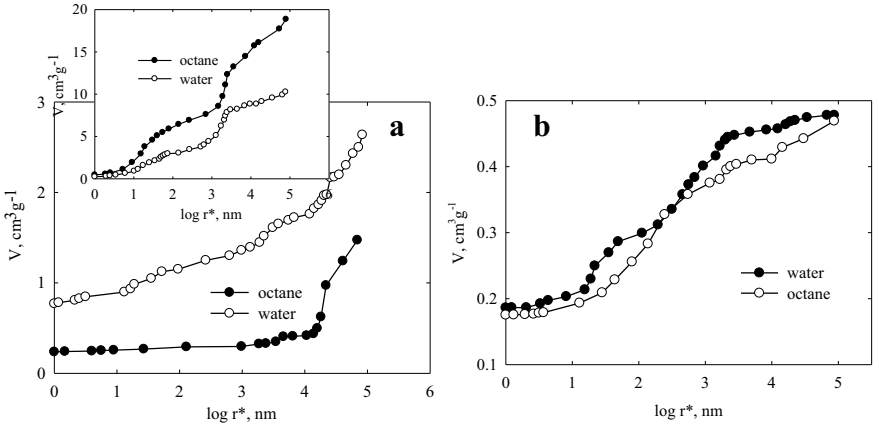

Fig. 8 Data of MSCP for GO (**a**), rGO (insertion of Fig. 8a) and HZD-GO composite (**b**). Adapted from [82] (**a**) and [74] (**b**)

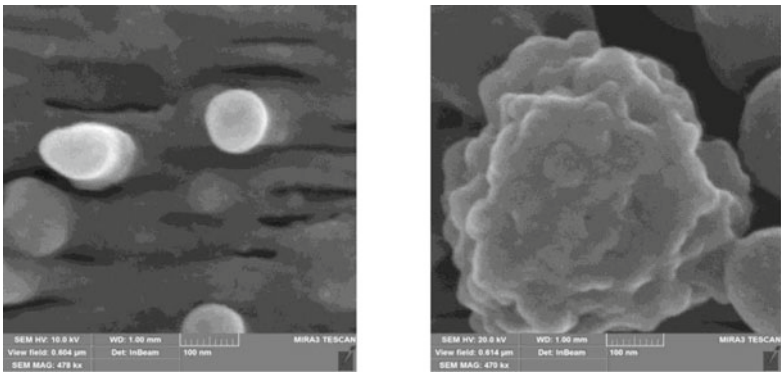

a b

Fig. 9 Active layer of polymer (**a**) and composite (**b**) materials for baromembrane separation. HZD-GO-containing composite was inserted into polyacrylonitrile active layer

two curves, is realized again at log$r$ = 0.5–0.6 (nm), 1.2–1.6 (nm), 2.5–3.5 (nm). Hydrophobicity can be expressed between these intervals.

Superhydrophilicity, which is due to GO: micropores, corresponds to voids between sheets. Further, this property is due to pores between GO aggregates, which are incorporated into the composite and between HZD aggregates, which are covered with GO. Hydrophilicity–hydrophobicity of HZD-GO composites give a possibility to use them as adsorbents for the removal of both inorganic and organic contaminants from water: U(VI)-containing cations [71], Pb^{2+}, $HCrO_4^-$, phenol, lactose [74], pesticides [75], arsenic and arsenate anions [76]. Adsorption involving this composite was integrated into electrodialysis process for desalination of milky whey [86]. The information about composites containing GO is summarized in [87].

The HZD-GO composite was used for modifying polymer membranes that contain thin polyacrylonitrile active layer [73] (Fig. 9a). The pristine polymer membranes were characterized by different cut-off against polyvinylpyrrolidone, molecular mass of which is 40 kDa indicating different pore sizes (Table 3). There are wide slits in active layer of the pristine membrane: their length is up to 250 nm. However, the pore width is 15–30 nm. White spheres are the polymer nodes, which are formed at the surface during the membrane casting. This morphology provides ultrafiltration ability of the polymer membrane.

Regarding modifying membranes, their pores are blocked by rose-like formations (Fig. 9b): the composite particles are also inside pores.

Modified membranes show lower water flux than the pristine materials (see Table 3). However, selectivity towards hardness ions appears: this tendency is enhanced, when one-component HZD modifier is changed to graphene-containing composite. The membrane with smaller pores of pristine membrane demonstrates stability against fouling when the solutions of OVA or BSA are filtered. In the case of pristine membranes, organic species are accumulated inside the membrane pores (pristine

Table 3 Water filtration and mechanism of fouling with proteins-calibrants (adapted from [73])

Modifier	PVP solution through unmodified membrane, J, $m^3\ m^{-2}\ s^{-1}$	Water filtration		Protein solution filtration: fouling mechanism	
		J, $m^3\ m^{-2}\ s^{-1}$	φ (Ca^{2+}, Mg^{2+}). %	OVA, 40 kDa	BSA, 69 kDa
–	5.5×10^{-6}	1.3×10^{-6}	0	Intermediate (pore constriction—cake formation)	Intermediate (pore constriction—cake formation)
HZD		5.9×10^{-7}	8	Cake formation	Cake formation
HZD-GO		3.3×10^{-7}	14	Cake formation	Cake formation
–	3.3×10^{-5}	3.5×10^{-6}	0	Intermediate (pore constriction—cake formation)	Intermediate (pore constriction—cake formation)
HZD		5.5×10^{-7}	5	Cake formation	Cake formation
HZD-GO		9.6×10^{-7}	10	Intermediate (pore constriction—cake formation)	Cake formation

membranes) or deposited onto their outer surface (membranes containing only HZD). As opposed to contaminants in pores, precipitate can be easy removed from the outer surface by scraping, by hydrodynamic pulsations or by the reverse flow of permeate. When the membrane contains a contaminant in pores, aggressive reagents are needed for regeneration. The membrane with smaller pores of active layer, which contains HZD-GO composites, is also stable against fouling with OVA and BSA. However, the membrane with larger pores accumulates OVA due to hydrophobic regions of the composite. BSA particles are not accumulated inside pores, since they are unavailable for larger particles of this protein. As opposed to water filtration, higher values of permeate flux have been found for the membranes containing HZD-GO comparing with membranes modified only with HZD.

Other approach, which allows us to obtain composite membrane, is the deposition of graphene on the outer surface of polymer support. The membrane demonstrating ultrafast nanofiltration can be obtained by this manner [72]. Hydrophilic GO nanoribbons (the angle of wetting with water is 41.4°), and hydrophobic rGOs (86.7°) were deposited simultaneously on commercial nylon support, the pore size of which is 0.22 μm (Fig. 10). The deposition was carried out by vacuum filtration followed by drying at 60 °C. The wetting angle decreased with a growth of the nanoribbon content in the mixture of carbon nanomaterials and reached 54.9° at the nanoribbon volume of 70% relatively the total volume of the mixed modifier. The material is stable in deionized water and also in acidic and alkaline solutions.

The membranes were tested in the processes of filtration of the solutions containing 10 mg dm^{-3} of organic dyes with various sizes and electrical charges: methyl red (hydrated radius of 4.87 Å, neutral), methyl orange (4.96 Å, negative),

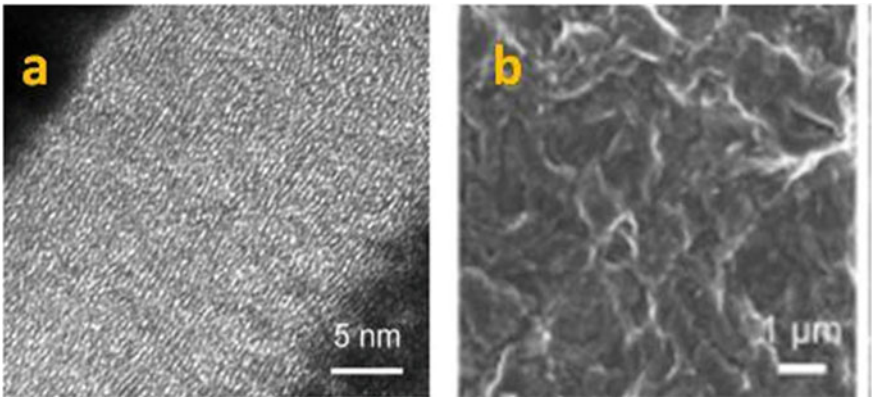

Fig. 10 Filtered layer of the membrane containing rGO and GO nanoribbons: high-resolution TEM (**a**) and SEM (**b**) images (adapted from [72])

methylene blue (5.04 Å, positive) and rose bengal (5.88 Å, negative). The feed solutions were filtered at 5 bar. As found, the filtration rate depends on the type of dye on the one hand and on the composition of filtering layer on the other hand. Comparing with the membrane containing only rGO, the permeate flux increases in 12–32 times for the membrane containing 70% of GO nanoribbons. The flux reached 664 $dm^3\ m^{-2}\ h^{-1}\ bar^{-1}$. It should be noted that the presence of any dye improves water transport. The best rejection (>99) is reached for methyl red (50–70 vol. % of nanoribbons) and rose bengal (both for rGO and for all mixtures). For regeneration, the membranes were washed with deionized water. The membrane containing equal volumes of rGO and nanoribbons is highly stable during the fifth recycling test, exhibiting a rejection rate of >97% for rose bengal and methylene blue. This high stability of the membrane is assumed to be caused by the strong π-π and van der Waals interactions between rGO sheets.

Liquids of different viscosity were filtered through the GO layer, which was deposited on macroporous nylon support [88]. In general, the permeate flux correlates with the liquid viscosity. However, the flux of acetone is higher in 2 times than that of water, though the viscosity ratio for these liquids is 3.

Composite membrane consisting of TiO_2 and GO was synthesized according to a new approach of manufacturing continuous nanochannels in a separating membrane with a two-dimensional laminar structure [89]. The membrane was formed by intercalation of TiO_2 particles, which are synthesized in situ in MXene nanosheets. Water permeability of the obtained membrane is about 90 $dm^3\ m^{-2}\ h^{-1}\ bar^{-1}$. This is higher in 7.3 times than the permeate flux of pristine GO membrane. The flux is higher in 2.4 times comparing with GO/TiO_2 membrane fabricated using traditional methods. The rejection rate for different organic dyes is above 97%. The membrane was also tested in the processes of the filtration of inorganic salts. It is interesting that the membrane demonstrates higher Na_2SO_4 rejection (60%) than the sulphate salt of divalent metal ($MgSO_4$, 35%). The rejection of organic and inorganic species is

partially caused by adsorption [90–92]. The effect of electric field on ion separation is considered in [93].

The membrane including polyvinylidene fluoride support, GO and Ag was obtained in [94], and further, it was impregnated with ionic liquids. This material was used for C_2H_4/C_2H_6 separation. The combination of ethylene-permeating in-plane nano-wrinkles and ethylene-facilitated plane-to-plane nanochannels provides high ethylene permeability and superhigh selectivity.

5 Inorganic Membranes Containing Carbon Nanoparticles

Advanced carbon nanomaterials, such as aerogels [95], graphene sponge [96] or MWCNTs [97], can be derived from natural polysaccharides: bacterial [95] or plant [97] cellulose or chitosan [96]. A very interesting direction is the formation of carbon in pores of inorganic membranes. As a rule, ceramic membranes are modified with oxides or phosphates of multivalent metals. Their nanoparticles are inserted to pores of ceramics [98–101] similarly to polymer membranes [6–8, 11, 102–104]. Since carbon is both hydrophilic and hydrophobic, the membranes modified with carbon nanomaterials are assumed to reject organic species, particularly due to adsorption.

First of all, this approach was developed for fumed silica matrix [105, 106]. The carbon constituent inside silica was obtained from the mixture of carboxymethylcellulose and polyisocyanate in a presence of $NiCl_2$. The interaction of −NCO groups of polyisocyanate with OH groups of cellulose results in copolymer formation inside the silica pore. Modified silica was annealed, the products of pyrolysis reduce nickel. Further, the metal particles provide the formation of nanostructured carbon from the copolymer. The product of its carbonization is carbon nanofibers and dendrites, which form sponge structure (Fig. 11a).

Further, this approach was adapted to ceramic membranes, which were produced from clay minerals [107, 108]. As a natural source of carbon, carboxymethyl cellulose [107] or milk [108] was used. The membranes contained the composite of silica with pyrocarbon [107] or only pyrocarbon [108]. Carbon particles are seen on the surface

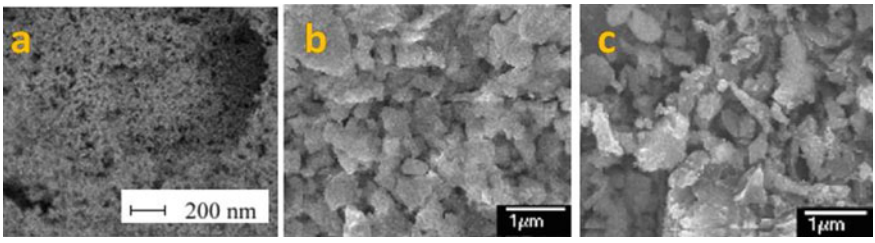

Fig. 11 TEM (**a**) and SEM (**b**, **c**) images of composites obtained by the carbonization of: copolymer of cellulose acetate with polyisocynate in SiO_2 matrix (**a**, adapted from [106]), polyisocynate and milk (**b**, **c**, adapted from [107]) in ceramics

of ceramics (compare Fig. 11b and c). Carbon phase cannot be recognized from XRD patterns, since its reflexes are masked by ceramics. Graphite phase is confirmed indirectly, since the intensity of reflexes at $2\theta = 26.6°$ and 44.0° increases.

The membranes were tested in the processes of removal of ions and dyes from water [107–110]. Synergic combination of the effect of size and charge exclusion due to inorganic and carbon constituents provides rejection of both organic and inorganic species. The rejection tends to decrease over time evidently due to shrinkage of the diffusion part of double electric layer caused by adsorption of organic and inorganic species.

Other approach, which allows us to graphene-containing inorganic membrane, is the filtration of mixed dispersion containing GO and clay mineral (for instance, attapulgite (ATP) [111]). The ATP nanorods were embedded between the laminar layers of GO influencing the interlayer distance and facilitating greater number of channels for enhanced water transportation. As found, Si–OH groups of attapulgite interact with the oxygen-containing groups of GO consequently forming GO/ATP composites. The surface charge density of the composite is more negative comparing with GO, The composite coated the surface of ceramic support, and the layer thickness was several microns. The contact angle depends on the composition of the layer: this value decreases from 67° for GO to 37° for the composite when a mass ratio of GO and ATP is 1:3. Comparing with the membrane modified only with GO, the composite provides increase of the water flux in several times. Very high rejection (99%) of Cu^{2+}, Ni^{2+}, Pb^{2+} and Cd^{2+} ions has been found, when the optimal composition of filtration layer is achieved. Filtration of Cu^{2+}-containing solution was performed during 6 h. Decrease of rejection over time has been also found. In this case, the rejection decrease is insufficient indicating dominating size effect provided by the filtration layer. In its small pores, diffusion parts of double electric layers are mainly overlapped promoting the rejection of ionic species.

6 Conclusions

Composite membranes containing advanced carbon nanomaterials, such as fullerenes and their derivarives, oxidized and reduced graphenes, nanotubes, graphite nanoparticles) are considered in this review. The modifiers were inserted into pores of ceramic or polymer supports (materials for baromembrane separation or proton-conducting membranes) or formed directly in ceramic matrix by carbonization of natural and synthetic polymers (ultrafiltration membranes). Other approaches are suspension filtration through macroporous support: a thin rejecting layer is deposited on its outer surface (normally graphenes are used for this purpose). At last, carbin addition is inserted into the polymer solution before casting of the membrane film. The materials for pervaporation, gas separation, baromembrane processes and low-temperature fuel cells are obtained by this manner.

The permeability of non-porous polymers depends on the packing density, the polymer chain mobility and the free volume. The hardsphere properties of fullerenes

provide high free volume of the polymer and compaction of its chains improving permeability. Ideally smooth surface of nanotubes provides fast transport of solvent. Oxidized graphene is responsible for fast ion transport through proton-conducting membranes or ion rejection during baromembrane separation. In the last case, this modifier enhances separation ability of the membranes and their antifouling properties due to additional hydrophilization.

According to our opinion, the prospective directions of investigations is involving derivatives of carbon nanomaterials, which contain different functional groups to the membrane preparation. Other approaches could be a sourch of the optimal combination of polymer support and carbon modifier, especially porous structure of the support is important. Moreover, similar functional groups of the polymer and modifier can show synergetic effect. The important task is the composition of two-component modifier, which includes both carbon nanomaterial and inorganic ion-exchanger. Regarding ceramic materials, carbonization of different types of polymers can provide different carbon structures inside pores affecting separation ability of composite membranes.

References

1. https://www.marketsandmarkets.com/Market-Reports/membranes-market-1176.html
2. Strathmann H (2001) Membrane separation processes: current relevance and future opportunities. AIChE J 47(5):107787
3. Souza V, Quadri M (2013) Organic-inorganic hybrid membranes in separation processes: a 10-year review. Braz J Chem Eng 30(4):683–700
4. Subasi Y, Cicek B (2017) Recent advances in hydrophilic modification of PVDF ultrafiltration membranes—a review: part II. Membr Technol 11:5–11
5. Sun W, ShiJ CC et al (2018) A review on organic–inorganic hybrid nanocomposite membranes: a versatile tool to overcome the barriers of forward osmosis. RSC Adv 8:10040–10056
6. Myronchuk V, Dzyazko Y, Zmievskii Y et al (2016) Organic-inorganic membranes for filtration of corn distillery. Acta Periodica Technologica 47:153–165
7. Zmievskii Y, Rozhdestvenska L, Dzyazko Y et al (2017) Organic-inorganic materials for baromembrane separation. Springer Proc Phys 195:675
8. Dzyazko Y, Rozhdestvenskaya L, Zmievskii Y et al (2015) Organic-inorganic materials containing nanoparticles of zirconium hydrophosphate for baromembrane separation. Nanoscale Res Lett 10:64
9. Abdulkarem E, Naddeo Y, Banat F et al (2020) Development of polyethersulfone/α-zirconium phosphate (PES/α-ZrP) flat-sheet nanocomposite ultrafiltration membranes. Chem Eng Res Design 161:206–217
10. Huang J, Arthanareeswaran G, Zhang K (2012) Effect of silver loaded sodium zirconium phosphate (nanoAgZ) nanoparticles incorporation on PES membrane performance. Desalination 285:100–107
11. Zmievskii Yu, Dzyazko Yu, Myronchuk V et al (2016) Fouling of polymer and organic-inorganic membranes during filtration of corn distillery. Ukrainian Food J 5(4):739–747
12. Pang R, Li X, Li J et al (2014) Preparation and characterization of ZrO_2/PES hybrid ultrafiltration membrane with uniform ZrO_2 nanoparticles. Desalination 332(1):60–66
13. Yogarathinam L, Gangasalam A, Ismail A et al (2018) Concentration of whey protein from cheese whey effluent using ultrafiltration by combination of hydrophilic metal oxides and hydrophobic polymer. J Chem Technol Biotechnol 93(9):2576–2591

14. Torbati S, Shahmirzadi M, Tavangar T (2018) Fabrication, characterization, and performance evaluation of polyethersulfone/TiO_2 nanocomposite ultrafiltration membranes for produced water treatment. Polym Adv Technol 10:2619–2631
15. Behboud A, Jafarzadeh Y, Yegani R (2016) Preparation and characterization of TiO_2 embedded PVC ultrafiltration membranes. Chem Eng Res Design 114:96–107
16. Díez B, Roldán N, Martín A et al (2017) Fouling and biofouling resistance of metal-doped mesostructured silica/polyethersulfone ultrafiltration membranes. J Membr Sci 526:252–263
17. Chen J, Ruan H, Wu L et al (2011) Preparation and characterization of PES-SiO_2 organic-inorganic composite ultrafiltration membrane for raw water pre-treatment. Chem Eng J 168(3):1272–1278
18. Li X, Janke A, Formanek P et al (2020) High permeation and antifouling polysulfone ultrafiltration membranes with in situ synthesized silica nanoparticles. Mater Today Proc 22:100784
19. Rahimi Z, Zinatizadeh A, Zinadini S (2019) Membrane bioreactors troubleshooting through the preparation of a high antifouling PVDF ultrafiltration mixed-matrix membrane blended with O-carboxymethyl chitosan-Fe_3O_4 nanoparticles. Environ Technol 40(26):3523–3533
20. Rahimi Z, Zinatizadeh A, Zinadini S (2014) Preparation and characterization of a high antibiofouling ultrafiltration PES membrane using OCMCS-Fe_3O_4 for application in MBR treating wastewater. J Appl Res Water Wastewater 1:13–17
21. Zhu J, Zhou S, Li M et al (2020) PVDF mixed matrix ultrafiltration membrane incorporated with deformed rebar-like Fe_3O_4–palygorskite nanocomposites to enhance strength and antifouling properties. J Membr Sci 612:118467
22. Sterescu D, Stamatialis D, Mendes E et al (2006) Fullerene-modified poly(2,6-dimethyl-1,4-phenylene oxide) gas separation membranes: why binding is better than dispersing. Macromolecules 39:9234–9242
23. Harun-Or M, Ralph S (2017) Carbon nanotube membranes: synthesis, properties, and future filtration applications. Nanomaterials 7:99
24. Safarpour M, Khataee A, Vatanpour V (2014) Preparation of a novel polyvinylidene fluoride (PVDF) ultrafiltration membrane modified with reduced graphene oxide/titanium dioxide (TiO_2) nanocomposite with enhanced hydrophilicity and antifouling properties. Ind Eng Chem Res 53(34):13370–13382
25. Kang S, Herzberg M, Rodrigues DF et al (2008) Antibacterial effects of carbon nanotubes: size does matter! Langmuir 24:6409–6413
26. Rubel RI, Ali MH, Jafor MA et al (2019) Carbon nanotubes agglomeration in reinforced composites: a review AIMS. Mater Sci 6(5):756–780
27. Miao M (2011) Electrical conductivity of pure carbon nanotube yarns. Carbon 49(12):3755–3761
28. Yu W, Liu Y, Shen L et al (2020) Magnetic field assisted preparation of PES-Ni@MWCNTs membrane with enhanced permeability and antifouling performance. Chemosphere 243:125446
29. Van Oss CJ, Good RJ, Chaudhury MK (1986) The role of van der Waals forces and hydrogen bonds in "hydrophobic interactions" between biopolymers and low energy surfaces. J Colloid Interf Sci 111:378–390
30. Khoerunnisa E, Rahmaha W, Ooic BS et al (2020) Chitosan/PEG/MWCNT/iodine composite membrane with enhanced antibacterial properties for dye wastewater treatment. J Environ Chem Eng 8:103686
31. Gumbi NN, Li J, Mamba BB et al (2020) Relating the performance of sulfonated thin-film composite nanofiltration membranes to structural properties of macrovoid-free polyethersulfone/sulfonated polysulfone/O-MWCNT supports. Desalination 474:114176
32. Guo J, Zhu X, Dong DD et al (2019) The Hybrid process of preozonation and CNTs modification on hollow fiber membrane for fouling control. J Water Proc Eng 31:100832
33. Khalid A, Abdel-Karim A, Atieh MA et al (2017) PEG-CNTs nanocomposite PSU membranes for wastewater treatment by membrane bioreactor. Sep Purif Technol 190:165–176

34. Rahimpoura A, Jahanshahi M, Khalili S et al (2012) Novel functionalized carbon nanotubes for improving the surface properties and performance of polyethersulfone (PES) membrane. Desalination 286:99–107
35. Alawada AR, Alshahrani AA, Aouak TA et al (2020) Polysulfone membranes with CNTs/chitosan biopolymer nanocomposite as selective layer for remarkable heavy metal ions rejection capacity. Chem Eng J 388:124267
36. Shah P, Murthy CN (2013) Studies on the porosity control of MWCNT/polysulfone composite membrane and its effect on metal removal. J Membr Sci 437:90–98
37. Shawky HA, Chae S-R, Lin S et al (2011) Synthesis and characterization of a carbon nanotube/polymer nanocomposite membrane for water treatment. Desalination 272:46–50
38. Song X, Wang L, Tang CY et al (2015) Fabrication of carbon nanotubes incorporated double-skinned thin film nanocomposite membranes for enhanced separation performance and antifouling capability in forward osmosis process. Desalination 369:1–9
39. Sun H, Li D, Liu B et al (2019) Enhancing the permeability of TFC membranes based on incorporating polyamide matrix into MWCNTs framework. Appl Surf Sci 496:143680
40. Hammond G, Kuck V (1992) Fullerenes: synthesis, properties, and chemistry of large carbon clusters. ACS, Washington, p 195
41. Hirsch A (1994) The chemistry of the fullerenes. Wiley-VCH Verlag GmbH, Weinheim, Germany, p 203
42. Bottero J, Rose J, Wiesner M (2006) Nanotechnologies: tools for sustainability in a new wave of water treatment processes. Integr Environ Assess Manage 2(4):391–395
43. Yevlampieva N, Vinogradova L, Ryumtsev E (2006) Effect of fullerene C_{60} as a branching point on molecular and polarization properties of star-shaped polystyrenes. Polym Sci 48:106–113
44. Shota S, Hidetoshi M, Keiichiro S et al (2008) Polyelectrolyte membranes based on hydrocarbon polymer containing fullerene. J Power Sources 176(1):16–22
45. Penkova A, Acquah S, Piotrovskiy L et al (2017) Fullerene derivatives as nano-additives in polymer composites. Russ Chem Rev 86(6):530–566
46. Đorđević A, Bogdanović G (2008) Fullerenol: a new nanopharmaceutic? Oncology 16(3–4):42–45
47. Dzyazko Y, Volfkovich Y, Perlova O et al (2019) Effect of porosity on ion transport through polymers and polymer-based composites containing inorganic nanoparticles (review). Springer Proc Phys 222:235–253
48. Gutru R, Nagaraju N, Santoshkumar D (2016) Functionalized fullerene embedded in Nafion matrix: a modified composite membrane electrolyte for direct methanol fuel cells. Chem Eng J 306(15):43–52
49. Saga S, Matsumoto H, Saito K et al (2008) Polyelectrolyte membranes based on hydrocarbon polymer containing fullerene. J Power Sources 176(1):16–22
50. Wang H, DeSousa R, Gasa J et al (2007) Fabrication of new fullerene composite membranes and their application in proton exchange membrane fuel cells. J Membr Sci 289:277–283
51. Tasaki K, DeSousa R, Hengbin W et al (2006) Fullerene composite proton conducting membranes for polymer electrolyte fuel cells operating under low humidity conditions. J Membr Sci 281(1):570–580
52. Rikame SS, Mungray AA, Mungray AK (2017) Synthesis, characterization and application of phosphorylated fullerene/sulfonated polyvinyl alcohol (PFSP) composite cation exchange membrane for copper removal. Sep Purif Technol 177:29–39
53. Gladchenko S, Polotskaya GA, Gribanov AV et al (2002) The study of polystyrene-fullerene solid-phase composites. Tech Phys 47(1):102–106
54. Dmitrenko ME, Penkova AV, Kuzminova AI et al (2019) Development and investigation of novel polyphenylene isophthalamide pervaporation membranes modified with various fullerene derivatives. Sep Purif Technol 226:241–251
55. Polotskaya G, Gladchenko S, Zgonnik V (2002) Gas diffusion and dielectric studies of polystyrene-fullerene compositions. J Appl Polym Sci 85(14):2946–2951

56. Penkova AV, Polotskaya GA, Toikka AM et al (2009) Structure and pervaporation properties of poly(phenylene-iso-phthalamide) membranes modified by fullerene C_{60}. Macromol Mater Eng 294(6):432–440
57. Polotskayaa G, Penkova A, Pientkac Z et al (2010) Polymer membranes modified by fullerene C_{60} for pervaporation of organic mixtures. Desalin Water Treat 14:83–88
58. Polotskaya G, Biryulin Y, Rozanov V (2005) Asymmetric membranes based on fullerene-containing polyphenylene oxide. Fullerenes, Nanotubes, Carbon Nanostruct 12(1–2):371–376
59. Chang S, Waite T, Schafer A et al (2002) Adsorption of trace steroid estrogens to hydrophobic hollow fibre membranes. Desalination 146:381–386
60. Hu J, Yuan T, Ong S et al (2003) Identification and quantification of bisphenol A by gas chromatography and mass spectrometry in lab-scale dual membrane system. J Environ Monit 5:141–144
61. Konieczny K, Klomfas G (2002) Using activated carbon to improve natural water treatment by porous membranes. Desalination 147:109–116
62. Berezkin V, Viktorovskii I, Vul A et al (2003) Fullerene microcrystals as adsorbents of organic compounds. Semiconductors 37(7):802–810
63. Ong S, Hu J, Biryulin Yu et al (2006) Fullerene-containing polymer membranes for rejection of estrogenic compounds in water. Fullerenes, Nanotubes, Carbon Nanostruct 14:463–466
64. Jin X, Hu J, Tint M et al (2007) Estrogenic compounds removal by fullerene-containing membranes. Desalination 214:83–90
65. Biryulin Y, Kostetskii Y, Kudoyarov M et al (2005) Fullerene-modified Dacron track membranes and adsorption of nitroxyl. Tech Phys Lett 31:506–508
66. Thines RK, Mubarak NM, Nizamuddin S et al (2017) Application potential of carbon nanomaterials in water and wastewater treatment: a review. J Taiwan Inst Chem Eng 72:116–133
67. Chen G-E, Zhu W-W, Xu S-J et al (2016) A PVDF/PVB composite UF membrane improved by F-127-wrapped fullerene for protein waste-water separation. RSC Adv 6:83510–83519
68. Novoselov KS, Geim AK, Morozov SV et al (2004) Electric field effect in atomically thin carbon films. Science 306(5696):666–669
69. Chen C-H, Hu S, Shih J-F et al (2017) Effective synthesis of highly oxidized graphene oxide that enables wafer-scale nanopatterning: preformed acidic oxidizing medium approach. Sci Reports 7:3908
70. Darkrim F, Levesque D (2000) High adsorptive property of opened carbon nanotubes at 77 K. J Phys Chem 104(29):6773–6776
71. Perlova OV, Dzyazko YS, Palchik AV et al (2020) Composites based on zirconium dioxide and zirconium hydrophosphate containing graphene-like additions for removal of U (VI) compounds from water. Appl Nanosci. https://link.springer.com/article/10.1007/s13204-020-01313-1
72. Cho K, Lee H, Nam Y et al (2019) Ultrafast-selective nanofiltration of an hybrid membrane comprising laminated reduced graphene oxide/graphene oxide nanoribbons. Appl Mater Interfaces 11(30):27004–27010
73. Rozhdestvenska LM, Kudelko KO, Ogenko VM et al (2020) Membranes modified by nano-composites of hydrated zirconium dioxide and oxidized graphene. Ukrainian Chem J 86(4):91–107
74. Dzyazko YS, Ogenko VM, Volfkovich YM et al (2018) Composite consisting of hydrated zirconium dioxide and grapheme oxide for removal of organic and inorganic components from water. Chem Phys Technol Surf 9(4):417–431
75. Dzyazko YS, Ogenko VM, Shteinberg LY et al (2019) Composite adsorbents including oxidized graphene: effect of composition on mechanical durability and adsorption of pesticides. Chem Phys Technol Surf 10(4):432–445
76. Luo X, Wang C, Wang L et al (2013) Nanocomposites of graphene oxide-hydrated zirconium oxide for simultaneous removal of As(III) and As(V) from water. Chem Eng J 220:98–106

77. Dreyer DR, Park S, Bielawski CW et al (2010) The chemistry of graphene oxide. Chem Soc Rev 39(1):228–240
78. Volfkovich YM, Rychagov AY, Sosenkin VE et al (2014) Measuring the specific surface area of carbon nanomaterials by different methods. Russ J Electrochem 50(11):1099–1101
79. Volfkovich YM, Filippov AN, Bagotsky VS (2014) Structural properties of different materials and powders used in different fields of science and technology. Springer, London, Heidelberg, New York, Dordrecht
80. Volfkovich YM, Sosenkin VE (2012) Porous structure and wetting of fuel cell components as the factors determining their electrochemical characteristics. Russ Chem Rev 81(10):936–959
81. Volfkovich YM, Sakars AV, Volinsky AA (2005) Application of the standard porosimetry method for nanomaterials. Int J Nanotechnol 2(3):292–302
82. Shulga YM, Baskakov SA, Baskakova YV et al (2015) Supercapacitors with graphene oxide separators and reduced graphite oxide electrodes. J Power Sources 279:722–730
83. Volfkovich YM, Lobach AS, Spitsyna NG et al (2019) Hydrophilic and hydrophobic pores in reduced graphene oxide aerogel. J Porous Mat 26(4):1111–1119
84. Kononenko NA, Berezina NP, Vol'fkovich YM et al (1985) Investigation of ion-exchange materials structure by standard porosimetry method. J Appl Chem USSR 58(10):2029–2033
85. Volfkovich YM, Sosenkin VE, Nikolskaya NF et al (2008) Porous structure and hydrophilic-hydrophobic properties of gas diffusion layers of the electrodes in proton-exchange membrane fuel cells. Russ J Electrochem 44(3):278–285
86. Myronchuk V, Zmievskii Y, Dzyazko Y et al (2019) Electrodialytic whey demineralization involving polymer-inorganic membranes, anion exchange resin and graphene-containing composite. Acta Periodica Technologica 50:163–171
87. Dzyazko Y, Volfkovich Y, Chaban M (2021) Composites containing inorganic ion exchangers and graphene oxide: hydrophilic-hydrophobic and sorption properties (review). Springer Proc Phys 246:93–110
88. Ding J-H, Zhao H-R, Ji D et al (2019) Ultrafast molecular sieving through functionalized graphene membranes. Nanoscale 11:3896–3904
89. Han R, Wu P (2019) High-performance graphene oxide nanofiltration membrane with continuous nanochannels prepared by in situ oxidation of MXene. J Mater Chem A 7:6475–6481
90. Tan P, Sun J, Hu Y et al (2015) Adsorption of Cu^{2+}, Cd^{2+} and Ni^{2+} from aqueous single metal solutions on graphene oxide membranes. J Hazard Mater 297:251–260
91. Ma F-f, Zhang D, Huang T et al (2019) Ultrasonication-assisted deposition of graphene oxide on electrospun poly(vinylidene fluoride) membrane and the adsorption behavior. Chem Eng J 358:1065–1073
92. Mahmoud KA, Mansoor B, Mansour A et al (2015) Functional graphene nanosheets: the next generation membranes for water desalination. Desalination 356:208–225
93. Lohrasebi A, Rikhtehgaran S (2018) Ion separation and water purification by applying external electric field on porous graphene membrane. Nano Res 11:2229–2236
94. Dou H, Xu M, Jiang B et al (2019) Bioinspired graphene oxide membranes with dual transport mechanisms for precise molecular separation. Adv Func Mat 29:1905229
95. Wu ZY, Li C, Liang H-W et al (2013) Ultralight, flexible, and fire-resistant carbon nanofiber aerogels from bacterial cellulose. Angewandte Chem Int Edit 125(10):2997–3001
96. Niu J, Domenech-Carb A, Primo A (2019) Uniform nanoporous graphene sponge from natural polysaccharides as a metal-free electrocatalyst for hydrogen generation. RSC Adv 9:99–106
97. Goodell B, Xie X, Qian Y et al (2008) Carbon nanotubes produced from natural cellulosic materials. J Nanosci Nanotechnol 8:2472
98. Dzyaz'ko YS, Belyakov VN, Stefanyak NV et al (2006) Anion-exchange properties of composite ceramic membranes containing hydrated zirconium dioxide. Russ J Appl Chem 79(5):769–773
99. Martí-Calatayud MC, García-Gabaldón M, Pérez-Herranz V et al (2015) Ceramic anion-exchange membranes based on microporous supports infiltrated with hydrated zirconium dioxide. RSC Adv 5:46348–46358

100. Dzyazko Y, Rozhdestveskaya L, Zmievskii Y et al (2019) Composite inorganic anion exchange membrane for electrodialytic desalination of milky whey. Mater Today: Proc 6(2):250–259
101. Myronchuk V, Zmievskii Y, Dzyazko Y et al (2018) Whey desalination using polymer and inorganic membranes: operation conditions. Acta Periodica Technologica 49:103–115
102. Dzyazko YS, Rozhdestvenska LM, Vasilyuk SL et al (2017) Composite membranes containing nanoparticles of inorganic ion exchangers for electrodialytic desalination of glycerol. Nanoscale Res Lett 12:438
103. Saki S, Uzal N, Ates N (2017) The size and concentration effects of Al_2O_3 nanoparticles on PSF membranes with enhanced structural stability and filtration performance. Desal Water Treat 84:215–224
104. Pang R, Li X, Li J et al (2014) Preparation and characterization of ZrO_2/PES hybrid ultrafiltration membrane with uniform ZrO_2 nanoparticles. Desalination 332:60–66
105. Dubrovina L, Naboka O, Ogenko V et al (2014) One-pot synthesis of carbon nanotubes from renewable resource: cellulose acetate. J Mater Sci 49:1144–1149
106. Goncharuk VV, Dubrovin IV, Dubrovina LV et al (2016) Carbon-silica composites with cellulose acetate, polyisocyanate and copper chloride. Phys Chem Solid State 17(2):241–246
107. Goncharuk VV, Ogenko VM, Dubrovina LV et al (2019) Modification of tubular ceramic membranes with pyrocarbon and silica. Ukrainian Chem J 85(11):52–61
108. Goncharuk VV, Kucheruk DD, Dubrovina LV et al (2019) Modification of tubular ceramic membranes by pyrocarbon from carbonized polymers. Ukrainian Chem J 85(6):97–103
109. Goncharuk VV, Ogenko VM, Kucheruk DD et al (2019) Water purification by microfiltration ceramic membranes modified with pyrocarbon and silica. J Water Chem Technol 41(4):246–252
110. Goncharuk VV, Dubrovina LV, Kucheruk DD et al (2016) Water purification of dyes by ceramic membrane modified by pyrocarbon from carbonized polymers. J Water Chem Technol 38(3):163–166
111. Liu W, Wang D, Soomro R et al (2019) Ceramic supported attapulgite-graphene oxide composite membrane for efficient removal of heavy metal contamination. J Membr Sci 591:117323

Dependence of the Nanocomposite Systems Resistance on the Initial Materials Dispersity

Ya. I. Lepikh, V. A. Borshchak, N. N. Sadova, and N. P. Zatovskaya

1 Introduction

With the development of nanophysics and nanoelectronics, at present, widespread use is made of composite materials, which are a multiphase heterogeneous system consisting of components with various physical and chemical properties. The analysis of the studies showed that the formation of the composite systems is accompanied by complex physicochemical processes between the conductive phase, on the one hand, and glass and organic bonds, on the other. Factors that control the rate of the chemical interaction (such as the starting material particle size, their acid-reducing properties) at the selected annealing temperature conditions determine the phase composition, microstructure and electrophysical properties of nanocomposites. That is, by providing for starting materials high level of stability, it is possible to solve the problems associated with the degradation processes that occur in the materials over time and often serve as causes of equipment failures.

2 Research Methods

It was found that a significant role in the reproduction and stability of the nanocomposites electrophysical parameters is played by the dispersion of the functional material and glass frit powders.

The dispersed composition (particle size distribution) is one of the most important characteristics of finely divided materials, determining their physicochemical properties. For the small particles (about 25 μm or less) size analysis, the method

Ya. I. Lepikh (✉) · V. A. Borshchak · N. N. Sadova · N. P. Zatovskaya
Odesa I.I. Mechnikov National University, 2 Dvoryanska Str., Odesa 65082, Ukraine
e-mail: ndl_lepikh@onu.edu.ua

O. Fesenko and L. Yatsenko (eds.), *Nanomaterials and Nanocomposites, Nanostructure Surfaces, and Their Applications*, Springer Proceedings in Physics 263, https://doi.org/10.1007/978-3-030-74741-1_11

of X-ray sedimentography is usually used. Determination of the material particle size distribution with different density, dispersion and, most importantly, different particle shapes other than spherical is carried out by the method of weight liquid sedimentation from the starting layer. The B-4 device was used, in which the use of more correct methods of measurement results mathematical processing, taking into account nonlinear resistance and particle shape laws, the use of mathematical approximation taking into account distribution multimodel provides the analysis high accuracy of a wide class of powders from 1 to 300 μm.

At present, the dispersion of powders is not regulated; according to the design documentation, powders with particle sizes less than 25 microns are used.

3 Results and Discussion

Our studies on samples made by standard technology showed a low level of the nanocomposites parameters reproducibility, which can be associated with large glass particles spread in their geometric dimensions [1–6].

Figure 1 shows a histogram of the glass powder particle size distribution

As can be seen from the figure, the particle size varies in a large range, which has a negative effect on the nanocomposite properties.

In addition, studies of samples obtained from powders of lead borosilicate glass (PbO, SiO_2, B_2O_3, Al_2O_3) with fixed particle sizes (0.5, 1, 3, 5 μm) and a functional material RuO_2 with a particle size of 3 μm at a fixed annealing temperature (870 °C) showed the nanocomposites resistance dependence on the ratio of the glass and conductive phases concentration. It has been determined that for samples with a low content of ruthenium dioxide, the influence of the glass frit particle sizes on the resistance is the largest. The resistance of the samples increases with increasing of the glass content, and the highest growth rate is observed for glass fiber with particle sizes of 0.5 μm shown in Fig. 2.

With an increase in the RuO_2 concentration, the resistance approaches a constant value and does not depend on the glass fiber particle sizes. The resistance dependence on the particle sizes for high-resistance nanocomposites can be associated with the processes of sintering and the effect of the components dispersion on the conductive

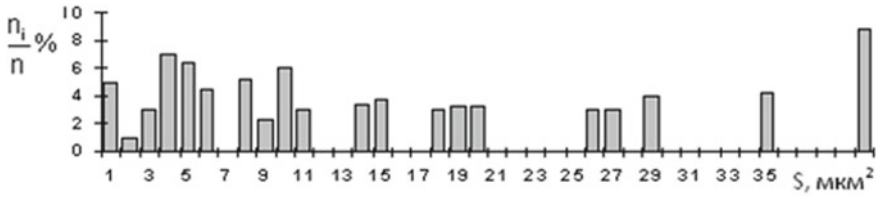

Fig. 1 Histogram of the glass powder 279–2 particle size distribution

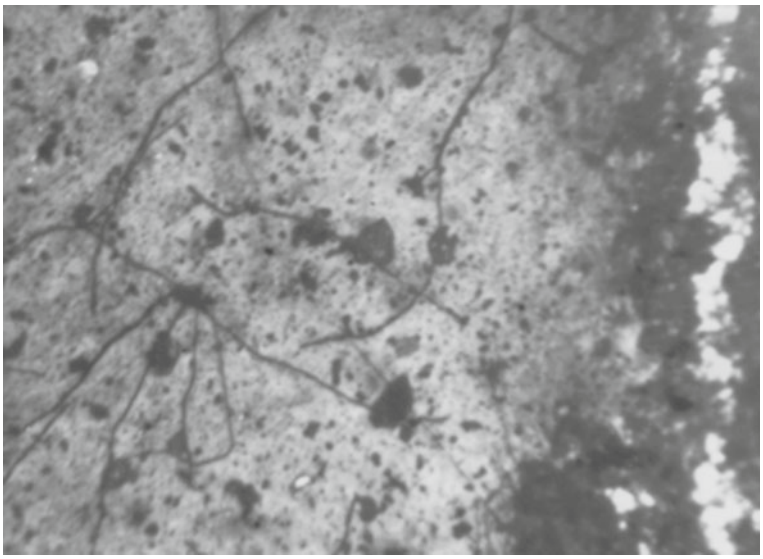

Fig. 2 Microcracks in thick films. Scanning microscopy. Secondary electron mode. Magnification 500

chains geometric dimensions. With a decrease in the glass particle sizes, the length increases and the cross-sectional area of the chains of the conducting phase decreases.

In RuO_2—glass systems, a mixed character of conductivity is observed, which is a combination of processes occurring in the conductive and glass phases. In high-resistance nanocomposites, the main contribution to the conductivity is made by glass fiber, so the properties of this phase play a significant role in the process of current transfer (Fig. 3).

4 Conclusion

It was found that with an increase in the conductive phase—glass ratio, the surface resistance decreases. The greatest influence on the nanocomposite resistance is the glass frit particle size for samples with a low content of ruthenium dioxide. With an increase in the glass content, the resistance rate growth increases, and the highest rate is observed when the glass particle size is about 0.5 μm. As the RuO_2 content increases, the resistance tends to a constant value and does not depend on the glass particle size.

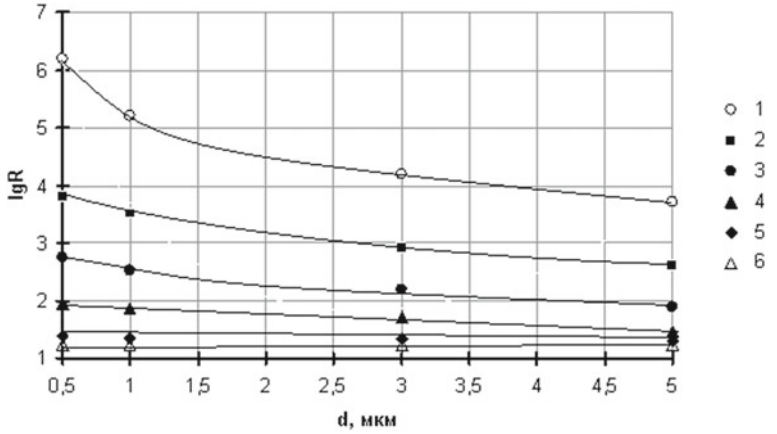

Fig. 3 R(Ohm/cm^2) dependence on the glass particles geometric sizes for different concentration ratios glass: RuO_2 (1–90:10; 2–80:20; 3–70:30;4–60:40; 5–50:50; 6–45–55)

References

1. YaI L, Lavrenova TI, Bugayova TN, Zatovskaya NP, Snigur PO (2014) Annealing temperature modes influence on properties of heterophase nanocomposites based on ceramics "glass—Ag-Pd" systems. Funct Mater 21(3):297–301
2. Smyntyna V, Borshchak V, Brytavskyi I (2018) Nonideal heterojunctions for image sensors. Nova Publishers, New York, USA
3. . Kurmashev ShD, Sadova NN, Lavrenova TI, Bugaeva TN (2005) Issledovanie vosproizvodimosti elektrofizicheskih parametrov tolstoplenochnyih struktur "RuO_2 – steklo". Tehnologiya i konstruirovanie v elektronnoy apparature 4(58): 62–64 (Kurmashev ShD, Sadova NN, Lavrenova TI, Bugaeva TN (2005) Investigation of the reproducibility of the electrophysical parameters of thick-film structures "RuO_2—glass". Technol Des Electron Equip 4(58):62–64
4. Kurmashev ShD, Bugaeva TM, Lavrenova TI, Sadova NN (2009) Influence of the glass phase structure on the resistance of the layers in sestem "Glass-RuO_2" Photoelectronics 18:99–102
5. Grinevych V, Smyntyna V, Filevska L (2018) Nanostructured SnO_2 as CBRN safety material. J. Bonca, S. Kruchinin (eds) Nanostructures materials for the detection of CBRN, NATO science for pease and security series a: chemistry and biology. Springer Science + Business Media B.V., part of Springer Nature, pp 107–127
6. Filevska LM (2018) Luminescence of nanoscale tin dioxide. Rev Photoelectron 27:52–59

Electrical Resistance of Modified Thermo-exfoliated Graphite

Iryna V. Ovsiienko, Lyudmila l. Vovchenko, Lyudmila Yu. Matzui, Tatiana l. Tsaregradskaya, Galyna V. Saenko, Oleh D. Marinin, and Tetiana A. Len

1 Introduction

The development of new composite materials based on different forms of nanocarbon and nanographite structure is quite a perspective direction in the creation of new materials with a wide range of functionality. Due to the unique combination of such properties as low density, high electrical conductivity, high thermal and corrosion resistance, these composite materials are used in the chemical industry, nuclear and thermal power, automotive and aircraft construction. The expansion of the areas of use of these materials can be achieved by creating new composites based on modified thermo-exfoliated graphite (TEG), i.e. composites formed by the deposition on the surface of TEG particles of metals, their salts and oxides.

The application of TEG as a basis for nanoscaled metal (or its compounds) deposition gives the possibility to create thermo-protective, rust-resisting materials possessing qualitatively new characteristics, which are specified by both the properties of metal and specific properties of graphite and do not inherent to the routine crystalline materials. So, the presence of a small amount of nanostructured phase (about 1–2%) could lead to an essential improving of electrical, magnetic and kinetic properties of composites. The application of TEG as supporter for nanoscaled metal particles is quite promising, due to the possibility to produce on the base of TEG-metal powders the products of different shape. Moreover, no binders are necessary for their production.

There are a number of methods for obtaining a modifying metal component on the surface of nanocarbon and graphite carriers, in particular, on the surface of the

I. V. Ovsiienko (✉) · L. Vovchenko · L. Yu. Matzui · T. Tsaregradskaya · G. V. Saenko · O. D. Marinin · T. A. Len
Departments of Physics, Taras Shevchenko National University of Kyiv, Volodymyrska 64/13, Kyiv 01601, Ukraine
e-mail: tsar_grd@ukr.net

O. Fesenko and L. Yatsenko (eds.), *Nanomaterials and Nanocomposites, Nanostructure Surfaces, and Their Applications*, Springer Proceedings in Physics 263, https://doi.org/10.1007/978-3-030-74741-1_12

TEG particles. These modification methods, as well as the effect of the metal modification of graphite surface on the transport, magnetic, mechanical and thermal properties of the obtained composites are described in the literature. In particular, a two-step method of producing "graphite-metal" compositions through intercalated graphite compounds is used to obtain an atomically distributed metal in a graphite matrix. Graphite is intercalated with metal salts, which is then reduced with various reducing reagents [1, 2]. Another method of obtaining composites based on graphite with metals is the reduction of metal from metal halides by intercalated compounds of graphite with potassium in organic solutions [3–5]. Modification of graphite by such methods significantly changes the properties of the source graphite. Modified according to these methods, graphite revealed a new interest effects, in particular, the anomalous Hall effect and linear asymmetric magnetoresistance [6–9]. However, these modification methods are very complex and require significant time and specific chemical equipment. In addition, these methods lead to partial destruction of the graphite layers and the graphite π-system, which can impair the conductive properties of graphite.

Other large groups of modification methods are physical methods of applying metal on the surface of a graphite carrier [9, 10]. The bases of these methods are phase transformations of the first order in the absence of chemical reactions. Such phase transformations are observed in the condensation of atoms on the substrate, condensation of liquid droplets followed by solidification, crystallization from a melt or solution, as well as in the decomposition of solid solutions. However, the use of these methods for the deposition of metal nanoparticles on the surface of dispersed carbon and graphite particles is quite problematic.

One of the most common methods of obtaining metal nanosized particles on the surface of a graphite carrier is a method of reducing the metal from the corresponding metal salts, aqua solution of which impregnates a graphite carrier. Recovery occurs using different types of reducing agents in the presence of stabilizers (surfactants, polymers, etc.) [11–14].

In the presented paper, the relationship between the parameters of structure, as well as between methods of obtaining a modifying coating on graphite surfaces and the concentration of metal in graphite and the electrical resistance of bulk specimens of modified TEG is investigated.

2 Experimental

2.1 Preparation of Bulk Specimens of Modified Thermo-exfoliated Graphite

As a source material for the production of TEG natural monocrystalline dispersive graphite (crystallite size L ~1 mcm, interplanar spacing $d_{002} = 0.335$ nm, parameter of preferred orientation of crystallites $\eta = 10^4$) has been used. Initially, natural

dispersive graphite has been intercalated with sulfuric acid by the standard liquid-phase technique up to the first stage compound [12]. Then obtained intercalated graphite has been thermo-exfoliated in ascending flow furnace at the temperature 1100 °C (the density of TEG powder is ~0.002 g/cm^3).

The modification of thermo-exfoliated graphite with metals has been performed by the two methods that are completely different in the succession of thermoexfoliation and modification processes [12]. In the first method, the graphite powder has been previously treated with a substance which contained the modifier as an element of chemical composition of this substance. The powder was then placed into cyclone gas-fired furnace where the processes of modification and thermoexfoliation were going on simultaneously at the temperature 1100 °C. This method allows to produce the specimens with concentration of modifier up to 5% mass and density ~(0.002–0.005) g/cm^3.

In the second method (chemical modification), the graphite was previously thermoexfoliated, and then the modifier was deposited on the surface of TEG particles during several successive chemical reactions. The powders of modified TEG produced by this method had the density ~(0.03–0.07) g/cm^3 which considerably exceeded the density of initial TEG. One of the advantages of this modification method is the possibility to produce the modified TEG with desired concentration of modifier (from 5 to 50% mass). The specimens of modified TEG with Ni, Co Fe and Cu (metals concentrations are 10, 30 and 50% mass) have been obtained with this method.

Methods of TEG modification, as well as the structural and morphological peculiarities and phase composition of obtained modified graphite are described in detail in [12].

For measurements of electrical resistance, the bulk specimens of modified TEG have been prepared by method of cold pressing without binder on automatic press with the following parameters: the range of allowable load p is from 1 ton up to 10 tons, and the rate of load growth v_p is from 0.1 up to 10 kN/s. For manufacturing bulk TEG specimens, such moulds have been used: the round press mould with diameter $D = 14$ mm and the rectangular press mould with linear dimensions $a \times b = (15 \times 3)$ mm^2. Thus, specimens for resistivity investigations have been in the form of pallets or rectangles.

The production of the (3–10)–mm-high pallets from the powders of low bulk density requires the application of large-sized press moulds. To avoid this, the powder of pure or modified TEG was previously tightened to a higher density ~(0.22–0.80) g/cm^3. The powder was poured into a glass tube with diameter 14 mm and height from 0.5 to 2 mm, and then the specimen prepared in this way was compressed to the density ~2 g/cm^3 using hydraulic press in the press mould with diameter 14 mm. Using this method, the specimens of modified TEG with nickel, cobalt, iron and nickel–iron have been obtained.

The density of bulk specimens prepared from modified TEG with high modifier concentration (up to 50 mass %) is (2.7–2.9) g/cm^3. So, to produce compacted specimens with high density, no supplementary compacting of TEG powders modified by this method is required. These density values exceed the density of bulk TEG

specimens and density of natural graphite, because the density of metal is considerably larger than the density of graphite. Wherefore for comparison properties of compacting modified TEG parameter of porosity, $\frac{\Delta V}{V}\frac{\Delta V}{V}$ has been used:

$$\frac{\Delta V}{V} = \frac{C_{\mathrm{GR}} A_{\mathrm{GR}} + C_M A_M}{d \cdot V} - 1, \tag{1}$$

where ΔV is the total volume of pores, V is the molar volume of source TEG or modified TEG, C_{GR} and C_M are, respectively, atomic concentrations of graphite and modifier, A_{GR} and A_M are, respectively, atomic masses of graphite and modifier, and d is the density of bulk specimen.

2.2 Measurement of Electrical Resistance

The measurements of electrical resistance of bulk specimens of modified TEG have been carried out at room temperature along compression axis ($\rho_{c)}$ and perpendicular to compression axis (ρ_a), and then anisotropy parameter ρ_c/ρ_a was determined for modified TEG specimens with different densities and different modifiers. Also, the temperature dependence of electrical resistance was measured perpendicular to compression axis for bulk specimens of modified TEG with different densities and modifiers in dependence on type and concentration of modifier.

For room temperature measurements of electrical resistance along compression axis and perpendicular to compression axis, specimens of cylindrical form with height $h = (3\text{–}10) \times 10^{-3}$ m and diameter $D = 1.4 \times 10^{-2}$ m have been used. Electrical resistance was measured by four-point method described in [7]. The principle schemes of arrangements specially designed for measuring resistance ρ_a perpendicular to compression axis and resistance ρ_c along compression axis are shown in Fig. 1.

The electrical resistance ρ_a was calculated according to the following formula:

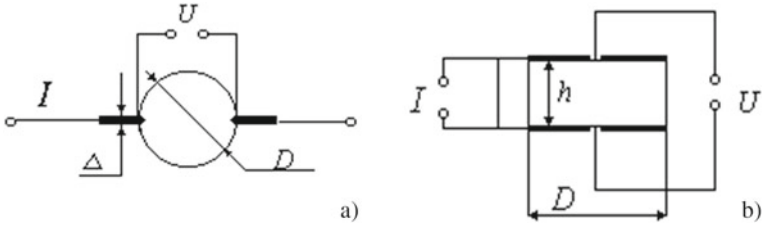

Fig. 1 Principle schemes of arrangements for measuring resistance ρ_a perpendicular to compression axis **a** and resistance ρ_c along compression axis **b**, (notation in the text)

$$\rho_a = \frac{\pi R h}{2\ln(D/\Delta)}, \quad R = R_{\text{et}}\frac{U_x}{U_{\text{et}}}, \tag{2}$$

where Δ is the thickness of electrodes supplying the specimen with power, R_{et} is the standard resistance equal to 0.01 Ω, U_x is the potential drop on the specimen, and U_{et} is the potential drop on the standard resistance.

The electrical resistance ρ_c was calculated by the following formula:

$$\rho_c = \frac{\pi D^2 R}{4h}, \tag{3}$$

where R is determined in the same way as in formula (2).

The measurements of temperature dependences of electrical resistance for bulk specimens of modified TEG have been carried out in temperature interval from 77 up to 293 K. The resistance was measured by standard four-probe method in direction perpendicular to pressure axis. The resistivity measurement error did not exceed 0.5%.

3 Results and Discussion

3.1 Resistivity of Modified TEG with Small Concentration of Modifier

The electrical resistances perpendicular to compression axis (ρ_a) and along compression axis (ρ_c) were investigated in source TEG and TEG modified with nickel, cobalt, iron as well as a mixture of nickel and iron by the method of simultaneous thermoexfoliation and modification. The concentration of modifier is ~1% at., and the range of densities was from 0.2 to 2 g/cm^3.

Figure 2 presents the dependence of resistance ρ_a (a) and ρ_c (b) on material density for TEG with different modifiers.

As it is clear from Fig. 2a, with increase of the material density, the value of electrical resistance perpendicular to compression axis decreases. As the density increases from nearly 0.2 to 0.4 g/cm^3, an abrupt decrease from (1.0–1.2) × 10^{-4} Ωm to 2 × 10^{-5} Ωm is observed, i.e. by five or six times. With further increase of density material to 2 g/cm^3, ρ_a slowly decreases almost two times. Thus, the increase of material density from 0.2 to 2 g/cm^3 leads to decrease of electrical resistance perpendicular to compression axis in almost ten times, and a small addition of metal does not influence the magnitude of resistance and behaviour of the dependence of ρ_a on density.

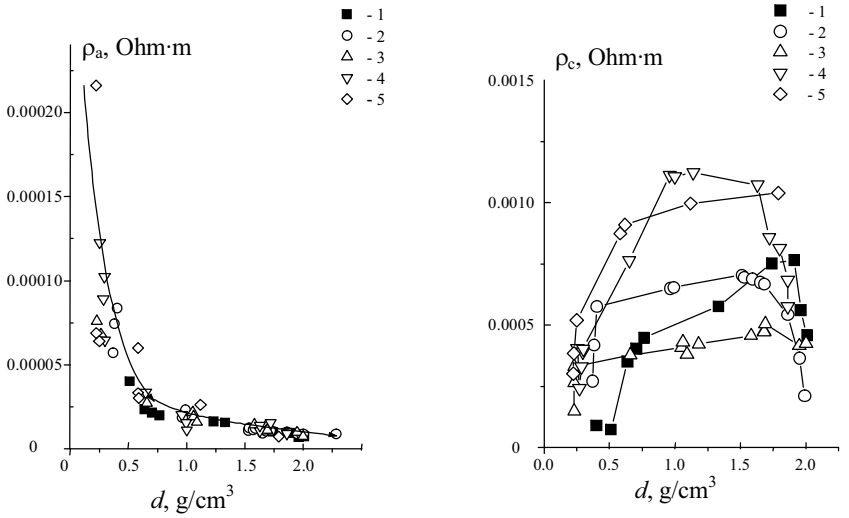

Fig. 2 Dependence of electrical resistance ρ_a **a** and ρ_c **b** on material density for bulk specimens of TEG with different modifiers: 1—TEG; 2—TEG-Ni; 3—TEG-Co; 4—TEG-NiFe; 5—TEG-Fe

As can be seen from the figure, the character of dependence ρ_c on TEG density d is rather complicated for source TEG. In the specimens with small densities d ~(0.2–0.5) g/cm^3, ρ_c is approximately 1×10^{-4} Ωm, i.e. has the same value as ρ_a. As TEG density increases, resistivity ρ_c gradually grows and comprises 7.5×10^{-4} Ωm for the specimens with the density d ~1.9 g/cm^3. Further insignificant increase of density to 2 g/cm^3 results in abrupt almost twofold decrease in ρ_c. The dependence $\rho_c(d)$ for modified TEG is very similar to that for pure TEG. But in contrast to ρ_a, which does not change its behaviour for TEG with small additions of metal, the value of ρ_c is different for the specimens with the same density but with different modifiers. For the specimens of modified TEG with nickel and cobalt, the value of ρ_c is close to those obtained for source TEG.

For modified nickel TEG, ρ_c is a little larger, and for modified cobalt TEG, ρ_c is a little smaller than for source TEG. For the specimens of TEG modified with iron and nickel, the value of ρ_c is almost two times larger than in source TEG and comprises ~$(1.1–1.2) \times 10^{-3}$Ωm.

As it is known from investigations [12], the modified TEG consists of microcrystallites which have the structure similar to the structure of natural graphite. Every microcrystallite consists of several graphite layers, the electrical resistance along the layers is small, below 10^{-6} Ωm, and electrical resistance perpendicular to the layers is large. The ratio ρ_c/ρ_a for natural monocrystalline graphite is ~10^5 and for high-oriented pyrolytic graphite is ~10^4. The source TEG and modified TEG with the density of (0.2–0.3) g/cm^3 are completely isotropic materials in which TEG particles are distributed chaotically. These have the same value of electrical resistance ~$(1.2–1.5) \times 10^{-3}$ Ωm both perpendicular and parallel to compression axis. In the

specimens of larger densities, i.e. in the specimens prepared under compression at larger pressures, the values of electrical resistance measured perpendicularly and in parallel to compression axis begin to differ. In such specimens, TEG particles are oriented in the same direction at high pressure of compression. As a result, a layered structure is formed perpendicular to compression axis which leads to considerable decrease of electrical resistance in the direction perpendicular to compression axis and its increase in the direction parallel to compression axis. This effect is observed for the specimens with the densities above (0.7–0.8) g/cm^3. With further increase of specimen's densities up to 2 g/cm^3, resistance ρ_a becomes still smaller but unessentially which is associated with the formation of more ordered layered structure. For TEG with the density ~2 g/cm^3, ρ_a is (9–10) $\times$ 10^{-5} Ωm, i.e. it is close to ρ_a value for pyrolytic anisotropic graphite. Small additions of metal (1% at.) practically have no effect on the magnitude of electrical resistance perpendicular to compression axis.

The electrical resistance of compacted materials is known to include electrical resistance of particles themselves that make up compacted material and electrical resistance of contact between these particles. The electrical resistance of metal modifier particles whose concentration is very small in given materials is smaller than that of graphite particles. But the decreased, in comparison with source TEG, electrical resistance in TEG metal system due to metal particles is compensated by electrical resistance of contacts between TEG particles and metal in these systems.

When the density of compacted materials is increased from 0.8 to 1.9 g/cm^3, the electrical resistance ρ_c along compression axis increases unessentially for the TEG specimens and practically does not change for the specimens of modified TEG. The value of ρ_c in the specimens of TEG modified with cobalt and nickel is close to that for source TEG, while in the specimens of TEG modified with iron as well as in TEG modified with iron and nickel, the value of ρ_c is considerably larger. The electrical resistance perpendicular to graphite layers has a jump-like character. Charge transfer takes place on the boundaries of crystallite, grains and defects. And it is in these places where the modifier is deposited in TEG. Therefore, the conductivity in the direction perpendicular to graphite layers takes place through metal impregnations located on the boundaries of crystallite, grains and defects. The decrease in electrical resistance along compression axis due to metal depositions is compensated by contact resistance, and in TEG nickel system as well as in TEG cobalt system, the value of ρ_c is close to that for source TEG. From the data on X-ray analysis, electron microscopy and Auger spectroscopy [12], it was found that iron is present as an oxide Fe_3O_4 in TEG iron and TEG iron–nickel systems, i.e. the boundaries of grains and graphite particles are covered with oxide films, and this results in the increase of contact resistance and growth of total electrical resistance of the system. The abrupt decrease of ρ_c both in source and modified TEG at the densities increasing insignificantly from 1.9 to 2 g/cm^3 is accounted for by the fact that at the pressure applied for producing TEG specimens with the density up to 2 g/cm^3, graphite grains are reduced, graphite layers are partially destroyed, and several graphite layers may be cut through by modifier particles. As a result, the electrical resistance ρ_c decreases.

Figure 3 presents the dependence of anisotropy parameter ρ_c/ρ_a on the density of source and modified TEG specimens.

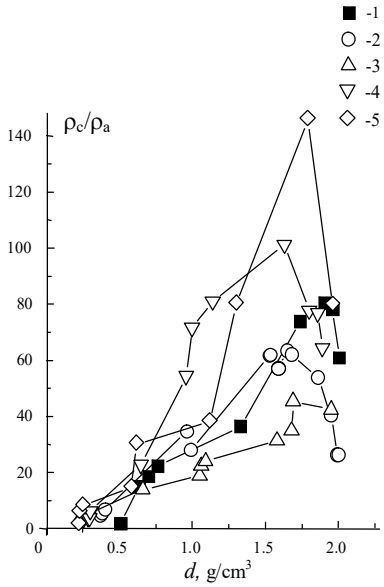

Fig. 3 ρ_c/ρ_a ratio for bulk specimens of TEG with different modifiers in dependence on density and type of modifier: 1—TEG; 2—TEG-Ni; 3—TEG-Co; 4—TEG-NiFe; 5—TEG-Fe

As Fig. 3 shows, the anisotropy parameter ρ_c/ρ_a slowly grows for all compact materials up to the density ~1.9 g/cm^3. After this point, anisotropy parameter decreases. For the specimens with small densities, ρ_c/ρ_a is almost the same for all materials, ρ_c/ρ_a ~1–5, which is typical for porous isotropic materials. The value of ρ_c/ρ_a becomes maximal in TEG with the density 1.91 g/cm^3 and equals to 80. In TEG modified with nickel or cobalt, the value of anisotropy parameter ρ_c/ρ_a is maximal at slightly smaller density, $\rho_c/\rho_a = 63$ in TEG with nickel and $\rho_c/\rho_a = 45$ for TEG with cobalt. The values ρ_c/ρ_a for TEG with cobalt are being smaller than those for source TEG at all densities of both materials. This is associated with the decrease of contact resistance between graphite and metal particles at higher pressures which results in smaller values in comparison with source TEG values of ρ_c. The maximal value of ρ_c/ρ_a ~100–145 in TEG modified with iron and nickel as well as for TEG modified with iron was observed at the density ~(1.6–1.79) g/cm^3. As it was mentioned above, this is accounted for by larger electrical resistance ρ_c for these compacted materials.

Thus, the maximal value of anisotropic parameter ρ_c/ρ_a for compacted source and modified TEG is ~100–140 which is 7–10 times smaller that in pyrolytic anisotropic graphite. This is explained, first, by partial destruction of graphite layers and reduction of graphite grains due to compression and, second, introduction of isotropic metal particles into graphite matrix which "shunt" the graphite layers. All this significantly reduces electrical resistance in the direction perpendicular to graphite layers (i.e. along compression axis of bulk specimen) in comparison with pyrolytic graphite. But at the same time, electrical resistance along graphite layers remains practically the same as in pyrolytic anisotropic graphite.

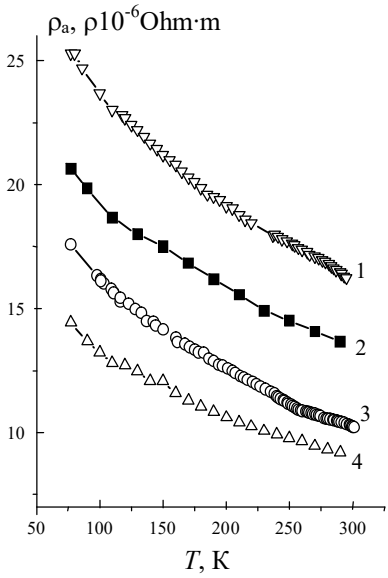

Fig. 4 Dependence $\rho_a(T)$ for compacted source (2) and modified TEG with 50% mass (1), 10% mass (3) and 30% mass (4) of nickel

3.2 The Temperature Dependence of Resistivity for Compacted Modified Thermo-Exfoliated Graphite

With the aim to study the influence of structure, type and concentration of modifier on temperature dependence of electrical properties of modified TEG, the electrical resistance in direction perpendicular to compression axis (ρ_a) in TEG modified with different concentrations of nickel, copper, iron and cobalt in the temperature range (77–300) K has been measured.

Figure 4 presents the results of measurements $\rho_a(T)$ dependence for compacted TEG modified with nickel. The nickel concentration in the samples is 10%, 30% and 50% mass. For comparison dependence, $\rho_a(T)$ for source TEG is also presented.

As it is seen from the figure, in general, the character of resistivity temperature dependence $\rho_a(T)$ is similar for all modified with different concentration of nickel TEG and source TEG. The ratio of resistivities at $T = 77$ K and room temperature ρ_{77}/ρ_r is near to that for source TEG and is about 1.5. For modified TEG with 5% mass of nickel, this ratio is nearly equal to that for TEG. For modified TEG with 30% mass and 50% mass of nickel ρ_{77}/ρ_r ~1.6 that is slightly larger than for modified TEG with 10% mass of nickel. The analogous results have been obtained for TEG modified with copper, cobalt and iron in different concentrations. For all these materials, the temperature dependence of electrical resistance is similar in it than for source compacted TEG. For all these compacted modified TEG, the values ρ_{77}/ρ_r are close to the values ρ_{77}/ρ_k for source compacted TEG. The exception is the specimens of TEG modified with 10 mass % of cobalt for which ρ_{77}/ρ_k is ~2.25. All specimens of compacted modified TEG including the specimens with the maximal concentration of

modifier 50% mass or 16–17% at. do not show considerable decrease of resistivity ρ_r in the temperature range from 77 to 300 K. This can be explained, first, by a large value of contact resistance between the particles of TEG and modifier which compensates the decrease in the specimen's resistance due to metal impregnation. Second, in terms of percolation theory, TEG-metal system can be viewed as a three-dimensional net with metal particles as conductivity sites. However, the metal concentration in TEG under study (beyond 50% mass) is small to reach a current threshold, i.e. at this concentration of metal in TEG metal system, the particles of metal have not been grouped into continuous cluster which results in abrupt drop of electrical resistance of the material.

The analysis of the properties of the modified TEG should take into account the whole complex of parameters including the type of modifier, its concentration and the parameter characterizing material structure, namely specimens porosity $\Delta V/V_0$, i.e. the volume of pores (ΔV) in specimen in comparison with the volume specimen.

Figure 5 presents the temperature dependences of electrical resistance $\rho_a(T)$ for compacted modifier TEG with the same concentration of modifier (nickel, cobalt, iron and copper) of 10% mass. For comparison, the figure also presents the temperature dependence $\rho_a(T)$ for source TEG and gives data on porosity for each material.

As can be seen from the figure, ρ_a for all specimens of modified TEG is smaller than for source TEG irrespective of modifier type and specimen's porosity. The comparison of specimens with the same porosity shows that ρ_a is the smallest in TEG with copper, it is almost two times smaller than in pure TEG and is slightly

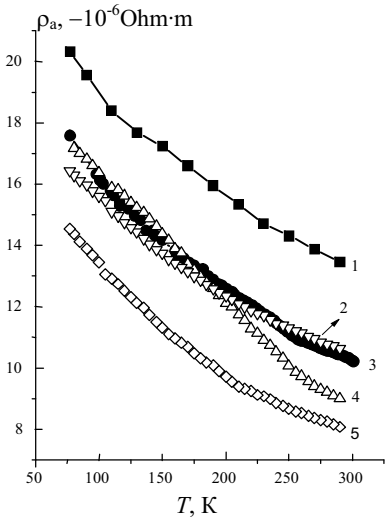

Fig. 5 Dependences $\rho_a(T)$ for bulk specimens of modified TEG with the same concentration of modifier of 10% mass: 1—pure TEG, $d = 1.8$ g/cm^3, $\Delta V/V_0 = 0.2$; 2—iron, $d = 1.94$ g/cm^3, $\Delta V/V_0 = 0.25$; 3—nickel, $d = 1.92$ g/cm^3, $\Delta V/V_0 = 0.27$; 4—cobalt, $d = 2.06$ g/cm^3, $\Delta V/V_0 = 0.18$; 5—copper, $d = 2$ g/cm^3, $\Delta V/V_0 = 0.22$

larger than in TEG with cobalt. The value of ρ_a in TEG with nickel and iron even with larger porosity is smaller than that in source TEG with $\Delta V/V_0 = 0.2$. That is, the modification of TEG with metal in concentration of 10% mass even in more porous material results in slight decrease of electrical resistance in the direction perpendicular to compression axis.

Figure 6 presents the temperature dependence ρ_a for TEG with different modifiers, different modifier concentrations and the same porosity.

As seen from the figure, bulk specimens of TEG with different modifiers, but the same porosity values, have identical temperature dependences of ρ_a, the value of ρ_a being smaller than that for less porous source TEG. The exception is bulk specimen of TEG with cobalt. For this specimen, the value of ρ_a is larger than in the other modified TEG, but this bulk specimen of modified TEG has the largest concentration of modifier (50% mass) among the other specimens shown in Fig. 6.

Thus, the above results show that the modification of TEG by metal results in a slight (less than twofold) decrease of electrical resistance in the direction perpendicular to compression axis. The type of modifier does not influence essentially the value of ρ_a in the materials with the same porosity and modifier concentration of 30% mass in the temperature range from 77 to 300 K.

Figure 7 presents the values of ρ_a at room temperature for all investigated bulk specimens of modified TEG with different modifiers and different concentrations in dependence of material porosity.

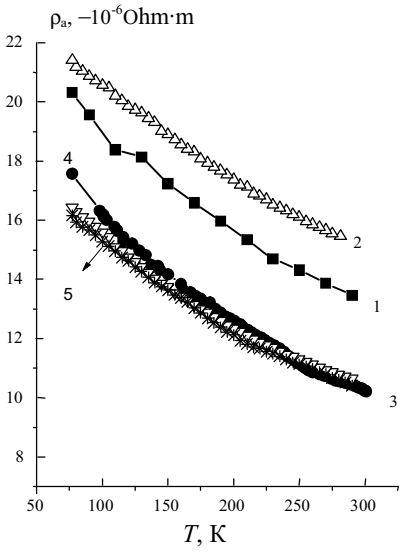

Fig. 6 Dependences $\rho_a(T)$ for bulk specimens of modified TEG with close values of porosity: 1— source TEG, $\Delta V/V_0 = 0.2$, $d = 1.8$ g/cm^3; 2—50% mass Co, $\Delta V/V_0 = 0.26$, $d = 2.85$ g/cm^3; 3—10% mass Ni, $\Delta V/V_0 = 0.27$, $d = 1.92$ g/cm^3; 4—10% mass Fe, $\Delta V/V_0 = 0.25$, $d = 1.94$ g/cm^3; 5—30% mass Cu, $\Delta V/V_0 = 0.26$, $d = 2.3$ g/cm^3

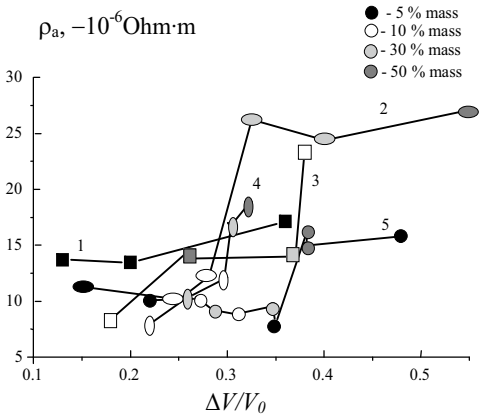

Fig. 7 Dependence $\rho_a(\Delta V/V_0)$ at room temperature for all bulk specimens of modified TEG with different modifiers and different concentrations: 1—source TEG; TEG modified by Fe (2); by Co (3); by Cu (4); by Ni (5). Each metal concentration has its mark on the figure

As it follows from figure the character of ρ_a dependence on porosity is the same for all bulk specimens of modified TEG regardless of the modifier's type. For each TEG modifier system, there is a limiting porosity beyond which the values of ρ_a are very similar and do not depend on modifier concentration in the interval up to 30% mass. At larger modifier concentrations, ρ_a increases abruptly 1.5–2 times. Further on as the porosity of bulk specimens grows to 0.6, ρ_a again changes insignificantly.

For bulk specimens of modified TEG with iron and copper, the limiting porosity is ~0.3, and for bulk specimens of modified TEG with cobalt and nickel, it is ~0.35.

4 Conclusion

Thus, the performed investigations of electrical resistance in bulk specimens of modified by metals TEG allow to make the following conclusions:

1. Impregnation of metal into TEG in small concentrations does not significantly influence the magnitude of electrical resistance of bulk specimens in the direction perpendicular to compression axis.
2. Impregnation of metal into TEG results in a significant decrease of anisotropy parameter ρ_c/ρ_a in modified TEG; the more uniform and even the distribution of metal particles in TEG, the greater is the increase of anisotropy parameter.
3. Impregnation of modifier from 10% mass to 50% mass into TEG results in insignificant (less than two times) decrease of electrical resistance perpendicular to compression axis of the specimens. The magnitude of resistance does not depend essentially on modifier type or modifier concentration (at the concentration below 30 mass %) but depends on material porosity.

4. There exists limit porosity for each TEG modifier system at which electrical resistance perpendicular to compression axis increases sharply. Electrical resistance in the specimens below or above this limit practically does not depend on modifier concentration. The more uniform and even the distribution of metal particles in TEG, the greater is the value of limit porosity.

References

1. Shirai M, Igeta K, Arai M (2000) Chem. Commun (7):623–624
2. Mendoza D, Morales F, Escudero R, Walter J (1999) J Phys Condens Matter 11:L317
3. Fagan SB, Mota R, da Silva AJR, Fazzio A (2003) Physica B 340–342:982:985
4. Ivanovskaya VV, Köhler C, Seifert G (2007) Phys Rew B 75:075410
5. Walter J, Wakita S, Boonchuduang W, Hara S, Suzuki M, Suzuki I (2002) J Phys Chem B 106:8547
6. Matzui D, Ovsiyenko I, Lazarenko O, Prylutskyy Yu, Matzui V (2011) Mol Cryst Liq Cryst 535:64–73
7. Tkachuk VY, Ovsiyenko IV, Matzui LY, Len TA, Prylutskyy YI, Brusylovets OA, Berkutov IB, Mirzoiev IG, Prokopov OI (2016) Mol Cryst Liq Cryst 639(1):137–150
8. Ovsiienko I, Matzui L, Berkutov I, Mirzoiev I, Len T, Prylutskyy Y, Prokopov O, Ritter U (2018) J Mater Sci 53(1):716–726
9. Muller U, Sattler K, Xhie J, Venkateswaran N, Raina GJ (1991) Vac Sci Technol B 9(2):829–832
10. Komiyama M, Kobayashi J, Morita S (1990) J Vac Sci Technol B 8(1):608–609
11. Ovsiyenko I, Matzui L, Pundyk I, Prylutskyy Yu (2012) J Mater Sci Res 1(3):19–24
12. Matzui L, Ovsiienko I, Vovchenko L, Brusilovets A, Tsurul M (2001) Functional materials 8(2): 345–350 (In Ukraine)
13. Len TA, Matzui LY, Ovsiienko IV, Prylutskyy YI, Andriievskyy VV, Mirzoiev I, Berkutov IB, Kolesnichenko YuV (2011) Low Temp Phys 37(10):819–823
14. Matzui L, Lysov V, Kharkov Y, Vovchenko L (2000) Metalurgija, 39(1):15–19

Methods for Controlling the Properties of Nanoporous Layers in Granules of Porous Ammonium Nitrate: Stage of Drying

N. O. Artyukhova, J. Krmela, V. Krmelova, and A. E. Artyukhov

1 Introduction

Porous ammonium nitrate (PAN) granules are obtained by the following methods [1–3]:

1. Granulation of melt in granulation towers with addition of pore-forming and modifying additives.
2. Heat treatment of granules.
3. Humidification and drying of the granules.

The main quality index of PAN is the absorptivity and retentivity to diesel fuel. Each of the noted methods provides the necessary value of these indices; at the same time, the environmental production indicators decrease (method 1), the strength of the granules is lost (method 2), the production scheme becomes more complicated (method 3).

N. O. Artyukhova (✉) · A. E. Artyukhov
Department of Marketing, Sumy State University, 2, Rymskogo-Korsakova Str., Sumy 40007, Ukraine
e-mail: n.artyukhova@pohnp.sumdu.edu.ua

A. E. Artyukhov
e-mail: a.artyukhov@pohnp.sumdu.edu.ua

J. Krmela
Department of Numerical Methods and Computational Modeling, Alexander Dubcek University of Trencin, 491/30, I. Krasku, 02001 Puchov, Slovak Republic
e-mail: jan.krmela@fpt.tnuni.sk

V. Krmelova
Department of Materials Technologies and Environment, Alexander Dubcek University of Trencin, 491/30, I. Krasku, 02001 Puchov, Slovak Republic
e-mail: vladimira.krmelova@fpt.tnuni.sk

O. Fesenko and L. Yatsenko (eds.), *Nanomaterials and Nanocomposites, Nanostructure Surfaces, and Their Applications*, Springer Proceedings in Physics 263, https://doi.org/10.1007/978-3-030-74741-1_13

A promising technique for obtaining PAN is to combine the heat treatment and humidification of granules in small-sized vortex granulators.

The main advantages of the PAN granules production in a vortex flow are:

- reduction of the residence time for granules in the workspace of the device and maintaining their strength properties;
- quantity reduction of heat treatment cycles for granules;
- combination of the humidification and drying stages in one device;
- classification of granules by size;
- decrease in the overall dimensions of the granulation equipment.

It is necessary to predict theoretically how the granule will be warmed up and moisture will be removed to obtain a high-quality porous structure. This mathematical model enables determining the conditions for uniform heat treatment and drying of granules in the hot heat transfer agent's flow.

Although there are many studies devoted to PAN production (e.g. [1–6]), they do not observe the nanoporous structure of the surface and deep layers of the granule. The granule absorptivity depends on the pore size on the surface of the granule. The retentivity of the granule depends on the size of the internal pores. The correct selection of the technology for obtaining PAN allows providing a given pore size on the surface and inside the granule.

One should note that the destruction of a granule can also occur at the stage of nanoporous structure formation during humidification and heat treatment, for example, in vortex granulators [7–11]. Despite the satisfactory results after introducing vortex granulators into the PAN production technology, the object of research includes the mechanisms for controlling the residence time of a granule in the workspace of this device. In this work, the authors continue the research on introducing the drying stage to eliminate the possible overheating of the granule and its collision with other granules and the wall of the device in the swirling heat transfer agent's intense flow. The necessity to introduce the final drying stage using multistage shelf units [8, 12, 13] is substantiated in works [14, 15]. The choice of this type of dryer is based on a comparative analysis of modern methods of effective dewatering of dispersed materials and effective two-phase systems such as fluidized bed [16–20].

The additional drying stage in the decreasing velocity regime in the active (but less turbulized) hydrodynamic mode will make it possible to achieve the following changes in the nanoporous structure of granules (in comparison with an undried sample):

- an increase in the number of micropores and mesopores of curvilinear configuration;
- an increase in the share of curvilinear macropores in the total number of nanopores;
- an increase in the surface nanopores depth.

These changes increase the retentivity rate of the granule and the reliable retention time of the diesel distillate in the granule.

The thermodynamic conditions to produce the PAN granules have a decisive effect on the nanoporous structure, features of pores, their number, relative porous surface area, etc. Based on the importance of this index, the authors modeled the thermodynamic operating conditions of a gravitational shelf dryer at the final drying stage.

Principal scheme of the PAN obtaining unit with the use of equipment with highly turbulized flows is shown in Fig. 1.

The target technological processes in PAN production are heat treatment of the ordinary ammonium nitrate after humidification and the PAN final drying, significant secondary process—cleaning of the waste drying agent before its release into the atmosphere or utilization. Given this, basic algorithm of the granulation unit's calculation (technological scheme of the unit is shown in Fig. 2) will be based on the defining of technological operation conditions and constructive characteristics of the vortex granulator (VG), gravitational shelf dryer (GSD), and absorber (A) with vortex mass transfer–separation contact elements.

In general, the algorithm to calculate the main technological equipment of the granulation unit to obtain PAN, can be presented as a scheme, as shown in Fig. 3. One or several software products, which together constitute automated complex of the granulation unit calculation, correspond each block of the scheme.

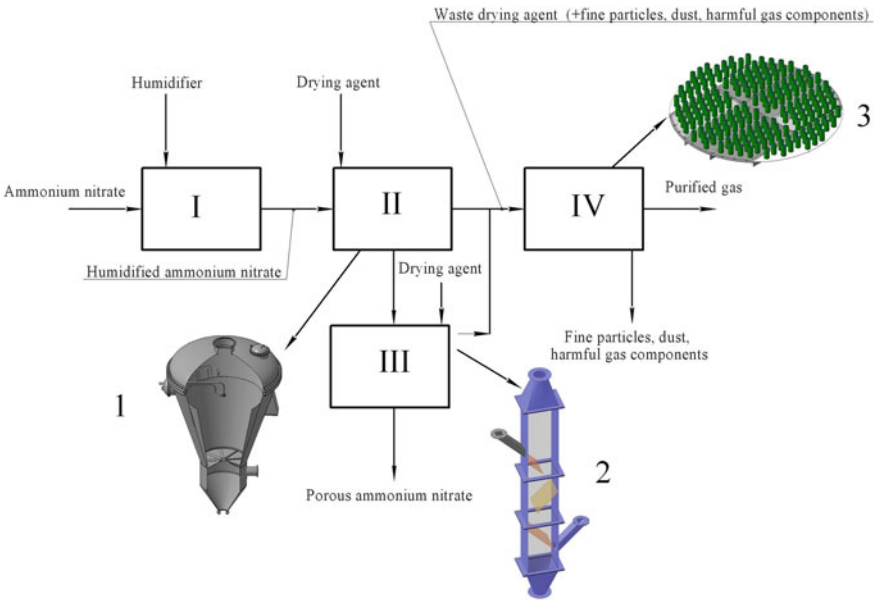

Fig. 1 Diagram of porous ammonium nitrate production according to the method [8, 11–15]: I—humidification of ordinary ammonium nitrate; II—heat treatment and drying of ordinary ammonium nitrate after humidification;—III—final drying PAN; IV—cleaning of exhaust gases; 1—vortex granulator; 2—multistage gravitational shelf dryer; 3—contact tray with heat and mass transfer–separation elements

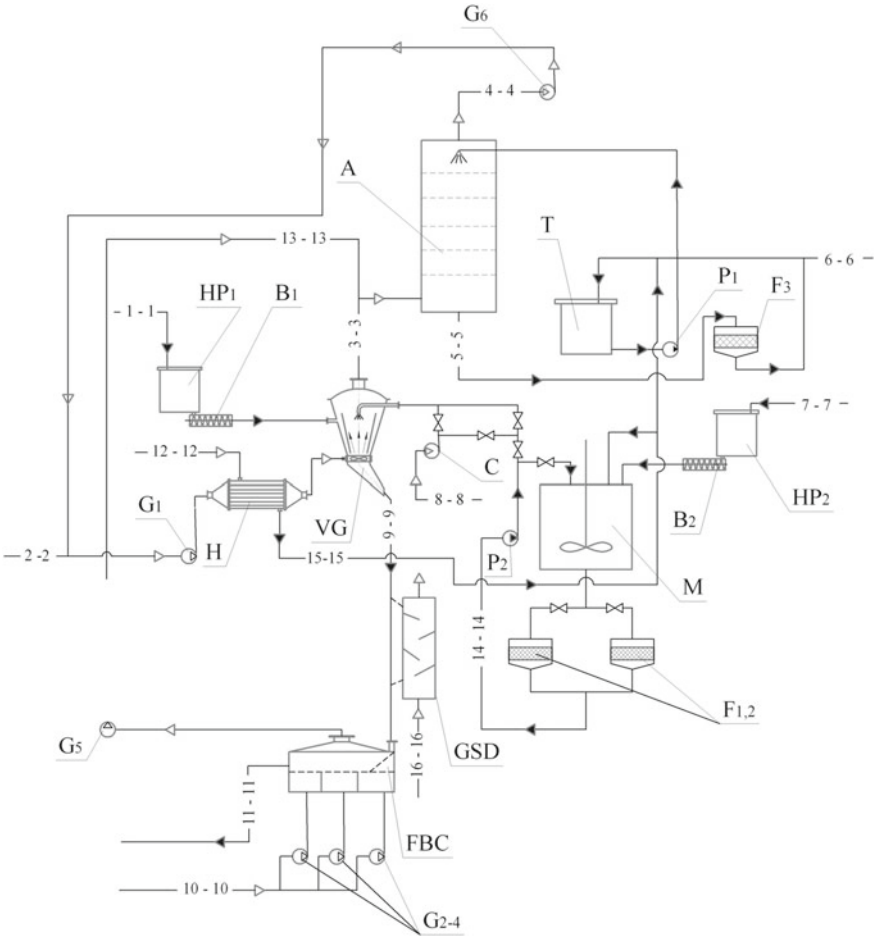

Fig. 2 Technological scheme of the porous ammonium nitrate production. *Elements of the installation: VG—vortex granulator; H—heater; GHD—gravitational shelf dryer; FBC – fluidized bed cooler; A—absorber; F—filter; M—mixer; B—batcher; HP—hopper; G—gas blower; P—pump; T—tank; C—compressor. The main flows*: 1–1—seeding agent; 2–2—manufacturing air; 3–3—polluted air; 4–4—purified air; 5–5—polluted water; 6–6—water; 7–7—substandard granules; 8–8—air for spraying of liquid material (solution, melt); 9–9—product; 10–10—air for cooling of granules; 11–11—granules for packaging; 12–12—steam; 13–13—dusty gas; 14–14—liquid material (solution, melt); 15–15—water condensate; 16–16—drying agent

2 Calculation of Technological Parameters

In order to study the influence made by the hydrodynamic regime of the gravitational shelf dryer's operation on the nanoporous structure of the granule after final drying, the experimental stand was created (Fig. 4).

Other devices and equipment include:

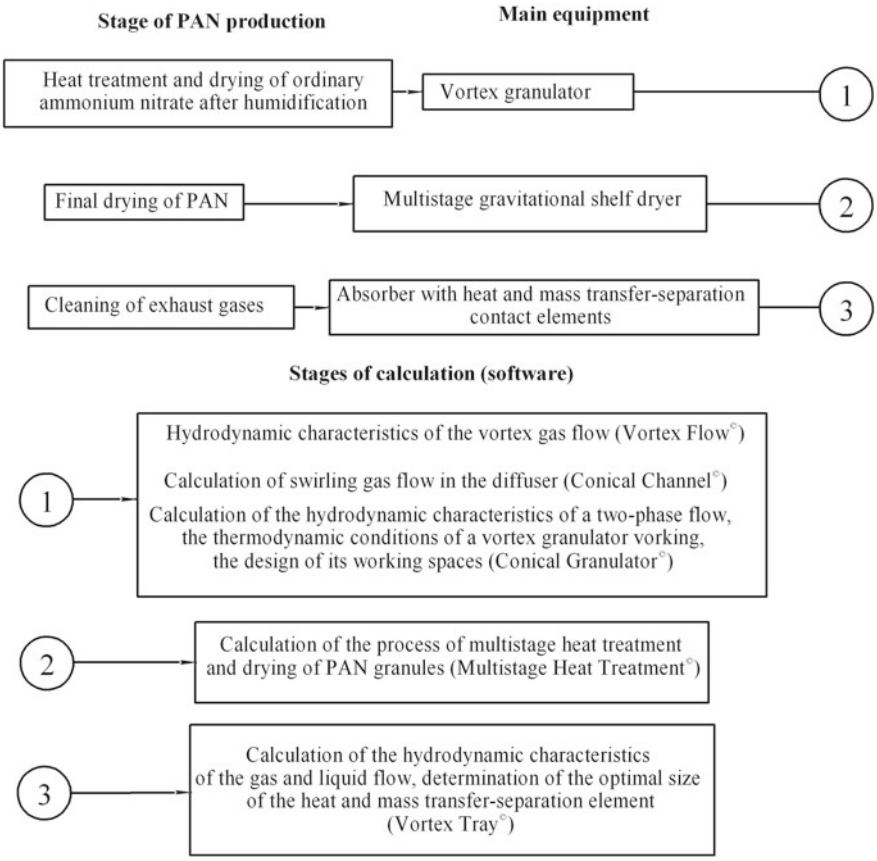

Fig. 3 Algorithm of the main technological calculation of the PAN obtaining granulation unit

- temperature in the calorifier is measured by TC10-C thermocouple; self-recording potentiometer КСП-3;
- temperature in the workspace of granulator is measured by thermal imager Fluke Ti25, pyrometer Victor 305B;
- humidity of granules and air is measured by the multimeter DT-838.

The theoretical calculation of the kinetics for the granule heating process and its mass changing are presented in Figs. 5 and 6.

Heating of the granule surface and removing moisture from it is carried out at a constant drying velocity. In this case, the heating and drying front are mixed in parallel. It enables obtaining a porous structure of the granule at low thermal stresses in the core. As the heating and drying front moves deeper into the granule, the drying velocity decreases. The heat treatment time must be increased to remove the required amount of moisture from the granule. Besides, it is essential to prevent overheating of the granule core. It will lead to the formation of pores in the form of cracks, not

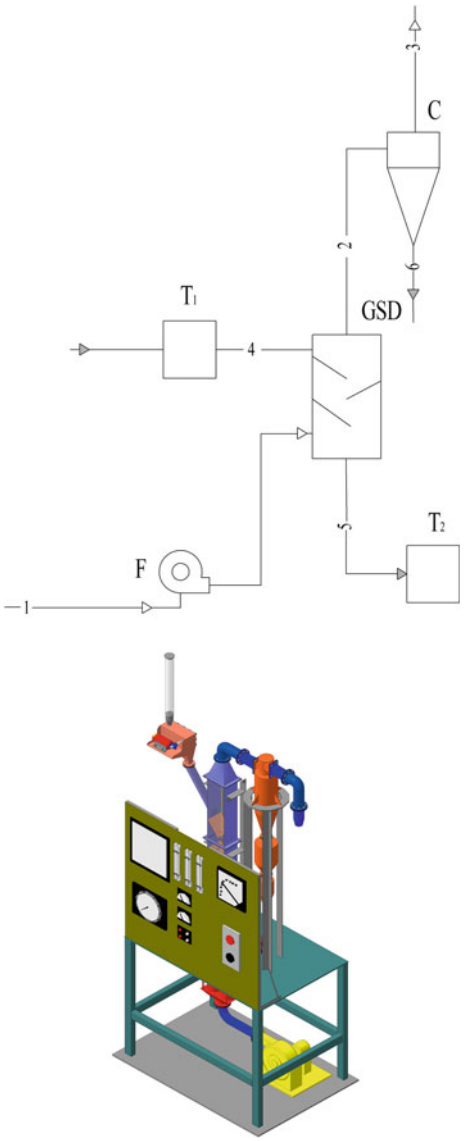

Fig. 4 Schematic diagram of the experimental setup for the study of shelf devices: F—fan; GSD—gravitational shelf unit; C—cyclone; T1, T2—containers (tanks); 1—drying agent; 2—waste drying agent; 3—purified gas; 4—PAN; 5—PAN after final drying; 6—fine particles

due to evaporation but due to the mechanical destruction. In this case, the strength of the granule is significantly reduced.

Multistage Heat Treatment© the mathematical model, underlying the software product, is demonstrated in [8, 11–13].

The Multistage Heat Treatment© program is necessary to calculate heat treatment and dehydration processes (if required) in the multistage drying, granulation and cooling devices of the weighted layer. The calculation results are the value of the

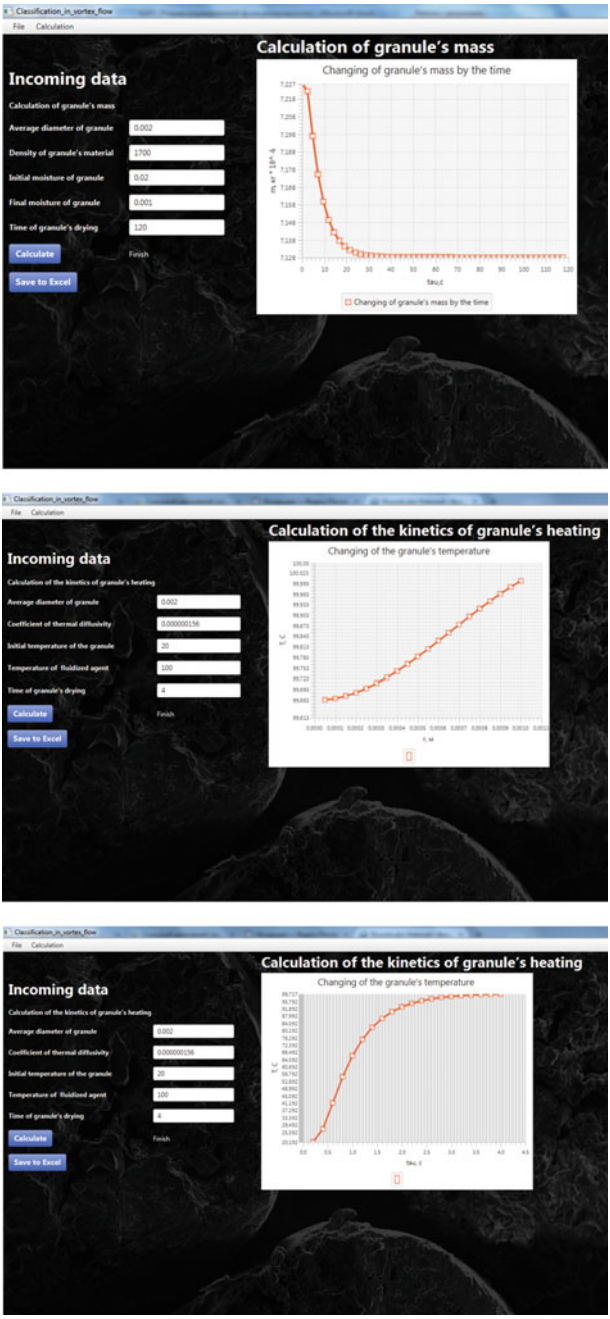

Fig. 5 Program interface for calculating the mass of a granule **a**, windows for calculating the heating kinetics of a granule **b**, **c**

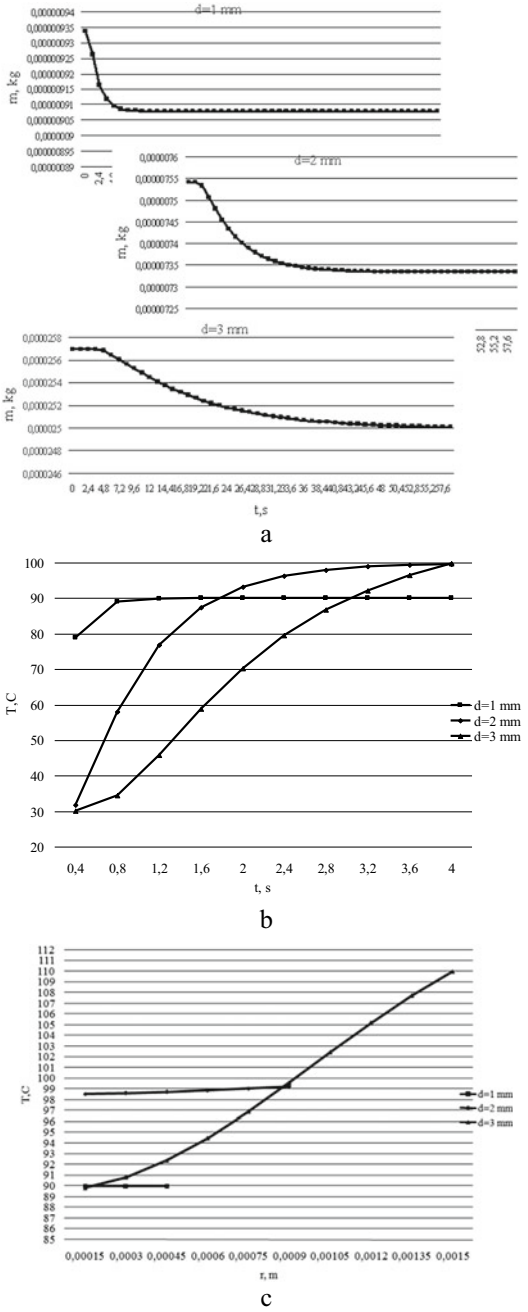

Fig. 6 Results of calculating the mass of the granule **a**, the heating kinetics of the granule **b**, **c**

temperature and humidity of the dispersed material and the gas flow (drying or heat transfer agent) before and after each stage of the multistage device. The heat treatment process is calculated in the gas flow direction (from the lower to upper sections of the device). The heat treatment process is calculated in the direction of the gas flow (from the lower to the upper sections of the device).

When starting work with the program, the equation system of the mathematical model appears on the screen (Fig. 7).

The user enters the initial data in the corresponding cells (Fig. 8).

The working field of the program after entering the initial data will have the form as shown in Fig. 9.

The next step is to carry out the calculation (Fig. 10). The corresponding command makes it possible to calculate the required values.

The calculation results are displayed in a separate window (Fig. 11).

```
k1:=(t1k1-t2k1)/(t1н1-t2н1)=E11;
k2:=(x2k1-x1k1)/(x2н1-x1н1)=E21;
k3:=G2*Cм*(t2k1-t2н1)+Gм*Cв*(x2k1*t2k1-x2н1*t2н1)=G1*Cc*(t1н1-t1k1)+Gc*Cв*
(x1н1*t1н1-x1k1*t1k1);
k4:=Gм*(x2н1-x2k1)=Gc*(x1k1-x1н1);
```

Fig. 7 Mathematical model for calculation

```
t1н1:=___;t2k1:=___;x1н1:=___;x2k1:=___;
G2:=___;G1:=___;Cм:=___;Cв:=___;Cc:=___;E11:=___;E21:=___;
```

Fig. 8 Input of initial data

$$k1 := \frac{t1k1 - t2k1}{t1н1 - t2н1} = E11$$

$$k2 := \frac{x2k1 - x1k1}{x2н1 - x1н1} = E21$$

$$k3 := G2\ Cм\ (t2k1 - t2н1) + Gм\ Cв\ (x2k1\ t2k1 - x2н1\ t2н1) = G1\ Cc\ (t1н1 - t1k1) + Gc\ Cв\ (x1н1\ t1н1 - x1k1\ t1k1)$$

$$k4 := Gм\ (x2н1 - x2k1) = Gc\ (x1k1 - x1н1)$$

$$t1н1 := \_\_\_$$
$$t2k1 := \_\_\_$$
$$x1н1 := \_\_\_$$
$$x2k1 := \_\_\_$$
$$G2 := \_\_\_$$
$$G1 := \_\_\_$$
$$Cм := \_\_\_$$
$$Cв := \_\_\_$$
$$Cc := \_\_\_$$
$$E11 := \_\_\_$$
$$E21 := \_\_\_$$

Fig. 9 Working area of the program

```
rez:=solve({k1,k2,k3,k4},{t1k1,t2н1,x2н1,x1k1});
```

Fig. 10 Calculation

$$rez := \{t1k2 = \quad , t2н2 = \quad , x1k2 = \quad , x2н2 = \quad \}$$

Fig. 11 Calculation results

```
t1н2:=t1k1;t2k2:=t2н1;x1н2:=x1k1;x2k2:=x2н1;
```

Fig. 12 Initial data to calculate the subsequent heat treatment stages

After the calculation of the first stage, the user proceeds to further calculations. The mathematical model equations at the next step are similar to the previous ones. The peculiarity of the calculation at each subsequent stage is to use the calculation results of the flow features in the previous stage, which are the initial data for the calculation (Fig. 12).

3 Properties of Nanoporous Layers in Granules of PAN

Figure 13 shows the electron microscopy results of the surface of PAN granules with various diameters after the final drying stage.

Analysis of these figures shows the following features of the nanoporous structure morphology:

- with an increase in the diameter of the granule, the nanoporous surface becomes more uniform thanks to the regular heating of the granule;
- an increase in the time for heat treatment with a slight decrease in temperature enables to avoid the formation of several “mechanical” pores arising from the thermal stress actions;
- the formation of a developed network of twisted nanopores occurs when the granule is not overheated;
- with an increase in the granule polydispersity degree, the small fraction is characterized by an uneven network of predominantly rectilinear nanopores;
- it is necessary to adjust the ratio between the drying agent’s flows and granules (dispersed material) to reduce the temperature stress effect on the granule. Such an optimization calculation is a task for further research.

The values of the relative porous surface of the PAN granule for different diameters are presented in Fig. 14.

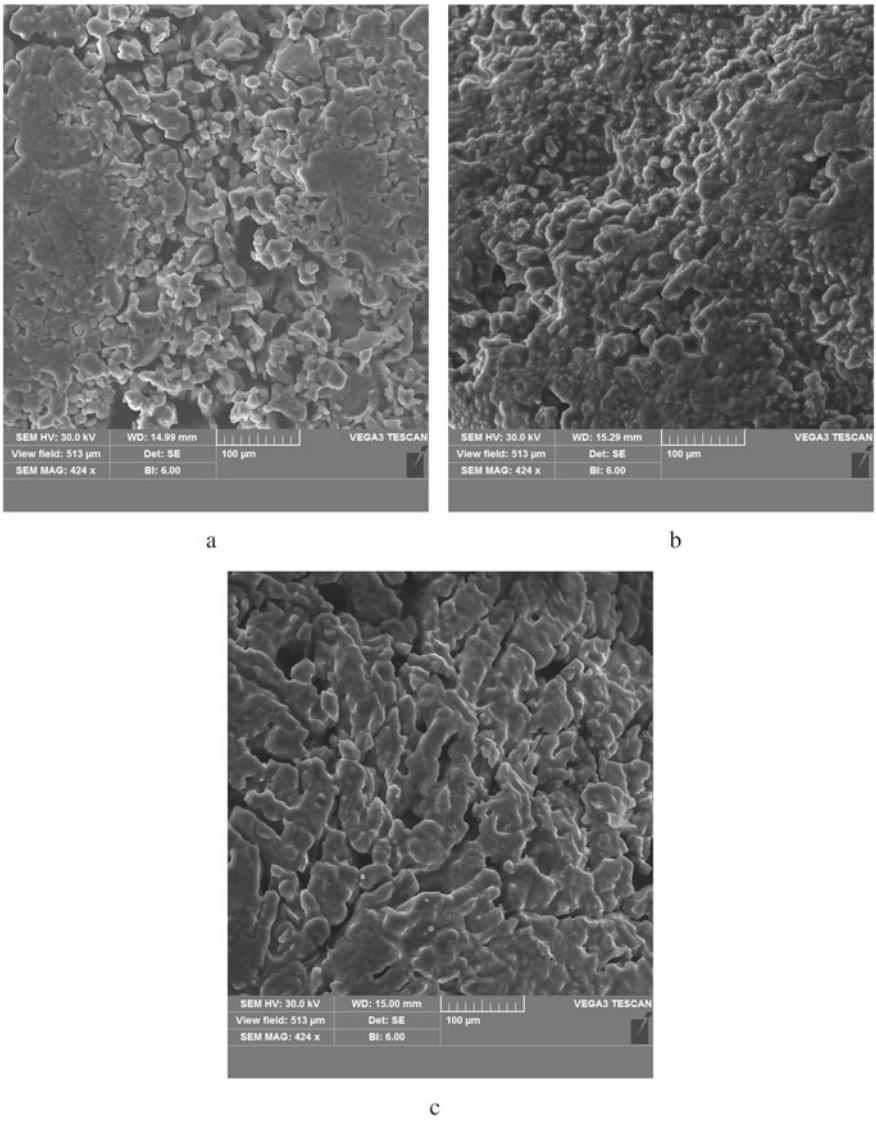

Fig. 13 Electron microscopy results of the surface of PAN granules with various diameters after the final drying stage: **a**–**d** = 1 mm; **b**–**d** = 2 mm; **c**–**d** = 3 mm

4 Conclusions

The obtained results indicate that the final drying stage of PAN granules provides an increase in their quality and shelf life without loss of retentivity toward diesel distillate.

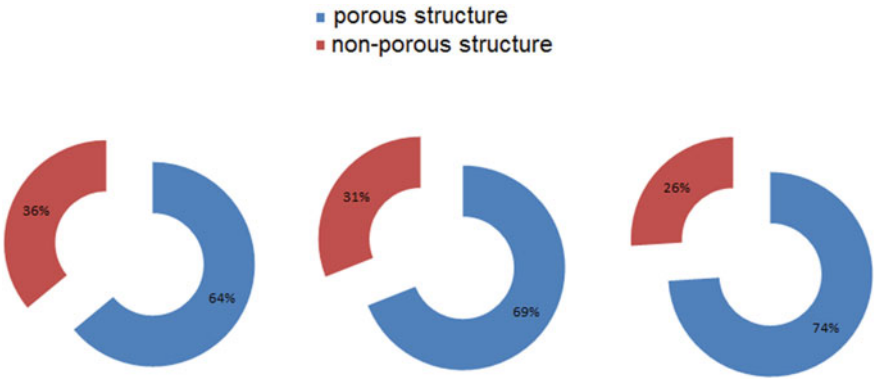

Fig. 14 Values of the relative porous surface of the PAN granule for different diameters: **a**–**d** = 1 mm; **b**–**d** = 2 mm; **c**–**d** = 3 mm

The introduction of this stage increases the total energy capacity of the production; however, the use of multistage shelf dryers enables:

- to section the internal space of the device with the formation of the heat–mass exchange steps;
- to differentiate the distribution of flows between stages;
- to provide gradual regulation for the driving force of heat–mass transfer;
- to achieve optimization of the cost ratio of interacting flows;
- to create an active hydrodynamic mode of flow interaction;
- to reduce the specific energy consumption for the intensification of the process.

Acknowledgements This research work had been supported by the Ministry of Science and Education of Ukraine under the project «Technological bases of multistage convective drying in small-sized devices with utilization and heat recovery units», project No. 0120U100476 and by the Cultural and Educational Grant Agency of the Slovak Republic (KEGA), project No. KEGA 002TnUAD-4/2019.

References

1. Zygmunt B, Buczkowski D (2007) Influence of ammonium nitrate prills' properties on detonation velocity of ANFO. Propellants Explos Pyrotech 32(5):41–414
2. Kubota N (2015) Propellants and explosives: thermochemical aspects of combustion, 3rd edn. Wiley-VCH Verlag & Co, Weinheim
3. Lipinska K (2005) Demilitarized propellants as ingredients in commercial explosives. In: European federation of explosives engineers: Brighton conference proceedings, Brighton, pp 493–498
4. Erode GM (2013) Ammonium nitrate explosives for civil applications: slurries, emulsions and ammonium nitrate fuel oils. Wiley-VCH Verlag & Co, Weinheim

5. Martin G, Barbour W (2003) Industrial nitrogen compounds and explosives. Watchmaker Publishing, Chemical Manufacture and Analysis
6. Janssen TJ (2011) Explosive materials: classification. Nova Science Publishers, Inc., Composition and Properties
7. Artyukhov AE, Artyukhova NO, Ivaniia AV (2018) Creation of software for constructive calculation of devices with active hydrodynamics. In: Proceedings of the 14th international conference on advanced trends in radioelectronics, telecommunications and computer engineering (TCSET 2018), 2018-April, pp 139–142
8. Obodiak V, Artyukhova N, Artyukhov A (2020) Calculation of the residence time of dispersed phase in sectioned devices: theoretical basics and software implementation. Lecture Notes Mech Eng 813–820
9. Artyukhov AE, Obodiak VK, Boiko PG, Rossi PC (2017) Computer modeling of hydrodynamic and heat-mass transfer processes in the vortex type granulation devices. CEUR Workshop Proc 1844:33–47
10. Artyukhov AE, Sklabinskyi VI (2017) Investigation of the temperature field of coolant in the installations for obtaining 3D nanostructured porous surface layer on the granules of ammonium nitrate. J Nano Electron Phys 9(1):01015-1–01015-4
11. Artyukhov AE, Sklabinskyi VI (2013) Experimental and industrial implementation of porous ammonium nitrate producing process in vortex granulators. Naukovyi Visnyk Natsionalnoho Hirnychoho Universytetu 6:42–48
12. Artyukhova N, Krmela J (2019) Nanoporous structure of the ammonium nitrate granules at the final drying: the effect of the dryer operation mode. J Nano Electron Phys 11(4):04006-1–04006-4
13. Artyukhova NA (2018) Multistage finish drying of the N_4HNO_3 porous granules as a factor for nanoporous structure quality improvement. J Nano Electron Phys 10(3):03030-1–03030-5
14. Artyukhov A, Artyukhova N (2018) Utilization of dust and ammonia from exhaust gases: new solutions for dryers with different types of fluidized bed. J Environ Health Sci Eng 16(2):193–204
15. Artyukhova N (2020) Morphological features of the nanoporous structure in the ammonium nitrate granules at the final drying stage in multistage devices. J Nano Electro Phys 12(4):04036-1–04036-6
16. Wan Daud WR (2008) Fluidized bed dryers—recent advances. Adv Powder Technol 19(5):403–418
17. Mujumdar AS (2006) Handbook of industrial drying. Taylor & Francis Group, Boca Raton
18. Sinaiski EG (2010) Hydromechanics: theory and fundamentals. WILEY-VCH Verlag GmbH & Co. KGaA, Weinheim
19. Crowe C (2006) Multiphase flow handbook. Taylor & Francis Group, Boca Raton
20. Kudra T, Mujumdar AS (2002) Advanced drying technologies. Marcel Dekker, New York

Nanoporous Organo-Mineral Fertilizers Obtained by Using of Granule Shell Technology

G. O. Yanovska, V. S. Vakal, A. E. Artyukhov, V. Y. Shkola, T. Y. Yarova, and S. V. Vakal

1 Introduction

Ensuring economic growth and achieving the goals of sustainable development requires the transition to resource-efficient economy, based on ecological balance, responsible production and consumption, the rational use of natural resources [1, 2]. The rational use of land [3] and ensuring the productivity of agriculture simultaneously are achieved by intensifying innovation activity in agriculture, aimed at increasing crop yields [4]. One of the directions of such activities is the use of new generation mineral fertilizers that meet the concept of innovative advancement [5]. According to agrochemical science [6], the share of mineral fertilizers in ensuring yield growth is 20–40%, and the ratio of the main nutrients of nitrogen, phosphorus and potassium for crops should usually be 1: 1: 1 [7]. At the same time, high doses of nitrogen fertilizers required in the initial growing season can have a negative impact on the environment due to significant nitrogen losses: the entry of gaseous nitrogen into the air and in the form of nitrates into the soil and groundwater. Thus, for such a common nitrogen fertilizer as urea, with its surface application only gaseous losses can be more than 50% [8].

In this connection, various ways are being developed to reduce the rate of nitrogen granules dissolution in the soil. The most well-known chemical methods are implemented by creating special slightly soluble fertilizers, introduction of nitrification inhibitors into the granules, as well as the granules encapsulation with the shells of different compositions [9–13].

V. S. Vakal · S. V. Vakal
Scientific Research Institute of Mineral Fertilizers and Pigments, 2 Rymskogo-Korsakova Street, Sumy 40007, Ukraine

G. O. Yanovska (✉) · A. E. Artyukhov · V. Y. Shkola · T. Y. Yarova
Sumy State University, 2 Rymskogo-Korsakova Street, Sumy 40007, Ukraine

O. Fesenko and L. Yatsenko (eds.), *Nanomaterials and Nanocomposites, Nanostructure Surfaces, and Their Applications*, Springer Proceedings in Physics 263, https://doi.org/10.1007/978-3-030-74741-1_14

The important step in microcapsules formation is the fabrication of proper wall materials that meets the criteria of encapsulation efficiency and the durability of microcapsules rely on the wall material structure. This shell should act as a barrier, storing the core material as well as protecting it against the oxygen, water and light, or initiate a controlled diffusion in the specific media [14].

The shell, which is applied to the surface of the granule (core), should have a porous surface, which consists mainly of curved nanopores of different depths. The size of the pores and their structure has a significant effect on the rate of the soil moisture penetration into the shell and after some time into the core of the granule. Due to the presence of nanopores in the shell, as well as in the interface of the granule, the process of dissolving the fertilizer will take place sequentially from the shell to the core. This path is optimal for the fertilizer assimilation. Thus, it will prevent against eco-destructive effects on the environment and loss of nutrients. In the case of increasing the pores size and changing their shape from curved to rectilinear, the groundwater will penetrate into the granule with greater speed and in greater quantities. This will lead to the simultaneous dissolution of both the shell and the core of the granule.

Nitrogen fertilizers with sulphur coating corresponding to the ecomarketing concept [15] have already been brought to the industrial production. Some of the promising components for encapsulation, in which there are no inert elements, are shells based on ammonium and calcium phosphates. Such shells allow the formation of complex NP and NPK fertilizers, in which the phosphate or phosphate-potassium coating acts as a membrane through which the nitrogen core of the granule diffuses. Our work showed that the dissolution rate of the nitrogen component of the fertilizer granule depends on the density of the formation of the phosphate-containing shell particles. It is possible to create shells with different permeability by varying the conditions of the application process.

The most important functions and benefits of the active compounds encapsulation are the following:

1. Increasing the stability of encapsulated materials by protecting them from environmental factors such as heat, high and low pH values, oxygen and light;
2. Controlled release of active components in the aqueous media;
3. Conversion of liquid formulations to solid, resulting in the convenience of handling and transportation [16].

When choosing the method of obtaining the organic-mineral fertilizers, preference should be given to the most effective for specific encapsulation conditions. For the production of mineral fertilizers (except for the technology of production in granulation towers), the most common methods are using devices with a fluidized bed and rolling machines [17–21]. Obtaining the multicomponent organic-mineral fertilizers with a shell of nutrients can be successfully carried out in plate granulators [22]. The coating technology on the surface of the granule in such devices allows you to use the nutrients that are difficult to disperse as a binder (plasticizer). In this case, the use of devices with active hydrodynamic modes (successful introduction of such devices in the technology of obtaining granules with a nanoporous structure

is described in [23–28]) is impractical. In combination with the main advantages of plate granulators [29], the technology described in this article can be considered a fairly simple and effective way in comparison with analogues [30, 31].

The performed investigations on studying the microstructure of the phosphate-containing coating revealed the features of the porous structure of the shell itself and the layer between the shell and the inner part of the encapsulated granule. The obtained microphotographs make it possible to study the pore size of the phosphate-containing shell and to determine the effect of the composition of the plasticizer on its porosity.

2 Materials and Methods

The development of the encapsulated fertilizers experimental samples was carried out on a model installation based on a plate granulator.

Figure 1 demonstrates the experimental stand scheme for organic-mineral fertilizers production process. The general view of pan granulator experimental sample is presented on Fig. 2.

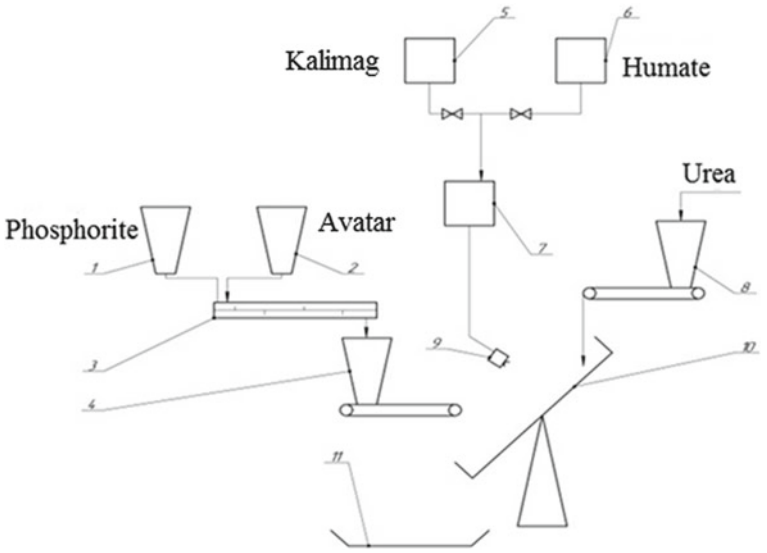

Fig. 1 Experimental stand scheme for organic-mineral fertilizers production process: 1—phosphate bunker; 2—bunker of microelements; 3—mixer; 4—dispenser; 5—potassium-magnesium solution tank; 6—humate solution tank; 7—potassium-magnesium mixing tank with humate; 8—urea granules feed unit; 9—nozzle; 10—pan granulator; 11—tray for granulated product

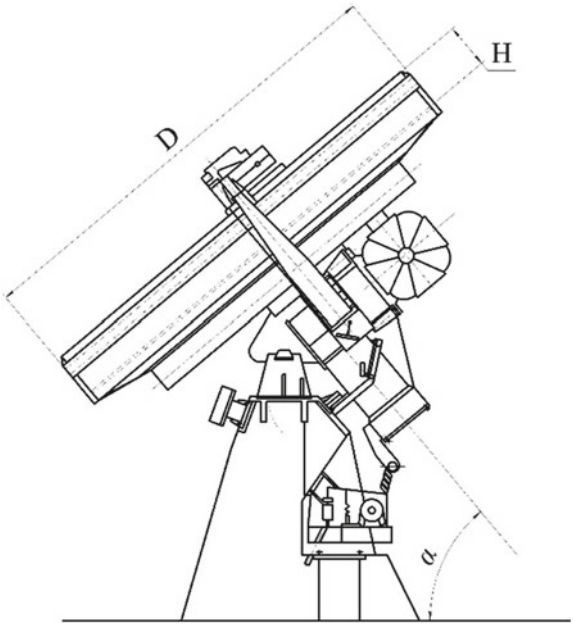

Fig. 2 Pan granulator: D—the diameter of the disc; H—the height of the disc; α—the tilt angle of the disc

The encapsulation process was carried out by applying a phosphate-containing coating to the urea granules. The composition of the plasticizer and its effect on the properties of the fertilizer shell were varied and studied.

The phosphate-glauconite concentrate from the Novo-Amvrosiivskyi deposit was used as a phosphate-containing component of the shell. The indicators of the concentrate are shown in Table 1.

The dispersed composition of phosphate-glauconite concentrate of the Novo-Amvrosiivskyi deposit is shown in Table 2.

Ballast calcium and potassium humates and an aqueous solution of potassium and magnesium (Kalimag) were used as a plasticizer. The choice of the first two types of plasticizer is justified by the need to introduce into the composition of the granule an organic component, which in addition to astringent properties has a positive effect on the humus content in the soil. Kalimag (46% K_2O) was used to enrich the encapsulated fertilizer with nutrient potassium and magnesium. Ballast

Table 1 Chemical composition of phosphate-glauconite concentrate

Indicator name and measurement unit	The result of the analysis
Mass fraction of total phosphates in terms of $P_2O_{5\ gen}$ (%)	15.0
Mass fraction of digestible phosphates in terms of $P_2O_{5\ dig}$ (%)	13.1
Mass fraction of water (%)	1.27

Table 2 Dispersed composition of phosphate-glauconite concentrate

Fraction of particle size (mm)	Mass fraction (%)
>0.4	0.85
>0.315	1.27
>0.28	2.54
>0.2	0.56
>0.1	37.88
>0.063	21.83
<0.063	35.07

Table 3 Chemical composition of calcium and potassium humates

Indicator name and measurement unit	The result of the analysis	
	Calcium humate	Potassium humate
pH (10% water solution)	9.0	11.65
Mass fraction of water (%)	89.5	83.4
Mass fraction of humates (in terms of dry matter) (%)	16.9	30.8
Mass fraction of total calcium (in terms of dry matter) (%)	6.0	–
Mass fraction of water-soluble calcium (in terms of dry matter) (%)	0.3	–
Mass fraction of magnesium (in dry matter) (%)	0.8	5.26
Mass fraction of total potassium K_2O (in dry matter) (%)	0.05	0.61

humates of calcium and potassium were obtained from lowland peat of the Glukhiv deposit in the Sumy region on a model homogenizer. The chemical composition of calcium and potassium humates is shown in Table 3.

Fertilizers samples were obtained as follows. Powdered phosphate-glauconite concentrate was fed to a plate granulator on urea granules with a size of 2–3 mm moistened by plastisizer. The encapsulation process took place by the mechanism of agglomeration for 5 min. Then the resulting product was sent for drying for 2 h at a temperature of 65 °C. In order to improve the nitrogen-phosphorus nutrition of plants, increase their stress resistance and productivity, an "Avatar" multicomponent microelement complex in the chelated form was added to the shell composition of the fourth test sample.

The chemical composition of the obtained encapsulated urea samples is presented in Table 4.

Table 4 Composition of the samples of fertilizers based on urea in the phosphate shell

Sample name	Composition			Plasticizer	Strength of granules (MPa)
	P_2O_5 (%)	N (%)	K_2O (%)		
Sample 1	7.20	23.8	0.31	Calcium humate	2.10
Sample 2	7.13	23.6	0.21	Potassium humate	2.07
Sample 3	7.84	21.8	0.42	Kalimag	2.09
Sample 4 with the addition of an "Avatar" trace-element complex	7.40	22.8	0.21	Calcium humate	1.71

3 Results and Discussion

The use of the phosphate-glauconite concentrate of the Novo-Amvrosiivskyi deposit involves the development of a coating containing the phosphate and potassium components. Plasticizers in the form of potassium and calcium humates—create an organic-mineral composition, which involves increasing the granules nutrients utilization. Potassium humate increases the potassium content in fertilizers, and calcium humate was used as a plasticizer due to its low solubility and positive effect on the formation of agronomically valuable, water-resistant soil structure.

The introduction of calcium into the fertilizer neutralizes the soil acidity and reduces the mineral components loss of the soil. The inclusion of trace elements in the chelate form allows to increase the agrochemical value of the fertilizer by improving the resistance of plants to diseases and adverse environmental factors. The introduction of the zeolites into the phosphate-containing shell involves the reduction of gaseous and infiltrative nitrogen losses and increases the productive moisture in the soil [7].

Carrying out of researches on an efficiency estimation of a phosphorus-containing coating on prolongation of dissolution of a nitrogen granule core demands studying of qualitative and quantitative characteristics of a coating and the interface between an external and internal layer by a scanning electron microscopy with elemental micro-analysis. Figure 3 presents a general view of the granules for four samples: a—general view of the granules at 100 times magnification, b—the surface of the granules at 1000 times magnification; c—general view of the cross-section of the granule at 100 times magnification; d is the slice of the granule at 1000 times magnification.

The study of the surface morphology showed that sample 1 has uniform surface, but uneven in shell thickness. The damage of the shell is probably formed during drying. The surface has coarse inclusions. The porous structure of the surface and the entire shell (cross-section) is developed, and the pores are mostly curved. The shell is not attached to the granule core due to the probable occurrence of temperature stresses during drying (Figs. 4 and 5; Table 5).

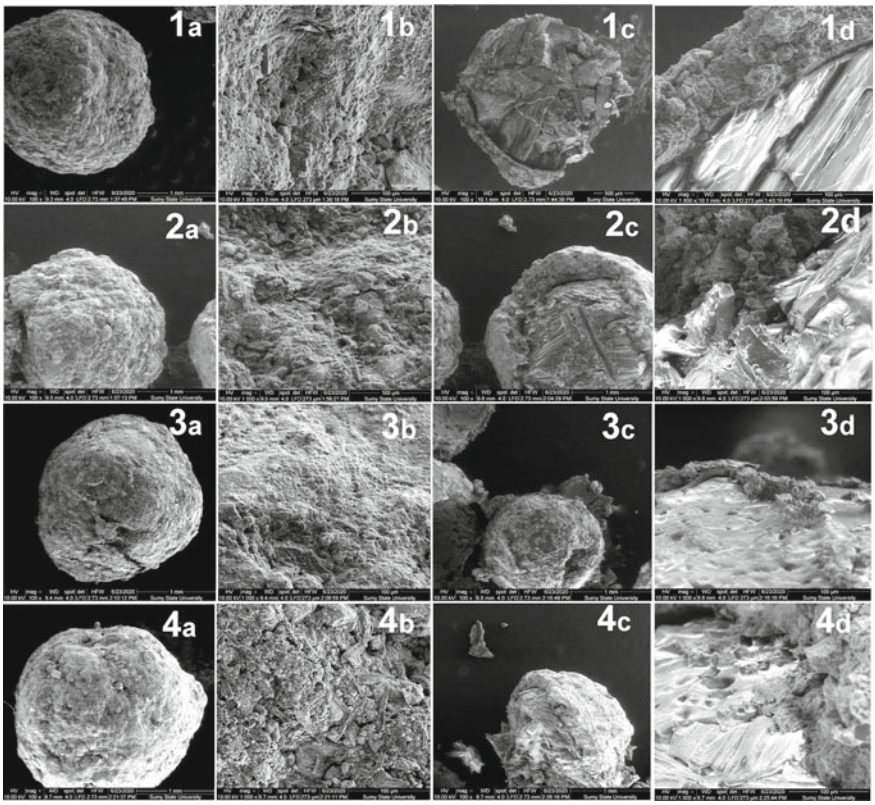

Fig. 3 General view of granules for samples 1–4: **a** general view of granule at a magnification ×100, **b** granule surface at a magnification ×1000; **c** general view of granule cross-section at a magnification ×100; **d** granule cross-section at a magnification ×1000

The elemental analysis shows increasing amount of C, N elements towards the granule core. The granule surface contains following elements: O, Al, Si, P, K, Ca, Fe, Mg, S, Cl, Na which amount is decreased from the surface to the core. Those elements as P, K, Fe, Mg, S, Cl, Na are absent in the core.

Sample 2 has a uniform surface, but has a non-uniform thickness of the shell. Compared with sample 1, the thickness of the shell is more uniform. There is damage of the shell, which probably formed during drying. The surface has fine inclusions. The porous structure of the surface and the whole shell (in section) is underdeveloped: there are mostly curved pores and pores that are formed mechanically (cracks, faults, cavities). The shell is not attached to the granule core due to the probable occurrence of temperature stresses during drying (Table 6).

The elemental analysis shows increasing amount of C, N elements towards the granule core. The granule surface contains following elements O, Al, Si, P, K, Ca, Fe, Mg, S, Na. The amount O, Si, P, Mg, Na is increased in the interface between granule and core compared with amount of elements in the shell. The amount Al, K,

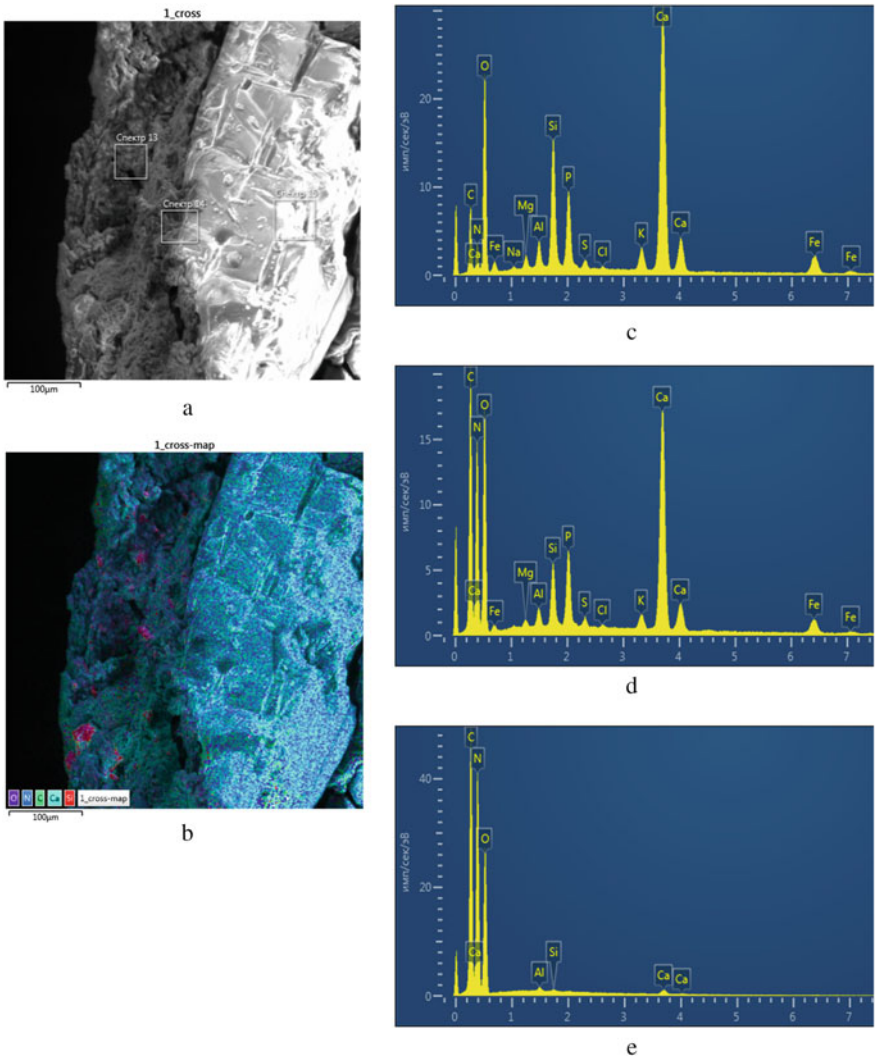

Fig. 4 Elemental composition analysis of the of the granule sample 1: **a** granule cross-section with areas where the elemental composition analysis was provided, **b** elements distribution on the sample cross-section surface, **c** the spectrum 13; **d** the spectrum 14; **e** the spectrum 15

Ca, Fe, S decreased in the direction from the surface to the core. Such elements as Al, P, K, Fe, Mg, S, Na are absent in the internal layer.

Sample 3 has a non-uniform surface and thickness of the shell, and there are areas without shell. Compared with samples 1 and 2, the thickness of the shell is more uniform. The surface has fine inclusions. The porous structure of the surface and the entire shell (in section) is developed and uniform in the form of closely spaced round

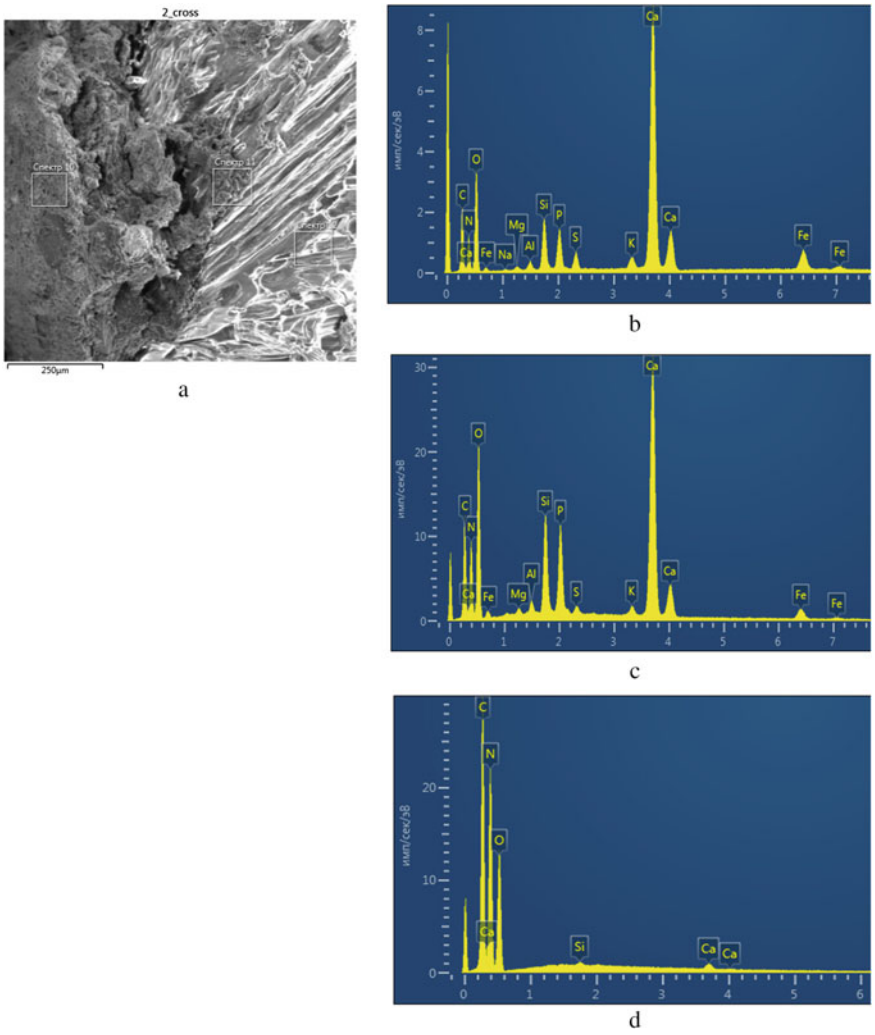

Fig. 5 Elemental composition analysis of the of the granule sample 2: **a** granule cross-section with areas where the elemental composition analysis was provided, **b** elements distribution on the sample cross-section surface (spectrum 10); **c** spectrum 11; **d** spectrum 12

cavities. The shell is not attached to the granule core due to the probable occurrence of temperature stresses during drying (Figs. 6 and 7; Table 7).

The elemental composition analysis shows the decrease of C, O, Al, Si, P, K, Ca, Fe, Mg, S, Na amount in the direction to granule core and increase of N amount.

Table 5 Elemental composition of fertilizer granule layers (Sample 1)

Sample 1	Sample 13	Sample 14	Sample 15
Element	Weight (%)	Weight (%)	Weight (%)
C	14.84	20.30	21.59
N	13.20	36.36	46.20
O	40.37	30.32	31.83
Al	0.95	0.35	0.11
Si	4.41	1.10	0.04
P	3.12	1.58	–
K	1.22	0.44	–
Ca	17.26	7.69	0.22
Fe	3.44	1.41	–
Mg	0.55	0.16	–
S	0.38	0.20	–
Cl	0.10	0.07	–
Na	0.16	0.00	–

Table 6 Elemental composition of fertilizer granule layers (Sample 2)

Sample 2	Spectrum 10	Spectrum 11	Spectrum 12
Element	Weight (%)	Weight (%)	Weight (%)
C	14.62	15.63	23.03
N	21.77	26.37	47.30
O	31.70	35.26	29.28
Al	0.37	0.35	–
Si	2.13	2.81	0.08
P	1.94	2.93	–
K	0.77	0.39	–
Ca	21.14	14.08	0.02
Fe	4.44	1.67	–
Mg	0.17	0.23	–
S	0.84	0.27	–
Na	0.11	0.00	–
Total amount	100.00	100.00	100.00

Sample 4 is uniform on the surface, but has a non-uniform thickness of the shell. This sample has no damage of the shell during drying. The surface has coarse inclusions. The porous structure of the surface and the entire shell (cros-section) is developed; the pores are mostly curved. The shell is not tightly bonded with the granule core due to the probable occurrence of temperature stresses during drying (Table 8).

On all samples, the granule surface has various damage, which occurred during the removal of moisture in the oven. These damages together with the formed porous

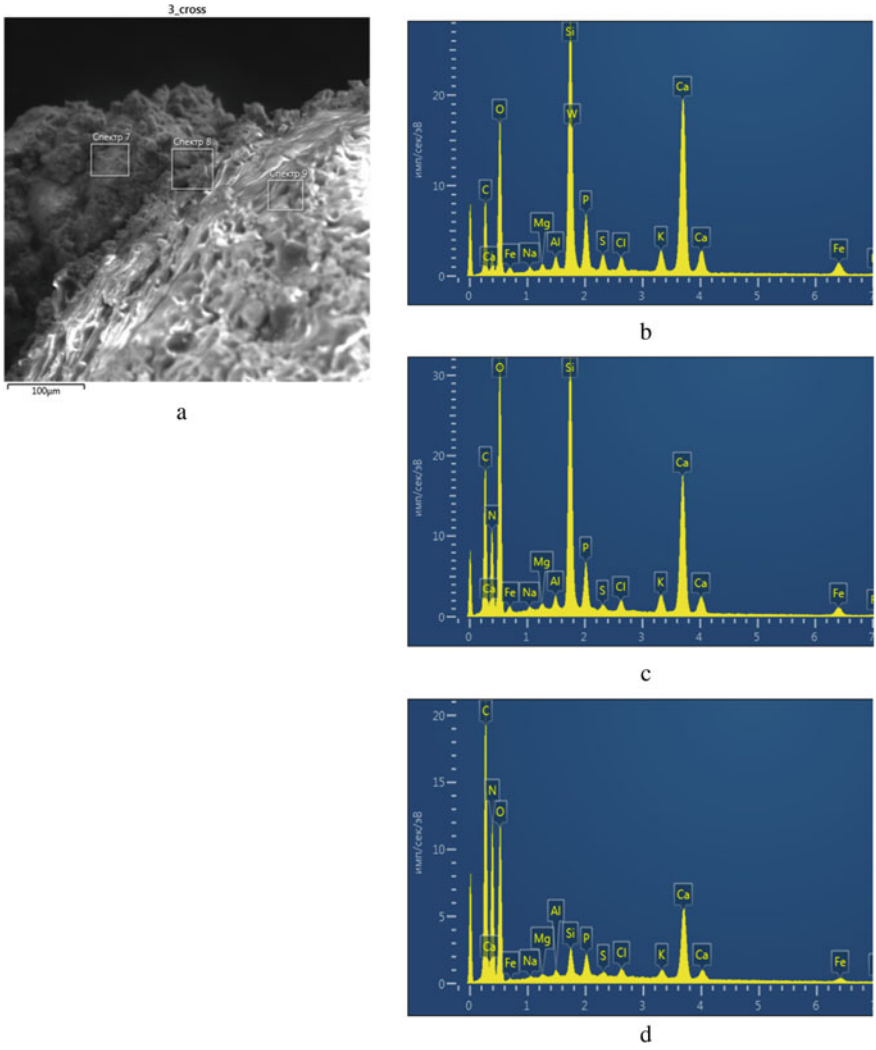

Fig. 6 Elemental composition analysis of the granule sample 3: **a** granule cross-section with areas where the elemental composition analysis was provided, **b** spectrum 7; **c** spectrum 8, **d** spectrum 9

structure allow moisture to penetrate into the shell and dissolve it in the soil. However, major damage can cause the shell to peel off the granule core during transport, as well as premature shell dissolution in the soil due to the large amount of moisture that enters the shell. Additional shell destruction can be caused by a loose fit of the shell to the granule core, which, according to the presented photos, is caused by the larger particle size of the phosphate-glauconite concentrate.

The uniformity of the granules shell thickness is not a determining factor that affects the quality of fertilizer. The required amount of concentrate (according to the

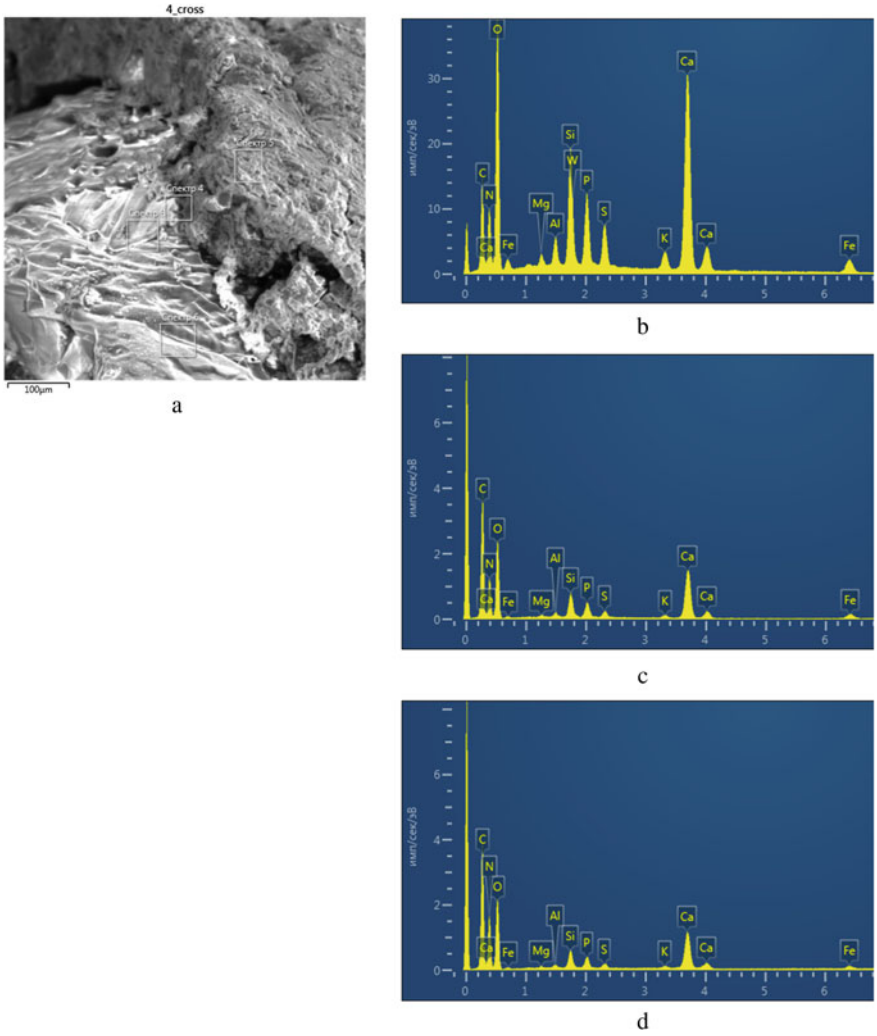

Fig. 7 Elemental composition analysis of the granule sample 4: **a** granule cross-section with areas where the elemental composition analysis was provided, **b** spectrum 3; **c** spectrum 4, **d** spectrum 5

technological calculation) is applied to each granule. The main quality indicators are:

- strength of the granule with a shell;
- the tight contact of the shell to the granule and the adhesion of the shell to the granule surface;
- developed porous structure with a minimum amount of surface mechanical damage caused by thermal stresses during drying.

Table 7 Elemental composition of fertilizer granule layers (Sample 3)

Sample 3	Spectrum 7	Spectrum 8	Spectrum 9
Element	Weight (%)	Weight (%)	Weight (%)
C	26.54	22.17	25.78/22.78
N	–	22.83	38.26/44.26
O	37.94	38.11	29.76
Al	0.59	0.32	0.16
Si	10.52	6.10	0.66
P	2.89	1.37	0.62
K	1.53	0.75	0.33
Ca	14.86	6.45	3.42/0.42
Fe	2.72	1.07	0.48
Mg	0.33	0.15	0.09
S	0.91	0.17	0.12
Na	0.34	0.14	0.08
Cl	0.83	0.36	0.26
Total amount	100.00	100.00	100.00

Table 8 Elemental composition of fertilizer granule layers (Sample 4)

Sample 4	Spectrum 5	Spectrum 4	Spectrum 7
Element	Weight (%)	Weight (%)	Weight (%)
C	15.97	29.61	27.93/22.93
N	19.76	28.32	45.42
O	42.06	31.89	30.91/28.91
Al	0.88	0.25	0.16
Si	3.32	1.32	0.99
P	2.40	0.98	0.75
S	1.45	0.30	0.30
K	0.83	0.27	0.20
Ca	10.75	5.52	4.14/0.14
Fe	2.08	1.40	0.09
Mg	0.41	0.13	0.11
W	0.10	–	–
Total amount	100.00	100.00	100.00

The main mechanisms involved in the core release are diffusion, degradation, use of solvent, pH, temperature and pressure. In practice, a combination of more than one mechanism is used. Diffusion occurs especially when the microcapsule coating is intact; the release rate is governed by the chemical properties of the core and the coating material and some physical coating properties.

The choice of the most suitable method depends on the core type, the application for the microcapsule, the size of the particles required, the physical and chemical properties of the core and the coating, the release mechanism required, the production scale and the cost [32].

Comparison of spectra 13, 10, 7 and 3 shows a slight changes in the elemental composition of the phosphate-containing shell during encapsulation. Comparison of spectra 14, 11, 8 and 4 shows a significant changes in the elemental composition at the interface of the granule core and phosphate-containing shell depending on the plasticizer, which can affect the carbamide dissolution rate. Comparison of spectra 15, 12, 9 and 5 shows that the change in the composition of the plasticizer has a significant impact on the physicochemical processes at the interface between the coating and the granule core. Addition of 0.3% of the "Avatar" microelement complex in chelated form allows to increase the permeability of the coating components and plasticizer into the granule core, which provides high-quality contact.

The dense packing of phosphate-glauconite concentrate particles, which is presented at the spectrum 3, allows us to conclude about the diffusion uniformity of the nitrogen solution of the granule core through the pores, which have an initial size of about 10 microns. Diffusion of the moisture through the phosphate-containing shell to the granule core allows to dissolve first the organic component of the shell to create a porous layer.

4 Conclusions

1. The obtained results have shown the possibility of phosphate-containing shell deposition on carbamide granules by agglomeration to obtain an encapsulated fertilizer with a sufficient characteristics for their application;
2. The most effective and technological is calcium humate plasticizer, which is modified with a trace elemental complex in chelated form;
3. The initial pore size of the phosphate-containing shell at the core–shell interface is 10 μm.
4. Phosphate-containing shell has a developed nanoporous structure with different pores depth and shape.
5. The phosphate-containing shell has nanoporous structure through all core thickness up to the granule interface.
6. On the surface and inside the shell, there is a small amount of "mechanical" pores caused by damage of the granules due to the release of moisture during drying.
7. The encapsulation technology needs to be further improved in studying of the control mechanisms of the nanoporous layer formation process.

References

1. Prokopenko OV, Shkola VY, Domashenko MD, Prokopenko MO (2015) Conceptual grounds to form motivational constituent of the international ecological policy. Market Manage Innov 4: 245–259. Available at: http://mmi.fem.sumdu.edu.ua/en/journals/2015/4/245-259
2. Brauweiler HC, Shkola V, Markova O (2017) Economic and legal mechanisms of waste management in Ukraine. Market Manage Innov 2:359–368. Available at: http://mmi.fem.sumdu.edu.ua/en/journals/2017/2/359-368https://doi.org/10.21272/mmi.2017.2-33
3. Yuriyivna SV, Dmytrivna DM, Volodymyrovych KA, Sergiivna NK (2016) Fundamentals of the Ukrainian land fund management. Market Manage Innov 2:235–345. Available at: http://mmi.fem.sumdu.edu.ua/sites/default/files/mmi2016_2_235_245.pdf
4. Prokopenko OV, Shkola VY, Omelyanenko VA (2013) Analysis of the use of international leasing in terms of improving the effectiveness of technology transfer by the example of agroindustrial complex. Market Manage Innov 3:185–199. Available at: http://mmi.fem.sumdu.edu.ua/en/journals/2013/3/185-199
5. Shkola V, Olshanska O, Kasyanenko T, Domashenko M (2021) Management of enterprise's advanced development for its international competitiveness. Distributed Sensing and Intelligent SystemsDistributed Sensing and Intelligent Systems. Proceedings of ICDSIS 2020. Springer International Publishing, Berlin. https://doi.org/10.1007/978-3-030-64258-7
6. Kisel VI (2000) Biologicheskoye zemledeliye v Ukraine: problemy i perspektivy [in Russian]. Shtrikh, Kharkov, 162 p
7. Mikhaylova LA (2015) Agrokhimiya. Nauchnyye osnovy primeneniya udobreniy pod osnovnyye polevyye kultury [in Russian] : course of lectures. PermIPTs "Prokrost", 2, 19
8. Baliuk SA et al (2012) Ekolohichnyi stan gruntiv Ukrainy. Ukrainskyi heohrafichnyi zhurnal [in Ukrainian] 2:38–42
9. Nagursky O, Gumnitsky Y (2012) Theoretical model of compounds release from capsulated particles and its experimental check. Chem Chem Technol 6(1):101–103. Available at: http://science2016.lp.edu.ua/sites/default/files/Full_text_of_%20papers/full_text_442.pdf. Accessed 15 Jan 2019
10. Du C, Zhou J, Shaviv A, Wang H (2004) Mathematical model for potassium release from polymer-coated fertiliser. Biosys Eng 88(3):395–400
11. Vacal VS, Pavlenko IV, Hurets LL, Vacal SV, Ochowiak M (2020) Mathematical modeling of nutrient release from capsulated fertilizers. Periodica Polytech Chem Eng 64(4):562–568
12. Gurets LL, Tsapko YuL, Malovany MS, Vakal VS (2019) Eksperymentalni doslidzhennia kinetyky rozchynennia kapsulovanykh azotnykh dobryv [in Ukrainian]. Sci Bul UNFU 29(2):94–98
13. Yuan G (2014) An organoclay formula for the slow release of soluble compounds. Appl Clay Sci 100:84–87. https://doi.org/10.1016/j.clay.2014.04.005
14. Jafari SM (2017) An overview of nanoencapsulation techniques and their classification. Nanoencapsulation Technologies for the Food and Nutraceutical Industries, 1–34
15. Prokopenko OV, Shkola VY (2012) Controlling of the ecological and economic enterprise security on the bases of ecomarketing. Market Manage Innov 4:337–346
16. Ghanbarzadeh B, Keivani F, Mohammadi. Encapsulation of food ingredients by solid lipid nanoparticles (SLNs M). Lipid-Based Nanostruct Food Encapsul Purposes 2:179–216
17. Stahl H (2010) Comparing granulation methods. GEA Pharma Systems, Hürth, 10 p
18. Litster J, Ennis B (2004) The science and engineering of granulation processes. Springer-Science+Business Media, Berlin, 250 p
19. Srinivasan S (2015) Granulation techniques and technologies: recent progresses. Bioimpacts 5(1):55–63
20. Solanki HK, Basuri T, Thakkar JH, Patel CA (2010) Recent advances in granulation technology. Int J Pharm Sci Rev Res 5(3):48–54
21. Saikh MA (2013) A technical note on granulation technology: a way to optimise granules. Int J Pharm Sci Rev Res 4:55–67

22. Reynolds GK , Le PK, Nilpawar AM (2007) High shear granulation
23. Artyukhov A, Artyukhova N (2018) Utilization of dust and ammonia from exhaust gases: new solutions for dryers with different types of fluidized bed. J Environ Health Sci Eng 16:193–204
24. Obodiak V, Artyukhova N, Artyukhov A (2020) Calculation of the residence time of dispersed phase in sectioned devices: Theoretical basics and software implementation. Lecture Notes in Mechanical Engineering, 813–820
25. Artyukhova NO (2020) Morphological features of the nanoporous structure in the ammonium nitrate granules at the final drying stage in multistage devices. J Nano- Electron Phys 12(4):04036-1–04036-6
26. Artyukhova NO, Krmela J (2019) Nanoporous structure of the ammonium nitrate granules at the final drying: the effect of the dryer operation mode. J Nano- Electron Phys 11(4):04006-1–04006-4. https://doi.org/10.21272/jnep.11(4).04006
27. Artyukhov AE, Artyukhova NO (2019) Technology and the main technological equipment of the process to obtain NH_4NO_3 with Nanoporous Structure. Springer Proc Phys 221:585–594
28. Artyukhov A, Artyukhova N, Ivaniia A (2018) Creation of software for constructive calculation of devices with active hydrodynamics. In: 14th International conference on advanced trends in radioelectronics, telecommunications and computer engineering, TCSET 2018 - Proceedings, pp 139–142
29. Hoeung P, Bindar Y, Senda SP (2011) Development of granular urea-zeolite slow release fertilizer using inclined pan granulator. Jurnal Teknik Kimia Indonesia 10(2):102–111
30. Patel P, Telange D, Sharma N (2011) Comparison of different granulation techniques for lactose monohydrate. Int J Pharm Sci Drug Res 3:222–225
31. Shanmugam S (2015) Granulation techniques and technologies: recent progresses. Bioimpacts 5(1):55–63
32. Da Silva PT, Martins Fries LL, de Menezes CR, Holkem AT, Schwan CL, Wigmann EF, de Oliveira Bastos J, de Bona da Silva C (2014) Microencapsulation: concepts, mechanisms, methods and some applications in food technology. Cienc Rural 44(7)

Influence of Changes in the Phase State of the Surface and External Factors of Laser Irradiation on the Nanocraters Formation

L. V. Shmeleva, A. D. Suprun, S. M. Yezhov, and V. V. Datsyuk

1 Introduction

Due to their unique properties, femtosecond lasers can be used in various fields of science, technology, and medicine. Femtosecond laser technology has attracted significant attention from the viewpoints of fundamental and application; especially, femtosecond laser processing materials present the unique mechanism of laser-material interaction. Under the extreme nonequilibrium conditions imposed by femtosecond laser irradiation, many fundamental questions concerning the physical origin of the material removal process remain unanswered [1–6]. Under the influence of powerful laser irradiation, a micro-explosion occurs on the solid surface with the formation of a nanocrater and luminous plasma [7–14]. From the start of the laser action process, the surface actively heated in the local area of the irradiated substance. When the light pressure on the surface and its temperature take critical values, a local phase transition occurs. Phase changes cause the substance ablation and are accompanied by a glow. The substance removed from the surface is plasma with a complex structure. Later on, the flying out from the surface solid and liquid particles (aerosol) affects the degree of laser exposure. To assess the consequences of such an influence, an analytical study of this process was carried out in the work. It was assumed that the aerosol formed near the surface has a complex drops-cluster structure.

On the basis of the inhomogeneous system of continuum mechanics, the boundary conditions were obtained [15], due to which a system of differential equations was formulated [16], which allowed to formulate a following system of two interconnected differential equations [17], namely:

L. V. Shmeleva (✉) · A. D. Suprun · S. M. Yezhov · V. V. Datsyuk
Taras Shevchenko National University of Kyiv, Kyiv, Ukraine
e-mail: lshmel@univ.kiev.ua

O. Fesenko and L. Yatsenko (eds.), *Nanomaterials and Nanocomposites, Nanostructure Surfaces, and Their Applications*, Springer Proceedings in Physics 263, https://doi.org/10.1007/978-3-030-74741-1_15

the equation of the dynamics of near-surface pressure:

$$\frac{\partial \Pi}{\partial \theta} = \left(-1 + \Lambda e_q \vartheta_\tau\right)\Pi^{\beta+\eta} - \Pi^{\beta+1} + \frac{e_q \vartheta_\tau \Pi^\eta}{\sqrt{1 + \left(\frac{\partial \Sigma}{\partial x}\right)^2 + \left(\frac{\partial \Sigma}{\partial y}\right)^2}}, \tag{1}$$

which determines the changes in near-surface pressure on the local area surface, arise by reason of the influence of laser radiation;

the crater dynamics equation:

$$\frac{\partial \Sigma}{\partial \theta} = \Pi^\beta \sqrt{1 + \left(\frac{\partial \Sigma}{\partial x}\right)^2 + \left(\frac{\partial \Sigma}{\partial y}\right)^2}, \tag{2}$$

which determines of the crater form at any time of the laser pulse and after its action.

There are the parameters Π, Σ in these equations. These parameters are accordingly dimensionless near-surface pressure and a dimensionless function of the shape of the crater formation. In Eq. (1), ϑ_τ is Heaviside stepped function and the parameter e_q determines the ratio of the flow that enters the surface of the matter q_s to the output flow q_{in}, i.e., in dimensionless units:

$$e_q \equiv \frac{q_s}{q_{\text{in}}} = f(x, y) \exp\left(-\Lambda M \Pi^{\eta+\beta} \Sigma\right), \tag{3}$$

where the function $f(x,y)$ determines the transverse shape of the stimulating impulse and adds to (1) an additional dependence on x, y, M is dimensionless parameter determined by equality

$$M = \frac{q_0 \gamma^2 L^2}{2\varphi_0^{3/2} \kappa^2 \rho_{0s} \alpha^{1/2}},$$

Λ is the parameter determining the degree of interaction of the evaporable matter with the incident radiation:

$$\Lambda = \frac{bL\gamma^3 q_{in}}{2\kappa\alpha\varphi_0} h(\omega), \tag{4}$$

where κ is polytropic index, $\alpha \equiv \kappa + 1$, $\gamma \equiv \kappa - 1$, $\beta \equiv \alpha/(2\kappa)$, $\eta \equiv 1/\kappa$, φ_0 is specific heat of the condensate—gas phase transition, ρ_{0s} is the density of the near-surface layer of solid, and L is the coefficient of heat loss. In (3):

$$b \equiv \frac{2R_\Gamma m_a^2}{3\pi\sqrt{\pi}\gamma\mu_a d_a^2 k_b},$$

where R_Γ is gas constant, μ_a is gas molecular weight, d_a is molecule effective diameter, m_a is evaporated matter atom mass, and k_b is Boltzmann constant. The function $h(\omega)$ determines constant part of absorption factor, which does not depend on pressure, but has a significant dependence on the frequency characteristics of the gaseous medium.

2 Analytical Solution of the Gas Phase Dynamics Problem in the One-Dimensional Approximation

Equation (1) is quite complex. To consider the problem analytically and to establish certain patterns, following assumptions were made. Namely, the width of the stimulating pulse is much larger than the depth of the crater, which is formed under the action of this pulse, and the pulse itself has no transverse structure. That is, in the area of the laser beam $f(x, y) = 1$. This will neglect the coordinate dependence in Eqs. (1) and (2). In this approximation:

$$N \equiv \sqrt{1 + \left(\frac{\partial \Sigma}{\partial x}\right)^2 + \left(\frac{\partial \Sigma}{\partial y}\right)^2} = 1.$$

The parameter e_q lose its dependence on coordinates and will depend only on time due to the functions Π and Σ.

An ideal gas model was used here. But when irradiated from the solid evaporates the aerosol, in which there are droplet-cluster formations. Therefore, the possibility of deviation of the gas from the ideal was taken into account. That is, it was assumed that the polytropicity index $\kappa \to 1$ (non-point molecules), while for point molecules $\kappa = 5/3$. The parameter e_q in the case of $\kappa \to 1$ can be defined as

$$\overline{e}_q = \exp\left(-\Lambda M \overline{\Pi}^2 \overline{\Sigma}\right),$$

where $\overline{e}_q$, $\overline{\Pi}$, $\overline{\Sigma}$ are the average values of the corresponding functions. That is, for $\kappa \to 1$ Eq. (1) can be approximately written as follows:

$$\frac{\mathrm{d}\Pi}{\mathrm{d}\theta} = \left(-2 + \Lambda \overline{e}_q \vartheta_\tau\right)\Pi^2 + \overline{e}_q \vartheta_\tau \Pi, \tag{5}$$

Due to Heaviside functions properties, Eq. (5) breaks out into two separate ones, each of them is responsible for part of process depending on time:

1. $\frac{\mathrm{d}\Pi_1}{\mathrm{d}\theta} = \left(\left(-2 + \Lambda \overline{e}_q\right)\Pi_1 + \overline{e}_q\right)\Pi_1$, when $\theta \le \theta_\tau$; with initial condition $\Pi_1(0) = \Pi_{\text{in}}$, where Π_{in} is dimensionless value of the initial pressure. The equation corresponds to the period when the pulse has not yet ended and its action still stimulates of the surface destruction.

2. $\frac{d\Pi_2}{d\theta} = -2\Pi_2^2$, when $\theta > \theta_\tau$.

The solution of Eq. (1) for case $\overline{e}_q = \text{const}$ in view of the entry condition will be:

$$\Pi_1(\theta) = \left(\left(\Pi_{in}^{-1} - 2/\overline{e}_q + \Lambda\right)\exp\left(-\overline{e}_q\theta\right) - \Lambda + 2/\overline{e}_q\right)^{-1} \tag{6}$$

For the case, $\kappa \to 1$ Eq. (2) is also simplified to the form: $\frac{d\Sigma}{d\theta} = \Pi$. As a result, the parameter $\overline{e}_q$ can be determined as follows:

$$\overline{e}_q = \exp\left(-\Lambda M\overline{\Pi}_1^3\theta_\tau/2\right), \tag{7}$$

2.1 *Influence of Radiation Absorption on Pressure Dynamics During Pulse Action*

The obtained function $\Pi_1(\theta)$ in (6) describes the process corresponding to the active removal solid to the gas phase until the action of the falling pulse on the surface cease. In order to analyze how the absorption of radiation by the gaseous medium affects the subsurface pressure during the action of the pulse, an averaging procedure (6) was performed within $0 < \theta < \theta_\tau$. As a result, we have a transcendental equation for $\overline{\Pi}_1$:

$$\overline{\Pi}_1 = \frac{1}{2e^{\Lambda M\overline{\Pi}_1^3\theta_\tau/2} - \Lambda} \cdot \left[1 - \frac{\ln\left\{e^{-\theta_\tau e^{-\Lambda M\overline{\Pi}_1^3\theta_\tau/2}} + \Pi_{in}\left(2e^{\Lambda M\overline{\Pi}_1^3\theta_\tau/2} - \Lambda\right)\left(1 - e^{-\theta_\tau e^{-\Lambda M\overline{\Pi}_1^3\theta_\tau/2}}\right)\right\}}{\theta_\tau e^{-\Lambda M\overline{\Pi}_1^3\theta_\tau/2}}\right], \tag{8}$$

The interaction of radiation with the gaseous medium is characterized by the dimensionless parameter Λ. The greater Λ the stronger the absorption. We looked for dependence by means of (8). This equation is transcendent, so it can only be analyzed numerically (Fig. 1).

Numerical analysis showed that at the beginning of the pulse, the values $\overline{\Pi}_1$ near to Π_{in} (Fig. 2). There is reason to believe that at the beginning of the pulse is the heating of the irradiated surface [18].

As the output flux q_{in} increases, this part of the curve $\overline{\Pi}_1(\theta_\tau)$ narrows, i.e., the substance begins to respond to external laser exposure at smaller destructive lengths θ_τ. Then, the average pressure $\overline{\Pi}_1$ increases rapidly and reaches its maximum. Further, with increasing Λ the average value of pressure $\overline{\Pi}_1$ decreases. This is understandable, because over time the range of interaction of radiation with the plasma - gas medium expands. From (8), it is seen that the pressure $\overline{\Pi}_1$ is approximately

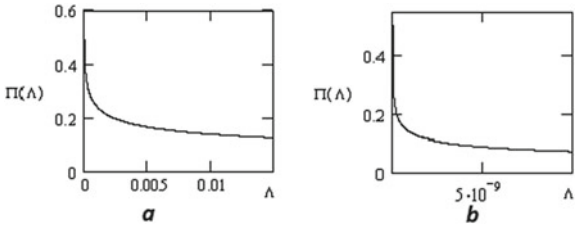

Fig. 1 $\overline{\Pi}_1(\Lambda)$ dependence for pulse length $\theta_\tau = 10^4$ which corresponds to real pulse length $\tau \sim 10$ fs (**a**) and $\theta_\tau = 10^{12}$ which corresponds to $\tau \sim 100ns$ (**b**)

Fig. 2 Dependence $\overline{\Pi}_1(\theta_\tau)$ at $\Lambda = 10^{-10}$

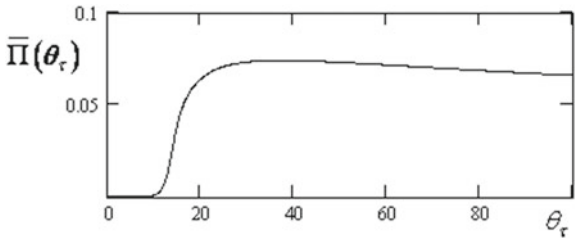

dependent on the product $\Lambda\theta_\tau$. The additional dependence on θ_τ is significant in the region of only small values of pulse lengths. Therefore, in the units of each specific experimental conditions, the pressure depends on the product $q_{\text{in}}^3\tau$, namely

$$\overline{P} \sim \frac{\gamma L_d^2\sqrt{\alpha\kappa}}{4\varphi_0^{5/2}} h(\omega) q_{in}^3 \tau,$$

where L_d is the optical loss factor. Such a definition follows from the definitions of Λ (4) and θ_τ [16].

The dependence of $\overline{\Pi}_1(\theta_\tau)$ was also investigated, which is shown in Fig. 3, at different values of the parameter that characterizes the interaction of radiation with the gaseous medium. Dependence between the absorption coefficient k of this medium and the parameter Λ has the form:

Fig. 3 Dependence of on a logarithmic scale for different possible (estimated) values of Λ

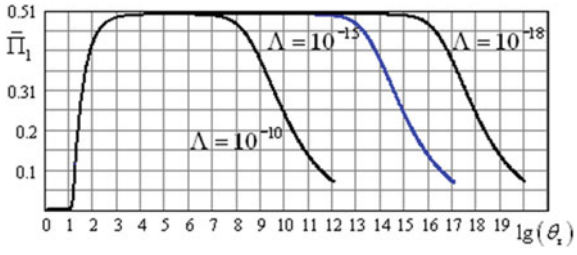

$$k = \frac{q_{\text{in}}\alpha^{3/2}\kappa^{1/2}}{2b\gamma^2\varphi_0^{3/2}} \cdot \frac{L}{L_d}\Lambda\Pi^{\eta+\beta} \sim 10^{12}\Lambda \ \text{sm}^{-1}.$$

In Fig. 3, value $\Lambda = 10^{-10}$ corresponds to the real absorption coefficient $k \sim 10^2$ sm^{-1}, the value $\Lambda = 10^{-15}$—the absorption coefficient $k \sim 10^{-3}$ sm^{-1}, and $\Lambda = 10^{-18} - k \sim 10^{-6}$ sm^{-1}. Accordingly, the radiation flux begins to be absorbed at times $t \sim 10^{-12}$ s when $k \sim 10^2$ sm^{-1}, $t \sim 10^{-7}$ s when $k \sim 10^{-3}$ sm^{-1}, and $t \sim 10^{-4}$ s when $k \sim 10^{-6}$ sm^{-1}.

For all the above curves (Fig. 1) with increasing length of the destructive part of the pulse θ_τ, the pressure initially increases rapidly and reaches its maximum value at $t \sim 10^{-13}$ s and then begins to decline, and the greater the value the sooner the pressure begins to decrease according to the exponential law. This pressure behavior is due to the fact that over time, the corrosion torch formed by the radiation takes up more volume. This reduces the amount of flow that reaches the surface of the solid. Mathematically, this fact tracks the effect of the factor e_q, which depends on the value of the parameter and takes into account the loss of intensity of the radiation flux on the way to the target.

The factor depends on Λ exponentially (4). The pressure Π_{in} increases from the value when $\theta = 0$ to the value $\left(2/e_q - \Lambda\right)^{-1}$ when $\to \infty$. Obviously, the behavior of the pressure varies depending on the magnitude of the flux incident on the surface and the interaction of radiation with the gas, i.e., the dynamics of the pressure on the surface of the substance are corrected by the values of Λ and e_q. As e_q decreases, the maximum value of pressure decreases in Fig. 4.

The effect of the radiation flux on the substance will be stronger when the absorption capacity of the gas (plasma torch) evaporated from the irradiated substance is minimal. A value of $e_q = 1$ means that the flux does not suffer any losses on the way to the substance, and this is possible only with the propagation of the laser pulse in vacuum. The results presented here are valid if we assume that e_q is constant over time. But it is obvious that the increase in pressure and depth of the crater leads to a decrease in the parameter e_q over time.

At the end of the pulse, the pressure dynamics are described by the solution defined by the second equation in (5). As soon as the pulse ceases, at the same time, there

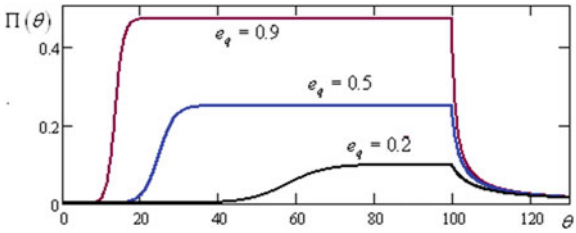

Fig. 4 Qualitative form of the dependence of gas pressure on time near the surface for different values of the parameter $\overline{e}_q$ and $\Lambda = 10^{-10}$ for the case when the destructive part of the pulse $\theta = 100$

are significant changes, namely the pressure drops sharply by the magnitude of the luminous flux in the pulse. Given this, the obtained piecewise continuous solution of Eq. (5):

$$\Pi_1(\theta) = \begin{cases} \left(\left(\Pi_{in} - 2\overline{e}_q + \Lambda\right)\exp\left(-\overline{e}_q\theta\right) - \Lambda + 2\overline{e}_q^{-1}\right)^{-1}, \theta \le \theta_\tau \\ 2(\theta - \theta_\tau) + \dfrac{\left(\Pi_{in}^{-1} - 2/\overline{e}_q + \Lambda\right)\exp\left(-\overline{e}_q\theta\right) - \Lambda + 2/\overline{e}_q}{1 - \overline{e}_q\Pi_q\left(\left(\Pi_{in}^{-1} - 2/\overline{e}_q + \Lambda\right)\exp\left(-\overline{e}_q\theta\right) - \Lambda + 2/\overline{e}_q\right)}, \theta > \theta_\tau \end{cases} \quad (9)$$

This dependence is shown in Fig. 4.

It is obvious that the pressure always acquires the maximum value during the action of the pulse at some point θ_1, where $\theta_1 \le \theta_\tau$. That is, $\Pi_{\max}$ can be defined as follows:

$$\Pi_{\max} = \Pi_1(\theta_1) = \left(\left(\Pi_{in}^{-1} - 2/\overline{e}_q + \Lambda\right)\exp\left(-\overline{e}_q\theta\right) - \Lambda + 2/\overline{e}_q\right)^{-1} \quad (10)$$

2.2 *Influence of Resonant Absorption of Radiation on Dynamics of a Torch*

The parameter Λ (4) depends on the frequency due to the presence of a factor $h(\omega)$. To find its explicit form, consider the absorption coefficient for this (one-dimensional) problem in more detail. Since we are talking about the absorption of electromagnetic radiation by gas, in the linear approximation [19], it is defined by the following expression:

$$k_l = \frac{\omega}{c}\frac{\pi e^2}{2m_e m_a}\rho \sum_{m(\neq 1)} \frac{f_{ml}\Gamma_{ml}}{\omega_{ml}\left(\omega_{ml} - \omega\right)^2} \quad (11)$$

Index l in absorption coefficient k defines that it concerns this coefficient value, which is responsible for atom excitation from state l into any given state m, on them summation is fulfilling; ω is electromagnetic radiation frequency; c is a velocity of light in vacuum; e is a charge of electron; m_e is its mass; ω_{ml} is atom radiation absorption proper frequency for its transition from state l into state m (it is resonance frequency); f_{ml}—oscillator strength for transition $l \to m$; Γ_{ml}—level width. For gases

$$\Gamma_{ml} = \frac{4\pi d_a^2}{m_a}\rho\left(\frac{k_b T}{m_a}\right)^{1/2},$$

It is common knowledge that the temperature can be determined from the state equation through pressure and density: Then:

$$\Gamma_{ml} = \frac{4\pi d_a^2}{m_a}(\rho P)^{1/2}.$$

If radiation emission frequency ω is close to one of resonance frequencies ω_{m0} (quasi-resonance system state), then in the expression for absorption coefficient k_l, they conserve only one dominant summand, and at the same time, before excitation atoms dwell in the fundamental state $l = 0$. Then taking it into account absorption coefficient becomes:

$$k = \rho(\rho P)^{1/2}\frac{2\pi e^2 d_a^2}{cm_e m_a}\frac{\omega f_{m0}}{\omega_{m0}(\omega_{m0}-\omega)^2} \tag{12}$$

As we see for one dimension case frequency, parameter $h_m(\omega)$ may be defined as:

$$h_m(\omega) \equiv \frac{2\pi^2 e^2 d_a^2}{cm_e m_a}\frac{\omega f_{m0}}{\omega_{m0}(\omega_{m0}-\omega)^2}, \tag{13}$$

where m represents some fixed state such that the frequency ω_{m0} is closest to ω.

Definition (13) makes it possible to determine the dependence of Λ on the radiation frequency. Substituting Λ in (10), we define $\Pi_{\max}$ as a function of the difference between the frequency of radiation and the natural frequency of gas absorption. After some transformations, the dependence of $\Pi_{\max}$ on the frequency can be reduced to the form:

$$\Pi_{\max}(\omega) = \left(\Pi_{\text{in}}^{-1}e^{-\theta_1 e^{-G}} + \left(2e^G - G\right)\left(1 - e^{-\theta_1 e^{-G}}\right)\right)^{-1}. \tag{14}$$

Here the following designations are introduced:

$$G \equiv W\frac{\omega}{\omega_{m0}(\omega_{m0}-\omega)^2} \quad \text{and} \quad W \equiv \frac{bLq_{\text{in}}}{\kappa\alpha\varphi_0}\frac{\pi^2 e^2 d_a^2 f_{m0}}{cm_e m_a}.$$

Expression (14) also takes into account the frequency dependence of the parameter $\overline{e}_q$. The graphical dependence $\Pi_{\max}(\omega)$ is shown in Fig. 5.

It is seen that at the point $\omega = \omega_{m0}$, the pressure formally becomes zero. But in reality, its value does not reach zero due to the presence of other, nonresonant terms, which was rejected when obtaining an explicit expression for the absorption coefficient k as a function of frequency ω, and also, due to the fact that in reality, the current pulse is not ideal Π–form.

Consequently, the qualitative character of evaporation intensity dependence from the incident radiation frequency is represented by Eq. (14). For all that, as we can see from Fig. 3, pressure is dropping when frequency ω approaches to ω_{m0} and formally

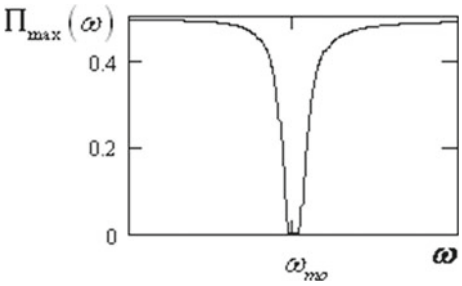

Fig. 5 Qualitative dependence of maximum pressure Π_{max} on frequency ω for arbitrary values W and θ_1

becomes equal to zero at $\omega = \omega_{m0}$ that is in qualitative accordance with obtained results. Merely resonance case $\omega = \omega_{m0}$ needs special investigation because for this case coefficient of absorption k dependence from ρ and P acquire quite different form, than in Eq. (12).

3 Conclusion

During laser irradiation of the solid, the surface is destroyed. The destruction of the surface is accompanied by the removal of the substance. The substance removed from the surface is plasma with a complex structure. Later on, the flying out from the surface solid and liquid particles (aerosol) affects the degree of laser exposure. To assess the consequences of such an influence, an analytical study of this process was carried out in the work. It was assumed that the aerosol formed near the surface has a complex drops-cluster structure. For this case, approximate piecewise continuous solutions were obtained during the time of the pulse and after its termination. The obtained solutions include two dimensionless parameters Λ and e_q, which are the characteristics of the interaction of radiation with ablative substance.

Based on these solutions, averaged expressions for pressure and crater function were obtained. Analysis of their behavior is carried out for various values of the parameters Λ and e_q. The quantity Λ is directly proportional to the absorption coefficient of radiation. The parameter e_q depends exponentially on Λ. Both parameters affect the value of the maximum pressure near the surface at the time of active laser exposure.

Also Λ depends on the frequency of the radiation and the frequency characteristics of the irradiated physical system. In the paper, the influence of the frequency parameter $h(\omega)$ to the absorption coefficient is studied. The influence of this parameter to the maximum pressure in the process under consideration is analyzed. It is shown that in the case of resonance, aerosol can to put up significant resistance to the laser action and practically stops the nanostructures formation on the substance surface.

When considering the dynamics of the surface pressure, it was found that its value is significantly affected by the increase in the length of the plasma torch due to the

magnitude of the interaction of radiation with the torch, which is determined by the parameter. Λ.

Our analysis of the dependence of pressure on the pulse length shows that there possibly exists a conservation law for the pulse intensity and its length product. It was also demonstrated that pressure reaches its maximum during action of a pulse, but this maximum do not necessarily coincides with time of the pulse termination.

The maximum pressure value Π_{max} dependence on frequency characteristics. It is shown that it is essential over the range of resonant frequencies.

References

1. Guo B, Sun J, Lu YF, Jian L (2019) Ultrafast dynamics observation during femtosecond laser-material interaction. Int J Extreme Manuf 1(3):032004 (23p). https://doi.org/10.1088/2631-7990/ab3a24
2. Mirza I, Bulgakova NM, Tomáštík J, Michálek V, Haderka O, Fekete L, Mocek T (2016) Ultrashort pulse laser ablation of dielectrics: thresholds, mechanisms, role of breakdown. Sci Rep 6, Article number: 39133. https://www.nature.com/articles/srep39133
3. Gattass RR, Mazur E (2008) Femtosecond laser micromachining in transparent materials. Nat Photon 2:219–225. https://www.nature.com/articles/nphoton.2008.47
4. Sugioka K, Cheng Y (ed) (2013) Ultrafast laser processing: from micro- to nanoscale. Pan Stanford. https://www.routledge.com/Ultrafast-Laser-Processing-From-Micro--to-Nanoscale/Sugioka-Cheng/p/book/9789814267335
5. Sugioka K, Cheng Y (2014) Ultrafast lasers-reliable tools for advanced materials processing. Light: Sci Appl 3:e149. https://www.nature.com/articles/lsa201430
6. Abramov DV, Arakelyan SM, Makov SA, Prokoshev VG, Khor'kov KS (2013) Formirovaniye sistemy mikrokraterov na poverkhnosti titana pri vozdeystvii femtosekundnym lazernym izlucheniyem v usloviyakh bystrogo okhlazhdeniya. Pis'ma v ZHTF 39(16):14–22 (in Russian)
7. Anisimov SI, Luk'yanchuk BS (2002) Selected problems of laser ablation theory. Physics-Uspekhi 45(3):293. https://doi.org/10.1070/PU2002v045n03ABEH000966
8. Hsu PS, Patnaik AK, Stolt AJ, Estevadeordal J, Roy S, Gord JR (2018) Femtosecond-laser-induced plasma spectroscopy for high-pressure gas sensing: enhanced stability of spectroscopic signal. Appl Phys Lett 113:214103. https://doi.org/10.1063/1.5054805
9. Kerse C et al (2016) Ablation-cooled material removal with ultrafast bursts of pulses. Nature 537:84–88. https://www.nature.com/articles/nature18619
10. Bulgakova NM et al (2014) Impacts of ambient and ablation plasmas on short- and ultrashort-pulse laser processing of surfaces. Micromachines 5:1344–1372. https://app.dimensions.ai/details/publication/pub.1045383007
11. Wu Z, Zhang N, Zhu X, An L, Wang G, Tan M (2018) Time-resolved shadowgraphs and morphology analyses of aluminum ablation with multiple femtosecond laser pulses. Chin Phys B 27(7):077901. https://doi.org/10.1088/1674-1056/27/7/077901/meta
12. Shugaev MV, Gnilitskyi I, Bulgakova NM, Zhigilei LV (2017) Mechanism of single-pulse ablative generation of laser-induced periodic surface structures. Phys Rev B 96(20):205429. https://doi.org/10.1103/PhysRevB.96.205429
13. Zhang N, Yang J, Zhu X (2012) Investigation of the ultrafast process of femtosecond laser ablation of highly oriented pyrolytic graphite. Chin J Lasers 39(5):0503002. http://en.cnki.com.cn/Article_en/CJFDTOTAL-JJZZ201205018.htm
14. Berezovska N, Dmitruk I, Kalyuzhnyy A, Dmytruk A, BlonskyiI (2018) Self-organized structuring of surface of metal-semiconductor composite by femtosecond laser processing. Ukrainian J Phys 63(5):406–412.

15. Shmeleva LV, Suprun AD, Yezhov SM, Datsyuk VV (2021) Specificity of boundary conditions for laser-stimulated destructive surface treatment without melting. In: Nanomaterials and nanocomposites, nanostructures surfaces, and their applications, vol 246 (Chap. 23). Springer International Publishing, pp 289–301. ISBN 978-3-030-51904-9. https://link.springer.com/chapter/10.1007/978-3-030-51905-6_23
16. Shmeleva LV, Suprun AD, Yezhov SM (2019) Simulation of the formation of a surface nanocrater under the action of high-power pulsed radiation—nanocomposites, nanostructures, and their applications part of the Springer Proceedings in Physics book series (SPPHY, vol 221), pp 505–515. https://doi.org/10.1007/2F978-3-030-17759-1_34
17. Shmeleva LV, Suprun AD, Yezhov SM, Datsyuk VV (2021) Theoretical modeling of laser-stimulated nanostructures. In: Nanomaterials and nanocomposites, nanostructures surfaces, and their applications, vol 246 (Chapter 22). Springer International Publishing, pp 277-287. ISBN 978-3-030-51904-9. https://link.springer.com/chapter/10.1007/978-3-030-51905-6_22
18. Suprun AD, Shmeleva LV, Razumova MA (2011) The influence of bulk absorption of substance on the threshold of destruction by the intensive pulse of electromagnetic radiation. Funct Mater 18(2):237–243. http://functmaterials.org.ua/contents/18-2/
19. Davydov AS (1963) Kvantovaya mekhanika. M. Fizmatgiz, 748s

Mechanisms of Magnetic Ordering in Quasi-2D BEDT-TTF Conductors

Yuriy Skorenkyy, Oleksandr Kramar, and Yuriy Dovhopyatyy

1 Introduction

BEDT-TTF family of quasi-two-dimensional organic conductors exhibits a variety of phases and transitions driven by temperature, pressure or anion doping [1–3]. Primarily, interest to $(BEDT\text{-}TTF)_2X$ compounds, where BEDT-TTF stands for bis(ethylenedithio)tetrathiafulvalene molecule and X denotes monovalent anion (I_3, ICl_2, IBr_2, $Cu[N(CN)_2]I$, $Cu[N(CN)_2]Cl$, $Cu[N(CN)_2]Br$, etc.), was induced by superconductivity of these materials at low temperatures. Though the mechanism of this superconducting phase stabilization is still unclear, other regions in phase diagram are interesting as well [4, 5], as they may give clues for explaining promising properties of many anisotropic molecular conductors.

Theoretical investigation of strong electron correlation effects in BEDT-TTF compounds based on the models for electron subsystem [6–8] in second quantization representation made it possible to attribute the paramagnetic metal to antiferromagnetic insulator transition to localization effects caused by electron interactions. These studies used models, which included every aspect of spatial structure of a particular BEDT-TTF compound [7, 9, 10] and required complex computations, however, due to this inherent structural complexity, neglected electron interactions of lower orders of magnitude [11] than on-site Coulomb repulsion parameter. At the same time, these matrix elements of electron interactions not included in previous studies may play an important role in magnetic ordering stabilization mechanism [12, 13].

Organic molecular crystals $(BEDT\text{-}TTF)_2X$ are composed of dimerized planar BEDT-TTF molecules and conducting anion planes (Fig. 1). The lattice unit cell contains one BEDT-TTF dimer, and electron capture by anion provides one hole

Y. Skorenkyy (✉) · O. Kramar · Y. Dovhopyatyy
Ternopil Ivan Puluj National Technical University, Ternopil, Ukraine

O. Fesenko and L. Yatsenko (eds.), *Nanomaterials and Nanocomposites, Nanostructure Surfaces, and Their Applications*, Springer Proceedings in Physics 263, https://doi.org/10.1007/978-3-030-74741-1_16

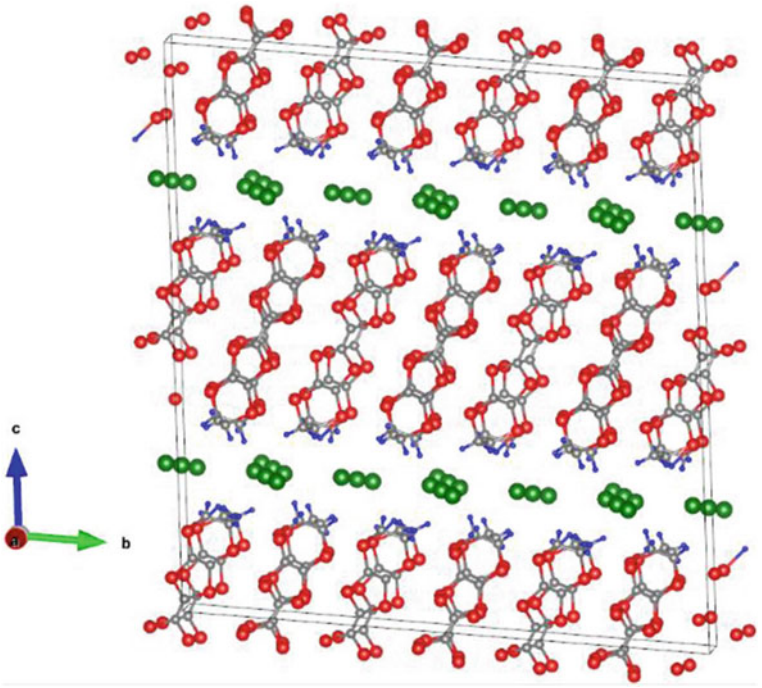

Fig. 1 Layered structure of α-(BEDT-TTF)$_2$I$_3$ [17]

carrier per dimer. Application of the external pressure leads to a considerable increase in conductance [14–16], therefore, it is to be described by the microscopical model of choice on the same footing as electron interactions.

2 Configurational Representation of the Model Hamiltonian

To take into account the electron interaction in the BEDT-TTF system, tight binding Hamiltonians in terms of electron operators have been introduced [7, 18]. Such an approach has a number of advantages. First, it allows to reduce complexity of theoretical description of electron transport through the molecular stacks to the problem of electron hopping through a lattice, where each site represents the (BEDT-TTF)$_2$ dimer. Second, it simplifies application of approaches developed for crystalline solid conductors with strong electron correlations [19–22].

We start from Hamiltonian of the extended the Hubbard model [23]

$$H = -\mu \sum_{i\sigma} a_{i\sigma}^{+} a_{i\sigma} + \sum_{ij\sigma}{}' t_{ij}(n) a_{i\sigma}^{+} a_{j\sigma} + \sum_{ij\sigma}{}' \left(T(ij) a_{i\sigma}^{+} a_{j\sigma} n_{\bar{\sigma}} + h.c.\right) + \\ + U \sum_{i} n_{i\uparrow} n_{i\downarrow} + \frac{1}{2} \sum_{ij\sigma\sigma'}{}' J(ij) a_{i\sigma}^{+} a_{j\sigma'}^{+} a_{i\sigma'} a_{j\sigma} + \frac{1}{2} \sum_{ij\sigma\sigma'}{}' V(ij) n_{i\sigma} n_{j\sigma'}, \tag{1}$$

where $a_{i\sigma}^{+}(a_{i\sigma})$ stand for operators of electron creation (annihilation) in second quantization formalism, $n_{i\sigma}$ is the number operator which measures occupancy of site i by electron of spin σ; μ denotes chemical potential; electron hoppings in the plane of molecules are described by the hopping integral $t_{ij}(n)$; $T(ij)$ characterizes reduction of hopping amplitude due to occupation of sites (correlated hopping [22, 24]); U is Coulomb repulsion of two electrons in the same site; $J(ij)$ stands for integral of direct intersite exchange interaction; $V(ij)$ is Coulomb repulsion of electrons in neighbouring sites.

The model Hamiltonian (1) takes into account the most important interactions in a narrow conduction band. By the second and third sums in (1) intersite electron hoppings are described, Coulomb repulsion of electrons on the same site is the fourth sum, whilst interatomic exchange interaction is the fifth sum and the last one describes interatomic Coulomb interaction. The peculiar structure of Hamiltonian (1) allows us to take into account three distinct types of electron hopping [25–27], namely the 'band' hopping

$$\sum_{ij\sigma}{}' t_{ij}(n) a_{i\sigma}^{+} a_{j\sigma} \tag{2}$$

the correlated hopping of the first type

$$\sum_{ij\sigma}{}' T_1(ij) a_{i\sigma}^{+} a_{j\sigma} \tag{3}$$

and the correlated hopping of the second type

$$\sum_{ij\sigma}{}' \left(T(ij) a_{i\sigma}^{+} a_{j\sigma} n_{\bar{\sigma}} + \text{h.c.}\right) \tag{4}$$

Using the relations [23] between the electron operators and transition (Hubbard) X-operators [28], Hamiltonian (1) can be rewritten in the configurational representation. This representation allows use of perturbation theory based on the operators of site transition and deriving effective Hamiltonians in which tendencies towards electron orderings are represented by respective exchange terms.

After the transition to Hubbard X-operators, the model Hamiltonian reads as

$$H = H_0 + H_1 + H_1^{'} + H_2, \tag{5}$$

where

$$H_0 = -\mu \sum_i \left(X_i^{\uparrow} + X_i^{\downarrow} + 2X_i^2 \right) + U \sum_i X_i^2 \tag{6}$$

$$H_1 = \sum_{ij\sigma}{}' t_{ij}(n) X_i^{\sigma 0} X_j^{0\sigma} + \sum_{ij\sigma}{}' \tilde{t}_{ij}(n) X_i^{2\sigma} X_j^{\sigma 2} \tag{7}$$

$$H_1' = \sum_{ij} t_{ij}'(n) \left(X_i^{\downarrow 0} X_j^{\uparrow 2} - X_i^{\uparrow 0} X_j^{\downarrow 2} + \text{h.c.} \right) \tag{8}$$

$$H_2 = \frac{1}{2} \sum_{ij\sigma\sigma'} V(ij) \left(X_i^{\sigma} + 2X_i^2 \right) \left(X_j^{\sigma'} + 2X_j^2 \right) - \frac{1}{2} \sum_{ij\sigma}{}' J(ij) \left(\left(X_i^{\sigma} + X_i^2 \right) \left(X_j^{\sigma} + X_j^2 \right) + X_i^{\sigma\bar{\sigma}} X_j^{\bar{\sigma}\sigma} \right). \tag{9}$$

H_0 describes an electron system in the absence of intersite hoppings and interactions (the 'atomic' limit). Characteristic feature of 'site' representation of H_0, in distinction from the electron creation and annihilation operators is a diagonal form of the on-site Coulomb repulsion term, which contains operators of $|{\downarrow}{\uparrow}>$—state occupancy. This peculiarity appears to be extremely useful for description of systems with strong interatomic interaction. Intersite Coulomb and exchange interaction, of lower orders of magnitude, are grouped in H_2.

H_1 describes translational motion of holes and doublons (doubly occupied states), exemplified by Figs. 2 and 3.

In the considered model, in distinction from the Hubbard model [29], hopping integrals for holes $t(n)$ and doublons $\tilde{t}(n)$ are different, which leads to a series of important effects.

Application of the external pressure to the narrow-band material can be adequately described as a hopping amplitude renormalization by the crystalline lattice strain

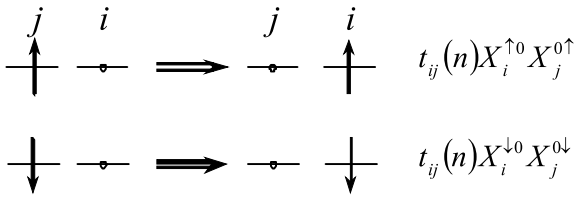

Fig. 2 Translational motion of holes. Arrow indicate transitions with operator representation shown to the right

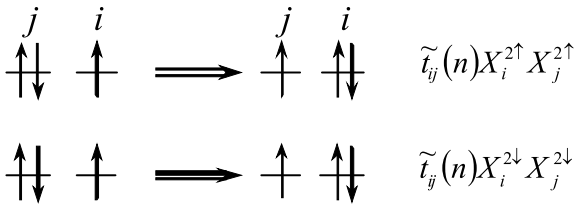

Fig. 3 Translational motion of doublons

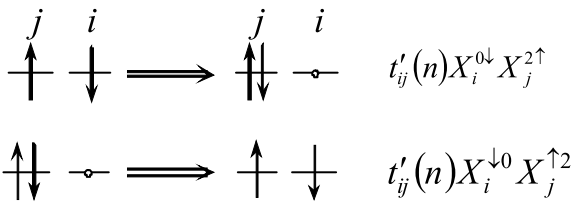

Fig. 4 Processes of pair creation and annihilation of holes and doublons

$u = \frac{\Delta V}{V_0} \sim p$ (here V_0 is the unit lattice volume). The bandwidth increases with the strain as

$$2w = 2w_0(1 + \alpha u) \quad \left(\alpha = \frac{V_0}{w_0} \cdot \frac{\partial w}{\partial V} < 0\right), \tag{10}$$

where w_0 is the unperturbed half-bandwidth. Thus, hopping integrals in a model with non-equivalent subbands are to be renormalized as

$$t \to t(1 + \alpha u), \quad \tilde{t} \to \tilde{t}(1 + \alpha u). \tag{11}$$

Similar renormalization is to be applied to all matrix elements describing electron hoppings.

$H_1^{'}$ describes processes of pair creation and annihilation of holes and doublons (Fig. 4):

Expressions for H_1 and $H_1^{'}$ prove that the configurational description is not only attractive for visualizing and classifying processes but also purposeful as it incorporates the correlation effects into the internal structure of H_1 and$H_1^{'}$. In the electron representation, the intersite hopping $\sim \sum t(ij)a_{i\sigma}^{+}a_{j\sigma}$ does not take into account the occupancy of sites i and j, and the processes shown in Figs. 2 and 4 are equally probable. Within the configurational approach, the effect of intra-atomic correlation is manifested in the structure of translational part of the Hamiltonian (5), from the expression for H_1 and $H_1^{'}$ one can see that the probability of state with spin σ electron on site i depends on both occupation of this site and site j, which electron is hopping from. One can also see that the hoppings corresponding to terms in H_1 and $H_1^{'}$ are not equivalent by energy cost; the processes described by $H_1^{'}$ are of 'activation' type in distinction from 'itinerant' motion of holes and doublons described by H_1. This energy non-equivalence allows considering the activation processes as a perturbation in the case of strong electron correlations.

3 Effective Hamiltonian of BEDT-TTF Electron Subsystem

Following the method of effective Hamiltonian derivation, proposed by work [30], we exclude hybridization processes described by $H_1^{'}$ with the canonical transformation

$$\tilde{H} = e^{S} H e^{-S}, \tag{12}$$

where S is chosen as

$$S = \sum_{ij} L(ij)\left(\left(X_i^{\uparrow 0} X_j^{\downarrow 2} - X_i^{\downarrow 0} X_j^{\uparrow 2}\right) - \text{h.c.}\right) \tag{13}$$

If we restrict ourselves to the quantities of the second order of magnitude (terms in H_0 are considered to be the values of the zeroth order of magnitude, S, H_1 and $H_1^{'}$ of the first order), then

$$\tilde{H} = H_0 + H_1 + H_1^{'} + H_2 + [SH_0] + [SH_1] + \left[SH_1^{'}\right] + \frac{1}{2}[S[SH_0]] \tag{14}$$

($[AB] = AB - BA$). Let us exclude non-activation-type hopping processes in the first order in $|t'_{ij}(n)|/U$

$$H_1^{'} + [SH_0] = 0. \tag{15}$$

When the exchange Coulomb correlation is taken into account in the mean-field approach, then from (15) we have

$$L(ij) = \frac{t_{ij}^{'}(n)}{\Delta}, \tag{16}$$

where

$$\Delta = U - V + zV\left(\left\langle X_i^0 \right\rangle + \left\langle X_i^2 \right\rangle\right) \tag{17}$$

is the energy of doublon-hole pair activation. Therefore, small parameter of the considered model is $|t'_{ij}(n)|/\Delta$ and not $|t(ij)|/U$ as in the Hubbard model [31]. This distinction, first, removes obstacles for transition to effective Hamiltonian, second, eliminates direct relation between $t_{ij}(n)$ and U.

Commutator $[SH_1]$ components have operator structure similar to $H_1^{'}$, but with hopping integrals of the second order of magnitude. In the considered approximation these do not contribute to $\tilde{H}$. Therefore, for a case when (σ − 0)— and (↑↓ −

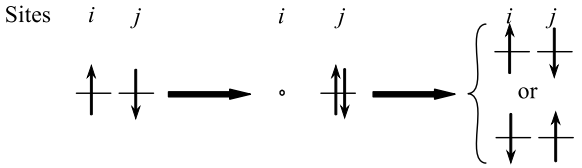

Fig. 5 Mechanism of superexchange ($\sim \frac{|t'_{ij}(n)|^2}{U}(X_i^{\uparrow} X_j^{\downarrow} + X_i^{\downarrow\uparrow} X_j^{\uparrow\downarrow})$

σ)-subbands are separated by energy gap $\left|t_{ij}^{'}(n)\right| << \Delta$, the effective Hamiltonian is

$$\widetilde{H} = H_0 + \sum_{ij}{}' t(n) X_i^{\sigma 0} X_j^{0\sigma} + \sum_{ij\sigma}{}' \widetilde{t_{ij}}(n) X_i^{2\sigma} X_i^{\sigma 2} + \widetilde{H_{ex}} + \widetilde{H_t}, \tag{18}$$

where

$$H_{ex} = -\frac{1}{2} \sum_{ij\sigma} J(ij)(X_j^{\sigma} \widetilde{X_j^{\sigma}} + X_i^{\sigma} \widetilde{X_j^{\sigma}}), \tag{19}$$

$$\widetilde{H_{ex}} = -\frac{1}{2} \sum_{ij\sigma} \widetilde{J}(ij)(X_i^{\sigma} \widetilde{X_j^{\sigma}} - X_i^{\widetilde{\sigma\sigma}} X_j^{\widetilde{\sigma\sigma}} - X_i^2 X_i^0), \tag{20}$$

$$\begin{aligned} \widetilde{H_t} = &-\frac{1}{2} \sum_{ijk\sigma}{}' J(ijk)\left(X_i^{\sigma 0} X_j^{\overline{\sigma}} X_k^{0\sigma} - X_i^{\sigma 0} X_j^{\overline{\sigma}\sigma} X_k^{0\overline{\sigma}}\right) \\ &-\frac{1}{2} \sum_{ijk\sigma}{}' J(ijk)\left(X_i^{2\sigma} X_j^{\sigma\overline{\sigma}} X_k^{\overline{\sigma}2} - X_i^{2\sigma} X_j^{\overline{\sigma}} X_k^{\sigma 2}\right). \end{aligned} \tag{21}$$

Here, the integral of indirect exchange through the polar states is

$$\tilde{J}(ij) = \frac{2t_{ij}^{'}(n) t_{ji}^{'}(n)}{\Delta}, \tag{22}$$

and the integral of indirect hopping through $(\sigma - 0)$- and $(\uparrow\downarrow - \sigma)$—subbands is

$$J(ijk) = \frac{2t_{ij}^{'}(n) t_{jk}^{'}(n)}{\Delta}. \tag{23}$$

Exclusion of the pair annihilation and creation of neighbouring $|\sigma>$- and $|\overline{\sigma}>$-states leads to formation of three terms in the expression for effective Hamiltonian, of which one describes indirect exchange interaction (Anderson's kinetic superexchange [32]), the others describe indirect electron hoppings. The superexchange mechanism induced by virtual transition of $|i\sigma>$-states to $|j\uparrow\downarrow>$—states stabilizes anti-parallel alignment of spins $|i\sigma>$ and $|j\overline{\sigma}>$ (Fig. 5). By analogy with superexchange, the indirect hopping of $|i\sigma>$-states through $|i0>$- or $|i\uparrow\downarrow>$—states can be termed superhopping (Fig. 6).

One may state that the transitions from the electron representation of hopping processes to the configurational one, with the following exclusion of activation-type hopping processes results in the effective Hamiltonian, which incorporates itinerant motion of $|i0>$ and $|i\uparrow\downarrow>$ configuration, exchange interaction of homeopolar states and indirect hopping of the polar states. At the first glance, effective Hamiltonian (18) appears more complex than the initial one, however, in the case of strong electron

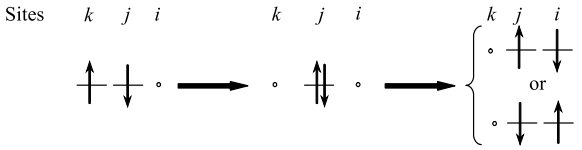

Fig. 6 Mechanism of superhopping ($\sim \frac{t'_{ij}(n)t+jk(n)}{U}(X_i^{\downarrow 0}X_k^{0\uparrow}X_j^{\uparrow\downarrow} - X_i^{\uparrow 0}X_k^{\uparrow 0}X_j^{\downarrow\downarrow})$

correlation the mathematical treatment of such Hamiltonians simplifies considerably and its physical interpretation becomes unambiguous.

4 Conditions for Antiferromagnetic State Stabilization

Since the pioneering work [31] the Hamiltonian of *s*-electrons with strong electron interaction in the case of half-filled band is known to be transformable to the exchange model with the effective nearest-neighbour exchange integral $J_\alpha = 2t_0^2/U$ (here t_0 is the unperturbed hopping integral of the Hubbard model) and antiferromagnetism in Mott–Hubbard insulator is stabilized by the virtual processes of doublons and holes pair creation and annihilation at neighbouring sites. In this case, we have clearly defined an antiferromagnetic state with two alternating sublattices with opposite magnetizations. Within molecular field approximation Neel temperature is given by expression

$$\theta_N = zt_0^2/U. \tag{24}$$

If $n \neq 1$ then for a consistent description of magnetic properties one has to take into account translational motion of extra electrons for $n > 1$ or holes for $n < 1$. However, treatment of antiferromagnetism from the initial Hamiltonian beyond the perturbation theory has known deficiencies [19–22]. For two-sublattices antoferromagnet within mean-field approximation at $n = 1$ one obtains the following equation for Neel temperature

$$1 = \frac{1}{2N}\sum_{\vec{k}} \frac{U}{t_0\left(\vec{k}\right)} th \frac{t_0\left(\vec{k}\right)}{2\theta_N} \tag{25}$$

which fails in the limit of $U \to \infty$. At large U and $n = 1$ only virtual hoppings of electrons can be realized and $\theta_N \sim 1/U$; if $t_0\left(\vec{k}\right) = 0$, then from (25) follows $\theta_N \sim U$, which is not satisfactory.

At $n = 1$ in the Hubbard approximation [28] for Neel temperature of two-sublattice antiferromagnet one has

$$1 = \frac{1}{2N} \sum_{\vec{k}} \frac{U}{\Delta(\vec{k})} \cdot \frac{Sh\Delta(\vec{k})/2\theta_N}{Ch\Delta(\vec{k})/2\theta_N - Cht(\vec{k})/2\theta_N}, \tag{26}$$

where

$$\Delta\left(\vec{k}\right) = \left(t_0^2\left(\vec{k}\right) + U^2/4\right)^{1/2}. \tag{27}$$

For small U this result is equivalent to mean-field approximation, however, in distinction from (25), Eq. (26) does not have solutions except of $\theta_N = 0$.

In the exchange model of two-sublattice antiferromagnet, the energy spectrum of spin waves has linear momentum dependency. Studies of the spin waves on basis of the initial Hamiltonian allow to reproduce correct momentum dependence, but also leads to incorrect linear dependency on the hopping integral. Equation for θ_N then reads as

$$1 = \frac{1}{N} \sum_{\vec{k}} \frac{1}{Ch\frac{U}{2\theta_N} + Ch\frac{t(\vec{k})}{2\theta_N}} \left(Sh\frac{U}{2\theta_N} + \frac{J_\alpha}{t\left(\vec{k}\right)} Sh\frac{t\left(\vec{k}\right)}{2\theta_N} \right). \tag{28}$$

If model rectangular density of states is used, from (28) one has for Neel temperature θ_N:

$$\theta_N = \frac{J_\alpha}{2} \cdot \frac{\int_0^{w/2\theta_N} \frac{Shx}{x} \mathrm{d}x}{Sh\frac{w}{2\theta_N}}. \tag{29}$$

One can see that the correct expression for θ_N can be obtained only at condition $w << \theta_N$. Here, the situation is analogous to the description of narrow-band ferromagnetism [20–22]. As was mentioned above, the exchange parameter is subject to renormalization if the external pressure is applied. This way the phase transition at change of interplane to intraplane coupling [33] can be reproduced.

Let us consider two alternating sublattices A and B, with opposite magnetizations and occupancy operators

$$\begin{aligned} \left\langle X_p^{\uparrow} \right\rangle &= \frac{n+m}{2}, \quad \left\langle X_p^{\downarrow} \right\rangle = \frac{n-m}{2}, \\ \left\langle X_l^{\uparrow} \right\rangle &= \frac{n-m}{2}, \quad \left\langle X_l^{\downarrow} \right\rangle = \frac{n+m}{2}, \end{aligned} \tag{30}$$

where index p marks sublattice A sites and indes l is reserved for B sublattice, m stands for the sublattice magnetization.

Equation for single electron Green function

$$G^{\uparrow}_{pp'}(E) = \left\langle\left\langle X^{0\uparrow}_{p} \;\middle|\; X^{\uparrow 0}_{p'}\right\rangle\right\rangle_{E} \tag{31}$$

with taking into account the exchange interaction in the mean-field approximation has the form

$$\begin{aligned}\left(E - z\left\langle X^{\downarrow}_{l}\right\rangle J_a\right)G^{\uparrow}_{pp'}(E) &= \frac{\delta_{pp'}}{2\pi}\langle X^{\uparrow}_{p} + X^{0}_{p}\rangle \\ &- \sum_{l} t(pl)\left(\left\langle\left\langle\left(X^{\uparrow}_{p} + X^{0}_{p}\right)X^{0}_{l}|X^{\uparrow 0}_{p'}\right\rangle\right\rangle + \left\langle\left\langle X^{\downarrow\uparrow}_{p}X^{0\downarrow}_{l}|X^{\uparrow 0}_{p'}\right\rangle\right\rangle\right).\end{aligned} \tag{32}$$

Let us apply the projection procedure

$$\left[X^{0\uparrow}_{p}, H_t\right] = \sum_{j}\varepsilon^{\uparrow}(pj)X^{0\uparrow}_{j}, \tag{33}$$

where H_t includes all the translational processes in the effective Hamiltonian. Anti-commuting of (33) with operators $X^{\uparrow 0}_{p}$, $X^{\downarrow 0}_{p}$, gives

$$\left(X^{\uparrow}_{p} + X^{0}_{p}\right)\varepsilon^{\uparrow}(pp) = -\sum_{l} t(pl)X^{\downarrow 0}_{p}X^{0\downarrow}_{l}, \tag{34}$$

$$\left(X^{\uparrow}_{l} + X^{0}_{l}\right)\varepsilon^{\uparrow}(pl) = \left(\left(X^{\uparrow}_{p} + X^{0}_{p}\right)\left(X^{\uparrow}_{l} + X^{0}_{l}\right) + X^{\downarrow\uparrow}_{p}X^{\uparrow\downarrow}_{l}\right)t(pl), \tag{35}$$

where $\varepsilon^{\uparrow}(ij)$ are non-operator expressions calculated by method of works [23, 30].

In an analogous way, we process Green function

$$T^{\uparrow}_{lp}(E) = \left\langle\left\langle X^{0\uparrow}_{l}|X^{\uparrow 0}_{p}\right\rangle\right\rangle_{E}. \tag{36}$$

After Fourier transformation, we obtain a closed set of equation for functions (31) and (36):

$$\left(E + \mu + \varepsilon^{\uparrow}_{p} - z\langle X^{\downarrow}_{p}\rangle J_a\right)G^{\uparrow}_{\vec{k}}(E) = \frac{\left\langle X^{\uparrow}_{p} + X^{0}_{p}\right\rangle}{2\pi} + \varepsilon^{\uparrow}\left(\vec{k}\right)T^{\uparrow}_{\vec{k}}(E), \tag{37}$$

$$\left(E + \mu + \varepsilon^{\uparrow}_{l} - z\langle X^{\downarrow}_{p}\rangle J_a\right)T^{\uparrow}_{\vec{k}}(E) = \tilde{\varepsilon}^{\uparrow}\left(\vec{k}\right)G^{\uparrow}_{\vec{k}}(E), \tag{38}$$

where $G^{\uparrow}_{\vec{k}}(E)$, $T^{\uparrow}_{\vec{k}}(E)$, $\varepsilon^{\uparrow}(E)$ are Fourier transforms of $G^{\uparrow}_{pp'}(E)$, $T^{\uparrow}_{pp'}(E)$, $\varepsilon^{\uparrow}(pl)$, respectively; $\tilde{\varepsilon}^{\uparrow}\left(\vec{k}\right)$ is obtained from $\varepsilon^{\uparrow}\left(\vec{k}\right)$ by substitution $m \to m$.

From Eqs. (37) and (38), we obtain

$$G_{\vec{k}}^{\uparrow}(E) = \frac{1}{2\pi} \cdot \frac{\left\langle X_p^{\uparrow} + X_p^{0} \right\rangle \left(E + \mu + \varepsilon_l^{\uparrow} - z \left\langle X_p^{\downarrow} \right\rangle J_a \right)}{\left(E + \mu + \varepsilon_{pl}^{\uparrow} - z \left\langle X_l^{\downarrow} \right\rangle J_a \right) \left(E + \mu + \varepsilon_l^{\uparrow} - z \left\langle X_p^{\downarrow} \right\rangle J_a \right) - \varepsilon^{\uparrow}\left(\vec{k}\right) \tilde{\varepsilon}^{\uparrow}\left(\vec{k}\right)}. \tag{39}$$

It is important that the spin-dependent shifts ε_p^{σ} and ε_l^{σ} of the corresponding subbands actually lead to the reduction of the indirect exchange interaction integral for the case of a partially filled band. To make an estimation of such renormalization let us compute ε_i^{σ} by averaging expression (34) and do the same for $\varepsilon_l^{\uparrow}$. We obtain

$$\varepsilon_p^{\uparrow} = -2\varepsilon/(2 - n + m), \quad \varepsilon_l^{\uparrow} = -2\varepsilon/(2 - n - m), \tag{40}$$

where

$$2\varepsilon = -\frac{2}{N} \sum_l t(pl) \left\langle X_p^{\downarrow 0} X_l^{0\downarrow} \right\rangle \tag{41}$$

is the mean energy of translational motion of electrons in the lower subband.

Thus, taking into account the spin-dependent shift of the subband centres leads to the renormalization of chemical potential

$$\mu + \frac{znJ_a}{2} - \frac{\varepsilon(2 - n)}{(2 - n)^2 - m^2} \to \mu \tag{42}$$

and indirect exchange integral

$$J_a + \frac{2\varepsilon}{(2 - n)^2 - m^2} \to \tilde{J}_a \tag{43}$$

whereas $\varepsilon < 0$, one always has $\tilde{J}_a < J_a$, which is a natural consequence of the destabilizing role of translational motion on antiferromagnetic ordering of localized magnetic moments. Therefore, the necessary (but not sufficient) condition for antiferromagnetism is

$$J_a > \frac{2|\varepsilon|}{(2 - n)^2}. \tag{44}$$

Similar results are obtained if ε_i^{σ} is calculated within the mean-field approach. Then, we have

$$\varepsilon^{\uparrow}(p) = w(1 - n)\left(n^2 - m^2\right)^{1/2}/(2 - n + m), \tag{45}$$

$$\varepsilon^{\uparrow}(l) = w(1 - n)\left(n^2 - m^2\right)^{1/2}/(2 - n - m), \tag{46}$$

the renormalized exchange integral is

$$\tilde{J} = J_a - \frac{2w(1-n)\left(n^2-m^2\right)^{1/2}}{(2-n)^2-m^2} \tag{47}$$

and instead of condition (44) one has

$$w(2-n)^2 > z(1-n)nU. \tag{48}$$

For calculation of averages $\left\langle X_p^{\uparrow}\right\rangle$, we rewrite Green function (39) in the form

$$G_{\vec{k}}^{\uparrow}(E) = \frac{\left\langle X_p^{\uparrow} + X_p^0\right\rangle}{2\pi}\left(\frac{A_{\vec{k}}}{E+\mu-\omega^{\uparrow}\left(\vec{k}\right)} + \frac{B_{\vec{k}}}{E+\mu+\omega^{\uparrow}\left(\vec{k}\right)}\right), \tag{49}$$

where, in analogy to result of [34]

$$\omega^{\uparrow}\left(\vec{k}\right) = \left(\frac{z^2m^2\tilde{J}^2}{4} + \varepsilon^{\uparrow}\left(\vec{k}\right)\tilde{\varepsilon}^{\uparrow}\left(\vec{k}\right)\right)^{1/2}, \tag{50}$$

$$A_{\vec{k}} = \frac{1}{2}\left(1 + \frac{zm\{\tilde{J}}{2\omega^{\uparrow}\left(\vec{k}\right)}\right), B_{\vec{k}} = \frac{1}{2}\left(1 - \frac{zm\{\tilde{J}}{2\omega^{\uparrow}\left(\vec{k}\right)}\right). \tag{51}$$

The spectral densities of Green functions $G_{\vec{k}}^{\uparrow}(E)$ are given by expressions

$$J_{\vec{k}}^{\uparrow}(E) = \frac{\left\langle X_p^{\uparrow} + X_p^0\right\rangle}{\exp(E/\theta)+1}\left(A_{\vec{k}}\delta\left(E+\mu-\omega^{\uparrow}\left(\vec{k}\right)\right) + B_{\vec{k}}\delta\left(E+\mu+\omega^{\uparrow}\left(\vec{k}\right)\right)\right). \tag{52}$$

Therefore,

$$\left\langle X_p^{\uparrow}\right\rangle = \frac{2-n+m}{4N}\sum_{\vec{k}}\left(\frac{A_{\vec{k}}}{\exp\left(\frac{-\mu+\omega^{\uparrow}\left(\vec{k}\right)}{\theta}\right)+1} + \frac{B_{\vec{k}}}{\exp\left(\frac{-\mu-\omega^{\uparrow}\left(\vec{k}\right)}{\theta}\right)+1}\right). \tag{53}$$

Expression for $\left\langle X_p^{\downarrow}\right\rangle$ can be obtained from (53) by substitution $m \to -m$. As a result, we obtain the system of equations for magnetization m and chemical potential μ

$$m = \left\langle X_p^{\uparrow}\right\rangle - \left\langle X_p^{\downarrow}\right\rangle, \tag{54}$$

$$n = \langle X_p^{\uparrow} \rangle + \langle X_p^{\downarrow} \rangle, \tag{55}$$

which may serve as a starting point for studies of effect of the lattice type (through density of states shape [35]), carrier concentration change and the external pressure application.

5 Spin Wave Spectrum for a Narrow-Band Antiferromagnet

Calculation of the antiferromagnon energy directly from the Hamiltonian in electron operators may result in dependency of the spin wave energy on the model parameter as $E_k \sim t_k$ instead of $E_k \sim J_a$ which causes inaccurate description of physical characteristics of antiferromagnetic material. Spin wave treatment of the effective Hamiltonian (18) does not have such deficiency. Let us introduce Green functions

$$G_{pk}(E) = \left\langle\left\langle X_p^{\uparrow\downarrow} \;\middle|\; X_k^{\downarrow\uparrow}\right\rangle\right\rangle_E, \tag{56}$$

$$T_{lp'}(E) = \left\langle\left\langle X_l^{\uparrow\downarrow} \;\middle|\; X_k^{\downarrow\uparrow}\right\rangle\right\rangle_E, \tag{57}$$

where $X_p^{\downarrow\uparrow}$ is an operator of antiferromagnon creation at site p of sublattice A, $X_l^{\downarrow\uparrow}$ is an operator of antiferromagnon creation at site l of sublattice B.

Equation for Green function for $G_{pk}(E)$ with exchange interaction treated in the mean-field approximation is

$$\begin{aligned}(E - zmJ_a)\, G_{pk}(E) = \frac{m}{2\pi}\delta_{pk} - m\sum_l J_a(pl)T_{lk} \\ + \sum_l t(pl)\left\langle\left\langle\left[X_p^{\uparrow\downarrow}, H_t\right]\middle|\; X_k^{\downarrow\uparrow}\right\rangle\right\rangle,\end{aligned} \tag{58}$$

where the result of $X_p^{\uparrow\downarrow}$-operator commutation with the translational terms of the Hamiltonian is

$$\left[X_p^{\uparrow\downarrow}, H_t\right] = \sum_l t\left(p'l\right)\left(X_p^{\uparrow 0}X_l^{0\downarrow} - X_l^{\uparrow 0}X_p^{0\downarrow}\right). \tag{59}$$

Using properties of X_i^{kl}—operators we may rewrite the last term as

$$\sum_l t\left(p'l\right)\left\langle\left\langle\left(X_p^{\uparrow\downarrow}X_p^{0\downarrow}X_l^{0\downarrow} - X_l^{\uparrow\downarrow}X_l^{\downarrow 0}X_p^{0\downarrow}\right)|X_{p'}^{\downarrow\uparrow}\right\rangle\right\rangle. \tag{60}$$

Let us assume that

$$\begin{aligned}\left\langle\left\langle X_p^{\uparrow\downarrow} X_p^{0\downarrow} X_l^{0\downarrow} \;\middle|\; X_{p'}^{\downarrow\uparrow}\right\rangle\right\rangle &\approx \left\langle\left\langle X_p^{\uparrow\downarrow} \;\middle|\; X_{p'}^{\downarrow\uparrow}\right\rangle\right\rangle\left\langle X_p^{0\downarrow} X_l^{0\downarrow}\right\rangle,\\ \left\langle\left\langle X_l^{\uparrow\downarrow} X_l^{\downarrow 0} X_p^{0\downarrow} \;\middle|\; X_{p'}^{\downarrow\uparrow}\right\rangle\right\rangle &\approx \left\langle\left\langle X_l^{\uparrow\downarrow} \;\middle|\; X_{p'}^{\downarrow\uparrow}\right\rangle\right\rangle\left\langle X_l^{\downarrow 0} X_p^{0\downarrow}\right\rangle.\end{aligned} \tag{61}$$

For Green function (57) one obtains the following equation

$$(E + zmJ_\alpha)T_{lp'}(E) = \sum_p t(lp)\left(X_l^{\uparrow 0} X_p^{0\downarrow} - X_p^{\uparrow 0} X_l^{0\downarrow}\right) - m\sum_p J_\alpha(pl)G_{pp'}(E), \tag{62}$$

Transformations of (62) allow obtaining the system of equations in $\vec{k}$-representation.

$$\begin{aligned}\left(E - zm\{\tilde{J}\alpha\right)G_{\vec{k}}(E) &= \frac{m}{2\pi} + m\tilde{J}_\alpha\left(\vec{k}\right)T_{\vec{k}}(E),\\ \left(E + zm\{\tilde{J}\alpha\right)T_{\vec{k}}(E) &= -m\tilde{J}_\alpha\left(\vec{k}\right)G_{\vec{k}}(E),\end{aligned} \tag{63}$$

where $G_{\vec{k}}(E)$ and $T_{\vec{k}}(E)$ are Fourier transforms of Green functions (56) and (57), and $\tilde{J}_\alpha$ is the exchange integral renormalized by taking into account electron hopping processes.

$$\tilde{J}_\alpha = J_\alpha + \frac{1}{zN}{\sum_{ij}}' t(ij)\left\langle X_i^{\uparrow 0} X_j^{0\uparrow}\right\rangle. \tag{64}$$

We obtain from (63) the Green function

$$G_{\vec{k}}(E) = \frac{1}{2\pi}\cdot\frac{m}{E - E\left(\vec{k}\right)}, \tag{65}$$

with

$$E\left(\vec{k}\right) = m\left(\tilde{J}_\alpha^2 - J_{\vec{k}}^2\right)^{1/2}. \tag{66}$$

Having in mind that

$$-\frac{1}{N}\sum_{ij} t(ij)\left\langle\left\langle X_i^{\uparrow 0} X_j^{0\uparrow}\right\rangle\right\rangle \sim w(1-n) \tag{67}$$

one can see that the translational motion destabilizes antiferromagntic order, as have already been shown above; the $E\left(\vec{k}\right)$ dependence is linear and includes Hubbard parameter U.

6 Conclusions

Electron-operator Hamiltonian for two-dimensional BEDT-TTF compound after transition to configurational representation and canonical transformation takes the form convenient for description of the peculiarities of indirect exchange effects and electron hopping. The obtained Hamiltonian can be tuned for a particular compound of the BEDT-TTF family by choosing appropriate single-electron density of states and model parameters. Such generalization allows one to highlight common features of antiferromagnetic order stabilization in materials with narrow conduction bands due to indirect hopping via localized subsystem. In distinction from standard approach, in the generalized model translational parameters are determined by the indirect exchange through sites with localized electrons. This may considerably renormalize band hopping parameter $t(ij)$ and favour electron localization or the compound metallization. This way in the proposed approach both processes of band and hybridization hopping are characterized.

The effective Hamiltonian in the case of strong electron correlation incorporates indirect exchange in $(\sigma - 0)$- and $(\uparrow\downarrow - \sigma)$-subbands, pair creation and annihilation of doublons and holes, indirect exchange and indirect hopping between localized magnetic moments and allows to obtain results, complimentary to both numerical and analytical studies in more sophisticated methods for less general models [10, 34, 36]. The presence of terms describing the correlated hopping of electrons in the Hamiltonian makes direct application of many standard theoretical methods impossible [23, 24], therefore, approaches of the nonperturbative character must be used for the energy spectrum calculation. In this method, electron processes described by the hybridization terms in the Hamiltonian allow to obtain correct contribution, caused by indirect (kinetic) exchange, to the energy spectrum which may contribute to Neel temperature increase.

References

1. Kino H, Fukuyama H (1996) Phase diagram of two-dimensional organic conductors (BEDT-TTF)$_2$X. J Phys Soc Jpn 65:215821–215869
2. McKenzie RH (1997) Similarities between organic and cuprate superconductors. Science 278:820–821
3. Ishiguro T, Yamaji K, Saito G (1998) Organic superconductors. Springer series in solid-state sciences, vol 88. Springer, Berlin, Heidelberg
4. Powell BJ, McKenzie RH (2006) Strong electronic correlations in superconducting organic charge transfer salts . J Phys: Condens Matter 18:R827–R866
5. Lebed AG (2008) The physics of organic superconductors and conductors. Springer series in materials science, vol 110. Springer, Berlin, Heidelberg
6. Demiralp E, Goddard WA (1997) Conduction properties of the organic superconductor κ-(BEDT-TTF)$_2$Cu(NCS)$_2$ based on Hubbard-unrestricted-Hartree-Fock band calculations. Phys Rev B 56:11907–11919
7. McKenzie R (1998) A strongly correlated electron model for the layered organic superconductors κ-(BEDT-TTF)$_2$X. Comments Cond Matter Phys 18:309–328

8. Scriven E, Powell BJ (2009) Toward the parametrization of the Hubbard model for salts of bis(ethylenedithio)tetrathiafulvalene: a density functional study of isolated molecules. J Chem Phys 130:104508
9. Kuroki K, Aoki H (1999) Superconductivity and spin correlation in organic conductors: a quantum Monte Carlo study. Phys Rev B 60:3060–3063
10. Painelli A, Girlando A, Fortunelli A (2001) Symmetrized mean-field description of magnetic instabilities in $\kappa-(BEDT-TTF)_2Cu[N(CN)]_2Y$ salts. Phys Rev B 64:054509
11. Fortunelli A, Painelli A (1997) On the ab initio evaluation of Hubbard parameters. II. The k-(BEDT-TTF)$_2$Cu[N(CN)$_2$]Br crystal. J Chem Phys 106(19):8051–8057
12. Skorenkyy Yu, Kramar O (2006) Energy spectrum of the organic quasi-1D conductors with NNN and correlated hopping. Condens Matter Phys 9:161–168
13. Skorenkyy Yu, Kramar O (2016) Antiferromagnetic ordering and pseudogap in a model of quasi-1D organic superconductor electronic subsystem. Mol Cryst Liq Cryst 639:24–32
14. Maesato M, Kaga Y, Kondo R, Kagoshima S (2001) Control of electronic properties of $\alpha-(BEDT-TTF)_2MHg(SCN)_4$ (M=K,NH_4) by the uniaxial strain method. Phys Rev B 64:155104
15. Tanatar MA et al (2002) Pressure-temperature phase diagram of the organic superconductor $\kappa-(BEDT-TTF)_2Cu[N(CN)_2I$. Phys Rev B 65:064516
16. Kanoda K, Kato R (2011) Mott physics in organic conductors with triangular lattices. Ann Rev Cond Matter Phys 2(1):167–188
17. Momma K, Izumi F (2011) VESTA 3 for three-dimensional visualization of crystal, volumetric and morphology data. J Appl Crystallogr 44:1272–1276
18. Jeschke HO et al (2012) Temperature dependence of structural and electronic properties of the spin-liquid candidate κ-(BEDT-TTF)$_2$Cu$_2$(CN)$_3$. Phys Rev B 85:035125
19. Fazekas P (1999) Lecture notes on electron correlation and magnetism. World Scientific Publishing, Singapore
20. Didukh L, Kramar O (2002) Metallic ferromagnetism in a generalized Hubbard model. Fizika Nizkikh Temperatur (Kharkov) 28:42–50
21. Didukh L, Kramar O (2005) Metallic ferromagnetism in the systems with strongly correlated electrons. Condens Matter Phys 8:547–564
22. Skorenkyy Y, Didukh L, Kramar O, Dovhopyaty Y (2007) Mott transition, ferromagnetism and conductivity in the generalized Hubbard model. Acta Phys Pol, A 111:635–644
23. Didukh L (2000) A modified form of the polar model of crystals. Acta Phys Pol, B 31(12):3097–3133
24. Skorenkyy Y, Kramar O, Dovhopyaty Y (2020) Electron-hole asymmetry in electron systems with orbital degeneracy and correlated hopping. Condens Matter Phys 23(4):43714
25. Didukh L, Skorenkyy Yu, Dovhopyaty Yu, Hankevych V (2000) Metal-insulator transition in a doubly orbitally degenerate model with correlated hopping. Phys Rev B 61:7893–7908
26. Didukh L, Skorenkyy Yu, Hankevych V, Kramar O (2001) Ground state ferromagnetism in a doubly orbitally degenerate model. Phys Rev B 64:144428
27. Didukh L, Hankevych V, Kramar O, Skorenkyy Yu (2002) Itinerant ferromagnetism of systems with orbital degeneracy. J Phys: Condens Matter 14:827–835
28. Hubbard J (1965) Electron correlation in narrow energy bands. The atomic representation. Proc Roy Soc A 285:542–560
29. Hubbard J (1963) Electron correlations in narrow energy bands. Proc Roy Soc A 276:238–257
30. Didukh L, Skorenkyy Yu, Kramar O (2008) Electron correlations in narrow energy bands: modified polar model approach. Condens Matter Phys 11:443–454
31. Chao KA, Spalek J, Oleś A (1977) The kinetic exchange interaction in double degenerate narrow bands. Phys Stat Sol (B) 84:747–759
32. Anderson PW (1961) Localized magnetic states in metals. Phys Rev 124:41–53
33. Vojta M, Becker KW (1999) Doped bilayer antiferromagnets: Hole dynamics on both sides of a magnetic ordering transition. Phys Rev B 60(22):15201–15213
34. Feldbacher M, Jurecka C, Assaad FF, Brenig W (2002) Single-hole dynamics in the half-filled two-dimensional Kondo-Hubbard model. Phys Rev B 66:045103

35. Kramar O, Skorenkyy Yu, Dovhopyaty Yu (2019) Effective masses of carriers in the degenerate conduction band: interplay of density of electronic states peculiarities and magnetization. J Nano- Electron Phys 11:05030(6)
36. Gorski G, Mizia J (2004) Magnetic ordering of itinerant systems: the role of kinetic interactions. Phys B: Cond Matter 344:231–242

Theoretical Basics of Final Drying of Ammonium Nitrate with Nanoporous Structure in Gravitational Shelf Dryers

N. O. Artyukhova, J. Krmela, and V. Krmelova

1 Introduction

The technology of the convection drying is one of the most efficient and widely used technologies in chemical and food industries [1, 2]. Complemented by the fluidization technique, this method allows achieving the high-quality dryable product [3, 4]. However, the fluidization technique involves high expenses for the drying agent charge and insurance of its motion in the device at the velocity, necessary for the formation of the fluidized system [5].

The most intensive dehydration (given the constant drying velocity) in the apparatus with a fluidized bed is conducted directly close to the gas-distributing lattice, in the so-called active zone [6]. Providing the high capacity of the apparatus, only a part of the dryable material is located in the "active" zone. Thus, the general rate of dehydration is lower, and it leads to the increasing volume of the drying device (the decreasing specific capacity of the device) [7]. A solution to the permanent residence of the disperse material in the "active" zone can be found through the implementation of the multistage shelf dryers with vertical sectioning of the workspace (Fig. 1).

N. O. Artyukhova (✉)
Department of Marketing, Sumy State University, 2, Rymskogo-Korsakova str, Sumy 40007, Ukraine
e-mail: a.artyukhov@pohnp.sumdu.edu.ua

J. Krmela
Department of Numerical Methods and Computational Modeling, Alexander Dubcek University of Trencin, 491/30, I. Krasku, 02001 Puchov, Slovak Republic
e-mail: jan.krmela@fpt.tnuni.sk

V. Krmelova
Department of Materials Technologies and Environment, Alexander Dubcek University of Trencin, 491/30, I. Krasku, 02001 Puchov, Slovak Republic
e-mail: vladimira.krmelova@fpt.tnuni.sk

O. Fesenko and L. Yatsenko (eds.), *Nanomaterials and Nanocomposites, Nanostructure Surfaces, and Their Applications*, Springer Proceedings in Physics 263, https://doi.org/10.1007/978-3-030-74741-1_17

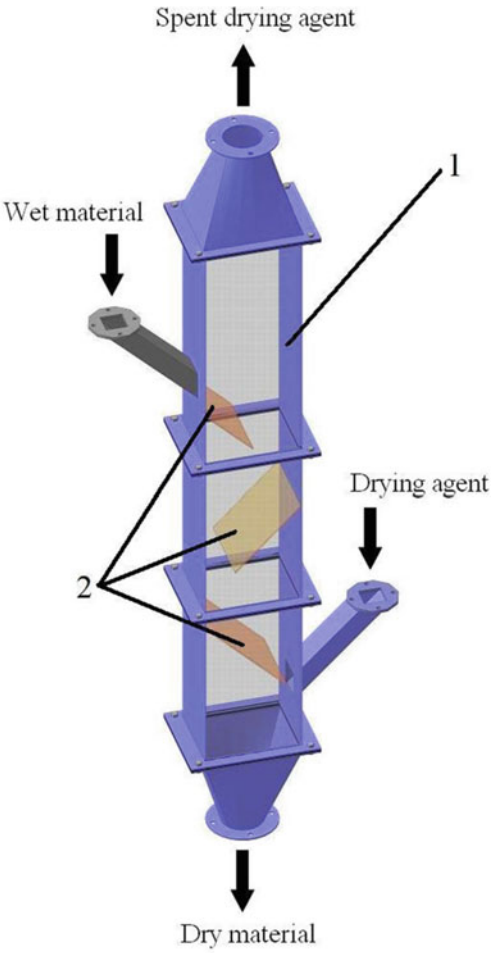

Fig. 1 Multistage shelf dryer: **1**—case; **2**—shelf

These devices operate in active hydrodynamic regimes with the formation of the developed phases contact areas. The use of the active hydrodynamic regimes in the drying [8–11] and the granulation [10, 12–15] technologies is a rather efficient method to boost the process and to downsize the equipment. Different constructions of the shelves (Fig. 2) enable us to control the residence time of the disperse phase in the workspace of the dryer.

The constructions of shelf dryers can be successfully applied to obtain porous ammonium nitrate granules (PAN) using the technology shown in Fig. 3. The final drying stage allows obtaining a developed network of deep curvilinear nanopores and reducing the residual moisture content of the granules. The system of deep curvilinear nanopores lets reliably retain diesel distillate in the PAN granule. The low residual moisture content of the PAN granule allows it be transported over long distances without losing its mechanical properties (in particular, strength).

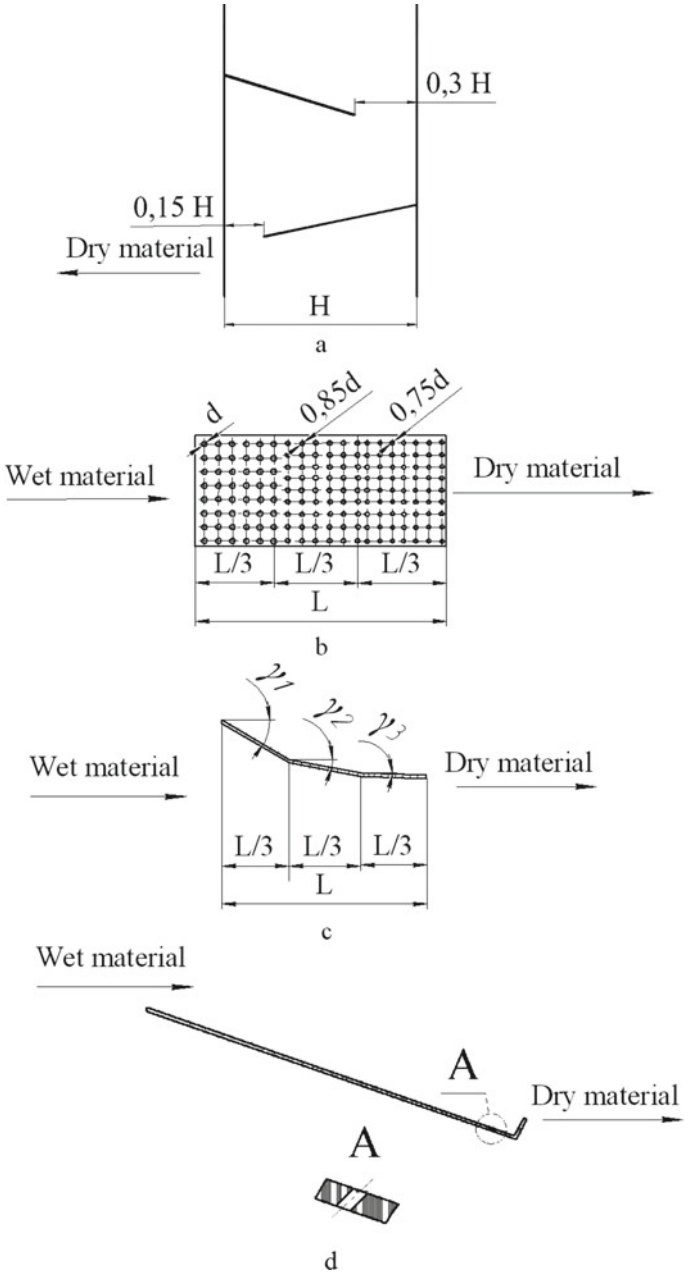

Fig. 2 Constructions of shelves of multilevel gravitational shelf dryer: **a**—shelf with different gap on height of dryer; **b**—sectioned shelf with variable perforation of sections; **c**—partitioned sections shelf with constant perforation and variable angle of inclination; **d**—shelf with stopper; d—diameter of hole of perforation; L—length of the shelf; H—width of device; γ_i—angle of inclination of shelf section to horizon

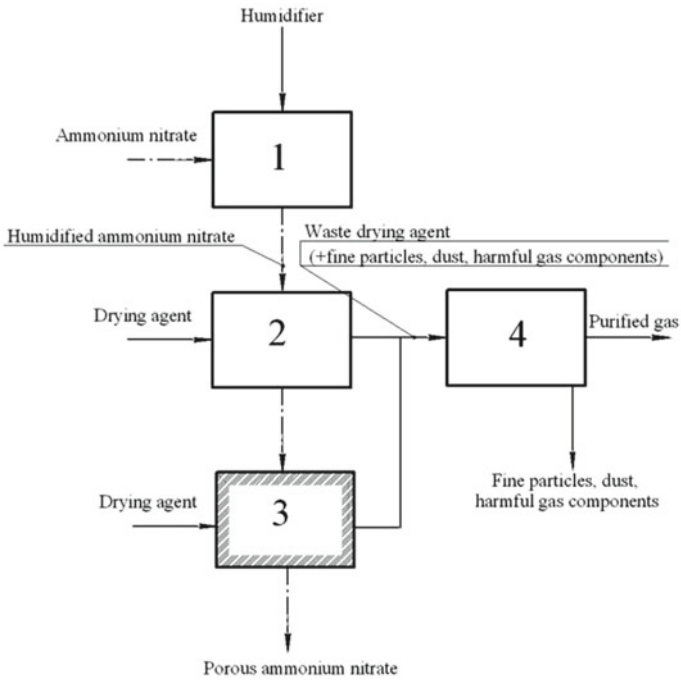

Fig. 3 Scheme of PAN obtaining process [16, 17]: **1**—humidification of ammonium nitrate granule; **2**—granulation drying; **3**—final drying; **4**—cleaning of waste gas

It is necessary to solve the following tasks to successfully simulate the formation of a nanoporous structure on the surface and near-surface layers of a PAN granule:

1. computer simulation of the hydrodynamic operating conditions for a gravitational shelf dryer to find the optimal hydrodynamic regime to obtain a developed nanoporous structure of PAN;
2. modeling the heating and dehydration kinetics to ensure optimal thermodynamic conditions for obtaining a nanoporous PAN structure;
3. investigation of the PAN nanoporous structure morphology, obtained in different periods of the drying process according to the classification adopted for this process.

Given the set tasks, the following three sections present the results of solution. A dryer with shelves with different gap on height of dryer is a prototype of those constructions shown in Fig. 2.

2 Hydrodynamics of Flows Motion

The multistage gravitational shelf dryer (Fig. 1):

- a type of the suspension bed—gravitational falling or cross-moving;
- a method of formation of various hydrodynamic conditions for the motion of the disperse phase in the device—sectioning of the workspace by the perforated shelf contacts with a varied angle of slope toward the horizon, a varied length and a varied level of perforation.

The hydrodynamic conditions of the dispersed phase and the gas flow movement provide a crucial impact on the operational character of the suspension bed of solid particles and their residence time in the workspace. Particles of different diameters under one and the same velocity of the gas flow may remain either fixed or suspended, or they are being removed from the device. Therefore, a velocity distribution profile of the presented devices is to be determined.

The objective of this part of work is to show how the optimal "geometry" of the workspace is selected as exemplified in the computer modeling of the hydrodynamics of the gas flow movement in the devices with various configurations of the suspension bed. The modeling is performed according to the original mathematical model, described in the works [10, 13–15] for multistage gravitational shelf dryers, and it is based on the Navier–Stokes equations (for instantaneous velocities) and the Reynolds equation (for average velocities) of the gas flow movement.

The proposed algorithm allows users to perform the optimization calculation for the main technological elements of the granulation unit at a stage of its design avoiding expensive multifactor experiment. The peculiarities of the software products also enable re-adjustment of the equipment to the changes in characteristics of raw materials and productivity of the unit.

The calculation results, for example, the following:

- minimal "hydrodynamic" residence time of the particles in the device, which will not exceed "thermodynamic" time (minimal time of the dehydration of particles to a standard indictor; is determined by the laws of dehydration kinetics and thermodynamic indicators of the dehydration);
- use of various temperature and moisture potentials of the heating agent in a separate parts of the unit;
- variations of the unit construction;
- possibility to apply recycling of the heating agent.

The calculations of the hydrodynamics of the highly turbulent flows are based on the classical equations of hydrodynamics. Considering that these equations are mostly nonlinear and there is no analytical solution without simplifications and suppositions, the numerical methods (DEM—discrete element method in particular) should be used to perform modeling. Herewith, instead of a continuous solution, a discrete set of target values is determined in the particular place (a cell or a grid node) of the area (given the stationary movement of flows). To achieve the maximum

precision of the solution, one should select a way of the presentation of the discrete values, which corresponds to the analogs of the algebraic equations for such a discrete sampling. Thus, a mathematical solution of the system of the differential and integral equations resolves into a solution of the system of algebraic equations.

The numerical solving of the equations of mathematical models is performed in one pass from the inlet section of the working volume to the outlet section. The finite volumes method with components of the finite element approach is used in the solution. Calculations are preceded by the building of the calculation grid, where unknown values of the velocities are found in the grid nodes.

The presented results are obtained through computer modeling of the installation, which is built according to the research and industrial samples of the equipment and the original analytical model, executed in the applied program.

Based on the results of the computer modeling (Figs. 4 and 5), the following functional zones in the workspaces of the vortex granulator and the multistage gravitational shelf dryer are separated:

- a stabilization zone for the gas flow movement;
- a separation zone;
- a drainage zone for the fine granules;
- a gas outlet zone.

The hydrodynamic characteristics of the gas flow movement in the mentioned zones allow a user to calculate the classification process of the granules and their separation after the outlet from the workspace.

The calculations of the hydrodynamics of the highly turbulent flows are based on the classical equations of hydrodynamics. Considering that these equations are mostly nonlinear and there is no analytical solution without simplifications and suppositions, the numerical methods (DEM—discrete element method in particular) should be used to perform modeling. Herewith, instead of a continuous solution a discrete set of target values is determined in the particular place (a cell or a grid node) of the area (given the stationary movement of flows). To achieve the maximum precision of the solution, one should select a way of the presentation of the discrete values, which corresponds to the analogs of the algebraic equations for such a discrete sampling. Thus, a mathematical solution of the system of the differential and integral equations resolves into a solution of the system of algebraic equations.

The numerical solving of the equations of mathematical models is performed in one pass from the inlet section of the working volume to the outlet section. The finite volumes method with components of the finite element approach is used in the solution. Calculations are preceded by the building of the calculation grid, where unknown values of the velocities are found in the grid nodes.

The presented results are obtained through computer modeling of the installation, which is built according to the research and industrial samples of the equipment and the original analytical model, executed in the applied program.

Based on the results of the computer modeling (Figs. 3 and 4), the following functional zones in the workspaces of the multistage gravitational shelf dryer are separated:

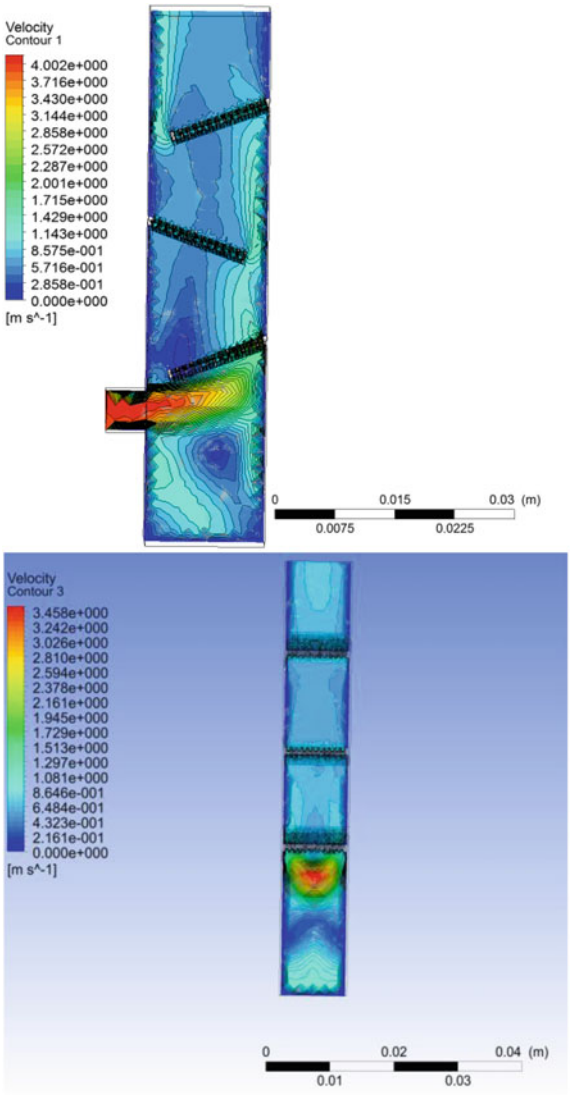

Fig. 4 Velocity field of the gas flow in the workspace of the multistage gravitational shelf dryer

- a stabilization zone for the gas flow movement;
- a separation zone;
- a drainage zone for the fine granules;
- a gas outlet zone.

The hydrodynamic characteristics of the gas flow movement in the mentioned zones allow a user to calculate the classification process of the granules.

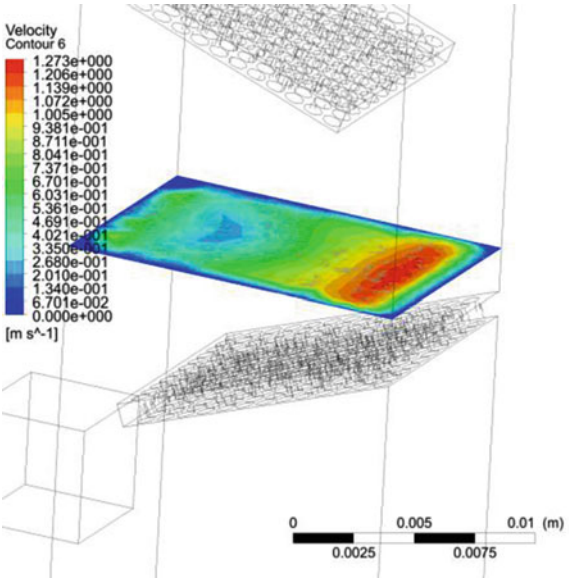

Fig. 5 Velocity field of the gas flow in the workspace of the multistage gravitational shelf dryer

3 Kinetics of Drying

Consider the typical diagram of the decreasing moisture of a particle from its initial heating (area AB), on the constant velocity area (BC) till the period of the reducing velocity of the process (CD) (Fig. 6).

The influence of one or another partial mass transfer mechanism on each stage is different. However, the gradient nature of the moisture transferring from the central layers of the particle into the drying agent flow may be considered as a generalized approach to the development of the optimization model.

Consider the flow moisture characteristics on the i-stage of the dryer (Fig. 7).

The calculation scheme shows that the maximum difference of moisture contents on the stage complies with the difference of the initial moisture of the disperse material (or the final moisture of the material, supplied from the preceding stage) and the initial moisture of the drying agent, that is, $\Delta x_{\max} = x_{i-1} - b_i$. The removal of moisture, on the other hand, is $\Delta x = x_{i-1} - x_i$ on the stage of the disperse material. $\Delta x / \Delta x_{\max}$ ratio characterizes the effectiveness of the moisture removal on the i-stage E_i.

Providing that the drying curve is exponential $U = \exp(-B_i \tau_i)$ [13], we assume that the drying effectiveness in relation to the moisture reduction is also an exponential function (Fig. 2b). This assumption is based on the theoretical approach to the description of other heat and mass transfer processes [10, 14] by considering that the increase of the moisture removal intensity is proportional to the increase of the drying effectiveness E_i. It should be mentioned that the quantity of the removed moisture per time unit decreases when the drying time increases, and the drying effectiveness

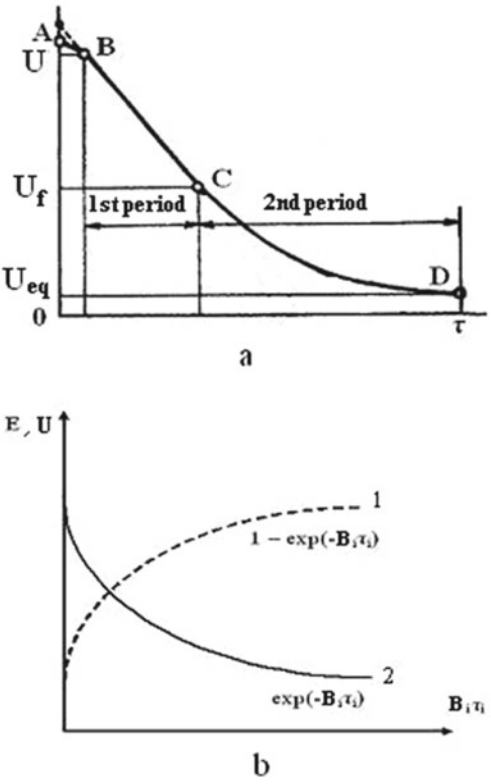

Fig. 6 Graphic visualization of the drying: **a**—a typical graph of the drying; **b**—an exponential model of the drying for one stage of the dryer: **1**—drying effectiveness; **2**—theoretical reduction of moisture on the i-stage of the dryer; $B_i\tau_i$—the kinetic characteristics of the process; τ_i—the contact time of the material with the drying agent on the i-stage of the dryer; U—current moisture of the material; U_{fin}—final moisture of the material in the first period; U_{eq}—equilibrium moisture of the material

E_i shows its peak growth in response to the increase of the drying time τ_i on the stage. When the drying time increases, $\frac{\Delta x}{\Delta x_{\max}} \to 1$ and $E_i \to 1$.

With the current drying time, the formula is

$$E_i = 1 - \exp(-B_i\tau_i) \tag{1}$$

To increase the difference $x_{i-1} - x_i$ and to reach the maximum possible value of E_i on the stage is possible due to the increase of the drying agent consumption G_{dr} in relation to the disperse material consumption $G_m\left(G_i^{-1} = {}^{G_m}/_{G_{dr}}\right)$. To determine an influence of the ratio of consumption to the drying effectiveness, put (1) to G_i^{-1} in the form of $1 + G_i^{-1}$ (and add this value to the pre-exponential expression).

Considering the above-mentioned assumptions, the drying effectiveness on the *i*-stage of the dryer is presented in the form of a ratio of differences between the moisture contents of the disperse material before and after the drying $x_{i-1} - x_i$ to the maximum possible (theoretical) difference between the moisture contents on the stage $x_{i-1} - b_i$, and also in the form of the function of the kinetic parameter of the moisture transfer B_i, the residence time of the material on the stage τ_i and the consumption ratio of the dispersed phase to the drying agent G_i^{-1}.

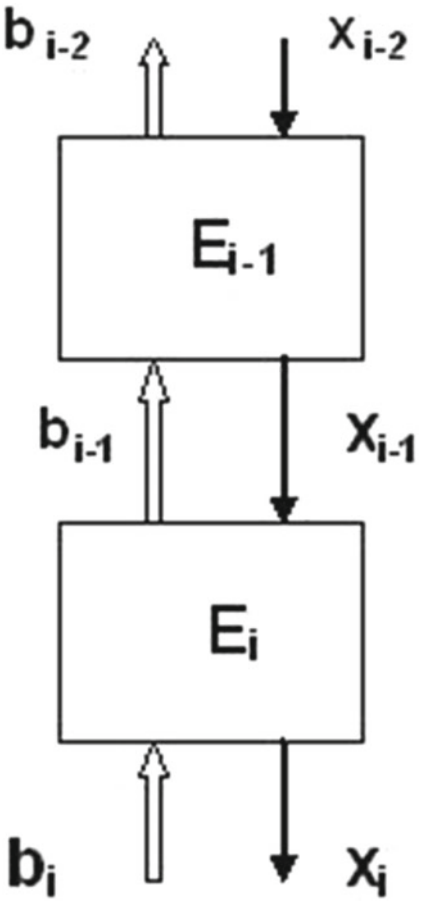

Fig. 7 Fragment of the calculation scheme for the multistage drying: x—moisture of the disperse material; b—moisture of the drying agent

$$E_i = \frac{\Delta x}{\Delta x_{\max}} = \frac{x_{i-1} - x_i}{x_{i-1} - b_i} = \frac{1 - \exp\left[-B_i \tau_i (1 + G_i^{-1})\right]}{1 + G_i^{-1}} \tag{2}$$

It should be mentioned that at large values of $B_i \tau_i$ (till the maximum point—perpetual residence time of the material on the stage), this expression will have the numerator of 1 $\left(\exp\left[-B_i \tau_i (1 + G_i^{-1})\right] = 0\right)$, and the effectiveness threshold will depend on the consumption ratio G_m / G_{dr}.

Consider the moisture values of the interacted flows on the last two stages of the drying process with the effectiveness E_i and $E_{i\text{-}1}$.

The system of equations connecting the kinetics and the moisture mass balance for the $i - 1$ stage of the dryer is

$$\begin{cases} x_{i-1} = \dfrac{x_i - E_i b_i}{1 - E_i}, \\ b_{i-1} = b_i + \dfrac{G_m}{G_{dr}} E_i (x_{i-1} - b_i). \end{cases} \tag{3}$$

Assume for simplicity that the drying agent (air) contains zero humidity, that is, $b_i = 0$, then the system will be

$$\begin{cases} x_{i-1} = \dfrac{x_i}{1 - E_i}, \\ b_{i-1} = \dfrac{G_m}{G_{dr}} E_i x_{i-1}. \end{cases} \tag{4}$$

For the $i - 2$ stage, the system (3) is

$$\begin{cases} x_{i-2} = \dfrac{x_{i-1} - E_{i-1} b_{i-1}}{1 - E_{i-1}}, \\ b_{i-2} = b_{i-1} + \dfrac{G_m}{G_{dr}} E_{i-1} (x_{i-2} - b_{i-1}) \end{cases} \tag{5}$$

Considering (4), the moisture of the disperse material before the $i - 1$ stage of the dryer will depend on the initial humidity of the air b_i and the final moisture of the material after x_i. Therefore

$$x_{i-2} = \frac{\frac{x_i}{1-E_i} - \frac{G_m}{G_{dr}} E_{i-1} E_i \frac{x_i}{1-E_i}}{1 - E_{i-1}} = \frac{x_i (1 - \frac{G_m}{G_{dr}} E_{i-1} E_i)}{(1 - E_{i-1})(1 - E_i)} \tag{6}$$

Thus, the simplest approximations of the effectiveness of two neighboring stages of the dryer with the fixed ratio of the interacted flows consumption to the drying agent consumption $G_i^{-1} = {G_m}/{G_{dr}}$ provide the maximum moisture excess of the material, supplied to the cascade, over the final moisture of the material x_i, providing the equal effectiveness of the stages, that is, $E_{i\text{-}2} = E_{i\text{-}1}$.

Figure 8 shows the calculation results regarding the moisture field of disperse material and drying agent at various stages of the shelf dryer.

4 Morphology of PAN Granule Structure

Physicochemical studies of the morphology of PAN samples were performed by scanning electron microscopy with EDX analysis.

Electron microscopy data are processed using the image processing proprietary software (Fig. 9). In the course of the analysis, the following morphological features are determined:

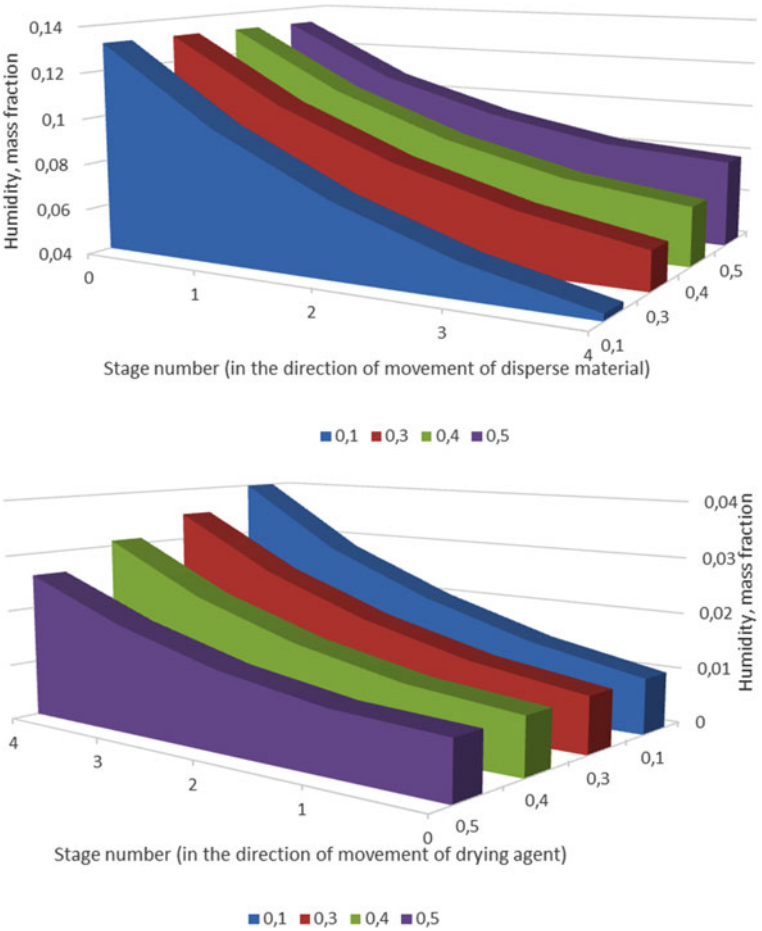

Fig. 8 Moisture field of the disperse material and drying agent

- the shape of nanopores;
- the depth of nanopores;
- the number of nanopores and the relative area of the nanoporous surface.

The results of the analysis (Fig. 10) provide the following conclusions:

- nanoporous structure is uniform over the entire surface of the shell and occupies from 65 to 75% for different samples;
- morphology of the porous structure includes rectilinear and curved nanopores, the depth of which ranges from 0.1 to 0.2 of the granule diameter;
- the pores create a developed structure throughout the specified thickness, connecting at different depths (thicknesses);

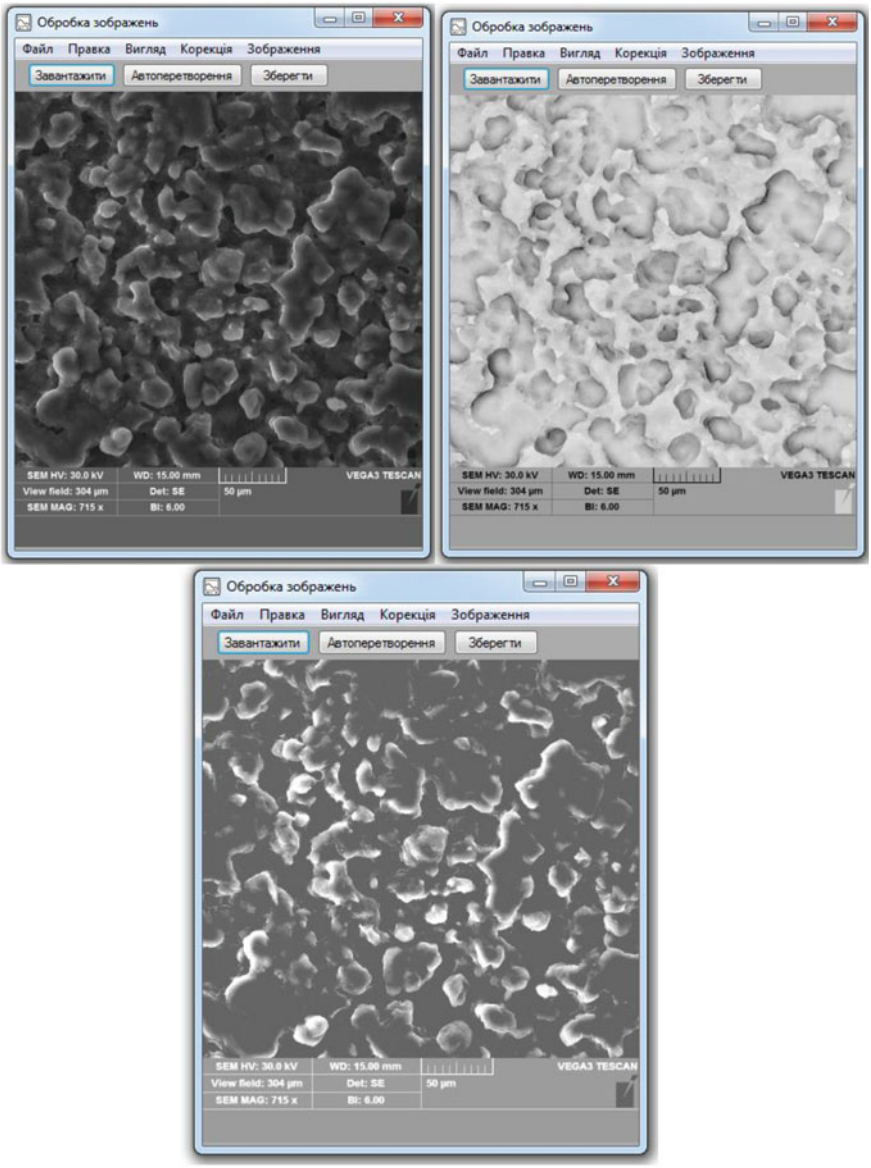

Fig. 9 Interface of the program for studying the morphology of granules

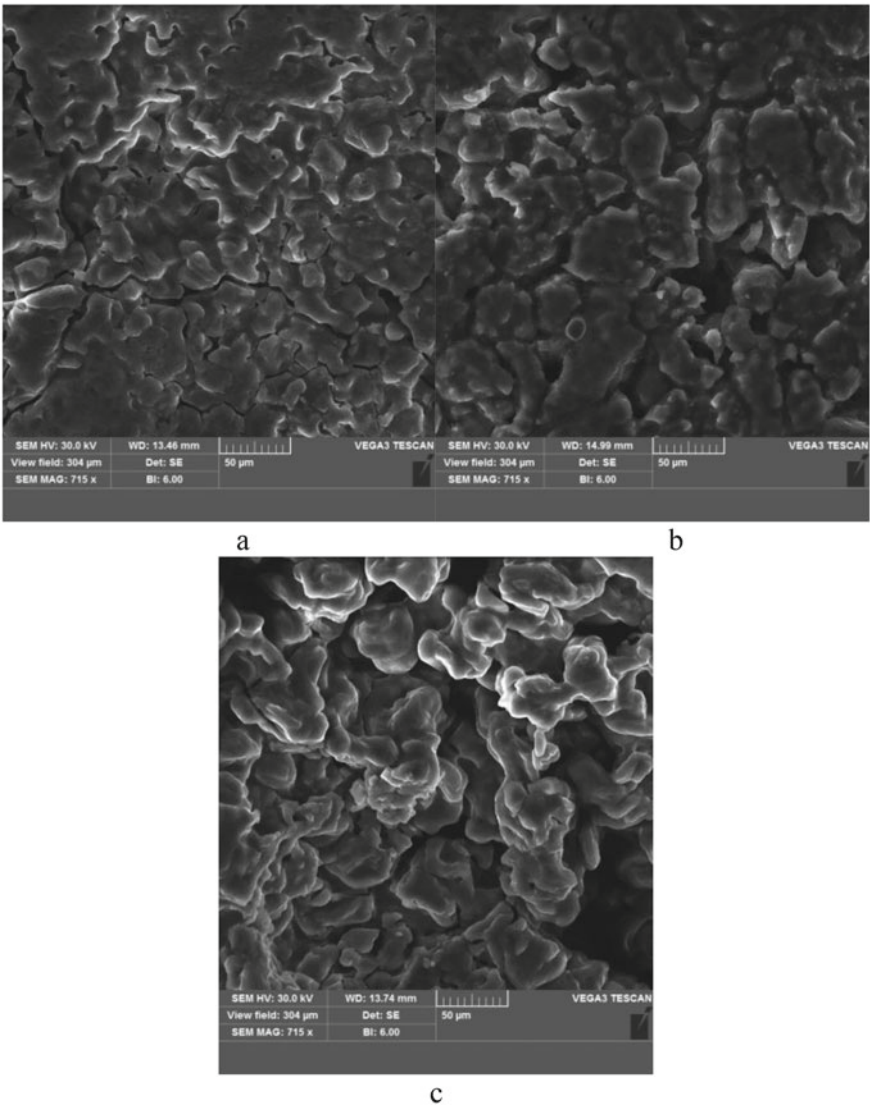

Fig. 10 Morphology of the nanoporous structure of PAN granules: **a**—heating of the granule; **b**—constant drying velocity mode; **c**—decreasing drying velocity mode

- there is a certain amount of "mechanical" pores on the surface, probably formed during the drying of the sample; such pores require further revision of the thermodynamic features in the drying process;
- the formation of a nanoporous structure is practically completed in the constant drying rate mode with optimal hydrodynamic features of the flow;

- drying in the decreasing velocity mode is necessary only to remove residual moisture from the PAN granule and create a network of "empty" pores for further filling with diesel distillate for an industrial explosive.

5 Conclusions

The computer modeling results of the hydrodynamic operating conditions regarding the shelf dryer's operation and theoretical modeling of the moisture content changing in the flow ensure the optimal operational parameters of the device to produce the PAN nanoporous structure successfully. The research results show that the final drying stage in the general technology to obtain PAN with a nanoporous structure makes it possible to create a developed nanoporous structure on the granule's surface and in the near-surface layers.

The PAN sample morphology study with a nanoporous structure shows that nanopores formation is practically completed during the constant drying velocity; it is inappropriate to use a dryer during a decreasing drying velocity period.

Acknowledgements This research work had been supported by the Ministry of Science and Education of Ukraine under the project "Technological bases of multistage convective drying in small-sized devices with utilization and heat recovery units," project No. 0120U100476 and by the Cultural and Educational Grant Agency of the Slovak Republic (KEGA), project No. KEGA 002TnUAD-4/2019.

References

1. Kudra T, Mujumdar AS (2002) Advanced drying technologies. Marcel Dekker, New York
2. Mujumdar AS (2006) Handbook of industrial drying. Taylor & Francis Group, Boca Raton
3. Sinaiski EG (2010) Hydromechanics: theory and fundamentals. WILEY-VCH Verlag GmbH & Co. KGaA, Weinheim
4. Crowe C (2006) Multiphase flow handbook. Taylor & Francis Group, Boca Raton
5. Wan Daud WR (2008) Fluidized bed dryers—recent advances. Adv Powder Technol 19(5):403–418
6. Artyukhova NA (2018) Multistage finish drying of the N HNO porous granules as a factor for nanoporous structure quality improvement. J Nano-Electron Phys 10(3):03030-1-03030-5
7. Artyukhov A, Artyukhova N, Ivaniia A, Gabrusenoks J (2017) Multilayer modified NH NO granules with 3D nanoporous structure: effect of the heat treatment regime on the structure of macro and mezopores. In: Proceedings of IEEE international young scientists forum on applied physics engineering (YSF-2017), pp 315–318
8. Artyukhov AE, Artyukhova NO, Ivaniia AV (2018) Creation of software for constructive calculation of devices with active hydrodynamics. In: Proceedings of the 14th international conference on advanced trends in radioelectronics, telecommunications and computer engineering (TCSET 2018), pp 139–142, April 2018
9. Artyukhova N, Krmela J (2019) Nanoporous structure of the ammonium nitrate granules at the final drying: the effect of the dryer operation mode. J Nano-Electron Phys 11(4). 04006-1-04006-4

10. Obodiak V, Artyukhova N, Artyukhov A (2020) Calculation of the residence time of dispersed phase in sectioned devices: theoretical basics and software implementation. Lect Notes Mech Eng 813–820
11. Artyukhova N (2020) Morphological features of the nanoporous structure in the ammonium nitrate granules at the final drying stage in multistage devices. J Nano-Electron Phys 12(4). 04036-1-04036-6
12. Artyukhov A, Artyukhova N, Krmela J, Krmelová V (2020) Granulation machines with highly turbulized flows: creation of software complex for technological design. IOP Conf Ser Mater Sci Eng 776(1). 012018
13. Artyukhov A, Artyukhova N, Krmela J, Krmelová, V (2020) Complex designing of granulation units with application of computer and software modeling: case vortex granulator. IOP conf ser Mater Sci Eng 776(1), 012016
14. Artyukhov A, Artyukhova N (2018) Utilization of dust and ammonia from exhaust gases: new solutions for dryers with different types of fluidized bed. J Environ Health Sci Eng 16(2):193–204
15. Artyukhov AE, Obodiak VK, Boiko PG, Rossi PC (2017) Computer modeling of hydrodynamic and heat-mass transfer processes in the vortex type granulation devices. CEUR Workshop Proc 1844:33–47
16. Artyukhov AE, Sklabinskyi VI (2017) Investigation of the temperature field of coolant in the installations for obtaining 3D nanostructured porous surface layer on the granules of ammonium nitrate. J Nano-Electron Phys 9(1). 01015-1-01015-4
17. Artyukhov AE, Sklabinskyi VI (2013) Experimental and industrial implementation of porous ammonium nitrate producing process in vortex granulators. Naukovyi Visnyk Natsionalnoho Hirnychoho Universytetu 6:42–48

Influence of the Preparation Method and Magnesium Ions Substitution on the Structure and Magnetic Properties of Lithium-Iron Ferrites

L. S. Kaykan and J. S. Mazurenko

1 Introduction

In recent years, ferrite-spinels of the general formula $(Me, Fe)_3O_4$, where M-divalent cation, attract considerable attention. This is due to not only to their excellent physical and chemical properties, but also to their technological applications, including magnetic storage devices, magnetic diagnostics, magnetic circuits, telecommunications, microwave devices, gas sensors, etc. [1–7] Each field of application requires from ferrites special properties, which can be reached by changing its synthesis conditions.

Ferrites have a high value of magnetization due to the imbalance of the magnetic moments of the lattice, a high value of resistance, low dielectric loss, and high Neel temperature [8–10]. These properties make ferrites universal materials for various technological applications. The crystallographic, electrical, and magnetic properties of ferrites are highly dependent on stoichiometry, as the parameters of the synthesis process, such as temperature, atmosphere, and pressure, affect the distribution of cations occupying tetrahedral (A) and octahedral (B) positions in the spinel lattice [11–14]. Control over the distribution of cations and oxygen parameters is important for the formation of physical properties that are necessary for the use of these materials in industry.

The morphology of the synthesized material, particle size, and their structure significantly affects their physicochemical properties. Thus, the preparation method is decisive even for ferrites of the same composition.

L. S. Kaykan (✉)
G.V. Kurdyumov Institute for Metal Physics, N.A.S. of Ukraine, 36 Academician Vernadsky Boulevard, Kyiv 03142, Ukraine

J. S. Mazurenko
Ivano Frankivsk National Medical University, Halytska Str. 2, Ivano-Frankivsk 76018, Ukraine
e-mail: yumazurenko@ifnmu.edu.ua

O. Fesenko and L. Yatsenko (eds.), *Nanomaterials and Nanocomposites, Nanostructure Surfaces, and Their Applications*, Springer Proceedings in Physics 263, https://doi.org/10.1007/978-3-030-74741-1_18

To establish the effect of the preparation method on the morphology and properties of magnesium-substituted ferrite with a spinel structure, the studied systems were synthesized in two ways. One system was obtained by the method of sol–gel auto combustion (system A) and the other by traditional ceramic method (system B). The structure and electrical properties of both systems are compared, and the influence of the method of preparation and substitution of magnesium ions on the physicochemical properties of the studied ferrites is revealed.

2 Experimental

Magnesium-substituted lithium ferrites of system A were synthesized by the sol–gel auto combustion method [15–17]. The production procedure was as follows: aqueous solutions of metal nitrates were used as starting reagents ($FeNO_3 \cdot 9H_2O$, $LiNO_3 \cdot 3H_2O$, $MgNO_3 \cdot 3H_2O$), taken in the appropriate molar ratio according to the stoichiometry of the expected compounds, as fuel used citric acid. Metal nitrates and citric acid were mixed dropwise on a magnetic stirrer in a molar ratio of metals to citric acid 1:1. The metal nitrate-citric acid solution slowly evaporated in the oven to form a viscous gel. Subsequent drying was performed to completely remove the adsorbed water at 110 °C. The resulting xerogel was placed in an oven, which was heated to a temperature of about 200–220 °C after which the mixture ignited and the exothermic reaction formed a product. Synthesized material was investigated using an X-ray diffractometer DRON-3 in CuK-α radiation. Figure 1 shows the precursor solution, the dried gel, and the product, formed after combustion.

Magnesium-substituted lithium ferrites of system B were synthesized by the ceramic method. Synthesis procedure included [18] the following mandatory steps:

1. Grinding of raw materials;
2. Preparation of the charging material;
3. Adding a plasticizer and forming a homogenized mixture;

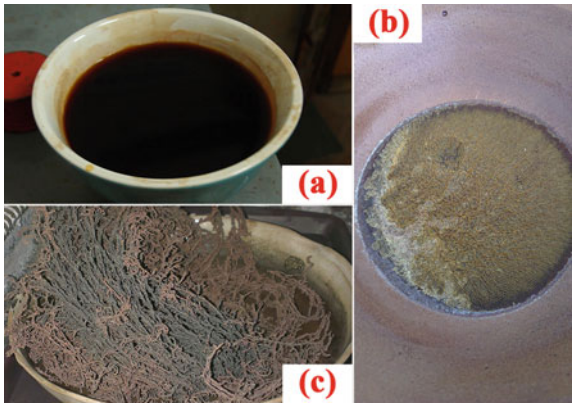

Fig. 1 Synthesis of lithium-iron spinel by sol–gel auto combustion method: **a** a solution of precursors; **b** dried xerogel; **c** the product, formed after the reaction

4. Formation of products;
5. Removal of the plasticizer;
6. Annealing of molded products.

To calculate the mixture of oxides (charging material) with the required ratio of components, we used the following procedure [19]: if the molar fraction of each of the components is a, b, c and the molecular weight is, respectively, a', b', c', the average molecular the weight of the mixture D is equal.

$D = aa' + bb' + cc'$. The weight percentages of the components of the mixture will be:

$$K_A = \frac{aa' \cdot 100}{D}; \quad K_B = \frac{bb' \cdot 100}{D}; \quad K_C = \frac{cc' \cdot 100}{D}$$

In our case, the composition of the charging material was calculated to obtain a spinel of general composition $Li_{0.5}Fe_{2.5-x}Mg_xO_4$, where $0.0 \leq x \leq 1.0$ with step 0.2. Starting oxides of Fe_2O_3 and MgO were of reagent grade (the content of the main component 98.8 and 98%) and LiOH—54.9%. The weight amounts of starting oxides to obtain 50 g of the substance are shown in Table 1.

The weighted portions of the starting oxides were thoroughly mixed and ground in a ball mill with the addition of distilled water for 2 h, after which the resulting mixture was evaporated, briquetted, air-dried at 120 °C, then pre-sintered in an oven at 900 °C for 5 h. The briquettes cooled together with the oven were carefully ground in a mortar to obtain a fine powder. Together with the plasticizer, the obtained powder was passed through a calibration grid with a cell size of 0.6 mm for homogenization. A 10% aqueous solution of polyvinyl alcohol is used as a plasticizer. As a result, we obtained a powder with an average particle size of ~0.1–0.2 μm. The obtained mass was used to form tablets 17 mm in diameter and 4 mm in height. To remove the plasticizer, the tablets were dried in air at a temperature of 120 °C for 8 h. The products obtained in this way were sintered in an oven at a temperature of 1000 °C for 5 h.

The obtained systems A and B were studied by X-ray structural, Mössbauer, and impedance methods.

Phase and structural analysis were performed using an X-ray diffractometer DRON-3 in CuK-α radiation. The full-profile Rietveld refinement method and the PowderCell program were used to analyze experimental diffractograms. Mössbauer absorption spectra of ^{57}Fe at room temperature were obtained in the mode of constant

Table 1 Amount of starting oxides, necessary to obtain spinel of general composition $Li_{0.5}Fe_{2.5-x}Mg_xO_4$

x	0.0	0.2	0.4	0.6	0.8	1.0
LiOH (g)	5.26471	5.34609	5.51663	5.79388	5.99472	6.20999
Fe_2O_3 (g)	48.78164	47.55424	44.98198	40.80041	37.77110	34.52423
MgO (g)	0.00000	1.00881	3.12297	6.55984	9.04965	11.71827

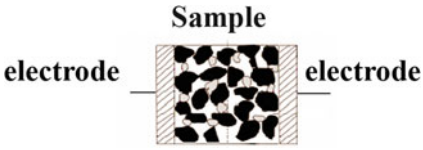

Fig. 2 Structure of the capacitor system for impedance spectroscopy

accelerations on a MS1104EM spectrometer using a source of γ-quanta ^{57}Co in a chromium matrix. Mathematical processing of the obtained spectra was performed using the universal computer program Univem [20].

To measure the spectrum of gamma-resonant absorption, which is the dependence of the intensity of resonant gamma radiation that has passed through the sample on the change in energy of resonant gamma quanta, the spectrometer used the principle of Doppler displacement of gamma quanta. To do this, the source is moved relative to the absorber, and at each value of the energy of gamma rays, which occurs during such a movement due to the Doppler effect, the intensity of gamma radiation passed through the sample is recorded.

Spinels of the composition $Li_{0.5}Fe_{2.5-x}Mg_xO_4$ ($x = 0.2$; 0.4; 0.6; 0.8) in powder form were used as an absorber. The density of the powder did not exceed 10 mg/cm^2.

Graphite electrode/sample/graphite electrode capacitor systems were fabricated for impedance studies (Fig. 2). Measurements were performed on an Autolab PGSTAT 12/FRA-2 impedance spectrometer in the frequency range 0.01 Hz–100 kHz.

3 Results and Discussion

3.1 Structure and Morphology of Magnesium-Substituted Lithium Ferrite

Figure 3 shows the experimental X-ray diffraction patterns of the system of magnesium-substituted lithium spinel, synthesized by the method of sol–gel auto combustion (system A) and by ceramic method (system B). As can be seen from the figure, all the obtained compounds are single-phase spinels; moreover, system with composition $Li_{0.5}Fe_{2.5}O_4$ ($x = 0.0$) belongs to the spatial group $P4_332$ [JCPDS No 76-1591], the so-called superordered spinel structure, as evidenced by the presence of superstructural peaks (110), (210), and (211). Such a superstructure arises due to the ordered arrangement of lithium and iron ions in a ratio of 1: 3 in the crystallographic direction [110]. All other compounds $Li_{0.5}Fe_{2.5-x}Mg_xO_4$, ($x = 0.2$; 0.4; 0.6; 0.8) found belonging to the spatial group Fd3m, because the presence of magnesium ions in the octa-lattice disrupts the order in the location of iron and lithium ions.

Figure 4 shows the experimental spectra of the samples of the composition

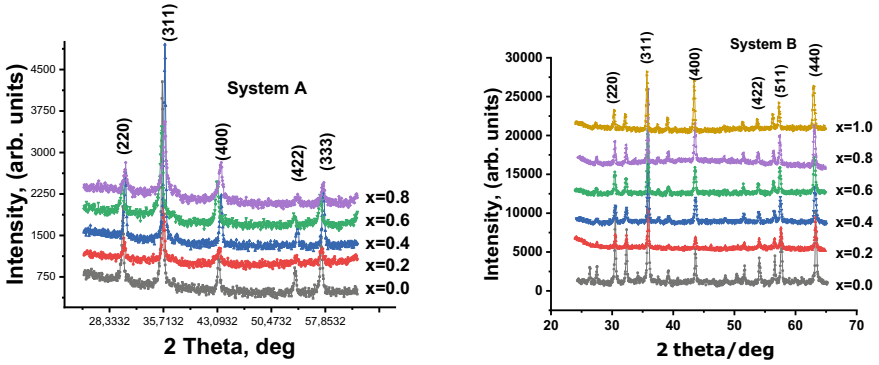

Fig. 3 Experimental X-ray diffraction patterns of systems $Li_{0.5}Fe_{2.5-x}Mg_xO_4$ ($x = 0.0; 0.2; 0.4; 0.6; 0.8$) obtained by sol–gel auto combustion method (system A) and experimental X-ray diffraction patterns of systems $Li_{0.5}Fe_{2.5-x}Mg_xO_4$ ($x = 0.2; 0.4; 0.6; 0.8; 1.0$), obtained by ceramic method (system B)

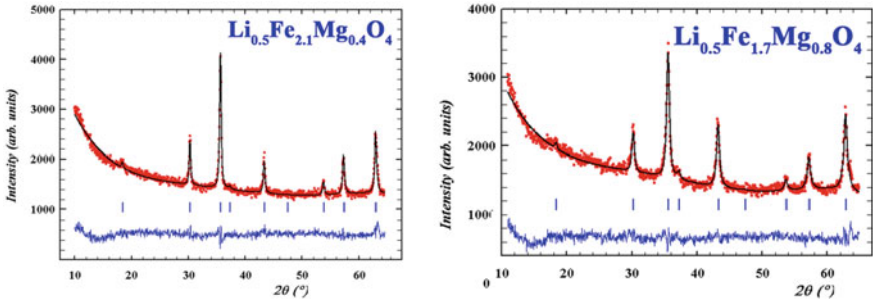

Fig. 4 X-ray spectra of compositions $Li_{0.5}Fe_{2.1}Mg_{0.4}O_4$ and $Li_{0.5}Fe_{1.7}Mg_{0.8}O_4$ (points) and their approximation by the full-scale Rietveld refinement method (solid line) (System B). Below is the difference spectrum

$Li_{0.5}Fe_{2.1}Mg_{0.4}O_4$ and $Li_{0.5}Fe_{1.7}Mg_{0.8}O_4$ (points) and their approximation by the full-profile Rietveld method (solid line). Below is the difference spectrum.

X-ray diffraction patterns of system B (samples obtained by ceramic method) for all Mg contents showed that the obtained system is identified as a single-phase defective cubic spinel structure from the spatial group Fd3m. Experimental X-ray diffraction patterns of samples in the vicinity of $20° \leq 2\Theta \leq 65°$ are presented in Fig. 3. The resulting system can be represented by the General formula $Li_{0.5}Fe_{2.5-x}Mg_xO_4$ ($x = 0.2; 0.4; 0.6; 0.8; 1.0$). Reflexes from the main reflecting planes (220); (311); (400); (511); (440); and (422) are observed in all diffractograms.

Figure 5 presents the experimental spectra of decoded using the FullProf software package.

The dependence of the constant lattice on the concentration with an accuracy of ± 0.002 Å, determined by X-ray diffraction for both systems is shown in Fig. 6.

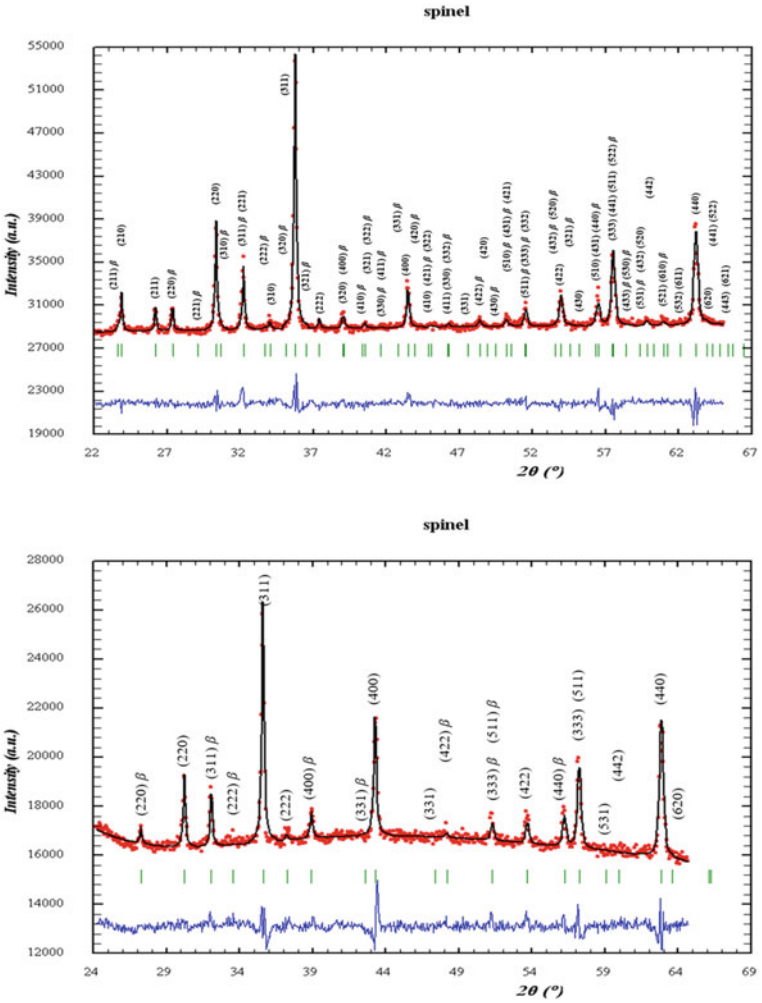

Fig. 5 Decoded X-ray diffraction patterns from a) the original (unsubstituted) sample $x = 0.0$ lithium-iron spinel b) from the sample of lithium-iron spinel, $x = 0.8$

The lattice constant value increases with increasing x for both systems. In the case of samples synthesized by the auto combustion method (system A), the values of the lattice constant are slightly higher than in system B. Obviously, this dependency of lattice constant behavior on the composition can be explained not so much by the substitution effect (because ions of approximately equal ionic radii Fe3 + (0.64) to Mg2 + (0.64) are replaced) but rather by the distortion of the unit cell caused by the formation of charged vacancies. Slightly larger values of the lattice constant for samples synthesized by ceramic method (system B) can be explained by the relatively

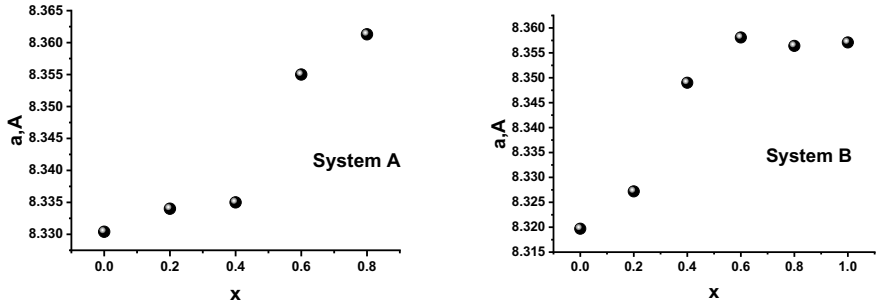

Fig. 6 Dependence of the lattice constant on the content of magnesium ions system A and system B

small size of the crystallites and, consequently, the influence of the surface. These results correlate well with the results obtained in [21].

For the system B, a small increase in the lattice constant a (Fig. 6) is associated with the formation of cationic and anionic vacancies, which occurs in nonstoichiometric substitutions and, according to [22], leads to an increase in the latter. And it should be noted the difference for both systems. For samples obtained by the ceramic method, the lattice undergoes changes at low levels of substitution, and in the case of auto combustion—at large. This difference is due to the fact that nonstoichiometric substitution in system B is accompanied by the formation of vacancies, which especially distort the lattice with small substitutions. With increasing magnesium content for such systems, the number of vacancies remains largely unchanged, as well as the magnitude of internal stresses increasing markedly with small substitutions, with increasing magnesium content remains almost the same. For samples obtained by auto combustion method (System A), the main reason for the increase in the lattice constant is the decrease in particle size observed during substitution.

The cationic distribution obtained from the analysis of experimental X-ray diffraction patterns using the full-profile Rietveld refinement method is shown in Table 2.

Table 2 shows that Li^+ cations occupy only the B position, while Fe^{2+} and Mg^{2+} ions occupy both A- and B-sublattice. Iron ions are redistributed on the A and B

Table 2 Distribution of cations by sublattices of systems $Li_{0.5}Fe_{2.5-x}Mg_xO_4$ ($x = 0.2$; 0.4; 0.6; 0.8) obtained by the method of sol–gel auto combustion

x	A-site	B-site	a (Å)	Δa (Å)
0.0	$Fe_{1.0}$	$Li_{0.5}Fe_{1.41}$	8.330	±0.002
0.2	$Mg_{0.16}Fe_{0.92}$	$Li_{0.5}Fe_{1.38}Mg_{0.04}$	8.334	±0.002
0.4	$Mg_{0.32}Fe_{0.84}$	$Li_{0.5}Fe_{1.26}Mg_{0.08}$	8.335	±0.002
0.6	$Mg_{0.48}Fe_{0.76}$	$Li_{0.5}Fe_{1.14}Mg_{0.12}$	8.355	±0.002
0.8	$Mg_{0.64}Fe_{0.68}$	$Li_{0.5}Fe_{1.02}Mg_{0.16}$	8.361	±0.002

Table 3 Distribution of elements by sublattices system B

x	Cationic distribution and phase composition	Spinel phase lattice parameters
0.0	$(Fe_{1.00})(Fe_{1.59}Li_{0.41})O_{4\pm\delta}$	8.3197 ± 0.0013
0.2	$(Li_{0.17}Fe_{0.76}Mg_{0.06})(Fe_{1.146}Li_{0.46}\ Mg_{0.08})O_{4\pm\delta}$	8.3272 ± 0.0013
0.4	$(Li_{0.16}Fe_{0.74}Mg_{0.09})(Fe_{1.57}Li_{0.33}\ Mg_{0.10})O_{4\pm\delta}$	8.3490 ± 0.0013
0.6	$(Li_{0.14}Fe_{0.66}Mg_{0.19})(Fe_{1.33}Li_{0.31}\ Mg_{0.36})O_{4\pm\delta}$	8.3581 ± 0.0013
0.8	$(Li_{0.19}Fe_{0.50}Mg_{0.31})(Fe_{0.94}Li_{0.41}\ Mg_{0.65})O_{4\pm\delta}$	8.3564 ± 0.0013
1.0	$(Li_{0.22}Fe_{0.35}Mg_{0.44})(Fe_{0.68}Li_{0.44}\ Mg_{0.88})O_{4\pm\delta}$	8.3571 ± 0.0013

sublattices in a ratio of approximately 4:6 and magnesium ions 8:2, respectively. According to the results of X-ray diffractometry, the advantages of the B position of the above ions are as follows: $Li^+ > Fe^{3+}Mg^{2+}$.

For samples of system B, the calculation of the cation distribution was carried out taking into account the ionic radii of each position (r_A and r_B) for different compositions. The results of calculations for all systems are presented in Table 3. In the unsubstituted lithium-iron spinel of stoichiometric composition $Li_{0.5}Fe_{2.5}O_4$, obtained under equilibrium synthesis conditions, all lithium atoms are localized in the octa-lattice, while iron ions are placed in tetra- and octa-positions (the case of the inverted spinel). Since one subsystem contains elements whose valence differs by 2 (in our case Li^+ and Fe^{3+}) at a low rate of synthetic cooling, the formation of a superstructure is possible [23], i.e., the process of atomic 1:3 ordering in the octa-sublattice, resulting in three Fe^{3+} ions and one Li^+ ion all are naturally located along the crystallographic directions <110> . In other words, as a result of a phase transition of the ordering type, a spatial group $O_h^7 - Fd3m$ decreases to $O^7 - P4, 3$. The diffraction pattern of the slowly cooled stoichiometric unsubstituted sample revealed the corresponding superstructural reflexes (110), (210), (211) (Fig. 6), which are absent on the diffractograms of the other samples: nonstoichiometric doping leads to the destruction of the superordination in the octa-sublattice.

Sintering of spinel at high temperatures and its subsequent cooling is accompanied by the following processes: redistribution of ions between the sublattices; ordering of ions within individual lattices, annihilation or association of point defects with cluster formation, spinel phase decay, as well as loss of volatile cations (Li^+) and oxygen [24]. Oxygen leaving the lattice at high temperatures comes from the atmosphere during cooling and is introduced into the structure, restoring the anionic sublattice. This oxygen can occupy both regular and irregular positions, causing minor tetragonal distortions [25]. Lack and excess of oxygen, as well as its presence in irregular positions causes significant changes in the structure and electrical properties of the studied materials.

Table 3 shows the distribution of system components by tetrahedral and octahedral positions of the spinel. A gradual decrease in the iron content in both sublattices and a simultaneous increase in magnesium indicates an almost uniform entry of Mg^{2+} ions in both sublattices in a ratio close to 1:2. Lithium ions are also redistributed in both sublattices almost evenly.

In general, according to system B, the substitution of Fe^{3+} ions for Mg^{2+} ions leads to a violation of electroneutrality, which increases with increasing magnesium content. In these systems, it is unlikely to provide a charge balance by increasing the valence of iron to the state of Fe^{4+}. Therefore, we can assume that electroneutrality is provided mainly by lithium vacancies and the introduction of cations in irregular positions, which, according to [26] leads to the formation of F-centers (the presence of a charged ion in the irregular position or the absence of the latter in the regular), strongly affects the processes of charge transfer in such systems.

The values of the sizes of the coherent scattering regions (CSR) for the samples of system A were calculated by the Selyakov-Scherrer formula.

$$\langle D \rangle = \frac{\lambda}{\beta_{\frac{1}{2}} \cos\theta},$$

where λ—X-ray wavelength, θ-diffraction angle, and $\beta_{1/2}$—half-width of reflection. Also, by the Williamson-Hall interpolation method, according to which the dependence of $\beta\cos\theta$ on the $\sin\theta$ equation

$$\beta \cos\theta = \frac{\lambda}{D} + 4\varepsilon \sin\theta$$

was constructed (if the approximation was performed by Lorentz or Cauchy functions) or equation

$$\beta^2 \cos^2\theta = \left(\frac{\lambda}{D}\right)^2 + (4\varepsilon \sin\theta)^2$$

(if the approximation was carried out by the Gaussian function). If we linearly approximate the obtained dependence, the angle of inclination of the line will be proportional to the magnitude of microstrains (ε or ε^2), and the intersection of the line with the y-axis is a quantity inversely proportional to the size of the CSR (D or D^2).

Figure 7 shows the Williamson-Hall dependence for the sample of $Li_{0.5}Fe_{2.5}O_4$ composition, and Table 4—calculated the CSR values for all synthesized systems by both the Scherrer method and the Williamson-Hall method.

The data in Table 4 indicate that all the synthesized samples are nanoscale, and larger values of the experimental constant lattice compared to the theoretical caused by the influence of the surface due to the small size of the crystallites. Slightly larger values of CSR in the Selyakov-Scherrer method are due to the fact that only one peak of intensity (the third) was taken into account, and the Williamson-Hall method takes into account all reflexes. It is known that with increasing the angle of reflection, the half-width of the peak increases, so taking into account, all the reflexes can give an average value, which may be slightly less than for one randomly selected reflex. Also, when determining the value of $\beta_{1/2}$ was taken into account the

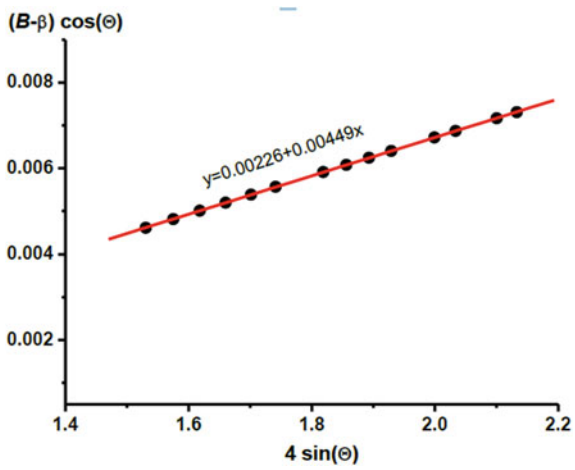

Fig. 7 Williamson-Hall dependence for the system $Li_{0.5}Fe_{2.5}O_4$

Table 4 Size of the coherent scattering (CSR) regions of the systems $Li_{0.5}Fe_{2.5-i}Mg_xO_4$ ($x = 0.0$; 0.2; 0.4; 0.6; 0.8) obtained by the method of sol–gel auto combustion, determined by the methods of Selyakov-Scherrer and Williamson-Hall

Concentration, x	CSR (nm) Selyakov-Scherrer method	CSR (nm) Williamson-Hall method
0.0	42.0	40.0
0.2	17.0	16.8
0.4	24.0	23.6
0.6	16.0	15.4
0.8	15.0	14.4

instrumental broadening caused by the discrepancy of the X-ray beam and the width of the limiting slits, which was determined using a reference sample. This sample was a well-annealed sample of lithium-iron spinel obtained by ceramic method.

3.2 Mössbauer Studies of Mg-Substituted Lithium-Iron Spinels

The spectrum of the unsubstituted sample ($x = 0.0$) consists only of magnetically ordered components. Of these, sextets with a magnetic field value of 507.78 and 496.87kOe can be attributed to iron ions in the octahedral and tetrahedral lattices, and a sextet with H = 455.53kOe can obviously be attributed to iron ions in the surface state, i.e., at the grain boundaries (Fig. 8).

With substitution on the spectra, a paramagnetic doublet appears, the intensity of which increases with increasing magnesium content.

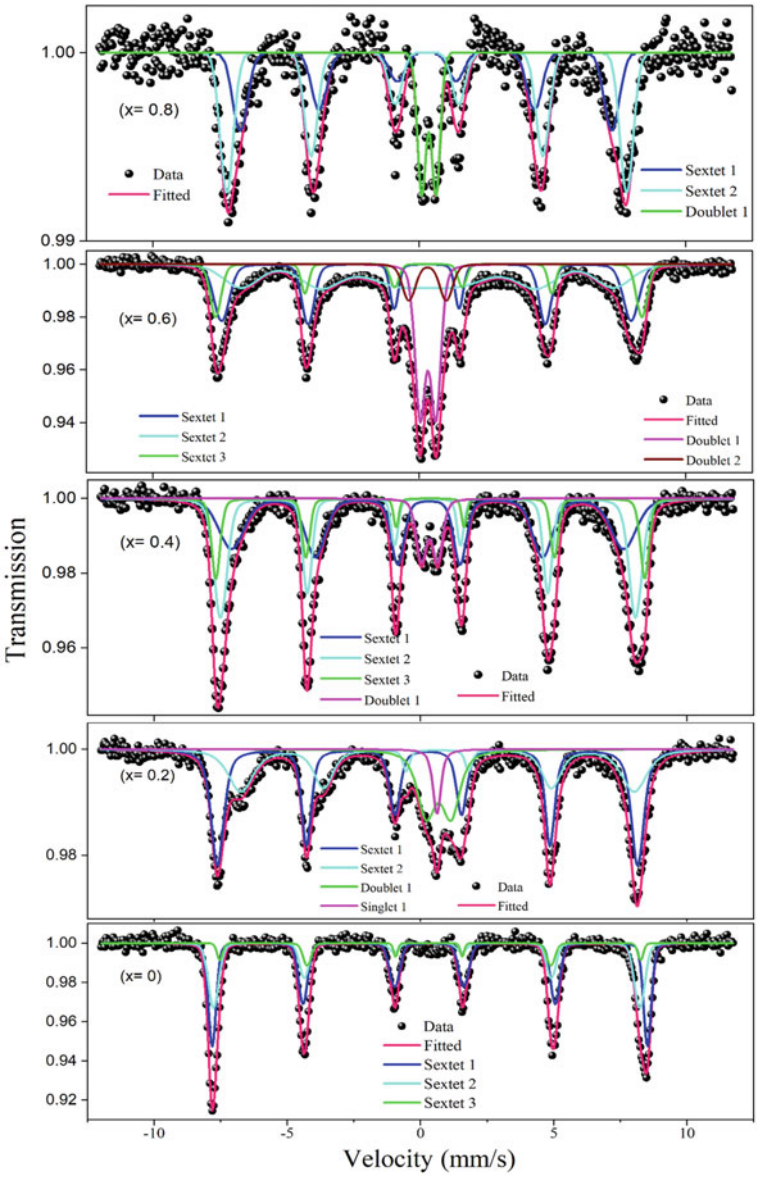

Fig. 8 Presents the Mössbauer spectra of 57Fe at room temperature of the system A $Li_{0.5}Fe_{2.5-x}Mg_xO_4$ ($x = 0.0; 0.2; 0.4; 0.6; 0.8$).

The parameters for decoding the Mössbauer spectra of all synthesized systems are given in Table 5.

Mössbauer spectra from ^{57}Fe, system B, obtained at room temperature for all samples, revealed an asymmetric Zeeman magnetic picture (Fig. 9). This magnetic sextet coexists with two paramagnetic doublets. The asymmetry of magnetically ordered components assumes the presence of two different superfine magnetic sextets, one of which can be attributed to the tetrahedral and the other to the octahedral environment of oxygen in the spinel lattice. However, when the content of magnesium ions in the structure increases, a central quadrupole doublet is observed along with the broadening of the magnetic sextet.

The intensity of this doublet increases with increasing concentration of Mg^{2+} ions, which for all systems coexists with the magnetically ordered phase, which remains pronounced at high concentrations of embedded magnesium. The observed general broadening of the Mössbauer lines for A- and B-sextets can be caused by a change in the chemical environment around different iron ions in the same sublattice. The value of the isomeric shift corresponding to the coordination of Fe^{3+} did not change significantly with increasing concentration of Mg^{2+} ions at room temperature. This fact indicates that the charge of s-electrons, which is distributed on Fe^{3+} ions, is almost independent of the content of substituted Mg^{2+} ions. The isomeric shift of the octahedral positions was found to be slightly less positive than for the tetrahedral ones (Table 6), which may be due to the slight sp3 covalence that occurs for ions at the B positions.

The parameters of the Mössbauer spectra of system B, calculated using the computer program MossWin (Table 6), give the characteristics of Fe^{3+} ions occupying tetrahedral (A) and octahedral (B) positions of the spinel structure.

The widths of the lines corresponding to the tetrahedral and octahedral environment of Fe^{3+} increase with increasing content of Mg^{2+} ions (Table 6), and accordingly, the superfine magnetic fields decrease (Fig. 9), which indicates the entry of magnesium ions into both octa- and tetrahedral positions.

Table 7 compares the data on the cationic distribution of iron obtained from Mössbauer and X-ray experiments.

The distribution of iron ions on the sublattice for X-ray data is taken from the proposed cationic distribution and expressed as a percentage relative to the total iron content in the sample. For Mössbauer data, the content of this distribution was calculated from the total area of sextets responsible for the tetra and octa, and the intensity of paramagnetic doublets was taken into account.

As can be seen from Table 7, the distribution of iron on octa- and tetra-sublattices calculated from Mössbauer data taking into account the intensity of paramagnetic doublets and X-ray diffraction patterns (Tables 5 and 6) generally coincides, which indicates the correctness of the results. Slight differences in the ratios can obviously be explained by the limitations of each of the methods and the disregard for the probability of the Mössbauer exit from different sublattices.

Mg^{2+} ions are known to have a weak advantage in the octahedral positions, as do Li^{+} ions, which also tend to occupy octahedral positions. According to Neel's molecular field theory [27], in spinels, the A-B-super-exchange interaction dominates the

Table 5 Parameters for decoding Mössbauer spectra of system A

Sample	$Li_{0.5}Fe_{2.5}O_4$	$Li_{0.5}Fe_{2.3}Mg_{0.2}O_4$	$Li_{0.5}Fe_{2.1}Mg_{0.4}O_4$	$Li_{0.5}Fe_{1.9}Mg_{0.6}O_4$	$Li_{0.5}Fe_{1.7}Mg_{0.8}O_4$
Is	0.3557	0.2761	0.2862	0.2330	0.2620
Qs	0.0080	−0.0271	0.0076	0.0592	−0.0336
H_{eff}	507.76	489.64	466.87	442.01	433.07
S	40.29	47.95	45.30	24.42	32.30
G	0.3500	0.5657	0.6631	0.7721	0.6697
Is	0.2606	0.6365	0.3102	0.3014	0.2801
Qs	−0.0169	0.0008	0.011	−0.0063	−0.0091
H_{eff}	496.87	458.42	494.40	490.24	465.98
S	51.04	29.83	44.87	40.17	51.34
G	0.4525	1.1230	0.4450	0.3677	0.5898
Is	0.3356				
Qs	−0.504				
H_{eff}	455.53				
S	8.67				
G	0.7760				
Is		0.6788	0.3512	0.3107	0.3555
Qs		0.9258	0.6723	0.6526	0.5293
S		18.14	9.82	35.40	16.36
G		0.8030	0.5205	0.6915	0.3896
Is		0.6141			
S		4.08			
G		0.3600			

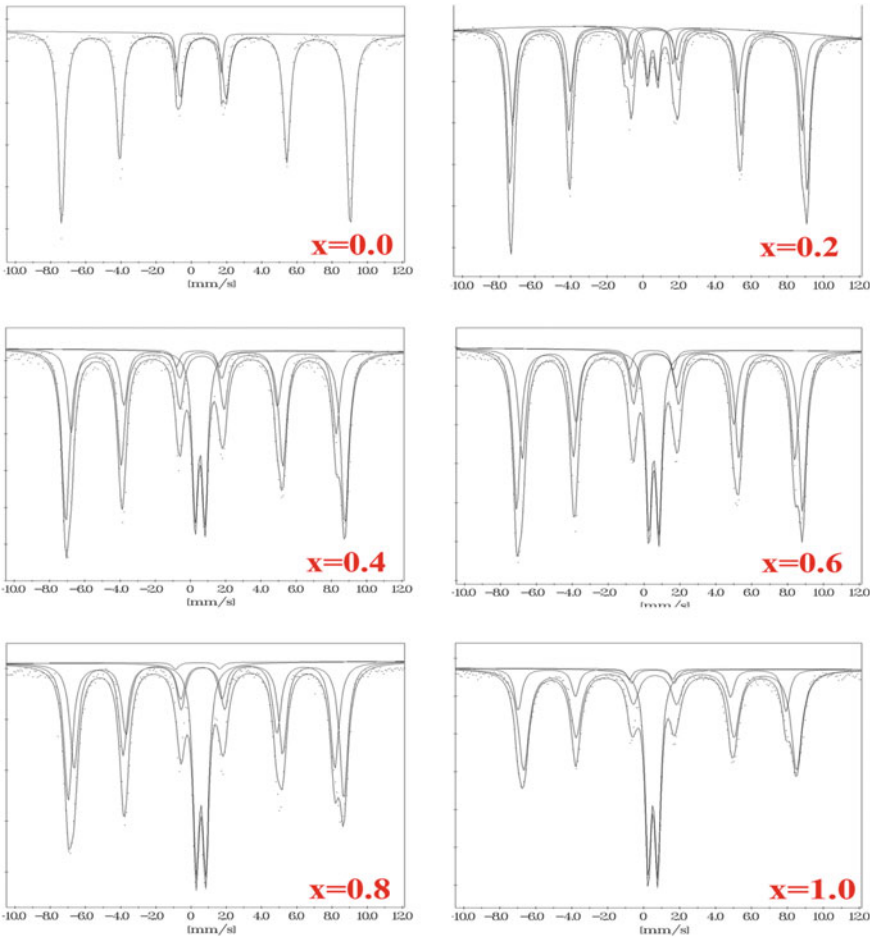

Fig. 9 Experimental ^{57}Fe Mössbauer spectra of synthesized systems B, measured at room temperature

intra-sublattice A-A and B-B interactions, and the internal superfine magnetic fields of the octa- and tetra-environment decrease with increasing Mg^{2+} substitution. In the unsubstituted sample, all lithium ions are concentrated in the octa-sublattice, and when substituted with magnesium, the latter displaces lithium in the tetra-sublattice. However, due to the weak advantage to the octa-positions, magnesium enters both sublattices, reducing the magnetic fields on the nuclei in both subsystems.

A paramagnetic doublet with a quadrupole close to 2.5 can be considered a sign of the presence of divalent iron, the concentration of which in the octahedral subsystem is quite small. The presence of Fe^{2+} in the tetra-sublattice is unlikely, due to its large ionic radius (0.83 nm). The second paramagnetic doublet, the intensity of which increases with increasing Mg^{2+} ion content, can be attributed to the manifestation of

Table 6 Parameters for decoding Mössbauer spectra of system B

Sample	$Li_{0.5}Fe_{2.5}O_4$	$Li_{0.5}Fe_{2.3}Mg_{0.2}O_4$	$Li_{0.5}Fe_{2.1}Mg_{0.4}O_4$	$Li_{0.5}Fe_{1.9}Mg_{0.6}O_4$	$Li_{0.5}Fe_{1.7}Mg_{0.8}O_4$
Is	0.755	0.7	0.67	0.70	0.68, 0.49
Qs	0.15	0.18	0.17	0.20	0.18, −0.05
H_{eff}	50.89	49.66	46.66	47.13	45.92, 46.27
S	95.40	33.65	24.76	32.49	34.05, 15.59
G	0.46	0.41	0.50	0.51	0.58, 0.49
Is		0.77	0.75	0.76	0.76, 0.77
Qs		0.19	0.19	0.19	0.17, 0.28
H_{eff}		51.07	49.15	49.43	48.55, 47.13
S		54.85	54.52	46.01	42.75, 54.24
G		0.41	0.53	0.50	0.56, 0.71
Is					
Qs					
H_{eff}					
S					
G					
Is		0.54	0.55	0.54	0.56, 0.51
Qs	–	0.56	0.56	0.57	0.55, 0.54
S		6.62	18.72	19.21	22.40, 28.58
G		0.30	0.39	0.39	0.42, 0.40
Is	0.45	0.33	0.43	0.40	0.38, 0.41
Qs	2.54	2.68	2.43	2.44	2.51, 2.41
S	4.61	4.88	1.99	2.29	0.80, 1.59
G	0.21	0.30	0.39	0.39	0.42, 0.40

Table 7 Cationic distribution of iron obtained from Mössbauer and X-ray experiments

X	X-ray analysis			Mössbauer analysis		
	Fe_{okt} (%)	Fe_{tetr} (%)	Fe_{okt} / Fe_{tetr}	Fe_{okt} (%)	Fe_{tetr} (%)	Fe_{okt} / Fe_{tetr}
0.2	60.0	37.5	1.6	61.9	38.1	1.6
0.4	65.9	34.1	1.9	65.9	34.1	1.9
0.6	66.0	34.0	1.9	67.5	32.5	2.0
0.8	66.1	33.9	1.9	65.9	34.1	1.9
1.0	69.4	30.6	2.3	70.1	29.9	2.3
Error	±0.1	±0.1	±0.1	±0.1	±0.1	±0.1

superparamagnetism, which is typical for the replacement of ferrites by nonmagnetic ions, for example, in Li–Zn ferrites [28], $CoFe_{2-x}Al_xO_4$ [29], and a number of others.

The presence of a central quadrupole doublet together with a widened magnetic sextet was observed in [28–30], and it was given various explanations. The possibility of a central doublet as a consequence of the presence of a paramagnetic impurity is incomplete, as the results of X-ray diffraction indicated the presence of only one pure spinel phase. Some samples were re-fabricated, but they did not show any changes in the presence of the center line. Moreover, it was found (Table 6) that the intensity of the doublet increases with increasing concentration of Mg^{2+} ions. It is known [29] that with increasing number of diamagnetic ions, some Fe^{3+} ions are isolated from other magnetic ions and have a short-term magnetic order. This promotes the growth of magnetic clusters of different sizes, known as superparamagnetic clusters, which have very little magnetic interaction with the environment, but which can have any type of magnetic arrangement within the cluster. Small clusters are characterized by a faster degree of relaxation, which causes the growth of the paramagnetic doublet. In such systems, magnetically ordered clusters are separated from others by nonmagnetic ions. A similar picture of the coexistence of magnetically ordered systems and a paramagnetic cluster (with a small quadrupole) was observed in [10] and explained on the basis of two relaxation mechanisms: spin–spin relaxation and relaxation between the possible direction of the spin slope in relation to "spin glass." In [31], the growth of the central doublet based on the Zeeman magnetic pattern in ferrites with diamagnetic substitution is explained by the formation and development of clusters with a decrease in magnetic A–B bonds. It was noted that when discrete subspectra, including the central component, were used to approximate the picture, Fe^{3+} ions did not have an advantage to any particular position.

A similar phenomenon of superimposition on the magnetic picture of the central paramagnetic line was observed in the study of the $ZnCr_xGa_{2-x}O_4$, $0.2 \leq x \leq 2$ system in [27]. However, in this case, the phenomenon is related to the existence of a dependence similar to spin glass, and the results are explained using the concept of two spin clusters. In other works, such as [10, 30], the presence of a central doublet was explained on the basis of the assumption of the presence of entropic clusters rather than superparamagnetic.

As the content of nonmagnetic Mg^{2+} ions increases both in the octa- and in the tetra-sublattices, there is a "break" of super-exchange bonds of type AB between the two sublattices, and as a consequence, there is an increase in the intensity of the quadrupole doublet with decreasing magnetic fields on the nuclei also in both subsystems, as observed in this work.

3.3 Frequency Behavior of Conductive and Dielectric Properties of Mg-Substituted $Li_{0.5}Fe_{2.5}O_4$ Spinels

Impedance spectroscopy is an effective method for studying the reproducibility of a cathode substance and the peculiarities of charge transfer processes in it. Experimental studies of complex impedance were used to study the properties of solid electrolytes [22] and ceramic oxides [23], and data analysis is based on the possibility of model representation of the test substance by an equivalent scheme. The determined parameters of such a scheme are compared with the corresponding values that characterize the conductive and dielectric properties of the components of the studied systems.

In this work, the influence of the conditions of synthesis and nonstoichiometric substitution of iron in the $Li_{0.5}Fe_{2.5}O_4$ matrix by divalent magnesium ions on the frequency behavior of the conductive and dielectric properties of the material was investigated by impedance spectroscopy methods.

System B is characterized by the presence of an ionic component of conductivity, as evidenced by hodographs (Fig. 10) in the form of a semicircle and a pronounced polarization branch, which goes to infinity with decreasing frequency [21] (Fig. 11).

The equivalent circuit (Fig. 12) is a series-connected two RC-elements, the resistance, and capacitance of which characterize the grain and intergranular regions and the area of the circle containing the Warburg element. The value of the Warburg element W is due to the diffusion transfer of lithium in the structure:

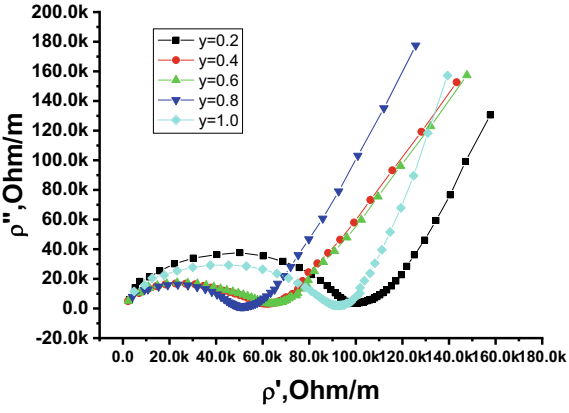

Fig. 10 Nyquist diagrams for specific values of real and imaginary part of resistance od system B

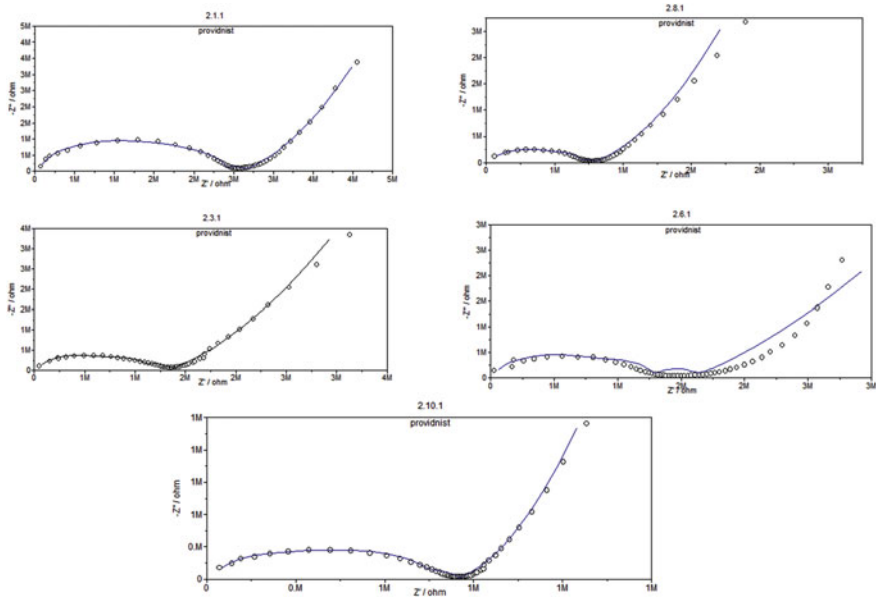

Fig. 11 Experimental (points) and frequency dependences calculated according to equivalent schemes (solid lines) of real and imaginary part of resistance

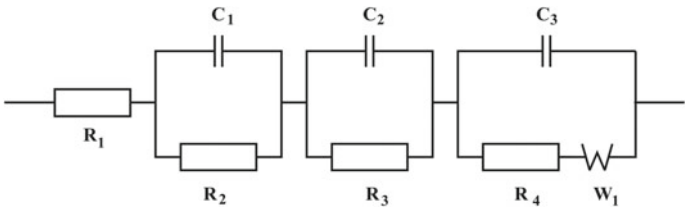

Fig. 12 Equivalent circuit

$$W = \frac{RT}{n^2 F^2 c_{Li} \sqrt{2D}}$$

where c_{Li}—volume concentration of lithium at a given electrode potential; D—diffusion coefficient; F—Faraday constant; T—absolute temperature.

However, in the nonstoichiometric system $Li_{0.5}Fe_{2.5-x}Mg_xO_4$, the degree of substitution of iron by magnesium determines different contributions to the specific conductivity of the ionic and electronic components, and the hodograph curves cannot be modeled in semicircles even for deposits with low values x. Therefore, the simulation should be performed taking into account the deformation of the circuits along the axis, which is expressed in the replacement of the capacitor by a constant phase

Table 8 Parameters of model representation of impedance measurements of magnesium-substituted lithium-iron spinels, which were slowly cooled by the synthesis temperature

x	R_1 (kΩ)	R_2 (kΩ)	R_3 (kΩ)	C_1 (pF)	C_2 (μF)	W
0.1	70.1	768.1	208.4	77.5	8.6	0.2
0.3	46.1	442.2	225.1	125.3	9.6	0.2
0.6	34.6	484.5	294.1	113.9	1.8	0.2
0.8	43.5	235.1	85.6	123.6	9.8	0.3
1.0	21.7	327.4	79.4	85.3	19.1	0.8
Error	±0.1	±0.1	±0.1	±0.1	±0.1	±0.1

element [31], the physical meaning of which is that the frequency impedance dispersion becomes similar to an inhomogeneous transmission line. Thus, the simulation of impedance hodographs should be performed taking into account both the multi-stage RC-system and the mass–charge transfer system. Table 8 shows the calculated values of the components, expressed by the electrical elements of the sections of equivalent circuits for sample of system B. In Table 8, the resistance R_1 corresponds to the resistance of the electrodes and contacts, and the resistances R_2 and R_3—the resistance of the crystallites and intercrystalline gaps. Since these systems are single-phase, the impedance hodograph is satisfactorily modeled by two sections, one of which expresses the electrophysical properties of the crystallites, and the other—the intercrystalline gaps. This partition, carried out on the basis of Wagner-Koops theory [32], is valid, as these structural components are characterized by strong differences in the values of the calculated parameters. The need to introduce the Warburg diffusion coefficient into an equivalent scheme was determined by the presence of a clearly expressed polarization branch in the Nyquist experimental diagrams, which indicates the presence of diffusion processes (Figs. 10 and 11).

In the study of electrical conductivity [33, 34], it is suggested that the electrons involved in the formation of electric current are localized mainly in the locations of

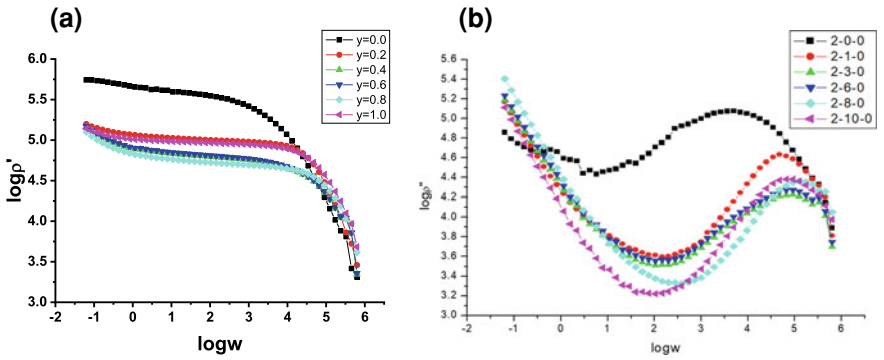

Fig. 13 Dependence of the real part (**a**) and imaginary part (**b**) of the resistivity on the frequency (system B)

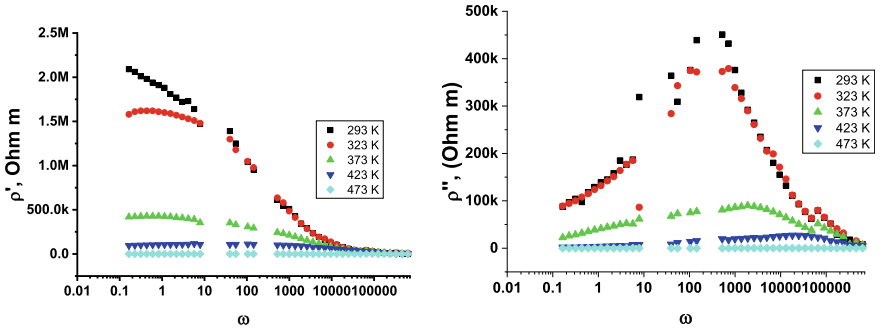

Fig. 14 Frequency dependence of real and imaginary parts of resistivity at different temperatures system A

ions. Based on the assumption of the localization of the states of 3d-electrons, we can imagine the process of electric current as a process of jumping electrons from one ion to another. Thus, it is considered that the corresponding valence states of the ions themselves migrate along the crystal, and at a sufficiently high concentration of ions with variable valence, the electrical conductivity is of high value and is characterized by low activation energy. In the presence of variable valence ions in the structure, in our case ions of ferrous and trivalent iron, 3d—the electron of the Fe^{2+} ion, overcoming the energy barrier, can jump to the Fe^{3+} ion, resulting in a process:

$$Fe^{2+} + Fe^{3+} \leftrightarrow Fe^{3+} + Fe^{2+}.$$

This process can occur in the absence of an external electric field. In this case, the system is in a state of dynamic equilibrium, in which the charge transfer is chaotic without a selected direction, so that the total current through an arbitrary cross section is zero. The situation changes in the case of applying an external electric field. The statistical distribution of electron jumps changes, their relative frequency increases in a certain direction, and there is a directed drift of electrons, so that the resulting current becomes different from zero.

Based on the hopping mechanism, the electrical conductivity of these systems largely depends on the content of divalent ions. The value of conductivity is directly dependent on the concentration of Fe^{2+} ions in the compound, which, in turn, depends on the composition of the initial oxides and the synthesis conditions. As can be seen from the results of Mössbauer analysis, almost every sample of system 2 includes iron in the divalent state. As shown by the results of the frequency dependence of conductivity, in the case of system B, the conductivity is greater than in system A. Thus, the amount of iron in the divalent state is responsible for the value of conductivity in the system.

Frequency dependences of the loss tangent (tan(δ)), for spinels of the composition $Li_{0.5}Fe_{2.5-x}Mg_xO_4$, where $x = 0.0; 0.1; 0.3; 0.6; 0.8; 1.0$ measured for the frequency

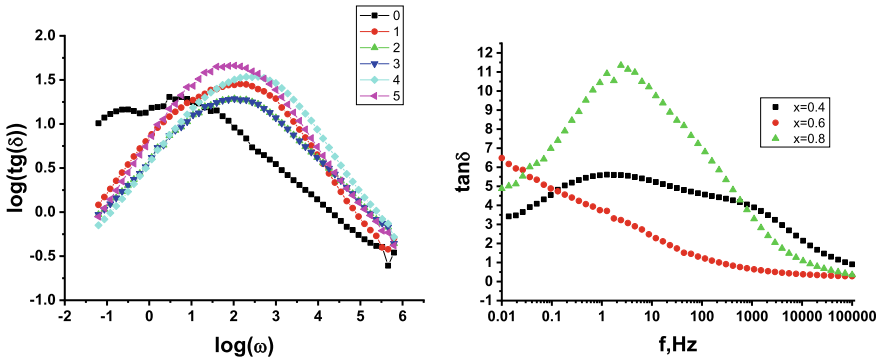

Fig. 15 Frequency dependences of the loss tangent (tan(δ)) of system B; dependence of the dielectric loss tangent (tan(δ)) on frequency of $Li_{0.5}Fe_{2.1}Mg_{0.4}O_4$, $Li_{0.5}Fe_{1.9}Mg_{0.6}O_4$, and $Li_{0.5}Fe_{1.7}Mg_{0.8}$, synthesized by the method of sol–gel auto combustion

range from 10^{-2} to 10^5 Hz. The change in tan(δ) with frequency at room temperature is shown in Fig. 15.

The figure shows that the dependence of the loss tangent on the frequency for systems $Li_{0.5}Fe_{2.1}Mg_{0.4}O_4$ and $Li_{0.5}Fe_{1.7}Mg_{0.8}$ characterized by the presence of a peak (for the system $Li_{0.5}Fe_{2.1}Mg_{0.4}O_4$ two of them, with vertices in the frequency range of 10 and 1000 Hz), indicating the resonant nature of the polarization processes in these systems. The maximum in tan$\delta(f)$ can be observed when the jump frequency is approximately equal to the frequency of the external applied field. The conditions for observing the maximum in tan$\delta(f)$ are given by the relation [35]:

$$\omega'\tau \approx 1$$

where $\omega' = 2\pi f_{\max}$ and $f_{\max}$ is proportional to the probability of a jump, τ—relaxation time.

Another explanation for the occurrence of the peak in the change of the tangent of losses with frequency can be made taking into account the dispersion of the dielectric constant. The presence of such a maximum can be explained by the fact that the rate of decrease of the real part of the dielectric constant in the frequency range $f < f_{\max}$ increases and at $f > f_{\max}$ decreases, as shown in Fig. 15, which may cause a peak in tan(δ) versus frequency. The double peak in the frequency dependence of the loss tangent for the system is obviously associated with both the processes of electron jump and the polarization of grain boundaries, which in fine materials make a significant contribution to both conduction and polarization processes due to the accumulation of defects and various kinds of inhomogeneities.

4 Conclusions

It is found that all magnesium-substituted systems are single-phase spinels of the spatial group Fd3m; the unsubstituted sample of the composition $Li_{0.5}Fe_{2.5}O_4$ ($x = 0.0$) belongs to the spatial group $P4_332$ [JCPDS No 76-1591], the so-called super-ordered spinel structure. The obtained systems belong to the nanometer range with CSR sizes of ~20–40 nm. As the concentration of magnesium (x) increases, the tetrahedral radii gradually increase, while the octahedral ones decrease. Total ionic radius $\overline{r}$ ($\overline{r} = \frac{r_A + r_B}{2}$) increases more slowly, which is reflected in the increase of the lattice constant. Thus, it is possible to note that substitution in a tetrahedral position plays a dominant role depending on change of a constant lattice on structure. It is shown that Li^+ cations occupy only B positions, while Fe^{3+} and Mg^{2+} ions occupy both A- and B-lattice. Iron ions are redistributed on the A and B sublattices in a ratio of approximately 4:6 and magnesium ions 8:2, respectively. According to the results of X-ray diffractometry, the advantages of the B position of the above ions are as follows: $Li^+ > Fe^{3+} > Mg^{2+}$.

X-ray density decreases with increasing x. This is due to the fact that the atomic weight of Mg^{2+} (24.31) is less than that of Fe^{3+} (55.8). Calculation of bond lengths between cations (b, c, d, e, f) (Me-Me) and between cation and anion (p, q, r, s) (Me-O), calculated on the basis of experimental values of the constant lattice and oxygen parameter (u), showed that both parameters increase with substitution, which leads to a weakening of the magnetic interaction in the system.

Studies of the conductive and dielectric properties of magnesium-substituted lithium-iron spinels based on impedance spectroscopy have shown: (1) the studied systems are characterized by the presence of two conduction mechanisms: electronic and ionic; (2) electronic conductivity is based on the jumping mechanism due to the presence of ferrous ions and is realized mainly by the volume of grains in the octa-lattice of spinel; (3) diffusion transfer of lithium ions is carried out at intergranular boundaries and point defects (vacancies), the number of which increases as the system deviates from stoichiometry; (4) with increasing number of ions of embedded magnesium system B, the value of conductivity at direct current does not change due to participation in the jumping mechanism of stable complexes $\left[Li^+_{tetra}Fe^{3+}_{octa}\right]$, formed during substitution; (5) the sharp increase in conductivity for system B is determined by the high content of ferrous ions, which is due to the use of high temperatures and long heat treatment times during synthesis; (6) the samples of system A are characterized by a decrease in conductivity with an increase in the content of embedded magnesium ions, which is due to a decrease in the number of Fe^{2+} ions; (7) the samples of system A and system B are characterized by different nature of the decrease in the real part of the dielectric constant, which is obviously due to differences in the microstructure. Moreover, the samples of system A show a significant dependence of the loss tangent on the composition; (8) polarization processes for system B are characterized by a constant relaxation time, and for system A, the relaxation time depends on the composition, which, obviously, is also determined by differences in the microstructure.

Thus, the study of the influence of synthesis conditions on the properties of magnesium-substituted lithium ferrites showed that in the case of synthesis by sol–gel auto combustion, there is a decrease in the size of synthesized particles by almost 10 times, which indicates high dispersion of Li-Mg ferrite system and increased 20 times the specific surface area of the substance.

Sol–gel synthesis results in nano disperse particles with higher porosity, higher lattice value, and degree of lithium stoichiometry, while remaining single-phase systems as in ceramic synthesis, but the samples obtained by sol–gel method have a more perfect structure and are high stoichiometry.

The obtained results showed the expediency of using the sol–gel method of auto combustion for the synthesis of high-quality nanosized ferrites with improved technological characteristics.

References

1. Akhtar MN, Yousaf M, Lu Y, Khan MA, Sarosh A, Arshad M, Niamat M, Farhan M, Ahmad A, Khallidoon MU (2021) Ceramics International
2. Fantechi E, Innocenti C, Bertoni G, Sangregorio C, Pineider F (2020) Nano Res 13:785
3. Thota S, Singh S (2017) Magnetic spinels—synthesis, properties and applications. InTech
4. Zhang Y, Yuan L, Zhang X, Zhang J, Yue Z, Li L (2017) Appl Surf Sci 410:99
5. Uhorchuk OM, Uhorchuk VV, Karpets MV (2015) J Nano-Electron Phys 7(2)
6. Deepty M, Srinivas Ch PN, Ramesh N, Mohan K, Singh MS, Prajapat CL, Verma A, Sastry DL (2020) Sens Actuators B Chem 316:128127
7. Hao X, Liu T, Li W, Zhang Y, Ouyang J, Liang X, Liu F, Yan X, Zhang C, Gao Y, Wang L, Lu G (2020) Sens Actuators B Chem 302:127206
8. Ostafijchuk BK, Bushkova VS, Moklyak VV, lnitsky RV (2015) Ukr J Phys 60:1234
9. Soman VV, Nanoti VM, Kulkarni DK (2013) Ceram Int 39:5713
10. Kotsyubynsky V, Moklyak V, Hrubiak A (2014) Mater Sci-Pol 32:481
11. Kopayev AV, Mokljak VV, Gasyuk IM, Kozub VV (2015) SSP 230:114
12. Sijo AK, Jha VK, Kaykan LS, Dutta DP (2020) J Magnetism Magnetic Mater 497:166047
13. Poudel TP, Rai BK, Yoon S, Guragain D, Neupane D, Mishra SR (2019) J Alloy Compd 802:609
14. Gajula GR, Buddiga LR (2020) J Magnetism Magnetic Mater 494:165822
15. Ostafiychuk BK, Kaykan LS, Kaykan JS, Ya B, Deputat, Shevchuk OV (2017) Nanoscale Res Lett 12
16. Kaykan LS, Kaykan JS, Yaremiy IP, Ugorchuk OM, Deputat BY, Nykoliuk MO (2016) J Nano-Electron Phys 8:04066
17. Almessiere MA, Slimani Y, Rehman S, Khan FA, Polat EG, Sadaqat A, Shirsath SE, Baykal A (2020) Mater Sci Eng C 116:111186
18. Agostini M, Matic A, Panero S, Croce F, Gunnella R, Reale P, Brutti S (2017) Electrochim Acta 235:262
19. Hagh NM, Amatucci GG (2010) J Power Sources 195:5005
20. Kotsyubynsky VO, Grubiak AB, Moklyak VV, Pylypiv VM, Lisovsky RP (2016) Metallofiz Noveishie Tekhnol 36:1497
21. Arshad MI, Arshad S, Mahmood K, Ali A, Amin N, Umaid-ur-Rehman, Isa M, Akram A, Sabir N, Ajaz-un-Nabi M (2020) Physica B Condensed Matter 599:412496
22. Yokozaki R, Kobayashi H, Honma I Ceramics Int (2020)
23. Zhang Z (2020) Mater Today Commun 101734
24. Jha VK, Alam SN, Roy M (2019) J Supercond Nov Magn 33:455

25. Kaykan LS, Mazurenko JS, Sijo AK, Makovysyn VI (2020) Appl Nanosci 10:2739
26. El-Fadl AA, Abd-Elrahman MI, Younis N, Afify N, Abu-Sehly AA, Hafiz MM (2019) J Alloy Compd 795:114
27. Ferchmin AR, Klama S, Krompiewski S (1979) Czech J Phys 29:883
28. Gul S, Yousuf MA, Anwar A, Warsi MF, Agboola PO, Shakir I, Shahid M (2020) Ceram Int 46:14195
29. Kumar L, Kumar P, Kar M (2013) J Mater Sci Mater Electron 24:2706
30. Zaki HM, AL-Heniti SH, Aljwiher MM (2020) Physica B Condensed Matter 597:412382
31. Poole CP Jr, Farach HA (1982) Z Physik B Condensed Matter 47:55
32. Mondal RA, Murty BS, Murthy VRK (2014) Curr Appl Phys 14:1727
33. Ostafiychuk BK, Gasyuk IM, Kaykan LS, Uhorchuk VV, Yakubovskiy PP, Tsap VA, Kaykan YuS (2016) Metallofiz Noveishie Tekhnol 36:89
34. Mazurenko J (2020) Phys Chem Solid St 21:453
35. Dutta DP, Roy M (2017) Ceramics Int 43:16915

All-Angled Perfect Transmission of the Ultra-relativistic Quasiparticles Through the Graphene Quantum Well

A. M. Korol, N. V. Medvid, A. I. Sokolenko, and O. Shevchenko

1 Introduction

Recently, much attention in the study of physical processes in modern nano-objects is paid to the so-called Dirac materials [1]. As graphene is the most-studied and very promising material in terms of practical applications among the Dirac materials, much attention has been paid to the study of graphene as well as of the various graphene-based structures in recent years. This is, in particular, due to non-trivial properties of graphene such as a linear dispersion relation for the quasiparticles, unusual quantum Hall effect, the property of chirality, the Klein tunneling, high mobility and ballistic transport (see, e.g., [2, 3]). And it should also be borne in mind that graphene is a promising material for modern electronics. One of the priority directions is to study the various possibilities of controlling the energy spectrum of the graphene-based structures. The key value that characterizes the dispersion relation of the Dirac quasiparticles is the Fermi velocity. Therefore, it is clear that significant efforts have been made to be able to control this value and also to use this control in practice [4–15]. For this purpose, a number of different methods were proposed and experimentally tested. The Fermi velocity of charge carriers in various structures is made to vary in space by some special techniques, e.g., by the appropriate doping, placing a grounded metal plane close to graphene sheet (which makes electron–electron interactions weaker and thereby modifies the Fermi velocity), stretching a small region of a graphene sheet and others. The electron wave propagation in the graphene-based structures with the tunable Fermi velocity was investigated in

A. M. Korol (✉) · N. V. Medvid · A. I. Sokolenko · O. Shevchenko
National University for Food Technologies, Volodymyrska street, Kyiv 68, Ukraine
e-mail: korolam@ukr.net

A. M. Korol
Laboratory on Quantum Theory in Linkoping, International Society for Independent Research (ISIR), box 8017, 58080 Linkoping, Sweden

O. Fesenko and L. Yatsenko (eds.), *Nanomaterials and Nanocomposites, Nanostructure Surfaces, and Their Applications*, Springer Proceedings in Physics 263, https://doi.org/10.1007/978-3-030-74741-1_19

[4–15] including the effect of the magnetic and the electric field. Immediately after graphene was fabricated, special attention was drawn to the fact that it can serve as a good energy filter for quasiparticles. The domain sub-barrier energies were more often meant in the relevant publications. At the same time, it was shown in the paper [3] that this statement applies equally to above-barrier energies. In this paper, we also investigate the region of above-barrier energies and focus on the fact that the transmission of quasi-electrons significantly depends on the values of the Fermi velocity in different regions of the structure under consideration. The main purpose of our investigation is to demonstrate the manifestation of the all-angled perfect transmission of the relativistic quasi-electrons in the graphene structure.

2 Model and Formulae

Consider the square well in graphene created by the external electrostatic potential. The massless quasiparticles low-energy spectrum can be described by the following Dirac-type equation [2]:

$$i\hbar\vec{\sigma}\nabla\left[\sqrt{\vec{v}(\vec{r})}\phi(\vec{r})\right]\sqrt{\vec{v}(\vec{r})} = (E-U)\phi(\vec{r}) \tag{1}$$

where $\vec{\sigma} = (\sigma_x, \sigma_y)$ are the two-dimension Pauli matrices, $\phi(\vec{r}) = \left[\phi_A(\vec{r}), \phi_B(\vec{r})\right]^T$—the two-component spinor consisting of the eigen functions for the A and B graphene sub-lattices, T—transposition symbol, v—the Fermi velocity which depends on the space coordinate r, U—the external electrostatic barrier height.

As in [3] we consider here those solutions of (1) which relates to standing waves in the quantum well and also to the propagating waves referring to free quasi-electrons. The first of them may be presented as follows:

$$\psi_w = \begin{pmatrix} a_2\cos(kx) + b_2\sin(kx) \\ a_2\left[\frac{ik_y}{E}\cos(kx) + \frac{ik}{E}\sin(kx)\right] + b_2\left[\frac{ik_y}{E}\sin(kx) - \frac{ik}{E}\cos(kx)\right] \end{pmatrix} \tag{2}$$

$$-\frac{d}{2} < x < \frac{d}{2}; k = \sqrt{E^2 - k_y^2}; k_y = E\sin\phi;$$

ϕ is the angle of incidence of the quasi-electrons on the well; the axes $0\times$ and 0y are directed across the well and along the well, respectively; the eigen functions in the left and in the right barriers with respect to the well are as follows:

$$\psi_{\text{bl}} = a_1\begin{pmatrix} e^{qx} \\ \frac{i(k_y-q)\beta}{E-U}e^{qx} \end{pmatrix}; x < -\frac{d}{2};$$

$$\psi_{\mathrm{br}} = a_1 \begin{pmatrix} e^{-qx} \\ \frac{i(k_y+q)\beta}{E-U} e^{-qx} \end{pmatrix}; x > \frac{d}{2};$$

$$q = \sqrt{k_y^2 - \frac{(E-U)^2}{\beta^2}}; \beta = \frac{\upsilon_{\mathrm{Fb}}}{\upsilon_{\mathrm{Fw}}},$$

υ_{Fb}, υ_{Fw} are Fermi velocities in the barrier and the well regions, respectively.

For the propagating waves, we have:

for the well area

$$\psi_l(x, y) = \begin{pmatrix} 1 \\ f^- \end{pmatrix} e^{i(k_x x + k_y y)} + r \begin{pmatrix} 1 \\ f^+ \end{pmatrix} e^{i(-k_x x + k_y y)}$$

$$\psi_r(x, y) = t \begin{pmatrix} 1 \\ f^- \end{pmatrix} e^{i(k_x x + k_y y)} \tag{3}$$

for the barrier area

$$\psi_b(x, y) = c \begin{pmatrix} 1 \\ g^+ \end{pmatrix} e^{i(q_x x + k_y y)} + d \begin{pmatrix} 1 \\ g^- \end{pmatrix} e^{i(-q_x x + k_y y)} \tag{4}$$

$$g^{\mp} = \frac{\mp i q_x + k_y}{(E-U)\beta^{-1}}; f^{\mp} = \frac{\mp i k_x + k_y}{E};$$

The corresponding states may interfere with each other resulting in the resonant tunneling spectra. Matching the eigen functions at the interfaces gives the expression for the transmission rates T:

$$t = \frac{(s_+ - s_-)(z_+ - z_-)e^{-iq_x}}{(s_+ - s_-)(z_+ - z_-)e^{2ik} - (s_+ - z_-)(s_- - z_+)} \tag{5}$$

$$s_{\pm} = \frac{k_y \pm i q_x}{E}; z_{\pm} = \frac{(k_y \pm ik)\beta}{E-U}; q_x = \sqrt{\frac{(E-U)^2}{\beta^2} - k_y^2};$$

$$T = |t|^2.$$

3 Results and Discussion

Figure 1 exposes the graph of the dependence of the transmission rates on the quasi-particle energy (transmission spectra) for the following set of the parameters: $U = 0.3$, $w = 0.5$, $\phi = 0.1$ for all lines, β =0.3, 0.5, 0.7, 1.3 for the solid (red online),

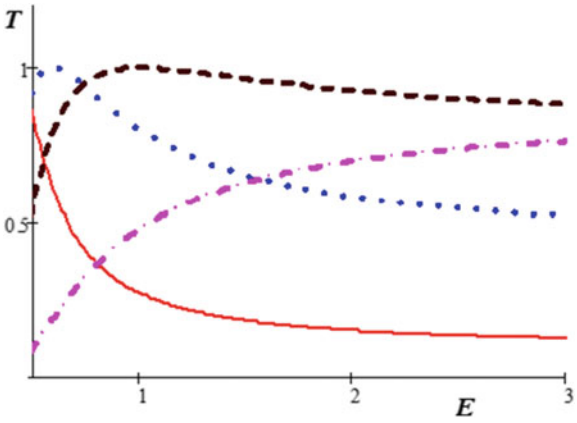

Fig. 1 Dependence of the transmission rates T on the quasi-electron energy E

dotted (blue), dashed (brown) and dashed-dotted (magenta) lines, respectively. Thus, the depicted curves relate to different values of β.

The main feature of these spectra is that, for a certain energy, the transmission rate T acquires the maximum value, namely it is equal to one. Lines with different beta values are very different from each other. The maxima with $T = 1$ are formed only for β values 0.5 and 0.7. This is explained as follows. As shown in [1], physically correct solutions of this problem are possible only in a certain range of energies (or quasi-momentums). For the given parameters in Fig. 1, in particular for $\beta = 0.3$, there are no such solutions in the region $E < 1$ (because of this, we start counting the energy on the corresponding axis not from zero). For $\beta = 1.3$, the resonance is observed at larger energy (see Fig. 4) than depicted in Fig. 1. Note that due to the above function $T(E)$ in Fig. 1, for a given energy interval, it is decreasing for small β values and increasing for large β values. The maximum at the point of resonant energy has the important feature that it is realized for any values of the incidence angle ϕ. This is evidenced, in particular, by Fig. 2, which shows the dependence of the transmission coefficient on the incidence angle of ϕ for such parameters: for all lines $E = 1$, $w = 2$, and $U = 0.3$ for the solid, dotted, dashed-dotted lines, $U = 0.1$ for the dashed line, $\beta = 0.5$ for the dotted and dashed lines, $\beta = 0.7$ for the solid line, $\beta = 0.3$ for the dashed-dotted line.

The straight line with $T(E) = 1$ corresponds to the energy $E = 1$, for which we see the maximum of the function of $T(E)$ in Fig. 1 for the same parameters. Therefore, in fact, the maximum value of $T = 1$ does not depend on the incidence angle of ϕ. Thus, in this structure there is a phenomenon of the perfect transmission independent of the incidence angle direction. A similar effect is known to occur in structures based on the dice lattice and on the topological insulators (see, e.g., [11, 12]). Here we show for the first time that an ideal transmission, regardless of the angles of incidence, is also possible in the graphene-based structures.

Figure 3 depicts the transmission spectra for another value of the barrier height U, namely for $U = 0.5$. It is seen that an increase in U led to the appearance of a resonance with $T = 1$ for $\beta = 0.3$ in the given energy interval. Parameters are as

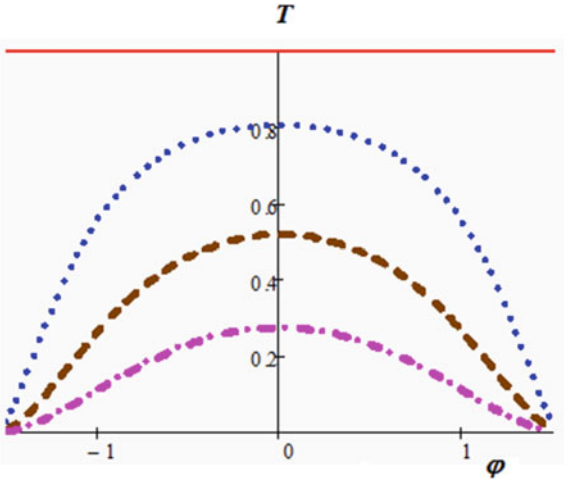

Fig. 2 Dependence of the transmission rates T on the incidence angle ϕ

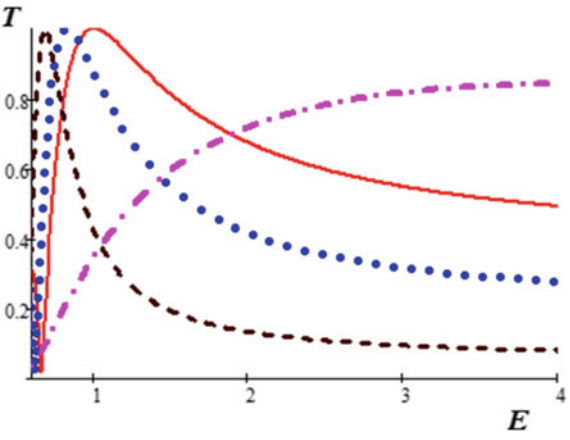

Fig. 3 Dependence of the transmission rates T on energy E for larger than in Fig. 1 U value

follows: $U = 0.5$, $w = 3$, $\phi = 0.1$ for all lines, β =0.5, 0.4, 0.3, 2 for the solid (red online), dotted (blue), dashed (brown), dashed-dotted (magenta) lines, respectively. Figures 1, 2 and 3 show that the all-angled transmission resonances are sensitive to changes in the quantities of U and β.

Figure 4 presents the graph of $T(E)$ in another larger-energy range. The parameter values are as follows: $U = 2$, $\phi = 0.5$ for all curves, and $\beta = 0.3$ for the dotted line, $\beta = 0.4$ for the dashed line $\beta = 0.5$ for the solid line. Here, too, the same as earlier phenomenon is observed: for resonant energies $T = 1$ for all angles of incidence. Analysis of the above formulas shows that the resonant energies E_s are subjected to the following expression:

$$E_s = \frac{U}{1-\beta}$$

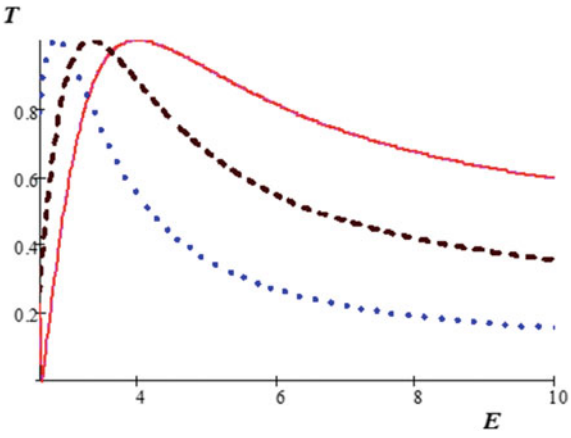

Fig. 4 Dependence of the transmission rates T vs E for larger, than in Figs. 1 and 3, energies

Thus, these energies significantly depend on the potential barrier height and the difference in the Fermi velocities.

Figure 5 presents the T versus ϕ dependence for the following parameters: $E = 1$, $U = 0.5$, $w = 3$, for all lines, β =0.5, 0.3, 0.4, 0.2 for the solid (red online), dotted (blue), dashed (brown), dashed-dotted (magenta) lines, respectively.

If the value of β is far enough away from that at which the phenomenon of omnidirectional transmission takes place, then an increase in the value of β leads to a significant decrease in the transmission coefficient. If the β values are close to those that give resonance, then the removal of β values from them in the direction of decrease or increase leads to a decrease in T in the whole range of the incidence angles. Also the range of allowable β values is also significantly reduced in this case. It should also be noted that the specific interaction of solutions in the quantum well

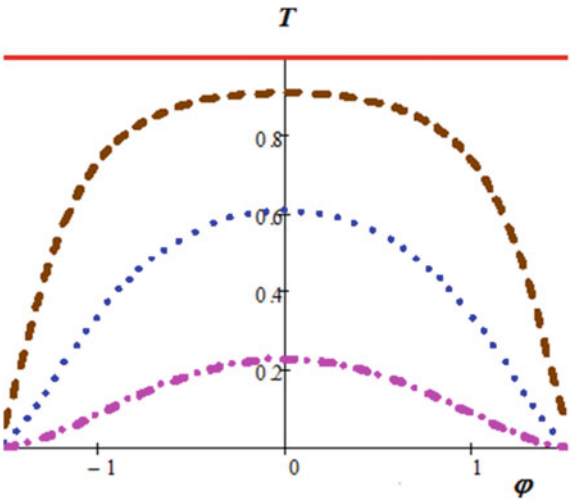

Fig. 5 Dependence of the transmission rates on the incidence angle for another, than in Fig. 2, set of the parameters values

and outside it suppressed the Klein tunneling in the considered system. (It is known that the presence of Klein tunneling is an obstacle to the creation of transistor-type devices based on graphene.) This significantly distinguishes this structure from that considered in [11, 12], where there is a Klein tunneling and the omnidirectional tunneling as well.

4 Conclusion

We consider the modern graphene-based nanostructure that can be used to regulate the energy spectrum of the quasi-electrons. Namely the structure of a graphene single quantum well with a rectangular cross section is studied. It is believed that the ultra-relativistic quasi-electrons whose motion obeys the Dirac-type equation can fall on a well at different angles. Based on this equation, the wave functions inside and outside the well are obtained within the continuum approach. We focus on the solution of the equation that is the interference of the confined states in the quantum well and of the states which propagate across the well. By matching the wave functions at the interfaces, the transmission coefficient of the quasi-electrons through a given structure T is determined. It is taken into account that the Fermi velocity can acquire different values in the region of the well and outside it.

The transmission spectra of quasi-electrons through a given structure, that is, the dependence of the transmission coefficient T on the charge carrier's energy E, are marked by a resonant nature. The most interesting feature of the studied spectra is the presence of the all-angled perfect transmission, that is, for a given set of parameter values, the transmission coefficient is maximum (equal to one) regardless of the angle of incidence of the quasi-electrons on the structure. The energy value for which this effect is realized depends essentially on the Fermi velocity values in different areas of the structure. This means that the transmission spectra can be flexibly adjusted by changing of the Fermi velocity. The dependence of the spectra on the direction of propagation of the electron wave and on the barrier height is also analyzed. Based on the results of this work, we can conclude that the structure considered in it can serve as an original energy filter, which passes quasi-electrons with the required energy from all directions of their incidence. This structure may be useful in the designing of the modern graphene-based nano-electronics.

References

1. Wehling TO, Black-Schaffer AM, Balatsky AV (2015) Dirac materials. Adv Phys 63:1
2. Castro Neto AH, Guinea F, Peres NMR, Novoselov KS, Geim AK (2009) The electronic properties of graphene. Rev Mod Phys 81:109
3. Pereira JM, Milnar V Jr, Peeters FM (2006) Confined states and direction-dependent transmission in graphene quantum wells. Phys Rev B 74:045424

4. Liu L, Li Y-X, Liu J (2012) Transport properties of Dirac electrons in graphene based double velocity-barrier structures in electric and magnetic fields. Phys Lett A 376:3342–3350
5. Wang Y, Liu Y, Wang B (2013) Resonant tunneling and enhanced Goos-Hänchen shift in graphene double velocity barrier structure. Phys E 53:186–192
6. Sun L, Fang C, Liang T (2013) Novel transport properties in monolayer graphene with velocity modulation. Chin Phys Lett 30(4):047201
7. Raoux A, Polini M, Asgari R, Hamilton AR, Fasio R, MacDonald AH (2009) Velocity-modulation control of electron-wave propagation in graphene. arXiv:0912.2608v1 [cond-mat.mes-holl]
8. Concha A, Tešanović Z (2010) Effect of a velocity barrier on the ballistic transport of Dirac fermions. Phys Rev B 82:033413
9. Yuan JH, Zhang JJ, Zeng QJ, Zhang JP, Cheng Z (2011) Tunneling of Dirac fermions in graphene through a velocity barrier with modulated by magnetic fields. Phys B 406:4214–4220
10. Krstajic PM, Vasilopoulos P (2011) Ballistic transport through graphene nanostructures of velocity and potential barriers. J Phys Condens Matter 23:000000(8pp)
11. Korol AM, Medvid' NV, Sokolenko AI (2018) Transmission of the relativistic fermions with the pseudo spin equal to one through the quasi-periodic barriers. Physica Status Solidi B 255(9):1800046
12. Korol AM, Medvid' NV, Sokolenko AI, Sokolenko IV (2019) Ballistic transmission of the Dirac quasielectrons through the barrier in the 3D topological insulators. Springer Proc Phys 221:517–525
13. Korol AM (2019) Tunneling conductance of the s-wave and d-wave pairing superconductive graphene–normal graphene junction. Low Temp Phys 45(5):A48
14. Takahashi R, Murakami S (2011) Gapless interface states between topological insulators with opposite dirac velocities. Phys Rev 10766805
15. Sen D, Deb O (2012) Junction between surfaces of two topological insulators. Phys Rev B 85:245402

Structure, Thermophysical Properties and Thermodynamics of Formation of Nanocomposites Based on Epoxy Resin and Carbon Nanotubes

Valery Korskanov, O. M. Fesenko, Tamara Tsebriinko, Andriy Yaremkevych, and Volodimir Dolgoshey

1 Introduction

Carbon nanotubes (CNT), due to their high mechanical properties, unique geometrical parameters (significant length-to-diameter ratio), high specific surface, thermal and electrical conductivity, are effective fillers for obtaining polymer nanocomposites (NC) with predetermined high-performance properties [1, 2]. In the twenty-first century, such NCs use broad applications in the field of biomedical science [3], as anode material for sodium and lithium-ion batteries [4], in high-performance supercapacitors [5], conductive aerospace adhesives [6], for advancing next-generation electronics [7], etc.

Epoxy resins (ER), which are characterized by high thermal stability, significant adhesion to various materials (metals, glass, ceramics, etc.), are widely used as adhesives, anti-corrosion coating or sealants, and promising as a polymer matrix for production NC [8, 9].

Therefore, nanocomposites based on ER and CNT which combine the beneficial properties of each of the components are of great interest to researchers [10, 11]. It is shown in the literature that the properties of such nanocomposites are determined by the properties of each of their components [12–15].

The purpose of this work was to study the thermodynamic of interaction between ER and CNT to determine the optimal conditions for the formation of NC on their basis.

V. Korskanov (✉) · O. M. Fesenko · T. Tsebriinko · A. Yaremkevych
Institute of Physics of the National Academy of Sciences of Ukraine, 46, Ave. Nauki, Kyiv 03039, Ukraine
e-mail: vk_dsc@ukr.net

V. Dolgoshey
National Technical University of Ukraine "Igor Sikorsky Kyiv Polytechnic Institute", 37, Ave. Peremohy, Kyiv 3056, Ukraine

O. Fesenko and L. Yatsenko (eds.), *Nanomaterials and Nanocomposites, Nanostructure Surfaces, and Their Applications*, Springer Proceedings in Physics 263, https://doi.org/10.1007/978-3-030-74741-1_20

2 Experimental

The Samples Preparation

The basis for the formation of NCs was an epoxydiane oligomer (EDO) based on bisphenol A, with a density of $\rho = 1150$ kg/m^3 at 293 K (trademark DER 321 from DOW Chemical). Polypox H354 (manufacturer UPPC (Germany)) was used as a hardener for EDO.

Carbon nanotubes with a density of 2100 kg/m^3, an outer diameter of 20 nm, and a specific surface of 196,000 m^2/kg were used as a nanofiller for the preparation of NCs [16].

The neat epoxy polymer was obtained by mixing EDO with Polypox H354 in a ratio of 100: 52 parts by weight, respectively. The mixture was kept for 24 h at room temperature according to the manufacturer's technological requirements (NC-I). Further, thermal postcuring was carried out for 4 h at a temperature of 473 K (NC-II).

A schematic diagram of the preparation process of the NC is presented in Fig. 1.

In general, the method for preparation of the epoxy composite material comprising a plurality of steps: ultrasonic dispersed of the carbon nanotubes in a EDO to form a homogeneous dispersion and for functionalization all high specific surface of CNT; adding a curing agent to the dispersion; stirring in a mechanical stirrer for 15 min until a homogeneous three-component mixture; curing during 24 h at temperature 293 K (NC-I); postcuring within 4 h at a temperature of 473 K (NC-II).

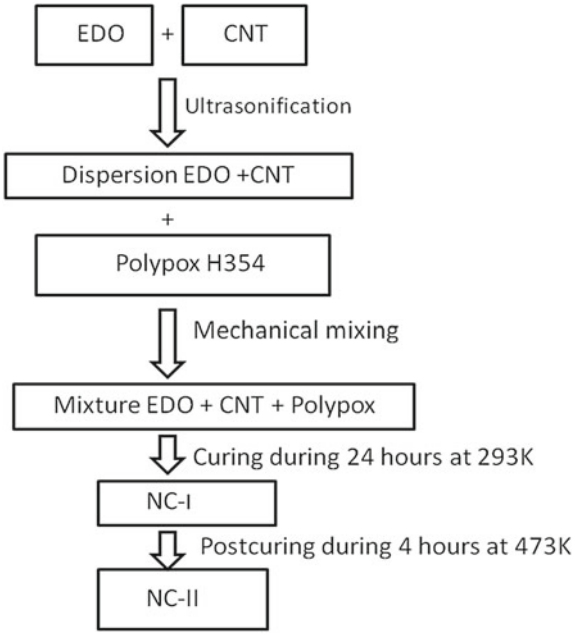

Fig. 1 Diagram of the preparation process of the NC

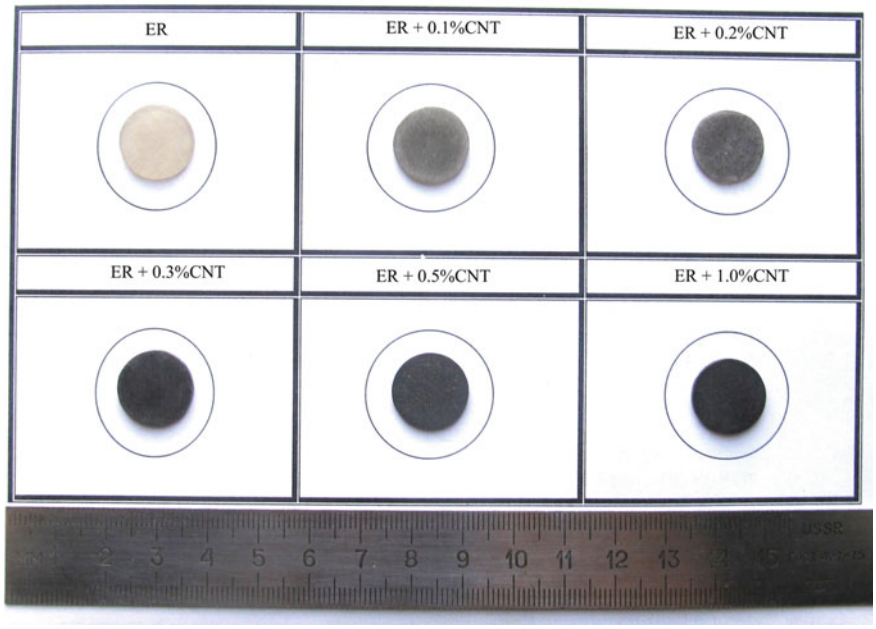

Fig. 2 Samples for research

Disk-like samples of pure ER and NC were prepared with CNT weight content (w) of 0.1, 0.05, 0.08, 0.2, 0.3, 0.4, 0.5, and 1.0% (Fig. 2).

Characterization of the Samples

Small-angle X-ray scattering (SAXS) curves were obtained in a Kratki-type vacuum chamber, in radiation from a copper anode monochromated by a nickel filter. The measurements were carried out in the mode of multiple-step scanning in the scattering range 2θ from 0.0124 to 12.0. The wavelength of the X-ray radiations is $\lambda = 0.154$.

The density ρ of the samples was determined by hydrostatic weighing in the reference isooctane.

DSC thermograms were obtained in the temperature range 203–443 K at a heating rate of 5 K/min with the Q2000 calorimeter (TA Instrument (USA).

Thermodynamic functions were calculated from DSC thermograms in the temperature range 253–373 K.

The change in enthalpy of samples ΔH during isobaric heating from temperature T_1 to $T_2$was calculated from the values of heat capacity at constant pressure C_p [17]:

$$\Delta H(T_1 \rightarrow T_2)\,(P = \text{const}) = \int_{T_1}^{T_2} C_p(T)dT \tag{1}$$

Entropy at each temperature T_i ($T_1 \leq T_i \leq T_2$) was found as [18]:

$$\Delta S_{T_i} = \Delta H_{T_i} / \Delta T_i \,. \tag{2}$$

The change in free energy or Gibbs energy (ΔG) was determined as follows [19]:

$$\Delta G_{T_i} = \Delta H_{T_i} - T_i \cdot \Delta S_{T_i}. \tag{3}$$

3 Results and Discussions

Figure 3 shows (SAXS) curves that were obtained for ER-II, CNT, NC-II +0.1%CNT, and NC-II +1.0%CNT.

The curve of pure EP-II (see Fig. 3) is characterized by a low level of X-ray scattering and a shape typical of amorphous systems. In contrast, the curve X-ray scattering from CNT has a high level of scattering and corresponds to the model of "defective balls" with an average size of about 7.17 nm (curve 2 on Fig. 3) [20]. For sample NC-II +0.1% CNT the SAXS curve is also typical of amorphous systems, but scattering intensity higher than for NC-II. On the scattering curve for NC-II + 1.0%CNT, we can see the plateau with characteristic average size of about 2.16 nm (curve 4 on Fig. 3). In our opinion, this plateau together with high level of scattering corresponds to the pores in the structure of the sample.

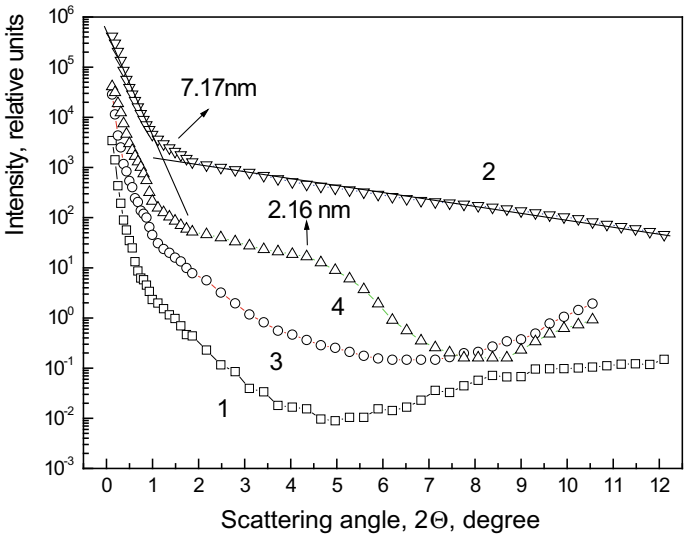

Fig. 3 SAXS curves for ER-II (1), CNT (2), NC-II +0.1%CNT (3), and NC-II +1.0%CNT (4)

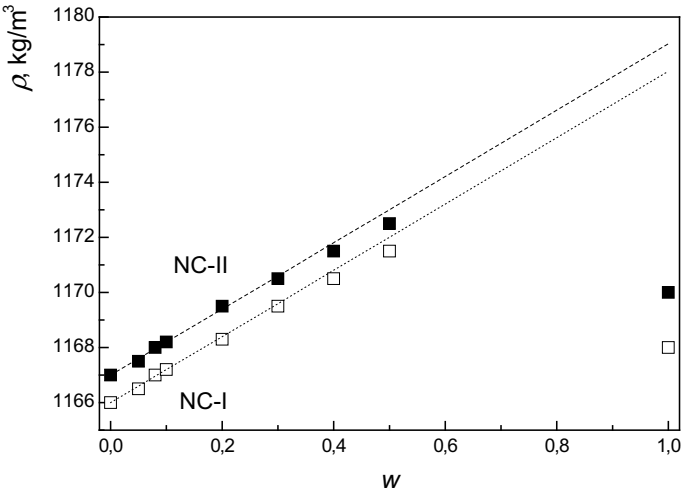

Fig. 4 Concentration dependences of the density of nanocomposites

Figure 4 shows that the concentration dependences of the density of nanocomposites are given.

The higher density of NC-II samples relative to NC-I is the effect of thermal postcuring of the samples. In the concentration range $w < 0.5$, the NC density increases with an increase in the CNT content according to linear relationships (see dashed lines in the figure):

$$\rho_{\text{NC - I}} = 1117 + 11.9\, w,$$
$$\rho_{\text{NC - II}} = 1167 + 12.0\, w.$$

The deviation from the linear concentration dependence $\rho = f\ (w)$ at $w \geq 0.5$ indicates a change in the morphology of the nanocomposites. In our opinion, at this concentration, saturation of bonds between EDO and CNT (see Fig. 1) occurs due to the very high specific surface of carbon nanotubes, mentioned above. As a result, at $w > 0.5$, a porous structure of the samples is formed.

Figure 5 presents the evolution of the ER formation.

After further thermal annealing of EP-II at temperatures above 473 K, the DSC thermograms did not change. Therefore, we assumed that EP-II is a fully cured system.

The resulting value $T_g = 305.7$ K for ER-I significantly exceeds the corresponding value for the uncrosslinked ER-0 ($T_{g0} = 242.0$ K), and the jump in heat capacity $\Delta C_p = 0.547$ kJ/(kg K) is much less than $\Delta C_{p0} = 0.951$ kJ/(kg K)—for ER-0 (Fig. 5). For the postcured sample (ER-II), these values are $T_g = 348.0$ K and $\Delta C_p = 0.382$ kJ/(kg K), respectively.

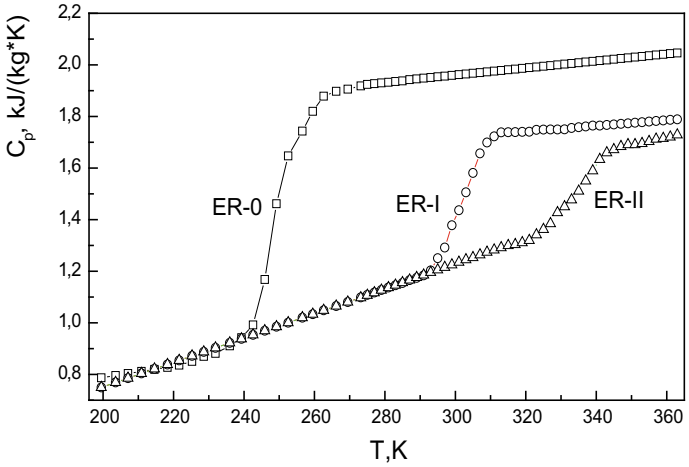

Fig. 5 Thermograms of the evolution of the ER formation. ER-0 is an uncured mixture EDO + CNT + Polypox; ER-I—after annealing for 24 h at 293 K, ER-II—after annealing for 4 h at 473 K

The degree of crosslinking of the studied polymers was estimated using the DiBenedetto equation which previously shown suitability for many network polymer systems, including epoxy-based polymer networks [21, 22]:

$$\alpha = \left[\frac{\Delta C_p}{\Delta C_{p0}} \cdot \frac{T_{g\infty} - T_g}{T_g - T_{g0}} + 1 \right]^{-1}, \tag{4}$$

where T_{g0}, ΔC_{p0}—is the glass transition temperature and a jump of heat capacity at glass transition of unhardened ER; T_g, ΔC_p—corresponding values for the test sample; $T_{g\infty}$—glass transition of fully hardened sample.

Substituting the corresponding values of thermophysical properties into Eq. 4, we obtain $\alpha = 0.724$ for ER-I and $\alpha = 1.000$ for ER-II. This means that the value α is numerically reflecting the effect of crosslinking of nanocomposites based on crosslinked polymers.

Comparative DSC thermograms for all studied samples are shown in Fig. 6.

The DSC thermogram for ER-I clearly shows a jump in heat capacity at the glass transition temperature T_g, which is superimposed on the endothermic relaxation effect in the temperature range 317–334 K (see Fig. 6). In a heat-treated sample (ER-II), the endothermic effect disappears, and the T_g increases significantly. On the thermograms of NC samples of the ER-I series, with an increase in the content of CNT, the endothermic effect becomes much less, and the jump in the heat capacity during glass transition ΔC_p decreases. In the samples of the EP-II series, both T_g and ΔC_p with an increase in w show a tendency to decrease (Fig. 6).

The thermophysical characteristics of all studied samples are collected in Table 1.

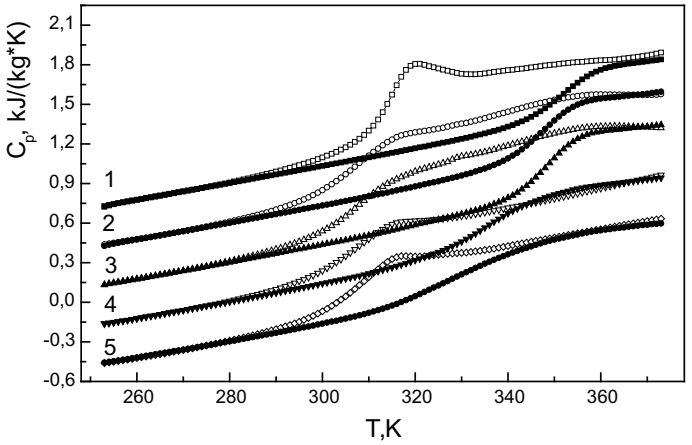

Fig. 6 DSC thermograms for all studied samples. Opened symbols are the samples from series ER-I, filled symbols are symbols of the samples from series ER-II. Thermograms No 2–No 5 shifted down on 0.3 kJ/(kg K). 1–ER, 2–ER + 0.05% CNT, 3–ER + 0.10% CNT, 4–ER + 0. 50% CNT, 5–ER + 1.00% CNT

Table 1 Thermophysical characteristics of the studied samples

No.	Sample	T_g, K	ΔT_g, K	ΔC_p, J/(kg K)	ρ, kg/m^3	α
1	ER-I	305.7	39.4	0.547	1166.0	0.724
2	NC-I + 0.05%CNT	306.6	45.2	0.530	1166.5	0.737
3	NC-I + 0.08%CNT	307.5	47.0	0.445	1167.0	0.776
4	NC-I + 0.1%CNT	309.3	48.6	0.408	1167.2	0.802
5	NC-I + 0.2%CNT	308.5	39.0	0.371	1168.0	0.812
6	NC-I + 0.3%CNT	308.8	39.6	0.358	1169.5	0.819
7	NC-I + 0.4%CNT	308.6	39.2	0.305	1170.5	0.840
8	NC-I + 0.5%CNT	308.7	39.4	0.291	1170.0	0.847
9	NC-I + 1.0%CNT	308.7	39.4	0.263	1168.0	0.912
10	ER-II	348.0	26.2	0.382	1167.0	1.000
11	NC-II + 0.05%CNT	346.5	25.3	0.454	1167.5	0.993
12	NC-II + 0.08%CNT	346.2	25.4	0.510	1168.0	0.991
13	NC-II + 0.1%CNT	345.5	25.3	0.530	1168.0	0.987
14	NC-II + 0.2%CNT	344.5	27.5	0.424	1169.0	0.985
15	NC-II + 0.3%CNT	342.0	30.2	0.420	1170.0	0.974
16	NC-II + 0.4%CNT	338.1	36.4	0.414	1171.0	0.957
17	NC-II + 0.5%CNT	336.0	40.4	0.410	1172.0	0.948
18	NC-II + 1.0%CNT	333.2	48.3	0.339	1168.2	0.945

Further, discussion of the obtained results was carried out by analyzing the concentration dependences of thermophysical properties according to the results of Table 1.

An increase in the glass transition temperature of samples T_g of the ER-I series, together with a corresponding expansion of the glass transition temperature range ΔT_g and a significant decrease in ΔC_p with an increase in the content of CNT to $w = 0.1\%$, indicates that in this region of compositions nanofiller acts as a reinforcing agent for the EP and leads to an increase in NC heterogeneity due to an increase in the total specific surface area of CNT.

This leads to the fact that the degree of NC crosslinking in this composition region increases with an increase in the CNT content (Table 1); i.e., the nanofiller acts as a crosslinking initiator for nanocomposites. This leads to the fact that the degree of NC crosslinking α in this region of the composition increases with an increase in the CNT content; i.e., the nanofiller acts as an initiator for the crosslinking of nanocomposites. Obviously, this is the result of ultrasonic dispersion of EDO with CNT at the initial stage of the formation of nanocomposites (Fig. 1).

With a further increase of w, the values of T_g and ΔT_g pass through a maximum at $w = 0.1 - 0.2\%$ and remain approximately the same at higher w. In our opinion, at $w = 0.1 - 0.2\%$, the thermodynamic state of ER-I remains constant, and a decrease in ΔC_p occurs due to an increase in the number of polymer–nanofiller contacts due to an increase in the total specific surface area of the CNT.

For samples of the ER-II series, the glass transition temperature in the entire range of compositions decreases with increasing w. This indicates that in nanocomposites CNT forms steric obstacles to the formation of a polymer network. The glass transition interval ΔT_g, passing through a minimum at $0.2\% \geq w \geq 0.1\%$, remains approximately constant. The value of the jump in heat capacity ΔC_p grows when the CNT content is $w < 0.1\%$, passes through its maximum 0.530 and tends to decrease at $w > 0.1\%$.

The discussion of the results of the effect of thermal annealing on the thermophysical properties of NC will be carried out by analyzing the components of Eq. (4).

The temperature difference $(T_g - T_{g0})$ formally reflects the general effect of NC crosslinking. A decrease in the values $(T_g - T_{g0})$ in the samples from series ER-II with an increase in w indicates the effect of CNT as steric obstacles to the formation of a network of bonds.

The value $\delta T_g = T_{g\infty} - T_g$ in Eq. (4) can be a measure of the completion of the crosslinking process (Table 1). At $w \leq 0.1$ in the ER-I, the value δT_g decreases and remains approximately constant with a further increase in w. For samples of the ER-II series, the δT_g value was taken as the effect of thermal annealing of the samples.

Since after heat treatment NC-I remains slightly uncured compared to NC-II, a decrease in the difference $T_{gER\text{-}II\infty} - T_{gNC\text{-}II\infty}$ (where $T_{gER\text{-}II\infty}$ is the glass transition temperature of fully formed ER-II, $T_{gNC\text{-}II\infty}$ is the glass transition temperature of fully formed NC-II) should be taken as a decrease in the crosslink density as a result of steric restrictions when increasing the content of CNT. The combination of these

components of Eq. (4) fully reflects the nature of the dependence of the degree of completeness of the crosslinking reaction in NC with a change in the composition (Table 1).

The analysis of the process of thermal crosslinking of EP and NC will be carried out within the framework of classical thermodynamics [5].

According to classical thermodynamics, for the transition of a substance from state I to state II, it is necessary to spend enthalpy (heat) $\delta H_{I\text{-}II} = (H_{II} - H_I)$. In NC with a change in the ratio of the components, the interaction energy of the polymer filler can be calculated as $(\delta H_{I\text{-}II})_{NC\text{-}CNT} = (\delta H_{I\text{–}II})_{\mathrm{NC}} - (\delta H_{I\text{–}II})_{\mathrm{ER}}$ (Fig. 7). According to thermodynamics [5], an increase in $(\delta H_{I\text{-}II})_{NC\text{-}CNT}$ should be regarded as an increase in the energy required for the formation of NC with increasing w.

The total enthalpy of interaction of epoxy resin with CNT in each of the nanocomposites was calculated from Fig. 7 as follows:

$$\delta \mathrm{H}_{ER-CNT} = \sum_{253k}^{373K} (\delta H_{I-II}).$$

The concentration dependence of the contribution of the interaction energy of the epoxy resin with the nanofiller to the total energy of NC formation is shown in Fig. 8.

If the degree of completion of the reaction changes by during thermal crosslinking of NC $\delta\alpha_{NC} = \alpha_{II} - \alpha_I$ and the total energy loss was $\delta H_{I,II}$, then the total energy of formation of the thermodynamic system is equal to $\delta H_{\infty} = \delta H_{I,II}/(\alpha_{II} - \alpha_I)$. The energy that should be lost for thermal postcuring of NC is equal to $\delta H_{NC} = \delta H_{ER} \cdot (\delta\alpha_{NC}/\delta\alpha_{ER})$. The contribution from the interaction of ER and CNT is calculated as

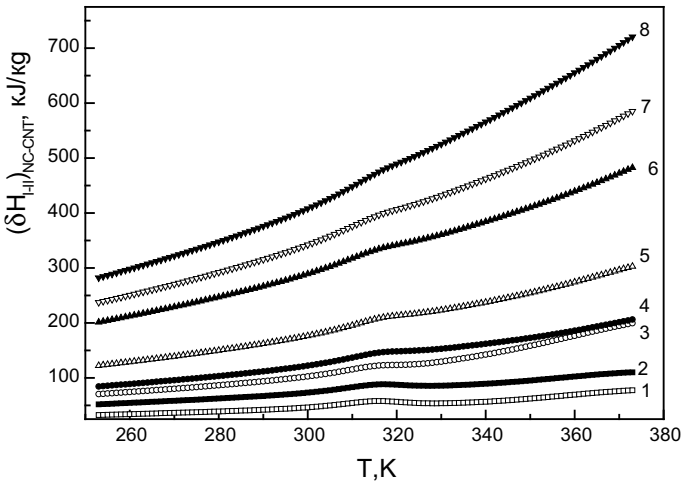

Fig. 7 Temperature dependence of the enthalpy of interaction of components in nanocomposites. Mass contain of CNT: 1–0.05%, 2–0.08%, 3–0.1%, 4–0.2%, 5–0.3%, 6–0.4%, 7–0.5%, 8–1.0%

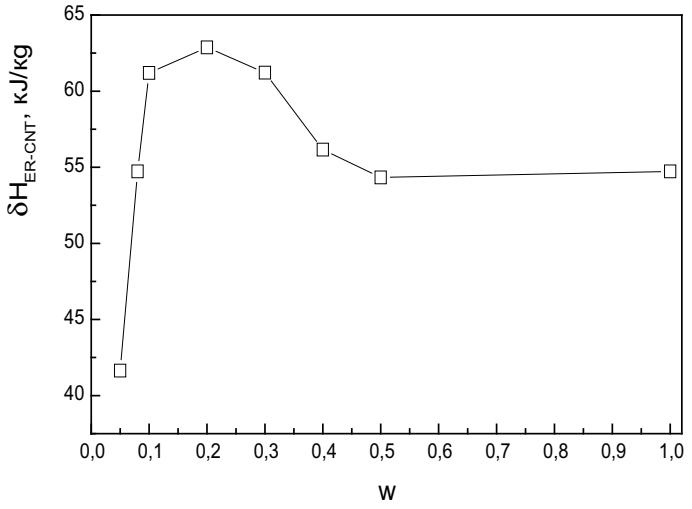

Fig. 8 Concentration dependence of the contribution of the epoxy resin–nanofiller interaction energy to the total energy of formation of NC

the difference between the energies that were spent on the formation of ER and NC, that is, $\delta H_{ER\text{-}CNT} = \delta H_{NC} - \delta H_{ER}$.

Figure 8 shows that the maximum polymer–nanofiller interaction energy is achieved at w from 0.1 to 0.4. Obviously, this is one of the main factors that ensure the achievement of optimal conduction properties of the investigated nanocomposites.

4 Conclusions

As a result of the studies carried out, it was found that with an increase in the content of CNT, a decrease in the glass transition temperature, an expansion of the glass transition temperature range in NC in relation to ER-II, and a reduced degree of completion of the crosslinking reaction of ER. It has been established that the maximum specific energy of the ER-CNT interaction is achieved at a mass content of nanofiller from 0.1% to 0.4%. Obviously, the position of this maximum corresponds to the saturation of the CNT bonds with the epoxy matrix.

5 Funding

This research did not receive any specific grant from funding agencies in the public, commercial, or not-for-profit sector.

Compliance with Ethical Standards

6 Conflict of Interest

The authors declare that they have no conflict of interest.

References

1. Kumar SD, Ravichandran M, Alagarsamy SV, Chanakyan C, Meignanamoorthy M, Sakthivelu S (2020) Processing and properties of carbon nanotube reinforced composites: a review. Materialstoday: processing. vol 27. pp 1152–1156. https://doi.org/10.1016/j.matpr.2020.02.006
2. Pantano A, Modica G, Cappello F (2008) Multiwalled carbon nanotube reinforced polymer composites. Mater Sci Eng: A 486(1–2):222–227. https://doi.org/10.1016/j.msea.2007.08.078
3. Anzar N, Hasan R, Tyagi M, Yadav N, Narang J (2020) Carbon nanotube—a review on synthesis, properties and plethora of applications in the field of biomedical science. Sens Int 1:100003. https://doi.org/10.1016/j.sintl.2020.100003
4. Zhong S, Liu H, Wei D, Hu J, Zhang H, Hou H, Peng M, Zhang G, Duan H (2020) Long-aspect-ratio N-rich carbon nanotubes as anode material for sodium and lithium ion batteries. Chem Eng J 395:125054. https://doi.org/10.1016/j.cej.2020.125054
5. Liu R, Sun S, Zhong R, Zhang H, Wu X Nitrogen-doped microporous carbon coated on carbon nanotubes for high performance supercapacitors. Microporous Mesoporous Mater 305:110300. https://doi.org/10.1016/j.micromeso.2020.110300
6. Jakubine MB, Ashrafi B, Zhang Y, Martinez-Rubi Y, Ch T, Kingston A, Simard B (2015) Single-walled carbon nanotube–epoxy composites for structural and conductive aerospace adhesives. Compos Part B: Eng 69:87–93. https://doi.org/10.1016/j.compositesb.2014.09.022
7. Niu T (2020) Carbon nanotubes advance next-generation electronics. Nanotoday 35:100992. https://doi.org/10.1016/j.nantod.2020.100992
8. Muñoz BK, Bosque A, Sánchez M, Utrilla V, Prolongo SG, Prolongo MG, Ureña A (2020) Epoxy resin systems modified with ionic liquids and ceramic nanoparticles as structural composites for multifunctional applications. Polymer 123233. https://doi.org/10.1016/j.polymer.2020.123233
9. Verma C, Olasunkanmi LO, Akpan ED, Quraishi MA, Dagdag O, El Gouri M, Sayed E, Sherif M, Ebenso EE (2020) Epoxy resins as anticorrosive polymeric materials: a review. Polymer 104741. https://doi.org/10.1016/j.reactfunctpolym.2020.104741
10. Chen J, Han J (2020) Effect of hydroxylated carbon nanotubes on the thermal and electrical properties of derived epoxy composite materials. Results Phys 18:103246. https://doi.org/10.1016/j.rinp.2020.103246
11. Aslan A, Salur E, Düzcükoğlu H, Sinan Şahin Ö, Ekrem M (2021) The effects of harsh aging environments on the properties of neat and MWCNT reinforced epoxy resins. Constr Build Mater 22:1211929. https://doi.org/10.1016/j.conbuildmat.2020.121929
12. Luo H, Qiu J (2019) Carbon nanotubes/epoxy resin metacomposites with adjustable radio-frequency negative permittivity and low dielectric loss. Ceram Int 45(1):843–848. https://doi.org/10.1016/j.ceramint.2018.09.253
13. Roy D, Tiwari N, Mukhopadhyay K, Kumar Saxena A (2014) The effect of a doubly modified carbon nanotube derivative on the microstructure of epoxy resin. Polymer 55(2):583–593. https://doi.org/10.1016/j.polymer.2013.12.012

14. Bui K, Brian Grady P, Dimitrios G, Papavassiliou V (2011) Heat transfer in high volume fraction CNT nanocomposites: effects of inter-nanotube thermal resistance. Chem Phys Lett 508(4–6):248–251. https://doi.org/10.1016/j.cplett.2011.04.005
15. Kharitonov AP, Simbirtseva GV, Tkachev AG, Blohin AN, Dyachkova TP, Maksimkin AA, Chukov DI (2015) Reinforcement of epoxy resin composites with fluorinated carbon nanotubes. Compos Sci Technol 107:162–168. https://doi.org/10.1016/j.compscitech.2014.12.002
16. Olenchuk MV, Gnatyuk OP, Dovbeshko G, Karakhim S (2019) Do carbon nanotubes inhibit or promote amyloid fibrils formation?. Biophys Bull 42:49–60. https://doi.org/10.26565/2075-3810-2019-42-04
17. Bejan A (2018) Thermodynamics today. Energy. 160:1208–1219. https://doi.org/10.1016/j.energy.2018.07.092
18. Greiner W, Neise L, Stocher H (1995) Thermodynamics and statistical mechanics. Springer 464
19. Rao Y (2004) An introduction to thermodynamics. Sangam Books Ltd. 479
20. Kim MK, Chirikjian GS, Jernigan RL (2002) Elastic models of conformational transitions in macromolecules. J Mol Graphics Model 21(2):151–160. https://doi.org/10.1016/S1093-3263(02)00143-2
21. Montserrat S (1995) Effect of crosslinking density on ΔC_p (T_g) in an epoxy network. Polymer 36(2):435–436. https://doi.org/10.1016/0032-3861(95)91337-7
22. Lee A, McKenna GB (1988) Effect of crosslink density on physical ageing of epoxy networks. Polymer 29(10):1812–1817. https://doi.org/10.1016/0032-3861(88)90396-5

Nanostructure Surfaces

Dispersion Kinetics of Thin Double Niobium-Nickel Films Deposited onto Oxide Ceramic Materials and Annealed in Vacuum

I. I. Gab, T. V. Stetsyuk, O. M. Fesenko, and D. B. Shakhnin

1 Introduction

Joining ceramic materials with each other and with metals is carried out by two main methods:

(1) Brazing with molten metallic solders;
(2) Solid-phase pressure welding.

Since ceramic materials, particularly oxide ones, are usually poorly wetted by molten metals, metal coatings are often used applied in various ways (electron beam sputtering, magnetron sputtering, chemical deposition etc.). Adhesive-active metals such as titanium, chromium, niobium and others are the most commonly used to make such coatings. Then, thus metallized ceramic parts are brazed in vacuum or an inert medium (argon, helium etc.) by molten metallic solders on the basis of tin, silver, copper, nickel etc. In this case, the thickness of the solder seam is from 50 to 100 μm up to several millimeters. Sometimes, multilayer metal coatings are used, but the thickness of the layers and brazed seams remains high [1–9].

At the same time, there is information that the reduction in the thickness of the brazed seam leads to a significant increase in the strength of the brazed joint [10–12]. Obtaining brazed or welded joints of metallized ceramics is possible through

I. I. Gab · T. V. Stetsyuk (✉)
Frantsevich Institute for Problems of Materials Science of National Academy Sciences of Ukraine, 3, Krzhyzhanovskogo st., Kyiv 03142, Ukraine
e-mail: tvst@ukr.net

O. M. Fesenko
Institute of Physics of National Academy Sciences of Ukraine, 46, Nauky ave., Kyiv 03680, Ukraine

D. B. Shakhnin
University «Ukraine», 23 Lvivska st., Kyiv 03115, Ukraine

O. Fesenko and L. Yatsenko (eds.), *Nanomaterials and Nanocomposites, Nanostructure Surfaces, and Their Applications*, Springer Proceedings in Physics 263, https://doi.org/10.1007/978-3-030-74741-1_21

reducing the thickness of both the metallization coating on the ceramics and the brazing layer by itself. This can be achieved if the soldering metal or alloy is also applied in the form of a rather thin film, the thickness of which does not exceed several μm. In addition, a thin soldering seam allows you to obtain precision welded or brazed ceramic and ceramic–metal units which can be used in microelectronics, radio engineering, microwave engineering etc.

This objective can be achieved by application onto the ceramic surfaces of double metal films, one of which is 100–200 nm thick and consists of an adhesion-active metal such as Ti, Cr etc., and the other is slightly thicker (2–3 μm) and serves as a solder, e.g. Cu, Ag etc., which will ensure joining of metallized ceramic materials during brazing or welding with fine (2–4 μm thick) solder seam.

The structure of such two- or multiphase coatings, determination of the optimal ratio of the thickness of each layer, processes of interaction at the phases interface, and behavior of these double films during annealing of them, is also an important area of research.

The study of dispersion kinetics two-layer niobium-nickel coatings (films) on oxide materials during annealing in vacuum and the creation of brazed and welded oxide ceramics joints based on them with super-thin brazed seam, the thickness of which does not exceed 5 μm, is the main task of the present work.

2 Materials and Experimental Methods

In this paper an electron-beam method for sputtering of metal (Nb, Ni) thin films was used.

The thickness of the deposited films was measured by two methods:

(1) The metal of the given weight (calculated for films of the required thickness) is completely evaporated, then the thickness of the film can be easily calculated according to the law of Lambert [13, 14];
(2) With the help of a special quartz sensor located in the vacuum sputtering chamber near the sample on which the film is deposited.

Solid non-metallic substrates were made of sapphire, alumina and zirconia ceramics as small thin plates 4 × 3 × 2 mm in size. One of the flat surfaces of each specimen was well polished to a roughness $R_z = 0.03 \div 0.05$ μm. After polishing, all specimens were thoroughly defatted and burned in air at 1100 °C for one hour.

As a metal deposited directly onto non-metallic surfaces, niobium was used. Metallized samples were then coated by nickel films serving as a solder when joining the samples.

The quality of all applied thin films was controlled using a XJL-17 metallographic microscope.

The specimens with deposited onto them metal films were annealed in a vacuum chamber for various periods of time (from 5 up to 20 min) and at different

temperatures (from 900 °C up to 1100 °C) in the vacuum not less than 2×10^{-3} Pa.

Annealed specimens were investigated using SEM and ASM microscopy with microphotographs storing. Using these microphotographs, the areas of metal islets on the surface of non-metallic samples were determined by the planimetric method [10]. The experimental data obtained were processed in the form of graphs showing the dependence of the surface area of the samples covered with metal thin films on the annealing parameters (temperature, time).

3 Results and Discussion

The thickness of the niobium metallization layer on the leucosapphire, alumina, and zirconium dioxide ceramics substrates was 150 nm, and the thickness of the nickel layer reached 1.5 μm.

The original niobium-nickel films on all three oxides were continuous and remained the same after five minutes of annealing at 1000 °C. Noticeable changes in the films appeared only after ten minutes at 1000 °C, but the films integrity was almost not violated as well. Only after twenty minutes of annealing at 1000 °C, the surface of the films has changed significantly, and even cracks appeared which are especially noticeable for films at the leuco sapphire surface (Fig. 1). The annealing temperature increase up to 1100 °C has of course accelerated the changes in the morphology of the films occurred after five minutes of annealing; these changes became more noticeable after ten minutes of annealing, but they did not violate the integrity of the films as well. Only after twenty minutes at 1100 °C, the films show cracks and tears (Fig. 2), but the film covers still about 90% of the substrate surface. The annealing of the films at 1200 °C further accelerated the process of their dispersion which is noticeable after five, and especially after ten, minutes (Fig. 3).

At high magnification under an atomic force microscope, niobium-nickel double films at the leuco sapphire surface show clearly that the film began to swell intensively

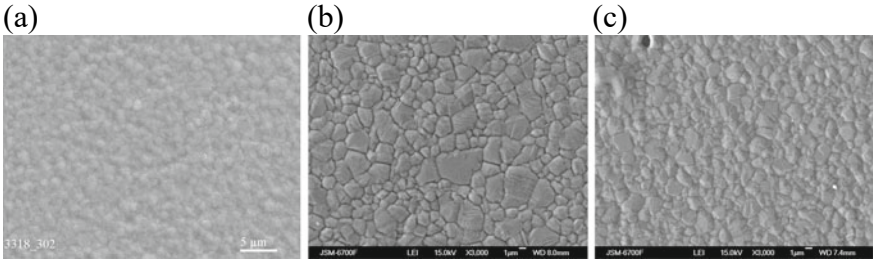

Fig. 1 SEM image of double niobium-nickel film deposited onto oxide materials and further annealed at 1000 °C during 20 min in vacuum, ×3000: **a** alumina ceramics; **b** leucosapphire; **c** zirconia ceramics

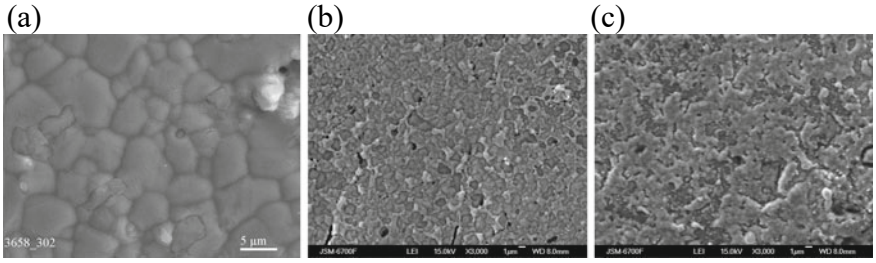

Fig. 2 SEM image of double niobium-nickel film deposited onto oxide materials and further annealed at 1100 °C during 20 min in vacuum, ×3000: **a** alumina ceramics; **b** leucosapphire; **c** zirconia ceramics

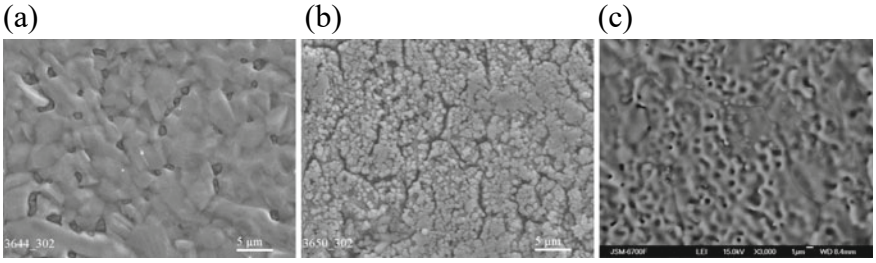

Fig. 3 SEM image of double niobium-nickel film deposited onto oxide materials and further annealed at 1200 °C during 10 min in vacuum, ×3000: **a** alumina ceramics; **b** leucosapphire; **c** zirconia ceramics

and to disintegrate after a ten-minute annealing at 1200 °C. The height of the swellings reached almost 200 nm.

Twenty-minute annealing at 1200 °C led not only to a significant dispersion of the films, but also to the interaction of nickel with niobium metallization layer at the oxide substrates because there is a eutectic in the Nb-Ni system at 1175 °C (Fig. 4).

Figure 5 shows the AFM image of a niobium-nickel double film at the zirconia

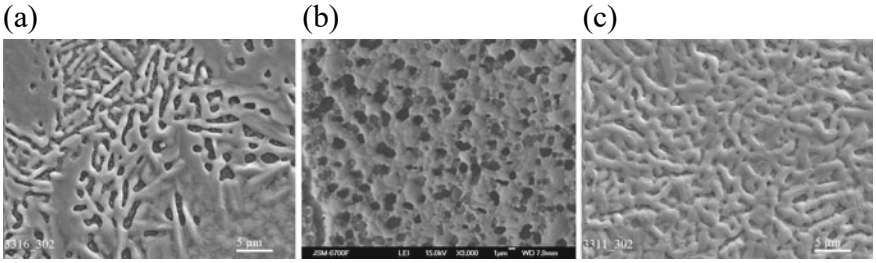

Fig. 4 SEM image of double niobium-nickel film deposited onto oxide materials and further annealed at 1200 °C during 20 min in vacuum, ×3000: **a** alumina ceramics; **b** leucosapphire; **c** zirconia ceramics

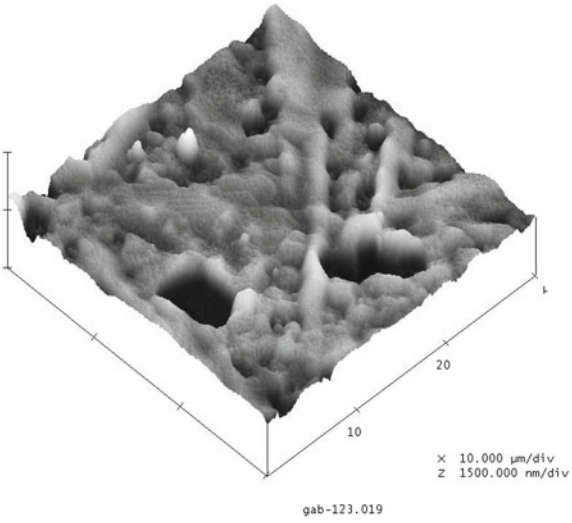

Fig. 5 Three-dimensional AFM image thin double niobium-nickel film deposited onto zirconia ceramics and further annealed at 1200 °C during 20 min in vacuum

ceramics surface annealed in vacuum at 1200 °C for 20 min. The photo shows that the interaction between niobium and nickel began in the film leading to a significant change in the primary relief of the film, and the height of the swelling of the film reached 350 nm.

Figure 6 shows the kinetic curves of dispersion of double niobium-nickel films at the oxide surfaces depending on annealing temperature and time, from which it follows that these films can be used to connect the studied oxides by pressure welding at temperatures up to 1100 °C without limiting the connection process time.

Using a double niobium-nickel film, a joint of zirconia ceramics was obtained by pressure welding at a temperature of 1150 °C under a pressure of 25 MPa (Fig. 7). The thickness of the seam was about 2,5 μm, and the shear strength of the joint reached 140 MPa.

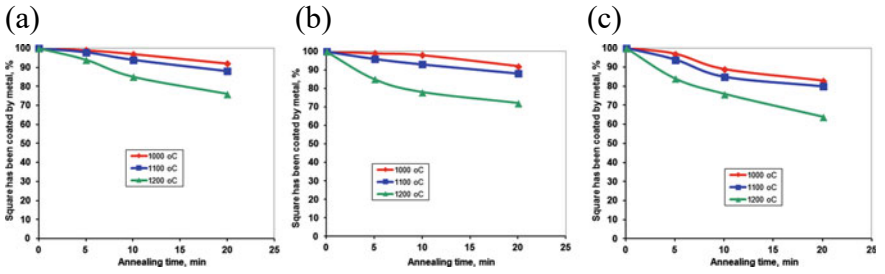

Fig. 6 Dependence of oxide materials area covered by double niobium-nickel film on annealing time at various temperatures (1000–1200 °C): **a** alumina ceramics; **b** leucosapphire; **c** zirconia ceramics

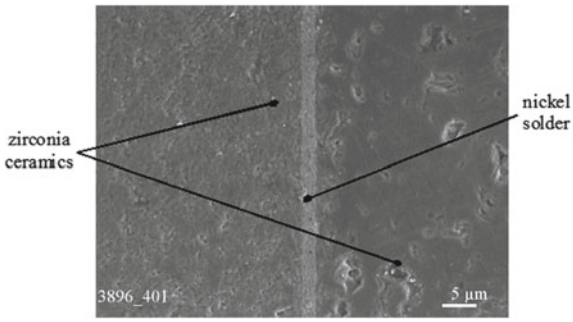

Fig. 7 Soldered joint of zirconia ceramics through double niobium-nickel film, with an ultrathin seam, ×400

4 Conclusions

The kinetics of decomposition of double niobium-nickel films deposited onto leuco sapphire, alumina, and zirconium dioxide ceramics was studied during vacuum annealing. Annealing was performed in vacuum not worse than 2×10^{-3} Pa at temperatures up to 1200 °C with different exposition times at each temperature (from 5 up to 20 min). The behavior of the films at the all three oxide surfaces during annealing was almost identical. It was found that the first slight changes in the films appear only after twenty minutes of annealing at 1000 °C. A further increase in the annealing temperature significantly accelerates the process of dispersing the films, especially with increasing annealing time. In particular, after a twenty-minute exposure at 1100 °C, the films already have a lot of cracks. At 1200 °C, the film disperses significantly after a five-minute exposure, and the interaction of nickel with niobium metallization layer at the oxide surfaces appears in it.

According to the research results, the kinetic curves of film dispersion are built, using which it is possible to select the optimal parameters (temperature, time) of the processes of metallized ceramics joining. Based on these graphs, the parameters of the joining of metallized dioxide-zirconium ceramics by pressure welding were selected, according to which the joints themselves were made with an ultra-thin seam about 2.5 μm thick, the shear strength of which reached 140 MPa.

References

1. Yevdokimov VR, Kashtanov SL, Lado LN, Shubin SN (1995) Diffuzionnaya svarka okhvatyvayushchego soyedineniya alyumooksidnoy keramiki s korrozionnostoykoy stal'yu. J Svarochnoye Proizvod 8:2 (in Russian)
2. Request 60-239373, C04B 37/02, B23K 20/00, (28 Nov 1985)
3. Request 380163, C04B 37/02, B23K 3/00, (4 Apr 1991)
4. Naidich Y (1999) High strength ceramics brazed joints: scientific and technological bases. J Ind Ceram 19(3):162
5. Andreyev AA, Kostyuk GI, Minayev NA (2012) Effektivnyye nanostrukturnyye mnogosloynyye pokrytiya dlya rezhushchikh instrumentov i detaley meditsinskogo

naznacheniya, rabotayushchikh v dinamicheskom rezhime. J Aviatsionno-kosmicheskaya Tekh i Tekhnol 2(89):28 (in Russian)
6. Zaytsev SV, Gerasimenko YuV, Lobanov MV, Khoviv AM (2014) Issledovaniye morfologii poverkhnosti oksidiro-vannykh plenok sistem Ti-Nb. J Kondensirovannyye Sredy i Mezh-faznyye Granitsy 16(2):153 (in Russian)
7. Lobanova TA, Volkhonskiy AO, Blinkov IV (2013) J Innovatsionnyye tekhnologii polucheniya iznoso-toykikh i triboadaptiruyemykh pokrytiy v industrii nanosistem 1(10):76. (in Russian)
8. Velikodnyy DV, Protsenko CI, Protsenko IY (2008) Tenzoeffekt v dvukhsloynykh plenkakh Cu/Cr i Fe/Cr. J Fiz Inzheneriya Poverkhnosti. 6(1–2):37. (in Russian)
9. Naveed M, Obrosov A, Weib S (2015) Investigation of the wear resistance properties of Cr/CrN multilayer coatings against sand erosion. Hindawi Publ Corp Conf Papers in Sci. Volume. Article ID 873543. https://doi.org/10.1155/2015/873543
10. Naydich YV, Gab II, Kostyuk BD, Stetsyuk TV, Kurkova DI, Dukarov SV (2007) Investigation of the ceramic materials connection processes (soldering) using metal nanofilms. J Rep Natl Acad Sci Ukr 35:97 (in Ukranian)
11. Naydich YV, Gab II, Kostyuk BD, Stetsyuk TV, Kurkova DI, Dukarov SV (2006) Issledovaniye struktury, morfologii i smachiva-niya metallami metallicheskikh nanoplenok, nanesennykh na po-verkhnost' oksida alyuminiya s tsel'yu polucheniya svarnykh i paya-nykh soyedineniy materialov na yego osnove. J Tekhnika Mashinostroyeniya 1:28 (in Russian)
12. Yakovich VM, Komarovskaya VM (2016) Mnogosloynyye pokrytiya. Inzhenerno-pedagogicheskoye obrazovaniye v XXI veke: materialy XII Respublikanskoy nauchno-prakticheskoy konferentsii molodykh uchenykh i studentov BNTU, Minsk, pp 215–218. (in Russian)
13. Metfessel S (1963) Tonkie plenki, sh szgotovlenie I izmerenie. Gosenergoizdat, Moscow-Liningrad (in Russian)
14. Khaas G, Tun PE (1968) Thin film physics, Mir, Moskow (in Russian)

Stripping Voltammetry of Nanoscale Films of Cu–Zn, Cu–Sn, Zn–Ni Alloys

A. Maizelis

1 Introduction

Coatings of Cu–Zn, Cu–Sn and Zn–Ni alloys have a number of functional properties that determine a wide range of their use. They are used in mechanical engineering for anti-corrosion and mechanical protection of steel surfaces. They are used in the form of a thick coating and a thinner sublayer under other coatings, as well as a replacement of other coatings, e.g. allergenic nickel, poisonous cadmium, chromium deposited using toxic compounds of Cr(VI). The properties of alloys directly depend on their chemical and phase composition. Therefore, analysis of the composition of alloy coatings is of great importance both in the development of new methods for their deposition and existing processes. Additionally, XRD method, which is mainly used to analyze the phase composition of classical electroplated coatings with a thickness of the order of 10 μm, has limitations both with a decrease in the thickness to nanoscale films and with the identification of amorphous phases and phases in the alloy in a low concentration.

The method of stripping voltammetry is a promising analysis method of alloy chemical and phase composition at the same time, especially in the analysis of nanoscale films that form multilayer coatings. It is based on the analysis of peaks on anodic voltammograms of dissolution of alloy thin films deposited on an inert substrate. Anodic branches of cyclic voltammograms are used for quick qualitative analysis. However, in this case, the entire spectrum of alloys deposited in a wide range of potentials of the cathode branch is analyzed, rather than alloys obtained at specific values of the current density or potential. Additionally, the analysis of the anodic voltammograms of the dissolution of alloys in the electrolyte, from which

A. Maizelis (✉)
Department of Technical Electrochemistry, National Technical University, "Kharkiv Polytechnic Institute", Kyrpychova str., 2, Kharkiv 61002, Ukraine

O. Fesenko and L. Yatsenko (eds.), *Nanomaterials and Nanocomposites, Nanostructure Surfaces, and Their Applications*, Springer Proceedings in Physics 263, https://doi.org/10.1007/978-3-030-74741-1_22

they were obtained under galvanostatic or potentiostatic conditions, is often complicated by the contact exchange of a surface containing an electronegative metal with an electrolyte, which contains ions of a less active metal.

The anodic peaks of the dissolution of copper-rich components of the Cu–Zn alloy were qualitatively recorded by cyclic voltammograms in alkaline electrolytes based on sorbitol [1], as well as under the conditions of anodic voltammetry of the obtained films in ammonium nitrate solution [2]. In [3], an attempt was made to stipping voltammetry in an ammonium nitrate solution of alloy films more enriched in zinc. The conclusion about the reliability and practicality of the ALSV method for the rapid determination of both the composition and the phase structure of electrodeposited brass was made as a result of a detailed comparative analysis of samples of coatings with Cu–Zn alloy and those obtained by metallurgy, XRD methods and stripping voltammetry in a solution of 0.3 mol dm-3 Na2SO4 [4], as well as in an alkaline electrolyte based on mannitol [5].

Separate dissolution of tin- and copper-rich phases was observed under cyclic voltammetry in non-aqueous electrolytes [6], a sulfate [7], ethylenediaminetetraacetate [8], methanesulfonate [9], pyrophosphate [10], alkali [11] et al. Stripping voltammetry of single-phase alloys Cu_6Sn_5 and Cu_3Sn in dilute sulfuric acid made it possible to identify the dissolution peaks of these phases on anodic voltammograms [12].

The anode response of CV for analysis of Zn–Ni is used for sulfate [13–15], ammonia electrolytes [16], and chloride [17, 18] electrolytes, in electrolytes with acetates [19], sulfamic acid [20], as well as in complex electrolytes based on citrate [21], pyrophosphate [22], amines [23], glycine, and ammonia [24]. The alloy dissolves more selectively in complex electrolytes that do not contain metal ions [25, 26]. In our previous studies [27–29], the examples of quantitative analysis of anodic voltammograms of Zn-Ni alloy films obtained in a polyligand ammonia-glycinate electrolyte are presented.

The purpose of this work is to make a quantitative analyze the change in the composition of nanoscale Cu–Zn, Cu–Sn, Zn–Ni films with the current density and deposition time by stripping voltammetry.

2 Experimental

The Cu–Zn alloy films of 100–150 nm thicknesses, Cu–Sn alloy films of 50–380 nm thicknesses and Zn–Ni alloy films of 50–100 nm thicknesses were deposited from polyligand electrolytes (Table 1). Alloys were anodically dissolved under potentiodynamic conditions in different solutions. Cu–Zn alloy films were dissolved in 0.3 mol L^{-1} Na_2SO_4 [4]. Cu-Sn alloy films were dissolved in 0.6 mol L^{-1} H_2SO_4 [12]. Zn-Ni alloy films were dissolved in dissolution contained 0.5 mol L^{-1} glycine and 0.5 mol L^{-1} NH_4Cl (pH 10.5) [27].

Cyclic voltammograms (CV) and anodic linear sweep voltammograms (ALSV) were obtained using Elins P-45X potentiostat. Plates made of Pt were used as working

Table 1 Electrolyte composition

Electrolyte composition	Electrolyte			
	"CuZn1"	"CuZn2"	"CuSn"	"ZnNi"
$CuSO_4 \cdot 5H_2O$, mol L^{-1}	0.08	0.04	0.08	–
$ZnSO_4 \cdot 7H_2O$, mol L^{-1}	0.17	0.18	–	0.04
$SnSO_4$, mol L^{-1}	–	–	0.4	–
$NiSO_4 \cdot 7H_2O$, mol L^{-1}	–	–	–	0.1
$K_4P_2O_7$, mol L^{-1}	0.5	0.22	1.4	–
$K_3C_6H_5O_7$, mol L^{-1}	0.13	0.66	–	–
EDTA, mol L^{-1}	–	–	0.4	–
$NH_3(NH_4^+)$, mol L^{-1}	–	–	–	0.66
Glycine, mol L^{-1}	–	–	–	0.25
KCl, mol L^{-1}	–	–	–	0.7
Hydroquinone, g dm^{-3}	–	–	10	–
Animal glue, g dm^{-3}	–	–	0.4	–

electrode (surface area of 1 cm^2) and as a counter electrode (surface area of 5 cm^2). Saturated silver-silver chloride reference electrode was connected to the electrolyte by a salt bridge. All the potentials are presented *vs.* this reference electrode.

3 Experimental Results and Discussion

Stripping voltammetry of Cu–Zn alloy films. Figure 1 shows the cyclic current–voltage dependences (CV) on platinum in polyligand pyrophosphate-citrate electrolytes ("CuZn1" electrolyte, Table 1) for the deposition of Cu–Zn alloy films (curve

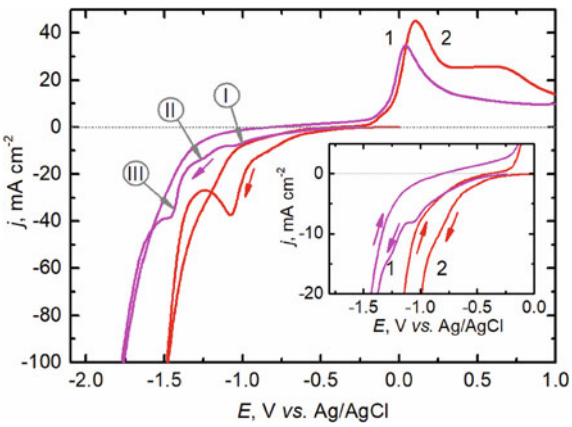

Fig. 1 CVs on Pt in electrolyte with $([Cu^{2+}]:[Zn^{2+}]):[Cit^{3-}]:P_2O_7^{4-}]$: 1—(1:2):0.5:2.0; 2—(1:0):0.5:2.0. Potential scan rate is 50 mV s^{-1}

1), as well as copper (curve 2). Two anode waves of copper dissolution correspond to two cathode waves of copper compounds reduction (curve 2). Scanning potentials in the cathode direction from the stationary potential leads to appearance of 3 peaks (I-III) of reduction of Cu–Zn alloys of different chemical and phase composition (curve 1). The anode branch of CV begins at −0.75 V with the dissolution of the phase enriched in zinc (inset in Fig. 1). The main dissolution peak of the copper-enriched phase appears at a potential of 0.0 V. Its potential almost coincides with copper dissolution peak (curve 2). The limiting current on the anode branch after the peak (this potentials region corresponds to the passive state of the surface) is not reduced until the region of oxygen evolution potentials not allowing to quantitatively dissolve all the deposit obtained during the cathode period CV.

The entire deposit is dissolved anodically, e.g. in a sulfate electrolyte that does not contain metal ions [4]. Anode voltammogram of dissolution of Cu–Zn alloy films obtained at different current density (Fig. 2) in the pyrophosphate-citrate electrolyte have peaks of dissolution of zinc-enriched phases and peaks of copper-enriched phases dissolution (at more positive potentials). It can be concluded that increase in current density of film deposition leads to increases the contribution of zinc-enriched phases, as the height of the group of peaks in the potential range −0.6…−0.4 V increase. Corresponding to the peak of copper dissolution (curve 1) peaks of copper-enriched dissolution phases are shifted to the left and decrease in height, first significantly (Fig. 2a), then insignificant with increase in current density of film deposition. The area of the peak at –0.05 V is stabilized (Fig. 2b) and decrease again (Fig. 2c).

After deconvolution of the anode voltammograms, the peaks were identified according to [4]. Alloys deposited in the region of potentials of wave I of CVA (Fig. 1), e.g. at a current density of 3 mA cm^{-2} (Fig. 2a, curve 2), are α-phase (solid solution of zinc in copper) and dissolve at one peak in the region of copper films dissolution potentials. Anodic voltammetry of dissolution of the alloy film, deposited at 5 mA cm^{-2} (Fig. 3a, curve 1), show the appearance of intermetallics in the deposit (γ- and β-phases), accompanied by significant decrease in the contribution of α-phase (Fig. 2a, curve 2). Increasing the deposition current density up to 10 mA cm^{-2} (Fig. 3a, curve 2) leads to the appearance of the epsilon phase dissolution peak on the anode voltammograms of the alloy film dissolution, the contribution of which increases with increase in current density (Fig. 3b).

It should be noted that the voltammograms of dissolution of films deposited on a platinum electrode until equal amount of electricity $Q_k = 0.4$ C cm^{-2} is reached, reflect the change in cathode current efficiency during deposition, as they allow to calculate the charge for their dissolution and to correlate it with the films deposition charge. Based on data from Fig. 2, the dependence of the current efficiency on the current density of the deposition of alloy films is presented in Fig. 4a. In the first part of this dependence, decrease in contribution of the α-phase of the alloy leads to decrease in current efficiency. Then increase in current efficiency corresponds to the current densities when γ-phase content in alloy increases. The drop in current efficiency at the last section of the dependence is probably due to an increase in content of ε-phase and hydrogen evolution rate increase.

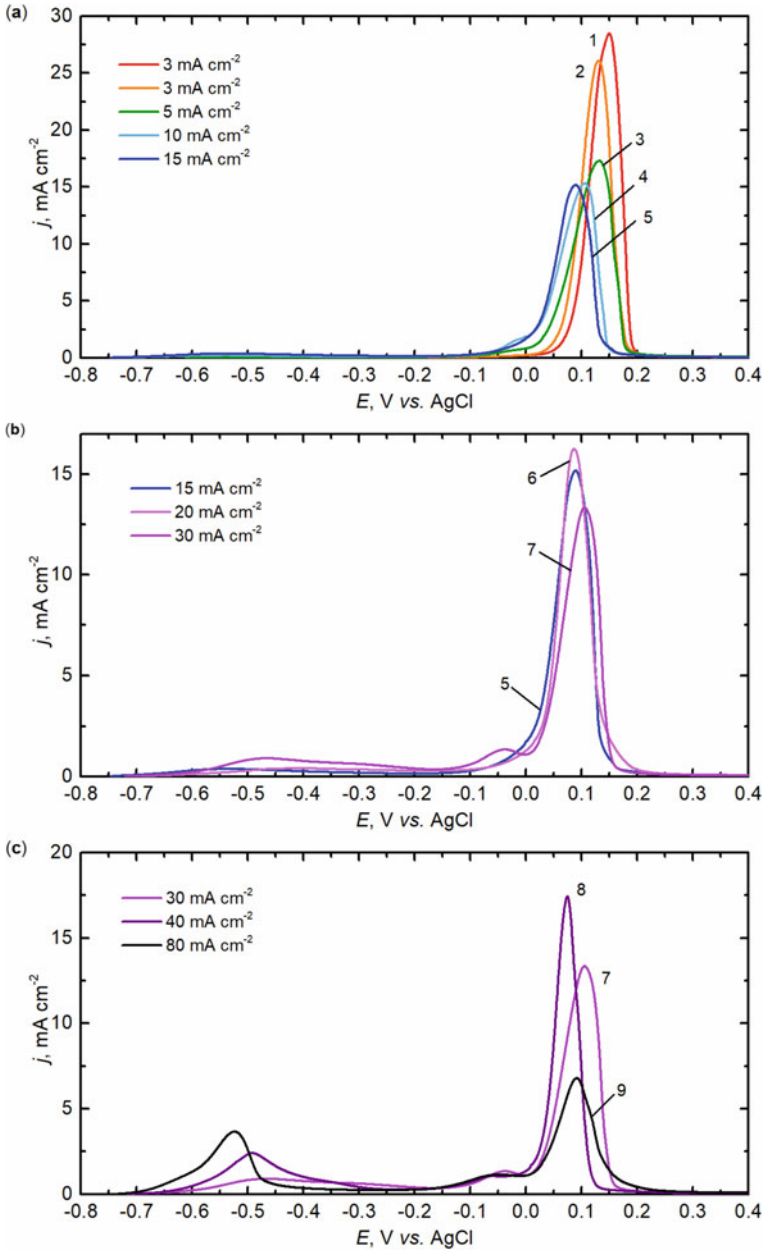

Fig. 2 Anodic CVs of Cu (1) and Cu–Zn (2–9) alloy films in 0.3 mol L^{-1} Na_2SO_4. Potential scan rate is 5 mV s^{-1}, and the films are deposited on Pt from "CuZn1" electrolyte (Table 1). Current density of films deposition, mA cm^{-2}: 1, 2–3; 3–5; 4–10; 5–15; 6–20; 7–30; 8–40; 9–80. The deposition charge is 0.4 C cm^{-2}

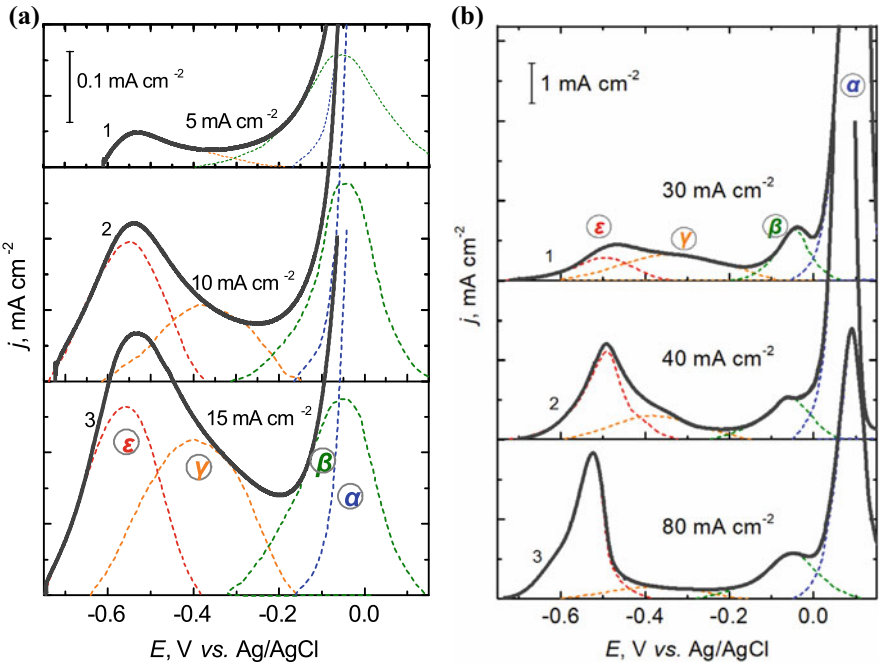

Fig. 3 Fragments of deconvoluted anodic polarization curves from **a** Fig. 2a and **b** Fig. 2c

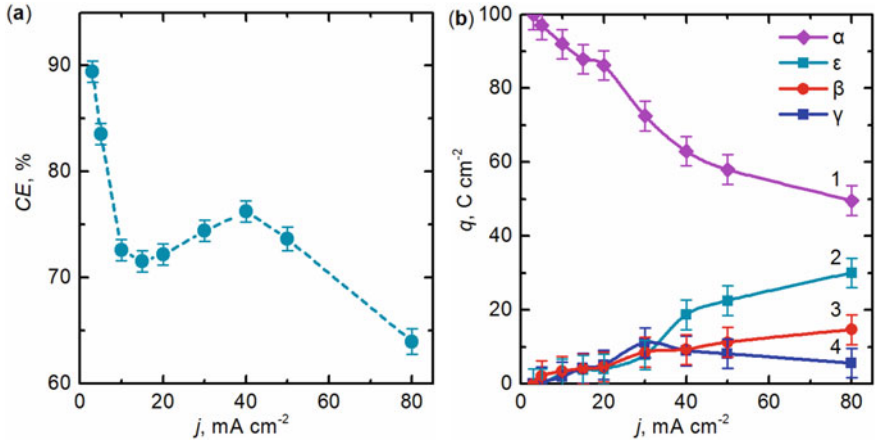

Fig. 4 **a** cathodic current efficiency of alloys films deposition and **b** and specific dissolution discharges α–(1), ε–(2), β–(3) i γ-phase (4)

The distribution of the specific charge for the dissolution of the phases in the films of Cu–Zn alloy deposited in a wide range of current densities is presented in Fig. 4b. It quantitatively reflects the decrease in the contribution of the α-phase (curve 1), sharper in the area of the first wave of polarization curve (Fig. 1, curve 1), the stabilization of the β-phase (Fig. 4b, curve 3), the growth of ε-phase (curve 2), and the extremum dependence of γ-phase content on the current density of films deposition (curve 5).

Increase in the ratio of metal ions concentrations in the direction of zinc ions (electrolyte "CuZn2", Table 1), the anode branch at CV (Fig. 5a) begins at more negative potentials than curve 1 in Fig. 1, and the peak of dissolution of the zinc-enriched phases is much higher than in Fig. 1. It should be noted that the cathode deposit does not dissolve completely in the peaks of the anode branch in this case of zinc-enriched deposit too.

The film deposited at a potential of −1.1 V (this potential corresponds to the region of potentials when Cu and Zn code position begins) contains zinc-enriched intermetallics besides α-phase (peak at −0.6 V, curve 1, Fig. 5b). With significant increase in polarization (Fig. 5b, curve 2) zinc content in the alloy film increases, and peak of ε-phase dissolution appears (it is approximately equal to the peak of α-phase dissolution).

Stripping voltammetry of Cu-Sn alloy films. CV on platinum in the "CuSn" electrolyte has 2 peaks of Cu-Sn alloys reduction. First peak corresponds to copper-enriched alloy, second peak corresponds to tin-enriched alloys (Fig. 6). On the anode branch of CV, we observe only 2 peaks of dissolution of free tin with the subsequent region of passivation of the copper-enriched deposit remaining on platinum electrode.

In 0.6 mol dm^{-3} H_2SO_4 solution (it is recommended for selective dissolution of Cu-Sn alloy components [12]), the tin component of the alloy (Fig. 7, curve

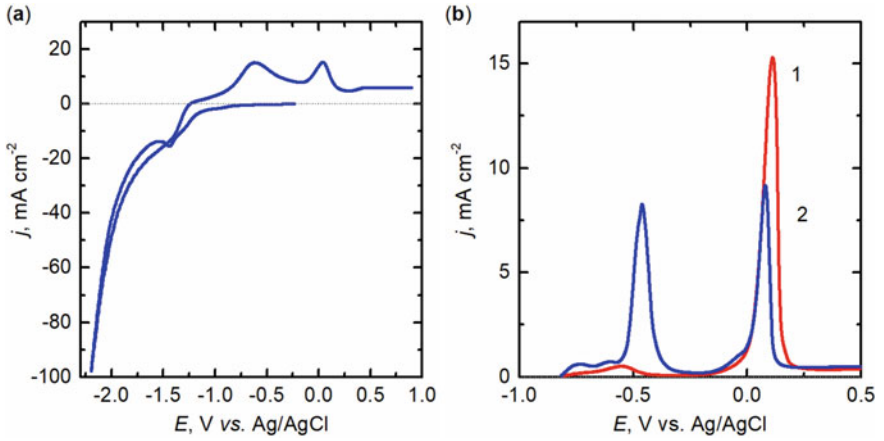

Fig. 5 **a** CV on Pt in the "CuZn2" electrolyte and **b** anodic voltammograms of Cu–Zn alloy films dissolution in the electrolyte of 0.3 mol dm^{-3} Na_2SO_4. Deposition potentials are: −1.1 V (1) and −1.5 V (2). Cathodic charge is 0.4 C cm^{-2}. Potential scan rate, mV s^{-1}: **a** 10, **b** 5

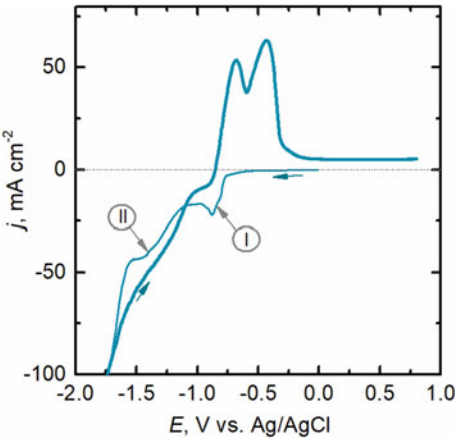

Fig. 6 CV on Pt in "1Cu5,3Sn" polyligand electrolyte. The potential scan rate is 50 mV s^{-1}

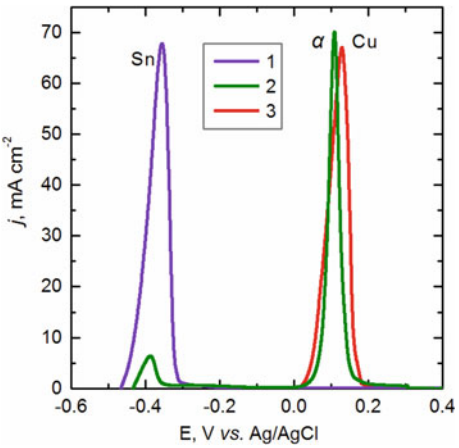

Fig. 7 Anode voltammograms of dissolution of films Sn (1), Cu (3) and Cu–Sn alloy (2), deposited on Pt from "CuSn" polyligand electrolyte (Table 1) at a potential of –1.15 V. Solution for dissolution is 0.6 mol dm^{-3} H_2SO_4. The deposition charge, C cm^{-2}: 1–0.2; 2–0.4; 3–0.6; 4–0.8; 5–1.0. Potential scan rate, mV s^{-1}: 1–20; 2–10; 3–6.6; 4–5; 5–4

2) dissolves at the peak in the region of tin dissolution potentials (curve1), and copper-enriched phase dissolves in the region of dissolution potentials of copper (curve 3).

Anode voltammograms of dissolution of alloy films of different thickness indicate a change in the composition of films with thickness, as they were obtained with constant product of the deposition charge and potential scan rate (Fig. 8) for correct comparison.

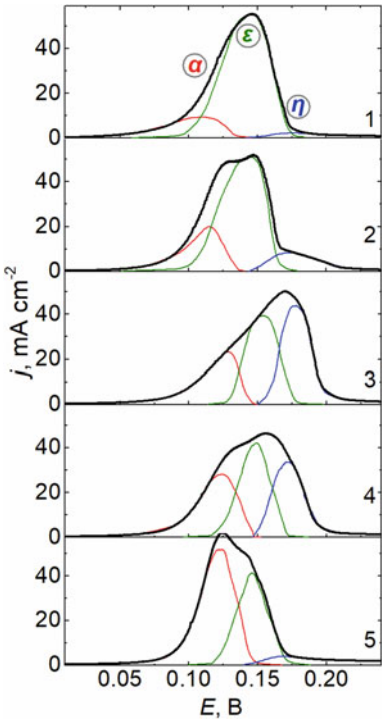

Fig. 8 Anode voltammograms of dissolution of Cu–Sn alloy films deposited on Pt from "CuSn" polyligand electrolyte (Table 1) at potential −0.9 V. Curves are deconvoluted into peaks of α-, ε-, and η-phases. Solution for dissolution is 0.6 mol dm^{-3} H_2SO_4. The deposition charge, C cm^{-2}: 1–0.2; 2–0.4; 3–0.6; 4–0.8; 5–1.0. Potential scan rate, mV s^{-1}: 1–20; 2–10; 3–6.6; 4–5; 5–4

All voltammograms of dissolution of films deposited at the potential of the first wave of CV (Fig. 6) have 3 peaks, which, according to [12], correspond to the dissolution of α-, ε- and η-phases. Increase in film deposition time leads to increase in α-phase dissolution peak and decrease in the dissolution peak of the ε-phase. Increase in the deposition charge to 0.6 C cm^{-2} (curve 3) leads to significant inhibition of film dissolution due to the increase in the content of the η-phase. Further increase in the film thickness leads to decrease in η-phase content.

The results of calculating the composition of the films are shown in Fig. 9. The content of α-phase in films increases with thickness increase (curve 1, Fig. 9a). The content of ε-phase (Cu_3Sn) in the films is reduced by more than a half. The film with a thickness of 265 nm has the highest content of η-phase (Fig. 3). The dependence of the total tin content in the films on their thickness (curve 6, Fig. 9b) suggests a tendency to decrease the total tin content in the films with thickness increase more. The current efficiency dependences have a maximum value of ~ 90% at a thickness of 350 nm (curve 5, Fig. 9b).

Stripping voltammetry of Zn-Ni alloy films. For stripping voltammetry of thin films of Zn-Ni alloy, an alkaline ammonia-glycinate electrolyte [27] is proposed. In this electrolyte, the dissolution potentials of zinc and nickel differ by almost 1 V, and all components of the Zn-Ni alloy dissolve selectively (Fig. 10).

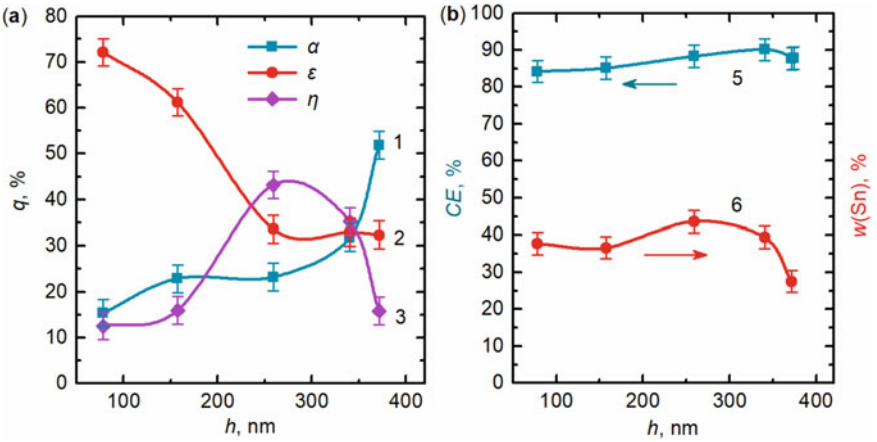

Fig. 9 Dependences of **a** specific charge of α- (1), ε- (2) and η-phases (3) dissolution, and **b** current efficiency (5) and the total tin content (6) on the thickness of alloy films deposited at potential of −0.9 V

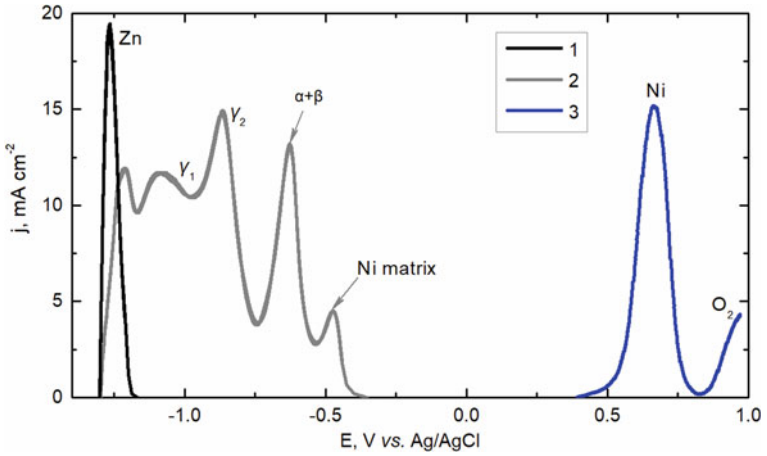

Fig. 10 Anode voltammograms of Zn (1), Zn-Ni (2), and Ni (3) films dissolution in solution of 0.5 mol L^{-1} glycine and 0.5 mol L^{-1} NH_4Cl (pH 10.5)

The Zn-Ni alloy films were deposited onto a Pt electrode from "ZnNi" ammonia-glycinate electrolyte (Table 1). Figure 11 shows series of anodic polarization curves in ammonia-glycinate electrolyte (0.5 mol L^{-1} glycine and 0.5 mol L^{-1} NH_4Cl, pH 10.5). Increase in the cathode current density leads to increase in their stationary potential in alkaline ammonia-glycine solution. It indicates increase in the content of more electropositive nickel. The height of the peaks increase approximately equally, therefore increase in cathodic current density increase with current density increase up to 20 mA cm^2.

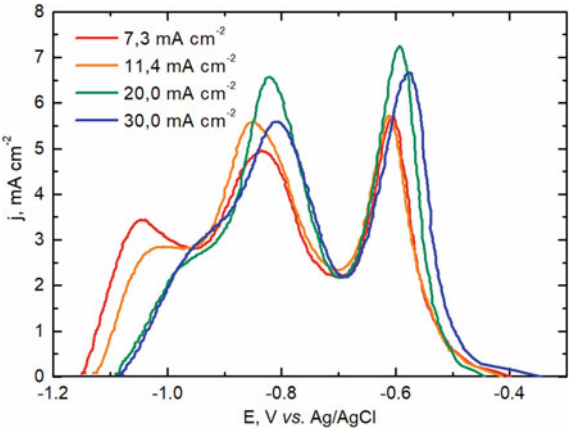

Fig. 11 Anodic voltammograms of Zn-Ni alloy films in alkaline ammonia-glycinate electrolyte. Zn-Ni alloys are deposited at current density, mA cm^{-2}: 1–7.3; 2–11.4; 3–14.5; 4–20; 5–25; 6–30

Deconvolution of anode voltammograms allow more accurate determination of area of picks (Fig. 12 a) of zinc dissolution from the γ_1-phase (peak I) (with formation of β-phase), zinc from the γ_2-phase (peak II) (with formation of α-phase) and nickel-enriched phase (peak III), which consists of residues of β-phase and α-phase, and also from initial β-phase [27].

Deconvolution of anode voltammograms allow more accurate determination of area of picks (Fig. 12a) of zinc dissolution from the γ_1-phase (peak I) (with formation of β-phase), zinc from the γ_2-phase (peak II) (with formation of α-phase) and nickel-enriched phase (peak III), which consists of residues of β-phase and α-phase, and also from initial β-phase [27].

Quantitative analysis of data from Fig. 12a shows reduce in the fraction of charge for γ_1-phase (curve 2) and increase in charge for zinc dissolution from γ_2-phase (curve 1) with increase in current density. Increase in current density leads to increase in the nickel content in the films above the stoichiometric γ-phase (curve 3). It is due to increase in the proportion of electricity spent on the dissolution of the β-phase (curve 4).

4 Conclusions

The chemical and phase composition of thin films (~50…300 nm) of Cu–Zn, Cu–Sn and Zn–Ni alloys were analyzed by stripping voltammetry.

Analysis in solution of sodium sulfate revealed that increase in current deposition of Cu–Zn alloy films from polyligand pyrophosphate-citrate electrolyte leads to decrease in the α-phase content, and stabilization of the β-phase content. There is an extremum on the dependence of γ-phase content on current density of deposition.

Stripping voltammetry of Cu–Sn alloy films (deposited in polyligand pyrophosphate-trilonate electrolyte) in a solution of sulfuric acid revealed that

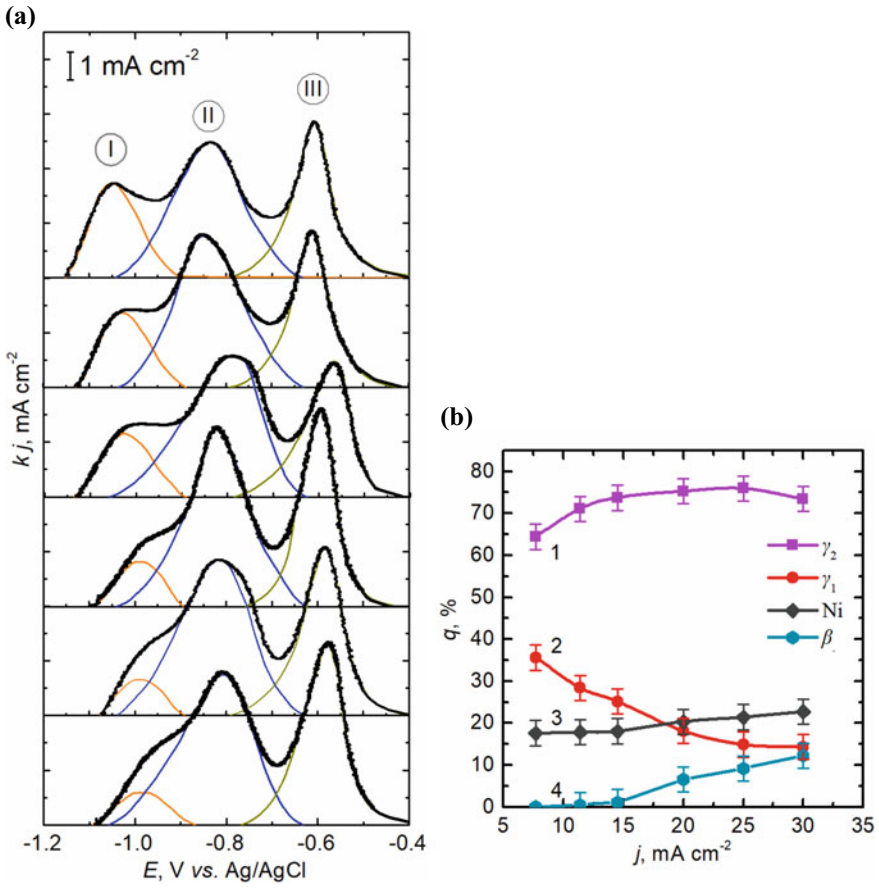

Fig. 12 A anodic voltammetry of alloys Zn-Ni in ammonia-glycinate electrolyte, and (**b**) fraction of charge q for dissolution of γ_2-phase (1), γ_1-phase (2), the initial β-phase (4) and whole Ni in the alloy (3). Current density for deposition, mA cm^{-2}: 1–7.3; 2–11.4; 3–14.5; 4–20; 5–25; 6–30

increase in deposition time leads to increase in α-phase content, decrease in ε-phase. Dependences of ε-phase content and whole tin content have maximum at thickness of 350 nm.

Stripping voltammetry in alkaline ammonia-glycinate solution revealed that increase in current density of Zn–Ni alloy films deposition from polyligand ammonia-glycine electrolyte leads to decrease in γ_1-phase content and increases in γ_2-phase content. Increasing in total nickel content is due to increase of β-phase content in films.

Therefore, it is shown that the method allows estimation of the content of both crystalline and amorphous phases, including films with their small content in the alloy.

References

1. Carlos IA, de Almeida MRH (2004) Study of the influence of the polyalcohol sorbitol on the electrodeposition of copper–zinc films from a non-cyanide bath. J Electroanal Chem 562(2):153–159. https://doi.org/10.1016/j.jelechem.2003.08.028
2. De Almeida MRH, Barbano EP, De Carvalho MF, Tulio PC, Carlos IA (2015) Copper–zinc electrodeposition in alkaline-sorbitol medium: electrochemical studies and structural, morphological and chemical composition characterization. Appl Surf Sci 333:13–22. https://doi.org/10.1016/j.apsusc.2015.02.005
3. De Almeida MRH, Barbano EP, De Carvalho MF, Carlos IA, Siqueira JLP, Barbosa LL (2011) Electrodeposition of copper–zinc from an alkaline bath based on EDTA. Surf Coat Technol 206(1):95–102. https://doi.org/10.1016/j.surfcoat.2011.06.050
4. Stevanović J, Skibina LJ, Stefanović M, Despić A, Jović VD (1992) Phase-structure analysis of brass by anodic linear-sweep voltammetry. J Appl Electrochem 22(2):172–178. https://doi.org/10.1007/BF01023820
5. Juškėnas R et al (2007) Electrochemical and XRD studies of Cu–Zn coatings electrodeposited in solution with d-mannitol. J Electroanal Chem 602(2):237–244. https://doi.org/10.1016/j.jelechem.2007.01.004
6. Abbott AP, Alhaji AI, Ryder KS, Horne M, Rodopoulos T (2016) Electrodeposition of copper–tin alloys using deep eutectic solvents. Transactions of the IMF 94(2):104–113. https://doi.org/10.1080/00202967.2016.1148442
7. Meudre C, David J, Ricq L, Hihn JY, Moutarlier V (2015) Elaboration of copper-tin alloys coatings: effect of glycine. J Mater Environ Sci 6(7):1834–1839
8. Barbano EP, de Oliveira GM, de Carvalho MF, Carlos IA (2014) Copper–tin electrodeposition from an acid solution containing EDTA added. Surf Coat Technol 240:14–22. https://doi.org/10.1016/j.surfcoat.2013.12.005
9. Low CTJ, Walsh FC (2008) Electrodeposition of tin, copper and tin–copper alloys from a methanesulfonic acid electrolyte containing a perfluorinated cationic surfactant. Surf Coat Technol 202(8):1339–1349. https://doi.org/10.1016/j.surfcoat.2007.06.032
10. Correia AN, Façanha MX, de Lima-Neto P (2007) Cu–Sn coatings obtained from pyrophosphate-based electrolytes. Surf Coat Technol 201(16–17):7216–7221. https://doi.org/10.1016/j.surfcoat.2007.01.029
11. Broggi RL, De Oliveira GM, Barbosa LL, Pallone EMJA, Carlos IA (2006) Study of an alkaline bath for tin deposition in the presence of sorbitol and physical and morphological characterization of tin film. J Appl Electrochem 36(4):403–409. https://doi.org/10.1007/s10800-005-9086-7
12. Murase K, Ito A, Ichii T, Sugimura H (2011) Preparation of Cu–Sn layers on polymer substrate by reduction-diffusion method using ionic liquid baths. J Electrochem Soc 158(6):D335. https://doi.org/10.1149/1.3573984
13. Nayana KO, Venkatesha TV (2014) Effect of ethyl vanillin on Zn–Ni alloy electrodeposition and its properties. Bull Mater Sci 37(5):1137–1146. https://doi.org/10.1007/s12034-014-0054-x
14. Roventi G, Cecchini R, Fabrizi A, Bellezze T (2015) Electrodeposition of nickel–zinc alloy coatings with high nickel content. Surf Coat Technol 276:1–7. https://doi.org/10.1016/j.surfcoat.2015.06.043
15. Soroor G, Kilmartin PA, Gao W (2015) Electrochemical studies of sol-enhanced Zn–Ni–Al_2O_3 composite and Zn–Ni alloy coatings. J Electroanal Chem 755:63–70. https://doi.org/10.1016/j.jelechem.2015.07.041
16. Lin ZF, Li XB, Xu LK (2012) Electrodeposition and corrosion behavior of zinc-nickel films obtained from acid solutions: effects of TEOS as additive. Int J Electrochem Sci 7:12507–12517
17. Basavanna S, Arthoba Naik Y (2009) Electrochemical studies of Zn–Ni alloy coatings from acid chloride bath. J Appl Electrochem 39(10):1975. https://doi.org/10.1007/s10800-009-9907-1
18. De Oliveira EM, Rubin W, Carlos IA (2009) Zn–Ni alloy electrodeposition from acid baths containing sorbitol or glycerol and characterization of Zn–Ni deposits. J Appl Electrochemy 39(8):1313–1321. https://doi.org/10.1007/s10800-009-9801-x

19. Petrauskas A, Grincevičienė L, Češūnienė A (2009) Influence of voltammetric parameters on Zn–Ni alloy deposition under potentiodynamic conditions. J Appl Electrochemy 39(9):1579–1585. https://doi.org/10.1007/s10800-009-9844-z
20. Gabriella R (2015) Electrodeposition of Nickel-Zinc alloy from a sulfamate bath. Advances in Materials 4(3):21
21. Tozar A, Karahan IH (2014) Structural and corrosion protection properties of electrochemically deposited nano-sized Zn–Ni alloy coatings. Appl Surf Sci 318:(15–23). https://doi.org/10.1016/j.apsusc.2013.12.020
22. Feng Z, Ren L, Zhang J, Yang P, An M (2016) Effect of additives on the corrosion mechanism of nanocrystalline zinc–nickel alloys in an alkaline bath. RSC Adv 6(91):88469–88485. https://doi.org/10.1039/C6RA18476F
23. Müller C, Sarret M, Benballa M (2002) Complexing agents for a Zn–Ni alkaline bath. J Electroanal Chem 519(1–2):85–92. https://doi.org/10.1016/S0022-0728(01)00725-2
24. Rodriguez-Torres I, Valentin G, Chanel S, Lapicque F (2000) Recovery of zinc and nickel from electrogalvanisation sludges using glycine solutions. Electrochim acta 46(2–3):279–287
25. Bajat JB, Mišković-Stanković VB (2004) Protective properties of epoxy coatings electrodeposited on steel electrochemically modified by Zn–Ni alloys. Prog Org Coat 49(3):183–196. https://doi.org/10.1016/S0013-4686(00)00583-1
26. Ivanov I, Kirilova I (2003) Corrosion resistance of compositionally modulated multilayered Zn–Ni alloys deposited from a single bath. J Appl Electrochem 33(3–4):239–244. https://doi.org/10.1023/A:1024179032045
27. Maizelis A, Kolupaieva Z (2020) Quantitative analysis of chemical and phase composition of Zn−Ni alloy coating by potentiodynamic stripping. Electroanalysis. https://doi.org/10.1002/elan.202060195
28. Maizelis A (2017) Voltammetric analysis of phase composition of Zn–Ni alloy thin films electrodeposited from weak alkaline polyligand electrolyte. J Nano- Electronic Phys 9(5):05010. https://doi.org/10.21272/jnep.9(5).05010
29. Maizelis AA (2017) Voltammetric analysis of phase composition of Zn–Ni alloy thin films electrodeposited under different electrolyze modes. IEEE 7th international conference on nanomaterials: applications and properties. 02NTF13-1-02NTF13-5. https://doi.org/10.1109/NAP.2017.8190373

The Stability Analysis of Stationary Modes of the Ice Surface Softening During the Friction Process

O. V. Yushchenko, A. Yu. Badalian, and O. V. Khomenko

1 Introduction

At present [1], ice and snow are often used in everyday life, nature, sports, and industry. The friction kinetics of ice is determined by processes such as frictional heating, creep and fracture, surface and melting pressure, and adhesion. Recently, experimenters and theorists have become interested in the process of boundary friction that occurs in nanoscale tribological systems [2–6].

In the tribological system, the main processes occur during the friction of contacting bodies. The question of the temperature or yield strength of ice during friction is still a matter of debate [7–11]. It was initially thought [1] that the cause of the friction decrease was an aqueous film that appeared on the ice surface due to frictional heating. Some researchers have developed this idea [1, 7–11], because understanding the conditions of formation of the water film is necessary for practical application. The film layer is formed with fluctuation domains of liquid water and solid ice, and it resembles a defective structure [11–13]. Studies have focused on the effect of thermal conductivity, which begins to decrease with increasing sliding speed [14].

Consider some concepts of theoretical models with quantitative estimates. It is generally accepted that the melting of the ice surface does not always occur during friction due to perfect mechanical heating. The results explained this feature by thermodynamic arguments. The dependences of the coefficient of friction on ice on the sliding speed, melting point, ambient temperature, and thermal conductivity of the slider have also been described for mild steel, copper, and organic glass. It was

O. V. Yushchenko · A. Yu. Badalian (✉) · O. V. Khomenko
Sumy State University, Sumy, Ukraine
e-mail: a.badalyan@mss.sumdu.edu.ua

O. V. Yushchenko
e-mail: o.yushchenko@phe.sumdu.edu.ua

O. Fesenko and L. Yatsenko (eds.), *Nanomaterials and Nanocomposites, Nanostructure Surfaces, and Their Applications*, Springer Proceedings in Physics 263, https://doi.org/10.1007/978-3-030-74741-1_23

found [14–18] that increased softening of ice at temperatures above −2 °C leads to significant wear. The study made it possible to extend the theory of Evans and others [1] to the case of hydrodynamic lubrication. Two regions with different dependences of the coefficient of friction on velocity were identified. In the first area, there is no melting of ice; while in the second due to frictional heating, a film of water is formed on the contact area. The idea of the mechanism of thermoregulation during ice friction was confirmed in [17]. This study describes the softening of ice in a material where there is a hydrodynamic friction and removal of the lubricating film. This approach allowed to obtain expressions for layer thickness, coefficient of friction, and wear, taking into account both hydrodynamic friction and surface roughness. Kolbek [16] believed that the kinetic friction on snow is regulated by the components:

(1) the dependence of the thickness of the water film on the temperature for perfectly insulated and aluminum sliders;
(2) the coefficient of lubricating friction from the speed at different temperatures;
(3) the dependence of the thickness of the water film on the distance along the lubrication zone for plastic and aluminum sliders at different temperatures;
(4) total friction along the aluminum slider at different temperatures.

These calculations show that the friction force that affects the slider varies over a wide range of speeds and temperatures. This theory is limited to the assumption that friction does not depend on the stress, and special attention is paid to the friction of water and an approximate estimate of the heat flow to the slider. But for the full disclosure of the processes occurring in the described system, it is necessary to take into account the effect of self-organization, to consider the equilibrium states and kinetics of the system [19–21].

2 Theoretical Model of the Ice Melting Process

Atomic models of ice friction have recently emerged. If we use the Ginzburg–Landau free energy in the first-order phase transition and the molecular dynamics method, we see that the film on the melted ice surface will previously consist of some molecular layers, and its thickness will increase with stress and temperature. This leads to a decrease in friction due to an increase in the lubricant layer due to the weakening of the hydrogen bonds between the ice molecules. The dependence of the friction force on the speed increases linearly due to the viscous component of the stress that occurs in the liquid film on the ice surface during shear.

Over time, there is a relaxation of the shear stress component.

Let us take as a basis the parameter from the hydrodynamic theory [5, 6]

$$\tau = \frac{\eta}{G}, \tag{1}$$

where η is the dynamic shear viscosity and G is the shear modulus.

There is an assumption that while the liquid freezes, η (the viscosity) becomes a modulus of G. But this situation is opposite to the usual second-order phase transition, where an infinite increase in τ at the critical point is also observed. If we move from a viscoelastic fluid to the general case, the expression (1) takes the form

$$\tau = \frac{\chi}{\gamma},$$

where χ is the generalized susceptibility and γ is the kinetic coefficient.

During the phase transition, an infinite increase in the susceptibility χ is observed, while the kinetic coefficient γ has no singularity. This is equivalent to the shear modulus G, which goes to zero at a finite viscosity η in Eq. (1).

The basis of our study is the softening of ice during friction, which is provided on the one hand by self-organization of stress components σ and deformation ε and on the other by temperature T. We know [22] the relationship between stress components σ and deformation ε; the Kelvin-Voigt model describes the simplest case, and the temperature effect is caused by critical increase of the shear modulus $G(T)$ at the reduced temperature: $G = 0$ for water and $G \neq 0$ for ice.

3 Main Equations

The model we take as a basis [22] consists of two planes: It is the friction of ice with some material, or the friction of ice against the surface of ice, which are separated by a lubricating softened layer of ice.

The kinetic equation for temperature T is obtained using the relation of the theory of elasticity. As a result, the mathematical model of the melting process is given by a system of differential equations

$$\dot{\varepsilon} = -\frac{\varepsilon}{\tau_\varepsilon} + \frac{\sigma}{\eta_\varepsilon}, \tag{2}$$

$$\tau_\sigma \dot{\sigma} = -\sigma + G(T)\varepsilon, \tag{3}$$

$$C_p \dot{T} = k\nabla^2 T - \sigma\frac{\varepsilon}{\tau_\varepsilon} + \frac{\sigma^2}{\eta_\varepsilon}. \tag{4}$$

In Eq. (2), τ_ε is the Debye relaxation time, η_ε is the effective shear viscosity coefficient. The second term of the right part describes the flow of viscous fluid due to the shear component of the· stress σ.

In Eq. (3), the first term of the right-hand side describes the relaxation with time $\tau_\sigma \equiv \eta/(G\ (T))$. Note that the effective viscosity $\eta_\varepsilon \equiv \tau_\varepsilon G_\varepsilon$ and the modulus $G_\varepsilon \equiv \eta_\varepsilon/\tau_\varepsilon$ do not coincide with the real viscosity η and the modulus $G(T)$. This is due to the different physical meaning of the Landau-Khalatnikov equations (3) and the

Kelvin-Voigt equations (2) [7, 13, 14]. The values of G_ε, η, η_ε weakly depend on the temperature of the surface layer of ice T, and the shear modulus $G(T)$ disappears at low temperatures to T_c, and then the approximations $G_\varepsilon(T)$, $\eta(T)$ are used for temperature dependences, $\eta_\varepsilon(T) = \text{const}$. Thus, we have

$$G(T) = G_0\left(\frac{T}{T_c - 1}\right). \tag{5}$$

In (4), C_p is the heat capacity; k is the thermal conductivity. The last term in the right part is responsible for the dissipative heating of the viscous fluid under the action of stress σ. On the other hand, single-mode approximation allows you to write

$$k\nabla^2 T \approx \frac{k}{l^2}(\tau_T Q_0 - T), \tag{6}$$

where l is the thermal conductivity scale, $\tau_T \equiv (l^2 C_p)/k$ is the thermal conductivity time.

Next, consider the thermal influence of friction surfaces, the value of which is not reduced to the Onsager component and is fixed by external conditions

$$Q = Q_0 + \frac{\sigma^2}{C_p \varepsilon \eta}, \tag{7}$$

where Q_0 is the heat of the environment from the solid to the surface layer. The quadratic stress contribution can be included in the friction temperature of the surface $T_e = \tau_T Q$. This complicates the analysis, which can be interpreted as a renormalization of values.

The above formulas are overloaded with many constants. Therefore, for further solution, we will use dimensionless variables, for which the main parameters of the system ε, σ, T, t are divided into scales, which we will define below.

$$\varepsilon_s = \left(\frac{\tau_\varepsilon^2 C_p T_s}{\eta_\varepsilon \tau_T}\right)^{1/2}, \sigma_s = \left(\frac{C_p T_s}{\tau_T}\right)^{1/2}, \quad T_s = T_c, t_s = \tau_\varepsilon$$

Then the basic Eqs. (2), (3), and (4) to describe the behavior of a viscoelastic medium in dimensionless form will be

$$\frac{d\varepsilon}{dt} = -\varepsilon + \sigma, \tag{8}$$

$$\alpha\frac{d\sigma}{dt} = -\sigma + g(T-1)\varepsilon, \tag{9}$$

$$\beta\frac{dT}{dt} = (T_e - T) - \sigma\varepsilon, \tag{10}$$

where the dimensionless constants are introduced

$$\alpha \equiv \frac{\tau_\sigma}{\tau_\varepsilon}, g = \frac{G_0 \varepsilon_s}{\sigma_s}, \beta = \frac{\tau_T}{\tau_\varepsilon}, T_e = \tau_T Q.$$

We omitted the strokes for reduction. It is constant here $g = G_0/G_\varepsilon$.

The system (8)–(10) is qualitative and can describe various features of the boundary mode. It has a form similar to the Lorentz scheme [16], which allows us to denote the thermodynamic phase and kinetic transitions.

4 Steady States of the System

To determine the stable states of the system in terms of the phase plane method, it is necessary to find the coordinates of the singular points [23], solving the system of equations

$$\begin{cases} 0 = -\varepsilon + \sigma, \\ 0 = \frac{1}{\alpha}[-\sigma + g(T-1)\varepsilon], \\ 0 = \frac{1}{\beta}[(T_e - T) - \sigma\varepsilon]. \end{cases} \tag{11}$$

Substitute $\sigma = 0$ in all Eqs. (11), then the stationary values of the corresponding parameters will be:

$$\sigma = 0, \varepsilon = 0, T = T_e(pointC).$$

When the value of $\sigma = 0$, the surfaces do not move and the boundary state hardens. This has been confirmed both theoretically and experimentally [22].

For the case $g(T-1) = 1$, coordinates of two points (A and B) depend on the initial conditions:

$$\varepsilon = \pm\sqrt{T_e - 1 - \frac{1}{g}}, \sigma = \pm\sqrt{T_e - 1 - \frac{1}{g}}, \quad T_e = 1 + \frac{1}{g}.$$

To determine the regions of existence of singular points and their types of stability, we construct the phase diagram of the system. For this, we use the condition for the existence of points A and B. Then using the Lyapunov substitution for the dimensionless system of equations (11), we find the condition for the equality of the discriminant of the cubic equation to zero for determining the Lyapunov exponents [23]. In addition, we consider the condition of complexity and loss of stability of the Lyapunov exponents. As a result, the phase diagram of various modes of realization of stable states of the system has the form shown in Fig. 1.

For the point C, we obtain the Lyapunov exponents in the form

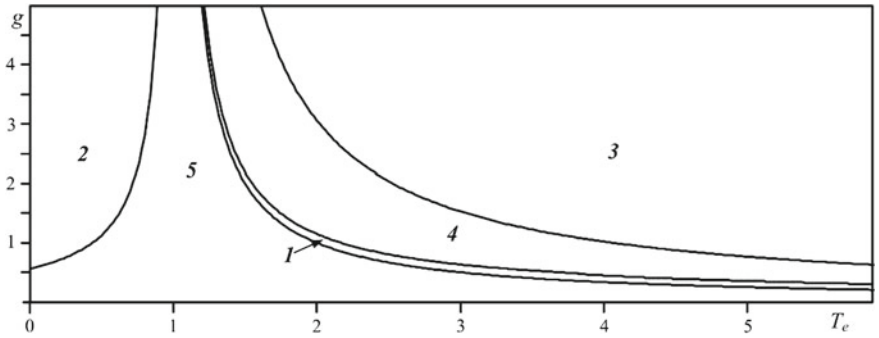

Fig. 1 Phase diagram of the system

$$\lambda_1 = -\frac{1}{\beta}, \lambda_{2,3} = \frac{-(1+\alpha) \pm \sqrt{(1+\alpha)^2 - 4\alpha[1 + g_\varepsilon(1 - T_\varepsilon)]}}{2\alpha}.$$

It should be noted that the root λ_1 is always negative. If we look at the complex-conjugate roots $\lambda_{2,3}$, we see that the real part is also negative, and it will always be. The type of stability of a stationary point depends on these roots.

The corresponding analysis of point C is shown in Table 1.

For point A, the coordinates are determined by the equations

$$\varepsilon_0 = +\sqrt{T_\varepsilon - 1 - \frac{1}{g}}, \sigma_0 = +\sqrt{T_\varepsilon - 1 - \frac{1}{g}}, \quad T_0 = 1 + \frac{1}{g}$$

The corresponding calculations are shown in Table 2.

Table 1 Values of coordinates and indicators of Lyapunov for point C, parameters g, T_e meet the relevant regions of the phase diagram; $\alpha = 4$, $\beta = 5$

Regions of the phase diagram		1	2	3	4	5
Parameters	g	0.27	0.8	0.88	0.4	0.4
	T_e	5	0,1	20	10	2
Coordinates	σ_1	0	0	0	0	0
	ε_1	0	0	0	0	0
	T_1	5	0,1	20	10	2
Lyapunov indicators	λ_{11}	−0.2	−0.2	−0.2	−0.2	−0.2
	λ_{12}	0.0158	$-0.625 + 0.19i$	1.4536	0.3951	−0.1344
	λ_{13}	− 1.2658	$-0.625–0.19i$	−2.7036	−1.6451	−1.1155
Type of stability		Saddle-stable knot	Stable knot-focus	Saddle-stable knot	Saddle-stable knot	Stable knot

Table 2 Values of coordinates and indicators of Lyapunov for point *A*, parameters g, T_e meet the relevant regions of the phase diagram; $\alpha = 4$, $\beta = 5$

Regions of the phase diagram		1	2	3	4	5
Parameters	g	0.27	0.8	0.88	0.4	0.4
	T_e	5	0,1	20	10	2
Coordinates	σ_2	0.5443	–	4.2265	2.5495	–
	ε_2	0.5443	–	4.2265	2.5495	–
	T_2	4.7037	2.25	2.1363	3.5	3.5
Lyapunov indicators	λ_{21}	−1.2523	−1.1911	−1.4718	−1.3114	−1.2319
	λ_{22}	−0.1571	−0.5309	$0.0109 + 1.0334i$	$-0.069 + 0{,}439i$	−0.3552
	λ_{23}	−0.0407	0.2720	$0.0109 - 1.0334i$	$-0.069 - 0{,}439i$	0.1371
Types of stability		Stable knot	–	Focus of complex architecture	Stable knot-focus	–

Point B is symmetric about the origin to point *A*, so the coordinate values are

$$\varepsilon_0 = -\sqrt{T_\varepsilon - 1 - \frac{1}{g}}, \sigma_0 = -\sqrt{T_\varepsilon - 1 - \frac{1}{g}}, T_0 = 1 + \frac{1}{g}.$$

To find the coefficients, it is necessary to perform actions similar to the analysis for point *A*. The corresponding results are presented in Table 3.

Table 3 Values of coordinates and indicators of Lyapunov for point *B*, parameters g, T_e meet the relevant regions of the phase diagram; $\alpha = 4$, $\beta = 5$

Regions of the phase diagram		1	2	3	4	5
Parameters	g	0.27	0.8	0.88	0.4	0.4
	T_e	5	0.1	20	10	2
Coordinates	σ_3	−0.5443	–	−4.2265	−2.5495	–
	ε_3	−0.5443	–	−4.2265	−2.5495	–
	T_3	4.7037	2.25	2.1363	3.5	3.5
Lyapunov indicators	λ_{31}	−1.2523	−1.1911	−1.4718	−1.3114	−1.2319
	λ_{32}	−0.1571	−0.5309	$0.0109 + 1.0334i$	$-0.069 + 0.439i$	−0.3552
	λ_{33}	−0.0407	0.2720	$0.0109 - 1.0334i$	$-0.069 - 0.439i$	0.1371
Types of stability		Stable knot	–	Focus of complex architecture	Stable knot-focus	–

5 Phase Portraits

Let us build phase portraits for all sets of parameters. For this purpose, we use the Runge–Kutta method [22, 23]. For the corresponding regions (see Tables 1, 2 and 3), we have phase portraits in Figs. 2, 3, 4, 5, and 6.

As can be seen from the tables and phase portraits, this mathematical model is characterized by the presence of five areas that differ in the implementation of the number of special points or in different types of their stability. In the second and fifth regions, only one point is realized, or only one stable state is possible for our physical system—the solid state of a thin layer of ice between the friction surfaces. In the last area, the type of stability of this state corresponds to a stable node and in the second area is somewhat more complex—a stable node-focus.

The first, third, and fourth regions are characterized by the implementation of three singular points. But symmetrical about the origin of points A and B, which

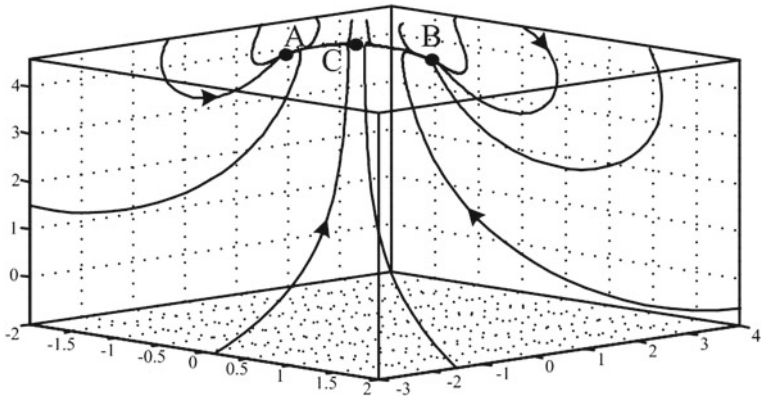

Fig. 2 Phase portraits for the 1st region for $\alpha = 4$, $\beta = 5$, $g = 0.27$, $T_e = 5$

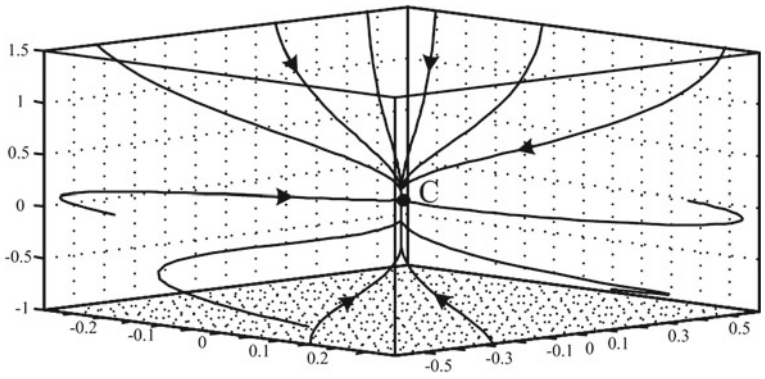

Fig. 3 Phase portraits for the 2nd region for $\alpha = 4$, $\beta = 5$, $g = 0.8$, $T_e = 0.1$

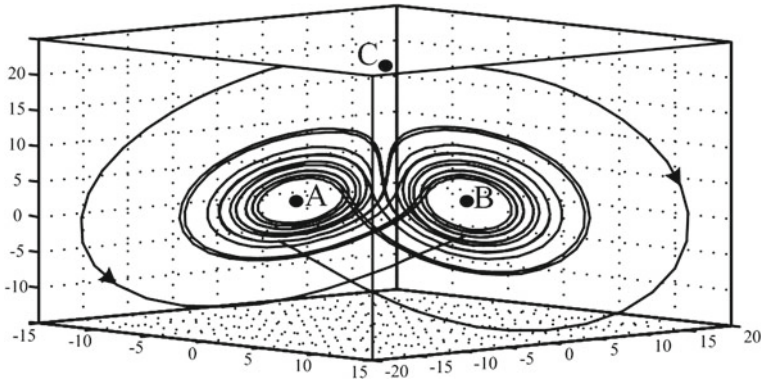

Fig. 4 Phase portraits for the 3rd region for $\alpha = 4$, $\beta = 5$, $g = 0.88$, $T_e = 20$

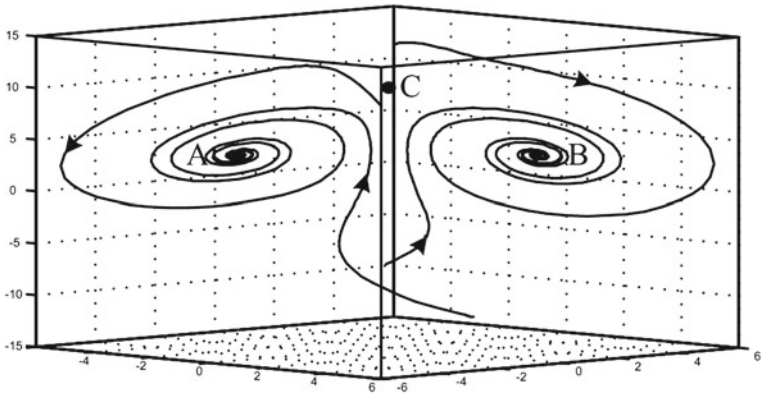

Fig. 5 Phase portraits for the 4th region for $\alpha = 4$, $\beta = 5$, $g = 0.4$, $T_e = 10$

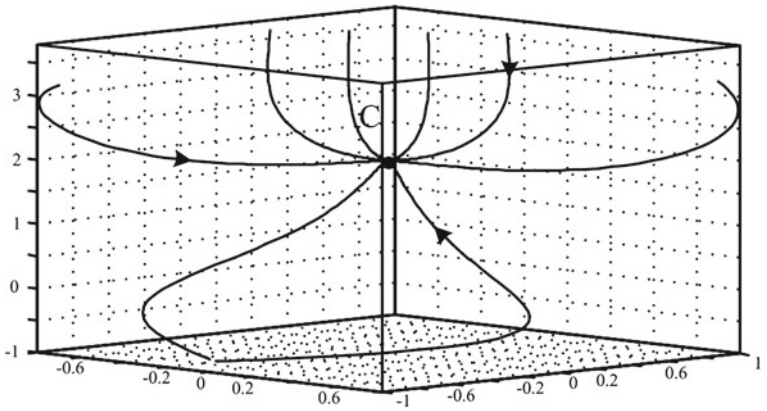

Fig. 6 Phase portraits for the 5th region for $\alpha = 4$, $\beta = 5$, $g = 0.8$, $T_e = 0.1$

correspond to different modes of deformation and characterize the state of softening or melting of a thin layer of ice, in the third region are unstable. In contrast to the previous cases, the first and fourth regions are characterized by three stable points. This indicates the coexistence of solid and liquid ice states, which is characteristic of the intermittent friction regime, which is often observed in the experiment. In the first region, the liquid state corresponds to the usual stable node, and the set of parameters of the third region gives complex kinetics, resembling a strange Lorentz attractor.

6 Conclusion

The paper considers a mathematical model of the process of melting an ultra-thin layer of ice between two solid smooth surfaces. This was thought that this layer may melt due to heat and shear deformation. The latter was described by the Voigt-Kelvin equation for a viscoelastic medium. For the control parameter—temperature—the relaxation equation of thermal conductivity was used, for the conjugate quantity—stress—the equation of Landau-Khalatnikov type. The result is a system of three differential equations, the analysis of which was performed by the phase plane method. The coordinates of the steady states of the system and the corresponding Lyapunov indices for all possible modes of realization of the solid and softened state of a thin layer of ice were determined. For each of these modes, the kinetics of the melting process of ice depending on external parameters was analyzed based on phase portraits.

References

1. Khomenko AV, Khomenko KP, Falko VV (2015) Nonlinear model of ice surface softening during friction. https://doi.org/10.5488/CMP.19.33002
2. Persson BNJ (2000) Sliding friction. In: Physical principles andapplications. Springer, Berlin
3. Yushchenko OV, Badalyan AY (2017) J Nano Electron Phys 9(4):04022
4. Pertsin A, Grunze M (2008) Langmuir 24:135
5. Lee S, Iten R, Müller M, Spencer ND (2005) Macromolecules 37:8349
6. Yamada Sh (2005) Langmuir 21:8724
7. Wiese K, Kessel TM, Mundl R, Wies B (2012) Tire. Sci Technol 40(2):124
8. Kietzig AM, Hatzikiriakos SG, Englezos P (2010) J Appl Phys 107(8):081101
9. Kennedy FE, Schulson EM, Jones DE (2000) Philos Mag A 80(5):1093
10. Khomenko AV, Lyashenko IA (2007) Phys Solid State 49(5):936
11. Khomenko AV, Yushchenko OV (2003) Phys Rev E 68:036110
12. Lifshits EM, Pitaevskii LP (1981) Course of theoretical physics, physical kinetics, 1st edn. Pergamon Press, Oxford
13. Khomenko AV (2004) Phys Lett A 329(1–2):140
14. Khomenko AV, Lyashenko IA (2007) Tech Phys 52(9):1239
15. Limmer DT, Chandler D (2014) J Chem Phys 141(18):505
16. Colbeck SC (1988) J Glaciol 34(116):78

17. Akkok M, Ettles CM, Calabrese SJ (1987) J Tribol 109:552
18. Olemskoi AI, Yushchenko OV, Badalyan AY (2013) Theor Math Phys 174(3):386
19. Yushchenko OV, Badalyan AY (2013) Ukr J Phys 58(5):497
20. Khomenko AV (2014) Condens Matter Phys 17(3):33401
21. Haken H (1983) Synergetics. In: An introduction. nonequilibrium phase transitions and selforganization in physics, Chemistry, and Biology, 3rd edn. Springer, Berlin
22. Khomenko AV, Khomenko KP, Falko VV (2016) Condens Matter Phys 19(3)
23. Khomenko A, Yushchenko O, Badalyan A (2020) Symmetry 12(11):1914

PALS Approach to Study of Water–Adsorption Processes in Nanostructured $MgAl_2O_3$ Ceramics: From Three- to Four-Component Fitting Procedures

H. Klym

1 Introduction

A long time nanostructured $MgAl_2O_4$ ceramics are interesting materials for humidity sensors due to their inner nanoporous structure and surface porosity, which promotes effective cooperative adsorption of water molecular [1–4]. The humidity-sensing application of these ceramics is known to be determinant of chemical and physical water–adsorption processes occurring within inner pores in ceramics bulk [5–7]. The presence of open porosity permits greater conductivity due to the enhancement of the specific surface area available for water–adsorption [8–10]. Recently, it was shown that amount of adsorbed water in these ceramics affects not only their electrical conductivity, but also other physical–chemical parameters [10, 11]. Such parameters can be the positron trapping modes of free volumes (or nanovoids) studied by positron annihilation lifetime spectroscopy (PALS)—one of the most informative experimental methods for studying of structurally intrinsic nanovoids in solids such as ceramics [12–15], thick films based on ceramics [15–17], and nanocomposites [18, 19] in the form of different modifications (clusters, agglomerates, nanopores, etc.) [20, 21].

We have achieved significant success in the study of spinel $MgAl_2O_4$ ceramics by the PALS method [8, 10, 11, 21]. It was shown that positrons injected in the studied $MgAl_2O_4$ ceramics can undergo two different processes such as positron trapping and ortho-positronium o-Ps decaying. The latter process (so-called "pick-off" annihilation) resulting from Ps interaction with electron from environment (including annihilation in liquid water) is ended by emission of two γ-quanta [20, 22]. In general, these two channels of positron annihilation are independent. However, if trapping sites will appear in a vicinity of grain boundaries neighboring with free-volume

H. Klym (✉)
Lviv Polytechnic National University, S. Bandery Str., 12, Lviv 79013, Ukraine
e-mail: halyna.i.klym@lpnu.ua

O. Fesenko and L. Yatsenko (eds.), *Nanomaterials and Nanocomposites, Nanostructure Surfaces, and Their Applications*, Springer Proceedings in Physics 263, https://doi.org/10.1007/978-3-030-74741-1_24

pores, these positron-positronium traps become mutually interconnected resulting in a significant complication of PALS data.

We have developed several approaches to the analysis of PALS spectra for the humidity-sensitive $MgAl_2O_4$ ceramics using different numbers of fitting parameters and algorithms to justify the obtained results [21, 23–25]. The goal of this work is to generalize in one work the previously presented approaches to the analysis of the PALS spectra of nanostructured spinel-type $MgAl_2O_4$ ceramics at adsorption of water. The trapping of PALS spectra is presented at the analysis on three and four components and also at the fixed values of some positron trapping parameters.

2 Sample Preparation and Experimental

The studied spinel-type $MgAl_2O_4$ ceramics were sintered from fine-dispersive Al_2O_3 and MgO powders using a special regime with maximal temperatures T_s of 1400 °C, the total duration being 2 h [21, 23]. In a result, the humidity-sensitive ceramics with a so-called trimodal pore size distribution and character values of pore radiuses centered near ~0.003, 0.09 and 0.4 μm were obtained [21]. The phase composition of ceramics obtained with X-ray diffraction [21, 23] was established that the studied ceramics contained the main spinel phase and small quantity of MgO phase (1.5%).

PALS measurements were performed using an ORTEC spectrometer [20, 26]. The ^{22}Na isotope was used as positron source, placed between two identical samples. The obtained PALS spectra were decomposed by LT computer program of Kansy [27]. In this work, three experimental and analysis approaches were presented to study of water–adsorption processes in the nanostructured $MgAl_2O_4$ ceramics using PALS method.

The first approach: analysis of PALS spectra by three-component fitting procedure in $MgAl_2O_4$ ceramics before and after water–adsorption. PALS measurements were performed at 20 °C and ~35% relative humidity [21]. We used three measured PALS spectra for each investigated pair of samples, the best results being chosen by comparing statistically weighted least-squares deviations between experimental points and theoretical curve. In order to change interrelation between positron trapping and Ps decay modes in the deconvoluted PALS spectra, we placed the samples into distillated water for 12 h. Then, the PALS measurements were repeated once more with water-immersed $MgAl_2O_4$ ceramics at the same conditions. We used three-component fitting of PALS spectra and obtained fitting parameters (positron lifetimes τ_1, τ_2, τ_3 and corresponding unity-normalized intensities I_1, I_2, I_3). Typical PALS spectra decomposed on three components using LT program (with τ_1, τ_2 and τ_3 lifetimes as well as I_1, I_2, and I_3 intensities) are shown in Fig. 1.

The second approach: analysis of PALS spectra by three-component fitting procedure in the $MgAl_2O_4$ ceramics at fixation of the lifetimes of the first and the second PALS components within row of relative humidity (*RH*). PALS measurements were performed at 20 °C. The selection of corresponding values for measuring chamber

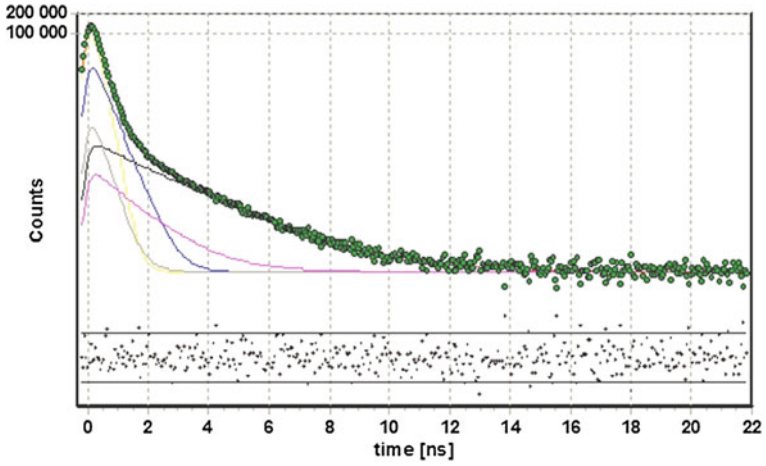

Fig. 1 Fitting of PALS spectra for $MgAl_2O_4$ ceramics on three components using LT computer program [28]

permit to investigation of samples at constant values of relative humidity in the range of 25–60% and 25–98% [24, 28].

Special testing procedure with a set of standard thermally treated non-defected Ni and Al probes was performed to correctly account for source input and other positron trapping channels in the measured lifetime spectra. The obtained data were mathematically treated at three-component fitting procedure with the fixed positron lifetimes of the first and second PALS components (τ_1 and τ_2). Only results with FIT (short abbreviation originated from "fitting") values close to 1.0 [24] were left for further consideration.

The third approach: analysis of PALS spectra by four-component fitting procedure in $MgAl_2O_4$ ceramics before and after water–adsorption [23]. The PALS measurements were performed at 22 °C and relative humidity RH = 35% after drying (initial samples) and after 7 days of water exposure (water vapor in desiccator at RH = 100%). Each PALS spectrum was collected within 6.15 ps channel width to analyze short and intermediate PALS components. To obtain data on longest-lived PALS components, the same ceramics were studied within a channel width of 61.5 ps as in [23, 29, 30]. At high-statistical measurements (more than ten millions of counts), the best results were obtained with four-term decomposition procedure. Such approach allows us to study nanopores of different sizes, responsible for o-Ps decaying. Each PALS spectrum was processed multiply owing to slight changes in the number of final channels, annihilation background, and time shift of the 0-th channel. In such a manner, we obtained fitting parameters (positron lifetimes τ_1, τ_2, τ_3, τ_4 and corresponding unity-normalized intensities I_1, I_2, I_3, I_4), which correspond to annihilation of positrons in the samples of interest.

In the all three approaches with using a well-developed formalism for two-state positron trapping model [21, 31, 32], the following parameters describing positron

lifetime spectra can be calculated according to Eqs. (1–3):

$$\kappa_d = \frac{I_2}{I_1}\left(\frac{1}{\tau_b} - \frac{1}{\tau_2}\right), \tag{1}$$

$$\tau_b = \frac{I_1 + I_2}{\frac{I_1}{\tau_1} + \frac{I_2}{\tau_2}}, \tag{2}$$

$$\tau_{av.} = \frac{\tau_1 I_1 + \tau_2 I_2}{I_1 + I_2}, \tag{3}$$

where κ_d is positron trapping rate in defect, τ_b—positron lifetime in defect-free bulk, and $\tau_{av.}$—average positron lifetime. In addition, the difference $(\tau_2 - \tau_b)$ can be accepted as a size measure of extended defects where positrons are trapped in terms of equivalent number of monovacancies, as well as the τ_2/τ_b ratio represents the nature of these defects.

3 Results and Discussion

3.1 Water–adsorption Processes in Nanostructured $MgAl_2O_3$ Ceramics Studied by Three-Component Fitting Procedure

The obtained PALS characteristics for the $MgAl_2O_4$ ceramics sintered at different T_s before and after water-immersion have a peak and region of smooth fading of coincidence counts in time (Fig. 2). Mathematically such curves describe by sum of exponential functions with different indexes (inversed to lifetimes).

As has been shown [21, 28], at three-component fitting procedure, the shortest (lifetime τ_1 and intensity I_1) and middle (lifetime τ_2 and intensity I_2) PALS components were ascribed to positron trapping modes. By accepting two-state positron trapping model [32], the longer τ_2 lifetime can be treated as defect-related one; these positron trapping defects being located near grain boundaries [33].

Obtained fitting parameters and positron trapping modes for initial and water-immersed $MgAl_2O_4$ ceramics are shown in Tables 1 and 2, respectively. The radii R_3 of spherical nanopores (given in Table 2) were calculated using of o-Ps-related τ_3 lifetime in known Tao-Eldrup model [34, 35]:

$$\tau_{o-Ps} = \left[2\left(1 - \frac{R}{R + \Delta R} + \frac{1}{2\pi}\sin\left(\frac{2\pi R}{R + \Delta R}\right)\right) + 0.007\right]^{-1} \tag{4}$$

where ΔR is empirically derived parameter ($\Delta R \approx 0.1656$ nm for polymers [18]), which describes effective thickness of the electron layer responsible for the "pick-off" annihilation of *o-Ps* in a hole.

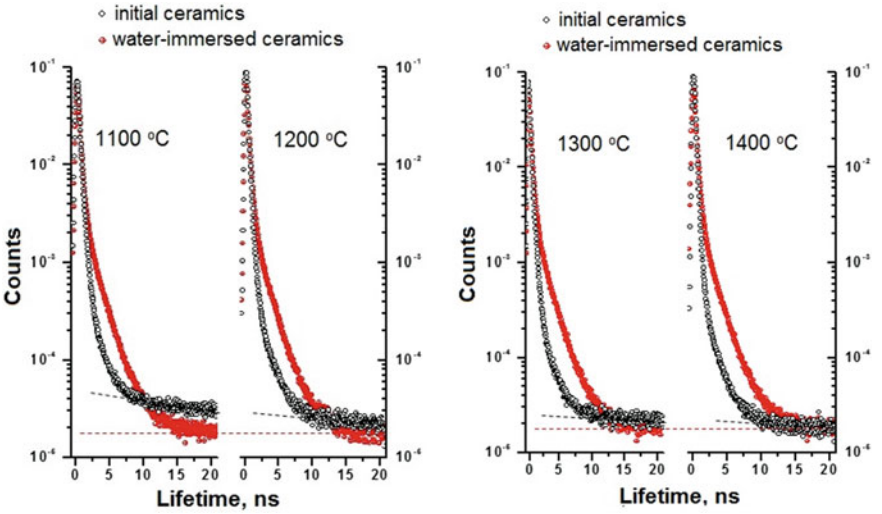

Fig. 2 Positron lifetime spectra for initial and water-immersed $MgAl_2O_4$ ceramics sintered at different T_s [28]

Table 1 Fitting parameters for initial and water-immersed $MgAl_2O_4$ ceramics mathematically treated within three-component procedure [21]

T_s, °C	Sample pre-history	τ_1, ns	I_1, a.u	τ_2, ns	I_2, a.u	τ_3, ns	I_3, a.u
1100	Initial	0.24	0.68	0.50	0.30	2.59	0.02
	Water-immersed	0.24	0.56	0.50	0.29	1.88	0.15
1200	Initial	0.23	0.70	0.47	0.28	2.39	0.02
	Water-immersed	0.22	0.54	0.45	0.34	1.87	0.12
1300	Initial	0.22	0.72	0.44	0.26	2.19	0.02
	Water-immersed	0.22	0.54	0.46	0.32	1.88	0.15
1400	Initial	0.19	0.76	0.36	0.22	1.90	0.02
	Water-immersed	0.21	0.56	0.43	0.32	1.94	0.12

As has been shown early [21–24] and above, the first component of PALS spectra with lifetime τ_1 and intensity I_1 as well as the second component with lifetime τ_2 and intensity I_2 are related to positron trapping modes. The lifetime τ_2 reflects positron trapping on defects located near grain boundaries on ceramic materials.

In initial ceramic samples obtained at different T_s, the shortest τ_1 and middle τ_2 positron lifetimes and intensities I_1 and I_2 reduced with rises of sintering temperature (see Table 1 and Fig. 3). In spate of structural distinction of ceramics sintered at different T_s, positrons are trapped in defects with the same rate of $\kappa_d = 0.60\ ns^{-1}$ (Table 2). The radii R_3 of spherical nanopores (given in Fig. 3) were calculated using τ_3 lifetimes in Tao-Eldrup model.

Table 2 Positron trapping modes for initial and water-immersed $MgAl_2O_4$ ceramics mathematically treated within three-component procedure [21]

T_s, °C	Sample pre-history	$\tau_{av.}$, ns	τ_b, ns	κ_d, ns^{-1}	τ_2- τ_b, ns	τ_2/τ_b	R_3, nm
1100	Initial	0.32	0.28	0.60	0.21	1.7	0.338
	Water-immersed	0.33	0.29	0.70	0.21	1.7	0.276
1200	Initial	0.30	0.27	0.60	0.20	1.7	0.322
	Water-immersed	0.31	0.27	0.90	0.18	1.7	0.275
1300	Initial	0.27	0.25	0.60	0.19	1.7	0.305
	Water-immersed	0.31	0.27	0.90	0.19	1.7	0.276
1400	Initial	0.24	0.21	0.60	0.15	1.7	0.278
	Water-immersed	0.29	0.26	0.90	0.17	1.7	0.282

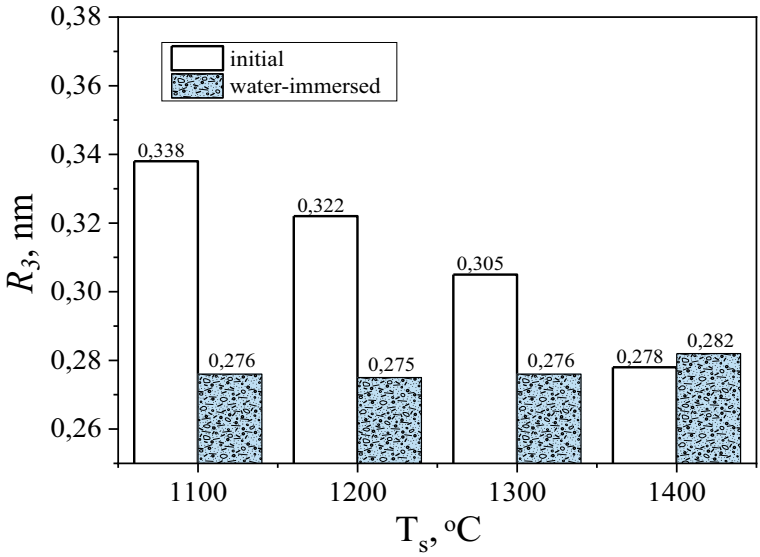

Fig. 3 Nanopore radii R_3 in $MgAl_2O_4$ ceramics sintered at 1100–1400 °C changed in water–adsorption cycles

The third PALS component with lifetime τ_3 is related with o-Ps decaying. In initial ceramic samples, this lifetime reduces from 2.6 to 1.9 ns with T_s, but intensity I_3 is closed to 0.02. In water-adsorbed ceramics, lifetime τ_3 is closed to 1,84 ns, while τ_3 ~ 1.88 ns is related to o-Ps "pick-off" decaying in water at 20 °C. In all cases, intensity I_3 rises from 2% to 0.12–0.15 a.u. testifying large amount of adsorbed water in ceramic samples. This change is accompanied by reduced in parameters of the first PALS component, but parameters of the second component are without changes.

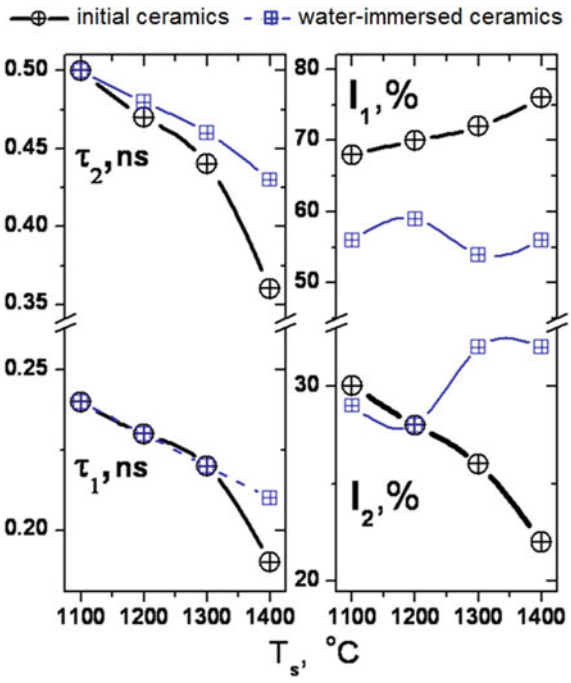

Fig. 4 Changes in lifetime components in dependence on sintering temperature of $MgAl_2O_4$ ceramics [28]

3.2 Water–Adsorption Processes in Nanostructured $MgAl_2O_3$ Ceramics Studied by Three-Component Fitting Procedure with Fixation of the Lifetimes

To study more considerable changes in positron trapping in the $MgAl_2O_4$ ceramics caused by absorbed water, the new algorithm is needed to treatment of PALS data [24]. This task can be permitted due to fixation of τ_1 and τ_2 parameters because adsorbed water not changes structure of spinel ceramics.

As was described above, the lifetime τ_2 is related to extended defects near grain boundaries in ceramic materials. Positrons are trapped in the same defects in $MgAl_2O_4$ ceramics independent on amount of adsorbed water by their nanopores. So, the first and second positron lifetimes (τ_1 and τ_2) can be considered near constant. Therefore, all changes in fitting parameters of these components will be reflected in intensities I_1 and I_2. The third lifetime τ_3 is non-fixed (see Table 3). Treatment of experimental PALS data was carried out at fixed lifetimes ($\tau_1 = 0.17$–0.2 ns and $\tau_2 = 0.36$–0.38 ns). At that, the best FIT parameters were obtained at constant lifetimes $\tau_1 = 0.17$ ns and $\tau_2 = 0.37$ ns [24].

The I_1 and I_2 intensities are changed dependently from amount of adsorbed water in $MgAl_2O_4$ ceramics. Thus, rising of *RH* from 25 to 98% results in reducing of intensity I_1 and increasing of intensity I_2. The changes of RH from 98 to 25% reflect inverse to previously described transformation in I_1 and I_2 intensities (Table 3). The

Table 3 PALS characteristics for $MgAl_2O_4$ ceramics sintered at 1300 °C (RH = 25%–60%–98%–60%–25%)

RH, %	Fitting prameters						Positron trapping modes				
	τ_1, ns	I_1, a.u	τ_2, ns	I_2, a.u	τ_3, ns	I_3, a.u	$\tau_{av.}$, ns	τ_b, ns	κ_d, ns^{-1}	τ_2-τ_b, ns	τ_2/τ_b
25	0.18	0.79	0.38	0.20	2.37	0.01	0.22	0.20	0.59	0.18	1.89
60	0.18	0.78	0.38	0.21	2.55	0.01	0.22	0.20	0.62	0.18	1.87
98	0.18	0.76	0.38	0.23	2.27	0.01	0.22	0.20	0.67	0.18	1.86
60	0.18	0.77	0.38	0.22	2.26	0.01	0.22	0.20	0.64	0.18	1.87
25	0.18	0.78	0.38	0.21	2.21	0.01	0.22	0.20	0.61	0.18	1.88

positron trapping in water-immersed defects related to the second component is more intensive. The lifetimes τ_3 are near 2.3–2.8 ns. The input of this component is not changed, and intensity is near 1% [36].

In contrast, most significant changes in positron trapping in $MgAl_2O_4$ ceramics caused by water-sorption reflect in positron trapping rate in defect κ_d (Fig. 5). Thus, the water-sorption effect in the studied spinel ceramics is accumulated in non-direct trapping κ_d parameter [24].

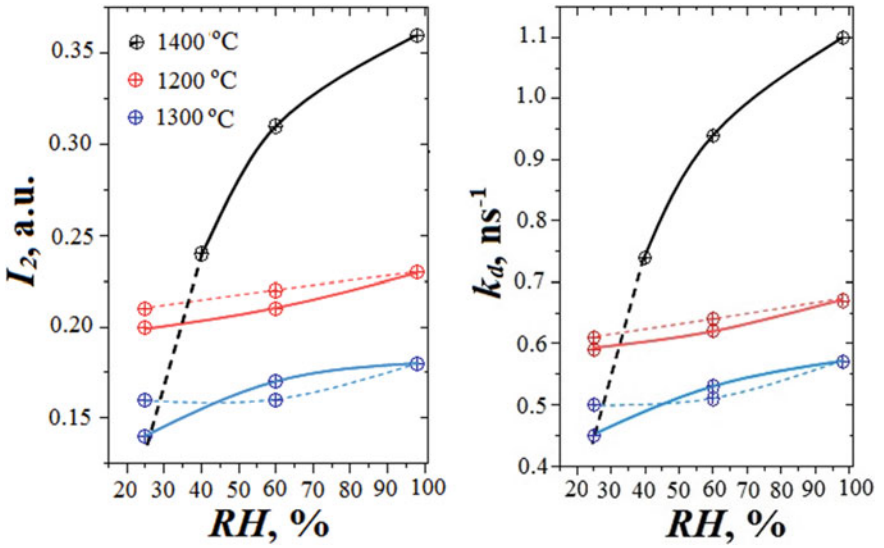

Fig. 5 Dependences of positron intensity I_2 and positron trapping rate κ_d on relative humidity in adsorption–desorption cycles for the $MgAl_2O_4$ ceramics sintered at different T_s [28]

3.3 *Water–Adsorption Processes in Nanostructured $MgAl_2O_3$ Ceramics Studied by Four-Component Fitting Procedure*

Fitting parameters obtained within four-component treatment of the reconstructed PALS spectra of initial and water vapor $MgAl_2O_4$ ceramics sintered at 1100–1400 °C are gathered in Table 4. It is established that τ_1 lifetime in the dried ceramics decreases with T_s, while I_1 intensity increases in respect to amount of main spinel phase like in [32]. Positrons are trapped more strongly in ceramics prepared at lower T_s, as reflected in the values of the second component of the reconstructed PALS spectra. As it follows from Table 4, the numerical values of this component (τ_2 and I_2) decrease with T_s.

As it follows from Table 5, the calculated values of positron trapping modes in

Table 4 Fitting parameters for $MgAl_2O_4$ ceramics sintered at different T_s obtained at four-component decomposition procedure [23]

T_s, °C	Sample pre-history	τ_1, ns	I_1, a.u	τ_2, ns	I_2, a.u	τ_3, ns	I_3, a.u	τ_4, ns	I_4, a.u
1100	Initial	0.169	0.68	0.462	0.28	2.240	0.017	70.14	0.025
	Water vapor	0.170	0.66	0.483	0.28	1.820	0.044	53.05	0.009
1200	Initial	0.164	0.73	0.443	0.24	2.347	0.011	70.51	0.020
	Water vapor	0.160	0.64	0.426	0.31	2.047	0.038	58.67	0.004
1300	Initial	0.155	0.82	0.414	0.16	2.426	0.008	68.74	0.014
	Water vapor	0.161	0.76	0.400	0.21	2.619	0.018	58.33	0.007
1400	Initial	0.152	0.88	0.388	0.11	2.504	0.007	62.32	0.008
	Water vapor	0.160	0.77	0.409	0.20	2.562	0.022	57.35	0.006

Table 5 Positron trapping modes and radii of nanopores determined from four-component fitting procedure for $MgAl_2O_4$ ceramics sintered at different T_s [23]

T_s, °C	Sample pre-history	Positron trapping modes					Radii of nanopores	
		$\tau_{av.}$, ns	τ_b, ns	κ_d, ns^{-1}	$\tau_2 - \tau_b$, ns	τ_2/τ_b	R_3, nm	R_4, nm
1100	Initial	0.289	0.215	1.260	0.349	2.627	0.309	1.844
	Water vapor	0.333	0.225	1.442	0.440	2.953	0.271	1.539
1200	Initial	0.257	0.199	1.074	0.327	2.643	0.319	1.852
	Water vapor	0.321	0.224	1.525	0.379	2.691	0.293	1.636
1300	Initial	0.176	0.764	0.334	2.901	0.176	0.325	1.818
	Water vapor	0.193	1.032	0.382	2.978	0.193	0.340	1.630
1400	Initial	0.195	0.166	0.544	0.349	3.108	0.331	1.701
	Water vapor	0.263	0.192	1.039	0.430	3.241	0.335	1.613

$MgAl_2O_4$ ceramics (average positron lifetime $\tau_{av.}$, bulk positron lifetimes in defect-free samples τ_b and positron trapping rates in defects κ_d) are decreased with sintering temperature T_s. These parameters are in good agreements with amount of additional MgO and Al_2O_3 phases in the ceramics [32].

At the same time, the principal water–vapor sorption processes in the studied $MgAl_2O_4$ ceramics sintered at 1100–1400 °C occur to be mostly determined by o-Ps related components in the PALS spectra reconstructed through four-term fitting procedure. As it was shown earlier [24, 29], the corresponding long-lived lifetimes τ_3 and τ_4 reflect sizes of nanopores, and their intensities I_3 and I_4 are directly related to the number of these nanopores.

So, in the initial $MgAl_2O_4$ ceramics sintered at 1100–1400 °C, the lifetime τ_3 increases with T_s, while intensity I_3 decreases (Table 4). These changes are due to the increase in the size of small nanopores with radius R_3, and their reduction is caused by increasing contact between grains. The lifetime τ_4 and intensity I_4 naturally decrease with T_s, indicating reduction in size and number of nanopores with radius R_4. The radii R_3 and R_4 of spherical nanopores (given in Table 5) were calculated using τ_3 and τ_4 lifetimes in Tao-Eldrup model. It is shown that radius of nanopores R_3 increases from 0.309 to 0.331 nm, and R_4 remains nearly at the same level (~1.8 nm) in the initially dried ceramics sintered at 1100–1400 °C (Fig. 6).

Preferential decreasing of the lifetime τ_2 in water vapor $MgAl_2O_4$ ceramics and increasing of their intensity I_2 demonstrate intensification of positron trapping in defects near grain boundaries filled with water. Thus, the water–adsorption processes in $MgAl_2O_4$ ceramics are accompanied by fragmentation of positron trapping sites near grain boundaries [23].

Water–vapor sorption processes in the studied ceramics result in essential evolution of third and fourth o-Ps-related components. The intensity I_3 increases in all initial samples after water–vapor exposure, thus confirming o-Ps annihilation in water-filled nanopores through a “bubble” mechanism (with corresponding o-Ps lifetime close to 1.8 ns) [37–39]. At the same time, the lifetime τ_3 decreases in more defective ceramics sintered at 1100 and 1200 °C, but increases in more perfect ceramics sintered at 1300 °C and 1400 °C.

Other mechanism of water–vapor sorption processes similar to one reported in [40] is realized in the studied $MgAl_2O_4$ ceramics through fourth component of the PAL spectra. Unlike the third component, the intensity I_4 decreases in water–vapor exposure ceramics samples. Since this intensity does not drop to zero being within 0.4–0.9% domain, it should be assumed that there exists a fraction of closed nanopores, where o-Ps are trapped [29].

4 Conclusions

Peculiarities of water–adsorption processes in nanostructured humidity-sensitive $MgAl_2O_4$ ceramics studied by positron annihilation lifetime at three- and four-component fitting procedures were generalized. The mathematical treatment of

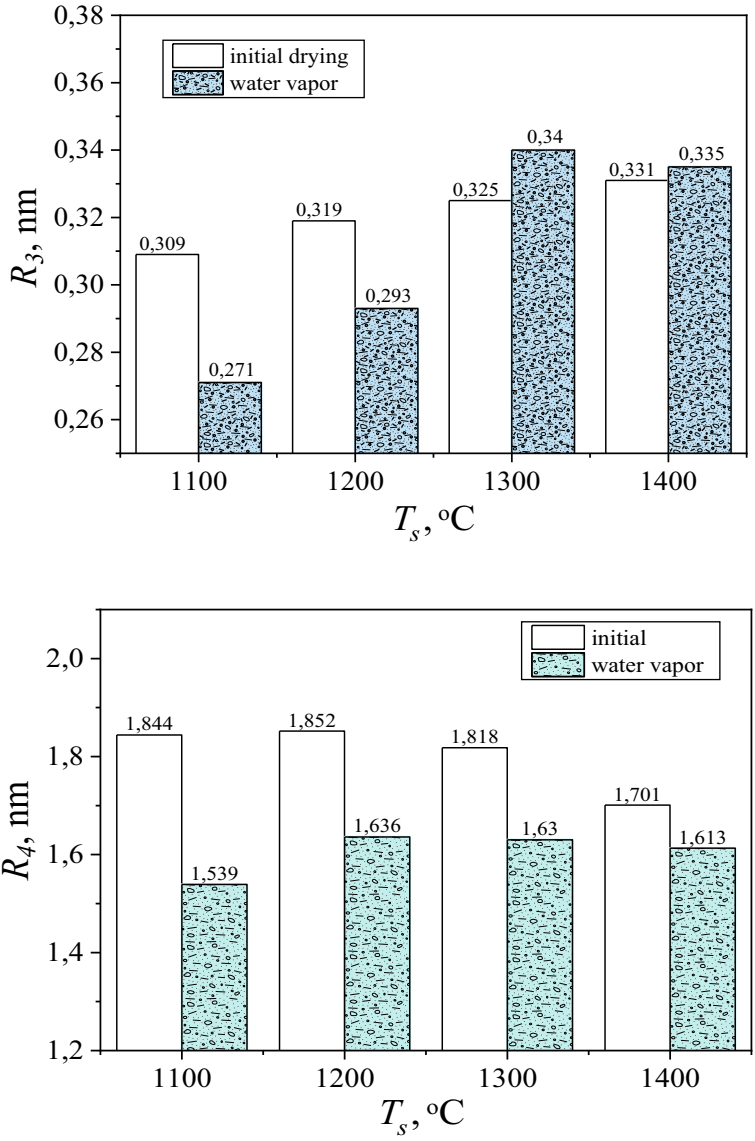

Fig. 6 Nanopore radii R_3 and R_4 in $MgAl_2O_4$ ceramics sintered at 1100–1400 °C changed in water–adsorption cycle

experimental PALS data at constant values of reduced bulk and defect-related lifetimes allows to refine the most significant changes caused by absorbed water in the functional ceramics.

It is shown that positrons are trapped more strongly in the ceramics obtained at lower T_s, which was reflected in the second component of the four-term decomposed PALS spectra. The positron trapping in defects occurs more efficiently in water-immersed ceramics due to increase in positron trapping rate of extended defects. The more perfect structure of ceramics, the more considerable changes occur in the water-absorbing pores.

The third and fourth longest-lived components in PALS spectra are due to annihilation of o-Ps atoms in the nanopores, the corresponding radii being calculated from τ_3 and τ_4 lifetimes using known Tao-Eldrup model. The Ps annihilation in nanopores with adsorbed water vapor is shown to occur via two mechanisms: o-Ps decaying in nanopores including "pick-off" annihilation in the "bubbles" of liquid water and o-Ps trapping in free volume of nanopores with physisorbed water molecules at the pore walls. The water vapor modifies defects in ceramics located near grain boundaries, and this process accompanied by void fragmentation at water–adsorption.

The fixation of all water-dependent positron trapping inputs allows to refine the most significant changes in positron trapping rate of extended defects located near grain boundaries. The water–adsorption processes in $MgAl_2O_4$ ceramics leads to corresponding increase in positron trapping rates of extended defects located near grain boundaries.

Acknowledgements H.K. thanks to Ministry of Education and Science of Ukraine for support, Prof. O. Shpotyuk for discussion, Dr. I. Hadzaman for sample preparation and Dr. A. Ingram for assistance in PALS experiment.

References

1. Gusmano G, Montesperelli G, Traversa E, Bearzotti A, Petrocco G, d'Amico A, Di Natal, C (1992) Magnesium aluminium spinel thin film as a humidity sensor. Sens Actu B Chem 7(1–3):460–463. https://www.sciencedirect.com/science/article/abs/pii/092540059280344W
2. Zhao X, Ren X, Sun C, Zhang X, Si Y, Yan C, Xu J, Xue D (2008) Morphology evolution at nano-to micro-scale. Funct Mater Lett 1(03):167–172. https://www.worldscientific.com/doi/abs/10.1142/S1793604708000393
3. Li JG, Ikegami T, Lee JH, Mori T (2000) Fabrication of translucent magnesium aluminum spinel ceramics. J Am Ceram Soc 83(11):2866–2868. https://ceramics.onlinelibrary.wiley.com/doi/abs/10.1111/j.1151-2916.2000.tb01648.x
4. Laobuthee, A, Wongkasemjit S, Traversa E, Laine RM (2000) $MgAl_2O_4$ spinel powders from oxide one pot synthesis (OOPS) process for ceramic humidity sensors. J Eur Ceram Soc 20(2):91–97. https://www.sciencedirect.com/science/article/abs/pii/S0955221999001533
5. Mordekovitz Y, Shoval Y, Froumin N, Hayun S (2020) Effect of structure and composition of non-stoichiometry magnesium aluminate spinel on water adsorption. Materials 13(14):3195. https://www.mdpi.com/1996-1944/13/14/3195
6. Wang Z, Chang CL, Zhao X, Qian W, Zhang X, Xie Z, Hwang B-H, Hu C, Shen J, Hui R (2009) $MgAl_2O_4$-based humidity-sensing material for potential application in PEM fuel cells.

J Power Sources 190(2):351–355. https://www.sciencedirect.com/science/article/abs/pii/S037877530801762X
7. Shah J, Kotnala RK (2012) Humidity sensing exclusively by physisorption of water vapors on magnesium ferrite. Sens Act B Chem 171:832–837. https://www.sciencedirect.com/science/article/abs/pii/S0925400512005497
8. Klym H, Ingram A, Shpotyuk O, Hadzaman I (2012) Water-sorption processes in nanostructured ceramics for sensor electronics studied with positron annihilation instruments. In: 28th International conference on microelectronics (MIEL), pp 155–158. https://doi.org/10.1109/MIEL.2012.6222821
9. Henninger SK, Schmidt FP, Henning HM (2010) Water adsorption characteristics of novel materials for heat transformation applications. Appl Therm Eng 30(13):1692–1702. https://www.sciencedirect.com/science/article/abs/pii/S1359431110001389
10. Klym H, Ingram A, Shpotyuk O, Hadzaman I, Chalyy D (2018) Water-sorption effects near grain boundaries in modified MgO-Al_2O_3 ceramics tested with positron-positronium trapping algorithm. Acta Phys Pol A 133(4):864–868. https://doi.org/10.12693/APhysPolA.133.864
11. Klym H, Ingram A, Hadzaman I, Karbovnyk I, Vasylchyshyn I, Popov AI (2019) Nanoporous characterization of modified humidity-sensitive MgO-Al_2O_3 ceramics by positron annihilation lifetime spectroscopy method. IOP Conf Ser Mater Sci Eng 503(1):012019. https://iopscience.iop.org/article/10.1088/1757-899X/503/1/012019/meta
12. Shpotyuk O, Balitska V, Brunner M, Hadzaman I, Klym H (2015) Thermally-induced electronic relaxation in structurally-modified $Cu_{0.1}Ni_{0.8}Co_{0.2}Mn_{1.9}O_4$ spinel ceramics. Phys B Condens Matter 459:116–121. https://www.sciencedirect.com/science/article/abs/pii/S0921452614008576
13. Karbovnyk I, Bolesta I, Rovetskii I, Velgosh S, Klym H (2014) Studies of CdI_2-Bi_3 microstructures with optical methods, atomic force microscopy and positron annihilation spectroscopy. Mater Sci Poland 32(3):391–395. https://link.springer.com/article/10.2478/s13536-014-0215-z
14. Bondarchuk A, Shpotyuk O, Glot A, Klym H (2012) Current saturation in In_2O_3-SrO ceramics: a role of oxidizing atmosphere. Rev Mex Fís 58(4):313–316. http://www.scielo.org.mx/scielo.php?script=sci_arttext&pid=S0035-001X2012000400005
15. Shpotyuk O, Brunner M, Hadzaman I, Balitska V, Klym H (2016) Analytical description of degradation-relaxation transformations in nanoinhomogeneous spinel ceramics. Nanoscale Res Lett 11(1):499. https://link.springer.com/article/10.1186/s11671-016-1722-0
16. Klym H, Hadzaman I, Shpotyuk O, Fu Q, Luo W, Deng J (2013) Integrated thick-film p-i-p^+ structures based on spinel ceramics. Solid State Phenom 200:156–161. https://www.scientific.net/ssp.200.156
17. Vakiv M, Hadzaman I, Klym H, Shpotyuk O, Brunner M (2011) Multifunctional thick-film structures based on spinel ceramics for environment sensors. J Phys Conf Ser 289(1):012011. https://iopscience.iop.org/article/10.1088/1742-6596/289/1/012011/meta
18. Karbovnyk I, Olenych I, Aksimentyeva O, Klym H, Dzendzelyuk O, Olenych Y, Hrushetska O (2016) Effect of radiation on the electrical properties of PEDOT-based nanocomposites. Nanoscale Res Lett 11(1):84. https://link.springer.com/article/10.1186/s11671-016-1293-0
19. Karbovnyk I, Collins J, Bolesta I, Stelmashchuk A, Kolkevych A, Velupillai S, Klym H, Fedyshyn O, Tymoshyk S, Kolych I (2015) Random nanostructured metallic films for environmental monitoring and optical sensing: experimental and computational studies. Nanoscale Res Lett 10(1):1–5. https://nanoscalereslett.springeropen.com/articles/10.1186/s11671-015-0855-x
20. Krause-Rehberg R, Leipner HS (1999) Positron annihilation in semiconductors. In: Defect studies. Springer, Berlin-Heidelberg-New York, p 378
21. Klym H, Ingram A, Shpotyuk O, Filipecki J, Hadzaman I (2007) Extended positron-trapping defects in insulating $MgAl_2O_4$ spinel-type ceramics. Physica Status Solidi c 4(3):715–718. https://onlinelibrary.wiley.com/doi/abs/10.1002/pssc.200673735
22. Jean YC, Mallon PE, Schrader DM (2003) Principles and application of positron and positronium chemistry. Word Scientific, Singapore

23. Klym H, Ingram A, Shpotyuk O, Hadzaman I, Solntsev V (2016) Water-vapor sorption processes in nanoporous MgO-Al_2O_3 ceramics: the PAL spectroscopy study. Nanoscale Res Lett 11(1):1. https://doi.org/10.1186/s11671-016-1352-6
24. Filipecki J, Ingram A, Klym H, Shpotyuk O, Vakiv M (2007) Water-sensitive positron-trapping modes in nanoporous magnesium aluminate ceramics. J Phys Conf Ser 79(1):012015. https://doi.org/10.1088/1742-6596/79/1/012015
25. Klym HI, Ivanusa AI, Kostiv YuM, Chalyy DO, Tkachuk TI, Dunets RB, Vasylchyshyn II (2017) Methodology and algorithm of multicomponent analysis of positron annihilation spectra for nanostructured functional materials. J Nano- Electron Phys 9(3):03037-1-6. https://doi.org/10.21272/jnep.9(3).03037
26. Shpotyuk O, Filipecki J: Free volume in vitreous chalcogenide semiconductors: possibilities of positron annihilation lifetime study. Wyd-wo WSP w Czestochowie, Czestochowa
27. Kansy J (1996) Microcomputer program for analysis of positron annihilation lifetime spectra. Nucl Instrum Methods Phys Res, Sect A 374(2):235–244
28. Klym H, Dunets R, Ivanusa A, Kostiv Y, Yurchak I (2017) Modified humidity-sensitive ceramics for microelectronics studied by PALS system. In: IEEE First Ukraine conference on electrical and computer engineering (UKRCON), pp 732–735. https://ieeexplore.ieee.org/abstract/document/8100341
29. Golovchak R, Wang Sh, Jain H, Ingram A (2012) Positron annihilation lifetime spectroscopy of nano/macroporous bioactive glasses. J Mater Res 27(19):2561–2567
30. Kobayashi Y, Ito K, Oka T, Hirata K (2007) Positronium chemistry in porous materials. Radiat Phys Chem 76:224–230. https://www.sciencedirect.com/science/article/abs/pii/S0969806X06001496
31. Nambissan PMG, Upadhyay C, Verma HC (2003) Positron lifetime spectroscopic studies of nanocrystalline $ZnFe_2O_4$. J Appl Phys 93:6320. https://aip.scitation.org/doi/abs/10.1063/1.1569973
32. Klym H, Ingram A (2007) Unified model of multichannel positron annihilation in nanoporous magnesium aluminate ceramics. J Phys Conf Ser 79(1):012014. https://iopscience.iop.org/article/10.1088/1742-6596/79/1/012014/meta
33. Klym H, Ingram A, Shpotyuk O, Filipecki J, Hadzaman I (2011). Structural studies of spinel manganite ceramics with positron annihilation lifetime spectroscopy. J Phys Conf Ser 289(1):012010. https://iopscience.iop.org/article/10.1088/1742-6596/289/1/012010/meta
34. Tao SJ (1972) Positronium annihilation in molecular substance. J Chem Phys 56(11):5499–5510. https://doi.org/10.1063/1.1677067
35. Eldrup M, Lightbody D, Sherwood JN (1981) The temperature dependence of positron lifetimes in solid pivalic acid. Chem Phys 63:51–58. https://doi.org/10.1016/0301-0104(81)80307-2
36. Klym H, Ingram A, Shpotyuk O, Hadzaman I, Hotra O, Kostiv Y (2016) Nanostructural free-volume effects in humidity-sensitive MgO-Al_2O_3 ceramics for sensor applications. J Mater Eng Perform 25(3):866–873. https://doi.org/10.1007/s11665-016-1931-9
37. Leifer I, Patro RK (2002) The bubble mechanism for methane transport from the shallow sea bed to the surface: a review and sensitivity study. Cont Shelf Res 22(16): 2409–2428. https://www.sciencedirect.com/science/article/abs/pii/S0278434302000651
38. Ljunggren S, Eriksson JC (1997) The lifetime of a colloid-sized gas bubble in water and the cause of the hydrophobic attraction. Colloids Surfaces A Physicochem Eng Aspects 129:151–155. https://www.sciencedirect.com/science/article/abs/pii/S0927775797000332
39. Grosman A, Ortega C (2005) Nature of capillary condensation and evaporation processes in ordered porous materials. Langmuir 21:10515–10521. https://pubs.acs.org/doi/abs/10.1021/la051030o
40. Dlubek G, Yang Yu, Krause-Rehberg R, Beichel W, Bulut S, Pogodina N, Krossing I, Friedrich Ch (2010) Free volume in imidazolium triflimide ($[C_3MIM][NTf_2]$) ionic liquid from positron lifetime: Amorphous, crystalline, and liquid states. J Chem Phys 133:124502. https://aip.scitation.org/doi/abs/10.1063/1.3487522

Thin Films of $La_{1-x}Sm_xVO_4$:Ca Luminescent Vanadate Nanoparticles Deposited with Various Methods on Glass Substrates

O. V. Chukova, S. A. Nedilko, S. G. Nedilko, T. A. Voitenko, M. Androulidaki, A. Manousaki, A. Papadopoulos, K. Savva, and E. Stratakis

Abbreviations

LED	Light emitting diode
PLD	Pulsed laser deposition
RE	Rare earth
SC	Spin coating
SE	Solution evaporation
SEM	Scanning electron microscopy
UV	Ultraviolet
XRD	X-ray diffraction.

1 Introduction

Luminescent oxide films are widely used for optical material science needs, in particular, as luminescent converters for adaptation of incident solar light to spectral sensitivity of silicon solar cells and for conversion of violet and blue LED radiation into white light [1–5]. All the noted applications require development of compounds with enhanced light harvesting from ultraviolet (UV) and violet spectral range (300–450 nm). Oxide materials are characterized by high radiation and thermal stability

O. V. Chukova (✉) · S. A. Nedilko · S. G. Nedilko · T. A. Voitenko
Taras Shevchenko National University of Kyiv, Volodymyrska Str., 64/13, Kyiv 01601, Ukraine
e-mail: chukova@univ.kiev.ua

M. Androulidaki · A. Manousaki · A. Papadopoulos · K. Savva · E. Stratakis
Institute of Electronic Structure & Laser (IESL) of Foundation for Research and Technology Hellas (FORTH), 711 10 Heraklion, Crete, Greece

O. Fesenko and L. Yatsenko (eds.), *Nanomaterials and Nanocomposites, Nanostructure Surfaces, and Their Applications*, Springer Proceedings in Physics 263, https://doi.org/10.1007/978-3-030-74741-1_25

that are important properties for such applications. Luminescent emission of the oxide compound can be related with electronic transitions in their own molecular oxyanions as well as with impure ions, especially RE ions.

Row of the orthovanadate compounds is one of the best oxide matrices for luminescent RE ions. A lot of compositions were synthesized over the world and considered for the noted purposes for the last years. There were bismuth, cerium and lanthanum orthovanadates, magnesium, copper, argentum and strontium vanadates and many others [6–9]. Up to now, mainly extensive approach to new compositions development was applied. We propose to develop common models predicting changes of characteristics of vanadate films by modification of their compositions.

Our own studies have also shown that some of developed oxide compositions in the form of micro/nanoparticles are able to demonstrate promising optical and structural characteristics [10–12]. In particular, we have developed vanadate nanoparticles with enhanced light harvesting from violet spectral range and intensive luminescence emission [13–15]. The next important task is to save the obtained high optical characteristics of oxide nanoparticles under their incorporation of the synthesized vanadate nanoparticles into composite film coatings. Noted that requirements to the properties of the films can be different for various practical tasks, and therefore, various methods of film application should be used in order to find the most suitable one for each practical application.

Thin films of oxide phosphors can be prepared by various methods such as chemical vapor, sol-gel, pulsed laser deposition, spin-coating, reactive sputtering, molecular beam and liquid phase epitaxy. [16–21]. Various methods are characterized by their advantages and disadvantages. Some of the noted methods require film matrices for dispersion of nanoparticles like a polymeric (silicon) matrix for the YAG:Ce particles used currently in commercial white LEDs. Liquid phase epitaxy methods use heavy metal solvents that lead to undesirable effects on optical properties of the films. Chemical vapor deposition and pulsed laser deposition methods use vacuum cameras that make process of deposition expensive. And all these factors can effect on luminescent efficiency of the RE-activated nanoparticles.

The present work is devoted to investigation of morphology and optical characteristics of the films obtained by various methods from the same initial nanoparticles. The methods applied here for deposition of the vanadate films were spin-coating, solution evaporation and pulsed laser deposition (PLD). Advantages and disadvantages of the noted methods for growth of luminescent films from vanadate nanoparticles for various applications are studied and discussed. All the films are applied on glass substrates. The choice of type of substrates is done taking into account possible application of luminescent vanadate films as light converting covering materials for the white LEDs.

2 Methods of the Vanadate Nanoparticles Synthesis and Their Deposition

2.1 Synthesis of the Nanoparticles

As methods those could be successfully used for synthesis of the orthovanadate nanoparticles, several authors have reported solid state, co-precipitation, hydrothermal, solution combustion and sol-gel synthesis [22–26]. We used in this work sol-gel synthesis of nanoparticles because these methods allowed to obtain particles with high luminescence efficiency of the RE activators [12, 15, 27].

Stoichiometric calculated amounts of $La(NO_3)_3$, $Sm(NO_3)_3$, NH_4VO_3, $Ca(NO_3)_2$ were taken as a starting reagents in the used sol-gel method. The necessary quantities of the reagents were gradually mixed in a 250 ml beaker. The solution system was homogenized using a magnetic stirrer. The content of metal ions in their solutions was estimated by trilonometric method: Solution of calcium nitrate was established by direct titration with murexide; the concentration of rare-earth ions in their respective nitrate solutions was established by direct titration with xylenol orange. At the next stage, a complexing agent was added to prevent the sedimentation process from the reaction mixture of a similar composition using the deposition method. Then, 5 g of citric acid were dissolved in a 100 ml distilled water, which was heated and added to the reagents solution. Such a mixture was poured into a graphite cup and placed on a sand bath. The solution gradually evaporated and turned into a gel and then a powder. The fine-grained powder was calcined for 5 h at a step-by-step heating with 100 °C steps up to 680 °C temperature (Fig. 1).

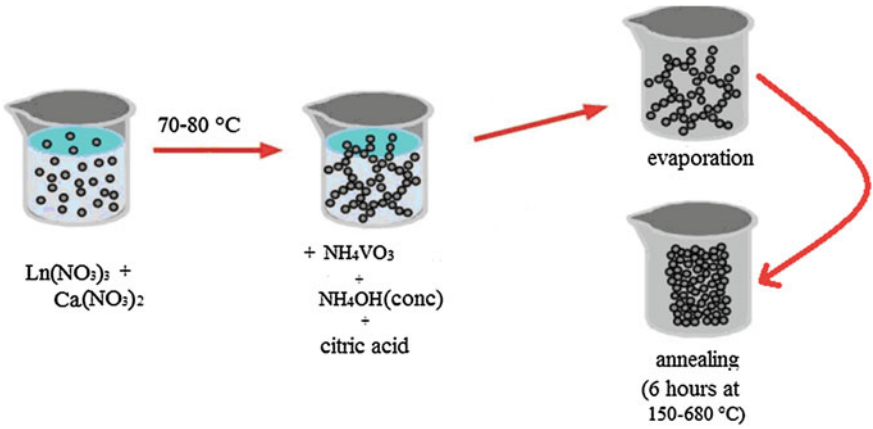

Fig. 1 Scheme of the sol-gel process of synthesis of the initial $La_{1-x}Sm_xVO_4$:Ca nanoparticles

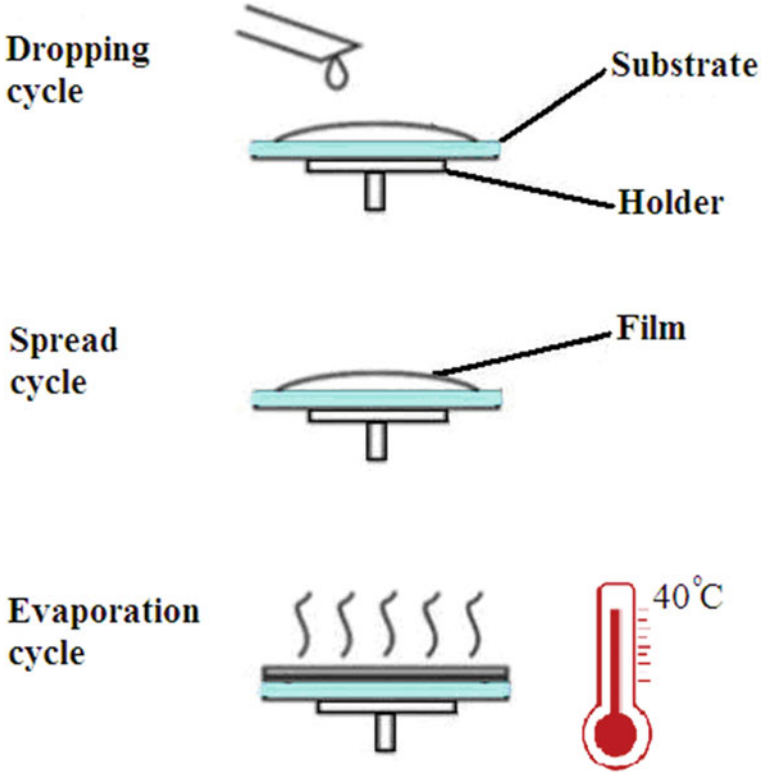

Fig. 2 Scheme of the SE deposition of the films

2.2 Solution Evaporation Method

In the solution evaporation (SE) method, the initial nanoparticles were dissolved in alcohol and placed in the ultrasonic dispergator for 20 min. Some of the samples were prepared using also film binding material (silicon gel). Then, the prepared suspension was deposited by 20 μg droplets on substrates. The deposited droplets were spread and then evaporated at 40 °C in air conditions for 24 h. Scheme of the SE process is presented in Fig. 2.

2.3 Spin-Coating Deposition of the Films

In the spin-coating (SC) method, the initial nanoparticles were dissolved in alcohol together with film binding material (silicon gel) and placed in the ultrasonic dispergator for 20 min. Then, prepared suspense was deposited on substrates by 20 μg droplets. The substrates containing suspension for the SC method were placed in a

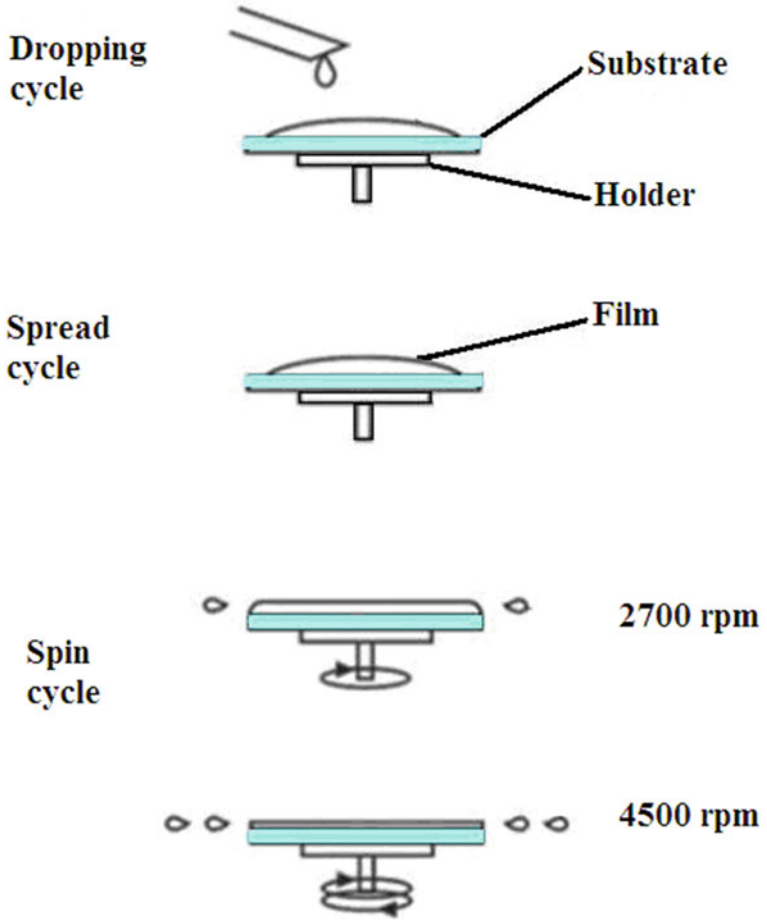

Fig. 3 Scheme of the SC deposition of the films

center of rotating disk and spin coated at 2700 or 4500 rpm for 5 min using MX-20 centrifuge. Scheme of the SC process is presented in Fig. 3.

2.4 Pulsed Laser Deposition

In the pulsed laser deposition (PLD) method, the initial nanoparticles were pressed into tablets of 15 mm diameter and 2–3 mm thickness. These tablets were used as targets for deposition of the films. Deposition was carried out in vacuum camera using KrF excimer laser with $\lambda_{gen} = 248$ nm, 10 Hz pulse repetition and 2000 J/cm^2 power. The substrates were heated to 300 °C.

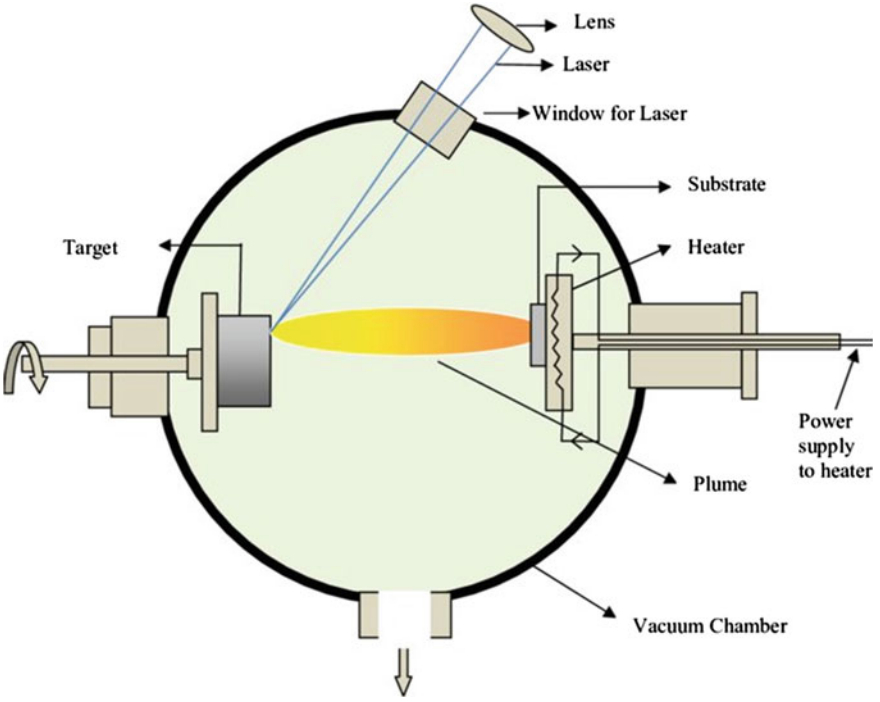

Fig. 4 Standard scheme of the PLD setup [28]

The used scheme of the PLD process is typical and similar to the described before in [28]. It is shown in Fig. 4.

3 Crystal Structure and Morphology of the Initial Nanoparticles

Knowledge about crystal structure and morphology of the initial nanoparticles is necessary for the correct analysis of the thin film characteristics.

Phase compositions of the initial nanoparticles were investigated at Shimadzu LabX XRD-6000 ($Cu_{K\alpha}$-radiation) diffractometer in $10 < 2\Theta < 90°$ angle range with a 2°/min step. It was found that $La_{0.9}Sm_{0.05}Ca_{0.05}VO_4$ is crystallized in monoclinic structure and the space group is P21/n. This result is well matched with a standard card of monoclinic $LaVO_4$ (JCPDS PDF2 50-0367). Increasing concentrations of the Sm^{3+} and Ca^{2+} impurities leads to formation of the monoclinic and tetragonal phases mixture. The latter is matched with standard card of tetragonal $LaVO_4$ (JCPDS PDF2 32–0504). Content of the tetragonal phase in the samples increases

with samarium concentration increase. The nanoparticles used for the films deposition have the $La_{0.8}Sm_{0.1}Ca_{0.1}VO_4$ and $La_{0.7}Sm_{0.15}Ca_{0.15}VO_4$ compositions with two-phase crystal structure, because just the same compositions doped with the Eu^{3+} ions have demonstrated the best luminescence characteristics before [12, 15, 27].

The microstructure of the initial nanoparticles was studied using scanning electron microscope (SEM) INCA X-max System from Oxford Instruments with 20 nm electronic beam diameter. The powder samples consist of nanoparticles that are densely agglomerated in solid grains with sizes about 1–3 microns. Agglomerates contain a lot of interspaces between nanoparticles. Sizes of nanoparticles are varied in a range from 50 to 200 nm. Nanoparticles were of round or polyhedral forms. Polyhedral particles are characterized by various proportions: Some of particles are near to cubic forms, whereas some of the particles are stretched along one of the axes (Fig. 5).

4 Morphology of the Films Obtained by Different Methods

Morphology of the obtained films is studied in comparison with SEM images of nanoparticles synthesized by co-precipitation and sol-gel methods. The SEM images of the film samples were obtained from JEOL JSM-7000F microscope. SEM images of the films in Figs. 2, 3 and 4 show as large areas up to ~2 × 2 μm for general view of samples as well as small separated areas up to ~0.8 × 0.8 μ.

4.1 Morphology of the SE Films

The SE films prepared without film binding material (pure films) consist of nanoparticles that are grouped in big agglomerates with dimensions up to 10 μ. Besides, small agglomerates with dimensions up to 1 μ and agglomerates of few nanoparticles with dimensions of 400–700 nm and lesser can be found in the SEM images of the synthesized films. Distribution of nanoparticles in these films is very inhomogenous (Fig. 6, left).

The SE films prepared with adding of the film binding material contain areas of very thin layers of silicon and mainly single nanoparticles or their small groups from few particles. Distribution of nanoparticles in these films is homogenous. No big agglomerates of nanoparticles were observed (Fig. 6, right).

The nanoparticles in the SE films both pure and grown with silicon (Fig. 6) are characterized by the shapes similar with ones observed for the initial nanoparticles (Fig. 5). Density of the particles in such films if much lower than for the films grown with silicon. Visually presence of silicon gel makes the film opaque, whereas the films prepared without silicon gel are semitransparent and homogenous.

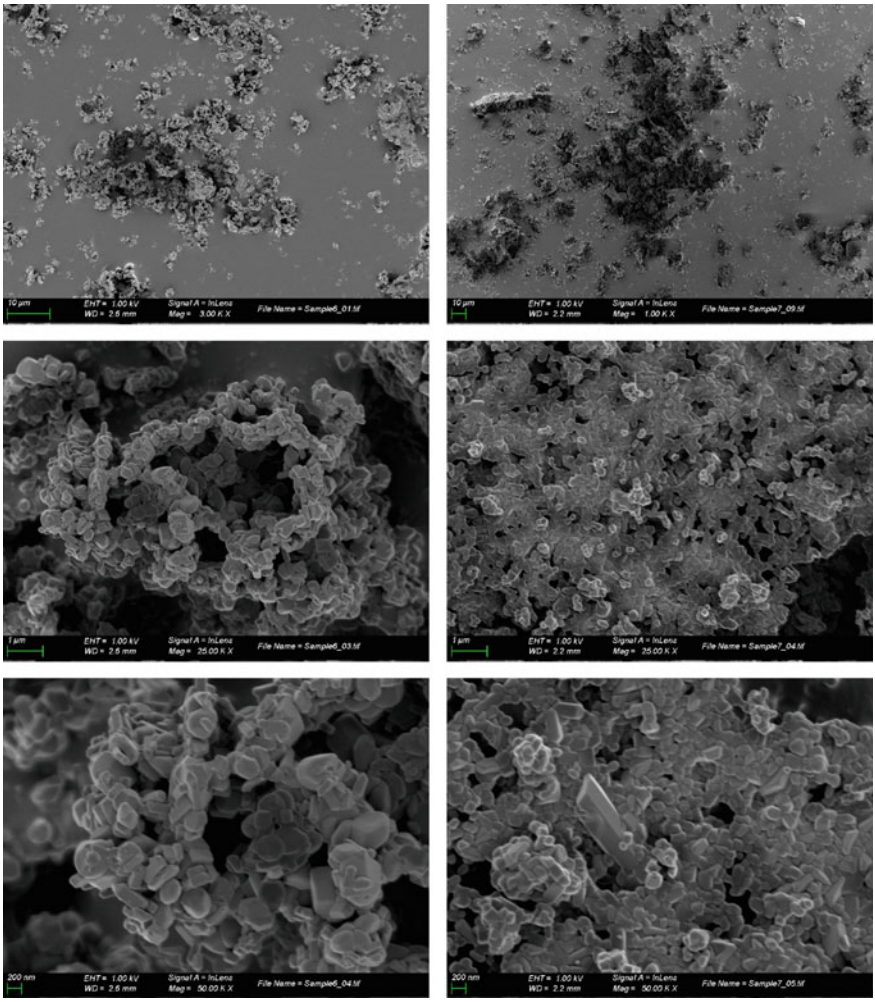

Fig. 5 SEM images of the $La_{0.8}Sm_{0.1}Ca_{0.1}VO_4$ (left) and $La_{0.7}Sm_{0.15}Ca_{0.15}VO_4$ (right) nanoparticles

4.2 Morphology of the SC Films

The most of the SC films are prepared with film binding materials in order to achieve better interaction of the films with substrate during spinning of the samples. Various spin rates were applied in order to study effects of growth conditions on properties of the films. Figure 7 presents comparison of SEM images of the SC films deposited with 2700 and 4500 rpm.

Microscopy of the SC films has shown that they are more homogenous and thinner than the SE films. Their SEM images contain many very small point inclusions and

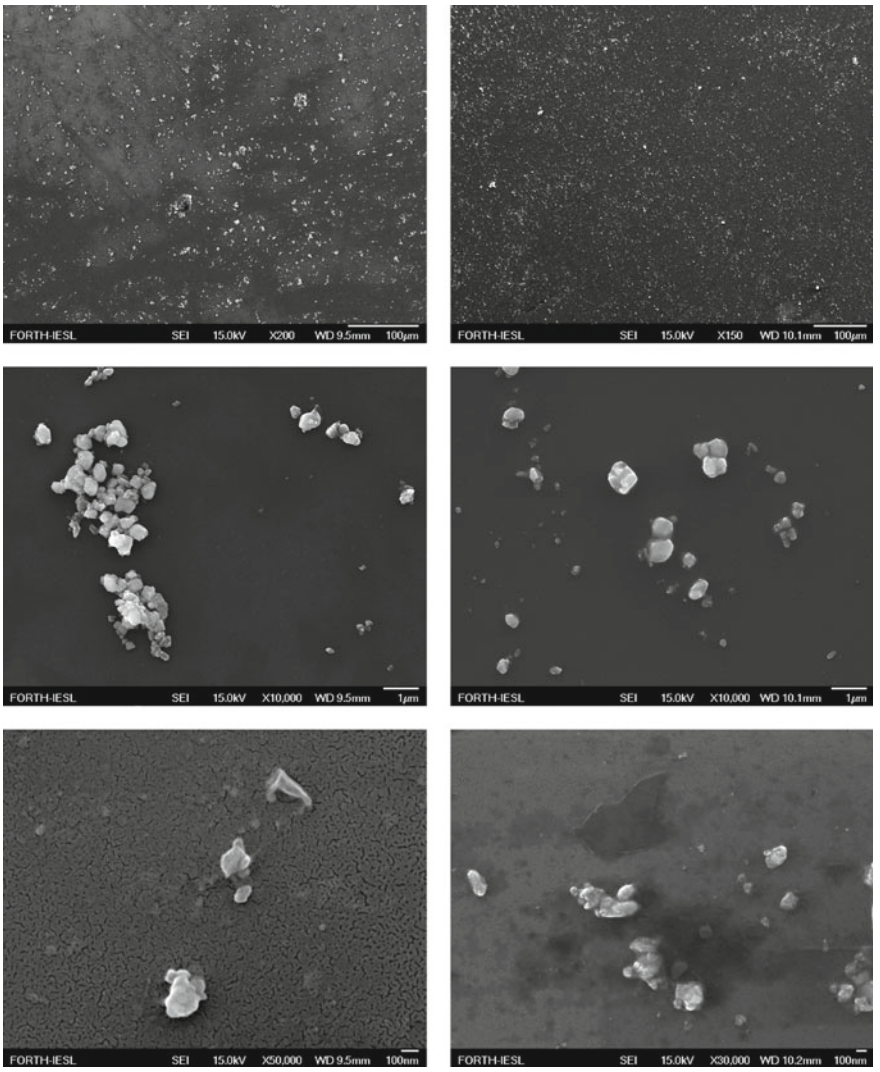

Fig. 6 SEM images of the $La_{0.8}Sm_{0.1}Ca_{0.1}VO_4$ SE films pure (left) and prepared with silicon (right)

some filled areas. Point inclusions are formed by single nanoparticles or by small groups of nanoparticles that are encapsulated inside the silicon film. Some filled areas are formed by agglomerates of nanoparticles with dimensions up to 5 microns and by smaller groups of nanoparticles homogenously distributed between the noted agglomerates.

Increase of spin rate of deposition from 2700 to 4500 rpm has a great impact on film morphology (compare left and right images in Fig. 7): Distribution of nanoparticles

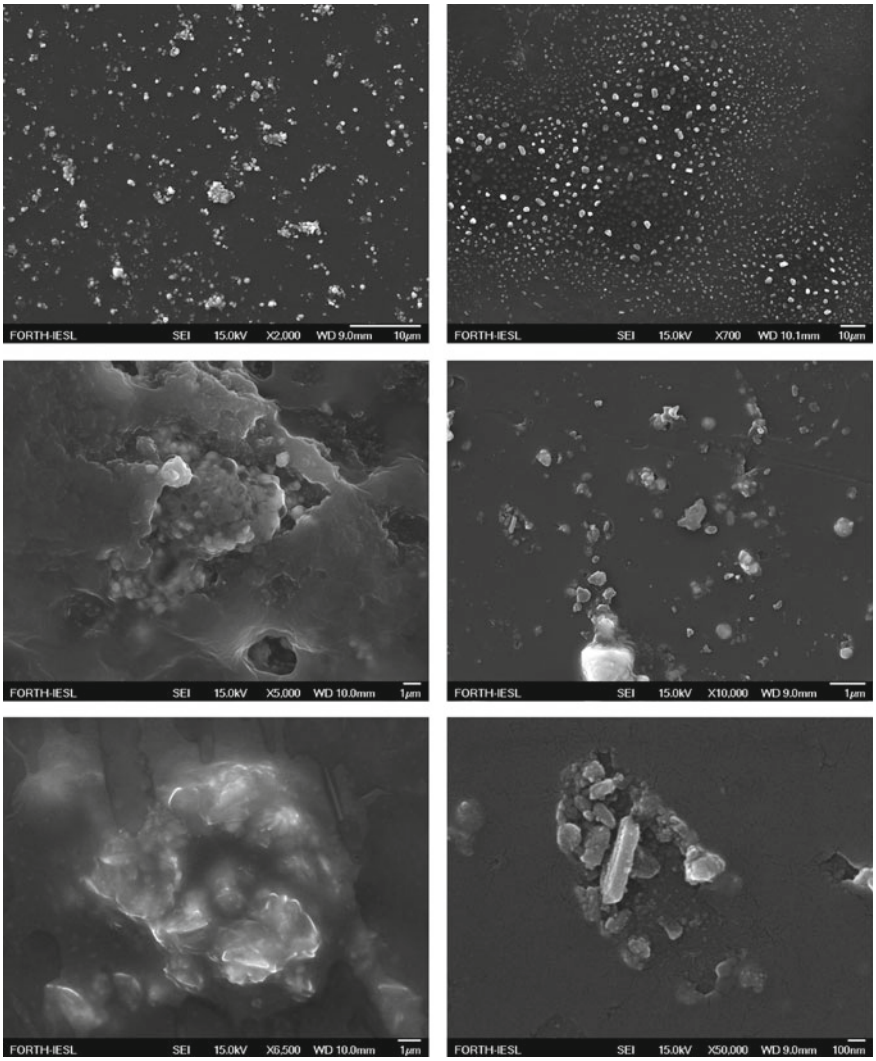

Fig. 7 SEM images of the $La_{0.8}Sm_{0.1}Ca_{0.1}VO_4$ SC films obtained with 2700 (left) and 4500 (right) rpm rates

in the films deposited with 4500 rpm rate is more homogenous, silicon layers are thinner, and agglomerates of nanoparticles are much more smaller. Obviously, the noted effects are achieved by better spreading of the nanoparticles in the film due to higher spin rate.

4.3 Morphology of the PLD Films

All the PLD films are prepared without adding any additional materials. Various number of pulses were used in order to study effects of growth conditions on properties of the films. Figure 8 presents comparison of SEM images of the PLD films deposited with 1000 and 2000 laser pulses. The $La_{0.8}Sm_{0.1}Ca_{0.1}VO_4$ PLD films deposited with 1000 and 2000 pulses on glass substrates have view of very light

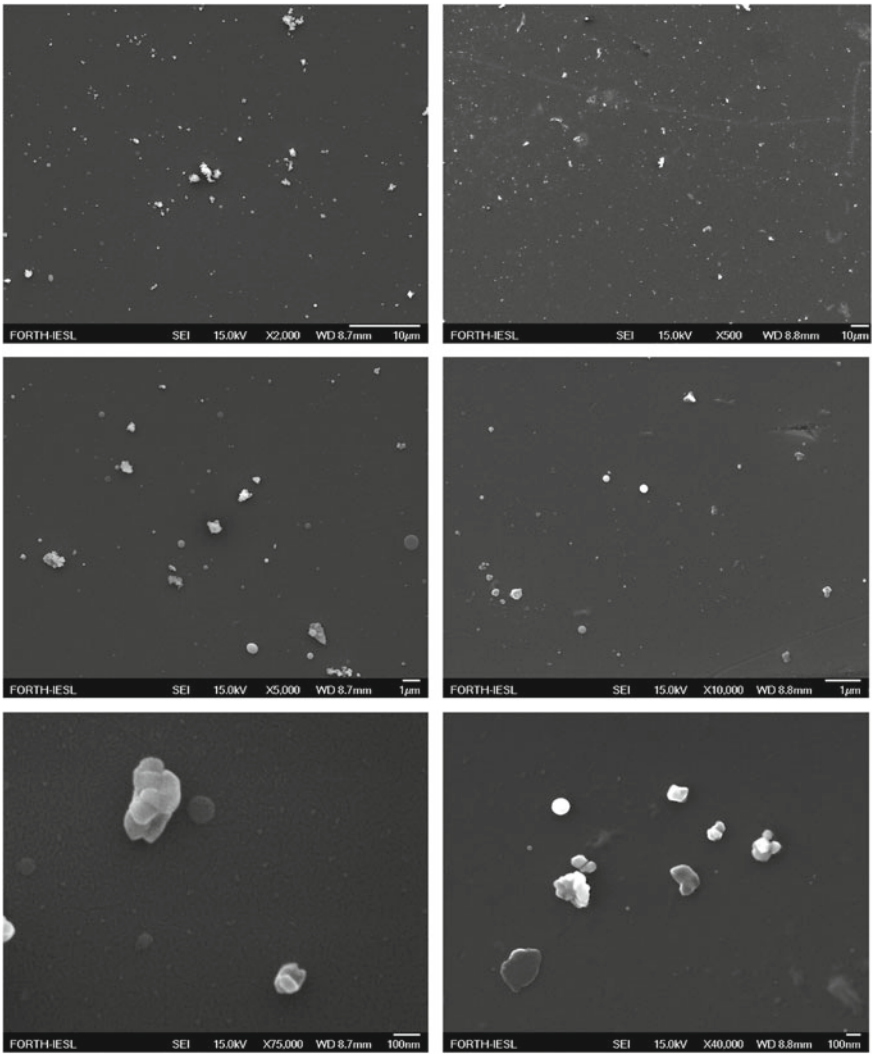

Fig. 8 SEM images of the $La_{0.8}Sm_{0.1}Ca_{0.1}VO_4$ PLD films deposited with 1000 (left) and 2000 laser pulses

and simply light gray homogenous smoke on the glass, respectively. In despite of the homogenous smoke view of the films at usual observation conditions, the SEM images of the samples have shown that the films contain the separated particles and their small agglomerates that are spread on the glass surface (Fig. 4). The detailed views prove that the applied particles and small agglomerates by their sizes and forms are related with the nanoparticles used for the PLD. Comparing morphology of the films deposited with different number of pulses (1000 or 2000), we have not observed essential differences in character of distribution of the particles dependently on number of pulses. The last influences only on densities of the particles in the films.

In despite of the films in their nanoscale structures contain the separated particles and their agglomerates homogenously distributed on the substrates, at usual scale they are looking as complete films. Therefore, we have supposed that the films are formed by grains that are too small to be recognized in the obtained SEM images.

The same situation has been reported formerly for the YVO_4:Eu PLD films deposited on silicon substrates [29]. The authors of that investigation have obtained SEM images of the YVO_4:Eu PLD films that are very similar to the reported here, and thus, we can use their results to estimate sizes of grains in our films. Kim et al. have supposed that their films are formed by very small grains that cannot be detected by the used SEM facility. After several steps of annealing, they achieved increase of grains in their films and have observed and estimated the grains. Noted, that investigated in our work films are thermally untreated and their SEM images are similar just with SEM images of thermally untreated films reported in [29]. We have estimated grain sizes in our films using comparison of our results with the results of [29]. From this comparison, we assumed that our films are formed by grains (particles) with dimensions from ~10 nm for the films on glass substrates to ~20 nm for the films on silicon substrates.

As it was noted above, the initial nanoparticles used here for deposition of the films consist of single nanoparticles with dimensions of nanoparticles from 50 to 200 nm. Thus, sizes of the film-forming grains (particles) from 10 to 20 nm are smaller than sizes of the nanoparticles in targets. We suppose the evaporated under action of laser pulses part of the target was dispersed as small-particle aerosol. It achieves the substrate and forms the films. Instead of this, some nanoparticles and their agglomerates can leave the target and achieve the substrates in their initial forms.

5 Optical Metrology of the Films

The next important step is to estimate thicknesses of the deposited films from technical point of view of optical technique. In the present work, thicknesses of the grown films were estimated using optical thin film metrology method based on the interference patterns in the reflectivity spectrum of the layered sample. Interference effects occurred between light reflected at the boundary and at the surface of the film were investigated with optical microscope and tabletop reflectometer. The light

Table 1 Thicknesses of the $La_{0.8}Sm_{0.1}Ca_{0.1}VO_4$ films deposited with various methods and different conditions

Method	Special conditions	Thickness, nm
SE	Pure vanadate film	30
SE	Silicon gel matrix	270
SC	2700 rpm	206
SC	4500 rpm	127
PLD	1000 pulses	180
PLD	2000 pulses	219

reflected from the sample is collected by pick-up optics connected to the camera adapter of a microscope. An optical fiber guides the light to the spectrometer, and the spectrum is detected by a high performance photo diode array. The measured spectrum from a layered sample shows typical interference effects that depend on the thickness and the optical properties of the materials. Therefore, the film thickness can be determined using optical constants (n and k) of film material and substrate [30]. The calculations were performed by non-commercial programs.

This investigation has shown that the applied method estimates the deposited samples as films with the certain thicknesses of nanoscale dimensions (Table 1). Thus, observed distributions of nanoparticles and their agglomerates do not influence metrology characteristics of the films. The measured thicknesses are varied from 30 to 270 nm for the films obtained by various methods.

Comparing results of SEM study and optical metrology, we should note that in despite of higher thickness of the SC films, they could satisfy the most homogenous distribution of the particles in the films and a lower density of agglomerated inclusions. At the same time, the PLD technology allows deposition of thin films of good quality from the vanadate nanoparticles without any additional matrices. In despite of the SE method allows to deposit the thinnest films, their homogeneity is still to be improved. Investigation of optical properties of the films should give more information about their quality.

6 Optical Spectroscopy

Comparison of optical properties of the initial nanoparticles and films is carried out mainly using reflection spectra because the initial nanoparticles are synthesized in powder state and it is not possible to directly measure their absorption spectra. Reflection spectra were measured using Perkin Elmer Lambda 950 spectrometer. The powder samples of initial nanoparticles were pressed in sample holder before measurements. The spectra of diffuse reflection were measured. In this mode, the monochromator is placed before the samples, and all light reflected from the powder

samples are collected by photometric sphere. In such experimental setup, luminescence and scattering from the investigated samples could give additional contribution in the recorded spectra, and this possibility should be taken into account under analysis of the obtained spectra.

Reflection spectrum of the initial $La_{0.8}Sm_{0.1}Ca_{0.1}VO_4$ nanoparticles consists of the main wide band with maximum in the UV range near 310 nm. This band is complex, and it contains at least one component spreading in the visible range with maximum near 400 nm. The 50% edge of reflection is located at 500 nm (Fig. 9, curve 1). The used glass substrate is characterized by reflection around 8–9% in all the visible range with some increase in the UV range (Fig. 9, curve 2). The pure SE film increases this reflection on 2% in all the measured range without any spectral features (Fig. 9, curve 3). The SE film deposited with silicon matrix increases the reflection on 6% and leads to appearance of two additional bands at 300 and 380 nm (Fig. 9, curve 4). These bands are corresponded, respectively, with 310 and 400 nm maxima of the main reflection band of initial nanoparticles. Therefore, we should assume here that using silicon binding material essentially increases contribution of the vanadate nanoparticles in the reflection spectra of the obtained film samples.

Reflection spectra of samples with the SC films deposited with 2700 rpm are similar to spectra of the substrate, and the film causes only increase of reflection on 4–5% (Fig. 10, curves 2 and 3). At the contrary, the SC film deposited with 4500 rpm does not cause distinctive increase of reflection, but it leads to appearance of

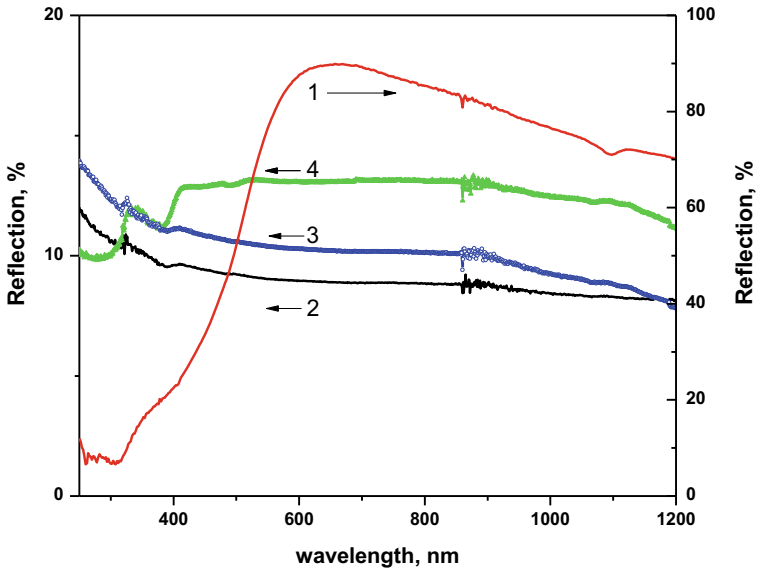

Fig. 9 Reflection spectra of the initial $La_{0.8}Sm_{0.1}Ca_{0.1}VO_4$ nanoparticles (1), glass substrate (2) and samples with the $La_{0.8}Sm_{0.1}Ca_{0.1}VO_4$ SE films pure (3) and deposited with silicon matrix (4)

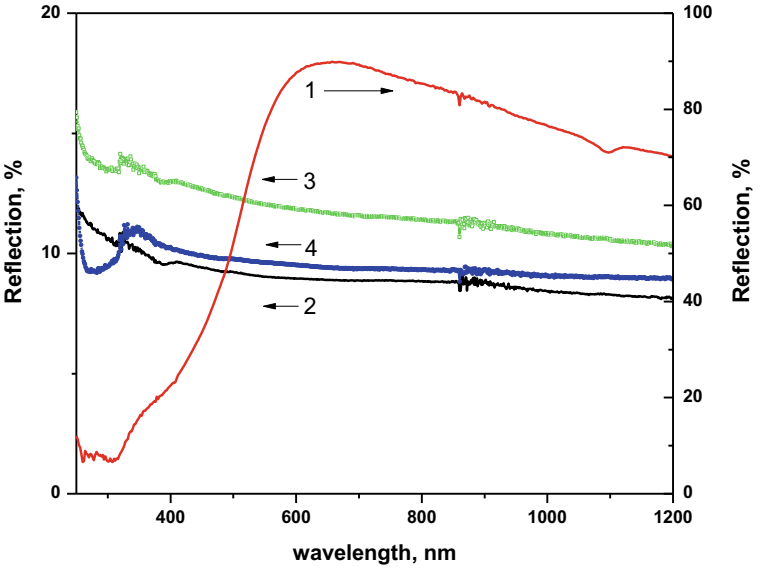

Fig. 10 Reflection spectra of the initial $La_{0.8}Sm_{0.1}Ca_{0.1}VO_4$ nanoparticles (1), glass substrate (2) and samples with the $La_{0.8}Sm_{0.1}Ca_{0.1}VO_4$ SC films deposited with 2700 (3) and 4500 rpm (4)

additional band at 300 nm that is corresponded to reflection of vanadate nanoparticles (Fig. 10, curves 4 and 1, respectively).

The PLD films increase reflection of the samples compared to substrate in 2–3 times from 8–9% to 20–30% in the spectral interval from 400 nm to near IR range. Increasing number of laser pulses increases the noted effect of the deposited films (Fig. 11, curves 1- 3). No additional spectral features were observed for this interval. The additional band at 300 nm corresponded to reflection of vanadate nanoparticles is revealed much more intensively for the PLD films as compared with the SE and SC films (Figs. 9–11).

The observed homogenous increase of reflection of the samples in all the visible range is obviously occurred due to scattering of light on vanadate nanoparticles and binding material. In particular, silicon matrix increases contribution of the SE films in reflection of the samples in 3 times compared to the pure SE films (Fig. 9, curves, 3–4).

From the other hand, increasing spin rates leads to decrease of contribution of the SC films in reflection of the samples (Fig. 9, curves, 3–4). This effect is occurred due to a higher quality of the SC film deposited with 4500 rpm compared to the SC film deposited with 2700 rpm (see Fig. 3 and description herein).

Thus, contributions of the SE and SC films in the reflection spectra of the corresponded samples are in good agreement with the results of SEM investigation of the films morphology. But, properties of the samples with PLD films have demonstrated some differences in their behavior. Contributions of the films in the reflection spectra are too much to be explained by simple scattering on vanadate particles. Besides,

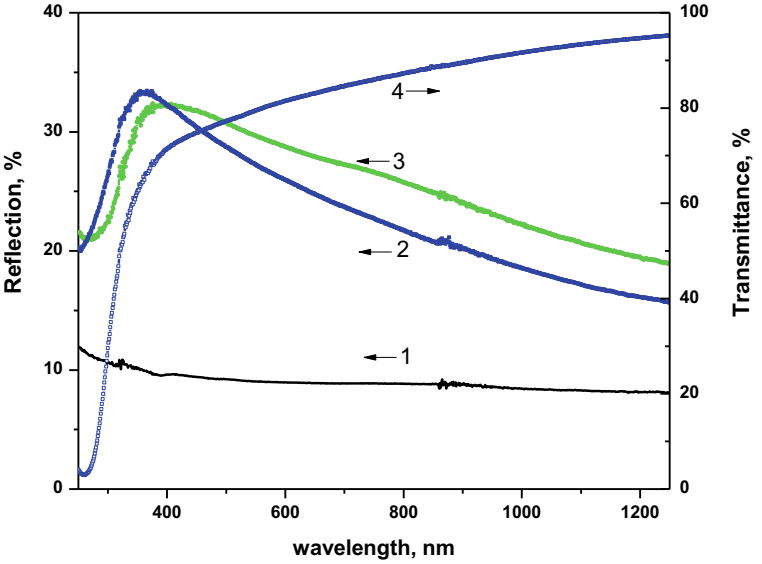

Fig. 11 Reflection (1–3) and transmittance (4) spectra of glass substrate (1) and the $La_{0.8}Sm_{0.1}Ca_{0.1}VO_4$ PLD films deposited with 1000 pulses (2, 4) and 2000 pulses (3)

estimated visually, the PLD vanadate films have view of gray smoke on the glass changing its light coloring dependently on a view angle, whereas the SE and SC films are characterized by white color of various transparencies dependently on the film. Note that the PLD films obtained without any additional binding material and they are characterized by a good homogeneity, especially if compared with the SE films. Vanadate nanoparticles in the PLD films have the lowest rate on agglomeration and the smallest film grains. And the PLD films are characterized by transparency around 90% measured in the transmittance mode (Fig. 11, curve 4). We suppose that contributions of the PLD films in the measured diffuse reflection spectra have another origin connected with the nanosize effects on the intermediate layers between film and substrate. Possibility of formation of nanostructures with special reflection properties under action of ultrafast laser pulses was reported recently [31]. We suppose that light interference on the randomly nanostructured profiles of the PLD films could contribute their diffuse reflection spectra.

7 Luminescence

Luminescence spectra were investigated using ACTONi (500) monochromator with grating 150 grooves/mm (blaze @ 300 nm), slit on 50 micron and liquid N_2—cooled CCD registration.

Luminescence emission spectra of all the grown films consist of four groups of lines in 550–725 nm spectral range that are corresponded to well-known inner f-f transitions in the Sm^{3+} ions incorporated in the $La_{1-x}Sm_{1-x}VO_4$:Ca luminescent nanoparticles. Groups of lines located in the 550–580, 580–620, 625–670 and 680–725 nm spectral ranges are caused by the $^4G_{5/2} \rightarrow {}^6H_{5/2}$, $^6H_{7/2}$, $^6H_{9/2}$ and $^6H_{11/2}$ transitions, respectively [32–35].

Distribution of lines in the emission spectra of the $La_{0.8}Sm_{0.1}Ca_{0.1}VO_4$ films is the same for the films obtained by various methods (Fig. 12). The lowest emission intensity is observed for the pure SE films. But, for the films deposited with silicon matrix, emission intensity of the SE films is higher than emission intensities of the SC films. Among the SC films, higher emission intensity is observed for the films deposited with lower spin rates (2700 rpm). It can be caused by lower film thickness formed under higher spin rates. Integral intensity ratio for the best films obtained by two different methods with silicon matrix I_{SE}/I_{SC} is about 1.4. Obviously, this difference is related with lower concentration of the vanadate nanoparticles in the SC films and with a more homogeneous morphology of the SC films. Inhomogeneous morphology of the SE films increases scattering of light inside the film, and in such a way, this increases excitation of luminescent centers in the SE films deposited with silicon matrix.

For the pure films prepared without binding matrix, the PLD films have shown higher emission intensity, especially it concerns the films deposited with 2000 laser

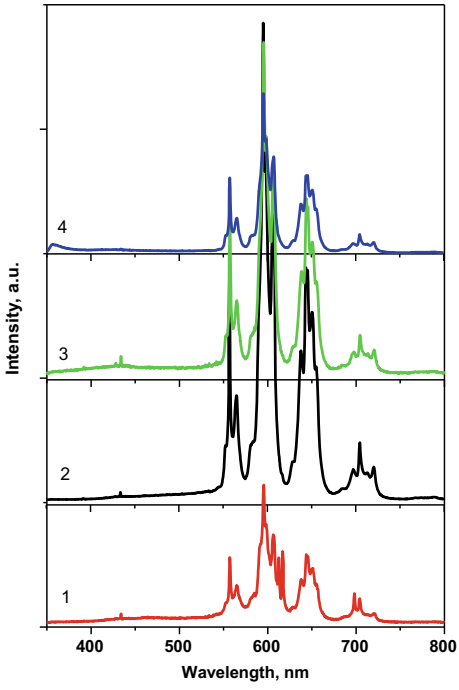

Fig. 12 Emission spectra of the $La_{0.8}Sm_{0.1}Ca_{0.1}VO_4$ SE films pure (1) and deposited with silicon matrix (2) and $La_{0.8}Sm_{0.1}Ca_{0.1}VO_4$ SC films deposited with 2700 (3) and 4500 rpm (4)

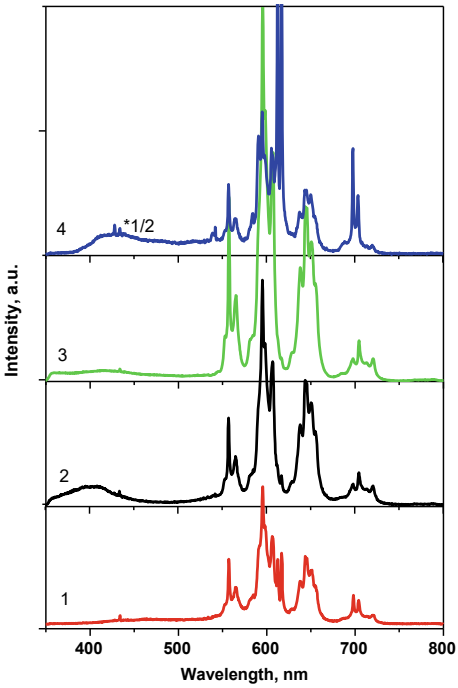

Fig. 13 Emission spectra of the $La_{1-x}Sm_xCa_xVO_4$ SE pure films (1) and PLD films (2–4) deposited with 1000 (2) and 2000 (3, 4) pulses, $x = 0.1$ (1–3) and 0.15 (4)

pulses (Fig. 13). Increase of number of pulses from 1000 to 2000 leads to increase of emission intensity of the PLD films in about 1.5 times (Fig. 13 curves 2, 3). Distribution of lines in emission spectra of the $La_{0.7}Sm_{0.15}Ca_{0.15}VO_4$ films has differences compared to distribution of lines in emission spectra of the $La_{0.8}Sm_{0.1}Ca_{0.1}VO_4$ films obtained by the same PLD method with the same conditions (Fig. 13, curves 3, 4). The observed redistribution of lines is corresponded to different luminescence properties of the initial nanoparticles that are caused by dependencies of their crystal phase composition on dopant concentrations [32]. This evidences that the deposited nanopartices have saved their crystal structure and luminescence properties in the prepared films.

Summarizing, we should note that the best luminescence characteristics of the pure films we have obtained for PLD method with 2000 pulses. The most intensive emission is observed for the SE films deposited with use of silicon matrix. From the other hand, as it was shown above, the SE films are characterized by inhomogeneous morphology, whereas the SC films are comparably homogenous. Therefore, different methods allow the deposition of films with different properties and this should be taken into account when choosing the method of deposition of films from luminescent vanadate nanoparticles.

8 Conclusions

Thin films containing luminescent active vanadate nanoparticles were applied by spin-coating, solution evaporation and pulsed laser deposition methods on glass substrates. The films are formed as by pure vanadate layers as well as by silicon binding matrices and incorporated with vanadate nanocrystallites. Morphology of the films was studied using scanning electron microscopy. It was shown that films obtained from the same compositions but under different procedures have different morphology.

Morphology and thickness of the films depend on a spin rate and a number of pulses. The obtained films are characterized by thicknesses from 30 to 270 nm. The films are formed by very small particles (up to 20 nm) and also can contain single nanoparticles with dimensions 40–60 nm and sometimes agglomerate of nanoparticles. The SE films are characterized by inhomogeneous morphology, whereas the SC and PLD films are comparably homogenous.

Spectroscopy properties of the obtained samples have been investigated. The best luminescence characteristics of the pure films have been obtained for the PLD method with 2000 pulses, whereas the most intensive emission is observed for the SE films deposited with silicon binding matrix. Therefore, different methods allow to obtain films with different properties and this should be taken into account at choice of method of luminescent vanadate nanoparticles films deposition.

Acknowledgements This work has received funding from Ministry of Education and Science of Ukraine (University's Science Grant Program and Bilateral Grant Program) and from the EU-H2020 research and innovation program under grant agreement No 654360 having benefited from the access provided by Institute of Electronic Structure & Laser (IESL) of Foundation for Research & Technology Hellas (FORTH) in Heraklion, Crete, Greece, Division of Microscopy, Universitat Autonoma de Barcelona, Spain, and Paul Scherrer Institut (PSI), Villigen, Switzerland, within the framework of the NFFA-Europe Transnational Access Activity. Authors thank Dr. Dimitrios Kazazis (PSI) for his kind support with the thin film metrology experiments.

References

1. Huang X, Han S, Huang W, Liu X (2013) Enhancing solar cell efficiency: the search for luminescent materials as spectral converters. Chem Soc Rev 42:173–201
2. Van der Ende BM, Aarts L, Meijerink A (2009) Lanthanide ions as spectral converters for solar cells. Phys Chem Chem Phys 11:11081–11095
3. Nakajima T, Isobe M, Tsuchiya T, Ueda Y, Kumagai T (2008) Direct fabrication of metavanadate phosphor films on organic substrates for white-light-emitting devices. Nat Mater 7:735–740
4. Panayiotakis G, Cavouras D, Kandarakis I, Nomicos C (1996) A study of X-ray luminescence and spectral compatibility of europium-activated yttrium-vanadate (YVO_4:Eu) screens for medical imaging applications. Appl Phys A 62(5):483–486
5. Higuchi T, Hotta Y, Hikita Y, Maruyama S, Hayamizu Y, Akiyama H, Wadati H, Hawthorn DG, Regier TZ, Blyth RIR, Sawatzky GA, Hwang HY (2011) $LaVO_4$:Eu Phosphor films with enhanced Eu solubility. Appl Phys Lett 98:071902

6. Sivakumar V, Suresh R, Giribabu K, Narayanan V (2015) $BiVO_4$ nanoparticles: Preparation, characterization and photocatalytic activity. Cogent Chem 1:1074647
7. Yang X, Zuo W, Li F, Li T (2015) Surfactant-free and controlled synthesis of hexagonal $CeVO_4$ nanoplates: photocatalytic activity and superhydrophobic property. ChemistryOpen. 4:288–294
8. Wang Q, Zhang Z, Zheng Y, Cai W, Yifei Yu (2012) Multiple irradiation triggered the formation of luminescent $LaVO_4$: Ln^{3+} nanorods and in cellulose gels. Cryst Eng Comm 14:4786
9. Li K, Van Deun R (2018) Eu^{3+} /Sm^{3+} -doped $Na_2BiMg_2(VO_4)_3$ from substitution of Ca^{2+} by Na^+ and Bi^{3+} in $Ca_2NaMg_2(VO_4)_3$: color-tunable luminescence via efficient energy transfer from $(VO_4)^{3-}$ to Eu^{3+} /Sm^{3+} ions. Dyes Pigm 155:258–264
10. Chukova OV, Nedilko SG. Slepets AA, Nedilko SA, Voitenko TA (2017) Crystal field effect on luminescent characteristics of Europium doped orthovanadate nanoparticles. In: Proceedings of the 2017 IEEE 7th international conference on nanomaterials: applications and properties, NAP 2017, 81903497-5
11. Chukova O, Nedilko SA, Nedilko SG, Sherbatsky V, Voitenko T (2013) Comparable structural and luminescent characterization of the $La_{1-x}Eu_xVO_4$ solid solutions synthesized by solid state and co-precipitation methods. Solid State Phenom 200:186–192
12. Chukova O, Nedilko SA, Nedilko SG, Slepets A, Voitenko T, Androulidaki M, Papadopoulos A, Stratakis EI (2019) Structure, morphology, and spectroscopy studies of $La_{1-x}RE_xVO_4$ nanoparticles synthesized by various methods. Springer Proc Phys 221:211–241
13. Chukova OV, Nedilko SG. Slepets AA, Nedilko SA, Voitenko TA (2018) Synthesis and investigation of La,Ca-doped $EuVO_4$ nanoparticles with enhanced excitation by near violet light. Physica Status Solidi A, 1700894–7.
14. Nedilko SG, Chornii V, Chukova O, Degoda V, Bychkov K, Terebilenko K, Slobodyanik M (2016) Luminescence properties of the new complex La, BiV_O4: Mo, Eu compounds as materials for down-shifting of VUV–UV radiation. Radiat Meas 90:282–286
15. Chornii V, Chukova O, Nedilko SG, Nedilko SA, Voitenko T (2016) Enhancement of emission intensity of $LaVO_4$:RE^{3+} luminescent solar light absorbers. Phys Status Solidi C 13(1):40–46
16. Inada R, Okuno K, Kito S, Tojo T, Sakurai Y (2018) Properties of lithium trivanadate film electrodes formed on garnet-type oxide solid electrolyte by aerosol deposition. Materials 11:1570–1613. https://doi.org/10.3390/ma11091570
17. Jeong SY, Choi KS, Shin HM, Kim TL, Song J, Yoon S, Jang HW, Yoon MH, Jeon C, Lee J, Lee S (2017) Enhanced photocatalytic performance depending on morphology of bismuth vanadate thin film synthesized by pulsed laser deposition. ACS Appl Mater Interfaces 9:505–512
18. Zorenko Y, Gorbenko V, Voloshinovskii A, Stryganyuk G, Nedilko S, Degoda V, Chukova O (2005) Luminescence of Sc-related centers in single crystalline films of $Lu_3Al_5O_{12}$ garnet. Phys Status Solidi C 2:105–108
19. Malashkevich GE, Chukova OV, Nedilko SG, Shevchenko GP, Bokshyts YV, Kouhar VV (2016) Influence of gold nanoparticles on luminescence of Eu^{3+} ions sensitized by structural defects in germanate films. J Phys Chem C 120:15369–15377
20. Yi SS, Bae JS, Shim KS, Moon BK, Seo HJ, Jeong JH, Kim JH (2006) Photoluminescence behaviors of Eu-doped $GdVO_4$ thin film phosphors grown by pulsed laser ablation. J Alloys Comp 408–412:890–893
21. Zhu Y, Wang Y, Zhu J, Zhou D, Qiu D, Xu W, Xu X, Lu Z (2018) Plasmon multiwavelength-sensitized luminescence enhancement of highly transparent Ag/YVO_4:Eu^{3+}/PMMA film. J Lumin 200:158–163
22. Chukova O, Nedilko SA, Nedilko SG, Voitenko T, Gomenyuk O, Sheludko V (2015) Study of temperature behavior of luminescence emission of $LaVO_4$ and $La_{1-x}Eu_xVO_4$ powders. Solid State Phenom 230:153–159
23. Xu Z, Li C, Hou Z, Peng C, Lin J (2011) Morphological control and luminescence properties of lanthanide orthovanadate LnVO4 (Ln = La to Lu) nano-/microcrystals via hydrothermal process. Cryst Eng Comm 13:474–482
24. Yoon SJ, Park K (2014) Synthesis and photoluminescent properties of white-emitting $Sr_{2.91}V_2O_8$:0.06:Eu^{3+} phosphors. Opt Mater 36:1305–1310

25. Chumha N, Kittiwachana S, Thongtem T, Thongtem S, Kaowphong S (2014) Synthesis and characterization of $GdVO_4$ nanostructures by a tartaric acid-assisted sol–gel method. Ceram Int 40:16337–16342
26. Liu G, Duan X, Li H, Dong H (2009) Hydrothermal synthesis, characterization and optical properties of novel fishbone-like $LaVO_4:Eu^{3+}$ nanocrystals. Mater Chem Phys 115:165–171
27. Chukova OV, Slepets NSG, AA, Nedilko SA, Voitenko TA, (2017) Synthesis and properties of the $La_{1-x-y}Eu_yCa_xVO_4$, ($0 \leq x$, $y \leq 0.2$) compounds. Nanoscale Res Lett 12:340–411
28. Mittra J, Abraham GJ, Kesaria M, Bahl S, Aman Gupta SM, Shivaprasad CS, Viswanadham UD, Kulkarni GK, Dey, (2012) Role of substrate temperature in the pulsed laser deposition of zirconium oxide thin film. Mater Sci Forum 710:757–761
29. Kim DK, Kang W (2004) Luminescence characteristics of red light emitting YVO_4: Eu thin film phosphors deposited on Si substrate using pulsed laser deposition. Bull Korean Chem Soc 25:1859–1862
30. Mochi I, Fernandez S, Nebling R, Locans U, Rajeev R, Dejkameh A, KazazisD, Tseng LT, Danylyuk S, Juschkin L, Ekinci Y (2020) Quantitative characterization of absorber and phase defects on EUV reticles using coherent diffraction imaging. J Micro/ Nanolithography MEMS MOEMS 19(1):014002
31. Papadopoulos A, Skoulas E, Mimidis A, Perrakis G, Kenanakis G, Tsibidis GD, Stratakis E (2019) Biomimetic omnidirectional antireflective glass via direct ultrafast laser nanostructuring. Adv Mater 31:1901123
32. Chukova O, Nedilko SA, Nedilko SG, Papadopoulos A, Slepets A, Stratakis EI, Voitenko T (2019) Structure and spectroscopy characterization of $La_{1-x}Sm_xVO_4$ luminescent nanoparticles synthesized co-precipitation and sol-gel methods. Opt Mater 95:109248
33. Chukova O, Nedilko S, Zayets S, Boyko R, Nagornyi P, Slobodyanik M (2008) Luminescent spectroscopy of sodium titanium orthophosphate crystals doped with samarium and praseodymium ions. Opt Mater 30:684–686
34. Sobszyk M, Szymański D (2013) A study of optical properties of Sm^{3+} ions in α-$Na_3Y(VO_4)_2$ single crystals. J Luminescence 142:96–102
35. Okram R, Ganngam Phaomei N, Singh R (2013) Water driven enhanced photoluminescence of Ln (= Dy^{3+}, Sm^{3+}) doped $LaVO_4$ nanoparticles and effect of Ba^{2+} co-doping. Mater Sci Eng, B 178:409–416

Carbon Solid Acids Prepared from the Surface-Brominated Nanoporous Activated Carbons

V. E. Diyuk, L. M. Grishchenko, A. N. Zaderko, G. G. Tsapyuk, O. V. Mischanchuk, O. Yu. Boldyrieva, and A. V. Yatsymyrskyi

1 Introduction

Activated carbons (AC) have a developed porous architecture and large specific surface area. They are widely used in catalysis and adsorption because of their high thermal and chemical stability. The properties of ACs significantly depend on the functional surface groups that are formed during its production or can be introduced into the surface layer during modification. Currently, we can identify the two most common methods used for their modification. The first is oxidation in the gas phase or in the liquid phase [1–5]. The main disadvantage of oxidation is the absence of selectivity [6, 7]. By oxidation, it is difficult to obtain both a significant number of basic and strongly acidic groups. The second modification method is based on the physical adsorption of substances in the micropores. The use of physical adsorption does not guarantee uniform distribution of the adsorbed substances on the surface and is often accompanied by their thermal desorption during application. Modern requirements for carbon materials and carbonaceous carriers, sorbents, and catalysts require a purposeful change of their physicochemical properties, which is achieved by introducing into the surface layer of specific nitrogen-, phosphorus-, oxygen-, sulfur-, and halogen-containing groups [8–15].

But, successful modification is impossible if not bear in mind the surface chemistry of various carbon materials. The preparation of solid acid catalysts can be carried out by chemical treatment, as a result of reactions with such sulfonating reagents as concentrated or fuming sulfuric acid, oleum, chlorosulfonic acid, etc. [16–18].

V. E. Diyuk (✉) · L. M. Grishchenko · A. N. Zaderko · G. G. Tsapyuk · O. Yu. Boldyrieva · A. V. Yatsymyrskyi
Taras Shevchenko National University of Kyiv, Kyiv 01601, Ukraine

O. V. Mischanchuk
Chuiko Institute of Surface Chemistry of the National Academy of Sciences of Ukraine, Kyiv 03164, Ukraine

O. Fesenko and L. Yatsenko (eds.), *Nanomaterials and Nanocomposites, Nanostructure Surfaces, and Their Applications*, Springer Proceedings in Physics 263, https://doi.org/10.1007/978-3-030-74741-1_26

These modifications with typical sulfonating reagents were undertaken to introduce sulfonic groups on the surface of ACs. This approach is effective for the sulfonation of carbonized biomass and carbonaceous materials [19–23], as they most easily react with these sulfonating agents. However, it rarely provides a significant concentration of grafted strongly acidic SO_3H groups on the surface of ACs. Because sulfuric acid is a strong oxidant, a parallel surface oxidation process often occurs simultaneously with sulfonation; this can lead to samples containing more oxygen-containing groups than sulfur-containing ones. The synthesis of sulfur-containing catalysts and the search for factors that impact the physicochemical properties, in particular catalytic, is a necessary actions for creating effective solid acid catalysts and controlling the catalytic process.

Modification of the carbon surface by compounds containing nitrogen and sulfur atoms is a promising direction in the creation of materials with specified properties. N- and S-containing carbon materials can be used as carriers and catalysts in redox and acid-base catalysis and can be employed as adsorbents to remove both inorganic and organic contaminants [24]. They also can act as fillers for chromatographic columns to separate substances that can be adsorbed directly on the surface of the fillers.

Apart from classical functional group inter-conversions that have already been discussed in [1, 16, 18], several interesting synthetic transformations of substituents attached to polycyclic aromatic honeycomb structures need to be mentioned. The formation of nitrogen- and sulfur-containing functional groups is often based on a common synthetic approach. It involves introducing an active halogen atom into the molecule, followed by replacing the resulting halogen group with the desired functional groups [25]. For introducing bromine-containing groups is often used quite aggressive reagents and complicated methods from the armory of plasma chemistry [14, 26].

In recent years, we reported on surface halogenation used to prepare precursors for aminated and sulfonated carbon layers [16, 27–30]. In the present chapter, we consider traditionally used room-temperature bromination to graft bromine-containing groups, being precursors to sulfo groups, to the surface of nanoporous activated carbons (NACs). In the framework of disclosing the synthetic paradigm, we will focus on some sulfur-containing reagents used to prepare sulfonated carbon layers. The choice of one of the selected sulfur-containing reagents was based on the fact that mercaptoacetic acid readily attaches to the acceptor-activated double C=C bonds and replaces active halogens in organic compounds. Also, the S–C bond in this acid is unstable and can be hydrolyzed to form thiol relatively easily. Another reagent, sodium disulfide, is commonly used in organic synthesis to alkylate sulfur to give organic disulfide, which is then oxidized or subjected to reduction cleavage of S–S bonds. Sodium hydrosulfide is also used to prevent double alkylation and disulfide formation. In the case of modifying the surface of carbons, small disulfide molecules can interact with the surface by only one sulfur atom, and therefore the modification methods are greatly simplified. Besides, when heated sodium sulfide heptahydrate, the resulting melt contains a significant amount of hydrosulfide HS^- ions because of hydrolysis passed at elevated temperatures.

2 Experimental

2.1 Materials

Several NACs were prepared and purchased to be used as starting materials. Here we use the NAC1 sorbent prepared from fruit pits by carbonization and steam activation [31]. The NAC2 sorbent was a spherical nitrogen-containing AC obtained by the standard method of the carbonization and vapor activation of vinyl pyridine rubber [32]. Hematological sorbent, NAC3 beads of Ukrainian trademark HSGD, was purchased from the Kavetsky Institute of Experimental Pathology, Oncology, and Radiobiology (Kyiv, Ukraine) and was used as received.

Reagent grade chemicals: molecular dibromine (Br_2, $\geq$ 99.5%), potassium bromide (KBr, $\geq$ 99.5%), sodium hydroxide (NaOH, 97%), sodium nitrate ($NaNO_3$, 99%), sodium carbonate (Na_2CO_3, $\geq$ 99.5%), methylamine ($MeNH_2$, 99%), sodium thiosulfate ($Na_2S_2O_3$, $\geq$ 99.5%), acetic acid (HAc, glacial 99–100%), silver nitrate ($AgNO_3$, 99.5%), potassium thiocyanate (KSCN, $\geq$ 99.0%), and potassium oxalate ($K_2C_2O_4$, $\geq$ 99.5%) used in this study were purchased from Sigma-Aldrich. The other chemicals, namely sodium mercaptoacetate ($NaSCH_2COONa$, SMA, $\geq$ 97%), sodium sulfide hexahydrate ($Na_2S{\cdot}6H_2O$, $\geq$ 98%), hydrogen peroxide (H_2O_2, 30%), and hydrochloric acid (HCl, 37%), were from Merck (Darmstadt, Germany). The dibromine was distilled to remove the impurities and then passed through a sulfuric acid dryer in a conventional drying process. Main reagents were used as received without extra purification. The concentrated chemicals were diluted with millipore deionized (DI) water, and the DI water was used for washing throughout the work. The high purity argon (Ar, 99.95%+) from the Linde Gas cylinders was purified further by passing it over magnesium metal at 400 °C and through absorbers containing ascarite and anhydrous alkali.

2.2 Modification

Bromination of NACs: NACs were subjected to bromination using liquid reagents, namely, the KBr_3 solution prepared by dissolving 100 g of liquid Br_2 and 150 g of KBr in 1 L of water and dry liquid dibromine (Br_2). In the bromination procedure, dried NACs (10 g) were placed in a tube, and 100 ml of KBr_3 solution or 10 ml of extra dried liquid Br_2 was added dropwise and allowed to infiltrate the pores, ensuring that the temperature of the reaction mixture remained below 40 °C. After soaking for 1 h, the immersed NACs were filtered, transferred to a conic flask, and then 100 ml of 10% (w/v) $K_2C_2O_4$ were added to the beads. This solution was added in a small portion under vigorous stirring, up to a cessation in carbon dioxide (CO_2) release. After filtration, the resulting NACs/KBr_3 and NACs/Br_2 were washed extensively with DI (under potentiometric control) until no bromide ions were left in the washing waters. The NACs were collected and dried at 80 °C under a vacuum for 2 h.

To study the chemical properties of the brominated NACs, they were also treated with $MeNH_2$. A sample of the brominated NACs (1 g) was suspended with an amine solution. This suspension was placed in a Teflon-lined, stainless steel autoclave reactor and kept in the sealed reactor for 40 min at 100 °C. After treatment, the excess amine solution was removed by filtration, and the resulting NACs were deep in 50 ml of 5% HCl solution. After that, these NACs on a filter funnel were washed several times with rinsed water until bromide ions could no longer be detected in the wash water. Finally, the filtered sample was collected, placed in a drying pistol, where dried overnight in a vacuum at 80 °C.

The brominated NACs were treated with nucleophilic reagents (SMA and Na_2S) to prepare solid acids as follows:

The preparation of solid acids by the method S1: 5 g of NACs/KBr_3 or NACs/Br_2 was placed in a 100 mL sealable Teflon beaker, where then 25 ml of concentrated SMA solution was added. The beaker was then tightly sealed and transferred to an autoclave to be kept at 120 °C. Following 10 h of autoclaving, the beads were filtered off, washed with H_2O, transferred to a flask with 50 ml of 25% (v/v) HCl, and then refluxed for 2 h. After hydrolysis of the S-containing surface species, the beads were filtered and washed with H_2O. After acidification, the resulting NACs have placed in 50 ml of 30% (v/v) H_2O_2 solution and allowed to infiltrate the pores for 3 h. The sulfonated NACs were filtered off, extensively washed with DI water on a filter, and then air-dried at 120 °C in a drying chamber. They were marked as NACs/KBr_3/S1 and NACs/Br_2/S1.

The preparation of solid acids by the method S2: 1 g of brominated precursor (NACs/Br_2) was added into the glassy carbon crucible with fused Na_2S and kept for 10 h. Fused Na_2S attacks most materials, including silica and alumina, but it does not appear to attack graphite, provided that the latter is of high quality and thoroughly baked out to remove any water and oxygen. After sulfuration (sulfidation), the melt was cooled, and the resulting NACs were washed from the slag with DI water and filtered to be washed on a funnel filter with 100 ml of 5% HCl water solution and again with DI water to remove chlorides and until the neutral pH of the rinse water. After hydrolysis and oxidation, the samples were treated analogously to the previous procedure, and they were marked as NACs/Br_2/S2.

2.3 Methods

The total bromine (C_{Br}) in the brominated NACs was found by the Volhard method. The total sulfur (C_S) in the sulfonated NACs was found by the Eschka method. Before the total bromine determination, the grafted bromine groups were pyrohydrolytically decomposed to bromide ions in the basic oxidative melt [33].

A Jeol JSM 6060LA scanning electron microscope (SEM) was employed in the surface morphology studies. High-resolution transmission electron microscopy (HRTEM) and transmission electron microscopy (TEM) images were collected on a JEOL JEM-2100F transmission electron microscope operated at an accelerating

voltage of 200 kV [34]. The samples for TEM were crushed in an agate mortar and then dispersed in a water-ethanol solution. A 10 μL of the prepared colloid solution was dropped onto a carbon-coated copper TEM microgrid and allowing the solvent to evaporate in a vacuum chamber. TEM image processing was done with inversed fast Fourier transform and two-dimensional fast Fourier transform (IFFT and 2D FFT) modules. Select area electron diffraction (SAED) patterns were recorded in a Philips TEM CM20 FEG operated at 200 kV on imaging plates utilizing the six orders of magnitude of a linear dynamic range of imaging plates.

Nitrogen adsorption/desorption isotherms were measured up to 1 atm at –196 °C on a Micromeritics ASAP 2010 unit. All the samples were outgassed at 150 °C under vacuum for 24 h before measurements. The specific surface area (S_{BET}) was calculated using the Brunauer–Emmett–Teller (BET) method. The total pore volume (V_{tot}) was estimated at a relative pressure of $p/p_0 = 0.99$. For pore size distribution (PSD) calculations, the adsorption branches of isotherms were analyzed with the SAIEUS program (http://www.nldft.com) and the kernel carbon–N_2 model for porous carbons having a heterogeneous surface [35, 36]; this model was derived from the 2D nonlocal density functional theory (NLDFT). Here the micropore surface area (S_{micro}) and micropore volume (V_{micro}) were found from the PSD data. The mesopore surface area (S_{ext}) and mesopore volume (V_{ext}) were found from a difference: $S_{ext} = S_{BET} - S_{micro}$ and $V_{ext} = V_{tot} - V_{micro}$. The parameters of the Dubinin–Radushkevich (DR) equation: The limiting micropore volume (V_{DR}) and the characteristic adsorption energy (E_{DR}) were found as in [31]. Bulk density γ was measured as reported in [2].

Thermoprogrammed desorption coupled with mass spectrometry (TPD MS) studies were performed on a monopole mass spectrometer MX 7304A with electron impact ionization [37, 38]. In a typical TPD MS run, a small amount of sample (0.3 mg) was placed in a quartz glass cell with controlled outer heating of 1000 °C. The cell had a brass connector for loss-free gas transfer to the mass spectrometer. After loading, the cell with the sample was evacuated for 2 h at 30 °C up to the residual pressure of about 10^{-4} Pa. And then, the vacuumed cell was heated at a linear heating rate by an outer resistance furnace. During the TPD MS characterizations, the heating rate was 7.5 °C min^{-1}. According to the TPD procedure, the sample in the cell was the source of a molecular gas beam. The gas was released from the heated sample, escaped from the cell, and passed into the mass spectrometer ion trap, where it was continuously scanned (in the positive ion mode) at m/z channels 16, 28, 44, and 64. And then, the intensity profiles for selected m/z were recorded against the temperature.

Thermal decomposition studies were conducted on a custom thermogravimetric analyzer [39]. At a typical thermogravimetric (TGA) experiment with thermal programmed desorption and IR spectroscopy (TPD IR) studies, a dried carbon sample (0.1 g) was heated from 30 to 800 °C, under the ramp of 10 °C min^{-1}. Thermogravimetric analysis (TGA) was performed by weighing in a dynamic argon atmosphere under a steady argon flow of 50 mL min^{-1}. Before the measurements, the samples were dried at 110–120 °C to a constant mass. In a typical experiment, the sample was heated from 30 °C up to 800 °C, at the heating rate of 10 °C min^{-1}. The weight loss (Δm), which was assigned to 1 g of the sample, was continuously registered, as a

function of temperature, in the form of thermogravimetric (TG) curves. The function of the first derivative (DTG) was calculated from the registered TG data. This calculation was done by a finite difference approximation using 6-second intervals, or 1 °C, at a scan rate of 10 °C min^{-1}. The DTG function was also expressed as a time-based rate by multiplying the data by the constant scan rate. At heating in dynamic argon, under a gas flow, only CO, CO_2, H_2O, and SO_2 gases can be thermodesorbed. All they are the products of thermal decomposition of surface acidic SO_3H groups and carboxylic (Cx) groups, aldehyde and lactone (A-L) groups, phenolic (Ph) groups, and other groups [40]. During the measurements, the temporal variation of CO, CO_2, and SO_2 concentration in the argon-diluted outlet mixtures was monitored using a Fourier transform infrared analyzer [41]. The temperature profiles for the release rate (r(CO), r(CO_2), and r(SO_2)) were plotted from the signal registered in the intensity–temperature(time) profiles. The concentrations of CO, CO_2, and SO_2 (C(CO), C(CO_2), and C(SO_2)) in the outlet gas mixtures were found per gram of NACs using evolved gas analysis (EGA) and the reference IR spectra recorded for the gas mixtures with the known concentrations of the measured gases.

Prepared solid acids were tested in the catalytic dehydration of 2-propanol to propene at atmospheric pressure. In a typical test, a catalyst bed (0.1 g) was packed inside a flow reactor. This reactor was heated under a thermoprogrammed ramp from 30 to 340 °C. The temperature inside the fixed catalyst bed was monitored with a USB thermocouple data logger, and the temperature readings were stored on a computer. Experiments were carried out with a gas mixture of 1.1 mmol of 2-propanol in argon at a total gas flow rate of 50 mL min^{-1}. The concentration of the product, propylene, was monitored at the C−H stretching frequency of 3105 cm^{-1}, as described in the earlier works [42, 43], and the conversion of 2-propanol to propylene (α) was calculated by the equation:

$$\alpha = \frac{C(\text{propene})}{C_0(\text{2-propanol})} \cdot 100\%, \tag{1}$$

where C(propene) and C_0(2-propanol) are the outlet propene and inlet 2-propanol concentrations, respectively. Temperatures at 50% ($t_{50\%}$) and 100% ($t_{100\%}$) conversion of 2-propanol were chosen to measure the effectiveness of the catalyst. Deactivation of catalysts was studied in a heating-and-cooling mode, considering the reaction productivity. In this study, the reactor with a catalyst was heated at a heating rate from 5 to 7 °C min^{-1}. When the highest α value was reached, at below 300 °C, the reactor was programmed to cool to 30 °C. The cooling rate was not exceeding 4 °C min^{-1}.

3 Results and Discussion

Nitrogen adsorption isotherms for the pristine NACs (Fig. 1a) are characterized by high nitrogen adsorption at low p/p_0. This observation indicates a large contribution of micropores with a size of less than 2 nm. All sorbents have a developed

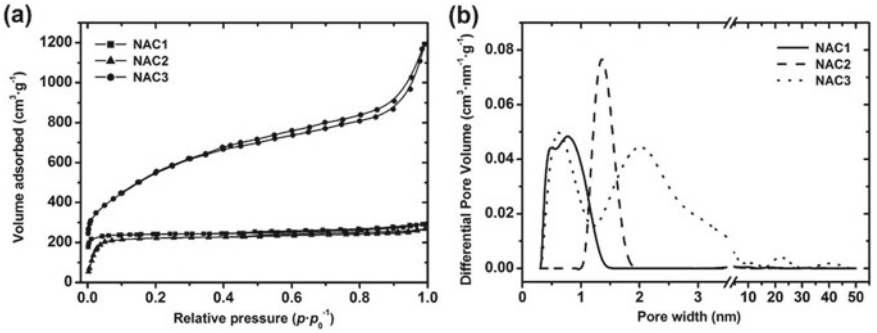

Fig. 1 **a** Nitrogen adsorption/desorption isotherms and **b** differential pore volume against pore width for NAC1, NAC2, and NAC3 sorbents

porosity, which increases from NAC1 to NAC3 (Table 1). For all materials, sorption hysteresis is observed on the isotherms, which indicates the presence of mesopores in the porous structure of NACs. Both NAC1 and NAC2 are mainly microporous; the contribution of mesopores to the porous structure is insignificant because S_{micro} significantly exceeds S_{ext}. The amount of mesopores in the NAC1 and NAC2 does not exceed 4% of the total S_{BET}. For NAC3, the contribution of mesopores to the total surface is ~28%; this material is microporous-mesoporous. The total pore volumes for the studied samples are very different because of various pore size distribution (Fig. 1b).

In the series of NAC2, NAC1, NAC3 sorbents, the volumes of micropores V_{micro} and mesopores V_{ext} increase by ~1.6 and 22 times, respectively. Using the DR equation gives close E_{DR} values for the NAC2 and NAC3 sorbents. For the NAC1 and NAC2 sorbents, the value of V_{micro} significantly exceeds that of V_{ext}. However, in the case of NAC3 sorbent, the value of V_{ext} is 2.2 times higher than that of V_{micro}. From the pore width distribution dependences (Fig. 1b), we can conclude that the porous structure of NAC1 sorbent consists almost entirely of small micropores, with a width of about 0.49 nm and 0.77 nm. In the porous structure of NAC2 sorbent, there are slightly larger micropores with a size of about 1.36 nm. As compared with NAC1 and NAC2 sorbents, the NAC3 sorbent contains small micropores of 0.63 nm wide and larger pores of 2.02 nm wide. NAC3 also has a significant number of mesopores with pore width in the range of 3–25 nm. Therefore, the NAC1 and NAC2 sorbents have a

Table 1 Bulk density γ and texture characteristics of NACs

Sample	γ, cm^3 g^{-1}	Specific surface area, m^2 g^{-1}			$\frac{S_{micro}}{S_{ext}}$	Specific volume, cm^3 g^{-1}				E_{DR}, kJ mol^{-1}
		S_{BET}	S_{micro}	S_{ext}		V_{tot}	V_{micro}	V_{ext}	V_{DR}	
NAC1	0.484	951	926	25	37	0.445	0.370	0.075	0.402	6.9
NAC2	0.423	1102	1064	38	28	0.414	0.356	0.058	0.357	5.6
NAC3	0.213	1997	1429	568	2.5	1.846	0.573	1.273	0.619	5.9

similar ratio of micropores and mesopores, while the structural–sorption parameters of NAC3 sorbent differ significantly from them. This unique material is difficult to assign to microporous materials since its S_{micro}/S_{ext} is about 2.5. Significant removal of the carbon matrix during long-term activation of NAC3 sorbent allowed obtaining a material with a very low bulk density γ and very large S_{BET} and V_{tot}. However, significant differences in the porous structure have little effect on the E_{DR} value (Table 1).

As can be seen from Fig. 2a, the porous structure of NAC1 sorbent maintains large channels with a width of 10–20 μm and smaller macropores whose width does not exceed 1 μm. These macropores are remnants of the structure of the raw material (fruit stones). They characterize the macrostructure of NAC1 sorbent. The existence of a developed system of transport channels in the NAC1 sorbent is critical in terms of the potential use of this material in adsorption–catalytic processes. The pristine NAC2 and NAC3 sorbents are spherical granules of 0.5–1 mm in diameter (Fig. 2b). Irregularities and dents on the surface of the granule are associated with the removal of part of the substance. It takes place during carbonization and subsequent activation

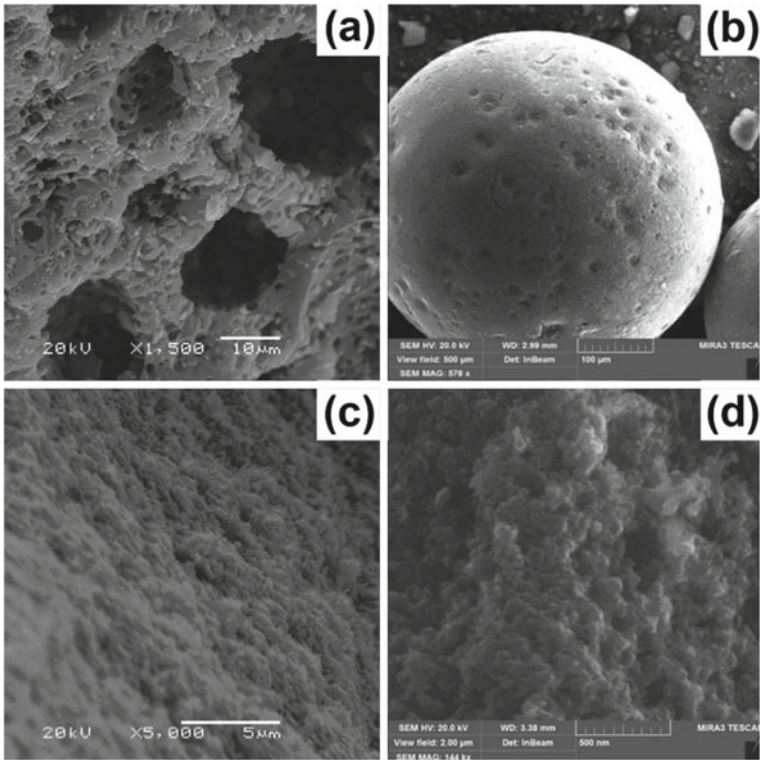

Fig. 2 **a–d** SEM images of the pristine NACs: **a**, **c**, **d** the surface morphology of NAC1, NAC2, and NAC3, correspondingly, and **b** spherical beads of NAC3

Table 2 Composition and surface chemistry of the pristine NACs

Sample	EDX, at%		TGA, g g^{-1}			TPD IR, C_{FG}, mmol g^{-1}		
	C	O	Δm	Δm_{FG}	$\Delta m(H_2O)$	Cx	A-L	Ph
NAC1	95.9	4.1	0.0515	0.0448	0.0180	0.06	0.07	0.69
[a]NAC2	96.1*	2.8	0.0325	0.0273	0.0077	0.10	0.03	0.49
NAC3	97.5	2.5	0.0151	0.0126	0.0031	0.03	0.04	0.22

[a]NAC2 contains 1.1 at% of N

of the raw material. There are only small transport channels in the macrostructure of NAC2 and NAC3 sorbents (Fig. 2c). The inner surface of these materials is formed by the combination of a large number of small rounded particles that have a close to spherical shape (Fig. 2c, d).

At high magnification, in the structure of NAC2 and NAC3, one can see many small channels and macropores (Fig. 2d). According to the EDX analysis, the pristine samples of NACs consist of carbon and contain only 2.5–4.1 mass% of oxygen (Table 2). Besides, the NAC2 sorbent contains 1.1 mass% of nitrogen that remained from the raw material, vinyl pyridine rubber. The NAC3 sorbent, which is also made of the same vinyl pyridine rubber, does not contain nitrogen because of its complete removal during much longer activation.

An IFFT TEM image shows the microporous structure typical for NACs (Fig. 3a). IFFT and 2D FFT HRTEM images show randomly distributed lattice fringes (Fig. 3b). These fringes indicate the presence of nanostructured graphene sheets. The fringe spacing of ~ 0.21 nm corresponds to the (002) plane of the graphite. Figure 3c shows the SAED pattern; smooth ring diffraction patterns are manifested the amorphous nature of the NACs, as found in the related carbon materials [44, 45]. One ring's position corresponds to 0.2 nm interplanar distance and the diffraction peak position of graphite at 44.2° (2θ).

Figure 4 shows the results of TGA, TPD IR, and TPD MS studies.

The total weight loss (Δm) for NAC3 is small; it reaches about 1.5% between 30 °C and 800 °C (Fig. 4a). By the TPD IR and TPD MS methods, we registered only

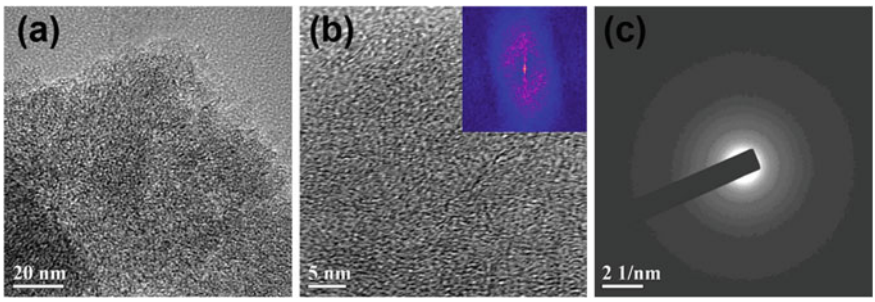

Fig. 3 Examples of IFFT **a** TEM and **b** HRTEM images, and **c** SAED pattern of NACs. Insert in **b** is 2D FFT HRTEM image

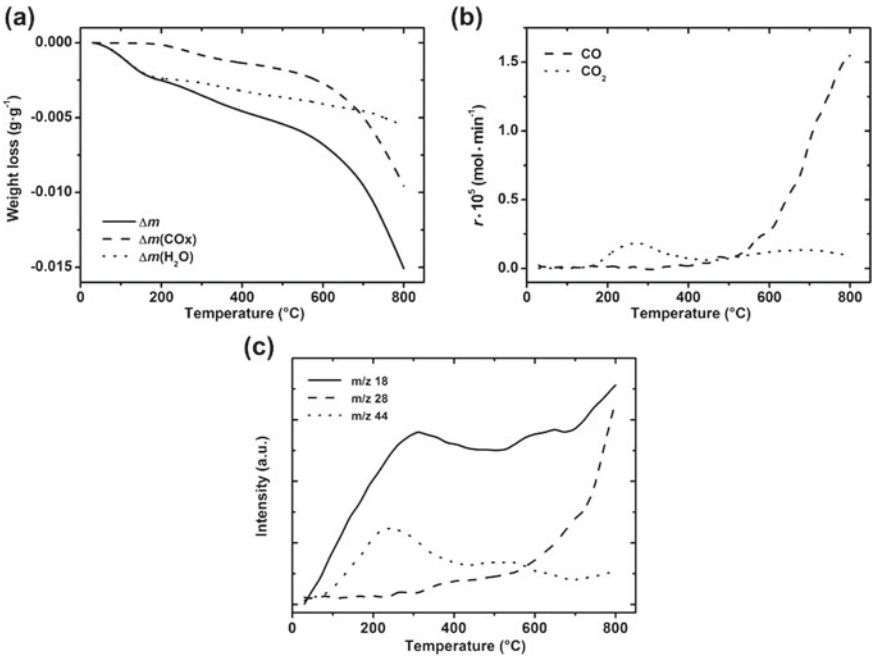

Fig. 4 Examples of thermograms: **a** TG/DTG, **b** EGA/TPD IR, **c** TPD MS for NAC3

H_2O, CO, and CO_2 in the products of thermal desorption. These gaseous products are released in a wide temperature range. Desorbed below and above 180 °C, they are from physisorbed gas and are the products of thermal decomposition of different oxygen-containing groups. In the temperature range of 30–800 °C, the total weight loss (Δm) sums the weight loss of physisorbed water, which is released up to 180 °C, and that of the functional oxygen-containing groups (Δm_{FG}) decomposed above 180 °C. In the process of thermal decomposition of functional groups, carbon oxides and chemisorbed water are released and caused the weight loss of $\Delta m(CO_x)$ and ($\Delta m(H_2O)$), respectively. The total water release is insignificant, about 0.5%, and about 40% of this amount is from physisorbed water (Fig. 4a). In the temperature range of 200–800 °C, about 0.17 mmol g^{-1} of chemisorbed water is released at an almost constant rate. For the samples of NAC1, NAC2, and NAC3, the TGA and TPD IR results are presented in Table 2.

Chemical analysis of NACs brominated with aqueous $KBr{\cdot}Br_2$ or liquid Br_2 showed that the bromine content C(Br) ranging from 0.4 to 0.6 mmol g^{-1} (Table 3). As can be seen, the bromination efficiency does not depend on the selected brominating agent. Moreover, reasonable questions remain with respect to the determining influence of the texture parameters on the bromination efficiency. As can be seen from Tables 1 and 3, the NAC1 sorbent, which has the smallest S_{BET}, can attach more bromine than the NAC2 and NAC3 sorbents, which have S_{BET} higher by about 150 and 1,040 m^2 g^{-1}, respectively.

Table 3 Bromine concentration C(Br) and the surface chemistry of the brominated NACs from the data of thermal analysis

Sample	C(Br), mmol g^{-1}	TGA				TPD IR, C_{FG}, mmol g^{-1}		
		Δm, g g^{-1}	Δm_{FG}, g g^{-1}	T_1, °C	$\Delta m(H_2O)$, g g^{-1}	Cx	A-L	Ph
NAC1/KBr_3	0.59	0.1345	0.1179	295	0.0103	0.18	0.43	0.96
NAC1/Br_2	0.51	0.1331	0.1157	282	0.0121	0.19	0.46	1.04
NAC2/KBr_3	0.41	0.1287	0.1127	298	0.0139	0.17	0.40	1.11
NAC2/Br_2	0.44	0.1196	0.1057	289	0.0133	0.12	0.32	1.09
NAC3/KBr_3	0.42	0.0873	0.0758	283	0.0078	0.09	0.10	0.83
NAC3/Br_2	0.44	0.0833	0.0748	279	0.0040	0.08	0.08	0.94

Further, bromination has a little effect on the outer surface relief, and no visible changes are registered (cf. Fig. 2b and Fig. 5a). During the mechanical grinding of beads, it is seen that their inner surface becomes more rough and spongy after bromination (cf. Fig. 2d and Fig. 5b, c). The bulk of the carbon solid is seen to be made of a soft, crepe-like, or spongy matrix.

For the brominated NACs, if compared to the pristine NACs, the weight loss effect in the temperature range of 180–800 °C (Fig. 6a), which is associated with the decomposition of different functional groups in the surface layer (Δm_{FG}), increases significantly. For the NAC3/Br_2 sample (Fig. 6b), in addition to the release of physisorbed water, there are two significant weight loss effects on ($d\Delta m/dT$) curve; they are between 180 °C and 450 °C and between 450 °C and 800 °C, respectively. The first effect for all brominated NACs has a peak at T_1 of 289 ± 10 °C (Table 3). The release of CO and CO_2 (Δm(COx)) is much lower than Δm_{FG} (Fig. 6a, b), which is due to the significant contribution of desorption of bromine and water in the overall process of thermal decomposition of the surface layer. The detachment of bromine atoms and the release of chemisorbed water ($\Delta m(Br + H_2O)$) can be quantified by the formula:

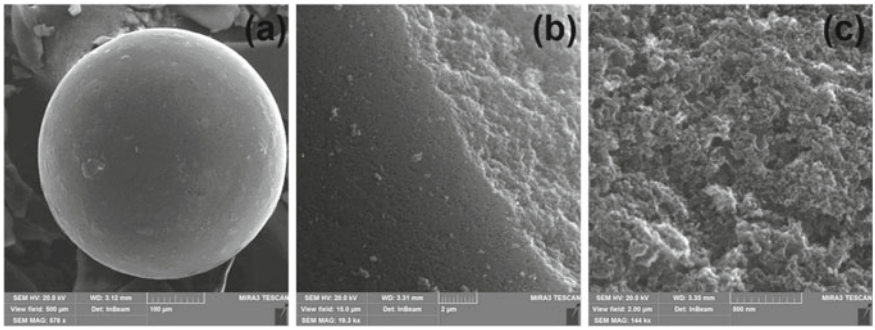

Fig. 5 **a** Typical SEM image of NAC3/Br_2 at low magnification, and **b**, **c** SEM images showing the surface morphology of crushed NAC3/Br_2 beads, at **b** low and **c** high magnifications

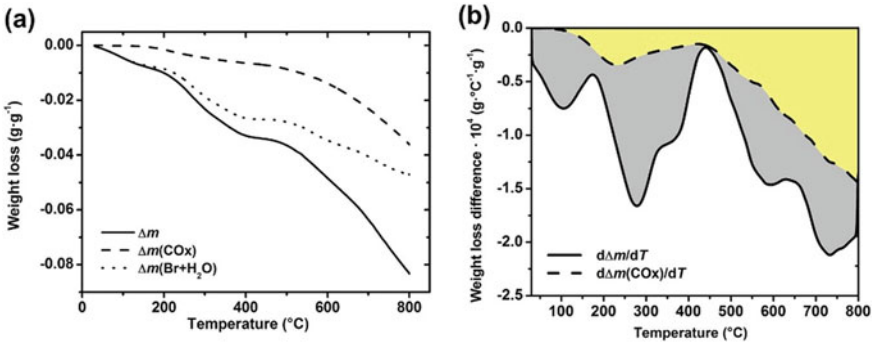

Fig. 6 Typical TGA for the brominated NACs: **a** TG and **b** DTG for NAC3/Br_2

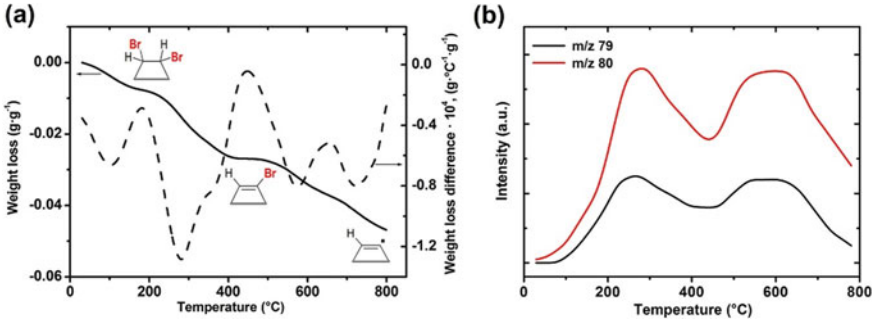

Fig. 7 Typical dependences **a** weight loss (TG/DTG) of (Br + H_2O) and **b** TPD MS profiles m/z 79 and 80 for NAC3/Br_2

$\Delta m(\mathrm{Br} + \mathrm{H_2O}) = \Delta m_{\mathrm{FG}} - \Delta m(\mathrm{COx})$. This contribution is clearly visible on the DTG curves; it is shown as the area shaded in gray in Fig. 6b.

Considering the temperature dependences for $\Delta m(\mathrm{Br} + \mathrm{H_2O})$ in Fig. 7a, one can see that the low-temperature weight loss effect corresponds to the release of physisorbed H_2O. The other two weight loss effects are mainly because of bromine detachment. The probable reason for the equality of these effects is the stepwise process of desorption of bromine. Above 180 °C and below 450 °C, approximately half of the bromine is detached, similarly, as it was reported in [46, 47]. In this temperature window, the easy elimination of HBr accompanies by the renewal of the C=C double bonds (see schema in Fig. 9). Detaching the residual bromine from the surface structures requires higher temperatures. They will stimulate homolytic or heterolytic C–Br bond cleavage. The TPD MS method confirmed the approximate equality of the bromine amounts detached in the stated temperature ranges (Fig. 7b). The total release of chemisorbed water from the surface of brominated NACs was found to be less than 0.4–1.4% (Table 3).

Comparison of the CO and CO_2 profiles obtained by the TPD IR and TPD MS methods for the brominated NACs (Fig. 8) proves the interaction of neighboring oxygen-containing groups when heated. In the process of thermal decomposition of the surface groups in a vacuum, the product of the thermal decomposition of Cx groups is CO_2, even if several such groups are located around. The reason of that is a very significant shift in the equilibrium toward the removal of CO_2, which makes other processes impossible. At atmospheric pressure, the probability of interaction of the two functional groups increases many times since the product is not removed quickly from the surface into the gas phase. Calculations show that the volume of gases released from the surface of brominated NACs, when heated, is about 0.25–0.69 mmol g^{-1} CO_2 and 1.13–1.89 mmol g^{-1} CO, which, under normal conditions, equals to a gas volume of 31.6–54.7 ml g^{-1}. That is, the entire inner volume of the porous structure of the brominated NACs filled with physisorbed gases is completely renewed. So, the total amount of the physisorbed CO and CO_2 is released in 1 to 3 min. In the TPD IR method, all processes of the surface groups' decomposition and thermal desorption should be considered being occurring with the participation of a gas phase consisting of a mixture of CO and CO_2. This condition will promote the reaction between adjacent groups or between groups and gaseous products.

For the brominated NACs, as compared to the pristine NACs, we registered an increased release of carbon oxides (Fig. 8), which indicates the oxidation of

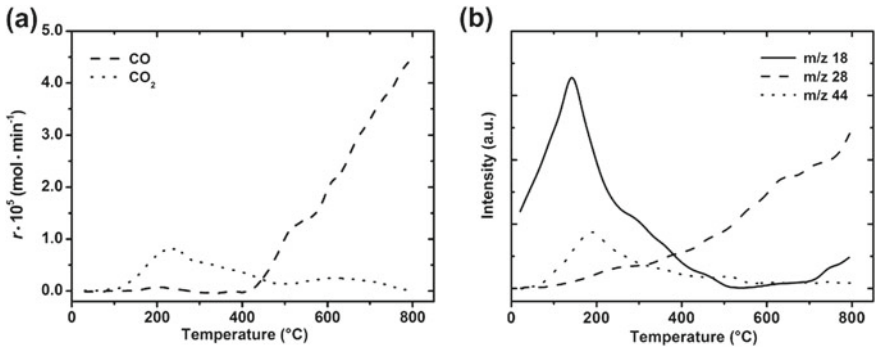

Fig. 8 Typical thermograms **a** TPD IR and **b** TPD MS for NAC3/Br_2

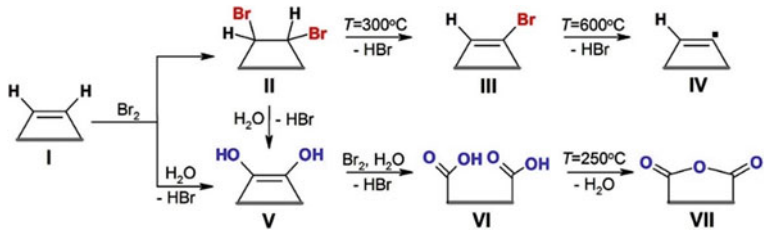

Fig. 9 Schematic diagram of the bromination and parallel oxidation of NACs

the carbon surface. The increase in $C(CO_2)$ during bromination is insignificant and is only 0.1–0.2 mmol g^{-1}; the increase in $C(CO)$ is significant of 0.6–2.3 mmol g^{-1}. The general process of bromination and oxidation of the surface of NACs can be described by the following scheme (Fig. 9) without considering the impact of the carbon edge magnetism and spin chemistry [48–53].

As a result of the interaction of the active center (I) with bromine, it is brominated to form the product (II). This product, when heated, can gradually detach bromine to form the product (III) and the bromine-free surface (IV), which was confirmed by thermal analysis (Fig. 7). A tandem reaction at the bromination is the oxidation of the active center (I) under the action of bromine and water to form the product (V). Obviously, the product (V) can also be formed because of the hydrolysis of the most active bromine in the product (II). As can be seen, the initial oxidation of the matrix and the hydrolysis of bromine are reasons for the formation of Ph groups. They present in the largest amount in the surface layer. The action of bromine can cause further oxidation of the surface product (V), as a result of which Ph groups are converted into Cb, the product (VI). At moderate heating, their dehydration with the formation of an anhydride cycle, the product (VII), is possible. The interaction between groups composed of the products (V) and (VI) can produce L groups [54], which are also found on the surface of brominated NACs.

Thus, the bromination of the NACs with liquid bromine or aqueous solution Br_2·KBr leads to the bromine addition of 0.41–0.59 mmol g^{-1} and the selective oxidation of the NACs' surface with the formation of Ph groups and a small amount of Cx and A-L groups. The total amount of additional oxygen-containing groups is much higher than the amount of the attached bromine (Fig. 10). The total amount of the groups formed during bromination (the attached bromine and oxygen-containing groups in sum, ΣC) for the brominated NAC1 and NAC2 samples is in the range of 2.2–2.5 mmol g^{-1}, while for the brominated NAC3 samples, it reaches only 1.5–1.6 mmol g^{-1}. Therefore, the reactivity of the NAC3's surface is significantly lower

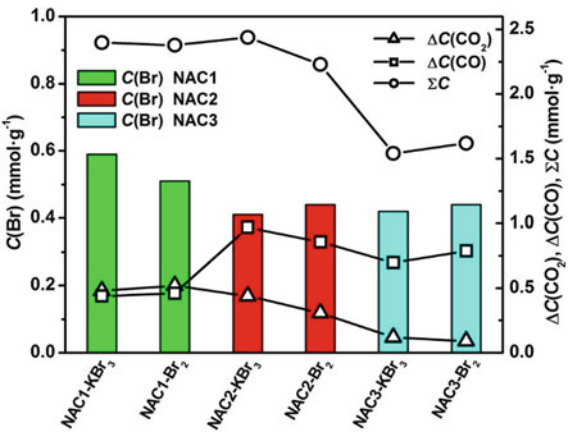

Fig. 10 The concentration of bromine (C(Br)), concentrations of oxygen-containing groups ($\Delta C(CO_2)$ and $\Delta C(CO)$), and concentration of all types of surface groups (ΣC) that are formed during bromination

Table 4 Bromine concentrations before and after debromination (C(Br) and C(Br40)) with $MeNH_2$ and the residual bromine percentage (Δ_{Br}) after basic treatment for 40 min

Sample	Bromine concentration, mmol g^{-1}		Δ_{Br}, %
	C(Br)	C(Br40)	
NAC1/KBr_3	0.59	0.32	46
NAC1/Br_2	0.51	0.26	49
NAC2/KBr_3	0.41	0.23	44
NAC2/Br_2	0.44	0.24	45
NAC3/KBr_3	0.42	0.22	48
NAC3/Br_2	0.44	0.23	48

than that of NAC1 or NAC2. This difference is associated with a large burnout during the production of NAC3.

Use the brominated NACs as precursors for S-containing solid acids, one should perform a preliminary study on the hydrolytic stability of attached bromine. It was found that the attached bromine is reasonably stable. It does not hydrolyze for prolonged storage of the brominated NACs at ambient conditions both in air and underwater, as proved by the absence of bromide ions in the liquid phase. In order to check hydrolytic stability, the brominated NACs were suspended in 100 ml of pure DW, and then the suspensions were boiled for 15 min. The brominated NACs did not hydrolyze, as confirmed by the absence of bromide ions in the filtrate.

To study their chemical properties, the brominated NACs were suspended in an alcohol solution of $MeNH_2$ and boiled at 100 °C for 40 min. After nucleophilic treatment, the total bromine (C(Br40)) in the samples was determined, and the residual bromine percentage(Δ_{Br}) was calculated (Table 4). About half of the attached bromine and more, of about 51–56%, is detached during the proposed treatment. At least two bromine forms, which have different natures, are present in the samples.

Since, the regardless of chemical nature of NACs and the used bromination method, the value of Δ_{Br} is usually almost the same; it is logical to assume that in all cases, the detached bromine is present in the form of HBr, as it was found at heating at 300 °C (Fig. 9). The bromine detaching restores the conjugate structure of the double C=C bonds. It is known that 1,2-dibromo derivatives are characterized by elimination reactions when the newly formed double C=C bonds are conjugated with other fragments of the molecule, such as the second C=C bond, carbonyl group, or aromatic nucleus. As a rule, slightly more than 50% of bromine remains on the surface. This fact can be explained since the cleavage or hydrolysis of the most active part of bromine occurs at the stage of treatment with potassium oxalate, the solution of which has an alkaline reaction.

In our opinion, the conjugate (edge) C=C double bonds are surface sites that can react with dibromine at room temperature. After bromination, these surface sites can participate in further interaction with nucleophiles, cleaving HBr and oxidizing to form Ph groups. Other surface sites, such as isolated C–H bonds, may also be involved in the bromination. However, the parallel reaction of hydrogen replacing with bromine does not occur intensively because of the low concentration or low

reactivity of aromatic hydrogen under the reaction conditions. This conclusion is confirmed by the rather high chemical homogeneity of surface bromine that participated in the nucleophilic substitution and elimination reactions. Likely, the content of the bromine attached as a result of the parallel substitution reaction is insignificant. Our assumption is also confirmed by the fact that the attached bromine should have thermal properties close to those observed experimentally. One type of the attached bromine atoms must be easily and rapidly detached at low temperatures (eliminating in the form of HBr) by the ionic mechanism. And, the remain bromine atoms must be slowly detached by the radical mechanism at high temperatures to form bromine radicals or HBr.

Data of chemical analysis show that the treatment of brominated precursors with sulfur-containing reagents leads to the complete removal of bromine from the surface and the formation of 0.34–0.55 mmol g^{-1} of sulfur-containing groups (Table 5).

Figure 11 shows the SEM images of the NAC3/Br_2/MA. As can be seen, the inner surface of the sulfonated beads does not undergo significant changes after sulfonation that followed bromination.

Figure 12 shows typical features of TGA, TPD IR, and TPD MS for the sulfonated NACs. The total weight loss Δm_{FG} sums the contribution of two weight loss effects in the temperature ranges of 200–400 °C and 500–800 °C.

Comparing to the pristine NACs (Fig. 4) and the brominated NACs (Fig. 6), the sulfonated NACs showed a significant weight loss effect that peaked at ~300 °C (Fig. 12a and b). Here, the most intensive thermal decomposition of the grafted SO_3H groups is a reason for the thermal desorption of SO_2. The evolution of SO_2 is accompanied by CO_2 gassing. This CO_2 is formed during the thermal decomposition of Cx groups, or it can be formed because of redox processes driven mainly by the thermal decomposition of SO_3H groups. As compared to the brominated NACs, the sulfonated NACs contain more Cx groups and fewer A-L groups. But, the total concentration of oxygen-containing groups during sulfonation changes slightly. Therefore, no significant parallel oxidation is observed during sulfonation.The formation of additional Cx groups can be explained as a consequence of reducing SO_3H groups to SO_2 at the expense of the carbon matrix.

Figure 12b shows the TPD MS profile m/z 64 (SO_2^+); this profile was fitted with two Gaussian functions. They describe a superposition of overlapping low-temperature and high-temperature components. Table 5 lists the peak temperatures (T_1 and T_2) and the total concentration of the SO_3H groups ($C(SO_2)$) evaluated from the analysis of temperature profiles. The ratio between components ($C_2(SO_2)$)/($C_1(SO_2)$) has a very complex dependence on the parameters, including the texture, preparation methods used, and concentration of oxygen-containing groups, etc. (cf. Figs. 12a and b).

The significant difference in the shape of the CO_2 release curves in the TPD IR and TPD MS experiments is because of the possibility of interaction between neighboring surface groups, with each other, and with the products of their decomposition during heating. As already mentioned, for the pristine and brominated NACs, the intergroup interaction leads to the formation of new surface groups (2Cx → A). For the sulfonated NACs, we observe the cooperative effect in the decomposition of

Table 5 Sulfur (C(S)) and SO_2 ($C_1(SO_2)$ and $C_2(SO_2)$) concentrations and the surface chemistry of the sulfonated NACs

Sample	Concentration, mmol g^{-1}			TPD peak temperature of SO_2, °C		Δm_{FG}, g g^{-1}	TPD IR, C_{FG}, mmol g^{-1}		
	C.A	TPD MS		T_1	T_2		Cx	A-L	Ph
	C(S)	$C_1(SO_2)$	$C_2(SO_2)$						
NAC1/KBr_3/S1	0.36	0.22	0.11	300	385	0.1287	0.50	0.33	1.08
NAC1/Br_2/S1	0.37	0.22	0.12	295	380	0.1390	0.59	0.40	1.17
NAC1/Br_2/S2	0.55	0.10	0.11	215	315	0.1312	0.43	0.28	1.25
NAC2/KBr_3/S1	0.38	0.13	0.11	310	385	0.1227	0.40	0.30	1.25
NAC2/Br_2/S1	0.34	0.12	0.12	295	350	0.1186	0.41	0.30	1.17
NAC2/Br_2/S2	0.43	0.11	0.11	240	315	0.1184	0.32	0.39	1.20
NAC3/KBr_3/S1	0.37	0.09	0.10	310	385	0.0918	0.19	0.15	0.96
NAC3/Br_2/S1	0.48	0.09	0.08	295	350	0.1076	0.31	0.19	0.97
NAC3/Br_2/S2	0.39	0.08	0.10	210	290	0.0895	0.12	0.14	1.07

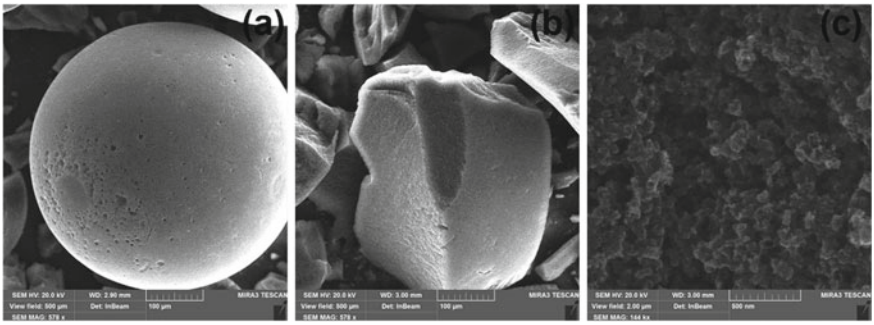

Fig. 11 **a**, **b** SEM images of the pristine NAC3 and crushed NAC3/Br_2/MA beads at low magnification, and **c** SEM image that showed the inner surface of the crushed NAC3/Br_2/MA bead at high resolution

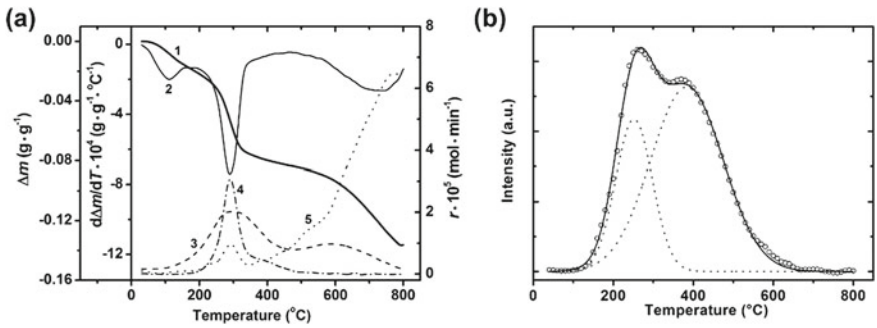

Fig. 12 **a** Thermograms (1, 2) TGA: (1) TG and (2) DTG curves, and (3, 4, 5) EGA profiles: (3) CO_2, (4) CO, (5) SO_2, and **b** TPD MS profile m/z 64 (SO_2^+) for NAC2/Br_2/SMA

neighboring groups determining their thermal stability. The decomposition of the least stable Cx groups and their interaction with the formation of A groups, which begins at about 100–150 °C (Fig. 12a), initiates the decomposition of neighboring SO_3H groups. As a result, many SO_3H groups are decomposed in a narrow temperature range, and the peaks on the CO_2 and SO_2 release curves very well coincide. This thermolytic process destabilizes the carbon matrix so that there is even a slight decomposition of A or Ph groups, as shown by the corresponding effect of CO release. In the TPD MS experiment, the decomposition of SO_3H groups occurs independently and is characterized by the presence of two forms, with the second form usually predominating (Fig. 12b). Therefore, TPD MS data were used to determine the amount of $C_1(SO_2)$ and $C_2(SO_2)$ (Table 5). According to Table 5, the sulfonation of the brominated NACs can introduce into the surface layer up to 0.55 mmol of sulfur per gram of NAC. However, the total sulfur concentration (C(S)) for some samples significantly exceeds the amount of SO_2 ($C_1(SO_2) + C_2(SO_2)$) released during the thermal decomposition of SO_3H groups. The maximum concentration of

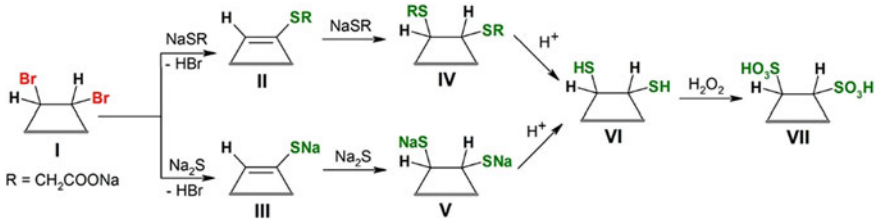

Fig. 13 Schematic of the sulfonation pathways starting from the brominated carbon surface

($C(SO_2)$) reaches from 40% to 60% of C(Br). The obtained sulfonation results can be explained using the scheme (Fig. 13).

On the brominated surface, the product (I) interacts with S-containing SMA or Na_2S nucleophiles. In this case, bromine is replaced to form the products (II) or (III). If the double C=C bond in these products is sufficiently reactive, further interaction with SMA and Na_2S produces the products (IV) and (V), respectively. Hydrolysis of products (IV) and (V) in an acidic environment leads to the formation of surface sulfides (VI). Their oxidation with hydrogen peroxide will give the final product (VII), which contains sulfo groups. The lower yield of SO_3H groups compared to the bromine content in the product (I) can be explained by several reasons. The first reason is the formation of the product (II) or (III), which unlike the product (IV) or (V) due to insufficient reactivity of the C=C bonds. Another reason for the small yields of SO_3H groups is the intensive hydrolysis of bromine in the alkaline medium of SMA or Na_2S. This process is most intense under the action of Na_2S, which leads to lower concentrations, as can be seen from $C(SO_2)$, and the lower thermal stability of the grafted SO_3H groups (Table 5). Another reason is the parallel oxidation of SMA and Na_2S with the formation of elemental sulfur or other S-containing products. Their presence can explain the higher concentration of C(S) as compared to $C(SO_2)$.

There is a positive correlation between the amount of bromine in the used precursors and the amount of SO_3H groups in the resulting solid acids (Fig. 14). Thus, an increase in the efficiency of sulfonation can be achieved by increasing the bromine content in the precursors.

The 2-propanol dehydration is a convenient model reaction for studying the acidic properties of carbon-based solid acids. This process is carried out in the gas phase between 30 °C and 300 °C. Under the action of acid centers, the dehydration of 2-propanol, as a rule, occurs by the following schema (Fig. 15).

In addition to propene and water, the reaction products may be diisopropyl ether and acetone. Additional investigations of the prepared solid acid catalysts confirmed their high selectivity to propene since no traces of diisopropyl ether and acetone were found in the reaction products. Below we report the results of testing the S-containing solid acids in the dehydration reaction that was performed to study the effect of halogenation. The methods of introducing sulfur-containing groups into the carbon surface layer were examined with respect to the catalytic activity of the resulting solid acids. Figure 16 shows the 2-propanol conversion against temperature over the

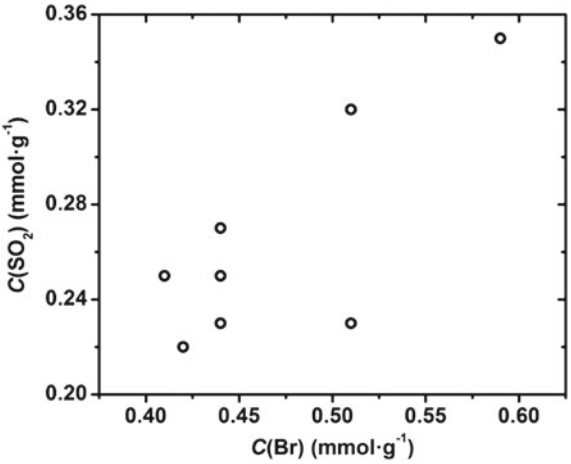

Fig. 14 Correlation between $C(SO_2)$ and $C(Br)$

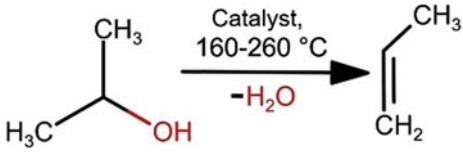

Fig. 15 Catalytic dehydration schema

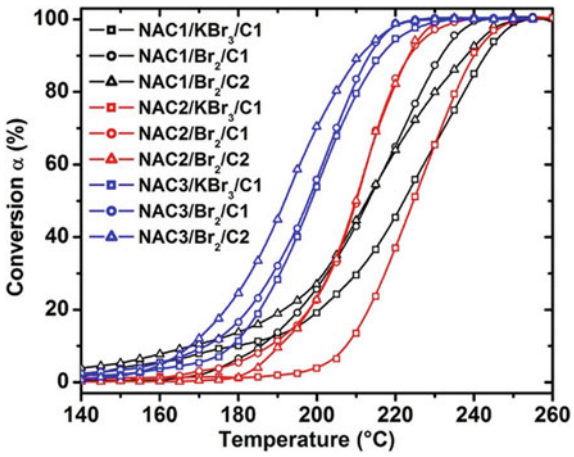

Fig. 16 Conversion of 2-propanol to propene against temperature

sulfonated NACs. As can be seen in Fig. 16, the brominated NACs modified with sulfur-containing compounds have significant catalytic efficiency. A 100% conversion of 2-propanol to propene is observed for all samples, and the $t_{100\%}$ ranges from 220 °C to 250 °C. The similar temperature behavior and close catalytic activity of all studied samples are due to the same nature of acid centers and approximately the same concentration of them. It should be noted that the pristine (unmodified) NACs

Table 6 Ratio ($C_2(SO_2)/C_1(SO_2)$) and catalysis temperatures on the sulfonated NACs

Sample	$C_2(SO_2)/C_1(SO_2)$	Catalysis temperatures, °C	
		$t_{50\%}$	$t_{100\%}$
NAC1/KBr_3/S1	0.50	222	250
NAC1/Br_2/S1	0.55	213	240
NAC1/Br_2/S2	1.10	213	245
NAC2/KBr_3/S1	0.85	225	250
NAC2/Br_2/S1	1.00	210	235
NAC2/Br_2/S2	1.10	210	230
NAC3/KBr_3/S1	1.11	199	230
NAC3/Br_2/S1	0.89	198	220
NAC3/Br_2/S2	1.25	192	220

do not show catalytic activity between 30 °C and 350 °C. The conversion α against temperature dependence has a fairly flat saturation, so we used the numerical values of $t_{50\%}$ and $t_{100\%}$ (Table 6) to characterize the catalytic activity of the samples.

The obtained series for catalytic activity at $t_{50\%}$ and $t_{100\%}$ has a similar sequence:

$$\begin{aligned}
&\text{NAC3/Br}_2\text{/S2} > \text{NAC3/Br}_2\text{/S1} > \text{NAC3/KBr}_3\text{/S1} \\
&\quad > \text{NAC2/Br}_2\text{/S2} = \text{NAC2/Br}_2\text{/S1} > \text{NAC1/Br}_2\text{/S2} \\
&= \text{NAC1/Br}_2\text{/S1} > \text{NAC1/KBr}_3\text{/S1} > \text{NAC2/KBr}_3\text{/S1}; \\
&\text{NAC3/Br}_2\text{/S2} = \text{AC3/Br}_2\text{/S1} > \text{NAC3/KBr}_3\text{/S1} \\
&= \text{NAC2/Br}_2\text{/S2} > \text{NAC2/Br}_2\text{/S1} > \text{NAC1/Br}_2\text{/S1} > \\
&\text{NAC1/Br}_2\text{/S2} > \text{NAC1/KBr}_3\text{/S1} = \text{NAC2/KBr}_3\text{/S1}.
\end{aligned}$$

The samples based on NAC3 have the highest catalytic activity, regardless of the treatment methods. If the modification methods (bromination and sulfonation) have similar efficiency, the surface layer structure should be alike. In this case, the structural parameters of the initial carbon matrix will play a significant role. The use of NAC3 having pores of different sizes leads to improved transport of the reagent to the active site, which intensifies the dehydration reaction of 2-propanol to propene. The major disadvantage of NAC3 is the lower reactivity of its surface, which is due to the intensive oxidative treatment when this material was prepared. Therefore, it is hard to expect a significant increase in the concentration of bromine and sulfo groups even when using other methods of modification. Using microporous NAC1 and NAC2 gives inferior results in catalysis, despite introducing more sulfo groups into the surface layer.

Comparison of the catalytic activity of the samples obtained based on one carbon matrix allows us to state that the most effective method of modification, in terms of the highest catalytic activity, is the treatment with Na_2S. This sulfonation agent and respective pathway do not always lead to the largest number of SO_3H groups.

However, they provide the highest ratio of $C_2(SO_2)/C_1(SO_2)$, and the prepared samples are the most thermally stable under catalysis conditions. With Na_2S used in the intermediate stage (see Fig. 13), one can get the products (III) or (V). They are easily transformed into surface sulfide groups. If one uses SMA for the modification, the hydrolytic conversion of the products (II) or (IV) depends on hydrolysis completeness. With partial hydrolysis, further oxidation will cause the formation of weak acid centers, as sulfoacetic acid derivatives, or sulfones, rather than SO_3H groups.

The most difficult to explain is why solid acids prepared from the NACs brominated with liquid bromine have the highest activity in catalysis. This situation seems paradoxical. The NACs/KBr_3/S1 solid acids are one of the best in terms of the amounts of released SO_2, and they have the highest thermal stability (see Table 5). Notably, the concentration of oxygen-containing groups is identical for NACs/KBr_3/S1 and NACs/Br_2/S1. The only difference can be in the distribution of oxygen-containing groups on the surface of NACs/KBr_3 and NACs/Br_2 and in the bromination media used (aqueous solution of Br_2·KBr and liquid Br_2). If we assume now that the stability of the acid center is determined by its neighboring groups, e.g., Cx groups, then the most stable will be centers that do not have adjacent Cx groups. On this point, see the earlier explanation to Fig. 12a given in the paragraph on the cooperative decomposition of Cx and SO_3H groups. Indeed, the NACs/KBr_3 samples have higher thermal stability than the NACs/Br_2 ones (cf. T_1 values in Table 3); This high stability confirms the different environments of bromine depending on the brominating agent used. For the NACs/KBr_3 samples, individual sites with chemisorbed bromine prevail, while for the NACs/Br_2 samples, other functional groups are located near chemisorbed bromine sites. Single active centers have higher thermal stability but may be less effective in catalysis due to the more energy-intensive formation of intermediate carbocations upon the dehydration of 2-propanol to propene [55]. The dehydration of 2-propanol to propene is possible with greater efficiency by the agreed mechanism on the catalytic SO_3H groups surrounded by adjacent polar centers. Alternatively, the impact of neighboring oxygen-containing groups on the course of the dehydration reaction of 2-propanol to propene could be in pre-concentrating the reagent near the active center (SO_3H group). This pre-concentration of 2-propanol takes place through weak interactions with the polar oxygen-containing groups.

4 Concluding Remarks

Techniques for modifying the surface of NACs with bromine-containing compounds under mild conditions have been developed. The obtained samples can be used as precursors to create sulfur-containing carbon materials with predetermined surface layer properties. It is shown that the bromination of the surface of NACs with an

aqueous solution of Br_2·KBr and liquid bromine leads to the attaching of 0.41–0.59 mmol g^{-1} of bromine. This bromination is accompanied by significant oxidation of the carbon surface with the formation of mostly phenolic groups. It has been shown that modification of bromine-containing precursors, where active bromine capable of further substitution, with sodium mercaptoacetate and sodium sulfide, followed by oxidation of mercapto groups, leads to carbon solids containing up to 0.34 mmol g^{-1} of sulfo groups. The obtained sulfur-containing NACs show catalytic activity in the 2-propanol dehydration reaction. It was found that the catalytic efficiency of the prepared NACs depends on the thermal stability and concentration of the acidic sulfur-containing sites. In comparison with the pristine NACs, the use of bromine-containing precursors result in obtaining catalysts with higher activity in the dehydration reactions. The optimal method that allows getting the highest catalytic activity is the treatment with Na_2S. When treating samples with SMA, it does not have much impact on their activity in the 2-propanol dehydration reaction. If forming the surface layer of acid catalysts with sulfo groups and oxygen-containing groups, it is necessary to take into account the number of surface groups and their surface distribution.

References

1. Berenguer R, Morallón E (2019) Oxidation of different microporous carbons by chemical and electrochemical methods. Front Mater 6:130. https://doi.org/10.3389/fmats.2019.00130
2. Uklein AV, Diyuk VE, Grishchenko LM et al (2016) Characterization of oxidized carbon materials with photoinduced absorption response. Appl Phys B 122:287. https://doi.org/10.1007/s00340-016-6561-2
3. Grishchenko LM, Diyuk VE, Konoplitska OP, Lisnyak VV, Maryichuk RT (2017) Modeling of copper ions adsorption onto oxidative-modified activated carbons. Adsorpt Sci Technol 35:884–900. https://doi.org/10.1177/0263617417729236
4. Ternero-Hidalgo JJ, Rosas JM, Palomo J, Valero-Romero MJ, Rodríguez Mirasol J, Cordero T (2016) Functionalization of activated carbons by HNO_3 treatment: influence of phosphorus surface groups. Carbon 101:409–419. https://doi.org/10.1016/j.carbon.2016.02.015
5. Veselovs'ka KI, Veselovs'kyi VL, Zaderko OM et al (2015) Effect of the oxidation and thermal treatment on bromination of activated carbon. J Superhard Mater 37:39–43. https://doi.org/10.3103/S1063457615010062
6. Berenguer R, Marco-Lozar JP, Quijada C, Cazorla-Amorós D, Morallón E (2012) A comparison between oxidation of activated carbon by electrochemical and chemical treatments. Carbon 50:1123–1134. https://doi.org/10.1016/j.carbon.2011.10.025
7. Saha B, Tai MH, Streat M (2001) Study of activated carbon after oxidation and subsequent treatment characterization. Proc Saf Environ 79:211–217. https://doi.org/10.1205/095758201750362253
8. Houshmand A, Daud WMAW, Lee M-G, Shafeeyan MS (2012) Carbon dioxide capture with amine-grafted activated carbon. Water Air Soil Pollut 223:827–835. https://doi.org/10.1007/s11270-011-0905-7
9. Diyuk VE, Yatsymyrskyi AV, Grishchenko LM, Horodetska DS, Vakaliuk AV, Mischanchuk AV, Zaderko AN, Lisnyak VV (2020) Surface phosphorylated activated carbons: preparation and acidity studies. Springer Proc Phys 240:235–248. https://doi.org/10.1007/978-981-15-1742-6-22

10. Jaramillo J, Álvarez PM, Gómez-Serrano V (2010) Oxidation of activated carbon by dry and wet methods surface chemistry and textural modifications. Fuel Process Technol 91:1768–1775. https://doi.org/10.1016/j.fuproc.2010.07.018
11. Shen W, Li Z, Liu Y (2008) Surface chemical functional groups modification of porous carbon. Rec Pat Chem Eng 1:27–40. https://doi.org/10.2174/2211334710801010027
12. Aldana-Pérez A, Lartundo-Rojas L, Gómez R, Niño-Gómez ME (2012) Sulfonic groups anchored on mesoporous carbon Starbons-300 and its use for the esterification of oleic acid. Fuel 100:128–138. https://doi.org/10.1016/j.fuel.2012.02.025
13. Zheng J, Liu H, Wu B et al (2012) Production of graphite chloride and bromide using microwave sparks. Sci Rep 2:662. https://doi.org/10.1038/srep00662
14. Hanelt S, Friedrich J, Orts-Gil G, Meyer-Plath A (2012) Study of Lewis acid catalyzed chemical bromination and bromoalkylation of multi-walled carbon nanotubes. Carbon 50:1373–1385. https://doi.org/10.1016/j.carbon.2011.11.009
15. Lockett MR, Smith LM (2009) Attaching molecules to chlorinated and brominated amorphous carbon substrates via Grignard reactions. Langmuir 25:3340–3343. https://doi.org/10.1021/la8039626
16. Grishchenko LM, Diyuk VE, Mariychuk RT et al (2020) Surface reactivity of nanoporous carbons: preparation and physicochemical characterization of sulfonated activated carbon fibers. Appl Nanosci 10:2923–2939. https://doi.org/10.1007/s13204-019-01069-3
17. Rechnia P, Malaika A, Kozłowski M (2015) Synthesis of (TAME) over modified activated carbon catalysts. Fuel 154:338–345. https://doi.org/10.1016/j.fuel.2015.03.086
18. Li Q, Chen S, Zhuang L et al (2012) Preparation of a sulfonated activated carbon fiber catalyst with γ-irradiation-induced grafting method. J Mater Res 27:3083–3089. https://doi.org/10.1557/jmr.2012.360
19. Toda M, Takagaki A, Okamura M et al (2005) Biodiesel made with sugar catalyst. Nature 438:178. https://doi.org/10.1038/438178a
20. Dawodu FA, Ayodele OO, Xin J, Zhang S (2014) Application of solid acid catalyst derived from low value biomass for a cheaper biodiesel production. J Chem Technol Biotechnol 89:1898–1909. https://doi.org/10.1002/jctb.4274
21. Russo PA, Antunes MM, Neves P et al (2014) Solid acids with SO_3H groups and tunable surface properties: versatile catalysts for biomass conversion. Green Chem 16:4292–4305. https://doi.org/10.1039/c4ta02320j
22. Pang Q, Wang LQ, Yang H et al (2014) Cellulose-derived carbon bearing –Cl and $–SO_3H$ groups as a highly selective catalyst for the hydrolysis of cellulose to glucose. RSC Adv 4:41212–41218. https://doi.org/10.1039/C4RA05520A
23. Hu S, Jiang F, Hsieh Y-L (2015) 1D Lignin-based solid acid catalysts for cellulose hydrolysis to glucose and nanocellulose. ACS Sustain Chem Eng 3:2566–2574. https://doi.org/10.1021/acssuschemeng.5b00780
24. Bonilla-Petriciolet A, Mendoza-Castillo DI, Reynel-Avila HE (eds) (2017) Adsorption processes for water treatment and purification. Springer, Cham, pp 2–19
25. Morrison RT, Boyd RN, Bhatacharjee KS (2010) Organic chemistry. 7th edn, Pearson, New Delhi
26. Friedrich JF, Hidde G, Lippitz A, Unger WES (2014) Plasma bromination of graphene for covalent bonding of organic molecules. Plasma Chem Plasma Process 34:621–645. https://doi.org/10.1007/s11090-013-9509-x
27. Diyuk VE, Zaderko AN, Grischenko LM, Tsapyuk GG, Vakaliuk AV, Lisnyak VV, Mariychuk R (2020) CO_2 adsorption on pristine, oxidized, and diethylamine-functionalized activated carbon sorbents. E_3S Web Conf 154:07001 https://doi.org/10.1051/e3sconf/202015407001
28. Bezugla TM, Grishchenko LM, Vakaliuk AV, Diyuk VE, Mischanchuk OV, Lisnyak VV (2018) Covalent bonding of sulfogroups to activated carbon fibers: the role of bromine plasma pretreatment. Molec Cryst Liquid Cryst 661:58–67. https://doi.org/10.1080/15421406.2018.1460240
29. Grishchenko LM, Vakaliuk AV, Diyuk VE, Mischanchuk OV, Boldyrieva OYu, Bezugla TM, Lisnyak VV (2018) From destructive CCl_4 adsorption to grafting SO_3H groups onto activated

carbon fibers. Molec Cryst Liquid Cryst 673:1–15. https://doi.org/10.1080/15421406.2019.1578488
30. Grishchenko LM, Tsapyuk GG, Novichenko NS, Mischanchuk OV, Yatsymyrskiy AV, Boldyrieva OY, Diyuk VE (2020) Amination of brominated nanoporous activated carbon beads for the preparation of CO_2 adsorbents. Molec Cryst Liquid Cryst 699:20–33. https://doi.org/10.1080/15421406.2020.1732535
31. Diyuk VE, Mariychuk RT, Lisnyak VV (2016) Barothermal preparation and characterization of micro-mesoporous activated carbons: textural studies, thermal destruction and evolved gas analysis with TG-TPD-IR technique. J Thermal Anal Calorim 124:1119–1130. https://doi.org/10.1007/s10973-015-5208-6
32. Khavryuchenko VD, Khavryuchenko OV, Shkilnyy AI, Stratiichuk DA, Lisnyak VV (2009) Characterization by SEM, TEM and quantum-chemical simulations of the spherical carbon with nitrogen (SCN) active carbon produced by thermal decomposition of poly(vinylpyridine-divinylbenzene) copolymer. Materials 2:1239–1251. https://doi.org/10.3390/ma2031239
33. Zaderko AN, Shvets RYa, Grygorchak II, Afonin S, Diyuk VE, Mariychuk RT, Boldyrieva OYu, Kaňuchová M, Lisnyak VV (2019) Fluoroalkylated nanoporous carbons: Testing as a supercapacitor electrode. Appl Surf Sci 470:882–892. https://doi.org/10.1016/j.apsusc.2018.11.141
34. Mariychuk R, Fejer J, Porubska J, Grishchenko LM, Lisnyak VV (2020) Green synthesis and characterization of gold triangular nanoprisms using extract of Juniperus communis L. Appl Nanosci 10:2835–2841. https://doi.org/10.1007%2Fs13204-019-00990-x
35. Jagiello J, Olivier JP (2013) Carbon slit pore model incorporating surface energetical heterogeneity and geometrical corrugation. Adsorption 19:777–783. https://doi.org/10.1007/s10450-013-9517-4
36. Jagiello J, Kenvin J, Celzard A, Fierro V (2019) Enhanced resolution of ultra micropore size determination of biochars and activated carbons by dual gas analysis using N_2 and CO_2 with 2D-NLDFT adsorption models. Carbon 144:206–215. https://doi.org/10.1016/j.carbon.2018.12.028
37. Ischenko EV, Matzui LY, Gayday SV, Vovchenko LL, Kartashova TV, Lisnyak VV (2010) Thermo-exfoliated graphite containing $CuO/Cu_2(OH)_3NO_3$:(Co^{2+}/Fe^{3+}) composites: Preparation, characterization and catalytic performance in CO conversion. Materials 3:572–584. https://doi.org/10.3390/ma3010572
38. Veselovskyi VL, Ischenko EV, Gayday SV, Lisnyak VV (2012) A high efficient two phase $CuO/Cu_2(OH)_3NO$ (Co^{2+}/Fe^{3+}) composite catalyst for CO-PROX reaction. Catal Commun 18:137–141. https://doi.org/10.1016/j.catcom.2011.11.024
39. Tsapyuk GG, Diyuk VE, Mariychuk R et al (2020) Effect of ultrasonic treatment on the thermal oxidation of detonation nanodiamonds. Appl Nanosci 10:4991. https://doi.org/10.1007/s13204-020-01277-2
40. Diyuk VE, Vakaliuk AV, Grishchenko LM, Mischanchuk OV, Brazhnyk DV, Lisnyak VV (2020) Barothermal Diels-Alder functionalization of multi-walled carbon nanotubes. Molec Cryst Liq Cryst 699:9–19. https://doi.org/10.1080/15421406.2020.1732533
41. Zabuga VY, Bochechka OO, Tsapyuk GG, Diyuk VE, Panova AM, Lisnyak VV (2018) On multiwalled carbon nanotubes oxidation: thermogravimetric, spectral and macrokinetic studies. Molec Cryst Liq Cryst 661:81–90. https://doi.org/10.1080/15421406.2018.1460257
42. Diyuk VE, Grishchenko LN, Yatsimirskii VK (2008) Kinetics of the dehydration of 2-propanol on modified activated charcoal containing acid sites. Theor Exper Chem 44:331–337. https://doi.org/10.1007/S11237-008-9046-5
43. Diyuk VE, Zaderko AN, Grishchenko LM, Yatsymyrskiy AV, Lisnyak VV (2012) Efficient carbon-based acid catalysts for the propan-2-ol dehydration. Catal Commun 27:33–37. https://doi.org/10.1016/j.catcom.2012.06.018
44. Khavryuchenko VD, Khavryuchenko OV, Shkilnyy AI, Lisnyak VV, Stratiichuk DA (2011) Structural effects of SKS active carbon modification with melamine, studied by SEM, TEM, EDX and quantum-chemical simulations. Int J Modern Phys B 25:1377–1383. https://doi.org/10.1142/S0217979211100059

45. Khavryuchenko VD, Tarasenko YA, Khavryuchenko OV, Shkilnyy AI, Lisnyak VV, Stratiichuk DA (2010) Nanostructurization in the SKS active carbon, characterized by SEM, TEM, EDX and quantum-chemical simulations. Int J Modern Phys B 24:1449–1462. https://doi.org/10.1142/S0217979210055627
46. Multian VV, Kinzerskyi FE, Vakaliuk AV et al (2017) Surface response of brominated carbon media on laser and thermal excitation: optical and thermal analysis study. Nanoscale Res Lett 12:146. https://doi.org/10.1186/s11671-017-1873-7
47. Diyuk VE, Zaderko AN, Veselovska KI, Lisnyak VV (2015) Functionalization of surface of carbon materials with bromine vapors at mediate high temperature: a thermogravimetric study. J Thermal Anal Calorim 120:1665–1678. https://doi.org/10.1007/s10973-015-4495-2
48. Khavryuchenko OV, Khavryuchenko VD, Lisnyak VV, Peslherbe GH (2011) A density-functional theory investigation of the electronic structure of the active carbon graphite-like and amorphous domains. Chem Phys Lett 513:261–266. https://doi.org/10.1016/j.cplett.2011.08.009
49. Khavryuchenko VD, Khavryuchenko OV, Lisnyak VV (2010) High multiplicity states in disordered carbon systems: ab initio and semiempirical study. Chem Phys 368:83–86. https://doi.org/10.1016/j.chemphys.2009.12.022
50. Khavryuchenko VD, Khavryuchenko OV, Lisnyak VV (2010) Effect of spin catalysis in H_2S oxidation: a quantum chemical insight. Catal Comm 11:340–345. https://doi.org/10.1016/j.catcom.2009.10.027
51. Khavryuchenko VD, Khavryuchenko OV, Tarasenko YA, Lisnyak VV (2008) Computer simulation of N-doped polyaromatic hydrocarbons clusters. Chem Phys 352:231–234. https://doi.org/10.1016/j.chemphys.2008.06.019
52. Khavryuchenko VD, Tarasenko YA, Strelko VV, Khavryuchenko OV, Lisnyak VV (2007) Quantum chemical study of polyaromatic hydrocarbons in high multiplicity states. Int J Modern Phys B 21:4507–4515. https://doi.org/10.1142/S0217979207037946
53. Khavryuchenko VD, Tarasenko YA, Strelko VV, Khavryuchenko OV, Lisnyak VV (2008) Interaction of the dioxygen molecule with the $C_{96}H_{24}$ polyaromatic hydrocarbon cluster: a quantum chemical insight. Int J Modern Phys B 22:2115–2127. https://doi.org/10.1142/S0217979208039289
54. Schönherr J, Buchheim JR, Scholz P, Adelhelm P (2018) Boehm titration revisited (Part II): a comparison of boehm titration with other analytical techniques on the quantification of oxygen-containing surface groups for a variety of carbon materials. C 4(2):22. https://doi.org/10.3390/c4020022
55. Diyuk VE, Mariychuk RT, Lisnyak VV (2016) Functionalization of activated carbon surface with sulfonated styrene as a facile route for solid acids preparation. Mater Chem Phys 184:138–145. https://doi.org/10.1016/j.matchemphys.2016.09.034

The Conductivity Mechanisms of ZnO Thin Films Structured Using Polyvinyl Alcohol

A. P. Chebanenko, L. M. Filevska, V. S. Grinevych, Yu. I. Bulyga, I. V. Brytavskyi, and V. A. Smyntyna

1 Introduction

Zinc oxide has recently been actively used to create cathodoluminophores, electroluminescent screens, acoustoelectronic amplifiers, various types of photo- and optoelectronic devices [1], as part of composite materials for electronic equipment [2]. Such a wide range of ZnO use is associated with the features of the surface and grain boundaries of the material [3–5]. Zinc oxide layers are used as a transparent conducting electrode in solar cells [6], as well as antireflection coatings in interference optics, in photoelectronic devices, lasers, and ultraviolet radiation LEDs [7]. The electrical conductivity changes of zinc oxide thin films in an environment, with hydrogen and oxygen-containing gases, together with their chemical resistance, nontoxicity, and low-cost fabrication make them a promising material for the active gas sensors elements [8–11]. The mechanisms of gas sensitivity of a material are usually associated with its electrical conductivity special feature. In the present work, the mechanisms of electrical conductivity in a dry air atmosphere of thin ZnO films obtained from a zinc acetate solution with the addition of polyvinyl alcohol were studied.

2 Methods

The variety of applications of thin films of zinc oxide is provided by a variety of methods for their production and subsequent processing [1, 5, 12–15]. Known methods of zinc oxide thin films forming such as atomic layer deposition technique

A. P. Chebanenko · L. M. Filevska (✉) · V. S. Grinevych · Yu. I. Bulyga · I. V. Brytavskyi · V. A. Smyntyna
Odessa I.I. Mechnikov National University, Dvoryanskaya str.,2, Odessa 65082, Ukraine

O. Fesenko and L. Yatsenko (eds.), *Nanomaterials and Nanocomposites, Nanostructure Surfaces, and Their Applications*, Springer Proceedings in Physics 263, https://doi.org/10.1007/978-3-030-74741-1_27

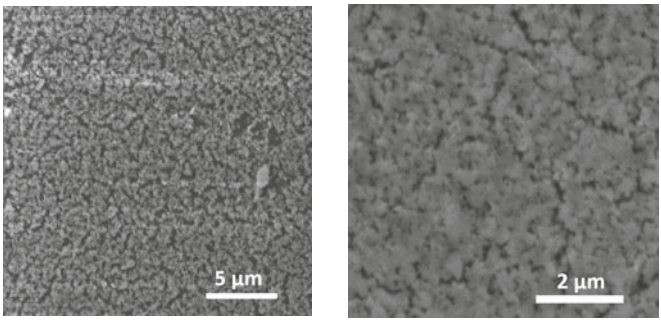

(a) (b)

Fig. 1 SEM image of the studied tin oxide film obtained by using polyvinyl alcohol, **a** magnification $10{,}000^{x}$, **b** magnification $30{,}000^{x}$)

[16, 17], magnetron sputtering in various modifications [18] require quite complex technical support. Widely used sol–gel technologies sometimes use relatively expensive and at the same time harmful reagents such as α-terpineol, 2-methoxyethanol, 2-aminoethanol.

In this work, zinc oxide films are formed by a simple method of chemical precipitation from zinc acetate solutions. ZnO films were obtained by immersing glass samples in an aqueous solution of zinc acetate with the addition of a 1% of polyvinyl alcohol (C_2H_4O) solution in equal proportions. The prepared solution was stirred on a magnetic stirrer and kept for several hours. The samples were obtained by reusable immersion of the substrates in the solution according to the technique described in [19]. Subsequently, the prepared films were annealed in air at 400 °C for 40–50 min.

The structure of the resulting film can be seen in the image of an electronic microscope shown in Fig. 1. The layers clearly show surface homogeneity and developed porosity.

For electrical characterization and clarification of the electrical conductivity mechanism in air, before and after several heatings to 440 K, the resistance, current–voltage characteristics, and dark current temperature dependences were measured.

3 Results and Discussion

The band gap of the obtained thin films was calculated in [19] from the absorption spectrum shown in Fig. 2 and was around 3.15–3.2 eV. In the same work, we have shown that the value of the band gap of films obtained by using polyvinyl alcohol is higher than that of films obtained by other methods used in this work. This means that the sizes of ZnO crystallites obtained in a zinc acetate solution with the addition of polyvinyl alcohol are smaller than those in ZnO films obtained from a solution

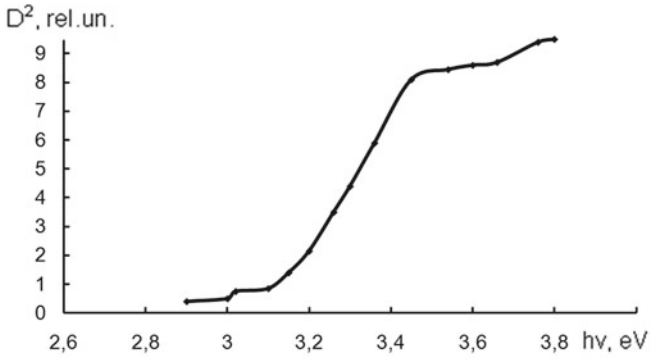

Fig. 2 Absorption spectrum of zinc oxide film

without PVA. The reason is that the polymer matrix with PVA limits the size of the reaction volumes, where the synthesis of zinc oxide crystallites occurs and, therefore, inhibits the growth of ZnO crystallites.

This result slightly exceeds such value for bulk material and indicates the nanoscale level of the film crystallites formed in the bounding volumes of the PVA polymer matrix.

The electrical conductivity of ZnO films and the type of their current–voltage characteristics (CVC) turned out to be significantly dependent on external conditions. The CVC of ZnO film at room temperature tends to an exponential dependency, specific for the potential barriers influence on conductivity. Thereby, in films obtained with PVA impurities, intercrystalline potential barriers are more pronounced, and these barriers affect the current flow.

The average value of the interelectrode resistance calculated from the initial linear section of the CVC on the Fig. 3 is about 2.8×10^9 Ω. Thereby, the addition of PVA leads to the growth of films resistance. This is explained by the fact that during high-temperature annealing, PVA (which plays the role of a polymer matrix) decomposes, decomposition products evaporate, and zinc oxide films become porous with a more developed surface. The porosity of the film can be seen on Fig. 1b. Nanoscale

Fig.3 CVC of ZnO film in the open air ($T = 293$ K)

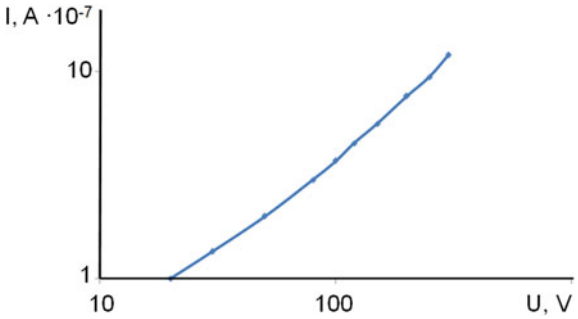

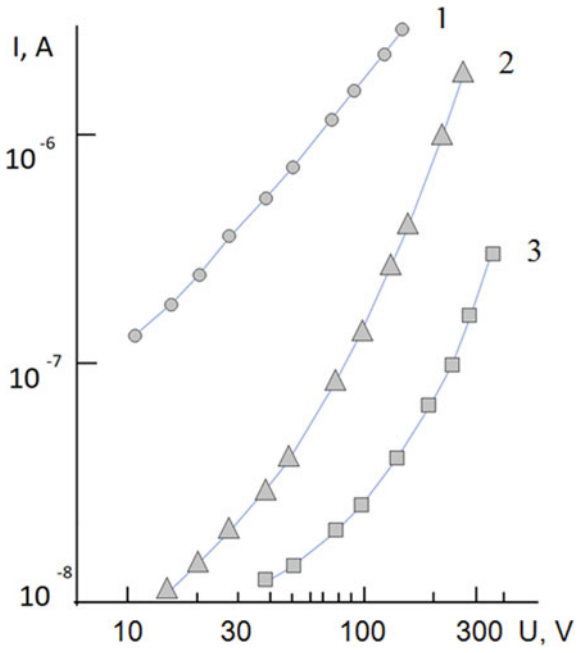

Fig.4 CVC of ZnO film in dry air ($T = 293$ K): 1—immediately after heating the film to 440 K and cooling in vacuum to 293 K, 2—after several measurement cycles in air, 3—after heating to 440 K and cooling to 293 K in air

crystallites might create a quantum well effect for carriers, which also leads to the resistance increase.

The electrical conductivity of ZnO films and the form of their current–voltage characteristics turned out to be significantly dependent on the external conditions. The cycles of heating–cooling of the films in the interval of 440–293 K were done in vacuum and in air. Curve 1 in Fig. 4 shows the CVC of the ZnO film measured in dry air atmosphere immediately after the cycle of heating the film to a temperature of 440 K and its further cooling in vacuum. CVC is almost linear, as it is seen from the figure. However, after carrying out a number of measurements on the indicated film in air atmosphere, the interelectrode resistance of the film increases by almost an order of magnitude, and its CVC becomes superlinear (see Fig. 4, curve 2). The curves reconstructed in different coordinates showed that better straightening of the CVC is observed in the coordinates $ln\ I - U^{1/4}$ (Fig. 5, curve 1). Such coordinates are characteristic for the barrier mechanism of current flow, in particular, over-barrier Schottky emission through intercrystalline potential barriers of small thickness [20].

Curve 3 (Fig. 5) shows the CVC of ZnO film measured after heating the film to a temperature of 440 K in an air atmosphere and then room temperature cooling. This procedure leads to a further increase in the resistance of the film and an increase in the superlinearity of its CVC (Fig. 5, curve 3). It turned out that the current–voltage dependence is straightened in the coordinates $ln\ I - U^{1/2}$ (Fig. 5, curve 2), which are characteristic for the above-barrier Schottky emission through "thick" intercrystalline barriers [20].

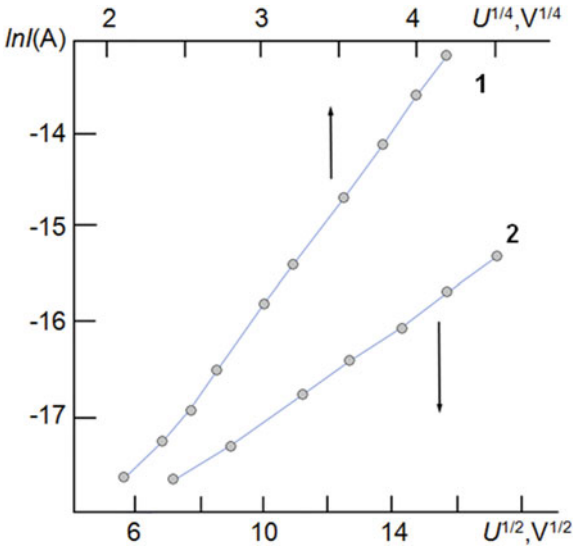

Fig. 5 CVC of ZnO film in special coordinates (T = 293 K): 1—after several cycles of measurements in air (corresponds to curve 2 in Fig. 4), 2—after heating to 440 K and cooling to 293 K in air (corresponds to curve 3 in Fig. 4)

Mentioned results may have the following explanation. The porosity of ZnO films obtained using PVA promotes the absorption of oxygen and its diffusion along the intercrystalline boundaries. Absorbed oxygen, by capturing conduction electrons, increases the surface locking bend of energy bands and also leads to an increase in the height of the intercrystalline potential barriers for electrons. Heating the film in air (where a large amount of oxygen is available) stimulates the process of chemisorption and diffusion of oxygen, which leads to an increase in the height and thickness of the intercrystalline barriers. The consequence of these processes is an increase in the electrical resistance of the film and the transition of barriers from "thin" to "thick" barrier behavior.

This explanation is consistent with the results of the temperature–current dependences measurements (TCD) on the studied films (Fig. 6), carried out in vacuum (curve 1 and curve 2) and in a dry air atmosphere (curves 3 and 4).

It can be seen that on the TCD, measured during heating in an air atmosphere, and in the high-temperature region, there is no section with the conductivity activation energy $E_A = 1.1$ eV, which was present on the TCD in vacuum and which was associated with desorption of molecular oxygen. When the film is heated in an air atmosphere at high temperatures, on the contrary, the growth of the current with temperature slows down, which is due to the diffusion of oxygen and an increase in the influence of intercrystalline barriers on the current transfer process.

It is characteristic that the conduction activation energy upon further cooling of the film (curve 4, Fig. 6) is $E_A = 0.43$ eV. This is consistent with the height of intercrystalline potential barriers in zinc oxide films calculated in [21] ($E_A = 0.45$ eV) and is explained by the model of an inhomogeneous semiconductor with large-scale potential fluctuations [22].

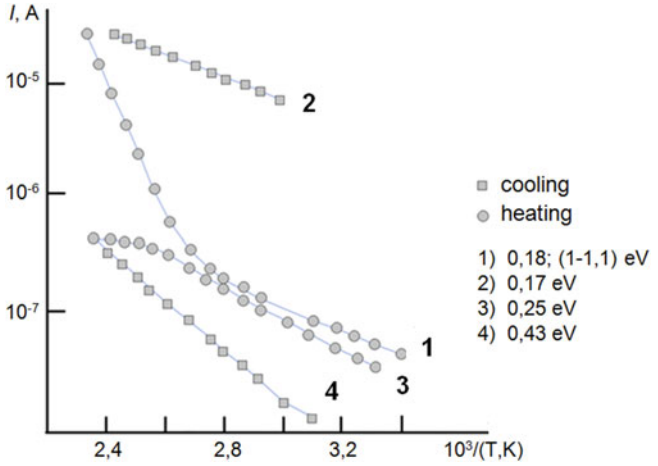

Fig. 6 Temperature dependences of the current in the ZnO film in vacuum (1, 2) and in air (3, 4), $U = 50$ V

4 Conclusions

The established character of current transport in vacuum is caused by the above-barrier Schottky emission over small intercrystalline potential barriers. Heating/cooling in the air atmosphere leads to the superlinearity of the current–voltage characteristic specific for the above-barrier Schottky emission over "thick" intercrystalline barriers.

The established barrier effects in the films conductivity are explained by the adsorption and subsequent diffusion of oxygen, which, capturing the conduction electrons, not only increases the surface locking curving of energy bands, but also increases the intercrystalline potential barriers height for electrons. The conductivity activation energy (0.43 eV) obtained from the TCD is consistent with the calculated height of intercrystalline potential barriers (0.45 eV) and is explained by the model of an inhomogeneous semiconductor with large-scale potential fluctuations.

References

1. Klingshirn CF, Meyer BK, Waag A, Hoffmann A, Geurts J (2010) Zinc oxide. From fundamental properties towards novel applications. Springer, Berlin, pp 254–263
2. Lepikh YI, Lavrenova TI, Sadova NM, Borshchak VA Balaban AP, Zatovska NP (2018) Strukturno-fazovi peretvorennya i elektrofIzichni vlastivostI kompozitsiynih materIaliv na bazi sistemi SiO_2-B_2O_3-Bi_2O_3-ZnO-BaO (Structural-phase transformations and electrophysical properties of composite materials based on the system SiO_2-B_2O_3-Bi_2O_3-ZnO-BaO). Sens Electron Microsys Technol 15(4):77–84 in Ukrainian

3. Pronin IA, Donkova BV, Dimitrov DT et al (2014) Relationship between the photocatalytic and photoluminescence properties of zinc oxide doped with copper and manganese. Semiconductors 48:842–847. https://doi.org/10.1134/S1063782614070173
4. Khomchenko VS, Kushnirenko VI, Papusha VP et al (2010) Luminescent and structural properties of ZnO-Ag films. Semiconductors 44:685–690. https://doi.org/10.1134/S1063782610050246
5. Lyadov NM, Gumarov AI, Kashapov RN et al (2016) Structure and optical properties of ZnO with silver nanoparticles. Semiconductors 50:43–49. https://doi.org/10.1134/S1063782616010139
6. Lee D, Bae WK, Park I, Yoon DY, Lee S, Lee C (2011) Transparent electrode with ZnO nanoparticles in tandem organic solar cells. Sol Energy Mater Sol Cells 95(1):365–368
7. Liu H, Liu Y, Xiong P et al (2017) Aluminum-doped zinc oxide transparent electrode prepared by atomic layer deposition for organic light emitting devices. IEEE Trans Nanotechnol 16:634–638
8. Moseley PT (2017) Progress in the development of semiconducting metal oxide gas sensors. A Rev J Meas Sci Technol 28(8):082001
9. .Kumar R, Al–Dossary O, Kumar G, Umar A (2015) Zinc oxide nanostructures for NO_2 gas–sensor applications: a review. J Nano–Micro Lett 7(2):97–120
10. Djurišić AB, Ng AMC, Chen XY (2010) Review ZnO nanostructures for optoelectronics: material properties and device applications. Prog Quant Electron 34:191–259
11. Ammaih Y, Lfakir A, Hartiti B et al (2014) Structural, optical and electrical properties of ZnO: Al thin films for optoelectronic applications. Opt Quant Electron 46(1):229–234
12. Semikina TV, Mamykin SV, Godlewski M et al (2013) ZnO as a conductive layer prepared by ALD for solarcells based on n-CdS/n-CdTe/p-Cu1.8S heterostructure. Semicond Phys Quant Electron Optoelectron 16(2):111–116
13. Krajewski TA, Luka G, Wachnicki L et al (2011) Electrical parameters of ZnO films and ZnO-based junction sobtained byatomic layer deposition. Semicond Sci Technol 26:085013–085018
14. Dostanko AP, Ageev OA, Golosov DA et al (2014) Electrical and optical properties of zinc-oxide films deposited by the ion-beam sputtering of an oxide target. Semiconductors 48:1242–1247. https://doi.org/10.1134/S1063782614090073
15. Gruzintsev AN, Volkov WT (2011) Modification of electrical and optical properties of ZnO films under ultraviolet irradiation. Semiconductors 45:1420–1424. https://doi.org/10.1134/S1063782611110121
16. Krajeski T, Guziewicz E, Godlewski M et al (2009) The influence of growth temperature and precursors' doses on electrical parameters of ZnO thin films grown by atomic layer deposition technique. Microelectron J 40:293–295
17. Luka G, Godlewski M, Guziewicz E, Stahira P, Cherpak V, Volonyuk D (2012) ZnO films grown by atomic layer deposition for organic electronics. Semicond Sci Technol 27:074006–074013
18. Dave PY, Patel KH, Chauhan KV, Chawla AK, Rawal SK (2016) Examination of zinc oxide films prepared by magnetron sputtering. Procedia Technol 23:328–335
19. Bulyga YI, Chebanenko AP, Grinevych VS, Filevska LM (2019) Electrophysical properties of zinc oxide thin films obtained by chemical methods. Photoelectronics 28:11–18
20. Vereshchagin IK (1987) Electroluminescence of crystals. Moscow, Nauka, p 376, In Russian
21. Vorobieva NA (2015) Nanocrystalline ZnO (M) (M = Ga, In) for gas sensors and transparent electrodes. Cand. Diss., Moscow, p 180, In Russian
22. Bonch-Bruevich VL, Zvyakin IP, Kaiper R, Mironova AG, Everline R, Esser B (1981) Electronic theory of disordered semiconductors. Moscow, Nauka, p 383, In Russian

Deposition and Growth of the AlCoCuFeNi High-Entropy Alloy Thin Film: Molecular Dynamics Simulation

O. I. Kushnerov, V. F. Bashev, and S. I. Ryabtsev

1 Introduction

High-entropy alloys (HEAs) are a relatively new class of metallic materials developed by Yeh et al. in 2004. Such alloys usually contain from 5 to 13 basic elements in equiatomic or close to equiatomic concentrations (from 5 to 35%). Due to the high mixing entropy, multicomponent high-entropy alloys typically consist of simple solid solutions with face-centered cubic (FCC) or body-centered cubic (BCC) lattices. Many high-entropy alloys possess unique properties, such as wear resistance, resistance to corrosion and oxidation, radiation resistance, high hardness, and strength [1–5]. Thus, the high-entropy alloys may find use as materials for nuclear reactors applications, medicine, electronics devices, mechanical equipment, rocket casings, and engines. The majority of HEAs were investigated in the as-quenched or homogenized state, whereas much less attention was paid to the study of thin films of high-entropy alloys. However, due to the very high cooling rates required to avoid the formation of complex crystallized phases and freeze the low-ordered structures, HEA is sometimes difficult to synthesize as bulk materials. The study of the growth characteristics of complex multi-element HEA films is an important topic of research considering that thin films can be used in various fields of technology [6]. Several papers [7–9] have been devoted to the study of thin film growth processes of one of the earliest and best-studied HEA of the AlCoCrCuFeNi system. However, a five-element AlCoCuFeNi HEA was later developed. This alloy does not contain Cr, which is commonly used in HEAs and helps to improve their performance, but significantly increases the cost of the alloy. In this work, the processes of deposition and growth of thin films of AlCoCuFeNi HEA on the surface of a monocrystalline silicon substrate were investigated by classical molecular dynamics (MD) simulation.

O. I. Kushnerov (✉) · V. F. Bashev · S. I. Ryabtsev
Oles Honchar Dnipro National University, Gagarin ave., 72, Dnipro 49010, Ukraine

O. Fesenko and L. Yatsenko (eds.), *Nanomaterials and Nanocomposites, Nanostructure Surfaces, and Their Applications*, Springer Proceedings in Physics 263, https://doi.org/10.1007/978-3-030-74741-1_28

2 Simulation Model and Methods

Classical MD simulation studies of deposition and growth of thin films of AlCoCuFeNi HEA have been performed using Large-Scale Atomic/Molecular Massively Parallel Simulator (LAMMPS, Sandia National Laboratory, USA) [10]. Visualization of snapshots and the coordination analysis was done using open visualization tool software OVITO [11]. A three-dimensional cell with periodic boundary conditions only in two horizontal directions x and y was used. The free boundary condition was used in the vertical z-direction to ensure surface growth. The monocrystalline Si (100) substrate was $10 \times 10 \times 2.2$ nm.

To prevent substrate displacement due to the impact of adatoms on the upper surface of the substrate, the positions of several lower atomic planes were fixed. The intermediate region of the substrate above the stationary atomic planes was controlled by a Berendsen thermostat and maintained at a temperature of 300 K which is similar to the experimental temperature mode to ensure isothermal growth conditions. The atoms of the upper layers of the substrate were not subjected to thermostating and were able to move freely under the impact of the deposited atoms (Fig. 1). The five atoms of metals Al, Co, Cu, Fe, and Ni in the equimolar ratio were directed to a substrate every 10 ps, this leads to the atomic flux density of 5×10^{23} atom/(cm^2 s). The rate of 0.5 atom/ps was carefully chosen to allow sufficient time for thermal relaxation with a Berendsen thermostat (i.e., energy relaxation of the substrate after collision). It should be borne in mind that the flux of atoms in the MD simulation is much more than in the experiment, but the obtained data on morphology, structure, and adhesion coefficient are quite adequate [9]. The velocities of the deposited atoms corresponded to the mean kinetic energy of 0.1 eV. The initial positions of the deposited atoms were chosen randomly in the $\{x, y\}$ plane above substrate so that they were outside the range of the potential that describes the interaction in the z-direction. All of Al, Co, Cu, Fe, and Ni atoms were deposited from an initial position 15.7–16 nm above the substrate.

The simulation was carried out using the embedded atom model (EAM) [12] to describe the interaction among Al–Co–Cu–Ni–Fe. EAM potentials include empirical formulas that simulate material characteristics such as surface energies, lattice constants, and the heat of solution. The EAM potential is based on the ideas of density functional theory, which generally states that the energy of a solid is a unique function of electron density.

The EAM potential is expressed as a multi-body potential energy function in the following form [12]

$$E = \sum_i f_i(\overline{\rho}_i) + \frac{1}{2} \sum_i \sum_{j \neq i} \phi_{ij}(r_{ij}) \tag{1}$$

where $f_i(\overline{\rho}_i)$ is the embedding energy function, $\phi_{ij}(r_{ij})$ is a pair interaction potential energy as a function of the distance r_{ij} between atoms i and j that have chemical

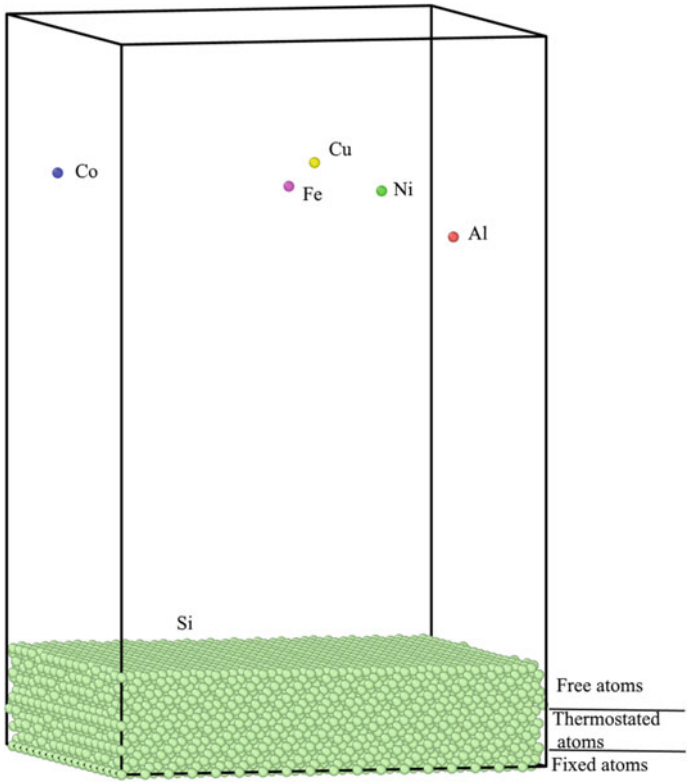

Fig. 1 Schematic picture of the simulation model

sorts a and b, $\overline{\rho}_i$ is the local host electron density. The energy E is the total energy of the atomistic system which comprises the sum of the embedding energy (first term of Eq. (1)) and the short-range pair potential energy (the second term). In the present research, the EAM potential developed by Zhou et al. [13] was used.

The interaction between the atoms of Al, Co, Cu, Fe, Ni, and the Si substrate was modeled using the Lennard–Jones potential

$$E_{ij}(r_{ij}) = 4\varepsilon\left[\left(\frac{\sigma}{r_{ij}}\right)^{12} - \left(\frac{\sigma}{r_{ij}}\right)^{6}\right] \tag{2}$$

with the parameters summarized in [7, 8], and the interaction between the silicon atoms was described using the Stillinger–Weber potential [14].

3 Results and Discussion

During simulation, 25,000 atoms were deposited to the substrate, which corresponds to the nominal equiatomic AlCoCuFeNi composition, but some of them escaping the surface and the resulting film contained only 24,433 atoms. So the sticking coefficient was ≈ 0.98. The composition of the simulated HEA film and the target composition is shown in Table 1.

Thus, the final composition of the simulated AlCoCuFeNi film was quite close to equiatomic.

According to the results of the simulation, it was found that in the initial stages of growth (0–2 ns) the film represents an islet-like structure formed by small clusters (Fig. 2). Later, the growth of the islands and the formation of continuous coating has begun. Due to the limited number of deposited atoms, it was impossible to obtain a completely continuous film even after 50 ns of simulation time. The film obtained at the end of the simulation is shown in Fig. 3. The maximum thickness of the film has

Table 1 Element composition in a simulated thin film of AlCoCuFeNi HEA

Number of atoms	Al	Co	Cu	Fe	Ni	Total
Nominal composition	5000	5000	5000	5000	5000	25,000
Resulting film	4909	4877	4865	4889	4893	24,433

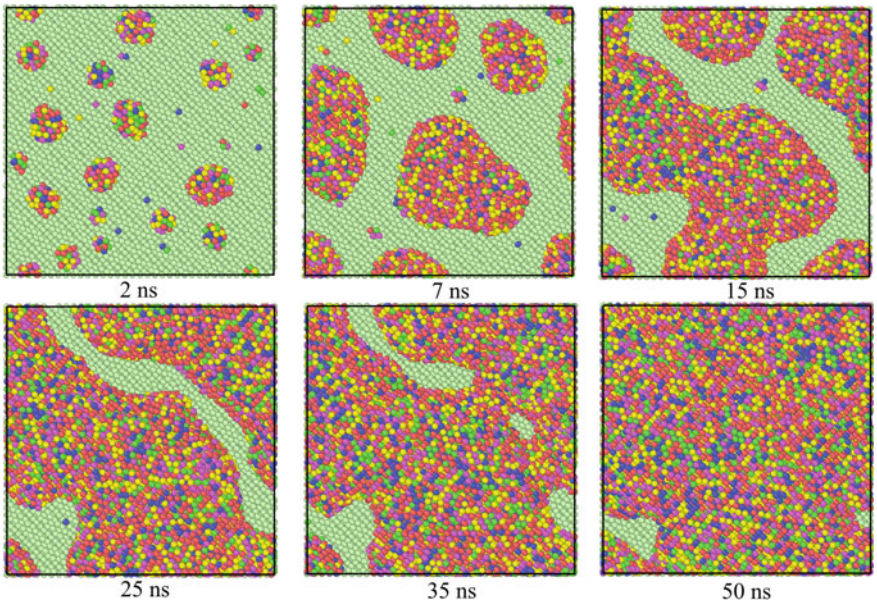

Fig. 2 Snapshots of AlCoCuFeNi thin film deposited on Si substrate at different times (top view): ●—Al, ●—Co, ●—Cu, ●—Fe, ●—Ni

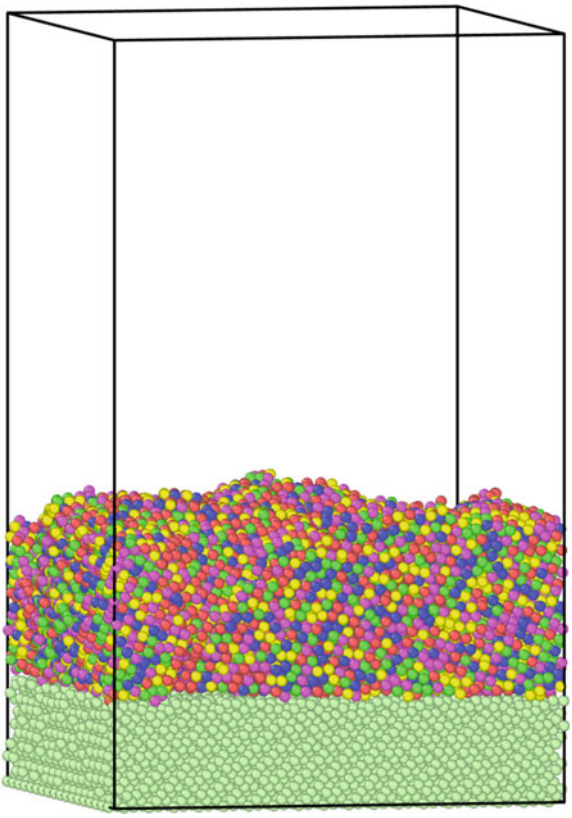

Fig. 3 AlCoCuFeNi thin film obtained after the 50 ns of simulation time

reached 4.3 nm.

Following the results of common neighbor analysis (CNA), the process of crystallization started after ~5 ns of simulation, at the characteristic sizes of islands (clusters) of about 2 nm. At the end of the simulation, after the 50 ns of modeling, the simulated film contains a face-centered cubic (FCC) phase (content 20.5%), a body-centered cubic (BCC) phase (content 13.2%), a hexagonal close-packed (HCP) phase (content 39.7%) (Fig. 4), and an indefinite phase (content 26.6%), which, according to the analysis of the radial distribution of atoms (RDF), has an amorphous structure. It should be noted that in bulk AlCoCuFeNi alloys only the presence of FCC and BCC phases was recorded [15], but at the same time in melt-spun films, the formation of the nanotwin structure and stacking faults in the FCC phase was noted [16]. Thus, the specific features of the distribution of the HCP phase atoms (Fig. 4) lead to the conclusion that this phase must be formed mainly of extrinsic (two HCP layers with an FCC layer between them) and intrinsic (two or more adjacent HCP layers) stacking faults in the lattice of the FCC phase. There are also twin boundaries between the FCC twins (a single layer composed of HCP atoms). As for the amorphous phase, its formation is explained by the high cooling rate that occurs during film deposition at

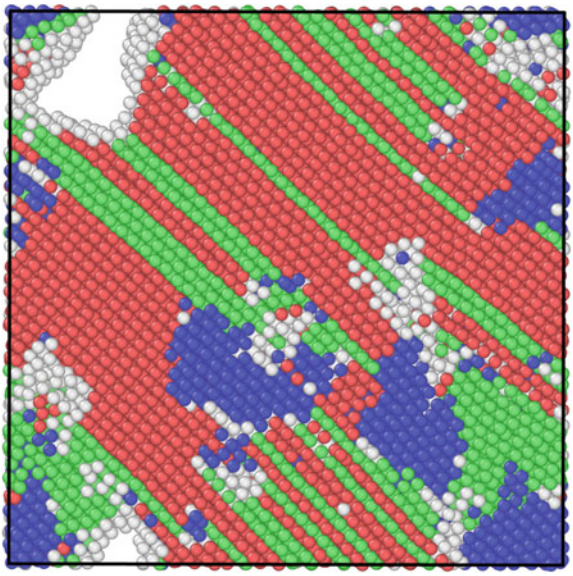

Fig. 4 Snapshot of AlCoCuFeNi thin-film sliced along the substrate plane (top view). Atoms are colored according to CNA analysis results: ●—FCC, ●—BCC, ●HCP, ●—amorphous phase

which some of the atoms do not have time to rearrange and form a crystalline phase. In the context of the present simulation, this concerns mainly atomic layers located near the film surface, while crystallization processes take place in deeper layers.

It is well known from the literature, that there are two main criteria by which the high-entropy alloys are usually characterized. This is the entropy of mixing ΔS_{mix} and the enthalpy of mixing ΔH_{mix}. However, to predict the phase composition of HEAs, some additional parameters were proposed [1, 2]. These parameters include in particular the valence electron concentration (VEC), the thermodynamic parameter Ω, which takes into account the melting temperature, mixing entropy, and the mixing enthalpy. The important parameter is an atomic-size difference between alloy components which is denoted as δ. Using the data from [17, 18], we calculated ΔS_{mix}, ΔH_{mix}, δ, VEC, and Ω for the AlCoCuFeNi HEA (Table 2).

According to [1, 2] the HEA alloys for which $\Omega \geq 1.1$ and $\delta \leq 6.6$ can form solid solutions without intermetallic compounds. However, simple (not ordered) solid solutions form if -15 kJ/mol $< \Delta H_{\text{mix}} < 5$ kJ/mol. The other useful parameter is VEC, which has been proven suitable in determining the phase stability of high-entropy alloys. As pointed in [19] at VEC ≥ 8.0, the sole FCC phase is expected in

Table 2 Electronic, thermodynamic, and the atomic-size parameters of the AlCoCuFeNi HEA

ΔS_{mix}, J/(mol K)	ΔH_{mix}, kJ/mol	Ω	VEC	δ
13.37	−5.28	3.847	8.2	5.323

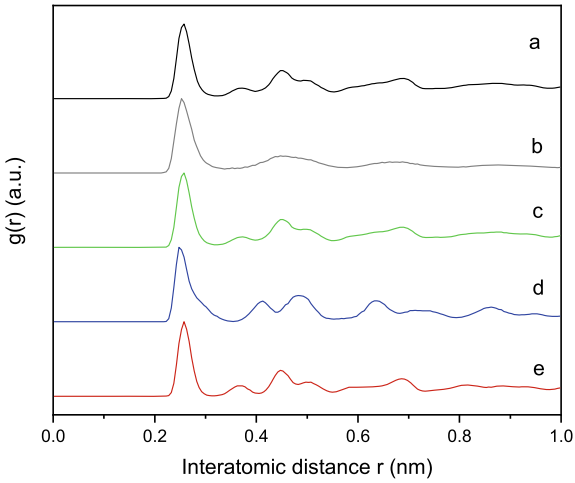

Fig. 5 RDF curves of AlCoCuFeNi thin film: a—whole film, b—amorphous phase, c—FCC phase, d—BCC phase, e—HCP phase

the alloy; at $6.87 \leq \text{VEC} < 8.0$, mixed FCC and BCC phases will coexist and the sole BCC phase is expected at $\text{VEC} < 6.87$. Thus, the simulation results, as well as the experimental results, generally confirm the validity of the above criteria, except for the VEC parameter. But, if the value of VEC is close to the boundary values, predictions of the phase compositions sometimes do not work [5].

Figure 5 presents the total RDF curves after 50 ns of simulation time. RDF patterns are obtained both for the film as a whole and for individual phases separated by CNA analysis. It is clearly visible, that the RDF form of an indefinite phase is intermediate between liquid and crystal, indicating an amorphous structure. The peaks on the RDF curves represent the successive distances between neighbors for different phases in the simulated film. So, from the RDF pattern for whole film these distances are: 1-st neighbor—0.2575 nm, 2-st neighbor—0.3725 nm, 3-st neighbor—0.4525 nm, 4-st neighbor—0.4925 nm.

Determining the distances between the nearest neighbors for the BCC and FCC lattices made it possible to estimate the lattice parameters for these phases. Table 3 shows the comparison between estimated parameters of the BCC and FCC lattices from the present MD simulation and the experimental results (Table 3).

As can be seen from Table 3, calculated lattice parameters are in good agreement with the experimental results, taking into account that the estimated average film temperature after 50 ns simulation was above room temperature and was ~350 K.

Table 3 Calculated and experimental lattice parameters for AlCoCuFeNi HEA

Lattice parameter *a*, nm	Experiment, bulk alloy	Experiment, melt-spun ribbon	Calculated
BCC phase	0.2878	0.2872	0.2895
FCC phase	0.3624	0.3618	0.3670

4 Conclusions

Molecular dynamics simulation was performed to describe the processes of growth and crystallization of thin AlCoCuFeNi HEA films. The structural characteristics and phase composition of films were examined utilizing CNA and RDF. According to simulation results, the growth of AlCoCuFeNi films occurs via a formation of three-dimensional adatom clusters or islands with subsequent coarsening and coalescence. The estimated lattice parameters of the BCC and FCC phases are in good agreement with the lattice parameters of AlCoCuFeNi alloy obtained from the experiment.

References

1. Murty BS, Yeh JW, Ranganathan S, Bhattacharjee PP (2019) High-entropy alloys. 2nd Edn. Elsevier
2. Gao MC, Yeh J-W, Liaw PK, Zhang Y (2016) High-entropy alloys: fundamentals and applications. Springer, Berlin
3. Miracle DB, Senkov ON (2017) A critical review of high entropy alloys and related concepts. Acta Mater 122:448–511. https://doi.org/10.1016/j.actamat.2016.08.081
4. Bashev VF, Kushnerov OI (2014) Structure and properties of high-entropy CoCrCuFeNiSn x alloys. Phys Met Metallogr 115:692–696. https://doi.org/10.1016/j.jallcom.2016.04.064
5. Bashev VF, Kushnerov OI (2017) Structure and properties of cast and splat-quenched high-entropy Al–Cu–Fe–Ni–Si alloys. Phys Met Metallogr 118:39–47. https://doi.org/10.1134/S0031918X16100033
6. Gulivets AN, Zabludovsky VA, Shtapenko EP, Kushnerev AI, Dergachov MP, Baskevich AS (2002) Multilayer compound Co-P films with controlled magnetic properties. Trans IMF 80:154–156. https://doi.org/10.1080/00202967.2002.11871457
7. Xie L, Brault P, Thomann A-L, Bauchire J-M (2013) AlCoCrCuFeNi high entropy alloy cluster growth and annealing on silicon: a classical molecular dynamics simulation study. Appl Surf Sci 285:810–816. https://doi.org/10.1016/j.apsusc.2013.08.133
8. Xie L, Brault P, Thomann A, Yang X, Zhang Y, Shang G (2016) Molecular dynamics simulation of Al–Co–Cr–Cu–Fe–Ni high entropy alloy thin film growth. Intermetallics 68:78–86. https://doi.org/10.1016/j.intermet.2015.09.008
9. Xie L, Brault P, Bauchire J-M, Thomann A-L, Bedra L (2014) Molecular dynamics simulations of clusters and thin film growth in the context of plasma sputtering deposition. J Phys D Appl Phys 47:224004. https://doi.org/10.1088/0022-3727/47/22/224004
10. Plimpton S (1995) Fast parallel algorithms for short-range molecular dynamics. J Comput Phys 117:1–19. https://doi.org/10.1006/jcph.1995.1039
11. Stukowski A (2010) Visualization and analysis of atomistic simulation data with OVITO–the Open Visualization Tool. Model Simul Mater Sci Eng 18:015012 . https://doi.org/10.1088/0965-0393/18/1/015012
12. Daw MS, Foiles SM, Baskes MI (1993) The embedded-atom method: a review of theory and applications. Mater Sci Reports 9:251–310. https://doi.org/10.1016/0920-2307(93)90001-U
13. Zhou XW, Johnson RA, Wadley HNG (2004) Misfit-energy-increasing dislocations in vapor-deposited CoFe/NiFe multilayers. Phys Rev B 69:144113. https://doi.org/10.1103/PhysRevB.69.144113
14. Stillinger FH, Weber TA (1985) Computer simulation of local order in condensed phases of silicon. Phys Rev B 31:5262–5271. https://doi.org/10.1103/PhysRevB.31.5262
15. Liu C, Peng W, Jiang CS, Guo H, Tao J, Deng X, Chen Z (2019) Composition and phase structure dependence of mechanical and magnetic properties for AlCoCuFeNix high entropy alloys. J Mater Sci Technol 35:1175–1183. https://doi.org/10.1016/j.jmst.2018.12.014

16. Yu PF, Cheng H, Zhang LJ, Zhang H, Ma MZ, Li G, Liaw PK, Liu RP (2016) Nanotwin's formation and growth in an AlCoCuFeNi high-entropy alloy. Scr Mater 114:31–34. https://doi.org/10.1016/j.scriptamat.2015.11.032
17. Takeuchi A, Inoue A (2005) Classification of bulk metallic glasses by atomic size difference, heat of mixing and period of constituent elements and its application to characterization of the main alloying element. Mater Trans 46:2817–2829. https://doi.org/10.2320/matertrans.46.2817
18. Li W-K, Zhou G, Mak TCW (2008) Advanced structural inorganic chemistry. Oxford University Press, Oxford, New York
19. Guo S, Ng C, Lu J, Liu CT (2011) Effect of valence electron concentration on stability of fcc or bcc phase in high entropy alloys. J Appl Phys 109:103505. https://doi.org/10.1063/1.3587228

Semiconductor Magnetosensitive Structure Two-Dimensional Model Representation

M. A. Glauberman and Ya. I. Lepikh

1 Introduction

The operation of all semiconductor magnetosensitive structures (MSS) used as magnetic field sensors is known to be based on the Lorentz force action on moving charge carriers. Depending on the carrier types that provide the effect of magnetic sensitivity, MSS are divided into unipolar and bipolar. Until the beginning of the last twenty years, only unipolar MSS were used—Hall plates and magnetoresistors, in which the fundamental galvanomagnetic effects (Hall and Gauss) are used directly in the form in which they were discovered more than 100 years ago. These effects to the present time have been quite deeply studied, which means the exhaustion of the capabilities and the appropriate sensors certain obsolescence.

A natural alternative to unipolar structures is bipolar magnetosensitive structures (BMS). The very fact of non-basic carriers using determines such structures variety in terms of physical features—in terms of methods of carrier generating and a useful signal obtaining, as well as the mechanisms of magnetic sensitivity. The latter, as a rule, act together, and each of them, manifesting itself to a greater or lesser extent depending on the design and technological parameters and the structure electrical regime, realize its influence on its electrophysical properties and thus stipulate the BMS functionality potential diversity. But the same circumstance creates significant difficulties in their study because of the difficulty of distinguishing the individual mechanism contribution to the observed total effect [1, 2].

On the other hand, when studying the BMS, as well as the MSS in general, there are difficulties associated with modeling. As opposed to the converters of other physical meanings, these structures due to the main vector magnitude specific orientation

M. A. Glauberman · Ya. I. Lepikh (✉)
Odesa I.I. Mechnikov National University, str. Dvoryanska, 2, Odesa 65982, Ukraine
e-mail: ndl_lepikh@onu.edu.ua

O. Fesenko and L. Yatsenko (eds.), *Nanomaterials and Nanocomposites, Nanostructure Surfaces, and Their Applications*, Springer Proceedings in Physics 263, https://doi.org/10.1007/978-3-030-74741-1_29

(current, magnetic induction, and Lorentz force) are purely three-dimensional. Even the simplest model approximation—the two-dimensional one, which is widely used today, is often presented without satisfactory justification.

2 Modeling Principles and Mathematical Problem Formulation

Construction of the adequate mathematical models that allow to take into account the multilayer systems all components mutual influence on each other, as well as various external factors (optical radiation, electric and magnetic fields, etc.) is an urgent task of semiconductor electronics [3–5]

The specificity of semiconductor magnetosensitive structures modeling is the principle impossibility of using linear one-dimensional models widely used in other fields of semiconductor physics and semiconductor devices because such structure action is based on the charge carrier's direction changing. If in the study of unipolar or non-injection bipolar structures, some important correlations can be obtained in a linear one-dimensional representation, reducing the magnetic field deflecting effect to changing the structure electrophysical parameters (occurrence of Hall potential difference in Hall sensors, change in the magnetoresistor sample resistance and the effective lifetime in the galvanomagnetic combination (GMR) converters, then for injection structures inevitably strictly have to issue from the equations of continuity for carriers of both types and the Poisson equation. In the stationary case, these equations can be written as [6]:

$$\operatorname{div} E = -e(p - n + N_D - N_A); \tag{1}$$

$$\operatorname{div} j = \pm e\,[g - R(p, n, \psi)], \tag{2}$$

where E—electric intensity; e—electron charge; N_D, N_A—donors and acceptors concentrations, respectively; j—the given type carriers current density; g—generation rate (of injection sources power density for non-equilibrium carriers); R—the recombination rate. Here in (2) the upper sign is chosen for holes, the lower—for electrons.

Here

$$j(B) = j_0 \pm m^*[j(B)'B], \tag{3}$$

where

$$j_0 = J(0) = ec\mu E \mp eD \operatorname{grad} c; \tag{4}$$

D is the given type carriers diffusion coefficient; μ—charge carrier mobility; μ^*—Hall mobility; c—charge concentration; B—magnetic field induction.

The boundary condition setting depends, generally speaking, on the choice of a specific physical model and electrical mode. In typical cases, Dirichlet conditions are chosen (ohmic contacts equipotency and non-basic carriers zero concentration on the boundary with the collector charge region volume) and Neumann homogeneous (the current density normal component zeroing on insulating surfaces) [2, 6, 7].

This problem solution is possible only by numerical methods. However, at the injection low level, an analytical approach becomes possible. In this case, ignoring the electric field dependence on the carrier concentration, which allows excluding from consideration the Poisson equation in the base volume. On the basis of (1)–(4) for the non-basic carriers, excess concentration can be written

$$\begin{aligned} &\mu \operatorname{div}(c\,E) \mp D \operatorname{div} \operatorname{grad} c \pm \mu^* \mu \operatorname{div}\{c[E \times B]\} \\ &\quad - \mu^* D \operatorname{div}[\operatorname{grad} c \times B] = \pm(g - R). \end{aligned} \tag{5}$$

At obtaining of (5), we used the assumption of mutual perpendicularity of the vectors j and B, which, without affecting the conclusion legitimacy, allows us to solve a problem on j and for weak magnetic fields to give the expression in more convenient form

$$j = \{j_0 \pm \mu^*[j_0 \times B]\}/\{1 + (\mu^* B)^2\} \approx j_0 \pm \mu^*[j_0 \times B]. \tag{6}$$

Assuming, in addition, the accelerating field is homogeneous and directed along the OX axis (Fig. 1), in Cartesian form can be written

$$L^2\left(\frac{\partial^2 c}{\partial x^2} + \frac{\partial^2 c}{\partial y^2} + \frac{\partial^2 c}{\partial z^2}\right) \mp 2\eta L \frac{\partial c}{\partial x} - 2\eta L \mu^*_{\text{eff}} B \frac{\partial c}{\partial y} - c = -g\tau \tag{7}$$

where $\eta = E_0 L/(2\varphi_T)$—field coefficient; E_0—basis electric intensity value at the emitter end; L—injected carrier diffusion length $\varphi = \mu^*_{mn} B \ll 1$, μ^*_{eff}—"effective Hall mobility"—parameter that characterizes the deviation (equal to μ^*_{mn} or $\mu^*_{mn} + \mu^*_{mj}$, respectively, when the deviation is only by the Lorentz force or together with the Hall field); g—source injection volumetric power density; τ—non-basic carrier lifetime.

It is important to note that in the accelerating field absence, the third term in the left part of (7), the only term containing the magnetic induction value, curl up to zero. This means that the concentration dependence on the magnetic field occurs only in the case of drift transfer, but not diffusion [5]—a fact ignored by the authors of the known works on modeling MSS [2, 4].

The combined effect of all MSS sensitivity mechanisms is taken into account by the continuity equation, but the difficulties associated with its analytical solution force us to look for simplified models [6], where idea of these mechanisms plays a

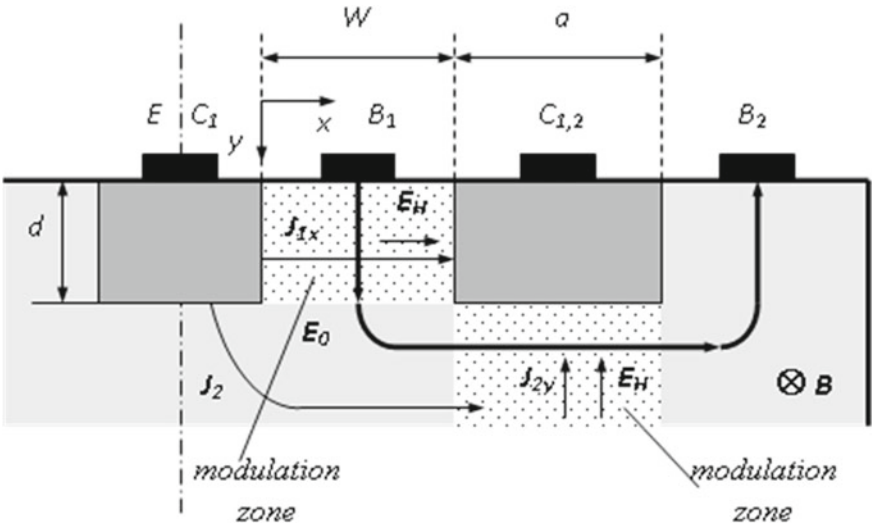

Fig. 1 Action of the transfer coefficient and deviation modulation in the MTS base with a longitudinal axis. E—emitter; B_1, B_2—basis; C_1, C_2—collectors; W—basis size (from emitter to collector); a—collector length; d—emitter and collector region depth; J_{1x}, J_{2y}—emitter current in X- and Y-directions; E_H—Hall field strength

key role. In the conditions of injection low level, it is accepted to allocate four such mechanisms:

– deviation of injected carriers by Lorentz force;
– deviation of injected carriers by Hall field force;
– modulation of the transfer coefficient;
– modulation of injection.

However, as was noted, these ideas themselves are not clearly defined, which makes it necessary to clarify them. It was also shown that qualitatively both mechanisms of deviation are identical and that injection modulation is not a characteristic for BMS effect. Then, considering the injection modulation as a side factor, but nevertheless such that it needs to be taken into account, we get two main effects:

1. Transfer coefficient modulation.
2. Flow redistribution.

The specificity of planar technology determines the MTS classification on the injected media current direction in the absence of a magnetic field and on the direction component of the magnetic induction which are registered relative to the structure technological surface [8]. According to the first feature, MTS is divided into vertical and horizontal, where the current direction is, respectively, perpendicular and parallel to the sample surface. For the second case, the MTS is divided into longitudinal and transverse magnetic axes (the magnetic induction component, respectively, parallel and perpendicular to this surface). It is obvious that for vertical MTS realization is

possible only with a longitudinal magnetic axis, while for horizontal—with either of the two directions.

Technological features [9, 10] also cause additional opportunities to create an accelerating electric field in drift structures:

1. The internal field due to the impurity exponential distribution in the basic diffusion;
2. The bulk charge field of the inversely displaced collector p–n junction.

According to [11], the effect of the MST transfer coefficient modulation with a longitudinal axis is explained in Fig. 1. The volume of the base can be conditionally divided into two active areas, in which, according to the accepted idea, the considered mechanism and the deviation mechanism are appeared.

In the modulation zone, the collector current in the absence of a magnetic field is determined by the current component of the injected carriers j_z, which has, due to the E_0 direction along the OY axis, diffuse nature. The inclusion of the magnetic field leads to the appearance of the current directed along the OX axis drift component due to the Hall field $E_н = \mu^*_{mj} B E_0$.

Because of the mathematical complexity, the continuity equation in all known works, even when using numerical methods and even in a simplified form (7), is solved exclusively in the two-dimensional approximation.

Figure 2a–c is shown two-dimensional structure models (in cross section with the XOY plane) of, respectively, vertical (2a) and horizontal with longitudinal (2b) and transverse (2c) magnetic axes.

Vertical structures with drift in the depleted region (Fig. 3c, d) are excluded from consideration [11] because of their physical discordance to MTS class, and, for the same reason, structures such as Fig. 3a, in which the effect of the magnetic field on the flux in the base was small in comparison with the deviation in the depleted layer.

As can be seen from the figure, in the active regions of all structures (highlighted in the figure) the conditions of the injected carriers transfer are identical.

Thus, in the two-dimensional approximation, the method of injected carrier's concentration field determining (including the boundary conditions setting) is independent on the MTS specific type [12].

However, as already noted, if for vertical (Fig. 3) and horizontal structures with a longitudinal axis (Fig. 4) two-dimensional consideration is quite legitimate (in extreme cases, with the appropriate geometry choice), then for structures such as Fig. 5 requires a special justification (which, incidentally, was ignored in the known works on their modeling [6, 13]).

The question of the legitimacy of MTS two-dimensional modeling with a transverse axis [14] includes two tasks—a two-dimensional description of the injected media transfer in the base and emitter two-dimensional modeling.

The first problem is easily solved by the transition from three-dimensional (volume) concentration c to two-dimensional (surface) C:

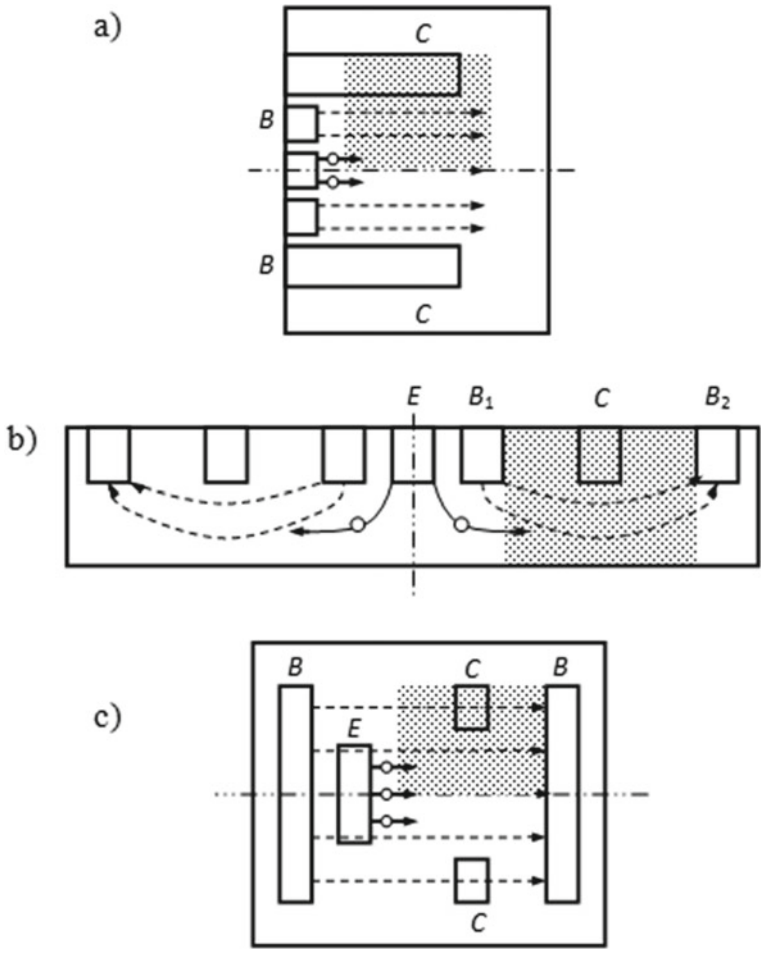

Fig. 2 Equivalence of the MTS two-dimensional model conception of different types

$$C \equiv \int_0^{z_0} c(x, y, z)\, \mathrm{d}z \tag{8}$$

where the coordinate origin is selected on the technological surface, and z_0 is the coordinate of the opposite surface. We also agree further on the capital letters *N, P* to denote the carrier surface concentrations of a specific type, corresponding to the volume—*n, p* (7).

Because of the mathematical difficulties, the continuity equations in all known works, even when numerical methods are used [15] and even in a simplified form, are solved exclusively in the two-dimensional approximation.

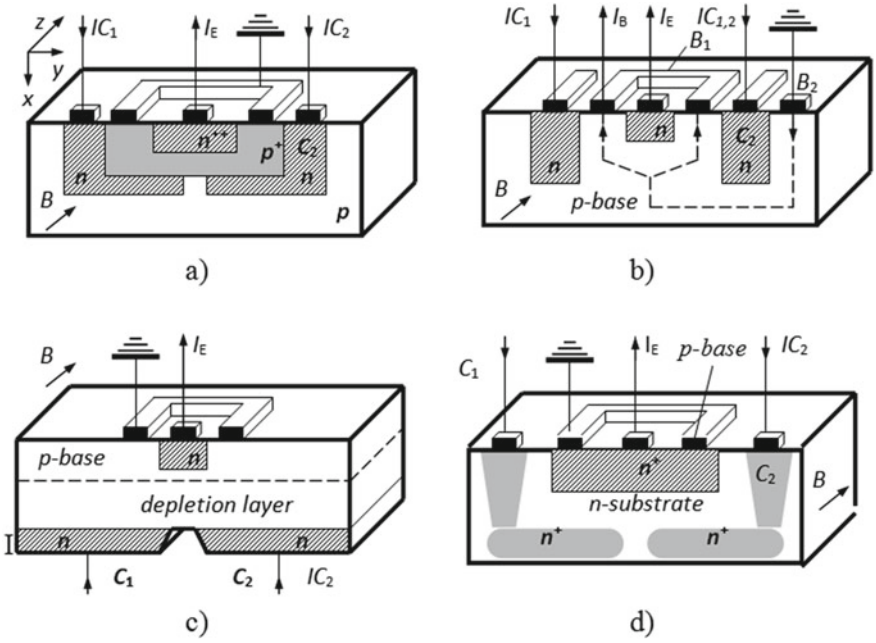

Fig. 3 Vertical MTS. Structures with a deviation in the base (**a**, **b**) and in the collector junction depleted region (**c**, **d**)

Then Eq. (7), after integration of both parts within (8) and under the natural assumption of the bulk injection sources absence ($g \equiv 0$), takes the form

$$L^2\left(\frac{\partial^2 C}{\partial x^2} + \frac{\partial^2 C}{\partial y^2}\right) \mp 2\eta L \frac{\partial C}{\partial x} - 2\eta L \mu^*_{\text{eff}} B \frac{\partial C}{\partial y} - C = -\Gamma\tau \tag{9}$$

where

$$\Gamma(X,\ y) = \frac{L^2}{\tau}\int\limits_0^{z_0} \frac{\partial^2 c}{\partial z^2}\mathrm{d}z = -D\left.\frac{\partial c}{\partial z}\right|_{z=0} \equiv \frac{1}{e} j_Z(x, y) \tag{10a}$$

From the comparison of the (7) and (9) right parts, it turns out that the Γ amount has a formal meaning of the surface (two-dimensional) power density of injection sources—the number of carriers generated per unit surface $z = 0$ (coming to the base through this surface unit). On the other hand, according to (10a), its physical content is a normal component of the real (three-dimensional) injection current density j_z through this surface, relating to the unit of charge.

Expression (10a) is written for the case $\partial c/\partial z = 0$ at $z = z_0$, which is realized in the MTS making on a single crystal or on an insulating substrate. For structures

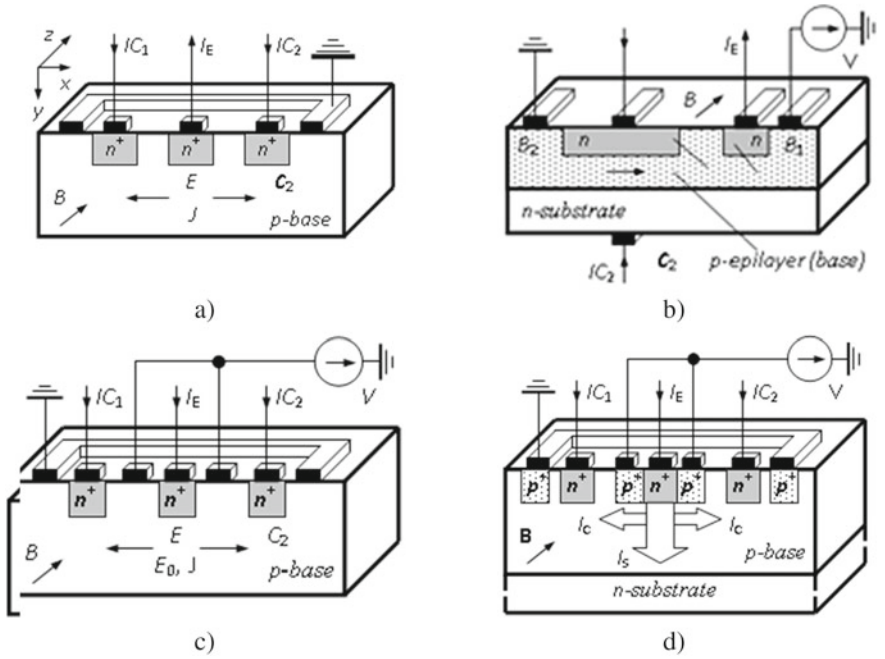

Fig. 4 Horizontal MTS with a longitudinal magnetic axis. **a**—with diffusion transfer; **b**, **c**, **d**—drift (the latter—with the lateral injection suppression)

made in the epitaxial layer on a substrate of the opposite conductivity type, the extracting effect of the *p–n* junction—substrate—epilayer can be taken into account by introducing of effective lifetime τ_{eff} instead of bulk τ. To determine τ_{eff}, it is convenient, assuming for simplification $E_0 = B = g = 0$, to represent Eq. (7) in the form.

$$D\left(\frac{\partial^2 c}{\partial x^2} + \frac{\partial^2 c}{\partial y^2}\right) = \frac{c}{\tau} - D\frac{\partial^2 c}{\partial z^2},$$

where the right part after integration by z is determined as the ratio of surface concentration to effective life:

$$\frac{C}{\tau_{\text{eff}}} \equiv \frac{C}{\tau} - D\frac{\partial c}{\partial z}\bigg|_{z=z_0}$$

from which

$$\tau_{\text{eff}} \equiv \left(\frac{1}{\tau} - \frac{D}{C}\frac{\partial c}{\partial z}\bigg|_{z=z_0}\right)^{-1} = \tau_{eff} \equiv \left(\frac{1}{\tau} + \frac{j_s}{eC}\right)^{-1} \tag{10b}$$

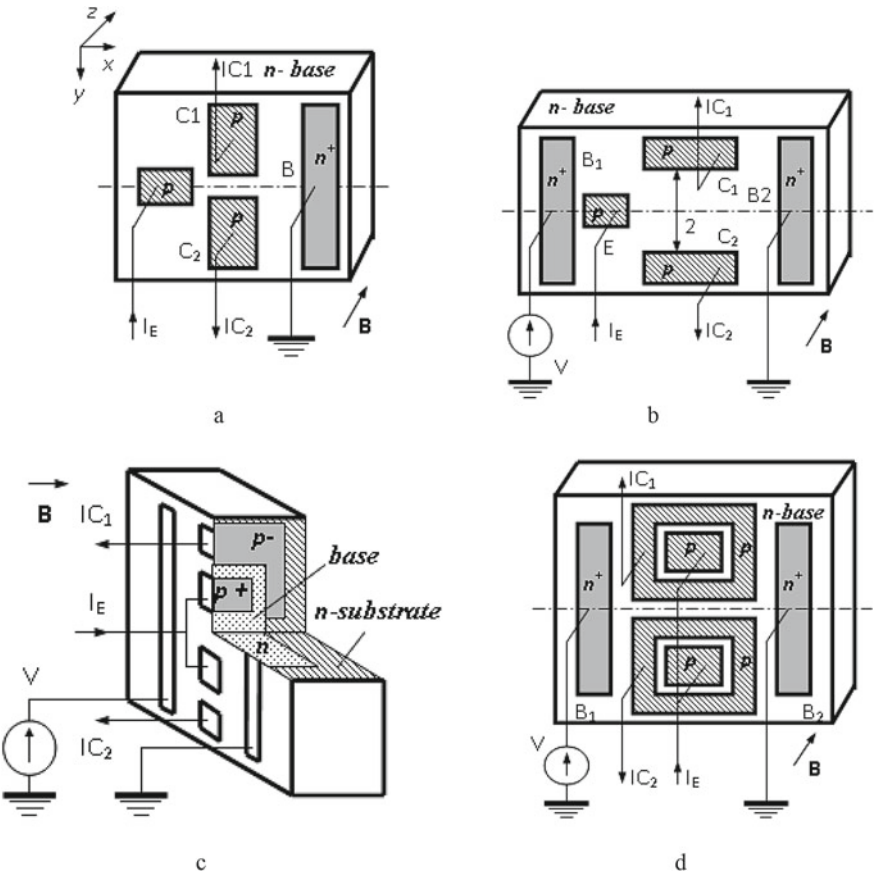

Fig. 5 Horizontal BMT with a transverse magnetic axis. **a**, **b**—in accordance with diffusion and drift transfer; **c**, **d**—optimized concerning the injection modulation

While the transition from three-dimensional configurations to two-dimensional through (8) is trivial and for non-injection ($\Gamma = 0$ in (9)) structures is widely used either with special cautions [15], or, more often, by threshed, the use of (10b) for injection structures modeling requires special consideration.

3 Conclusions

1. The considered two-dimensional representation of MTS model of different types allows to construct such structure physical and mathematical models that give the chance to define the MTS magnetosensitivity mechanisms, in particular of

the two-collector magnetotransistor (TMT) which can be useful in the practical design of devices of various constructions.
2. The drift component of charge current flow is adequately described by the continuity equation, which takes into account the Lorentz force action, when the boundary conditions of the first kind are superimposing on the collector transition boundaries.
3. The flow diffusion component does not feel the influence of the magnetic field in the transistor structure volume.

References

1. Glauberman MA, Kozel VV, Nakhabin AV (2000) Charge-carrier transport in a double-collector magnetotransistor. Semiconductors 34:603–605. https://doi.org/10.1134/1.1188036
2. Glauberman MA, Egorov VV, Kanishcheva NA, Kozel VV (2010) Zavisimost effektivnosti preobrazovaniya magnitotranzistora ot vremeni zhizni inzhektirovannykh nositeley (Dependence of the conversion efficiency of the magnetotransistor on the lifetime of the injected carriers), 4th International Scientific and Technical Conference "Sensor Electronics and Microsystem Technologies" SEMST-4. Odessa, June 28–July 2, 2010, Abstracts, Odesa Astroprint: 194
3. Gordiєnko YuO, Larkin SYu, Lepikh YaI ta in. (2011) Teoretichni aspekti modelyuvannya ta proyektuvannya rezonatornikh zondiv dlya skanuyuchoï mikroskopiï (Theoretical aspects of the modeling and design of resonator probes for scanning microscopy). Sens Electron Microsyst Technol 2(3):97–107
4. Glauberman M, Egorov, Kulinich O (2012) Magnetotransistors: physics, modeling, application of LAP LAMBERT Academic Publishing GmbH & Co.KG:136
5. Lepikh YaI, Gordiєnko YuO, Dzyadevich SV ta in (2011) Intelektualni vimiryuvalni sistemi na osnovi mikroyelektronnikh datchikiv novogo pokolinnya (Intelligent visual systems based on microelectronic sensors of the new generation). Monograph Odesa Astroprint: 352
6. Guvenc MG (1988) Finite-element analysis of magnetotransistor action. IEEE Trans Electron Dev 35(11):1851–1860
7. Nathan A, Maenaka K, Allegretto W, Baltes H, Nakam T (1989) The Hall effect in integrated magnetotransistors. IEEE Trans Electron Dev 36(1):108–117
8. Vikulina LF, Glauberman MA (2000) Fizika sensoriv temperaturi i magnitnogo polya (Physics of temperature and magnetic field sensors) Odesa Mayak, 244
9. Krasyukov AYu, Krupkina TYu, Chaplygin YuA (2015) Modelirovaniye kharakteristik i optimizatsiya konstruktivno-tekhnologicheskikh parametrov integralnykh magnitochuvstvitelnykh elementov v sostave mikro- i nanosistem MIyeT. Izvestiya vysshikh uchebnykh zavedeniy. Elektronika (Modeling of characteristics and optimization of constructive and technological parameters of integral magnetosensitive elements as part of micro- and nanosystems MIET, Izvestiya of higher educational institutions. Electronics 20 (5):489–496
10. Kozlov AV, Krasjukov AY, Krupkina TY (2016) Simulation of characteristics and optimization of the constructive and technological parameters of integrated magnetosensitive elements in micro and nanosystems. Russ Microelectron 45:522–527. https://doi.org/10.1134/S1063739716070088
11. Rahman M, Hassan A, Imamuddin M (1987) Effect of magnetic field on the electrical paramters of the junction transistors with theoretical explaination. Indian J Pure Appl Phys 25(5 & 6):231–234
12. Zieren V (1984) Geometrical analysis of the offset in buriedcollector vertical magnetotransistor. Sens Actuators 5(3):199–206

13. Persiyanov TV, Barabich IN, Parsamyan DK, Tairova DA (1986) Chislennyy dvumernyy analiz raspredeleniya neosnovnykh nositeley zaryada v baze mnogokollektornykh magnitotranzistorov(Numerical two-dimensional analysis of the distribution of minority charge carriers in the base of multi-collector magnetotransistors) In Matematicheskoye modelirovaniye i eksperimentalnyye issledovaniya elektricheskoy relaksatsii v elementakh mikroskhem (Mathematical modeling and experimental research of electrical relaxation in microcircuit elements) Moscow, pp 66–72
14. Davies LW, Wells MS (1971) Magneto-transistor incorporated in an integrated circuit. In: Proceedings IREE Australia, June, pp 235–238
15. Baltes GP, Popovich RS (1986) Integralni napivprovidnikovi datchiki magnitnogo polya TIIER (Integral magnetic field sensors TIIER) 74(8):60–90

Thermodynamic States and Transitions Diagrams in Surface Engineering for the Material Degradation Prevention

V. M. Ledovskykh, Yu. P. Vyshnevska, I. V. Brazhnyk, and S. V. Levchenko

1 Introduction

Development of the degradation prevention methods for metallic materials and alloys remains a challenging topic. Metal surface modification for obtaining in situ nano- and sub-nanoscaled protective layers constitutes a promising approach that may also be used for functionalization.

Furthermore for continuously operated systems where favorable conditions could be engineered the sustainable protection with the layers regeneration may be implemented. At the same time, surface engineering methods based on in situ synthesis and deposition of non-metallic phase layers are found to be highly dependent on the accuracy of theoretical models that represent electrochemical processes in target systems.

In the present work, the application of the thermodynamic states and transitions diagram for analysis of the phase layers formation in a multicomponent environment has been demonstrated and the theoretical model that represents coaction mechanism of the additives of different nature has been further improved and refined.

V. M. Ledovskykh · S. V. Levchenko
National Aviation University, Liubomyra Huzara Ave, 1, Kyiv 03058, Ukraine

Yu. P. Vyshnevska (✉)
National Technical University of Ukraine "Igor Sikorsky Kyiv Polytechnic Institute", 37, Peremohy Ave., Kyiv 03056, Ukraine
e-mail: vishnevsk@ukr.net

I. V. Brazhnyk
Gimasi SA, Piazzale Roncàa, 4, 6850 Mendrisio, Switzerland

O. Fesenko and L. Yatsenko (eds.), *Nanomaterials and Nanocomposites, Nanostructure Surfaces, and Their Applications*, Springer Proceedings in Physics 263, https://doi.org/10.1007/978-3-030-74741-1_30

2 Materials and Experimental Methods

Corrosion tests and determination of the inhibitor efficiency were performed gravimetrically according to the standard procedure. Tests were performed on steel 08 kp in the aqueous saline solutions with the composition: 0.3 g/l NaCl; 0.3 g/l Na_2SO_4; and 0.3 g/l $NaHCO_3$, exposure time at 25 °C temperature was 72 and 168 h.

The ratio of the solution volume (ml) to the area of metal sample (cm^2) was 10:1. The inhibition efficiency was determined by the equation $Z = \left[\left(K_m - K'_m\right)/K_m\right] \cdot 100\%$, the inhibition coefficient—by the equation $\gamma = K_m/K'_m$, where K_m, K'_m—is the corrosion rate of metal in solutions without and with inhibitor ($K_m = \Delta m/(S \cdot \tau)$, where Δm is the loss of the sample weight, g; S is the sample area, m^2; τ is the exposure time, h).

Polarization measurements were carried out in potentiostatic and potentiodynamic regimes in a three-electrode cell with separated cathodic and anodic compartments. Carbon steel 08 kp was used as the working electrode, platinum—as the counterelectrode and an Ag|AgCl|KCl(sat.) electrode—as the reference one. In this paper, the potential values are given with respect to the normal hydrogen electrode potential.

Investigation of the morphological characteristics and elemental composition of the surface protective films of the inhibitive compositions and distribution of elements within the phase film were carried out with the scanning electron microscope (EVO-50, Zeiss, Germany) equipped with the energy-dispersive detector (INCA PENTA FET × 3, Oxford Instruments,. Co., UK) and using Auger microprobe JAMP-9500F in the scanning electron microscopy mode. The energy of electron beam—3 keV, current—0.5 μA. During the profiling, the surface of the samples was bombarded with argon ions (ion etching) with the energy of 4 keV. The pickling rate is 40 Å/min.

3 Results and Discussion

3.1 Theoretical Background

During contact of the metals with aqueous solutions of electrolytes, the corrosion process may occur that leads to the metal oxidation and formation of more stable compounds with the components of the environment. Corrosion in the oxidizing medium is accompanied by the weight loss of metal and degradation of its mechanical and functional properties.

Metal corrosion in conductive solutions follows the electrochemical mechanism and obeys to its general regularities. Immersion of the metal into a solution where only its ions are present, an equilibrium will be established between the reduced and oxidized forms of the metal, the electric double layer appears and the metal electrode acquires a certain potential:

$$\mathrm{Me} + \mathrm{mH_2O} \rightleftarrows \mathrm{Me(H_2O)_m^{n+}} + \mathrm{n}e^-$$

The equilibrium potential of the metal electrode under constant conditions and the composition of the system remains constant indefinitely while its dependence on activity (for highly dilute solutions—on the molar concentration) of the potential-determining ions is represented by the Nernst equation. Electrode equilibrium is characterized by equal rates of ionization of the metal and the reduction of its cations. Thus, the weight loss of metal does not occur ($\Delta m = 0$) [1, 2].

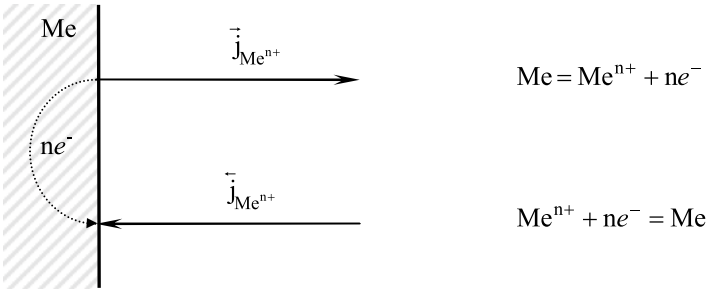

Equilibrium state may be described as follows: $\vec{j}_{Me^{n+}} = \overleftarrow{j}_{Me^{n+}} = j_0$, where j_0—the density of exchange current.

In the case, when the solution along with the oxidant (the metal cations) also contains other particles that are able to attach electrons (depolarizers D), the balance of the metal electrode is shifted transferring the system to a disequilibrium state that causes the corrosion process and loss of metal weight ($\Delta m > 0$):

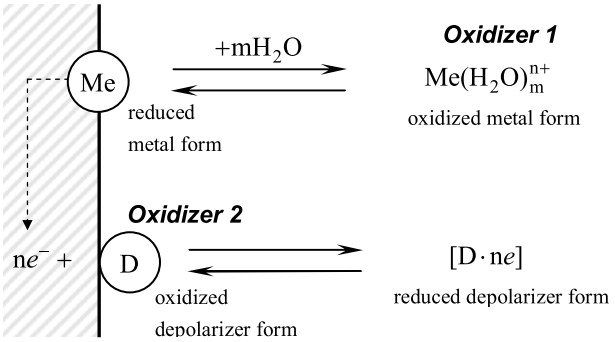

Reaction schema for the stationary corrosion process may be presented as:

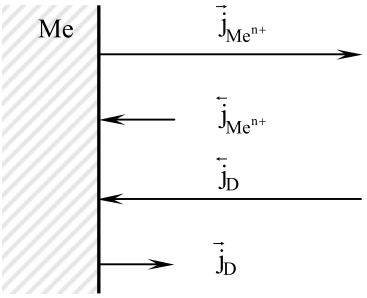

where $\vec{j}_{Me^{n+}} + \vec{j}_{D} = \overleftarrow{j}_{D} + \overleftarrow{j}_{Me^{n+}}$

If $\underset{Me^{n+}}{\overleftarrow{j}} \ll \vec{j}_{Me^{n+}}$ and $\overrightarrow{j_D} \ll \overrightarrow{j_D}$ then the following approximate representation may be applicable:

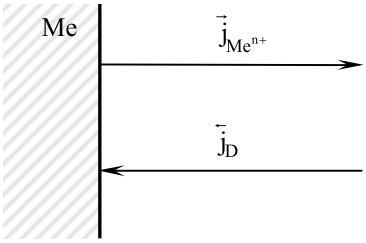

$\vec{j}_{Me^{n+}} \approx \overleftarrow{j}_{D} \approx j_{corr}$, A/cm^2

where j_{corr} represents metal corrosion rate in current units.

During corrosion with oxygen depolarization, the oxidant 2 is oxygen molecules. Depending on the pH of the medium, they are able to reduce according to the following reactions:

$$\text{Neutral and alkaline media } O_2 + 2H_2O + 4e^- = 4OH^-$$
$$\text{Acidic media } O_2 + 4H^+ + 4e^- = 2H_2O$$

In the case of corrosion with hydrogen depolarization, the conjugate cathodic reactions are:

$$\text{Neutral and alkaline media } 2H_2O + 2e^- = H_2 + 2OH^-$$
$$\text{Acidic media } 2H^+ + 2e^- = H_2$$

For the electrochemical system with joint presence of two oxidants in the solution (*oxidant* 1—metal cation and *oxidant* 2—depolarizer), the stronger oxidant will be reduced on a metal surface with the assimilation of electrons which corresponds to a higher electrode potential. Thus, the spontaneous electrochemical corrosion process is thermodynamically possible when the following criteria are met:

$$E_{O_2} > E_{Me}\ or\ E_{O_2} - E_{Me} > 0$$
$$E_{H_2} > E_{Me}\ or\ E_{H_2} - E_{Me} > 0.$$

3.2 Thermodynamic States and Transitions Diagrams

For analytical studying and determination of stability of certain forms of the reaction products as well as the ranges and conditions for thermodynamic possibility of corrosion, it is advisable to use diagrams of the thermodynamic states and transitions (Pourbaix diagrams) [3–5].

The diagrams consist of graphical dependences of the equilibrium electrode potentials of all possible equilibria in the systems Me–H_2O against pH of aqueous solutions. They include equilibria where the metal, its ions, hydrogen, oxygen, water, and its ions are involved.

The equations of electrode equilibria and corresponding graphical lines of the E-pH dependence for the Fe–H_2O system are shown in Table 1 and Fig. 1, respectively. For the purpose of this study, the concentrations of iron ions are taken as 1×10^{-6} mol/l. If the equilibria include electrons and ions H^+ or OH^-, then the lines of dependence of their potentials on pH are inclined, if they include only electrons—horizontally, if only water ions—vertically.

$$Fe(OH)_{2(S)} \rightleftarrows Fe^{2+} + 2OH^-$$

According to this equation, when x mol of $Fe(OH)_2$ is dissolved the x mol Fe^{2+} cations and 2 × mol of OH^--ions are released into solution. Thus, K_s $Fe(OH)_2 = x \cdot (2x)^2$. Due to the stoichiometry and the given concentration of iron (II) ions as 1×10^{-6} mol/l, as well as reference values of the solubility equilibrium, a sequence of calculations for the determination of the hydrate formation pH value may be presented as follows:

$$K_{s\,Fe(OH)_2} = 1 \times 10^{-6}(2s_{OH^-})^2 = 8 \times 10^{-15};$$

$$C_{OH^-} = \sqrt{\frac{8 \times 10^{-15}}{4 \times 10^{-6}}} = 4.47 \times 10^{-5}\ \text{mol/l}$$

$$C_{H^+} = \frac{K_w}{C_{OH^-}} = \frac{1 \times 10^{-14}}{4.47 \times 10^{-5}} = 2.237 \times 10^{-10};$$

$$pH = -\lg\left(2.237 \times 10^{-10}\right) = 9.65$$

Table 1 Electrode equilibria in the system Fe–H_2O and equations for calculating their potentials depending on the activity of potential-determining ions and pH of solutions ($T = 298$, 15 K)

Electrode potential, V	Electrode equilibrium	Line designation on Fig. 1
$E_1 = -0.440 + 0.0296 \lg a_{Fe^{2+}}$	$Fe^{2+} + 2e^- \rightarrow Fe$	(Line 1)
$E_2 = 0.047 - 0.059\,pH$	$Fe(OH)_2 + 2H^+ + 2e^- \rightarrow Fe + 2H_2O$	(Line 2)
$E_3 = 0.493 - 0.0886\,pH + 0.0296 \lg a_{HFeO_2^-}$	$HFeO_2^- + 3H^+ + 2e^- \rightarrow Fe + 2H_2O$	(Line 3)
$E_4 = 1.057 - 0.1766\,pH - 0.0592 \lg a_{Fe^{2+}}$	$Fe(OH)_3 + 3H^+ + e^- \rightarrow Fe^{2+} + 3H_2O$	(Line 4)
$E_5 = 0.179 - 0.0592\,pH$	$Fe(OH)_3 + H^+ + e^- \rightarrow Fe(OH)_2 + H_2O$	(Line 5)
$E_6 = -0.810 - 0.059\,lg a_{HFeO_2^-}$	$Fe(OH)_3 + e^- \rightarrow HFeO_2^- + H_2O$	(Line 6)
$pH^* = 1/2\left(13.29 - \lg a_{Fe^{2+}}\right)$	$Fe^{2+} + 2H_2O \rightarrow Fe(OH)_2 + 2H^+$	(Line 7)
$pH = 18.30 - \lg a_{HFeO_2^-}$	$HFeO_2^- + H^+ \rightarrow Fe(OH)_2$	(Line 8)
$E_9 = 0.771 + 0.0592 \lg \frac{a_{Fe^{3+}}}{a_{Fe^{2+}}}$	$Fe^{3+} + e^- \rightarrow Fe^{2+}$	(Line 9)
$pH^* = 1/3\left(4.84 - \lg a_{Fe^{3+}}\right)$	$Fe^{3+} + 3H_2O \rightarrow Fe(OH)_3 + 3H^+$	(Line 10)
$E_{H_2} = -0.0592\,pH$	$2H^+ + 2e^- \rightarrow H_2$ $2H_2O + 2e^- \rightarrow H_2 + 2OH^-$	(Line a)
$E_{O_2} = 1.218 - 0.0592\,pH$	$O_2 + 4H^+ + 4e^- \rightarrow 2H_2O$ $O_2 + 2H_2O + 4e^- \rightarrow 4OH^-$	(Line b)

*Lines 7 and 10 are arranged vertically and their position corresponds to the pH of the hydrate formation of the corresponding slightly soluble $Fe(OH)_2$ and $Fe(OH)_3$. The pH value of the beginning of their formation can be calculated on the basis of the solubility equilibrium (K_s). For example, heterogeneous dissociation equilibrium of $Fe(OH)_2$:

Since the studied system Fe–H_2O uses water as a medium, the diagram contains the dependences of the equilibrium electrode potentials against the pH for the hydrogen (*line a*) and oxygen (*line b*) electrodes.

Lines *a* and *b* of the diagram enable us to determine which conjugate cathodic depolarization reactions may take place as part of the metal corrosion process depending on its potential and pH of the medium. Thus, at potentials less than the equilibrium potentials of the hydrogen electrode (below *line a*), the equilibrium of the hydrogen electrode shifts toward the reduction of H^+ ions enabling the electrons assimilation in corrosion processes with hydrogen depolarization. On the contrary, at potentials lying above the *line a*, the electrode equilibrium of the hydrogen electrode

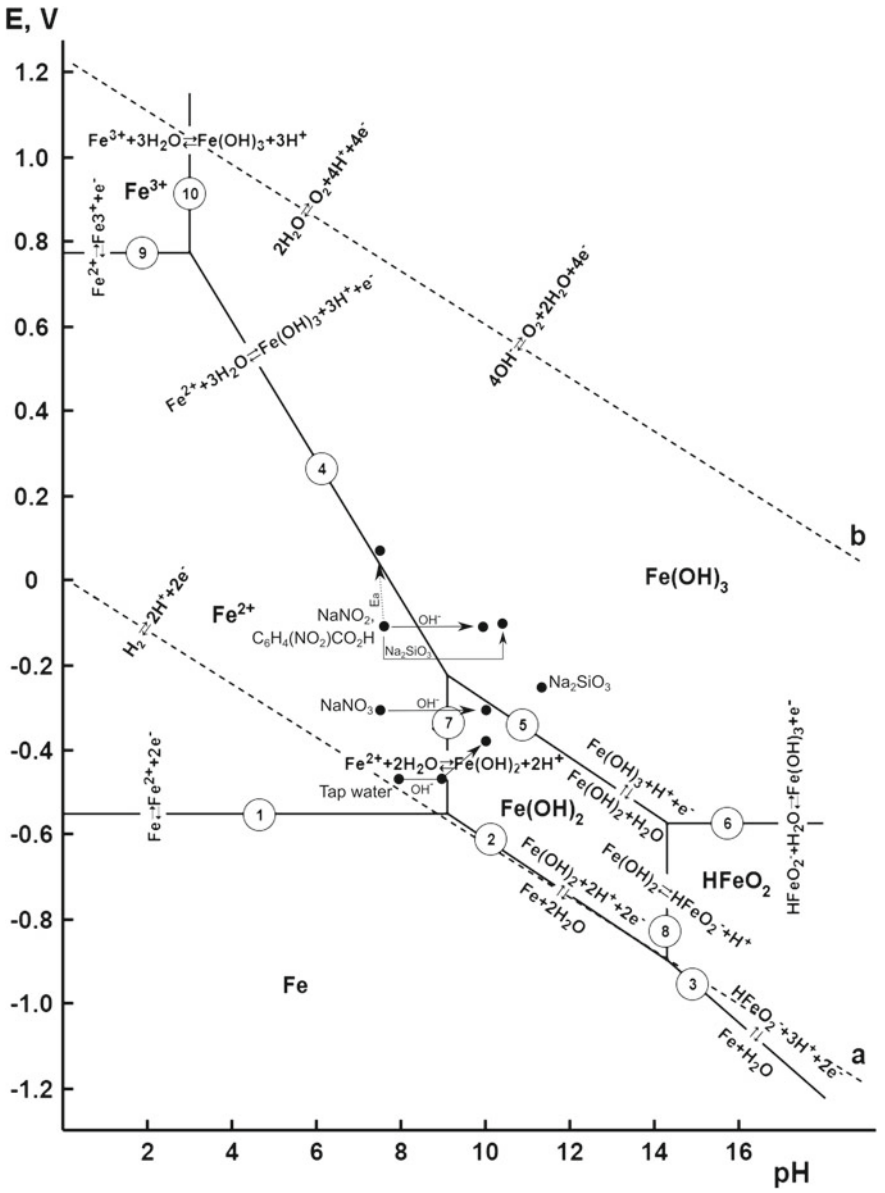

Fig. 1 Pourbaix diagram of the Fe–H_2O system

is shifted in the opposite direction with the release of electrons, which prevents the corrosion with hydrogen depolarization. Similarly, at potentials less than the equilibrium potentials of the oxygen electrode (below *line b*), the electrode equilibrium is shifted toward the oxygen reduction that requires electrons, and thus under these conditions oxygen can act as a depolarizer in metal corrosion. At metal potentials higher than the oxygen electrode potentials (above *line b*), there is a region of water decomposition with the formation of oxygen, which eliminates the process of oxygen depolarization.

The equilibrium lines divide the plane of the Pourbaix diagram into regions, each of which corresponds to the existence of one thermodynamically stable component of the Fe–H_2O system.

Within the zone, which is located under the lines 1, 2, 3, the metallic state of iron is thermodynamically stable. At these potentials and pH, the metal does not undergo corrosion damage in aqueous solutions.

In the region bounded by lines 1, 7, 4, 9, the thermodynamically stable form of the substance in the system is the hydrated Fe^{2+} cations. The metal under these conditions is unstable and undergoes electrochemical corrosion with the formation of the Fe^{2+} ions. In the part of this zone that lies below *lines a* and *b*, corrosion can occur simultaneously with hydrogen and oxygen depolarization due to conjugated reduction reactions of ions H^+ and molecules O_2, while above line *a*—only with oxygen depolarization.

In the area between *lines 9* and *10,* the thermodynamically stable state is Fe^{3+} ions; thus, at these potentials and pH all other forms of substances in the Fe–H_2O system are converted into Fe^{3+}. Iron undergoes corrosion destruction at potentials below the *line b* with oxygen depolarization, and above–only due to a significant shift of the metal potential in the positive direction.

The area between lines 2, 7, 5, 8 is characterized by the thermodynamic stability of the non-metallic phase—iron (II) hydroxide $Fe(OH)_2$, which is formed due to metal corrosion. Under these conditions, the metal is thermodynamically unstable, but due to the formation of a non-metallic phase on its surface a slight inhibition of the subsequent corrosion process may be observed.

At potentials and pH, which lie in the area to the right of the vertical line 8 and between 3 and 6, there is a corrosion of iron with the formation of the $HFeO_2^-$ anions.

The region bounded by lines 4, 6, 5, 10 corresponds to the conditions of thermodynamic stability of solid iron (III) hydroxide, more precisely of iron (III) oxohydroxide—FeOOH. The metallic iron state is unstable, and the metal undergoes corrosion with oxygen depolarization, while the formation of a dense protective oxide film with the participation of iron (III) ions on its surface can significantly inhibit the metal corrosion due to the passivation of the surface.

Steel corrosion in aqueous saline media occurs mainly with oxygen depolarization and is limited by the cathodic process of the oxidant (oxygen) diffusion to the metal surface, while the anode process usually occurs in the region of active metal ionization and is limited by the electrochemical act of charge transfer. Due to the possibility of both frontal and side supply of molecular oxygen to the metal surface, inhibition of

the cathodic process of the depolarizer (O_2) reduction is a challenging task even if a significant surface coverage ratio of adsorbed inhibitor particles could be achieved.

Due to the difficulties of slowing down the cathodic corrosion reaction by limiting the diffusion of the oxidant the development of the inhibitor methods for the protection of steel in neutral medium is primarily focused on inhibiting the anodic process of ionization of the metal. This approach may be implemented due to the fact that under certain conditions the Fe–H_2O system may be shifted toward a state of the formation and thermodynamic stability of new solid non-metallic phases that can deposit on the metal surface transferring it into a passive state.

The diagram shows that the passive state of steel can be expected in the area of formation on its surface of hydrated iron (III) oxides, which have the ability to provide effective protection of the metal. Oxidative and salt passivators are widely used to protect steel in neutral and aqueous saline media [5–7]. Of particular interest are inhibitory mixtures, which are characterized by the synergism phenomenon within its components [8–16].

Passivation of steel can be achieved by applying external anodic polarization or by creating an internal cathode current by reducing the inhibitor and substantially accelerating the cathodic corrosion process.

As has been shown in previous studies [17–21] that despite an ability to adsorb and reduce on a metal surface the oxidative inhibitors may transfer the metal to a passive state only in cases where the transition of the Fe–H_2O system to thermodynamically stable state of hydrated iron (III) oxides may be achieved.

Such typical behavior of the system can be illustrated by the analysis of the sodium nitrite inhibitive efficiency at different pH. In a neutral aqueous saline solution (pH 7.3), despite it shows high rated protective efficiency that marginally increases at higher inhibitor concentrations (Fig. 2), it tends to provoke localized corrosion damage that limiting its application as individual inhibitor.

According to the results of the polarization measurements, $NaNO_2$ at pH 7.3 shifts the electrode corrosion potential in a positive direction due to the inhibition of the anodic reaction. At the same time, under these conditions the influence on cathodic

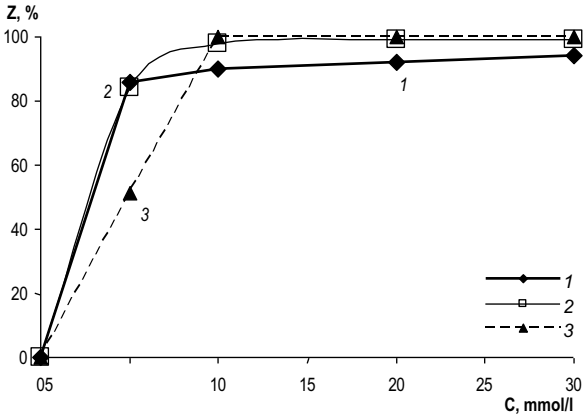

Fig. 2 Dependence of the inhibition efficiency for carbon steel in the aqueous saline solution on the concentration: 1—$NaNO_2$ at pH 7.3; 2—$NaNO_2$ at pH 10; 3—Na_2SiO_3 at pH 11.2

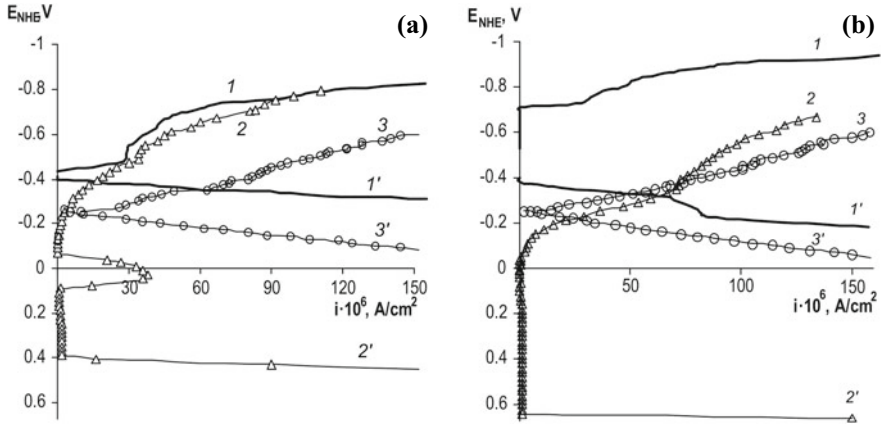

Fig. 3 **a** Cathodic (*1, 2, 3*) and anodic (*1′, 2′, 3′*, polarization curves for carbon steel in: *1, 1′*—background aqueous saline solution, *2, 2′*—in the presence of $NaNO_2$ (30 mmol/l), *3, 3′*—in the presence of $NaNO_3$ (30 mmol/l) at pH 7.3. **b** Cathodic (*1, 2, 3*) and anodic (*1′, 2′, 3′*,) polarization curves for carbon steel in: *1, 1′*—background aqueous saline solution, *2, 2′*—in the presence of $NaNO_2$ (30 mmol/l), *3, 3′*—in the presence of $NaNO_3$ (30 mmol/l) at pH 10

reduction is virtually have not been observed (Fig. 3). It can be assumed that the initial act of the inhibitor action is its adsorption with the participation of a sp^2—hybrid electron pair of the central nitrogen atom. This theoretical representation is in line with the results obtained for sodium nitrate that does not have such an electron pair and contains a coordinationally saturated central atom. In contrast to nitrite (NO_2^-), the nitrate ions (NO_3^-) do not show significant inhibitory effect on steel corrosion at different pH values and can even promote corrosion under certain conditions (Fig. 3a, b).

Comparative analysis of the polarization measurements for NO_2^- and NO_3^- ions at different pH values shows that the sodium nitrite efficiency improved significantly at pH 10 as compared to pH 7.3 greatly widening the full passivation zone (Fig. 3, 4e). In contrast, no improvement in electrochemical behavior in the presence of NO_3^- ions has been observed which is in line with theoretical expectations.

To ensure effective passivation of the steel surface, it is necessary to establish conditions (potential and pH) for the transition of the system to a state where thermodynamically stable form of products is a hydrated iron (III) oxides:

$$Fe^{2+} + 3H_2O \rightleftarrows Fe(OH)_3 + 3H^+ + e^-$$

Ability of NO_2^- ions to reduce on the metal surface contributes to a greater potential shift at pH 10 that leads to a system transition to a region of the thermodynamic stability of $Fe(OH)_3$ that results in efficient passivation of the metal surface with phase non-metallic protective layer. At the same time, the obtained results for NO_3^- system correspond to an area of the thermodynamic stability of hydrated iron (II)

ions. Such products are not capable to form dense protective films to efficiently slow down further corrosion processes.

Proposed theoretical representation of the NO_2^- inhibition mechanism that implies its reduction on the metal surface may be further supported by the analysis of other oxidative anions with the coordination-saturated central atoms. Inhibitory effect of such compounds is due to the inhibition of the anodic partial reaction, thus the corrosion potential of the metal is shifted to the positive direction.

At the same time, similar to the NO_3^- ions the oxidative anions CrO_4^{2-} does not show improvement in protection efficiency at the pH 10 compared to pH 7.3 that is attributed to its inability to reduce on the metal surface. According to the Pourbaix diagram (Fig. 1), the thermodynamically stable products for such potentials and pH are hydrated iron (II) ions.

3.3 Inhibitive Mechanism Aliasing Effects

Individual passivating inhibitors are usually considered as "dangerous" due to the high risk of pitting in the case of local damage to the protective film (Fig. 4d) that may lead to rapid structural degradation and premature equipment failure. To address this disadvantage, increase the protective efficiency and reduce the effective inhibitor concentrations, it is advisable to complement oxidative inhibitors with salt passivators that are capable to form slightly soluble salts with iron (II) cations, which occur as a result of local damage to protective phase films.

Oxidative and salt passivators are able to form synergistic compositions with high efficiency of anticorrosive action [19–21]. It has been previously shown that marked synergistic effect may be observed within mixtures based on sodium nitrite as well as oxohalides with sodium silicate, phosphate, carbonate, and others. Depending on the molar concentration ratio of the components, they are characterized by synergistic extremes and demonstrate wide areas of complete passivation that may be considered as full protection of the metal against corrosion. The wide range of concentration ratio where inhibitive mixture may exhibit improved protective efficiency is extremely important for practical applications as the protection will sustain even in the case if the concentration of one component will be depleted.

In particular, synergistic inhibitive mixture $NaNO_2 + Na_2SiO_3$ demonstrate excellent protective efficiency both in terms of rated reduction in corrosion rate and resulting surface morphology (Fig. 5, 6).

Preconditions and regularities of the phase protective layer formation in presence of such inhibitive mixtures have been previously covered in detail [20].

Results obtained in the present work are found to be in a good agreement with theoretical expectations that imply reduction of: NO_2^- and ClO_3^- ions that facilitate to a formation of protective film of hydrated iron (III) oxides with the inclusion of slightly soluble salts originating from the salt passivator components of the mixture [19–21]. Other studied inhibitive mixtures based on $NaNO_2$ or $KClO_3$ also exhibit synergistic behavior (Fig. 7a–c, f) with salt passivators and tend to improve finish of

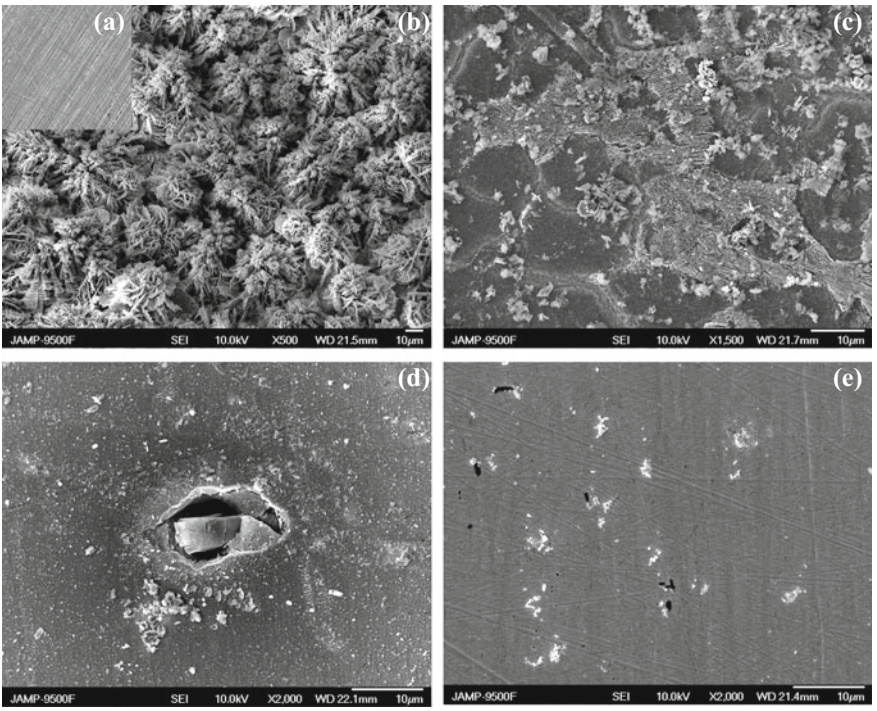

Fig. 4 Sample morphology: **a**—without exposition, **b**—after 168 h exposition in blank solution at pH 7.3; **c**—after 168 h exposition in blank solution at pH 10, after168h exposition in presence of $NaNO_2$ (30 mmol/l) at pH 7.38 **d** and pH 10 **e**

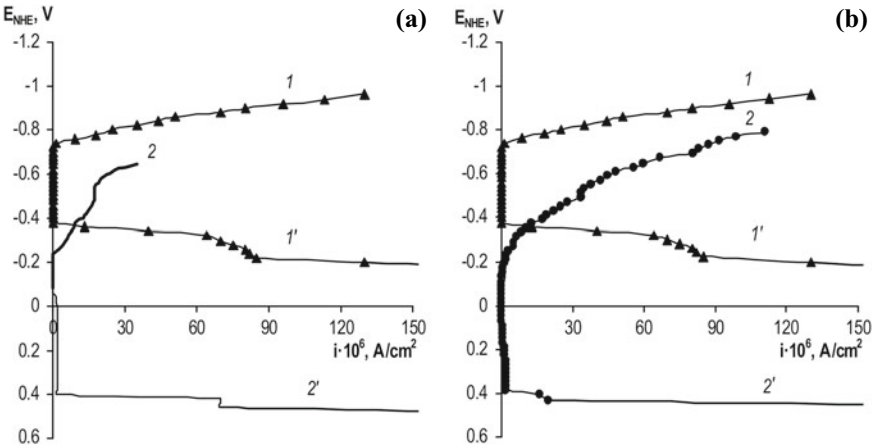

Fig. 5 Cathodic (1, 2,) and anodic (*1′, 2′*) polarization curves for carbon steel in the presence of: **a**—*1*, *1′*—background aqueous saline solution at pH 10; *2*, *2′*—in the presence of Na_2SiO_3 (30 mmol/l). **b**—*1*, *1′*—background aqueous saline solution at pH 10; *2*, *2′*—$NaNO_2$ (10 mmol/l) + Na_2SiO_3 (20 mmol/l)

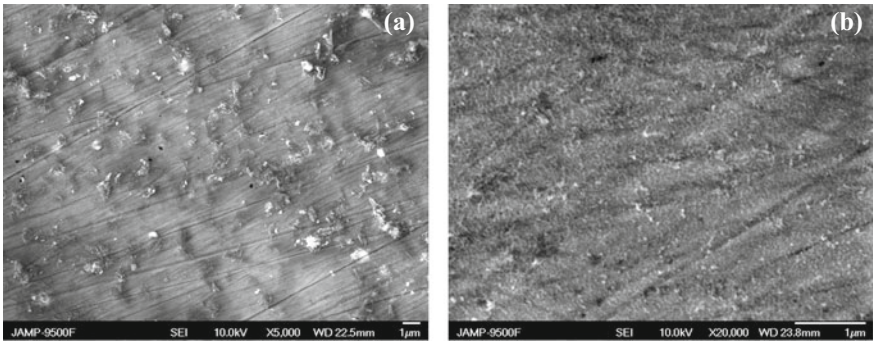

Fig. 6 Morphology of the protective film after 168 h exposition in solution with: **a**—Na_2SiO_3 (30 mmol/l); **b**—$NaNO_2$ (10 mmol/l) + Na_2SiO_3 (20 mmol/l)

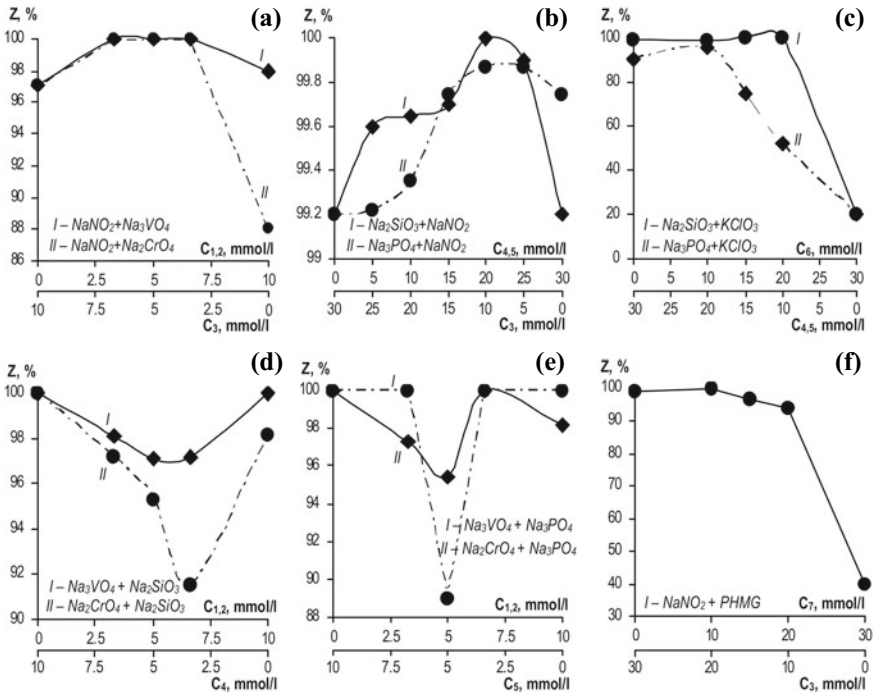

Fig. 7 Inhibitive efficiency vs concentration ratio of the binary mixture components. Key: 1—Na_3VO_4; 2—Na_2CrO_4; 3—$NaNO_2$; 4—Na_2SiO_3; 5—Na_3PO_4; 6—$KClO_3$; 7—PHMG

the metal surface.

In contrast, binary inhibitive mixtures composed according to a similar schema as oxidative passivators (Na_3VO_4, Na_2CrO_4) but with coordinately saturated acidizing anions with the addition of salt inhibitors (Na_2SiO_3, Na_3PO_4) demonstrate negative

mechanism aliasing that results in noticeable antagonistic effects both in terms of protection efficiency and the amount of surface corrosion damage (Fig. 7d, e). Such behavior may be attributed to a concurrence among the individual inhibitive action factors that take place between the mixture components due to structural similarities that reduce efficiency at specific concentration ratio [21].

Nitroaromatic compounds—nitrobenzoates and nitrofuroates also are promising component of synergistic inhibitive mixtures due to the presence of nitro group ($-NO_2$) attached to an aromatic ring. For further research to clarify the criteria for the selection of components for synergistic composition 3-nitrobenzoic acid (contain nitro group) and benzoic acid (without nitro group) were investigated. According to the gravimetric measurements, 3-nitrobenzoic acid and benzoic acid at pH 7 does not show significant inhibitory effect on steel corrosion and can even promote corrosion under certain conditions (Figs. 8 and 9), while at pH 9–11 efficiency as corrosion inhibitors for 3-nitrobenzoic acid increases greatly, while benzoic acid tends to promote corrosion (Fig. 8). It may be attributed to the reduction process of 3-nitrobenzoic acid. Thereby, the mechanism of the action of NO_2^--ion (Fig. 3) and organic nitroaromatic substances is similar.

Investigation of the kinetics of the electrode processes in the presence of 3-nitrobenzoic acid under pH 10 using the polarization measurements shows notable deceleration in the anodic reaction rate owing to a passivation of the metal surface (Fig. 9b).

For improving the inhibition efficiency and surface morphology, the synergistic mixture 3-nitrobenzoic acid (oxidative-type inhibitor) with Na_2SiO_3 (salt type inhibitor) has been investigated. The isomolar series method has been employed for determining the optimal concentration ratio and synergistic maximum (Fig. 10).

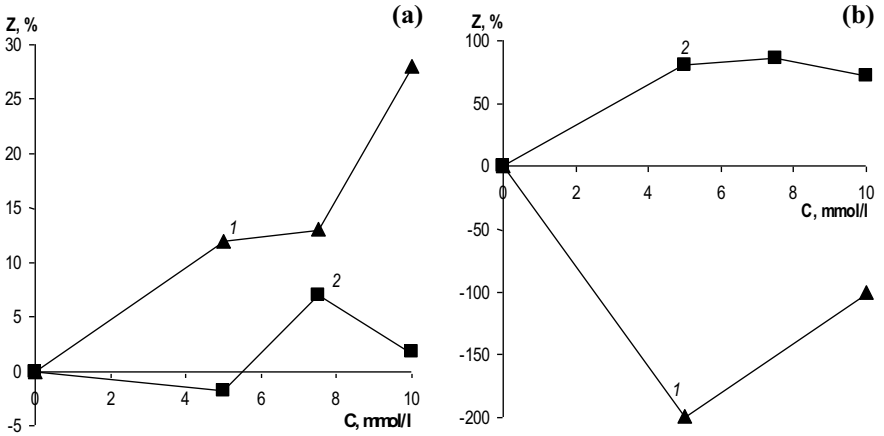

Fig. 8 Dependence of the inhibition efficiency for carbon steel in the aqueous saline solution on the concentration: **a** 1—benzoic acid at pH 6.8; 2—benzoic acid at pH 10; **b** 1—3-nitrobenzoic acid at pH 5.8; 2—3-nitrobenzoic acid at pH 10

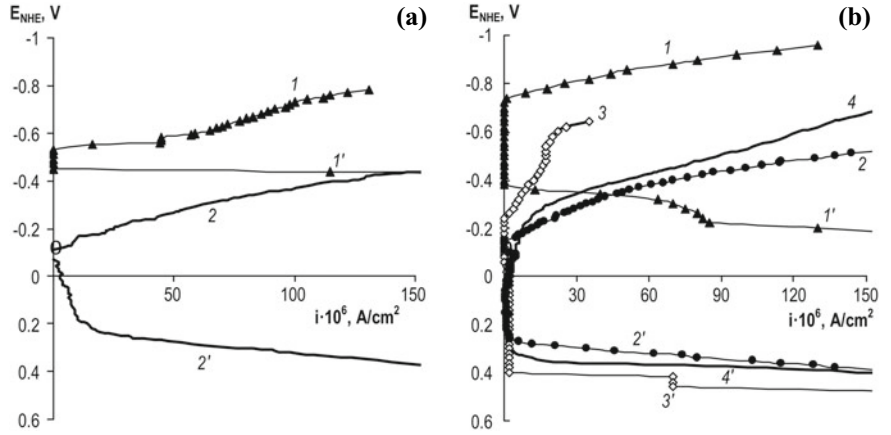

Fig. 9 **a** Cathodic (*1, 2*) and anodic (*1′, 2′*) polarization curves for carbon steel in: *1, 1′*—background aqueous saline solution, *2, 2′*—in the presence of 3-nitrobenzoic acid (10 mmol/l). **b** Cathodic (*1, 2, 3*) and anodic (*1′, 2′, 3′*, polarization curves for carbon steel in: *1, 1′*—background aqueous saline solution, *2, 2′*—in the presence of 3-nitrobenzoic acid (10 mmol/l) at pH 10, *3, 3′*—in the presence of Na_2SiO_3 (30 mmol/l), *4, 4′*—in the presence of 3-nitrobenzoic acid (2.5 mmol/l) + Na_2SiO_3 (7.5 mmol/l)

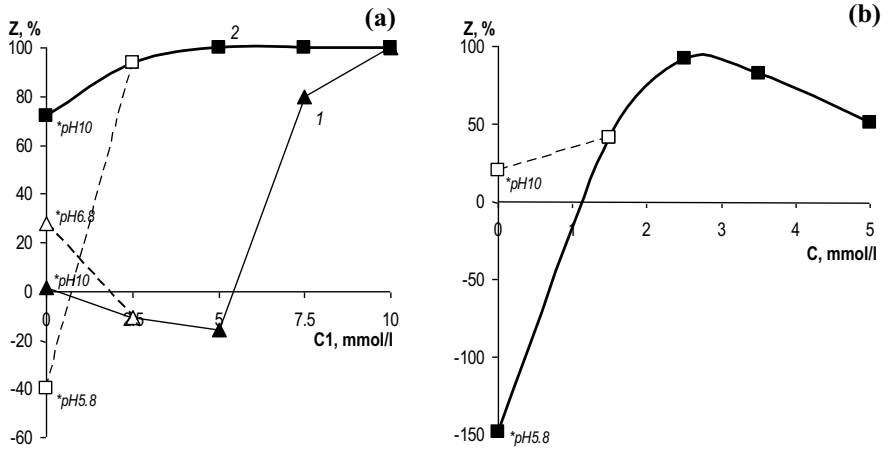

Fig. 10 Inhibitive efficiency vs concentration ratio of the binary mixture components. **a** *1*—benzoic acid + Na_2SiO_3, *2*—3-nitrobenzoic acid + Na_2SiO_3 (total concentration 10 mmol/l); **b** 3-nitrobenzoic acid + Na_2SiO_3 (total concentration 5 mmol/l)

Investigation of the kinetics of the electrode processes in the presence of synergistic mixture under pH 10 using the polarization measurements shows notable shift of the potential to the positive direction and significant deceleration of the anodic process owing to a passivation of the metal surface even when the total concentration

of the synergistic composition is reduced by 6 times compared to the concentration of sole Na_2SiO_3.

It was found that protective efficiency of the mixture against the concentration ratio has extreme character reaching the peak value of 99.99% at the 3-nitrobenzoic acid with Na_2SiO_3 ratio as 1:1. This inhibitive composition demonstrates significant improvement in morphology and continuity of the protective phase film (Fig. 11).

At the same time, the benzoic acid in mixtures with Na_2SiO_3 demonstrates antagonistic effect that in line with theoretical expectations and shows the applicability of the proposed inhibitive mechanism model for additives of different nature (Fig. 10a).

Based on a comprehensive analysis of studied systems [17–21], the overall action of a given additive has been splitted to individual factors of specific influence and further interpretation of the mixture behavior has been performed on the basis of the positive and negative mechanism aliasing model. Depending on the nature of the interaction between individual factors the supplementary, complementary and tandem action may be distinguished while antagonistic effects are attributed to negative mechanism aliasing.

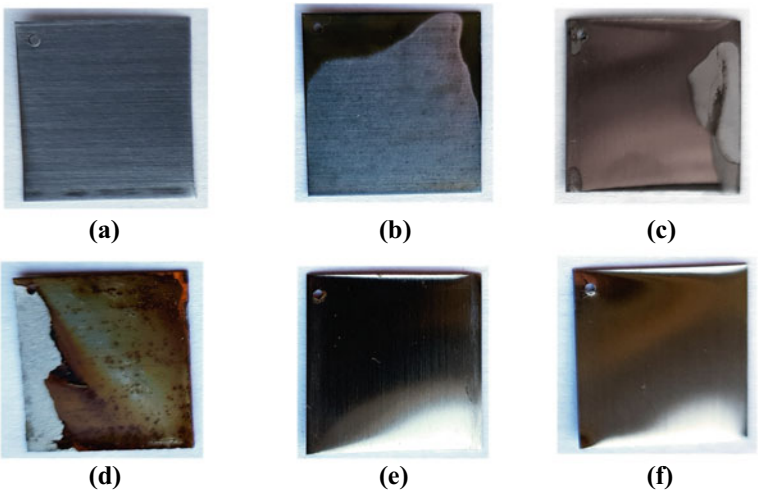

Fig. 11 Sample morphology: **a**—without exposition, **b**—after 168 h exposition in blank solution at pH 7.3; **c**—after 168 h exposition in the presence of Na_2SiO_3 (5 mmol/l); **d**—after 168 h exposition in the presence of 3-nitrobenzoic acid (5 mmol/l); **e**—after 168 h exposition in the presence of the binary mixture3-nitrobenzoic acid + Na_2SiO_3 (total concentration 5 mmol/l); **f**—after 168 h exposition in the presence of the binary mixture3-nitrobenzoic acid + Na_2SiO_3 (total concentration 10 mmol/l)

4 Conclusions

A range of additives of different nature and their binary mixtures have been investigated in regard to their influence on the corrosion processes. It was shown the applicability of the thermodynamic state and transitions diagrams for analysis of electrochemical processes and interactions during the development and optimization of synergistic inhibitive compositions.

It has been demonstrated that the possible positive and negative mechanism aliasing effects between mixture components may be predicted analytically for well-defined systems that is crucial for development of the synergistic mixtures.

Employment of the refined theoretical models for a mechanism coaction within a multicomponent environment provides an ability for development novel materials degradation prevention methods based on the phase layers formation that may be considered as controlled in situ synthesis.

References

1. Rozenfeld IL (1977) Corrosion inhibitors. Khimiya, Moscow
2. Antropov LI, Makushin EM, Panasenko VF (1981) Inhibitors of the corrosion of metals, Tekhnika, Kiev
3. Pourbaix M (1974) Atlas of electrochemical equilibria in aqueous solutions. National Association of Corrosion Engineers, Houston, Texas, p 551
4. Pourbaix M, Pourbaix A (eds) (1982) Diagrams of chemical and electrochemical equilibria: their setting-up and applications. In: Proceedings of a NATO advanced research workshop, CEBELCOR's reports techniques 142, RT 263, CEBELOR, Brussels
5. Beverskog B, Puigdomenech I (1996) Revised Pourbaix diagrams for iron at 25–300 °C. Corros Sci 38(12):2121–2135. https://doi.org/10.1016/S0010-938X(96)00067-4
6. Garcés P, Saura P, Zornoza E, Andrade C (2011) Influence of pH on the nitrite corrosion inhibition of reinforcing steel in simulated concrete pore solution. Corros Sci 53(12):3991–4000. https://doi.org/10.1016/j.corsci.2011.08.002
7. Hussain RR (2014) Passive layer development and corrosion of steel in concrete at the nanoscale. J Civ Environ Eng 4:e116. https://doi.org/10.4172/2165-784X.1000e116
8. Min J, Park JH, Sohn H-K, Park JM (2012) Synergistic effect of potassium metal siliconate on silicate conversion coating for corrosion protection of galvanized steel. J Ind Eng Chem 18(2):655–660. https://doi.org/10.1016/j.jiec.2011.11.057
9. Truc AT, Pébère N, Xuan HT, Hervaud Y, Boutevin B (2002) Study of the synergistic effect observed for the corrosion protection of a carbon steel by an association of phosphates. Corros Sci 44:2055–2071. https://doi.org/10.1016/S0010-938X(02)00013-6
10. Omotosho Olugbenga A, Okeniyi Joshua O, Ajayi Oluseyi O, Loto Cleophas A (2012) Effect of synergies of $K_2Cr_2O_7$, K_2CrO_4, $NaNO_2$ and aniline inhibitors on the corrosion potential response of seel reinforced concrete in saline medium. Int J Environ Sci 2(12):2346–2359.https://doi.org/10.6088/ijes.00202030116
11. Mohana KN, Badiea AM (2008) Effect of sodium nitrite-borax blend on the corrosion rate of low carbon steel in industrial water medium. Corros Sci 50(10):2939–2947. https://doi.org/10.1016/j.corsci.2008.07.002
12. Eyu GD, Will G, Dekkers W, MacLeod J (2016) The synergistic effect of iodide and sodium nitrite on the corrosion inhibition of mild steel in bicarbonate-chloride solution. Materials 9(11):868. https://doi.org/10.3390/ma9110868

13. Ramanauskas R, Girčienė O, Gudavičiūtė L, Selskis A (2015) The interaction of phosphate coatings on a carbon steel surface with a sodium nitrite and silicate solution. Appl Surf Sci 327:131–139. https://doi.org/10.1016/j.apsusc.2014.11.120
14. Girčienė O, Ramanauskas R, Gudavičiūtė L, Martušienė A (2011) Inhibition effect of sodium nitrite and silicate on carbon steel corrosion in chloride-contaminated alkaline solutions. Corrosion 67(12):125001-1–125001-12. https://doi.org/10.5006/1.3665355
15. Chong AL, Mardel JI, MacFarlane DR, Forsyth M, Somers AE (2016) Synergistic corrosion inhibition of mild steel in aqueous chloride solutions by an imidazolinium carboxylate salt. ACS Sustain Chem Eng 4(3):1746–1755. https://doi.org/10.1021/acssuschemeng.5b01725
16. Ioffa ZA (1972) Synergetic and antagonistic effects at adsorption and impact of surfactants on the electrochemical reactions and corrosion of iron. Prot Metals 8(2):139–145
17. Ledovskykh VM, Vyshnevska YuP, Brazhnyk IV, Levchenko SV (2017) Metal surface modification for obtaining nano- and sub-nanostructured protective layers. Nanoscale Res Lett 12:186–191. https://doi.org/10.1186/s11671-017-1964-5
18. Ledovs'kykh VM, Vyshnevs'ka YuP, Brazhnyk IV, Levchenko SV (2017) Development and optimization of synergistic compositions for the corrosion protection of steel in neutral and acid media. Mater Sci 52(5):634–642. https://doi.org/10.1007/s11003-017-0002-1
19. Ledovskykh VM, Vyshnevska YuP, Brazhnyk IV, Levchenko SV (2019) Thermodynamic approach to purposeful design of synergistic inhibitive compositions for corrosion protection in aqueous saline medium. Mater Sci 54(4):485–495. https://doi.org/10.1007/s11003-019-00208-z
20. Ledovskykh VM, Vyshnevska YuP, Brazhnyk IV, Levchenko SV (2019) Metal surface engineering based on formation of nanoscaled phase protective layers. Nanocompos Nanostruct Their Appl Springer Proc Phys 221:69–84. https://doi.org/10.1007/s11003-014-9680-0
21. Ledovskykh VM, Vyshnevska YuP, Brazhnyk IV, Levchenko SV (2021) Mechanism of the oxidative and salt passivators coaction within binary inhibitive mixtures. Mater Sci 56(5) (In press)

The Investigation of Morphology, Topography, and Surface Fractality of Heterooxide Composite Coatings

Iryna Yu. Yermolenko, Hanna V. Karakurkchi, Maryna V. Ved, and Nikolay D. Sakhnenko

The scientific and practical interest to heterooxide oxide composite coatings is explained by a wide range of their functionality. Such coatings are used as decorative [1], anti-corrosion [2], magnetic [3], as carriers of catalytic systems [4], etc. To obtain them, cathodic electrodeposition by direct [5] and pulsed current [6] as well as plasma-electrolyte oxidation [7–9] is used.

An important point in the electrochemical deposition of multicomponent alloys is the prediction of their functional properties, which is based on the results of the analysis of the composition and structure of coatings, including the morphology and topography of the surface.

The establishing of the relationship between the composition, structure, and properties of alloys, as well as correct interpretation of the results obtained, contributes to the solution of very specific practical problems of controlling the composition and structure of electrolytic coatings. This is the basis for the predicted electrochemical synthesis of modern materials with the required properties and performance characteristics.

The inclusion of refractory metals (tungsten, molybdenum, etc.) into the composition of galvanic alloys promotes the formation of an amorphous structure of coatings. This has a favorable effect on the structurally dependent properties of the synthesized materials, such as microhardness, corrosion resistance, and catalytic activity [10–12].

Safizadeh et al. [13] deposited X-ray amorphous coatings of Fe–Mo with a molybdenum content of 47% and Fe–Mo–P with a content of 21–30% molybdenum and 9–16% phosphorus, which was confirmed by XRD analysis. The authors note a greater roughness of phosphorus-containing coatings and an improvement in catalytic properties by 16.5% compared with binary Fe–Mo in the reaction of electrolytic evolution

I. Yu. Yermolenko (✉) · H. V. Karakurkchi · M. V. Ved · N. D. Sakhnenko
National Technical University «Kharkiv Polytechnic Institute», 2, Kyrpychova str., Kharkiv 61002, Ukraine

O. Fesenko and L. Yatsenko (eds.), *Nanomaterials and Nanocomposites, Nanostructure Surfaces, and Their Applications*, Springer Proceedings in Physics 263, https://doi.org/10.1007/978-3-030-74741-1_31

of hydrogen in a model environment for the production of chlorate. According to the presented data, the overvoltage of hydrogen evolution at the Fe54Mo30P16 electrode is reduced by 30% compared to the low-carbon steel electrode.

The results of studies by Gomez and Pellicer [14, 15] show a tendency to the manifestation of soft magnetic properties in binary Co-Mo coatings during the transition from crystalline to spheroidal structure of the alloy.

Gong et al. [16] showed an increase in the coercive force of galvanic deposits of Co–Ni–Fe sympatically surface roughness. The authors show that dependence of coercive force on the thickness of the coating it has pointed out the extreme in the range of 5–50 nm at a maximum film thickness at 20 nm. Gong et al. [16] attribute this dependence to the regulation of the coercivity mechanism by anisotropy, in particular by changing the elemental composition, grain size, surface roughness, and internal stresses during film formation.

Along with the morphology, sufficiently comprehensive information on the structure of the coatings is provided by the analysis of the topography and the determination of the class of surface roughness of electrodeposited films. In materials science, roughness is a characteristic of surface quality and depends on the method of processing (grinding, polishing, etc.) of the material. During the deposition of electroplated coatings, this parameter not only reflects the degree of roughness of the substrate, but is the result of the process of nucleation on the substrate of foreign material and crystal growth during the formation of the alloy [17]. Together with topography, roughness can be an additional indicator of the degree of surface development. Among the criteria for evaluating roughness, the most used are the arithmetic mean roughness Ra and root-mean-square roughness (rms) Rq. The method of contact scanning using an atomic force microscope (AFM) is considered the most informative for determining the roughness parameters [18]. However, the Ra and Rq values can be very different for different scan areas (48 × 48 um, 20 × 20 um, 10 × 10 um, 5 × 5 um) and sample position, as noted Shuyi Gan и Qing Zhou [19].

To eliminate this dependence, many methods are proposed, among which fractal analysis can be distinguished [20]. In modern materials science, a fractal is considered as a kind of universal chemical-structured unit that carries information about the structure and properties of materials. According to Kotowski [21], multifractal spectra may differ for different samples; however, they are identical for one sample even if its size or position is accidentally changed. The positive experience of using fractal analysis to assess the mechanical and corrosion damage of metal structures [22, 23] confirms the feasibility of determining fractality when studying the structure of galvanic alloys. The self-similarity and identity of fractals, in combination with the parameters of the surface roughness, makes it possible to objectively assess the structure of the coatings in the transition from nano- to macro-relief.

1 Experimental

1.1 The Obtaining Composites Fe–Co–MoO_x

The Fe–Co–MoO_x were deposited on a copper M1 and onto a mild steel substrate from electrolytic bath of composition, mol/dm^3: iron(III) sulfate 0.05–0.075, cobalt sulfate 0.15–0.2, sodium molybdate 0.04–0.06, sodium citrate 0.4–0.5, sodium sulfate 0.15, and boric acid 0.1; the pH value was adjusted within the range 4.0–4.6 by addition of sulfuric acid or sodium hydroxide.

The acidity of electrolyte was controlled by pH-meter pH-150 M with the glass electrode ESL-6307. The electrolyte solutions were prepared using the certified reagents of chemically pure grade on the distilled water. The electrolyte temperature at a level of 25–30 °C was maintained. Pretreatment of samples surface includes mechanical polishing, polishing, degreasing, chemical etching in a mixture of the 50% nitric and 50% sulfuric acids, thorough washing with distilled water and drying.

Electrolysis was performed in the two-electrode glass cell using radially positioned anodes of AISI 304 steel. The Fe–Co–MoO_x films were deposited by two modes: (i) direct current (dc) with the current density i of 2–3 A/dm^2 and (ii) pulse current (pc) with amplitude i of 3–5 A/dm^2 at the range on/off time of 2–50 ms. The ratio of the cathode to the anode area was 1: 5, and volume current density was kept at the level 2 A/dm^3. For deposition of coatings in a galvanostatic regime with the current density i 2–9 A/dm^2, stabilized B5-47 power sources were used. The magnetic stirrer with heating of MM-5 was used for mixing intensity and heating of the electrolyte to the required temperature.

1.2 The Obtaining Heterooxide Coatings $Al_2O_3 \cdot MO_x$(M–Co, Mn)

The oxide coatings $Al_2O_3 \cdot MO_x$(M–Co, Mn) were formed on substrates of Al alloys in alkaline electrolytes by plasma electrolytic oxidation (PEO). The electrolytes composition is given in Table 1. The distilled water and certified reagents of chemically pure grade were used for the electrolytes preparing. The surface of samples for

Table 1 Composition of electrolytes for obtaining of heterooxide PEO coatings

Substrate	Coating	Electrolyte, mol/dm^3
Al alloys: AD0, D16, AMn, AL25	Al_2O_3	$K_4P_2O_7$—1.0
	$Al_2O_3 \cdot CoO_x$	$K_4P_2O_7$—0.4; $CoSO_4$—0.1
	$Al_2O_3 \cdot MnO_y$	NaOH—0.005; $KMnO_4$—0.05

oxidation was prepared by grinding with subsequent degreasing, washed twice with cold and hot water, and dried at the temperature of 30–40 °C.

The heterooxide coatings formation was conducted in a galvanostatic mode. The current density (j) was varied in the range: 3–5 A/dm^2 for $Al_2O_3 \cdot CoO_x$ coatings and 10–20 A/dm^2 for $Al_2O_3 \cdot MnO_y$. The electrolyte temperature was maintained within the interval of 20–25 °C. Processing time was 15–30 min.

1.3 The Research Methods

The chemical composition of the coatings was determined by energy-dispersive X-ray spectroscopy by an Oxford INCA Energy 350 electron probe microanalysis integrated into the system of the SEM. The X-rays were excited by exposure of the samples to a beam of 15 keV electrons. The surface morphology of the deposits was studied with a Zeiss EVO 40XVP scanning electron microscope (SEM). Images were made registering secondary electrons (SEs) via scanning with an electron beam; this mode made it possible to study the topography with a high resolution and contrast ratio.

The elemental composition was determined by X-ray fluorescence method.

The surface morphology and topography were examined by an atomic force microscopy AFM using NT–206 microscope. Scanning was performed by contact probe CSC-37 with a cantilever lateral resolution of 3 nm. The scan areas were fixed in the range of 40.0 × 40.0 μm, 20.0 × 20.0 μm, 10.0 × 10.0 μm and 5.0 × 5.0 μm, and the height of the surface relief was recorded with a resolution of 256 × 256 pixels. Areas for scanning were selected in the center of the samples, to compare the diversity of the surface of the study which was repeated for two areas spaced at a distance of 1500 μm [24].

The visualization of the results was carried out by means of relief reconstruction in the form of 2D and 3D topography maps (the height is reflected in color).

The AFM data were processed using Explorer software by analyzing the average amplitude parameters of the surface roughness: (1) the arithmetic mean Ra (ISO 4287/1), which determines the surface roughness as a two-dimensional arithmetic value; (2) the root mean square Rq (ISO 4287/1), which is a determinant characteristic of surface roughness.

The fractal dimension was estimated by the «perimeter–area» method («slit-island method» (SIM)). For this, the surface was cut at a level of 20% of the highest peak of the map. A graph was built in coordinate's lg$P$ – lg$S$, and the fractal dimension was determined through the slope of the straight line k:

$$D = k/2.$$

2 The Research of the Morphology and Surface Topography of Fe–Co–MoO_x Coatings

Previously, the kinetic regularities of the deposition process of iron and cobalt with molybdenum into a ternary alloy were investigated. It was shown that, firstly, competitive reduction of alloy-forming components (iron, cobalt, and molybdenum) occurs during co-deposition into a ternary alloy [25]. Secondly, the reduction of oxometallate MoO_4^{2-} occurs both during the electrochemical stage and during the subsequent chemical reaction between the adsorbed hydrogen atoms and intermediate molybdenum oxides. The contribution of each of these reactions to the cathodic process, among other things, on the type of polarization is depended. The pulsed current use promotes a more complete reduction of molybdenum. The last significantly affects the content of both the refractory component and the oxygen content in the alloy. Obviously, this will affect on the coating structure and its properties.

Analysis of the energy dispersive X-ray spectra of the coatings indicates that the components are co-deposited into the alloy in the ratio ω(Fe): ω(Co): ω(Mo) = ~1: 1: 1 in the galvanostatic mode. However, we observe an uneven distribution of alloy components over the surface. Also, the alloys are characterized by a high oxygen content both on the hills (21 Fe, 22 Co, 26 Mo, and 31 O at. %) and valleys (16 Fe, 17 Co, 20 Mo, and 47 O at. %). The high concentration of oxygen in the alloy composition indicates incomplete reduction of molybdate-ions to molybdenum oxides MoO_x.

In the valleys, the oxygen content is higher than on the hills, which is associated with the inclusion of intermediate molybdenum oxides MoO_x in the coating (Fig. 1a–c).

The molybdenum content increases, and the oxygen content decreases on the relief hills due to the localization of a higher current density and a more complete reduction of intermediate molybdenum oxides by ad-hydrogen atoms. But the oxygen content at the same high enough—32 to 34 at. %.

The results obtained make it possible to consider the obtained coatings as composite electrolytic coatings of the general composition Fe–Co–MoO_x.

For deposits obtained by pulsed current, the ratio of the components in the alloy is defined as ω(Fe): ω(Co): ω(Mo) = ~3: 2: 1 (Fig. 1d, f, g). Probably, this behavior of the system is associated with the peculiarities of the co-deposition mechanism, including a change in the rate of partial reactions of alloy-forming components reduction and evolution of gaseous hydrogen. The molybdenum content in the alloy is reduced by only 2–6 at. %, and the oxygen content is halved and does not exceed 25 at. %. This is due to the participation of ad-hydrogen atoms in the chemical reduction of intermediate molybdenum oxides to metal during polarization interruption.

It should be noted that the optimal current density for deposition Fe–Co–MoO_x coatings is 3 A/dm^2. Further increase in the current density (up to 5 A/dm^2) leads to cracking of the coatings (Fig. 1f, g), which indicates the internal stresses increase in the films obtained at increased current densities.

DC

$i = 2$ A/dm^2

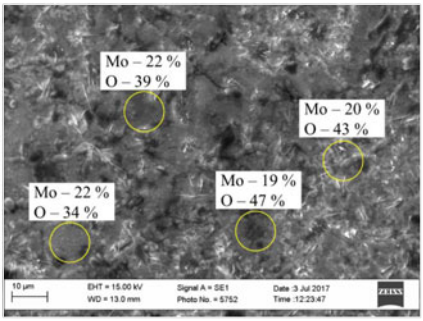

$Fe_{14}Co_{15}Mo_{18}O_{53}$ (at. %)

a

$i = 2{,}5$ A/dm^2

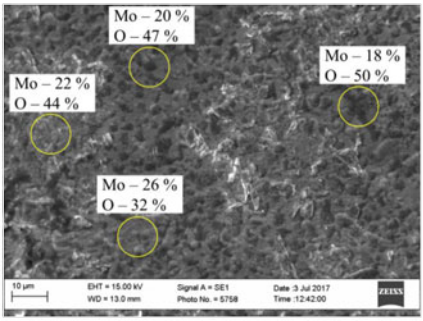

$Fe_{16}Co_{15}Mo_{19}O_{50}$ (at. %)

b

$i = 3$ A/dm^2

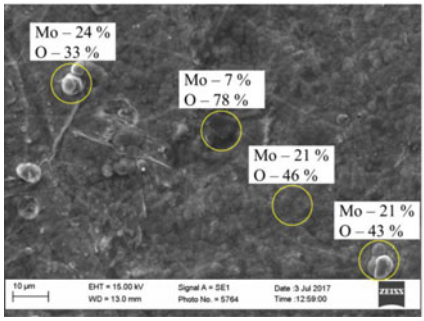

$Fe_{14}Co_{13}Mo_{18}O_{55}$ (at. %)

c

PC

$i = 3$ A/dm^2, $t_{on}/t_{off} = 2$ms/5ms

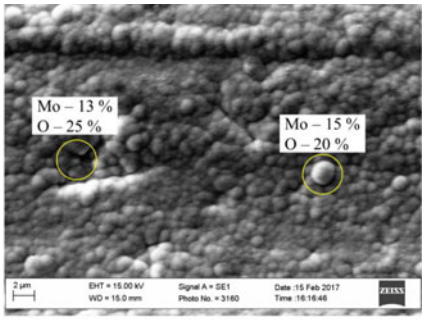

$Fe_{36}Co_{26}Mo_{13}O_{25}$ (at. %)

d

$i = 5$ A/dm^2, $t_{on}/t_{off} = 2$ms/10ms

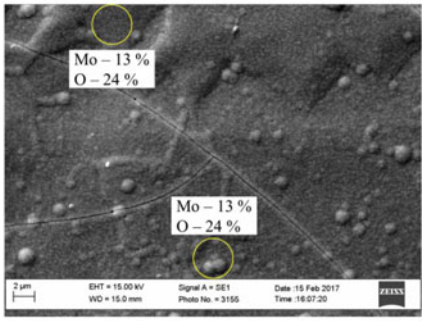

$Fe_{37}Co_{26}Mo_{13}O_{24}$ (at. %)

f

$i = 5$ A/dm^2, $t_{on}/t_{off} = 2$ms/50ms

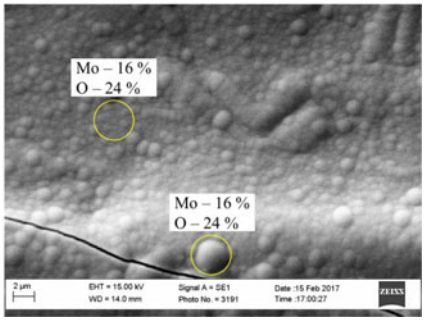

$Fe_{34}Co_{27}Mo_{16}O_{23}$ (at. %)

g

Fig. 1 Composition and morphology of Fe–Co–MoO_x coatings deposited by direct (**a**, **b**, **c**) and pulse current (**d**, **f**, **g**)

Atomic force microscopy (AFM) made it possible to study in more detail the surface topography of Fe–Co–MoOx coatings.

For AFM analysis, we selected samples of coatings deposited onto a mild steel substrate which are containing (a) iron 31, cobalt 31, and molybdenum 38 at. %, obtained in galvanostatic mode, and (b) iron 44, cobalt 35, and molybdenum 21 at. % are deposited by pulse current (in terms of metal).

Films obtained in the galvanostatic mode are characterized by a globular surface with an agglomerate size of 1–3 um formed by spheroids 0.3–0.5 um in size (Fig. 2a, b). The formation of a globular structure is also confirmed by the pattern of the tilt angles distribution of the elementary sections of surface (Fig. 2c).

Analysis of the heights distribution histogram and CS-topography the surface sections show a pronounced alternation of hills and valleys (Fig. 2b, c). The periodicity of the valleys is 1–2 um, and their depth varies from 0.5 to 2.0 um, which indicates a substantial development of the surface. This is confirmed by the values of R_a and R_q for Fe–Co–MoO_x alloy were defined as 0.29 um and 0.37 um, respectively, that much higher than those for the polished mild steel substrate ($R_a = 0.007$ um and $R_q = 0.010$ um).

The fractal dimension was determined by the «slit-island method» (SIM). The scan research results at area of 48 × 48 um show that the fractal dimension D for Fe–Co–MoO_x coating is of 2.64 with, which reflects three-dimensional nucleation

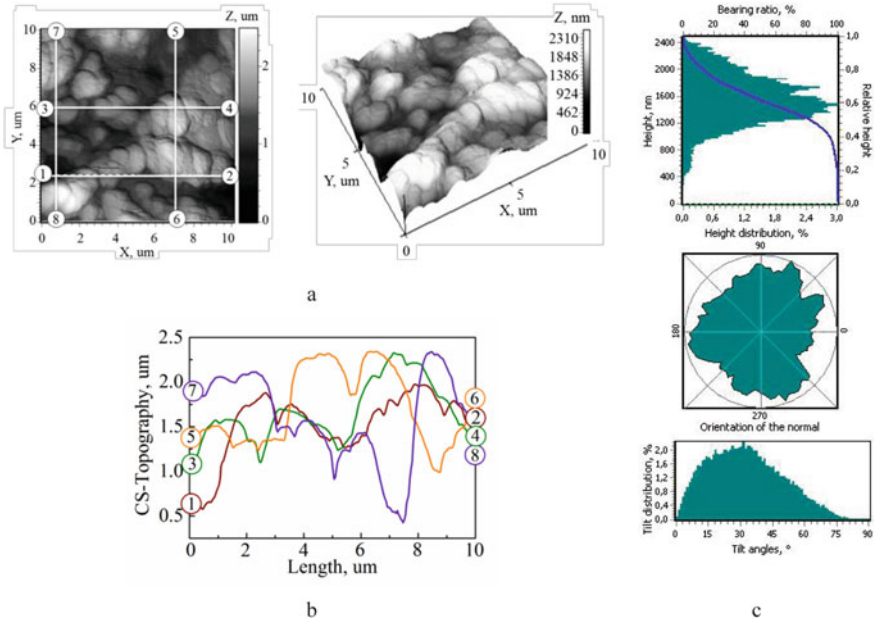

Fig. 2 2D, 3D surface maps **a**, cross-sectional profiles **b** and histogram of height distribution, tilt angles distribution of the elementary sections of surface, and orientation angles to the normal (**c**) of Fe–Co–Mo alloy deposited by direct current. Scan area 10 × 10 um

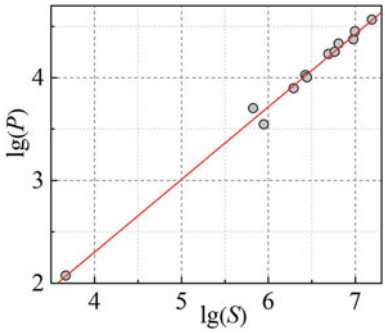

Fig. 3 Self-similarity of Fe–Co–MoO_x coating, obtained by direct current. Scan area 10 × 10 um

during coating growth. Fractal dimension ranges from 2.42–2.48 with decreasing the scan area to 10 × 10 um (Fig. 3) and becomes lower $D = 2.05$ in the nanoscale relief (5 × 5 um). The above parameters indicate a local leveling of the surface during the transition to a nanoscale relief.

In addition, the uniform distribution of orientation angles to the normal indicates the isotropy of the surface properties of Fe–Co–MoO_x coatings.

The formation of intermetallic Fe_7Mo, Fe_7Co, FeCo phases, confirmed by the X-ray diffraction analysis results [26], and developed structure of surface layers determine high anticorrosive, mechanical, and electro-catalytic properties of Fe–Co–MoO_x coatings.

This is a favorable factor for the use of such materials as electrodes in the reactions of hydrogen and oxygen electrochemical reduction, as well as the oxidation of low molecular weight alcohols, as shown by testing [26].

The morphology of coatings deposited by pulse current differs significantly from films obtained in galvanostatic mode. Earlier, we reported about the inhomogeneity of the surface coating deposited in a pulsed mode [27]. The presence of two type's fields was established. The first field has a globular structure with a grain size of 0.2–0.3 and with singly located cone-shaped hills. The diameter of the cone-shaped hills is 3 um, and the height is 2.4 nm, which determines the value of the parameter $R_q = 0.13$ within one scanning area [27].

The second type of field is shown in Fig. 4. On 2D and 3D maps of surface topography, a structure with hills and valleys is visualized, identically to the crystal lattice of cobalt. In truth, the X-ray patterns of Fe–Co–MoO_x coatings obtained by PC visualize lines corresponding to metallic cobalt, but the lines of intermetallic iron compounds with cobalt are disappearing [26]. The histogram of tilt angles distribution of the elementary sections of surface also indicates the formation of sharp hills on the film surface (Fig. 4c).

The periodicity of the valleys is 0.2–0.5 um, and their depth varies does not exceed 1 um, as shown in Fig. 4. The histogram of height distribution in this area indicates a rather smooth transition between heights and a more even distribution of sharp hills of different heights, which indicates a leveling of the surface also (Fig. 4c).

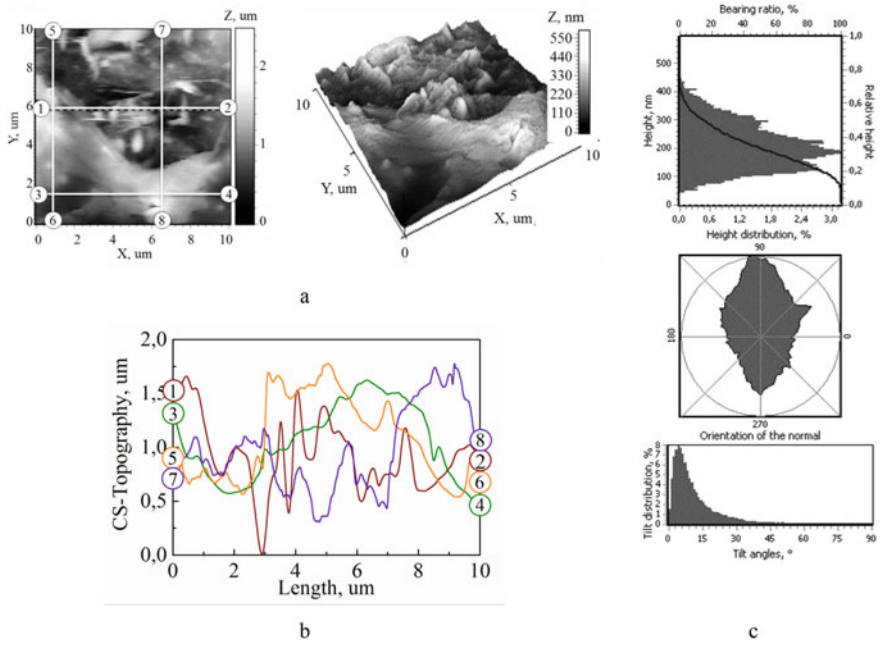

Fig. 4 2D, 3D surface maps **a**, cross-sectional profiles **b** and histogram of height distribution, tilt angles distribution of the elementary sections of surface, and orientation angles to the normal (**c**) of Fe–Co–Mo alloy deposited by pulse current. Scan area 10 × 10 um

Surface roughness values R_a and R_q were defined as 0.064 um and 0.078 um, respectively, which is much less compared to samples obtained in galvanostatic mode.

Analysis of the surface cross-sectional profiles of the between the markers (Fig. 4b) indicates the formation of small cone-shaped grains with a size of 0.2–0.3 um and their association into crystallites, the size of which ranges at 0.5–3.5 um.

Fractal dimension D on samples with scanning areas of 48 × 48 μm, 20 × 20 μm, 10 × 10 μm, and 5 × 5 μm is defined as 2.69; 2.47; 2.54; and 2.51, respectively. The pattern of the location of points in the coordinate's $\lg P - \lg S$ (Fig. 5), as well as a slight deviation of the fractal dimension from the mean value, indicates a uniform distribution of self-similar structures in the transition from micro- to nano-relief. Analysis of the histogram of the orientation angles to the normal allows us to talk about the anisotropy of the surface properties of coatings deposited in a pulsed mode, which will favorably affect the magnetic properties of the synthesized materials (Fig. 5c).

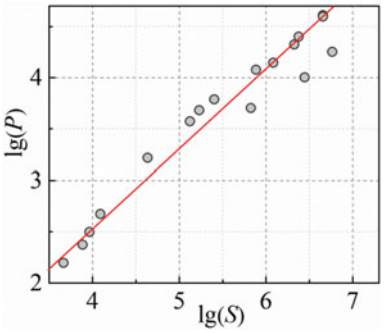

Fig. 5 Self-similarity of Fe–Co–MoO_x coating structure, obtained by pulse current. Scan area 10 × 10 um

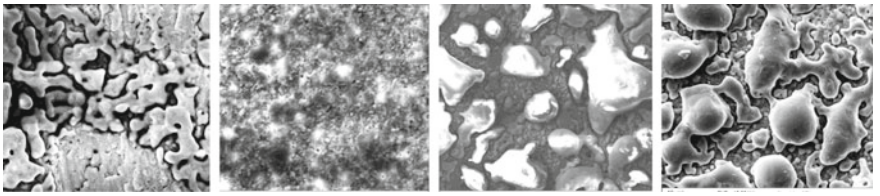

ω(Co) – 21.5 at.% ω(Co) – 18.7 at.% ω(Co) – 13.6 at.% ω(Co) – 23.6 at.%

a b c d

Fig. 6 Surface morphology of the heterooxide coatings $Al_2O_3 \cdot CoO_x$ on Al alloys: AD0 **a**, AMn **b**, D16 **c**, AK12M2MgN, **d** Magnification × 1000

Studies of physicochemical properties prove that coatings obtained by a pulse mode exhibit soft magnetic properties (Coercive force = 7–10 Oe) and demonstrate higher microhardness indices compared to the galvanostatic mode [28]. At the same time, the films deposited on direct current are characterized by higher electrocatalytic properties.

3 Research of Plasma-Electrolyte Coatings $Al_2O_3 \cdot CoO_x(MnO_y)$

The heterooxide coatings doped with transition metals in particular Co and Mn are of practical interest as catalytic materials for electrochemical and hetero-phase transformations.

The inclusion of metal-dopants into the composition of the synthesized oxide coatings changes surface morphology of the treated materials.

In the proposed modes of PEO, aluminum alloys are formed uniform cobalt-containing coatings, which are characterized by a “spheroidal-mosaic” morphology

of the surface, the protrusions of which are enriched with the target active component. For the studied alloys, the cobalt content varies from 13.6 to 23.6 at. % and increases in a number of alloys D16 < AMn < AD0 < AK12M2MgN.

Synthesis of manganese-enriched (up to 35.0 at. %) heterooxide layers with uniform distribution of the active component is provided in the mode of "decreasing power" at a polarization current density of 10–20 A/dm^2 for 15–30 min. The higher values of *j* (20 A/dm^2) at the initial stage provide the formation of the oxide matrix Al_2O_3 and the removal of alloying elements of alloy from the surface layers. The further reduction of j to 10–15 A/dm^2 after achieving stable sparking allows forming uniform strongly adhered heterooxide layers. The heterooxide coatings doped with manganese are finely dispersed with a uniform distribution of the active ingredient on the surface (Fig. 7).

The manganese content in the synthesized oxide layer varies from 23.7 to 33.2 at. % and increases in a number of alloys AMn < D16 < AD0 < AK12M2MgN. The obtained dependence can be explained by the kinetic features of the formation of heterooxide coatings in manganese-containing electrolytes.

Analysis of the surface morphology of the formed oxide coatings indicates a high degree of its development and the presence of globular spheroidal or conical structures.

This is the reason for certain limitations in the use of atomic force microscopy for the study of the obtained systems, in particular by the contact method. It was found that the scanning of the studied samples in the areas of 20–50 μm occurs under conditions when the probe, taking into account the resolution of 3 nm, fixes only the outer part of the formed coating and does not reach the main surface of the sample (Fig. 8).

However, these results are important for the comparative analysis of plasma-electrolyte treatment for the formation of heterooxide coatings.

The reducing the size of the scan areas of the formed PEO coatings on aluminum alloys of different chemical composition allows us to observe differences in the topography of the surface oxide layers. The crater-like fused holes formed during the combustion of spark and micro-arc discharges were found on small areas of the scan on the surface (Fig. 9). Such depressions are probably the outer part of the

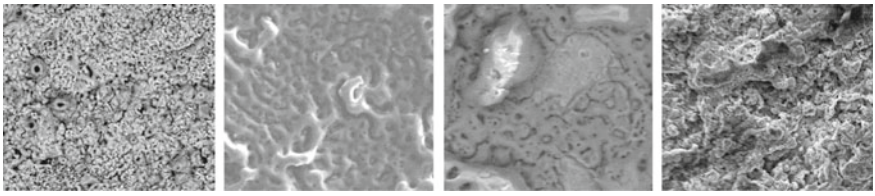

Fig. 7 Surface morphology of the heterooxide coatings $Al_2O_3 \cdot MnO_y$ on Al alloys: AD0 **a**, AMn **b**, D16 **c**, AK12M2MgN **d**, Magnification × 1000

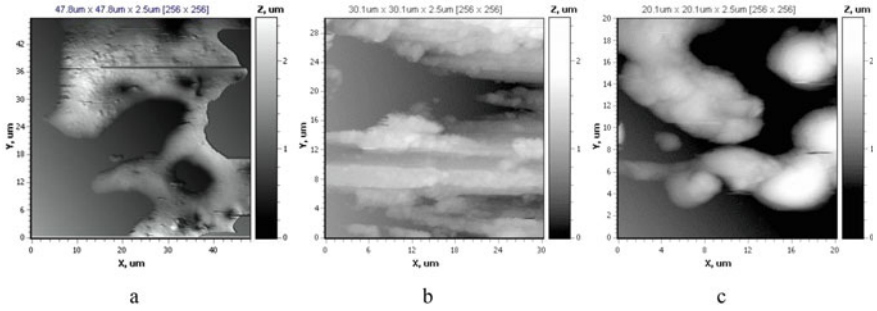

Fig. 8 2D maps of the surface of heterooxides coatings: Al_2O_3 **a**; $Al_2O_3 \cdot CoO_x$ **b**, **c**. Scanning area: 47.8 × 47.8 μm **a**; 30.0 × 30.0 μm **b**; 20.0 × 20.0 μm **c**

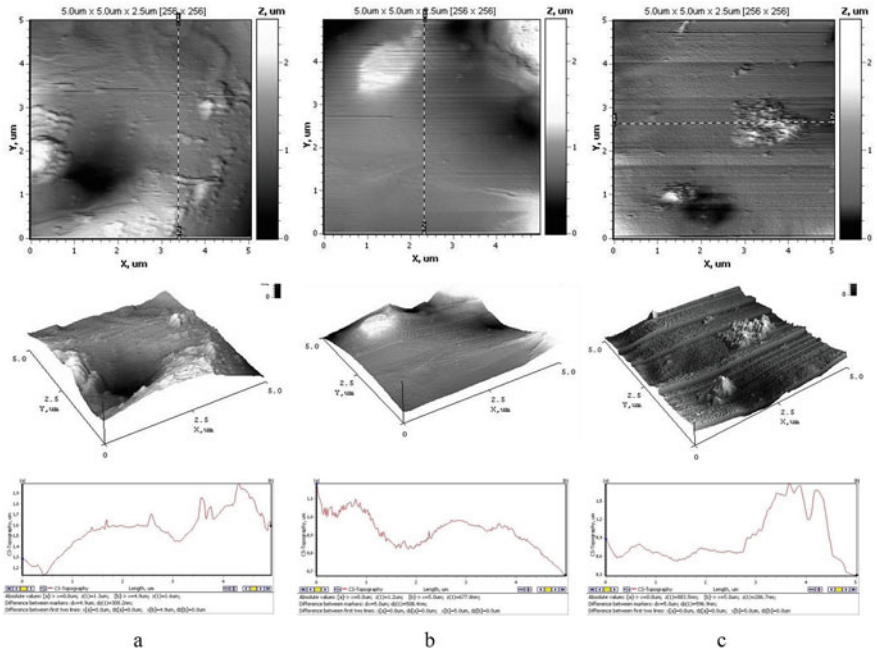

Fig. 9 2D , 3D surface maps and cross-sectional profiles of coatings Al_2O_3 obtained on Al alloys: AD0 **a**; D16 **b**; АК12М2MgN **c**

combustion channel—a closed (dead-end) pore [29].

The pore size of oxide coatings changes from tens of nanometers to micrometers and more and decreases in the number of alloys AD0 (Fig. 9a) > D16 (Fig. 9b) > АК12М2MgN (Fig. 9c). The revealed regularity correlates with the kinetic dependences of the formation of plasma-electrolyte coatings on these alloys. The determined topography of the surface layer is also fully consistent with the data on

the morphology of the surface by SEM analysis. The obtained results confirm the peculiarities of the formation of oxide coatings on alloys of different composition [30].

Oxide layers of Al_2O_3 are very rough and formed by sets of crystallites with rather sharp angles. Analysis of the absolute relief height of these coatings shows that the most developed oxide layer is formed on a technical aluminum alloy AD-0 ($z = 1.3$ μm, where z is the height). This indicator for alloy D16 is 1.2 μm. For the alloy AK12M2MgN at an average height of relief $z = 0.9$ μm, the presence of sharp crystallites with a size of 1.0–1.5 μm. They are probably oxides of the alloying components of the alloy, mainly silicon, in the surface layer, given the analysis of the chemical composition of the coating.

As previously established, the factors influencing the morphology and topography of surface layers during PEO are changes in the composition of working solutions, as well as variations in the energy parameters of oxidation.

It is shown that the incorporation of cobalt and manganese into the coatings causes a change in the morphology and, consequently, the topography of their surface.

Based on the size of the areas for efficient scanning (Fig. 8), we can say that the coating $Al_2O_3 \cdot CoO_x$ has a higher degree of surface development compared to the oxide system Al_2O_3.

Taking into account the "mosaic" morphology of the surface layer of cobalt-containing systems, it is assumed that the AFM probe effectively "scanned" only the outer part of the $Al_2O_3 \cdot CoO_x$ coating. Therefore, to get a more complete idea of the topography of the formed cobalt-containing structures is possible only when moving to smaller areas of scanning (Fig. 10).

According to the results of AFM analysis, it was found that heterooxide coatings $Al_2O_3 \cdot CoO_x$ are formed by agglomerates of grains that are close in shape to spherical. In general, the formed oxide layer is micro globular, but at the same time quite uneven along the *x*-, *y*-, and *z*-axes, which is consistent with the analysis of the morphology of the surface layers [30].

Changes in the cobalt content in the coating affect the topography of the surface and the size of the structures that form the surface oxide layer (Fig. 11).

With increasing cobalt content in the $Al_2O_3 \cdot CoO_y$ coating, the size of the crystallites increases and averages 1–2 μm. They combine to form areas of smooth surface with spherical agglomerates 6–8 μm in size.

The roughness of the oxidized surface can be characterized by the cross section of the agglomerated formation between markers 1 and 2. Also, the topography of the surface of the coatings is characterized by a fairly large difference between the heights of the protrusions and depressions from 0.3 to 1.2 μm.

In contrast to cobalt-doped "mosaic" coatings, manganese incorporation results in the formation of a fine heterooxide layer. The surface is even more developed, therefore AFM-study of samples of $Al_2O_3 \cdot MnO_y$ contact method can be performed on scan areas with a size of not more than 5×5 μm (Fig. 12).

The formed $Al_2O_3 \cdot MnO_y$ coating is non-porous and evenly rough. The height difference between the highest and lowest points of coverage in the area of the surface scan is within only 100 nm. A certain sharpness of the crystallites on the

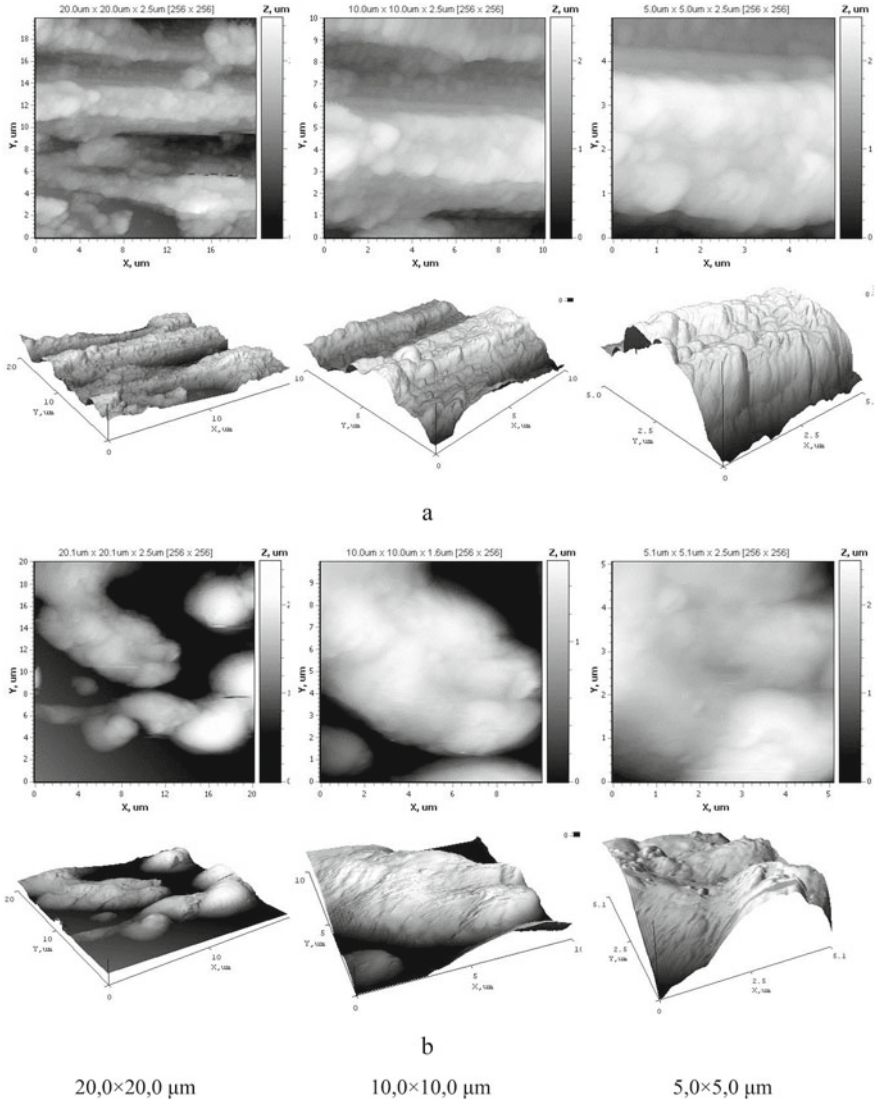

Fig. 10 2D-a and 3D-maps of the surface of $Al_2O_3 \cdot CoO_x$ with Co containing, at. %: 8 **a**; 13 **b**

cross-sectional profile of the surface can be explained by "failures" of the probe when moving to the next scan line.

Quantitative assessment of the degree of surface development of mono- and heterooxide coatings are roughness indicators (*Ra* and *Rq*) (Table 2).

For the studied oxide systems we have established the following pattern: roughness of $Al_2O_3 \cdot CoO_x$ coatings are on 20–25% higher than that of Al_2O_3 oxide systems

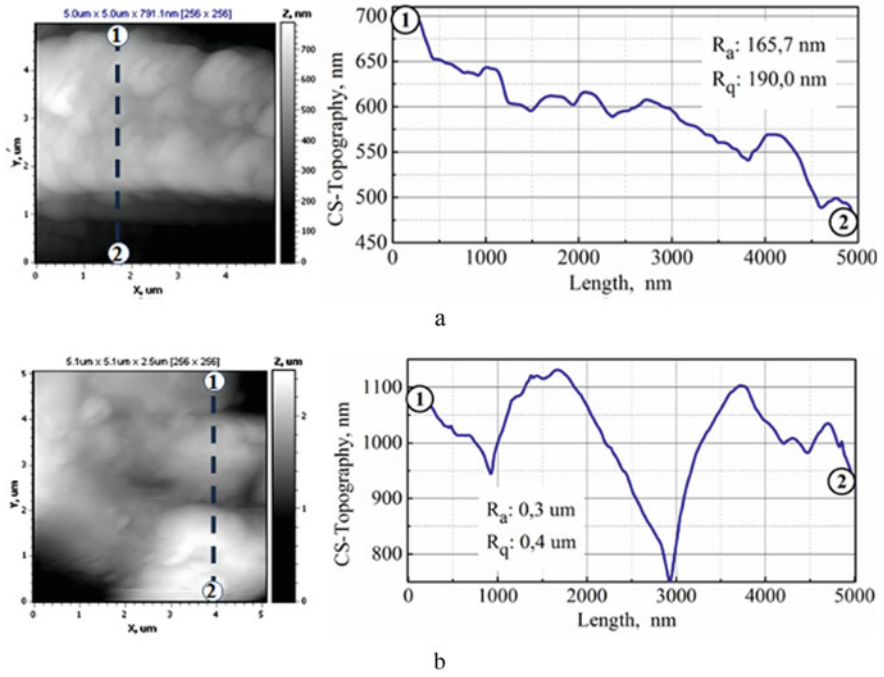

Fig. 11 2D surface maps and cross-sectional profile of coatings with Co containing, at. %: 8.0 **a**; 23.6 **b**

and manganese-doped systems. The lowest roughness values are inherent for the system $Al_2O_3 \cdot MnO_y$. They decrease almost 5 times compared to Al_2O_3 coating.

Thus, we can conclude that the incorporation of manganese into the oxide matrix of the carrier metal and the formation of a heterooxide layer of $Al_2O_3 \cdot MnO_y$ helps to align the relief of the treated surface compared to the oxide layers of Al_2O_3. The obtained results also correlate with the results of the analysis of the surface morphology of oxide coatings on aluminum alloys.

Another quantitative parameter that can be used to assess the degree of ordering (structural organization) of the synthesized oxide materials is the fractal dimension D_F.

Fractal analysis of the formed coatings is based on the properties of self-similarity, so it is sufficient to analyze a small part of the microstructure of the material to obtain information about the object of study as a whole. Thus, on the Fig. 13 are SEM-images of the morphology and the graphical analysis of the fractal dimension of the aluminum alloys surface modified in the diphosphate electrolytes.

It is established that with increasing number of alloying elements in the composition of aluminum alloys the fractal dimension increases from 2.27 to 2.66 in a number of alloys AD0 < D16 < AK12M2MgN. The D_F for oxide coatings on alloys

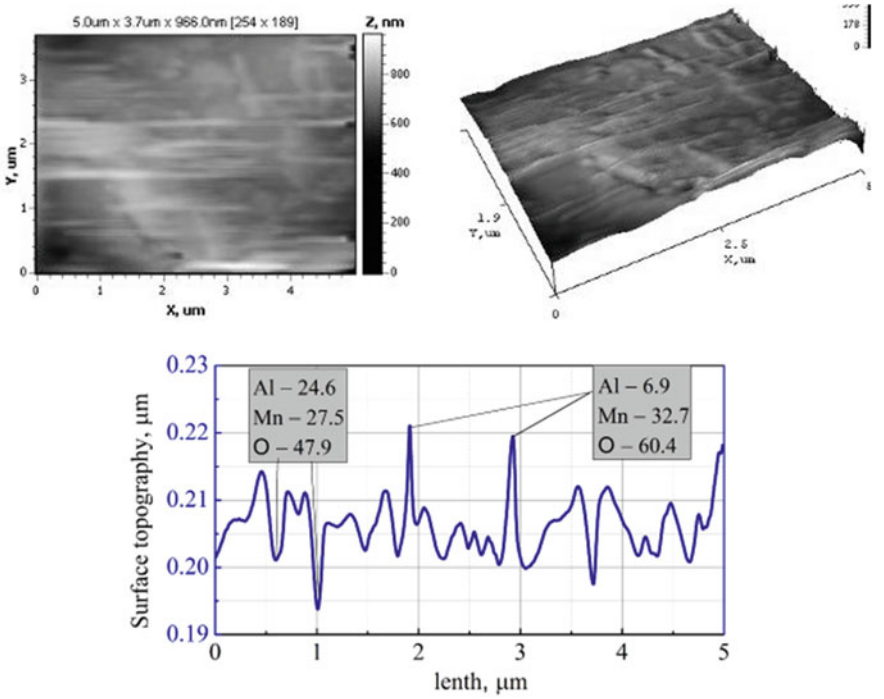

Fig. 12 2D, 3D surface maps and section profile coating surface $Al_2O_3 \cdot MnO_y$

Table 2 Roughness indices of PEO coatings on Al alloys

Oxide system	Content of dopant (at. %)	Roughness index (nm)	
		Ra	*Rq*
Al_2O_3	–	229.27	294.39
$Al_2O_3 \cdot CoO_x$	23.6	284.25	387.59
$Al_2O_3 \cdot MnO_y$	33.5	47.85	62.40

D16 and AK12M2MgN does not differ significantly (within 0.05 units), while for technical aluminum AD0 fractal dimension is 0.4 units lower.

Taking into account the obtained results, it is possible to draw a conclusion about the influence of the treated surface composition on the morphology and topography of obtained oxide coatings. This is an additional confirmation of the formation of a more complex in shape (relief) oxide layer on alloyed Al alloys compared to pure metals, which is fully consistent with the established patterns of plasma-electrolyte synthesis of oxide coatings [31].

According to the fractal analysis, the quantitative parameters of the topography of heterooxide coatings on alloyed aluminum alloys were specified (Fig. 14).

It is determined that the fractal dimension of the formed heterooxide systems is in the range from 2.66 to 2.83, which is characteristic of three-dimensional structures

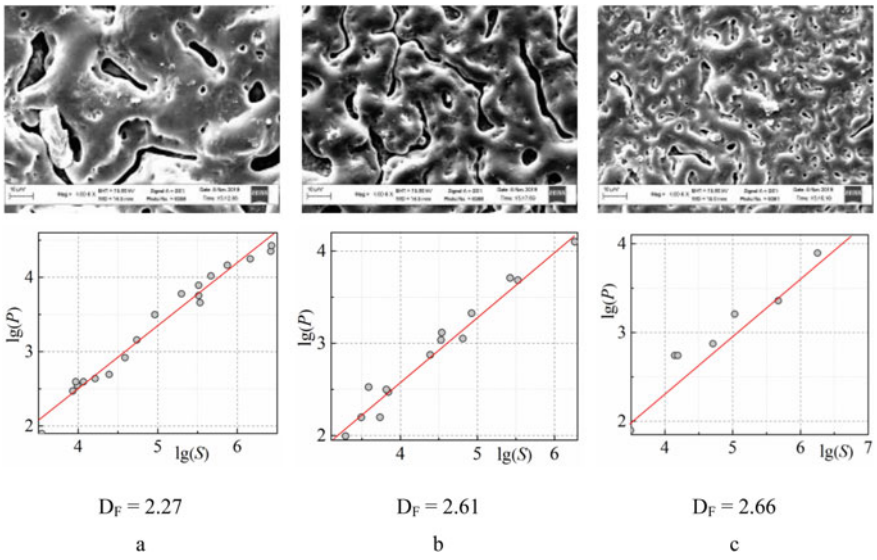

Fig. 13 Morphology of surface layers (× 1000) and graphical fractal analysis of oxide coatings on alloys: AD0 **a**; D16 **b**; AK12M2MgN **c**

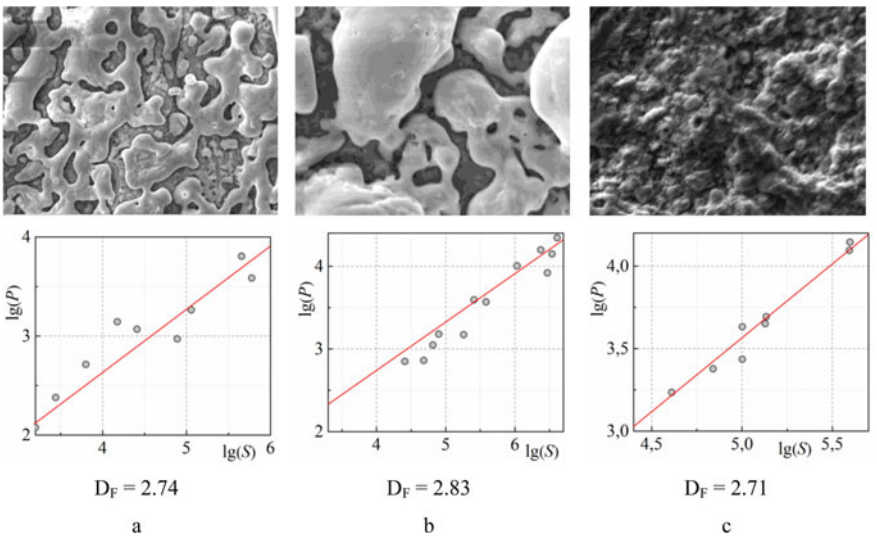

Fig. 14 Morphology of surface layers (× 1000) and graphical fractal analysis of heterooxide coatings: $Al_2O_3 \cdot CoO_x$ **a**, **b**; $Al_2O_3 \cdot MnO_y$ **c**. The contain of dopant metal in the coating, at. %: ω(Co)—8 **a**; ω(Co)—23 **b**; ω(Mn)—33 **c**

with complex surface relief. The fractality of PEO coatings increases in the series $Al_2O_3 < Al_2O_3 \cdot MnO_y < Al_2O_3 \cdot CoO_x$.

The analysis of the obtained results allows to determine certain regularities that generally coincide with the established tendencies regarding the characteristics of the surface of aluminum alloys modified by the PEO method. The fractal dimension of the coatings increases with the incorporation of dopant metals into the oxide matrix of the carrier metal. Cobalt-doped systems have the largest fractal dimension, and Al_2O_3 oxide coatings have the smallest.

The obtained results on the features of the surface topography of the synthesized materials allow us to expect a synergistic combination of functional properties of the obtained composite materials.

The results of metallographic studies have shown that the formed mono- and heterooxide coatings have high adhesion to the carrier metal. Introduction to the synthesized oxide coating of dopant metals, along with the transformation of its morphology, topography, and chemical composition, leads to the strengthening of the surface. The microhardness of the studied systems increases in a number $Al < Al_2O_3 \cdot MnO_y < Al_2O_3 \cdot CoO_x < Al_2O_3$. The identified patterns are explained by the structural features of the synthesized oxide layers. Coatings on multicomponent alloys, given the presence of alloying elements in their composition, are characterized by higher microhardness than non-alloy metals [32].

Thus, the complex of physicochemical and physico-mechanical properties of heterooxide systems, taking into account the morphology, topological, and structural features of the coatings is a prerequisite for increasing their corrosion resistance and catalytic activity.

Tests of the obtained materials on the basis of heterooxide systems in model oxidation reactions of CO and benzene have proved that their catalytic activity is not inferior to contacts containing precious metals [32]. This is due to the high affinity of nonstoichiometric oxides of manganese and cobalt to oxygen and the corresponding decrease in the activation energy of the destruction of the double bond O = O. The bench tests of a single-cylinder diesel with a catalytic coating on the surface of the combustion chamber of the piston showed that the use of $Al_2O_3 \cdot CoO_x$, $Al_2O_3 \cdot MnO_y$ allows to influence the fuel burnout in the wall areas, which in turn reduces hourly consumption 3% and improves its environmental friendliness [32].

4 Conclusions

(i) Methods of scanned electronic and probe microscopy confirmed a high stage of the surface of synthesized heterooxide coatings. It is indicated that the fractal dimension of the composite systems, supplemented with additional components, is in the interval from 2 to 3, which is typical for trivial structures with a folding surface relief.

(ii) It has been established that the method for the synthesis of electrochemical coating and storage material for the lining is injected into the indicators of

shortness and fractality. In particular, a more developed surface is formed when using the pulse mode and processing of multicomponent alloys. It is concluded that the fractality is influenced by the modes of formation and defects of the treated surface, due to the chemical and phase composition of the base material. The obtained results correlate with the analysis of the morphology and structure of the untreated surface and the formed oxide coatings in electrolytes of different composition.

(iii) Features of morphology and topography of surface layers in combination with their chemical composition cause increase in functional properties of the synthesized materials, in particular indicators of microhardness, corrosion resistance, and catalytic activity. Thus, the established regularities expand the possibilities of synthesis on structural materials of heterooxide coatings with the predicted composition, structure, and properties.

References

1. Tsyntsaru N, Cesiulis H, Donten M, Sort J, Pellicer E, Podlaha-Murphy EJ (2012) Modern trends in tungsten alloys electrodeposition with iron group metals. Surf Eng Appl Electrochem 48(6):491–520
2. Paulo N, Casciano S, Benevides RL, Lima-Neto P, Adriana N (2014) Corrosion resistance of electrodeposited Ni-Mo-W coatings. Correia Int J Electrochem Sci 9:4413–4428
3. Kublanovskii VS, Yapontseva YuS, Troshchenkov YuN et al (2010) Corrosion and magnetic propetries of electrolytic Co-Mo alloys. J Appl Electrochem 8(3):440–444
4. Rudnev VS, Lukiyanchuk IV, Vasilyeva MS, Medkov MA, Adigamova MV, Sergienko VI (2016) Aluminum- and titanium-supported plasma electrolytic multicomponent coatings with magnetic, catalytic, biocide or biocompatible properties. Surf Coat Tech 307(C):1219–1235. https://doi.org/10.1016/j.surfcoat.2016.07.060
5. Tsyntsaru N, Bobanova J, Ye X, Cesiulis H, Dikusar A, Prosycevas I, Celis J-P (2009) Iron-Tungsten alloys electrodeposited under direct current from citrate–ammonia plating bath. Surf Coat Technol 203:3136–3141
6. Su F-H, Huang P (2012) Microstructure and tribological property of nanocrystalline Co-W alloy coating produced by dual-pulse electrodeposition. Mater Chem Phys 134:350–359
7. Martin J, Leone P, Nomine A, Veys-Renaux D, Henrion G, Belmonte T (2015) Influence of electrolyte ageing on the plasma electrolytic oxidation of aluminium. Surf Coat Technol 269:36–46
8. Mohedano M, Lu X, Matykina E, Blawert C, Arrabal R, Zheludkevich ML (2017) plasma electrolytic oxidation (PEO) of metals and alloys. In: Book: reference module in chemistry, molecular sciences and chemical engineering, pp 432–437. https://doi.org/10.1016/B978-0-12-409547-2.13398-0
9. Jiang BL, Wang YM (2010) Plasma electrolytic oxidation treatment of aluminium and titanium alloys. Surf Eng Light Alloys 110–154
10. Capel H, Shipway PH, Harris SJ (2003) Wear 255:917. https://doi.org/10.1016/S0043-1648(03)00241-2
11. Yapontseva YS, Dikusar AI, Kyblanovskii VS (2014) Study of the composition, corrosion, and catalytic properties of Co-W alloys electrodeposited from a citrate pyrophosphate electrolyte. Surf Eng Appl Electrochem 50:330. https://doi.org/10.3103/S1068375514040139
12. Donten M, Cesiulis H, Stojek Z (2000) Electrodeposition and properties of Ni-W, Fe-W and Ni-Fe-W amorphous alloys. A comparative study. Electrochim Acta 45(20):3389–3396

13. Safizadeh F, Sorour N, Ghali E, Houlachi G (2017) Study of the hydrogen evolution reaction on Fe-Mo-P coatings as cathodes for chlorate production. Intern J Hydrogen Energy 42(8):5455–5463
14. Gomez E, Pellicer E, Valles E (2001) Electrodeposited cobalt_molybdenum magnetic materials. J Electroanal Chem 517:109–116
15. Gomez E, Pellicer E, Alcobe X, Valles E (2004) Properties of Co-Mo coatings obtained by electrodeposition at pH 6.6. J Solid State Eletrochem 8:497–504
16. Gong J, Riemer S, Morrone A, Venkatasamy V, Kautzky M, Tabakovic I (2012) Composition gradients and magnetic properties of 5–100 nm thin CoNiFe films obtained by electrodeposition. J Electrochem Soc 159(7):D447–D454
17. Tabakovic I, Gong J, Riemer S, Kautzky M (2015) Influence of surface roughness and current efficiency on composition gradients of thin NiFe films obtained by electrodeposition electrochemical/electroless deposition. J Electrochem Soc 162:D102–D108
18. Frederix P, Linford MR (2017) Surface analysis by atomic force microscopy (AFM): its various modes, capabilities, and comparison to and integration with other techniques. Vacuum technology & coating
19. Gan Sh, Zhou Q, Xu X, Hong Y, Liu Y, Fu Sh (2007) Study on the surface roughness of substrate with multi-fractal spectrum. Microelectron Eng 84:1806–1809. https://doi.org/10.1016/j.mee.2007.01.273
20. Stout K, Blunt L (2000) Three-dimensional surface topography, 2nd edition (Ultra precision technology). Penton Press, London, p 285
21. Kotowski P (2006) Fractal dimension of metallic fracture surface. Int J Fract 141:269–286. https://doi.org/10.1007/s10704-006-8264-x
22. Menchaca-Campos EC, Villalba-Enciso ER, Juarez-Nuñez V, Flores-Dominguez M, Mayorga-Cruz D, Tapia RG, Uruchurtu-Chavarín J (2020) Fractal dimension analysis of aluminum corrosion roughness by electrochemical and optical methods. Euro J Eng Res Sci 5(3)
23. Xu S, Weng Y (2006) A new approach to estimate fractal dimensions of corrosion images. Pattern Recognit Lett 27(16):1942–1947
24. Garcia R, Perez R (2002) Dynamic atomic force microscopy methods. Surf Sci Rep 47:197–301
25. Yermolenko IYu, Ved MV, Sakhnenko ND (2019) The kinetics peculiarities and the electrolysis regime effect on the morphology and phase composition of Fe-Co-W(Mo) coatings. Chapter 28: In: Fesenko O, Yatsenko L (eds) Nanocomposites, nanostructures, and their applications. NANO 2018. Springer proceedings in physics, vol 221. Springer, Cham, Switzerland AG 2019, pp 403–423. https://doi.org/10.1007/978-3-030-17759-1_28
26. Ved MV, Sakhnenko ND, Yermolenko IYu, Nenastina TA (2018) Nanostructured functional coatings of iron family metals with refractory elements. In: Fesenko O, Yatsenko L (eds) Chapter 1: in the book nanochemistry, biotechnology, nanomaterials, and their applications, Springer proceedings in physics 214. Springer International Publishing AG, part of Springer Nature 2018, pp 3–34. https://doi.org/10.1007/978-3-319-92567-7_1
27. Yermolenko IY, Ved MV, Sakhnenko ND, Sachanova YI (2017) Composition, morphology, and topography of galvanic coatings Fe-Co-W and Fe-Co-Mo. Nanoscale Res Lett 12(1):352. https://doi.org/10.1186/s11671-017-2128-3
28. Yermolenko IYu, Ved MV, Sakhnenko ND, Shipkova IG, Zyubanova SI (2019) Nanostructured magnetic films based on iron with refractory metals. J Mag Magn Mater 475:115–120. https://doi.org/10.1016/j.jmmm.2018.11.104
29. Karakurkchi AV, Sakhnenko ND, Ved MV, Luhovskyi IS, Drobakha HA, Mayba MV (2019) Features of plasma electrolytic formation of manganese- and cobalt-containing composites on aluminum alloys. Adv Mater Sci Eng 6381291:13. https://doi.org/10.1155/2019/6381291
30. Sakhnenko M, Ved MV, Karakurkchi A (2017) Nanoscale oxide PEO coatings forming from diphosphate electrolytes. Nanophys Nanomater Interface Stud Appl NANO 2016 195:507–531. https://doi.org/10.1007/978-3-319-56422-7_38
31. Karakurkchi AV, Sakhnenko MD, Ved' MV, Tulenko MV, Dzheniuk AV (2020) Analysis of technological approaches to electrochemical surface treatment of aluminum alloys. Eastern-Euro J Enterp Technol Mater Sci 3(12(105)):44−55. https://doi.org/10.15587/1729-4061.2020.206014

32. Parsadanov IV, Sakhnenko ND, Ved MV, Rykova IV, Khyzhniak VA, Karakurkchi AV, Gorokhivskiy AS (2017) Increasing the efficiency of intra-cylinder catalysis in diesel engines. Voprosy Khimii i Khimicheskoi Tekhnologii 6:75–81